THE UNIVERSITY
of ADELAIDE

Proterozoic Crustal Growth in the Southeastern Gawler Craton;
The Development of the Barossa Complex, and an Assessment of the Detrital Zircon Method.

Kieran James Meaney

Geology and Geophysics
School of Physical Sciences
University of Adelaide

This thesis is submitted in fullfillment of the
requirements for the degree of Doctor of Philosophy

December 2017

Abstract

The Barossa Complex, southeast Gawler Craton, South Australia, forms the southeastern-most exposure of pre-Neoproterozoic crust in Australia. Understanding the geodynamic evolution of this area can improve paleogeographic reconstructions of the economically significant Gawler Craton, as well as global reconstructions in the Proterozoic. The first part of this thesis addresses the geological development of the Barossa Complex during the Palaeo-Mesoproterozoic.

The Barossa Complex is composed of metasedimentary and metaigneous gneisses. These include calcsilicate, quartzofeldspathic, psammopelitic, and pelitic gneisses. In the northern inliers, the protoliths to these gneisses are indicative of a progressively deepening basin. Syndepositional felsic orthogneisses and mafic amphibolites indicate a tectonically active basin.

Deposition of the metasedimentary protoliths to the Barossa Complex occurred between 1730-1655 Ma, synchronous to the onset of the Kimban Orogeny in the Gawler Craton and the deposition of the Willyama Supergroup in the Curnamona Province. U-Pb and Hf isotopic analyses from detrital zircon indicates sediment was largely derived from the Gawler Craton. Syndepositional granite intrusions occurred in the northern extent of the Barossa Complex at 1717 ±7 Ma.

Metamorphism initiated in the Barossa Complex at c. 1630 Ma with the development of a low angle metamorphic fabric. Peak granulite conditions of approximately 8-9 kbar and 800-850 ^{o}C occurred at c. 1590 Ma in the southern Barossa Complex. The northern Barossa Complex preserves lower grade metamorphic features and c. 1600 Ma zircon with hydrothermal Rare Earth Element (REE) signatures, which are potentially linked to the Hiltaba event in the Gawler Craton. Post peak metamorphism continued until c. 1550 Ma and is associated with retrograde shear zones in the southern Barossa Complex, and late pegmatites in the northern inliers.

The Barossa Complex shares a depositional and metamorphic history with the Willyama Supergroup in the Curnamona Province and Mt. Isa Inlier basin sequences, and was part of a transcontinental plate margin system during the Late Palaeo- Early Mesoproterozoic. East dipping subduction was the likely driver for extensive rift basin development across the eastern margin of Proterozoic Australia before the Isan-Olarian Orogeny inverted these basins. The Barossa Complex is the southern-most exposure of this system.

The second part of this thesis addresses the use of detrital zircon in modern sediment as a means of characterising the bedrock of a catchment area, which has been used previously in the Gawler Craton and Curnamona Province.

In the Broken Hill area of the Curnamona Province, stream sediments were sampled from drainage pathways with catchments that have stratigraphically and chronologically well characterised bedrock lithologies. Zircon ages from the modern sediment found up to 30% of the zircons were significantly younger than what expected from the bedrock sources (>1.6 Ga). Aeolian dune sands from the Strzelecki Desert to the north of the study area are found to contain zircon with U-Pb and Lu-Hf isotopic compositions matching the ‘exotic’ zircon populations in Broken Hill. Aeolian detritus is considered to have contributed zircon to the stream sediments in Broken Hill, and should be considered in any study utilising modern detritus in arid environments. Detrital zircon provenance studies of the geological record should be interpreted cautiously if aeolian input may have occurred.

Declaration

I, Kieran Meaney, certify that this work contains no material which has been accepted for the award of any other degree or diploma in my name, in any university or other tertiary institution and, to the best of my knowledge and belief, contains no material previously published or written by another person, except where due reference has been made in the text. In addition, I certify that no part of this work will, in the future, be used in a submission in my name, for any other degree or diploma in any university or other tertiary institution without the prior approval of the University of Adelaide and where applicable, any partner institution responsible for the joint-award of this degree.

I give permission for the digital version of my thesis to be made available on the web, via the University's digital research repository, the Library Search and also through web search engines, unless permission has been granted by the University to restrict access for a period of time.

I acknowledge the support I have received for my research through the provision of an Australian Government Research Training Program Scholarship.

Kieran Meaney Date 21/12/2017

This is possibly the most difficult bit of the whole thesis to write because, looking back, the vast number of people that have helped me over these last couple of years is phenomenal. But first and foremost, the biggest thanks must go to Martin Hand. You've had my back at every step of the way, which is good because if you were in front of me I'd probably be blinded by a freshly tie-dyed pair of jeans… Keep rocking the Mohawk, it suits you!

Thanks as well to Alan who got me started in honours, where I developed a deep seeded frustration from needing to know what the heck happened to those rocks. Who knows what would have happened if I picked a different project back then. Thanks as well to Karin for all the proofreading, and for throwing the odd bit of demonstrating my way. A big thankyou has to go to Wolfgang for sharing his wealth of knowledge with me over the years.

A big thanks go to the staff at Adelaide Microscopy, but in particular Ben and Aoife for all their help with the SEM and Laser (especially on the weekends!). Thanks as well to Justin for all the days out at Waite, and for knowing how Hafnium works. I think I'm starting to get the hang of it now.

To everyone I ever shared an office with – CERG Tank old and new – Thanks for just being there, feeling the same pain when the laser or probe died, knowing where the spare ethanol was, and just generally being amazing. Sorry for all the pacing, all the frantic scribbles on the whiteboard, and the occasional frustrated thumping of rock or computer…

Then of course there's my army of field hands; you were all brilliant. Craig, who helped me to do so much of the mapping, I can't thank you enough! The Warren Inlier would not have been the same without you. Special mention as well to Renee who has followed me to the furthest reaches of the Barossa Complex and even to Broken Hill; Thankyou. And to everyone else as well! I haven't forgotten you; Richard, Kam, and Brett – the Para Wirra Dream Team; Ava and Heather – My Heroes of the South; Meg, Kate, Coralie – My ever reliable go anywhere crew.

Thankyou to my 1984 Subaru L-series touring wagon, who carried me to the furthest reaches of the Barossa Complex, whose ample boot space was ideal for fieldwork, and who could successfully pull a U-turn on the narrowest of dead end tracks. We had to retire you when you couldn't go up hills anymore. Sorry for driving you over that Yakka.

Nearly done, bear with me!

To my Mum and Dad; thanks for keeping me in a general state of alive-liness since, well, ever really. But the last few years especially. You were always there, always supportive, and I probably don't say thanks enough. Coralie, thanks for being my emergency backup fieldie. Sorry for all the snakes. And finally Emi; you kept me sane through a lot of it, I dragged you out to find a rock more than once, and I appreciate every minute of it.

If I've forgotten anyone, well, thank you too.

One final shout out to all the zircon currently resting in the sand dunes, creeks, and rivers in deserts everywhere – keep doing what you're doing, you'll catch out many more geologists before you're done.

CHAPTER 1

Introduction and Thesis Outline

1.1 Project Overview and Aims

The Gawler Craton and Curnamona Province form the two major crustal elements of the South Australian Craton (Figure 1). Both of these regions are economically significant, as both host world class ore bodies such as the Broken Hill Pb-Zn-Ag deposit in the Curnamona Province (e.g. Conor and Preiss 2008), and numerous Iron-Oxide-Copper-Gold (IOCG) and gold deposits in the Gawler Craton, including the Olympic Dam IOCG-Uranium-Rare-Earth-Element deposit (Hand et al. 2007, Ehrig et al. 2013). While many of these deposits were generated during the Late Palaeo- Early Mesoproterozoic in association with magmatic and hydrothermal activity (Skirrow et al. 2007, Ehrig et al. 2013, Schlegel and Heinrich 2015), the tectonic regime in Australia during this interval is still poorly understood.

Numerous models exist which attempt to describe the development of, and relationships between, the Australian crustal elements throughout the Proterozoic (Myers et al. 1996, Betts et al. 2002, Giles et al. 2004, Betts and Giles 2006, Wade et al. 2006, Cawood and Korsch 2008, Payne et al. 2009, Johnson 2013, Betts et al. 2015, Aitken et al. 2016). In many of these models, the Gawler Craton often presents a challenge to interpret. This is due to much of the craton being obscured by Neoproterozoic to recent sedimentary units, and in many areas data are limited to samples obtained from drill core that lack a regional context (e.g. Payne et al. 2006, Thomas et al. 2008, Howard et al. 2011, Armit et al. 2017). Regional geophysical signatures are commonly used to identify large scale structures in such poorly exposed areas (e.g. Betts et al. 2003, Direen et al. 2005, Thiel et al. 2005, Stewart and Betts 2010). This can still lead to misinterpretation of the significance of regional features without adequate assessment of the basement lithologies. An example of this is the interpretation of regional scale shear zones as continental suture zones in some models, despite an absence of critical evidence such as appropriate igneous and metamorphic associations (e.g. Giles et al. 2004, Betts and Giles 2006). Such interpretations, if incorrect, drastically influence the models for the geodynamic regime which drove the lithospheric evolution.

Continental scale models of crustal development feed into global reconstruction models, which aid the understanding of how the Earth has evolved through time. Numerous supercontinent reconstruction models have been proposed for the Proterozoic Eon, which address two periods of supercontinent formation and breakup; the Palaeoproterozoic Columbia or Nuna supercontinent (e.g. Rogers and Santosh 2002, Zhao et al. 2004, Evans and Mitchell 2011, Zhang et al. 2012, Meert and Santosh 2017), and the Neoproterozoic Rodinia supercontinent (e.g. Hoffman 1991, Pisarevsky et al. 2003, Li et al. 2008, Merdith et al. 2017). Australia's position within these supercontinents and its relationship to other continental fragments, such as the North American Craton Laurentia, are rarely consistent between these models. This highlights the ambiguity of the relationship between the Australian continent and formerly contiguous continental elements.

Numerous different configurations are proposed for a connection between eastern Proterozoic Australia and western Laurentia (i.e. Dalziel 1991, Karlstrom et al. 1999, Wingate et al. 2002; Figure 2). In some Neoproterozoic reconstructions the South China Craton (e.g. Li et al. 1995, Li et al. 2008; Figure 2d) is proposed to be positioned between Laurentia and Australia, although this is contested (e.g. Merdith et al. 2017).

While the Australia-Laurentia connections are typically presented in the context of the Neoproterozoic Rodinia supercontinent, similar connections are proposed for the Columbia/Nuna supercontinent (e.g. Moores 1991, Wingate et al. 2002, Li and Evans 2011, Mulder et al. 2015, Betts et al. 2015), making it likely that any connection between eastern Australia and another continental fragment was

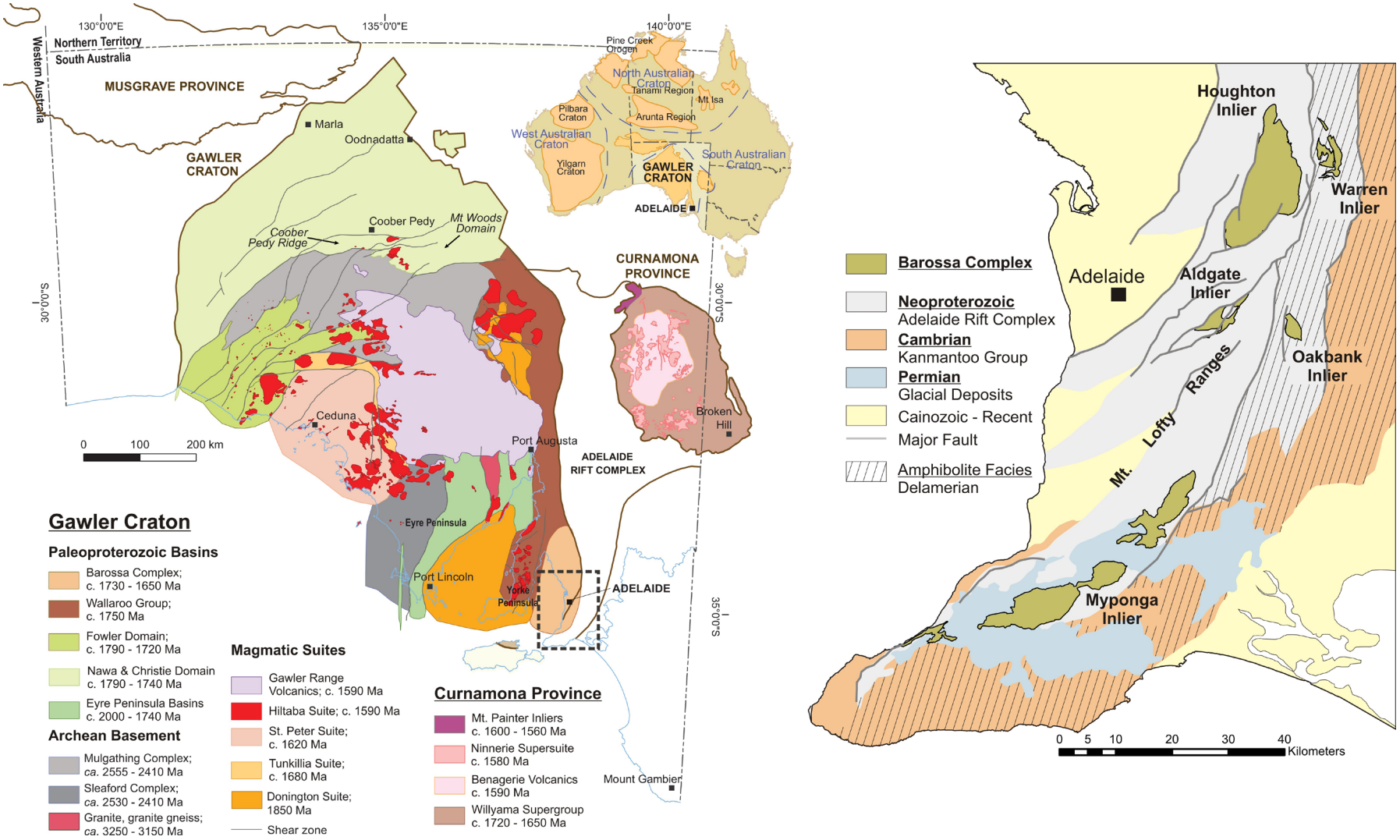

Figure 1: Geological map of the Gawler Craton and Curnamona Province after Reid et al. (2017), with inset geological domains of the Mount Lofty Ranges after Preiss (1993), with focus on the Barossa Complex basement inliers.

established in the Palaeo-Mesoproterozoic. This may also simply be a by-product of the poor understanding about the relationship between Australia and other Proterozoic crustal elements. This makes establishing the geological histories of western Laurentia and Eastern Proterozoic Australia essential, as meaningful reconstruction models rely on the accurate characterisation and correlation of these two regions.

In the case of Australia, regions such as the Mount Isa Inlier, the Curnamona Province, and Eastern Gawler Craton mark the easternmost exposures of the Proterozoic Australian continent. As such these are the best regions to target in order identify potential correlations to other formerly contiguous continental elements. While regions such as the Mount Isa Inlier and the Curnamona Province have well characterised geological histories (e.g. Betts et al. 2006, Conor and Preiss 2008, and references therein), some areas of eastern Gawler Craton remain enigmatic. One such area is the Barossa Complex, which forms the southeastern-most exposure of the Gawler Craton (Figure 1). Limited work has been done on the Barossa Complex, and the stratigraphy, depositional history, and the significance of metamorphic events is largely unknown. The position of the Barossa Complex makes it the southeastern-most exposure of pre-Neoproterozoic crust in Australia, and therefore could potentially be linked to formerly contiguous lithosphere (e.g. Figure 2). Understanding this enigmatic region may significantly influence continental evolution models for eastern Australia during the early Proterozoic.

This thesis is presented in two parts, which aim to investigate crustal growth in southeast Proterozoic Australia. In the first part of the thesis, Chapters 2 to 5 focus on the development of the Barossa Complex on the southeastern margin of the Gawler Craton. In the second part of the thesis, Chapter 6 addresses the validity of the use of zircons sourced from modern detritus to assess the bedrock characteristics of a catchment area. This technique has been used to assess the crustal development of the Gawler Craton and Curnamona Province (Condie et al. 2005, Belousova et al. 2009, Howard et al. 2009), but has yielded zircon age populations which have yet to be identified from in situ samples and which are extremely difficult to account for in the known bedrock geology. One way to evaluate such records is to undertake a case study in a region of well characterised basement zircon, and to assess how well represented those basement lithologies are within the modern sediments.

1.2 Previous Work on the Barossa Complex

Crystalline basement rocks have been recognised in the Mount Lofty Ranges since the earliest geological surveys, but their development and significance has never been meaningfully addressed. Howchin (1906) first described the metamorphic basement in a stratigraphic context, noting its exposure in anticlinal cores and the primarily metasedimentary nature of the rocks, with the caveat that the metamorphism and often extensive weathering of the rocks obscured any stratigraphic boundaries. Numerous studies followed this which focussed on either the petrology of well outcropping lithologies (Benson 1909, England 1935, Alderman 1938), or the structure and stratigraphy of the Mount Lofty Ranges in general (Howchin 1926, Sprigg 1946). Several of these early works described the distinctive calcsilicate (Benson 1909, England 1935), which occurs in what is now known as the Houghton Inlier. Benson (1909) incorrectly described this calcsilicate as a metamorphosed diorite, which was later corrected (Spry 1951, Talbot 1963). Several works retained this incorrect nomenclature and refer to a “Houghton Diorite” type lithology (e.g. Davies 1972, Wicks 1972).

The production of regional geological maps in the Mount Lofty Ranges (e.g. Sprigg et al. 1951, Sprigg and Wilson 1954) identified 5 basement exposures, which were

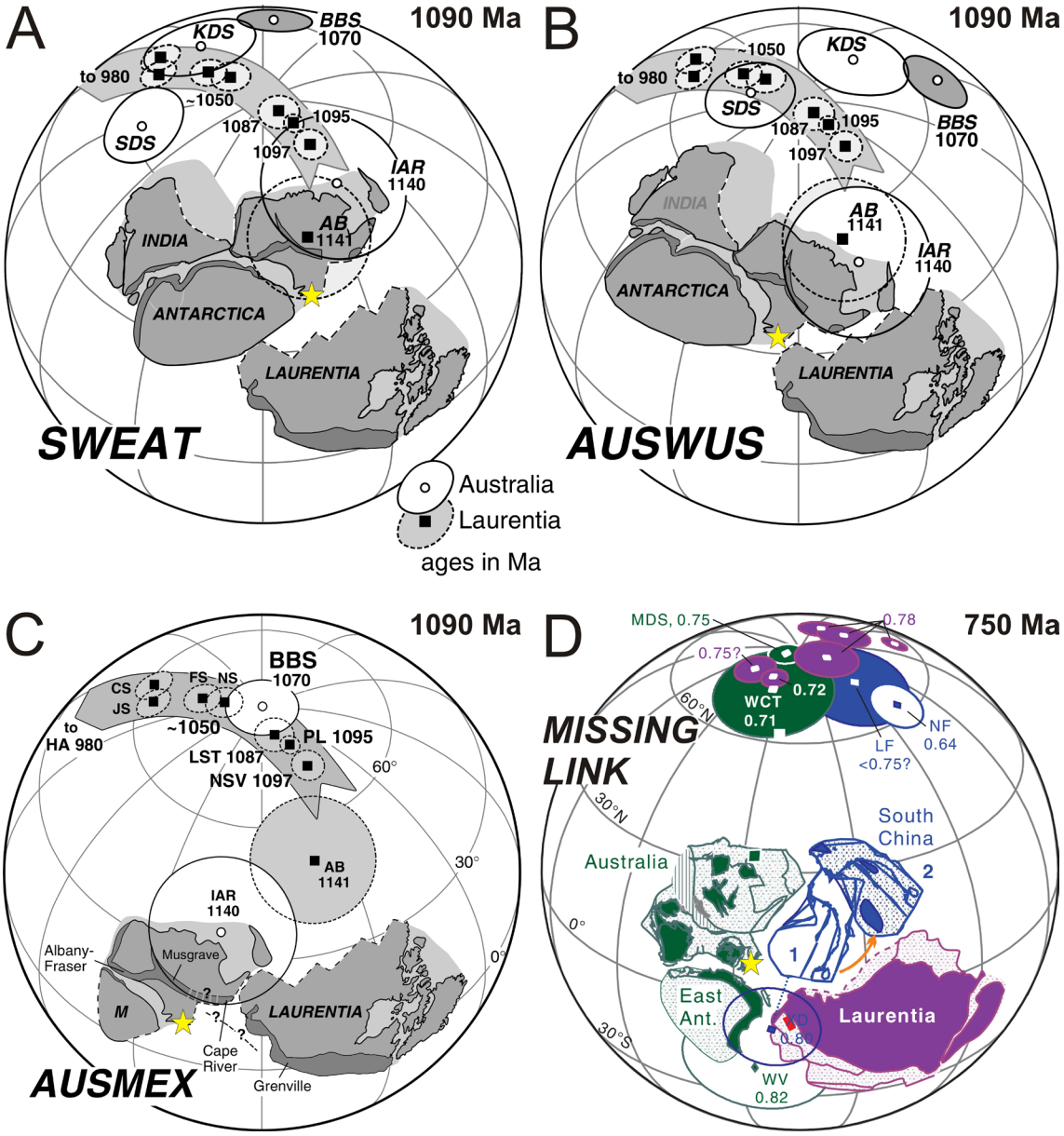

Figure 2: Proposed reconstruction models from the Meso- to Neoproterozoic featuring Australia and Laurentia. The approximate position of the Barossa Complex is marked with a yellow star. A) The Sout-West Laurentia – East Antartica (SWEAT) Model (Moores 1991). B) The Australia – Western United States (AUSWUS) model (Karlstrom et al. 1999). C) The Australia – Mexico (AUSMEX) model (Wingate et al. 2002). D) The Australia- South China-Laurentia "Missing Link" Model (Li et al. 1995). Figures Modified after Wingate et al. (2002) and Li and Evans (2011).

later termed the Houghton, Warren, Aldgate, Oakbank, and Myponga inliers (Preiss 1993; Figure 1). The internal stratigraphy of the inliers remains largely undescribed. Minor exceptions to this include the descriptions of calcsilicate occurrences in the Houghton, Aldgate, and Myponga inliers which have been proposed to be a potential marker unit (Talbot 1963). Several attempts at mapping small portions of the different inliers have been conducted (Talbot 1963, Callen 1966, Chappel 1964, Davies 1972, Wicks 1972, Heaslip 1972, McEwin 1972, Mills 1973). These Previous efforts have largely been done with inconsistent levels of detail which has led to difficulty in correlating different lithologies

and structures. A number of common rock types occur throughout the five inliers including sillimanite- and garnet- bearing metapelite gneisses, quartzites and psammites, calcsilicates, psammopelites, retrograde schists, and metaigneous granitic gneisses and amphibolites (Preiss 1993). The relationships between these different lithologies is largely undescribed.

More recent work focussing on geochronology has highlighted the potential significance of the Barossa Complex. Detrital zircon U-Pb analysis from across the 5 inliers reveals maximum depositional ages ranging between c. 1720 Ma and 1655 Ma (Jagodzinski et al. 2017). Early, likely syndepositional, granite occurs in the northern Houghton Inlier which has preserves an igneous crystallisation age of 1717 ±7 Ma (Jagodzinski et al. 2017). These ages correspond to the deposition of the Willyama Supergroup and the intrusion of early syndepositional granitoids in the Curnamona Province to the north east (Raetz et al. 2002; Figure 1, Page et al. 2005b, Page et al. 2005a, Stevens et al. 2008), and a correlation between the Barossa Complex and the Willyama Supergroup is proposed (Kositcin 2010, Jagodzinski et al. 2017).

Metamorphic zircon and monazite from across the Barossa Complex have yielded age populations at c. 1630 Ma, 1610 Ma, 1590-1580 Ma, and 1570-1550 Ma (Belousova et al. 2006, Szpunar et al. 2007, Morrissey et al. 2013, Jagodzinski et al. 2017). The metamorphic grade in the Barossa Complex appears to increase in grade ffrom amphibolite facies in the north to granulite facies in the south (Preiss 1993, Morrissey et al. 2013). Peak metamorphic conditions of approximately 800-850^{o}C and 8-9 Kbar have been determined from the southern Houghton and southern Myponga Inliers (Morrissey et al. 2013); however it is unclear at which of the possible metamorphic time periods that peak conditions were reached. Undeformed granitic pegmatite in the southern Myponga Inlier yields a zircon crystallisation age of 1580 ±4 Ma (Jagodzinski et al. 2017), suggesting that pervasive deformation had ceased by this time. Monazite obtained from discrete retrograde greenschist facies shear zones and other retrogressed rocks record ages between 1570-1550 Ma (Morrissey et al. 2013). Some of these shear zones from the southern Myponga Inlier contain east side down extensional kinematic indicators, and it is possible that this retrograde phase was associated with extension. However, these kinematic indicators could have also developed during the Neoproterozoic in the rifting event which produced the Adelaide Rift Complex (Preiss 2000) and be unrelated to the monazite grains within the shear zones.

Between 850-812 Ma during the onset of rifting and the deposition of the lower Adelaide Rift Complex, A-type granites intruded the Barossa Complex and are now exposed in the Warren and Oakbank Inliers (Preiss et al. 2008).

Deposition of the Neoproterozoic Adelaide Rift Complex and Cambrian Kanmantoo Group continued until the onset of the Delamerian Orogeny (Preiss 2000) which occurred between 514-490 Ma (Foden et al. 2002, Foden et al. 2006). The Delamerian Orogeny variably metamorphosed and deformed the rocks of the Mount Lofty Ranges, including the Barossa Complex (Offler and Fleming 1968). The Houghton, Aldgate, and Myponga Inliers all lie within the sub-greenschist to greenschist domain in the western section of the Delamerian Orogen, and have been variably retrogressed to greenschist facies (Talbot 1963, Offler and Fleming 1968, Mancktelow 1990). The Williamstown-Meadows Fault juxtaposes the lower grade zone of the Delamerian Orogen in the west against the lower to upper amphibolite facies zone in the east, where the Warren and Oakbank inliers experiences comparatively higher grade Delamerian conditions (Figure 1; Offler and Fleming 1968, Mancktelow 1990). In the Warren Inlier in particular, Delamerian retrograde fabrics and deformation appear

to dominate the macroscopic textures of the exposed rocks (Mills 1963, Mills 1973).

In most areas of the Barossa Complex, the advanced state of weathering and Permian to recent sedimentary cover obscures much of the outcrop (Talbot 1963, Davies 1972). The presence of weakly lithified Permian sediments directly overlying some of the Barossa Complex exposures in the Myponga Inlier illustrates that many of these rocks have been in a near surface environment since at least 250 Ma.

The present lack of stratigraphic subdivision and structural understanding of the Barossa Complex makes comparing this region to other Palaeo-Mesoproterozoic regions of Australia and elsewhere difficult to do with any certainty. Before techniques such as detrital zircon analysis can be meaningful, the stratigraphy of the inliers involved needs to be established. The determination of a structural or deformational history is also necessary to aid interpretations of metamorphic development and lend context to geochronology. As well as the standard U-Pb geochronology techniques the analysis of additional geochemical systems, such as the Lu-Hf isotopic system in zircon, or the distribution of the Rare Earth Elements (REEs) in different metamorphic minerals, can provide further insight into the geological processes which have influenced the development of the Barossa Complex over time.

1.3 Thesis Outline

Part 1

The first part of this thesis systematically addresses the lack of basic groundwork in the Barossa Complex, and builds up a systematic investigation of the stratigraphy, depositional setting and timing, and subsequent metamorphism.

Chapter 2 & 3: Mapping the Barossa Complex

Chapters 2 and 3 present the stratigraphy and large scale structures within the Barossa Complex. In existing work on the Barossa Complex, lithological mapping has been restricted to localised areas which has hampered the understanding of the stratigraphic relationships and structures. Chapter 2 addresses the stratigraphy and structure of the two northern inliers, the Houghton and Warren Inliers, which contain the best exposures and allows for the best assessment of these features. Chapter 3 presents lithological maps of three smaller exposures including the Aldgate, Oakbank, and the southernmost portion of the Myponga Inlier, and highlights potential stratigraphic correlations.

Chapter 4: Depositional Timing Constraints on the Barossa Complex

Building on the stratigraphic framework outlined in Chapters 2 and 3, Chapter 4 assesses the detrital and igneous zircon U-Pb geochronology from across the stratigraphy of the Houghton Inlier, with additional samples from the Warren and Myponga inliers. Zircon U-Pb dating is used to further constrain the depositional timing of the Barossa Complex. Lu-Hf isotopes are also presented for detrital zircon in order to further characterise the likely sediment sources and allow for better correlations to other similarly aged basins in eastern Proterozoic Australia.

Chapter 5: Metamorphic Zircon Geochronology

Chapter 5 builds upon the existing body of metamorphic geochronology from the Barossa Complex with the aim of evaluating the multiple periods of metamorphism, and determining at which stage peak metamorphism occurred. Distribution partition coefficients of the REEs between metamorphic zircon and garnet are used in combination with zircon U-Pb geochronology in order to directly link the growth of metamorphic minerals to U-Pb ages.

Part 2

The second part of the thesis addresses the validity of the detrital zircon technique in modern and ancient environments. The use of detrital zircon as a sediment provenance indicator is widely used around the world, and often plays a significant role in identifying and linking formerly contiguous crustal elements (e.g. Goodge et al. 2008, Li et al. 2008, Evans and Mitchell 2011, Medig et al. 2014). In the modern environment, detrital zircons have been used to characterise the bedrock evolution of river and stream catchments (e.g. Griffin et al. 2004, Condie et al. 2005, He et al. 2014, Malusà et al. 2016). The use of modern detrital zircon has been used to produce large U-Pb and Lu-Hf isotope datasets for many areas in Australia such as the Gawler Craton and Curnamona Province (e.g. Condie et al. 2005, Belousova et al. 2009, Howard et al. 2009).

Some recent studies have begun to identify and highlight inconsistencies between bedrock zircon ages and isotopic compositions and the detritus contained in the streams which drain that bedrock (e.g. Bonich et al. 2017), or the ambiguity arising from recycling sediment (Andersen et al. 2016). These studies are particularly significant when considering modern detrital zircon studies in Australia which produced zircon age populations that cannot be easily reconciled with the basement geology (Condie et al. 2005, Belousova et al. 2009). Despite these obvious problems, modern detrital zircon datasets are still used to interpret the development of Proterozoic Australia (e.g. Belousova et al. 2006, Medig et al. 2014, Smits et al. 2014, Armit et al. 2017).

Chapter 6: Modern Detrital Zircon

Chapter 6 addresses detrital zircon age populations identified in modern stream sediments from the Broken Hill region in the Curnamona Province. A number of streams in the geologically well described Broken Hill area have been sampled in order to test how well stream sediments represent the zircon populations of the catchment bedrock. Chapter 6 uses U-Pb and Lu-Hf isotopes to link detrital zircon back to a primary source region, and in doing so address the methods of zircon transport in arid environments, and the usefulness of detrital zircon as a sediment provenance indicator both in the modern environment and the geological record.

Additional Works

In addition to the work presented in this thesis, during the course of my Ph.D., I have also co-authored a report book by the Geological Survey of South Australia which presents Sensitive High Resolution Ion Microprobe (SHRIMP) zircon U-Pb geochronology from across the Barossa Complex. This report book is attached as Appendix 1, and will be published as:

Jagodzinski, E.A., Meaney, K., Szpunar, M., and Fraser, G., 2017. *SHRIMP U-Pb dating of the Barossa Complex, South Australia: exploring tectonic links between the Gawler Craton and Curnamona Province.* Report Book 2017/00017. Department of the Premier and Cabinet, South Australia, Adelaide.

References

Aitken, A. R. A., Betts, P. G., Young, D. A., Blankenship, D. D., Roberts, J. L. & Siegert, M. J., 2016. The Australo-Antarctic Columbia to Gondwana transition. Gondwana Research, 29(1), 136-152.

Alderman, A. R., 1938. Augen-Gneisses in the Humbug Scrub Area, South Australia. Transactions of the Royal Society of South Australia, 62, 168-191.

Andersen, T., Kristoffersen, M. & Elburg, M. A., 2016. How far can we trust provenance and crustal evolution information from detrital zircons? A South African case study. Gondwana Research, 34, 129-148.

Armit, R., Betts, P. G., Schaefer, B. F., Yi, K., Kim, Y., Dutch, R. A., Reid, A., Jagodzinski,

L., Giles, D. & Ailleres, L., 2017. Late Palaeoproterozoic evolution of the buried northern Gawler Craton. Precambrian Research, 291, 178-201.

Belousova, E. A., Preiss, W. V., Schwarz, M. P. & Griffin, W. L., 2006. Tectonic affinities of the Houghton Inlier, South Australia: U - Pb and Hf-isotope data from zircons in modern stream sediments. Australian Journal of Earth Sciences, 53(6), 971-989.

Belousova, E. A., Reid, A. J., Griffin, W. L. & O'Reilly, S. Y., 2009. Rejuvenation vs. recycling of Archean crust in the Gawler Craton, South Australia: Evidence from U–Pb and Hf isotopes in detrital zircon. Lithos, 113(3–4), 570-582.

Benson, W. N., 1909. Petrographical Notes on Certain Pre-Cambrian Rocks of the Mount Lofty Ranges, With Special Reference to the Geology of the Houghton District. Transactions of the Royal Society of South Australia, 33, 101-140.

Betts, P. G., Armit, R. J., Stewart, J., Aitken, A. R. A., Ailleres, L., Donchak, P., Hutton, L., Withnall, I. & Giles, D., 2015. Australia and Nuna. Geological Society, London, Special Publications, 424.

Betts, P. G. & Giles, D., 2006. The 1800–1100 Ma tectonic evolution of Australia. Precambrian Research, 144(1–2), 92-125.

Betts, P. G., Giles, D., Lister, G. S. & Frick, L. R., 2002. Evolution of the Australian lithosphere. Australian Journal of Earth Sciences, 49(4), 661-695.

Betts, P. G., Giles, D., Mark, G., Lister, G. S., Goleby, B. R. & Aillères, L., 2006. Synthesis of the proterozoic evolution of the Mt Isa Inlier. Australian Journal of Earth Sciences, 53(1), 187-211.

Betts, P. G., Valenta, R. K. & Finlay, J., 2003. Evolution of the Mount Woods Inlier, northern Gawler Craton, Southern Australia: an integrated structural and aeromagnetic analysis. Tectonophysics, 366(1), 83-111.

Bonich, M. B., Samson, S. D. & Fedo, C. M., 2017. Incongruity of Detrital Zircon Ages of Granitic Bedrock and Its Derived Alluvium: An Example from the Stepladder Mountains, Southeastern California. The Journal of Geology, 125(3), 337-350.

Callen, R. A., 1966. A comparison of the genesis of copper orebodies at Kuitpo and Moonta in South Australia, with particular reference to the economic potential of each district. Unpub. BSc (Hons) Thesis, University of Adelaide.

Cawood, P. A. & Korsch, R. J., 2008. Assembling Australia: Proterozoic building of a continent. Precambrian Research, 166(1–4), 1-35.

Chappel, B. E. E., 1964. The geology of the Willunga Hill - Kuitpo area. Unpub. BSc (Hons) Thesis, University of Adelaide.

Condie, K. C., Beyer, E., Belousova, E., Griffin, W. L. & O'Reilly, S. Y., 2005. U–Pb isotopic ages and Hf isotopic composition of single zircons: The search for juvenile Precambrian continental crust. Precambrian Research, 139(1–2), 42-100.

Conor, C. H. H. & Preiss, W. V., 2008. Understanding the 1720–1640 Ma Palaeoproterozoic Willyama Supergroup, Curnamona Province, Southeastern Australia: Implications for tectonics, basin evolution and ore genesis. Precambrian Research, 166(1–4), 297-317.

Dalziel, I. W. D., 1991. Pacific margins of Laurentia and East Antarctica-Australia as a conjugate rift pair: Evidence and implications for an Eocambrian supercontinent. Geology, 19(6), 598-601.

Davies, M. B., 1972. The geology and petrology of an Archaean inlier south of Normanville – the geochemistry of the Houghton granulite. Unpub. BSc (Hons) Thesis, University of Adelaide.

Direen, N. G., Cadd, A. G., Lyons, P. & Teasdale, J. P., 2005. Architecture of Proterozoic shear zones in the Christie Domain, western Gawler Craton, Australia:

Geophysical appraisal of a poorly exposed orogenic terrane. Precambrian Research, 142(1), 28-44.

Ehrig, K., McPhie, J. & Kamenetsky, V., 2013. Geology and mineralogical zonation of the Olympic Dam iron oxide Cu–U–Au–Ag deposit, South Australia. In: Geology and Genesis of Major Copper Deposits and Districts of the World, a Tribute to Richard Sillitoe (eds Hedenquist, J. W., Harris, M. & Camus, F.) Society of Economic Geologists Special Publication, Vol. 16, pp. 237-268.

England, H. N., 1935. Petrographic Notes on Intrusions of the Houghton Magma in the Mount Lofty Ranges. Transactions of the Royal Society of South Australia, 58, 1-15.

Evans, D. A. D. & Mitchell, R. N., 2011. Assembly and breakup of the core of Paleoproterozoic–Mesoproterozoic supercontinent Nuna. Geology, 39(5), 443-446.

Foden, J., Elburg, M. A., Dougherty-Page, J. & Burtt, A., 2006. The timing and duration of the Delamerian orogeny: Correlation with the Ross Orogen and implications for Gondwana assembly. Journal of Geology, 114(2), 189-210.

Foden, J. D., Elburg, M. A., Turner, S. P., Sandiford, M., O'Callaghan, J. & Mitchell, S., 2002. Granite production in the Delamerian Orogen, South Australia. Journal of the Geological Society, 159(5), 557-575.

Giles, D., Betts, P. G. & Lister, G. S., 2004. 1.8-1.5-Ga links between the North and South Australian Cratons and the Early-Middle Proterozoic configuration of Australia. Tectonophysics, 380(1-2), 27-41.

Goodge, J. W., Vervoort, J. D., Fanning, C. M., Brecke, D. M., Farmer, G. L., Williams, I. S., Myrow, P. M. & DePaolo, D. J., 2008. A Positive Test of East Antarctica–Laurentia Juxtaposition Within the Rodinia Supercontinent. Science, 321(5886), 235-240.

Griffin, W. L., Belousova, E. A., Shee, S. R., Pearson, N. J. & O'Reilly, S. Y., 2004. Archean crustal evolution in the northern Yilgarn Craton: U–Pb and Hf-isotope evidence from detrital zircons. Precambrian Research, 131(3–4), 231-282.

Hand, M., Reid, A. & Jagodzinski, L., 2007. Tectonic framework and evolution of the Gawler craton, Southern Australia. Economic Geology, 102(8), 1377-1395.

He, M., Zheng, H., Bookhagen, B. & Clift, P. D., 2014. Controls on erosion intensity in the Yangtze River basin tracked by U–Pb detrital zircon dating. Earth-Science Reviews, 136, 121-140.

Heaslip, J. E., 1972. Review of the Geology of the Mt. Magnificent Area, University of Adelaide.

Hoffman, P. F., 1991. Did the Breakout of Laurentia Turn Gondwanaland Inside-Out? Science, 252(5011), 1409-1412.

Howard, K. E., Hand, M., Barovich, K. M., Payne, J. L. & Belousova, E. A., 2011. U–Pb, Lu–Hf and Sm–Nd isotopic constraints on provenance and depositional timing of metasedimentary rocks in the western Gawler Craton: Implications for Proterozoic reconstruction models. Precambrian Research, 184(1–4), 43-62.

Howard, K. E., Hand, M., Barovich, K. M., Reid, A., Wade, B. P. & Belousova, E. A., 2009. Detrital zircon ages: Improving interpretation via Nd and Hf isotopic data. Chemical Geology, 262(3–4), 277-292.

Howchin, W., 1906. The geology of the Mount Lofty Ranges - Part II. Transactions of the Royal Society of South Australia, 30, 227 - 263.

Howchin, W., 1926. The geology of the Barossa Ranges and neighborhood in relation to the geological axis of the country. Transactions of the Royal Society of South Australia, 50, 1-16.

Jagodzinski, E.A., Meaney, K., Szpunar, M.,

and Fraser, G., 2017. SHRIMP U-Pb dating of the Barossa Complex, South Australia: exploring tectonic links between the Gawler Craton and Curnamona Province. Report Book 2017/00017. Department of the Premier and Cabinet, South Australia, Adelaide.

Johnson, S.P., 2013. The Birth of supercontinents and the Proterozoic Assembly of Western Australia. Geological Survey of Western Australia, 72p

Karlstrom, K. E., Harlan, S. S., Williams, M. L., Geissman, J. W. & Åhäll, K., 1999. Refining Rodinia: Geologic Evidence for the Australia–Western U.S. connection in the Proterozoic GSA Today, 9(10), 1-7.

Kositcin, N., 2010. Geodynamic Synthesis of the Gawler Craton and Curnamona Province. Geoscience Australia, Record, 2010/27, 113p.

Li, Z.-X. & Evans, D. A. D., 2011. Late Neoproterozoic 40° intraplate rotation within Australia allows for a tighter-fitting and longer-lasting Rodinia. Geology, 39(1), 39-42.

Li, Z.-X., Zhang, L. & Powell, C. M., 1995. South China in Rodinia: Part of the missing link between Australia–East Antarctica and Laurentia? Geology, 23(5), 407-410.

Li, Z. X., Bogdanova, S. V., Collins, A. S., Davidson, A., De Waele, B., Ernst, R. E., Fitzsimons, I. C. W., Fuck, R. A., Gladkochub, D. P., Jacobs, J., Karlstrom, K. E., Lu, S., Natapov, L. M., Pease, V., Pisarevsky, S. A., Thrane, K. & Vernikovsky, V., 2008. Assembly, configuration, and break-up history of Rodinia: A synthesis. Precambrian Research, 160(1–2), 179-210.

Malusà, M. G., Resentini, A. & Garzanti, E., 2016. Hydraulic sorting and mineral fertility bias in detrital geochronology. Gondwana Research, 31, 1-19.

Mancktelow, N. S., 1990. The structure of the southern Adelaide Fold Belt, South Australia. In: The evolution of a Late Precambrian-Early Paleozoic Rift Complex: The Adelaide Geosyncline (eds Jago, J. B. & Moore, P. J.), pp. 483-495, The Geological Society of Australia Special Publication

McEwin, A. J., 1972. Geology and petrology of part of the Archaean Inlier north-east of Yankalilla on the Fleurieu Peninsula. Unpub. BSc (Hons) Thesis, University of Adelaide.

Medig, K. P. R., Thorkelson, D. J., Davis, W. J., Rainbird, R. H., Gibson, H. D., Turner, E. C. & Marshall, D. D., 2014. Pinning northeastern Australia to northwestern Laurentia in the Mesoproterozoic. Precambrian Research, 249, 88-99.

Meert, J. G. & Santosh, M., 2017. The Columbia supercontinent revisited. Gondwana Research, 50, 67-83.

Merdith, A. S., Collins, A. S., Williams, S. E., Pisarevsky, S., Foden, J. D., Archibald, D. B., Blades, M. L., Alessio, B. L., Armistead, S., Plavsa, D., Clark, C. & Müller, R. D., 2017. A full-plate global reconstruction of the Neoproterozoic. Gondwana Research, 50, 84-134.

Mills, K. J., 1963. The geology of the Mount Crawford granite gneiss and adjacent metasediments. Transactions of the Royal Society of South Australia, 87, 167-183.

Mills, K. J., 1973. The structural geology of the Warren National Park and the western portion of the Mount Crawford State Forest, South Australia. Transactions of the Royal Society of South Australia, 97(Part 4), Pages: 281-315.

Moores, E. M., 1991. Southwest U.S.-East Antarctic (SWEAT) connection: A hypothesis. Geology, 19(5), 425-428.

Morrissey, L. J., Hand, M., Wade, B. P. & Szpunar, M., 2013. Early Mesoproterozoic metamorphism in the Barossa Complex, South Australia: links with the eastern margin of Proterozoic Australia. Australian Journal of Earth Sciences, 60(8), 769-795.

Mulder, J. A., Halpin, J. A. & Daczko, N. R., 2015. Mesoproterozoic Tasmania: Witness

to the East Antarctica–Laurentia connection within Nuna. Geology, 43(9), 759-762.

Myers, J. S., Shaw, R. D. & Tyler, I. M., 1996. Tectonic evolution of Proterozoic Australia. Tectonics, 15(6), 1431-1446.

Offler, R. & Fleming, P. D., 1968. A synthesis of folding and metamorphism in the Mt Lofty Ranges, South Australia. Journal of the Geological Society of Australia, 15(2), 245-266.

Page, R. N., Stevens, B. P. J. & Gibson, G. M., 2005a. Geochronology of the sequence hosting the Broken Hill Pb-Zn-Ag orebody, Australia. Economic Geology, 100(4), 633-661.

Page, R. W., Conor, C. H. H., Stevens, B. P. J., Gibson, G. M., Preiss, W. V. & Southgate, P. N., 2005b. Correlation of Olary and Broken Hill Domains, Curnamona Province: Possible relationship to Mount Isa and other North Australian Pb-Zn-Ag-bearing successions. Economic Geology, 100(4), 663-676.

Payne, J. L., Barovich, K. M. & Hand, M., 2006. Provenance of metasedimentary rocks in the northern Gawler Craton, Australia: Implications for Palaeoproterozoic reconstructions. Precambrian Research, 148(3–4), 275-291.

Payne, J. L., Hand, M., Barovich, K., Reid, A. & Evans, D. A. D., 2009. Correlations and Reconstruction Models for the 2500-1500 Ma evolution of the Mawson Continent. In: Paleoproterozoic Supercontinents and Global Evolution (eds Reddy, S. M., Mazumder, R., Evans, D. A. D. & Collins, A. S.), pp. 319-357, Geological Society, London.

Pisarevsky, S. A., Wingate, M. T. D., Powell, C. M., Johnson, S. & Evans, D. A. D., 2003. Models of Rodinia assembly and fragmentation. Geological Society, London, Special Publications, 206(1), 35-55.

Preiss, W. V., 1993. Basement Inliers of the Mount Lofty Ranges. In: The Geology of South Australia, Volume 1, The Precambrian (eds Drexel, J. F., Preiss, W. V. & Parker, A. J.), pp. 102-105, Geological Survey of South Australia, Adelaide.

Preiss, W. V., 2000. The Adelaide Geosyncline of South Australia and its significance in Neoproterozoic continental reconstruction. Precambrian Research, 100(1-3), 21-63.

Preiss, W. V., Fanning, C. A., Szpunar, M. A. & Burtt, A. C., 2008. Age and tectonic significance of the Mount Crawford Granite Gneiss and a related intrusive in the Oakbank Inlier, Mount Lofty Ranges, South Australia. MESA Journal, 49, 38-49.

Raetz, M., Krabbendam, M. & Donaghy, A. G., 2002. Compilation of Pb zircon data from the Willyama Supergroup, Broken Hill region, Australia: Evidence for three tectonostratigraphic successions and four magmatic events? Australian Journal of Earth Sciences, 49(6), 965-983.

Reid, A. J., Jourdan, F. & Jagodzinski, E. A., 2017. Mesoproterozoic fluid events affecting Archean crust in the northern Olympic Cu–Au Province, Gawler Craton: insights from 40Ar/39Ar thermochronology. Australian Journal of Earth Sciences, 64(1), 103-119.

Rogers, J. J. W. & Santosh, M., 2002. Configuration of Columbia, a Mesoproterozoic Supercontinent. Gondwana Research, 5(1), 5-22.

Schlegel, T. U. & Heinrich, C. A., 2015. Lithology and Hydrothermal Alteration Control the Distribution of Copper Grade in the Prominent Hill Iron Oxide-Copper-Gold Deposit (Gawler Craton, South Australia). Economic Geology, 110(8), 1953–1994.

Skirrow, R. G., Bastrakov, E. N., Barovich, K., Fraser, G. L., Creaser, R. A., Fanning, C. M., Raymond, O. L. & Davidson, G. J., 2007. Timing of Iron Oxide Cu-Au-(U) Hydrothermal Activity and Nd Isotope Constraints on Metal Sources in the Gawler Craton, South Australia. Economic Geology, 102(8), 1441-1470.

Smits, R. G., Collins, W. J., Hand, M., Dutch,

R. & Payne, J., 2014. A Proterozoic Wilson cycle identified by Hf isotopes in central Australia: Implications for the assembly of Proterozoic Australia and Rodinia. Geology, 42(3), 231-234.

Sprigg, R. C., 1946. Reconnaissance geological survey of portion of the western escarpment of the Mount Lofty Ranges. Transactions of the Royal Society of South Australia, 70, 313 - 346.

Sprigg, R. C., Whittle, A. W. G. & Campana, D., 1951. Adelaide 1:1 Mile Geological Sheet (ed Dickinson, S. B.), Department of Mines, Adelaide, Adelaide, South Australia.

Sprigg, R. C. & Wilson, B., 1954. Echunga 1:1 Mile Geological Sheet (ed Dickinson, S. B.), Departmen of Mines, Adelaide, Adelaide.

Spry, A. H., 1951. The Archaean complex at Houghton, South Australia. Transactions of the Royal Society of South Australia, 74(1), 115-134.

Stevens, B. P. J., Page, R. W. & Crooks, A., 2008. Geochronology of Willyama Supergroup metavolcanics, metasediments and contemporaneous intrusions, Broken Hill, Australia. Australian Journal of Earth Sciences, 55(3), 301-330.

Stewart, J. R. & Betts, P. G., 2010. Late Paleo–Mesoproterozoic plate margin deformation in the southern Gawler Craton: Insights from structural and aeromagnetic analysis. Precambrian Research, 177(1), 55-72.

Szpunar, M., Wade, B., Hand, M. P. & Barovich, K. M., 2007. Timing of Proterozoic high-grade metamorphism in the Barossa Complex, southern South Australia; exploring the extent of the 1590 Ma event. MESA Journal, 47, 21-27.

Talbot, J. L., 1963. Retrograde metamorphism of the Houghton Complex, South Australia. Transactions of the Royal Society of South Australia, 87, 185-197.

Thiel, S., Heinson, G. & White, A., 2005. Tectonic evolution of the southern Gawler Craton,South Australia, from electromagnetic sounding. Australian Journal of Earth Sciences, 52(6), 887-896.

Thomas, J. L., Direen, N. G. & Hand, M., 2008. Blind orogen: Integrated appraisal of multiple episodes of Mesoproterozoic deformation and reworking in the Fowler Domain, western Gawler Craton, Australia. Precambrian Research, 166(1–4), 263-282.

Wade, B. P., Barovich, K. M., Hand, M., Scrimgeour, I. R. & Close, D. F., 2006. Evidence for Early Mesoproterozoic Arc Magmatism in the Musgrave Block, Central Australia: Implications for Proterozoic Crustal Growth and Tectonic Reconstructions of Australia. The Journal of Geology, 114(1), 43-63.

Wicks, S. P., 1972. Geology of part of basement inlier north-east of Mt. Compass. Unpub. BSc (Hons) Thesis, University of Adelaide.

Wingate, M. T. D., Pisarevsky, S. A. & Evans, D. A. D., 2002. Rodinia connections between Australia and Laurentia: no SWEAT, no AUSWUS? Terra Nova, 14(2), 121-128.

Zhang, S., Li, Z.-X., Evans, D. A. D., Wu, H., Li, H. & Dong, J., 2012. Pre-Rodinia supercontinent Nuna shaping up: A global synthesis with new paleomagnetic results from North China. Earth and Planetary Science Letters, 353–354(0), 145-155.

Zhao, G., Sun, M., Wilde, S. A. & Li, S., 2004. A Paleo-Mesoproterozoic supercontinent: assembly, growth and breakup. Earth-Science Reviews, 67(1–2), 91-123.

CHAPTER 2

This Chapter is written for submission to
The Australian Journal of Earth Sciences as;

Meaney, K., Hand, M., Collins, A. S.,
The Palaeo-Mesoproterozoic Stratigraphy and Structure of the Northern Barossa Complex, Mount Lofty Ranges, South Australia

Statement of Authorship

Title of Paper	The Paleo-Mesoproterozoic Stratigraphy and Structure of the Northern Barossa Complex, Mount Lofty Ranges, South Australia
Publication Status	☐ Published ☐ Accepted for Publication ☐ Submitted for Publication ☑ Unpublished and Unsubmitted w ork w ritten in manuscript style
Publication Details	Written to be submitted to The Australian Journal of Earth Sciences

Principal Author

Name of Principal Author (Candidate)	Kieran Meaney		
Contribution to the Paper	Project design, Fieldwork, Data interpretation, Manuscript design, Creation of figures		
Overall percentage (%)	80		
Certification:	This paper reports on original research I conducted during the period of my Higher Degree by Research candidature and is not subject to any obligations or contractual agreements with a third party that would constrain its inclusion in this thesis. I am the primary author of this paper.		
Signature		Date	21/12/2017

Co-Author Contributions

By signing the Statement of Authorship, each author certifies that:

i. the candidate's stated contribution to the publication is accurate (as detailed above);
ii. permission is granted for the candidate in include the publication in the thesis; and
iii. the sum of all co-author contributions is equal to 100% less the candidate's stated contribution.

Name of Co-Author	Martin Hand		
Contribution to the Paper	Assistance with fieldwork and data interpretation, Manuscript review		
Signature		Date	21/12/2017

Name of Co-Author	Alan Collins		
Contribution to the Paper	Assistance with fieldwork and data interpretation, Manuscript review		
Signature		Date	30/11/2017.

ABSTRACT

The Barossa Complex is a domain of late Palaeo- to early Mesoproterozoic crust on the southeastern margin of the Gawler Craton. The Barossa Complex occurs as a series of inliers enclosed by Neoproterozoic to Palaeozoic sedimentary units. Stratigraphic and structural mapping of the northernmost inliers reveal a sequence of metasediments that include calcsilicate, psammopelitic, and pelitic gneisses. An early low-angle metamorphic fabric formed parallel to lithological boundaries and is interpreted to have developed in an extensional, high temperature setting before being deformed in east-west and then north-south oriented compressional environments. This work provides context to existing geochronology indicates that deposition occurred between ca. 1720-1655 Ma, and that high-grade metamorphism likely occurred at ca. 1625 Ma with subsequent Proterozoic deformation between ca. 1590-1550 Ma. The protoliths to the Barossa Complex were deposited in one of a series of basins that formed on the eastern margin of the Gawler Craton during the Late Palaeoproterozoic, and were subsequently deformed during the 1600 Ma Olarian and Kararan Orogenies.

1. Introduction

In recent years numerous models have been proposed which attempt to describe Australia's continental evolution through the Palaeoproterozoic (e.g. Giles et al. 2004, Betts and Giles 2006, Wade et al. 2006, Cawood and Korsch 2008, Morrissey et al. 2011, Johnson 2013, Smits et al. 2014, Betts et al. 2015, Aitken et al. 2016). In many of these models the Archean-Mesoproterozoic Gawler Craton and the Palaeo-Mesoproterozoic Curnamona Province are often grouped together as the South Australian Craton. However, the evolution of these two cratonic domains are often considered separately, and in some cases as exotic to one another (e.g. Betts and Giles 2006). This is largely because Gawler Craton and Curnamona Province are separated by the Neoproterozoic Adelaide Rift Complex (Preiss 2000). One of the few places where the basement to the Adelaide Rift Complex is exposed is in the southern Mount Lofty Ranges in a series of inliers, referred to collectively as the Barossa Complex (Preiss 1993).

The Barossa Complex is considered to be the easternmost extent of the Gawler Craton (Figure 1; Preiss 1993, Szpunar et al. 2007, Morrissey et al. 2013), although it is frequently left out of evolutionary schemes for the craton. This exclusion is largely the result of the small amount of detailed work that exists for the Barossa Complex, and this creates ambiguity as to its place in the development of the Palaeoproterozoic domains within the South Australian Craton. The Barossa Complex inliers sit adjacent to the Tasman line, which marks the eastern limit of exposed Palaeoproterozoic rock in Australia, and as such they provide an opportunity to examine the closest in situ exposure to the edge of the Proterozoic continent (e.g. Morrissey et al. 2013). This makes the Barossa Complex a valuable region in terms of reconstruction models that seek to identify the continuation of Proterozoic Australia into now separated continental systems.

Existing geological maps of the Barossa Complex tend to focus on small isolated areas and are largely restricted to unpublished Honours and PhD theses (Chappel 1964, Callen 1966, Davies 1972, Heaslip 1972, McEwin 1972, Wicks 1972, Crowhurst 1988, Paul 1998). Although many of the Barossa Complex lithologies have been described in detail by these and other workers (e.g. Spry 1951, Talbot 1963), the lithological relationships are often largely undescribed and a stratigraphic column has never been

formulated. Additionally, the majority of structural work within the Barossa Complex has focussed on the overprinting structures and retrogressive effects of the Cambro-Ordovician Delamerian Orogeny (Webb 1953, Talbot 1963, Mills 1973).

This chapter aims to provide context for further work in the northern Barossa Complex with the intention to establish lithology maps, a basic stratigraphic column, and an outline of the Proterozoic structural history in the northern Barossa Complex. While the effects of the Delamerian Orogeny are dominant in some areas of the northern Barossa Complex, the nature and structural evolution of this event have been studied extensively (e.g. Offler and Fleming 1968, Mancktelow 1990 and references therein, Flöttmann et al. 1994, Flottmann and James 1997). As such, the primary focus of this chapter will be on the structures which predate the Delamerian Orogeny.

2. Background

The Barossa Complex is a collective term used to describe the five metamorphic basement inliers exposed in the Mount Lofty Ranges (Preiss 1993). These extend from the Warren Inlier, located approximately 7km southeast of Williamstown, to the Myponga Inlier, the southernmost extent of which reaches 5km south of Normanville on the Fleurieu Peninsula (Figure 1). The Barossa Complex is overlain by sequences belonging to the Neoproterozoic-Cambrian Adelaide Rift Complex, and is exposed within partially fault bound anticlinal cores generated during the Cambro-Ordovician Delamerian Orogeny (Offler and Fleming 1968, Mancktelow 1990).

The Barossa Complex contains extensive areas that are deeply weathered, or covered by Permian, Tertiary, and Quaternary sediments (e.g. Chappel 1964, Horsfall 1973, Preiss 1993) which contribute in many areas to poor exposure of the bedrock. Despite this, the two most northern inliers, the Houghton and Warren Inliers (Figure 1), have areas of good exposure.

Common rock types which have been identified and described throughout the Barossa Complex include sillimanite- and garnet- bearing gneisses, quartzites and psammites, calcsilicate gneisses, retrograde micaceous rocks, as well as metaigneous rocks including amphibolites and granitic orthogneisses (Preiss 1993 and references therein). SHRIMP U-Pb dating of detrital zircon from across the Barossa Complex suggests that deposition occurred between 1720-1650 Ma (Jagodzinski et al. 2017). Granite gneiss from the northern Houghton Inlier records a protolith crystallisation age of c. 1717 Ma (Belousova et al. 2006, Jagodzinski et al. 2017), indicating that it intruded relatively early in the depositional history.

The Barossa Complex was metamorphosed to upper amphibolite-granulite facies conditions during the Late Palaeoproterozoic to Early Mesoproterozoic, and later retrogressed to greenschist facies during the Delamerian Orogeny (Talbot 1963, Szpunar et al. 2007, Morrissey et al. 2013, Jagodzinski et al. 2017).

Zircon and monazite U-Pb geochronology indicate that metamorphism occurred between 1630-1580 Ma (Szpunar et al. 2007, Morrissey et al. 2013, Jagodzinski et al. 2017). Three apparent pulses of zircon growth have been identified at 1630 Ma, 1610 Ma, and 1590 Ma (Szpunar et al. 2007, Jagodzinski et al. 2017). Monazite records a later stage of metamorphism, with U-Pb ages between 1580-1550 Ma (Szpunar et al. 2007, Morrissey et al. 2013). Undeformed pegmatitic granite in the southern Myponga Inlier records a crystallisation age of 1580 ±4 Ma and marks the end of the deformation period (Jagodzinski et al. 2017). Metamorphic conditions calculated by Morrissey et al. (2013) for garnet-sillimanite bearing metapelite from the north and south of the Barossa Complex suggest that peak metamorphism occurred at approximately 800-850^{o}C and 8-9 Kbar, Although it is uncertain when during the 1630-

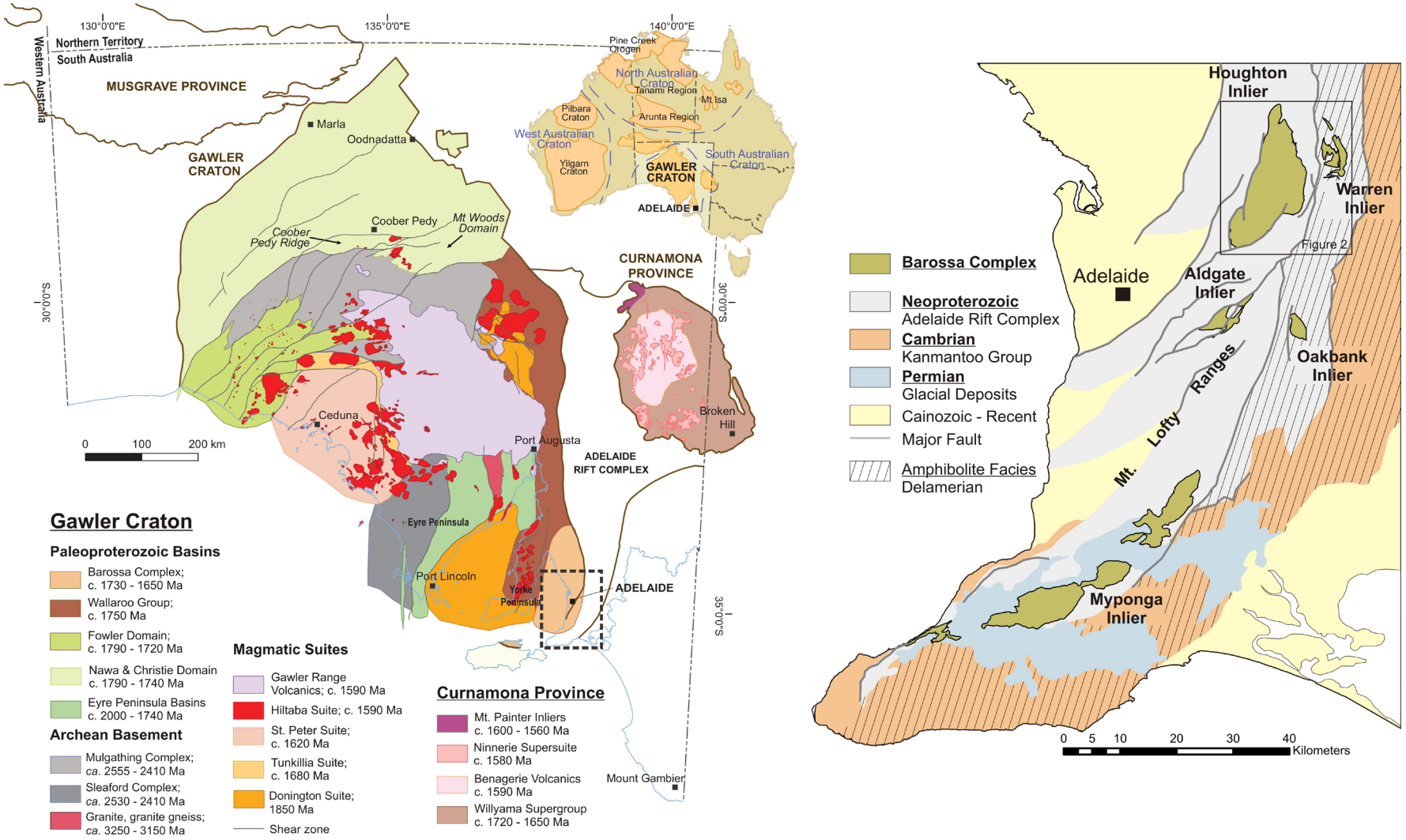

Figure 1: Location Map of the Gawler Craton and Curnamona Province in South Australia after Reid et al. (2017). The blow up shows the location of the various Barossa Complex Inliers exposed within the Mount Lofty Ranges (after Preiss 1993).

1580 Ma period peak metamorphism occurred. Monazite recording ages between 1570-1550 Ma from the Houghton and Myponga inliers are interpreted to represent a period of retrograde metamorphism (Morrissey et al. 2013). This is consistent with the pre-Delamerian retrograde phase suggested by Talbot (1963).

Post dating high grade Late Palaeo- Early Mesoproterozoic metamorphism are bodies of Neoproterozoic granite in the Warren and Oakbank inliers which are dated at approximately 850-810Ma (Preiss et al. 2008). These are interpreted to have intruded during the onset of rifting and the deposition of the basal sequences of the Adelaide Rift Complex.

During the Cambro- Ordovician Delamerian Orogeny, the Barossa Complex was retrogressed and variably deformed. Between the Houghton and Warren Inliers lies the Williamstown-Meadows Fault (WMF; Figure 1, 2), which is a major thrust fault that juxtaposes the greenschist and amphibolite grade zones of the Delamerian Orogen (Figure 2; Mills 1973, Mancktelow 1990). The Houghton Inlier lies to the west of the WMF in the lower greenschist grade zone of the Delamerian Orogeny that is dominated by Delamerian D_1 structures. The Warren Inlier lies to the east of the WMF in an area where Delamerian metamorphic grades reach the lower amphibolite facies, forming fibrolitic sillimanite and partial melt, and where Delamerian D_2-D_3 structures dominate (Offler and Fleming 1968).

3. Stratigraphy of the Houghton and Warren Inliers

Existing studies within the Barossa Complex have focussed only on small areas which have prevented the formulation of a generalised stratigraphy. This study has examined the whole of the Houghton and Warren inliers (Figure 2), revealing a repetition of rock types interpreted to represent stratigraphy. Due to a lack of preserved sedimentary structures, the lithologies could not be ordered into depositional youngest to oldest, and are presented here in their current structural orientation. It must also be noted that the rock names and descriptions used here reflect their present characteristics and mineral assemblages, which in some instances differ dramatically from the primary metamorphic mineral assemblages that would have existed at the end of Late Palaeo- Early Mesoproterozoic metamorphism due to the retrogressive affects of the Delamerian Orogeny.

3.1 Houghton Inlier

3.1.1 East Kersbrook Calcsilicate

Southeast of the Kersbrook township lie a series of interlayered calcsilicate and quartzofeldspathic gneisses (Figure 2). These have previously been correlated to calcsilicate gneiss which occurs in the Inglewood township (Figure 2; Spry 1951). It is here proposed that these calcsilicate occurrences are separate stratigraphic units (see below).

This calcsilicate is composed primarily of actinolite and plagioclase, with abundant retrograde epidote. The unit is usually coarse-grained, with grain sizes up to but rarely exceeding 1-2mm. Gneissic layering is typically weakly developed, and the actinolite is aligned. In many places this unit is retrogressed to a much finer grained rock where epidote becomes the dominant mineral. Hematite occurs infrequently, and where present is adjacent to actinolite where it is partially replaced by epidote.

In rare occurrences, pegmatites occur which are mineralogically similar to the host calcsilicate, which was likely the melt source. The pegmatites are composed of quartz, plagioclase, and occasionally with crystals of actinolite up to 5cm long. These have been described previously by Benson (1909) who termed them ‘Yatalite’, and attributed the actinolite to the alteration of primary diopside.

The quartzofeldspathic gneiss which occurs in association with this calcsilicate is dominated by quartz and plagioclase, with

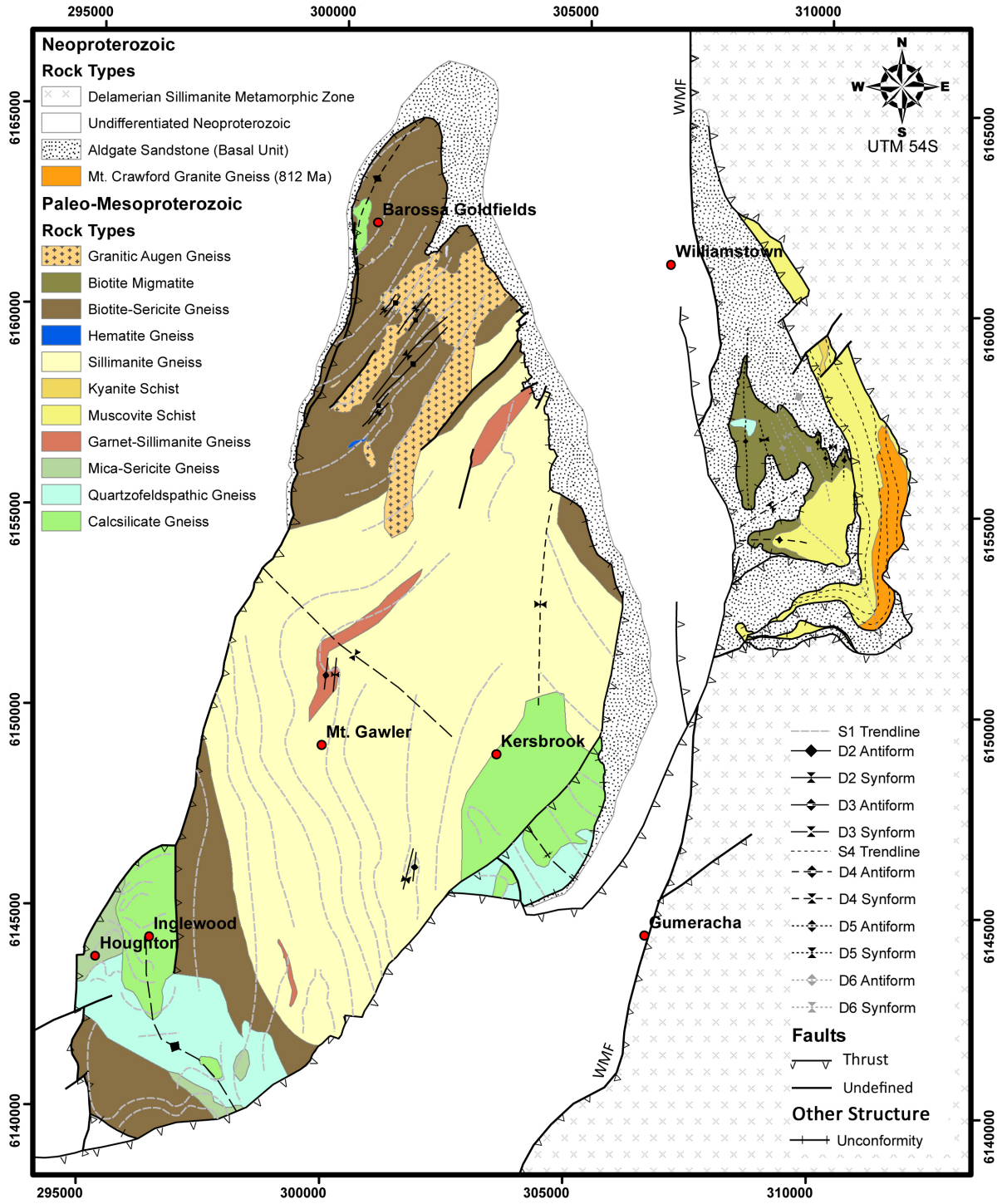

Figure 2: Lithology map of the Houghton and Warren Inliers with simplified structures. The smaller Warren Inlier lies within the sillimanite grade metamorphic zone of the Delamerian Orogen, east of the Williamstown-Meadows Fault (WMF).

minor biotite defining the foliation. Biotite is almost always replaced by sericite. Remnant biotite also occurs, confirming the identity of the original mica.

The extent of this unit is partially inferred due to poor outcrop in the Kersbrook area, but appears to correspond to a significant magnetic low observed in this area of the inlier (Figure 3) which has been used to infer the extent of this unit.

3.1.2 Sillimanite Gneiss

This unit is the most abundant lithology in the Houghton Inlier. The primary metamorphic mineralogy is almost impossible to distinguish in the majority of outcrops due to the extent of weathering and retrogression. Despite this, in many instances the retrogressive minerals and weathering products pseudomorph the primary mineralogy, allowing identification of distinctive minerals such as sillimanite (Figure 4a) and garnet. In thin section, the majority of the matrix of this unit is highly weathered and the mineralogy is indistinguishable. Relict twinning occurs in some sericitic masses which is reminiscent of plagioclase or cordierite. It is possible that these minerals were part of the peak assemblage. Leucosomes and pegmatites occur in many outcrops, although less frequently in the northern areas of the inlier. These bodies typically preserve a quartz-K-feldspar dominated assemblage, and generally occur aligned with the S_1 metamorphic fabric.

Weathered garnet porphyroblasts occur in distinct layers which have been mapped as marker units, and likely reflect a primary compositional variation. These layers are discontinuous, and it is unclear as to whether this reflects protolithic variation or is a result of metamorphic processes. The now clay-replaced garnet porphyroblasts average approximately 2 cm in size, but are up to 10 cm in diameter in some instances. The metamorphic fabric typically wraps these porphyroblasts.

Psammitic layers also occur infrequently within this unit on scales of up to several meters thickness. These psammites are typically quartz dominated with plagioclase, K-feldspar and minor biotite. In some instances leucosomes occur within the psammite layers and are parallel to the metamorphic layering.

3.1.3 Biotite-Sericite Gneiss

This lithology is composed of a well layered gneiss with alternating bands of micaceous and quartzofeldspathic material (Figure 4b). The micaceous layers are now dominantly composed of sericite and fine grained muscovite, but relict biotite is frequently present and was likely the primary mineral prior to retrogression. The micaceous bands occur on the scale of 2-5 mm, but are commonly obliterated by an overprinting cleavage associated with the Delamerian Orogeny (discussed below). Quartz and plagioclase occur in the leucocratic layers of the gneiss and do not exceed 0.5 mm in grain size. Minor amounts of hematite and magnetite are common throughout the unit. In rare cases, small areas dominated by coarse grained hematite occur. In these instances hematite, quartz, and K-feldspar occur up to 5 mm, with hematite composing up to 80% of the rock. Plagioclase rich domains define a layering in the same orientation as the S_1 metamorphic layering in the surrounding rocks. These occurrences have been mapped as a separate subunit (Figure 2). Leucosomes are common, with a greater abundance occurring in the southern areas of the inlier. Leucosomes are aligned with the S_1 metamorphic foliation.

The biotite-sericite gneiss has a gradational contact with the sillimanite gneiss, which commonly occurs over a scale of approximately 100 to 200 meters. In this transition zone, the rocks maintain the characteristic gneissic banding but retrograde muscovite becomes the dominant mica. The presence of sillimanite (or former presence) was taken as the boundary between these two units for the purpose of map representation.

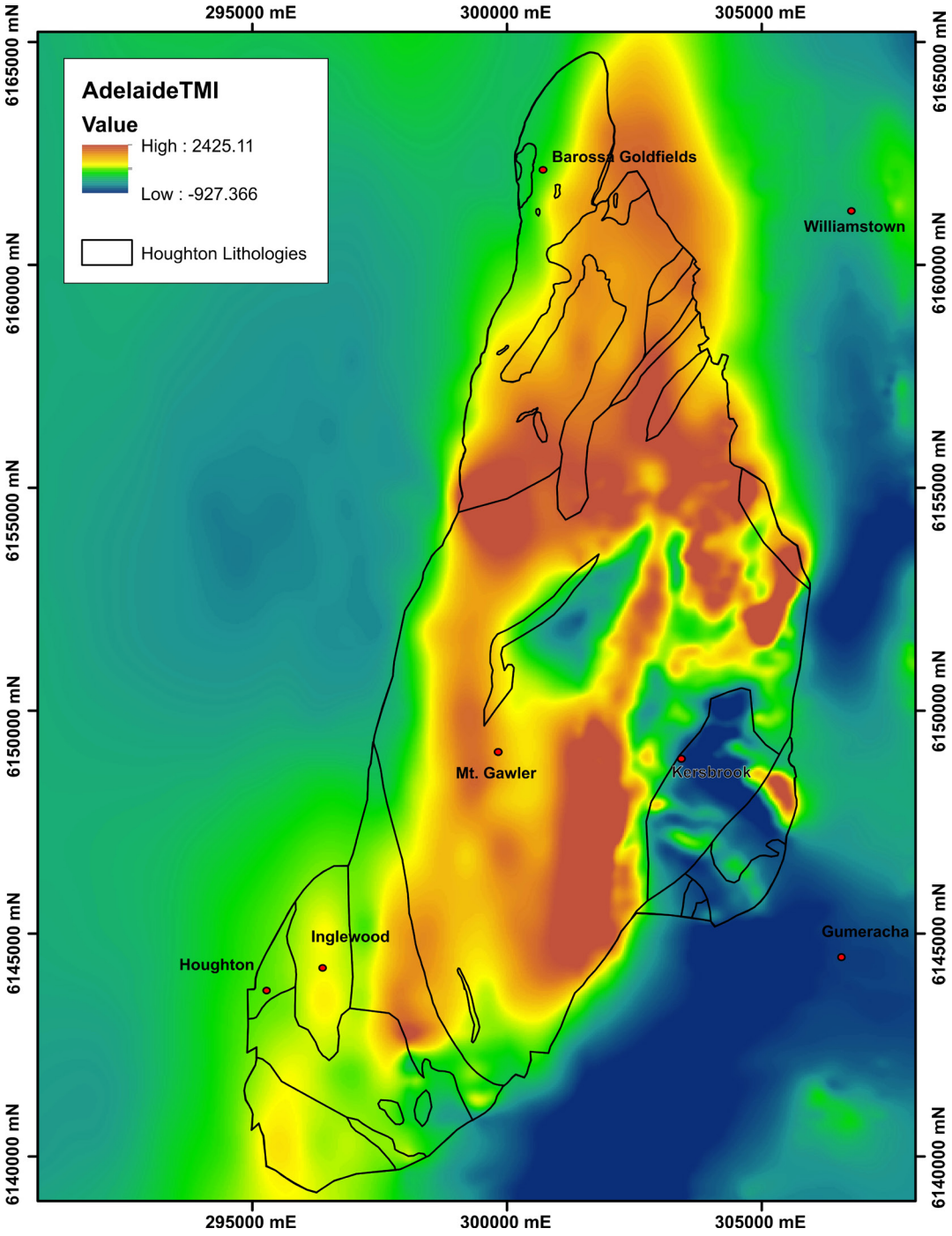

Figure 3: Total Magnetic Intensity Map (reduced to poles) of the Houghton and Warren Inliers. The magnetic high which continues beyond the margin of the Inlier in the NE corresponds to the area where the unconformity with Neoproterozoic sediments is intact. Relative Magnetic lows on the western and southern margins correspond to areas of faulting and strong retrogression. Data source: South Australian Resources Information Geoserver (SARIG).

3.1.4 Southern Houghton Inlier lithologies

In the Houghton-Inglewood-Paracombe area in the southern Houghton Inlier (Figure 2), and also in a small exposure in the north western Houghton Inlier, are a group of metasediments which appear to be discontinuously interlayered with one another. This includes the Houghton calcsilicate, formerly referred to as the Houghton Diorite (Benson 1909, Preiss 1993 and references therein), a quartzofeldspathic gneiss, and mica-rich gneiss, described below.

Mica-rich gneiss

The mica-rich gneiss outcrops best within the township of Houghton. In outcrop this rock contains layers of up to 5 cm thickness that are interpreted to be the relict sedimentary layering. At the microscopic level however, the rock is homogeneously retrogressed to fine grained sericite, so any primary metamorphic mineralogical descriptions can only be made using relict crystal shapes preserved in hand specimens. The layering observed appears to alternate between what was once a mica dominated and feldspar dominated assemblage. Sericite pseudomorphs after mica occur in grains up to 5 mm diameter, while the sericite pseudomorphs after feldspar record grain sizes not exceeding 2 mm. The sub-greenschist facies retrograde minerals in this unit preserve a cleavage which is attributed to the Delamerian Orogeny.

Quartzofeldspathic Gneiss

In this unit, plagioclase and quartz dominate the mineralogy in varying amounts, in addition to minor hematite and biotite. The foliation in this unit is defined by biotite, as well as elongation of quartz grains. Elongate quartz is up to 5mm long and 1-2 mm wide, while plagioclase forms a finer grained matrix. Small concentrations of hematite also follow the foliation. Plagioclase is frequently weathered or retrogressed to sericite which preserves a cleavage attributed to the Delamerian Orogeny, and gives this unit a phyllite-like appearance in some instances.

Houghton Calcsilicate

This unit is well exposed and comparatively fresh in contrast to most of the exposure in the Houghton Inlier. It is dominated by plagioclase, with well defined layers of diopside and retrograde actinolite defining the gneissic foliation (Figure 4c). Quartz commonly occurs with the plagioclase but typically does not exceed 10% of the rock. Diopside is commonly retrogressed to actinolite , with small amounts of hematite and epidote in association with actinolite. Other trace minerals include rutile and zircon.

3.1.5 South Para Orthogneiss

A large body of granite gneiss occurs in the northern Houghton Inlier and is best exposed in the South Para Gorge. This rock is composed of up to 3-4 cm microcline augen in a groundmass of quartz, plagioclase, and biotite (Figure 4d). The biotite is commonly concentrated into domains which define the dominant foliation. Typical grain sizes of the groundmass are approximately 2-5mm. In most outcrops, plagioclase and biotite are weathered to clays, although extensive fresh outcrops occur in the South Para River. Magnetite is also present in trace amounts.

The South Para Orthogneiss is most commonly found in association with the biotite-sericite gneiss and sillimanite gneiss. In some areas the contact between these lithologies are high strain zones which parallel the dominant S_1 metamorphic fabric (see below). An intrusive contact is also preserved in many areas. This intrusive contact is best preserved with the biotite-sericite gneiss where migmatites, now deformed, occur with increasing leucosome abundance in proximity to the granite body.

The South Para Orthogneiss has been dated by Jagodzinski et al. (2017) as having a magmatic zircon U-Pb age of 1717 ±7 Ma, and preserve metamorphic zircon ages of 1632 ±4

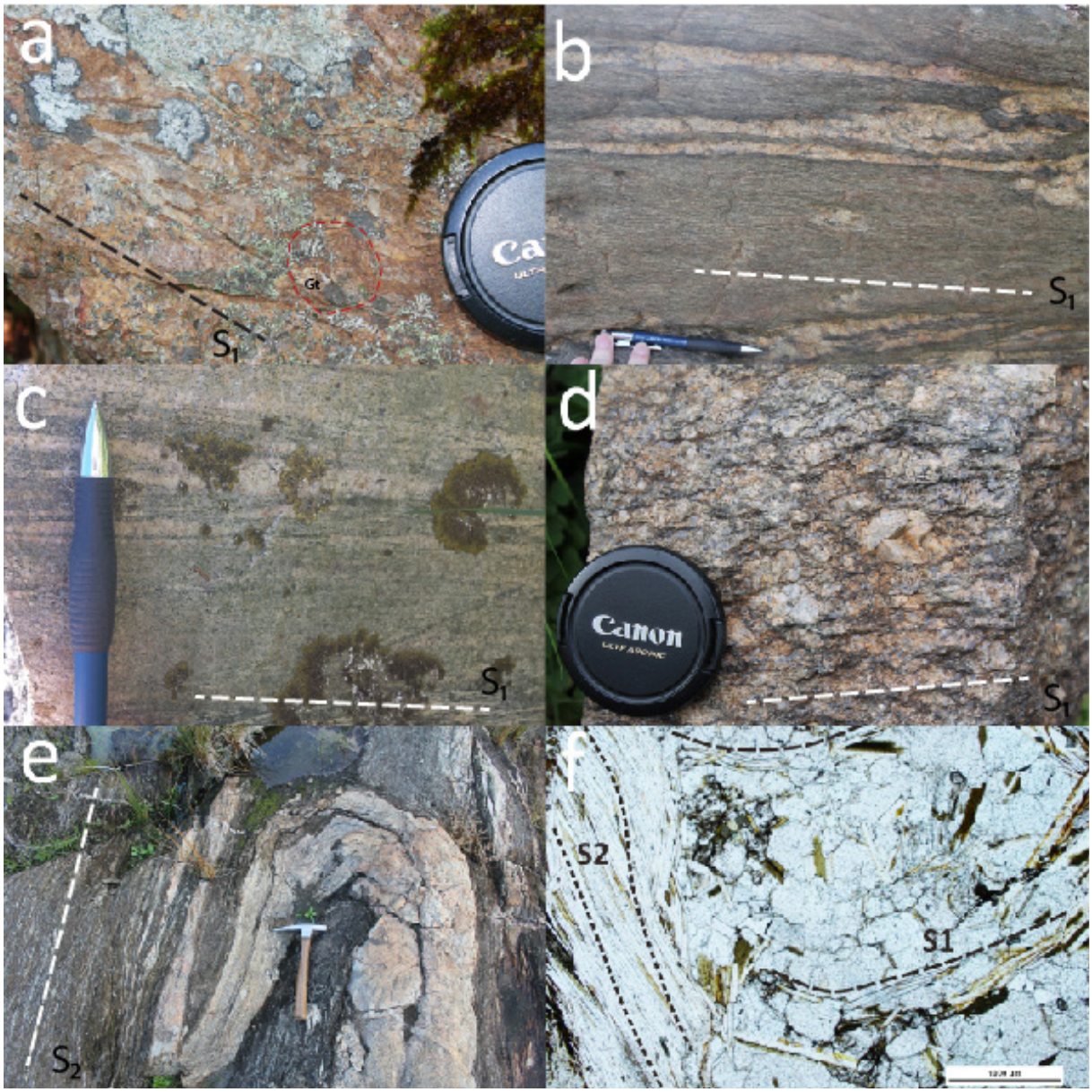

Figure 4: Photos of outcrops within the Houghton and Warren Inliers. a) Deeply weathered sillimanite gneiss in the Houghton Inlier showing mats of sillimanite (garnet absent). b) Biotite-sericite gneiss in the northern Houghton Inlier showing layer parallel leucosomes and a strong S_4 cleavage at an angle to the leucosomes. c) Calcsilicate Gneiss in the southern Houghton Inlier showing banding of feldspars and green diopside-actinolite. d) Granitic augen texture in the South Para Orthogneiss in the northern Houghton Inlier. e) Folded and boudinaged early pegmatite in the Warren Inlier. f) Photomicrograph of relict S_1 fabric overprinted by the dominant S_2 fabric in the Warren Inlier. Scale bar is 1000 µm.

Ma, 1609 ±5 Ma, and 1589 ±10 Ma. This unit was also interpreted to be the source of zircon in the stream sediment samples collected in the South Para River by Belousova et al. (2006), who identified zircon of magmatic origin recording a U-Pb age of 1718 ±8 Ma, consistent with the age identified by the in situ sample of Jagodzinski et al. (2017).

3.2 Warren Inlier Stratigraphy

3.2.1 Quartzofeldspathic gneiss

This lithology is only observed in the northwestern Warren Inlier, and is exposed in the South Para Gorge. This lithology is very similar to the quartzofeldspathic rocks found in the Houghton Inlier. Plagioclase dominates the mineralogy, with varying amounts of quartz that can make up to 50% of the rock. Minor biotite is present and creates a weak gneissic foliation. Grain sizes average 3-4mm and are homogeneous throughout all samples. Partial melting is not obvious in the limited exposure, although pegmatites have intruded this unit.

3.2.2 Biotite Migmatite Gneiss

This lithology is dominated by coarse grained biotite, quartz, plagioclase, and minor K-feldspar. Retrograde muscovite is also common but is not the dominant mica. A strong gneissic fabric is present in most outcrops defined by the segregation of the biotite from the quartzofeldspathic minerals (S_2, see below). This foliation is intensely folded in all exposures, and is described in detail below.

Some quartz rich layers occur up to 1 meter thick, and it is possible that these represent relict sedimentary layering. Infrequent amphibolites occur within this unit which appear to be parallel to the compositional layering. These amphibolites typically occur on the scale of 0.5-1 m thickness.

This unit contains leucosomes and intrusive pegmatites. The earliest of these are a series of strongly deformed pink K-feldspar rich pegmatites with aligned concentrations of biotite that forms a fabric (Figure 4e). A younger series of leucosomes and pegmatite veins parallel the dominant S_2 foliation (see below). Unlike the older pegmatites, the younger generation have white k-feldspar and minor muscovite, with no clear foliation. These leucosomes occur on the scale of 1-15 cm thickness throughout this unit, and are commonly aligned with the S_2 fabric.

3.2.3 Sillimanite-Muscovite Schist

This lithology dominates the eastern Warren Inlier and the fault block on the eastern side of the inlier which was previously defined as the Springfield Shear zone (Mills 1973). It is most commonly expressed as a coarse-grained muscovite schist, which overprints an older sillimanite-bearing assemblage. The muscovite-dominated retrogression is extensive and obscures older macroscopic structures. Minor fine grained (< 1mm) quartz and plagioclase occasionally form minor bands. Sillimanite occurs as small fine grained mats in areas where the muscovite overprint is not as extensive. In some areas in the eastern fault block, kyanite overprints the foliation of this unit. The kyanite usually forms unoriented masses, and is often weathered which gives it a pale green colour. Large bodies of pegmatite intrude this unit, which are described below. Tourmaline bearing assemblages commonly form halos around these minor intrusions.

3.2.4 Mount Crawford Granite Gneiss

This unit has been described in detail by previous workers, and is one of the better understood lithologies in the Barossa Complex (Mills 1963, Mills 1973, Preiss et al. 2008). This granite gneiss contains quartz, plagioclase, K-feldspar, muscovite, biotite, and minor apatite and zircon. Micas occur in varying amounts, with some areas being mica poor, while other areas are semi-schistose. Xenoliths of country rock occur frequently, up to several meters in size, and are usually muscovite or biotite schists with rare garnet. This unit was dated using U-Pb zircon geochronology as having an intrusive age of 812 ±6 Ma. It is interpreted to be the result of rift related magmatism (Preiss et al. 2008) and is associated with the development of the Adelaide Rift Complex. A strong foliation is present in this lithology defined by biotite and muscovite. This is typically a planar fabric with some minor crenulations, both of which formed during the Delamerian Orogeny.

3.2.5 Late Pegmatites

Throughout all the lithologies in the Warren Inlier a series of late pegmatites are present. These are typically dominated by quartz and K-feldspar, often with muscovite and common accessory minerals include beryl and tourmaline. These minor intrusions occur at varying scales with the largest in the central Warren Inlier measuring approximately 20 meters wide and over 50 meters in length. These pegmatites are largely undeformed and contain no discernable fabric. Pegmatites of identical minerlogy occur in the Neoproterozoic cover sequences, and are thus interpreted to have been generated during the Delamerian Orogeny.

3.3 Lithological Relationships and Correlations

Due to the poor outcrop in the majority of the Houghton Inlier, and to a lesser extent the Warren Inlier, the lithological relationships are often difficult to determine. Structual modification during the Palaeo- Mesoproterozoic and Palaeozoic also complicates the primary relationship of the lithological units. In spite of this complexity in both the Houghton and Warren Inliers the same general lithological sequence is evident. The major lithological difference between the two inliers is that the Warren Inlier has coarser grained retrograde minerals, which is not surprising as the Warren Inlier lies within a higher grade zone of the Delamerian Orogen.

In the Houghton Inlier, calcsilicate and quartzofeldspathic gneiss occur in the north and southwest areas of the inlier, and are structurally overlain by biotite-sericite gneiss. This gneiss then grades structurally upward into the sillimanite gneiss which makes up the majority of the inlier. Similarly in the Warren Inlier, quartzofeldspathic gneiss occurs in the northwest of the inlier and is structurally overlain by biotite migmatite, which grades into a muscovite-sillimanite schist. As such it is proposed that these lithologies correlate across the two inliers, as is summarised in the column in Figure 5. However, the lack of sedimenta-

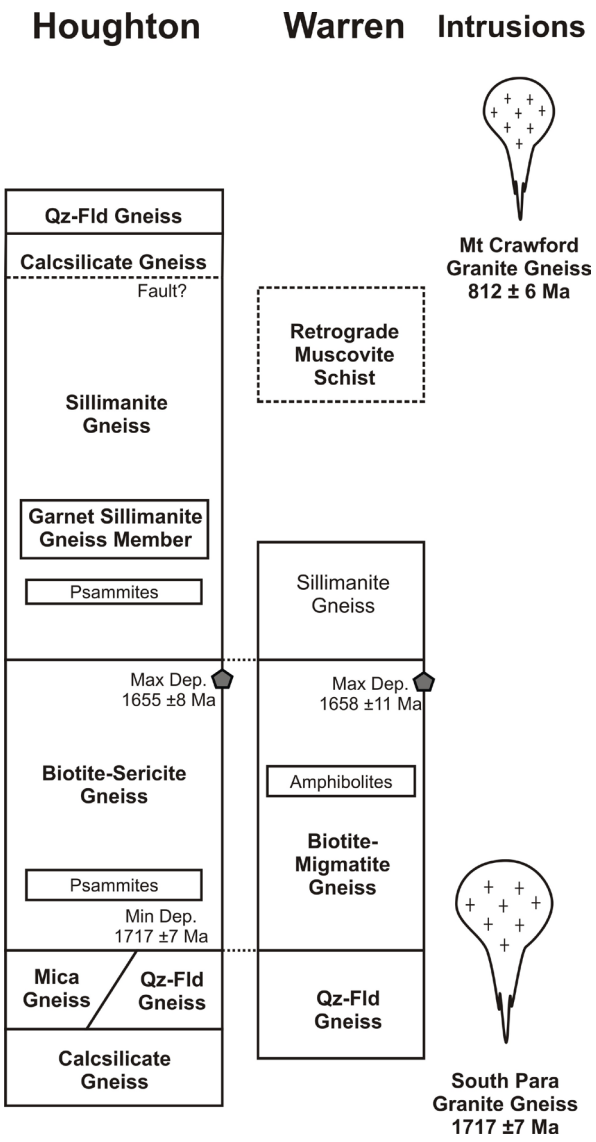

Figure 5: Summary of stratigraphy and correlations between Houghton and Warren Inliers, presented in the current structural orientation. The Calcsilicate at the top of the Houghton Inlier Column is the Kersbrook Calcsilicate. Quartzofeldspathic Gneiss abbreviated to Qz-Fld Gneiss. The approximate stratigraphic locations of samples analysed for detrital zircons by Jagodzinski et al. (2017) are marked on the columns with the determined age constraints.

ry younging indicators, such as cross bedding or grading, means that directly identifying the younging direction of these lithologies is not possible. Age constraints derived from zircon U-Pb geochronology and intrusive relationships suggest that the sedimentary pile is the correct way up (discussed below).

4. Structure and Metamorphism

Figure 6 shows a structural map of the Houghton and Warren inliers. Assessing the structural and metamorphic history of the Houghton and Warren inlier is made challenging by the sparse outcrop and degree of weathering, and the amount of structural and metamorphic reworking during the Cambro-Ordovician Delamerian Orogeny. Most outcrops in the Houghton Inlier appear to only preserve planar fabrics, and it is not until the inlier is considered at much larger scales that folding becomes evident. Microstructural analysis is hampered by the extensive weathering and sericisation which has largely obliterated the majority of primary minerals, making reliable interpretations difficult without extensive detailed work which is beyond the scope of this chapter. The sparse outcrop in many places also makes it likely that some structures such as minor faults or macroscopic folds are under-represented in the structural map shown in Figure 6.

4.1 Houghton Inlier

4.1.1 hD_1 event

The earliest deformation event recognised in the Houghton Inlier is the generation of a strong metamorphic fabric (S_1) which is pervasive in the majority of outcrops. This fabric is typically parallel or near-parallel to relict sedimentary layering. It is associated with the development of high grade minerals including sillimanite and garnet in metapelites. Layer parallel leucosomes also occur, and become more common in the southern part of the inlier. This suggests S_1 is associated with a high grade metamorphic event. In the areas where garnet and sillimanite are preserved, the sillimanite defines the fabric which wraps around large garnet porphyroblasts, implying garnet growth initiated relatively early in the deformation, or even pre D_1. This S_1 fabric is also consistently present within the South Para Orthogneiss, indicating that the D_1 event occurred after the intrusion of the granite protolith to the orthogneiss.

Minor shear zones parallel the S_1 fabric. These are best developed at the contact between different lithologies, in particular the South Para Orthogneiss and the biotite-sericite gneiss. It remains unclear whether these shears developed syn-D_1 or whether they developed at a later stage, exploiting the S_1 fabric.

4.1.2 hD_2 event

The second recognisable deformational event in the Houghton Inlier is a series of open to tight folds with axial traces that parallel the average trends of the S_1 fabric (Figure 6). These folds occur at large scales with wavelengths ranging 20 to 200 m. F_2 folds are best preserved in the area south of the Barossa Goldfields (Figure 6), where they form a series of S folds with long east limbs and short west limbs (Figure 8). Some examples also exist further south near the Millbrook Reservoir. It is likely these folds are much more common than have been mapped, and have not been identified due to sparse outcrop. Although the metamorphic fabric is further disturbed by larger F_3 structures (see below) the axial traces of these F_2 folds are consistently oriented parallel to the local trend of the S_1 fabric. The S_1 remains dominantly east dipping due to the short west limb of the D_2 folds, implying that the F_2 folds verge westward.

Orientations of the S_1 fabric across the Houghton Inlier (Figure 7a) cluster to show predominantly SE or NE dipping trends, which reflects a larger D_3 fold (see below), as well as some scatter of SW or NW dipping which are the result of F_2 folds. The red highlighted data on Figure 7a shows an example of F_2 folds from south of the Barossa Goldfields

in the northern Houghton Inlier with NE-SW trending axial traces, which plunge shallowly to the S-SE.

4.1.3 hD_3 event

The third deformation recorded in the Houghton Inlier caused large scale regional folding. The best example of this is the large ESE plunging open synformal fold which trends NW-SE through the central part of the inlier (Figure 6, Figure 8). Poles to S_1 foliations from the Houghton Inlier show a spread around a NW-SE axis, with a shallow plunge to the SE (Figure 7a).

A second D_3 fold occurs in the south of the Inlier, with an antiform near Inglewood and Torrens Gorge trending approximately NNW-SSE (Figure 6). A stereonet considering this fold separately to the main body of the Houghton Inlier (Figure 7b) shows a spread of poles to S_1 fabric about a NE-SW axis. It is likely that the orientation of this antiform has been disturbed by the numerous later faults in the area.

During either the D_2 or D_3 events, pegmatites intruded in the northern part of the inlier. These rare intrusions cross cut the S_1 gneissic fabric in the South Para orthogneiss. They are also partially offset by small faults and appear otherwise undeformed. This would suggest that they belong to either the D_2 or D_3 generation of events. With limited cross cutting relationships, it is difficult to assign them to a specific event.

4.1.4 hD_4 event

The final phase of deformation recorded in the Houghton Inlier is the development of the large overturned anticline in the core of which the inlier is exposed. The overturned western limb of this anticline is faulted out. This anticline is defined by the basement-Adelaidean relationship. Previous workers have attributed this structure to the D_1 phase of the Delamerian Orogeny (Offler and Fleming 1968).

Minor faulting associated with this stage of deformation is common and is often associated with voluminous quartz veins and hydrous alteration. Zones of sericitic alteration commonly occur around quartz veins, and where this occurs, any older structure or mineralogy is completely overprinted. The quartz veins frequently contain intact cavities with prismatic quartz crystals, which suggests that they have not experienced any major deformational event since their formation. In the northern Houghton Inlier, these quartz veins may be mineralised, and have historically been mined for gold (Brown 1885).

In the more micaceous units such as the biotite – sericite gneiss, a strong steeply east dipping cleavage is commonly developed, and can be traced into the overlying Neoproterozoic units in areas where the unconformity is intact (Figure 7c). This cleavage obliterates the earlier fabrics in some areas, giving some rocks a slate or phyllite-like appearance. Previous workers have referred to such rocks and structures as 'phylonnites' – phyllite-like rocks formed through retrogression (Talbot 1963). This feature is particularly common in the southernmost areas of the inlier where small D_4 faults are abundant. Webb (1953) mapped many small to regional scale folds in this southern part of the inlier using cleavage-layering relationships as the hinges of folds were rarely obvious. As the cleavage is strongest in the most retrogressed rocks, the folds defined by this method are attributed to D_4 deformation.

4.2 Warren Inlier

4.2.1 wD_1 event

The D_1 event in the Warren Inlier is largely not preserved. Foliations present in some pegmatites (Figure 4e) are the only occurrences of this early fabric identified in outcrop. These pegmatites have been extensively structurally reworked, making any interpretation of its significance difficult. Relict features in thin section, first identified

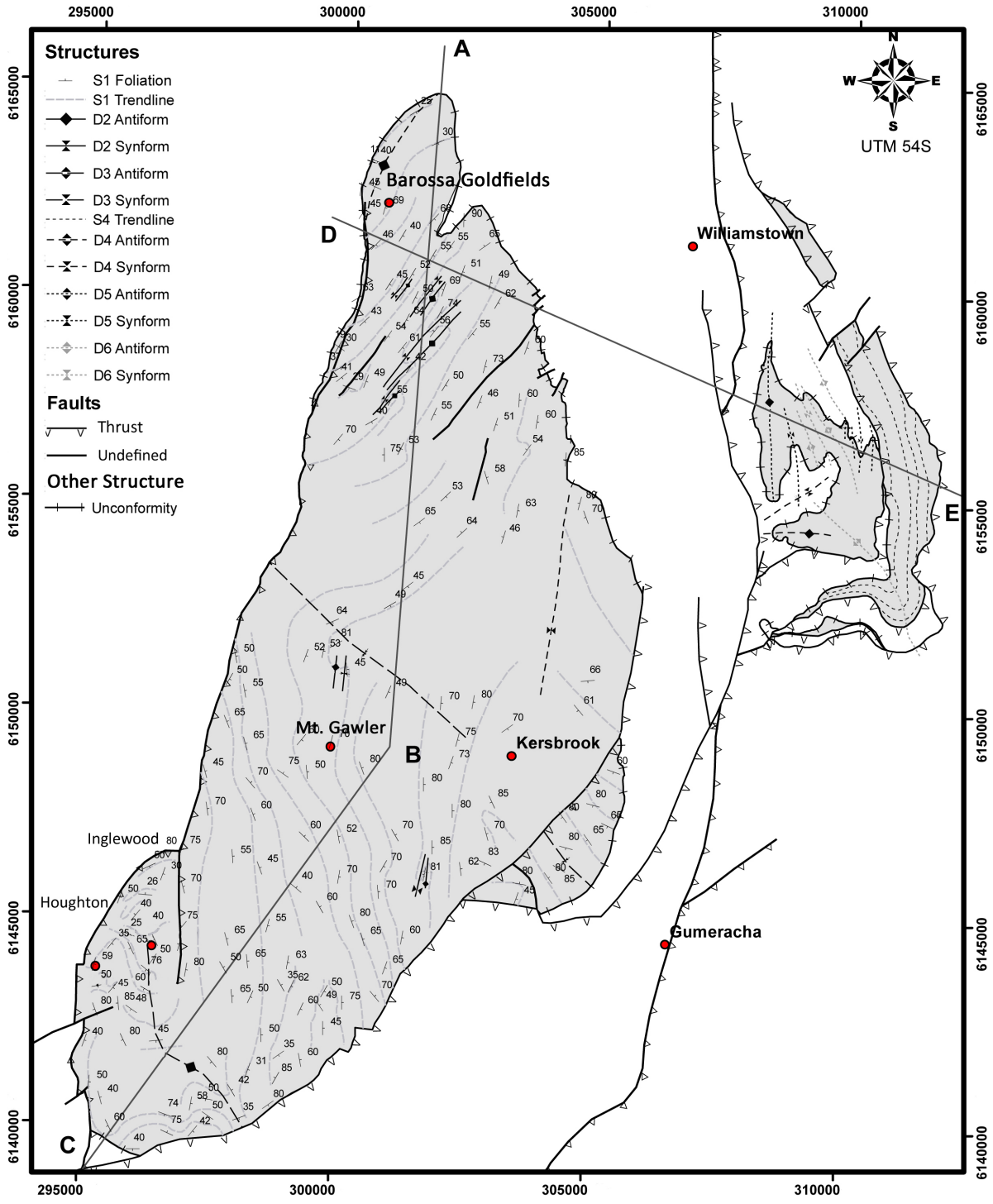

Figure 6: Map of the Houghton and Warren Inliers showing Proterozoic and Phanerozoic deformation. Cross section lines for Figure 8 marked A-C, D-E.

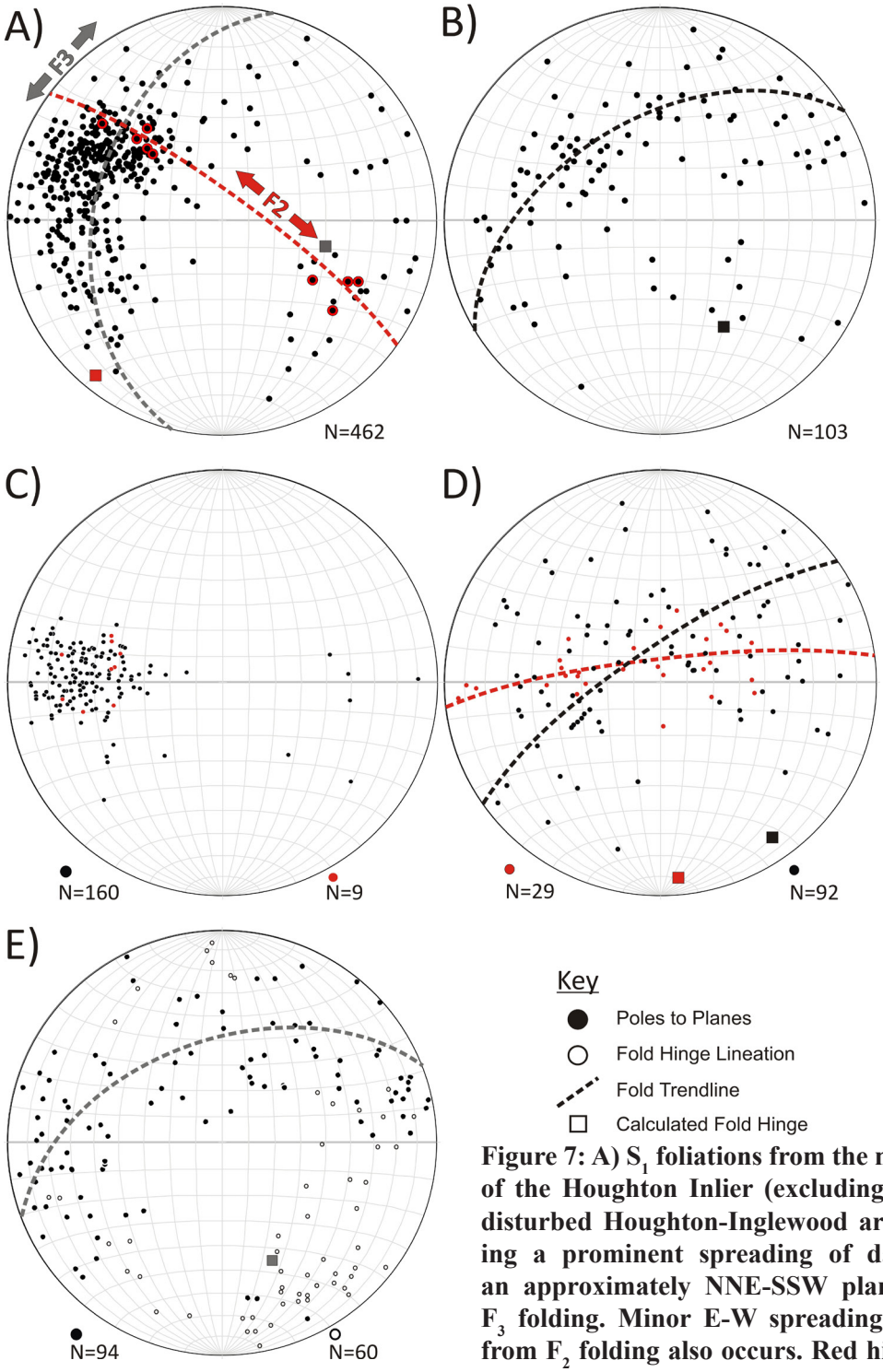

Figure 7: A) S_1 foliations from the main body of the Houghton Inlier (excluding the fault disturbed Houghton-Inglewood area) showing a prominent spreading of data along an approximately NNE-SSW plane due to F_3 folding. Minor E-W spreading resulting from F_2 folding also occurs. Red highlighted data from selected F_2 Folds in the Northern Houghton Inlier. B) Poles to S_1 fabric from the Inglewood-Torrens Gorge area showing spreading around a NE-SW trending plane due to D_3 folding. C) Poles to D_4 cleavage in the Houghton Inlier showing a strong unimodal cluster. Red points are from cleavage planes in the overlying Neoproterozoic sedimentary rocks. D) Poles to S_2 fabric from the Warren Inlier. Data highlighted red is from the northwest of the inlier showing folding along an E-W trending plane of a D_5 fold. Black data from the eastern part of the inlier shows folding along a NE-SW trending plane of the D_6 folds. E) Poles to F_5 fold axial planes being spread over a NE-SW trending plane due to D_6 folding. Unfilled symbols shows hinge lineations to these folds clustering in the SE with some spread.

by Mills (1973), show the remnants of an early S_1 fabric perpendicular to the dominant S_2 (Figure 4f). It is evident that the S_2 is a well developed crenulation cleavage. However the without further observable features of the S_1 fabric in the Warren Inlier, this event remains undefined.

4.2.2 wD_2 event

A well developed S_2 fabric is the dominant fabric in the Warren Inlier, and is easily identifiable through the segregation of micaceous and quartzofeldspathic minerals in the biotite migmatite, or as the dominant schistocity in the muscovite schists. In the biotite migmatite unit, coarse grained muscovite occurs in alignment with the mineral segregation layering, indicating it grew during this segregation process. In some outcrops, pegmatites are tightly folded with axial planes parallel to the S_2 fabric, and is some cases are boudinaged within this fabric. In the muscovite schists of the eastern Warren Inlier this fabric continues into the Mt. Crawford Granite Gneiss, indicating that it developed after 812 Ma, and therefore is likely to have formed during the Delamerian Orogeny.

4.2.3 wD_3 event

During this event upright open folds were produced on the regional scale, as can be seen clearly in the north-west of the inlier (Figure 6, 7d). Mesoscopic folds of this generation occur commonly on the scale of 5-10cm and are also extensive throughout the biotite migmatite. These folds are typically open upright folds with north-south trending axial traces and are frequently refolded by the later wD_4 folds (Figure 7e).

4.2.4 wD_4 event

The final stage of deformation in the Warren Inlier is the development of NW-SE trending folds which commonly refold the folds of the D_3 deformation (Figure 7e). These are more prevalent in the eastern areas of the inlier (Figure 6) and produced tight folds with east dipping axial planes (Figure 8). Crenulations of this generation overprint the folds of the wD_2-wD_3 events, and are not reoriented by later folding events.

4.3 Correlation of structures

In the Houghton Inlier, the S_4 cleavage continues into the Neoproterozoic cover and therefore formed during the Delamerian Orogeny. The Delamerian-aged structures to the west of the Willimastown Meadows Fault are predominantly Delamerian D_1, characterised by folding and thrust faulting which generated the faultbound anticline which exposes the Houghton Inlier (Offler and Fleming 1968). Delamerian D_2 and D_3 structures are largely absent from this zone, and without evidence for additional deformation, the S_4 cleavage in the Houghton Inlier is interpreted to correlate with the Delamerian D_1 deformation phase.

The structures in the Neoproterozoic metasedimentary rocks that overlie the Warren Inlier were described in detail by Mills (1973), allowing for an easy comparison between the structural elements of the basement and cover. In the overlying metasediments a low angle foliation associated with the growth of coarse grained muscovite in the pelitic members of the lower Aldgate Sandstone is attributed to the earliest phase of the Delamerian Orogeny. A similarly oriented low angle fabric also occurs in other areas of the Delamerian Orogen, such as in the Rathjen Gneiss (Oliver and Zakowski 1995, Foden et al. 1999). The S_2 fabric in the Warren Inlier appears to be a low angle fabric at larger scales. The folds preserved within this S_2 fabric mimic the open upright shape of the Delamerian D_2 and D_3 folds in the Neoproterozoic cover (Figure 8). This, in addition to being largely defined by coarse muscovite overprinting an older fabric, suggests that the S_2 fabric in the Warren Inlier correlates to Delamerian S_1 fabric observed in the overlying sediments. This consequently would make the S_2 fabric observed in the Warren Inlier an S_4 fabric in the overall context

Table 1: Correlation of structural generations between the Houghton and Warren Inliers

	Proterozoic (Olarian?) Orogeny	Delamerian Orogeny	Houghton Inlier	Warren Inlier	**Final Basement Nomenclature**
Oldest	D_1	-	hD_1/S_1	wD_1/S_1	**D_1**
	D_2	-	hD_2/S_2	-	**D_2**
	D_3	-	hD_3/S_3	-	**D_3**
	-	D_1	hD_4/S_4	wD_2/S_2	**D_4**
	-	D_2	-	wD_3/S_3	**D_5**
Youngest	-	D_3	-	wD_4/S_4	**D_6**

of the northern Barossa Complex.

The S_4 fabric of the Warren Inlier is subsequently folded by two further generations of Delamerian-aged deformation, and the folds observed in the Warren Inlier from this time (wD_3, wD_4) can be traced into the Neoproterozoic cover. These are mapped as Delamerian D_2 and D_3 folds by Mills (1973), and thus makes them D_5 and D_6 folds relative to basement.

A summary of structural nomenclature and correlations is given in Table 1. The nomenclature used in the cross sections in Figure 8 is the final overall nomenclature for the Barossa Complex.

5. Discussion

5.1 Protoliths to the Barossa Complex Metasediments

The proposed stratigraphic column for the northern Barossa Complex (Figure 5) shows a succession of calcsilicate and quartzofeldspathic gneiss structurally underlying biotite sericite gneiss which grades into sillimanite gneiss, before a return to quartzofeldspathic and calcsilicate assemblages. The protolith to the calcsilicate gneiss was likely a marl or other carbonate cemented siliciclastic sediment. The calcsilicate gneiss in the Houghton Inlier is always found in association with quartzofeldspathic gneiss. The absence of biotite or other micaceous minerals in the quartzofeldspathic gneiss is suggestive of a low clay or silt content in the protolith, making the precursor a well sorted quartz-feldspar arenite, and is reflective shallow water conditions. The biotite-sericite gneiss and sillimanite gneiss are indicative of psammopelitic to pelitic protoliths which likely reflects a gradational change in depositional setting, such as a marine incursion. Psammitic layers of various sizes are also common throughout these lithologies, which may indicate minor environmental changes such as storm surge or turbidite sequences. These units are overlain by a further calcsilicate and quartzofeldspathic assemblage, indicating a return to shallow water environments.

Similar sequences of calcareous to pelitic sediments are also observed in other Proterozoic sequences throughout Australia, and commonly reflect depositional settings such as continental shelf (e.g. Parker and Lemon 1982, Dirks 1990, Szpunar et al. 2011) or rift basins (e.g. Conor and Preiss 2008, Maidment et al. 2013, Tucker et al. 2015). One notable absence from the stratigraphy is the presence of volcanic unnits, as may be expected in a rift setting. While minor

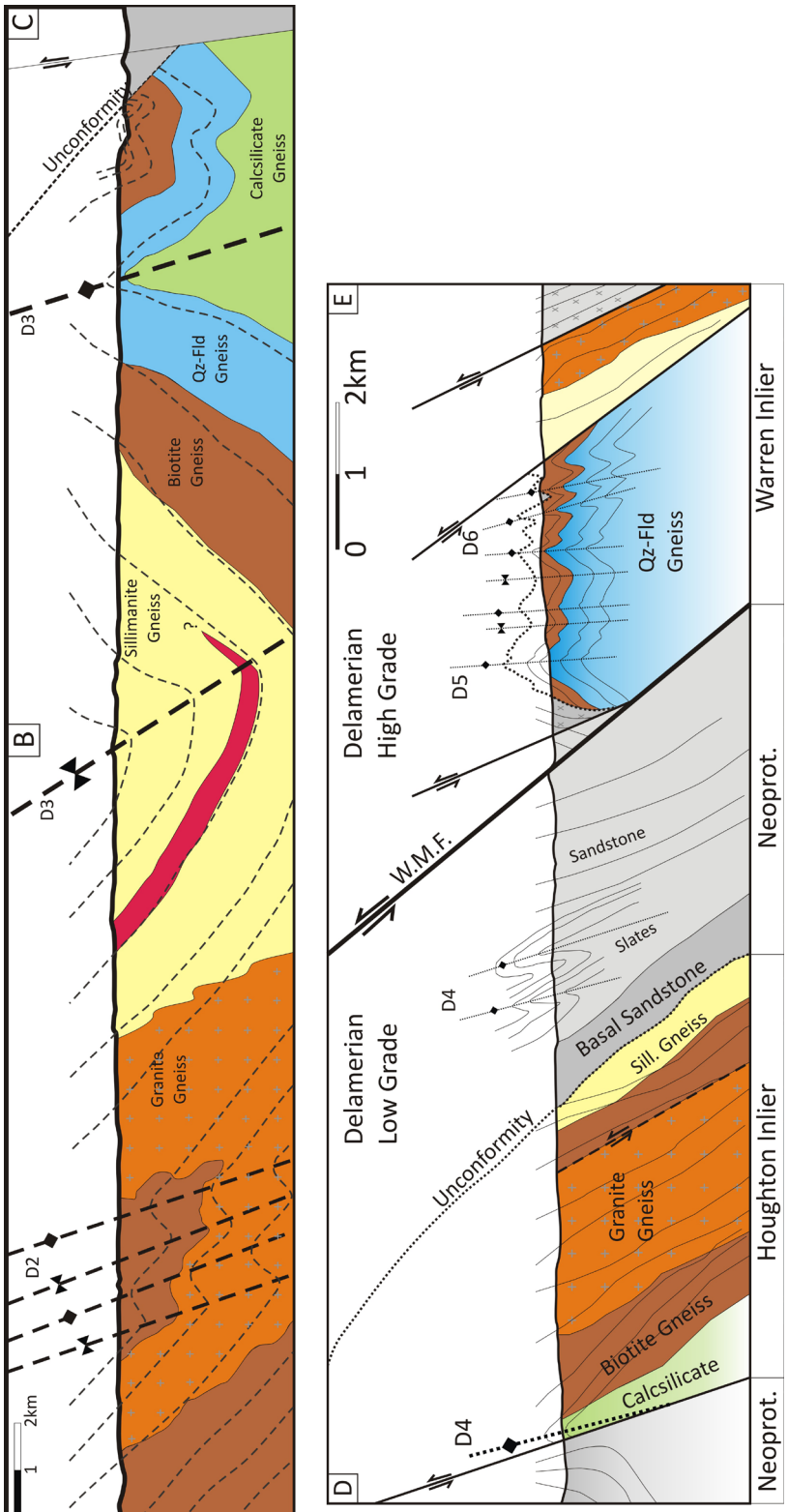

Figure 8: Cross sections of the Houghton and Houghton-Warren Inliers. The North-South (A-C) section through the Houghton Inlier shows the Proterozoic deformation features as the S_1 fabric is deformed by D_2 and D_3 folds. The East West transect through the Houghton and Warren nliers (D-E) shows the deformation associated with the Delamerian Orogeny with D_4 folds dominant in the low grade zone to the west, and D_5-D_6 folds dominating the deformation in the Warren Inlier.

occurrences of amphibolite in the Warren Inlier indicate some mafic magmatism, the structural reworking of this inlier make it impossible to determine whether these represent syn- or post depositional magmatism.

The lack of preserved sedimentary structures makes assessing the depositional tectonic setting difficult. A gradual change in depositional energies indicates is apparent, which is reminiscent of a marine setting. The meta-carbonate sequences are also suggestive of a marine shelf type setting (Grotzinger 1989). The transition from siliciclastic-carbonate sediments to clay rich sediments and back to siliciclastic-carbonate sediments is consistent with a setting that evolved initially to a deep water setting before returning to a shallow water environment.

5.2 Constraints on depositional timing

The depositional timing of the sedimentary protoliths to the Barossa Complex has been examined by (Jagodzinski et al. 2017). The South Para Orthogneiss records a magmatic zircon U-Pb age of 1717 ±7 Ma and intrudes the biotite-sericite gneiss and sillimanite gneiss in the northern Houghton Inlier. However, two samples from the biotite-sericite gneiss yielded maximum depositional ages of 1707 ±5 Ma and 1655 ±8 Ma. These age constraints contradict the preserved field relationships. The maximum depositional age (MDA) of the biotite sericite gneiss at 1707 ±5 Ma is significantly younger than the crystallisation age of the granitic gneiss which intrudes that unit. The biotite-sericite gneiss sample comes from a sample adjacent a sheared boundary between the South Para Orthogneiss and the biotite-sericite gneiss, while more regionally, an intrusive contact is apparent. The maximum depositional age of 1707 ±5 Ma was calculated from only two grains, and may not be a representative MDA as these grains may have been partially reset during one of the multiple subsequent thermal events. Therefore, a more reliable constraint is the intrusive relationship which indicate the protolith to the biotite-sericite gneiss is older than 1717 ±7 Ma.

The sample yielding a maximum depositional age of 1655 ±8 Ma comes from the southern Houghton Inlier from where the biotite-sericite gneiss transitions into the sillimanite gneiss. In the northern Houghton Inlier, the sillimanite gneiss occurs in contact with the South Para Orthogneiss. However, the contact is not directly observed between these two units and may be tectonic or unconformable. The approximately 70 m.y. difference between the lower and upper age constraints of the biotite-sericite gneiss may be reflecting a stratigraphic break which is now unrecognisable due to metamorphism. If a now obscured unconformity exists within the biotite sericite gneiss, this would provide an opportunity for the granitic precursor to the South Para Orthogneiss to be exposed and unconformably overlain by the protolith to the sillimanite gneiss in what is now exposed as the northern Houghton Inlier. Irrespective, the age constraints demonstrate deposition of the protoliths to the Houghton Inlier initiated prior to 1717 ±7 Ma and continued until at least 1655 ±8 Ma. These constraints also show that the structurally lowest part of the biotite-sericite gneiss is older than the structurally overlying parts of the unit and means that the overall stratigraphic sequence is the right way up.

In the Warren Inlier, a sample of the upper biotite migmatite gneiss yielded a MDA of 1658 ±11 Ma. The two younger MDAs of c. 1655 Ma strengthen the correlation of the biotite sericite gneiss in the Houghton Inlier and the biotite migmatite in the Warren Inlier. Throughout the other inliers of the Barossa Complex, detrital zircon maximum depositional ages range between c. 1700-1650 Ma (Jagodzinski et al. 2017).

5.3 Metamorphism and deformation

Three Palaeo-Mesoproterozoic deformation

phases are recorded in the northern Barossa Complex. The earliest of these formed the dominant S_1 metamorphic fabric. S_1 forms a low angle to minor psammitic layers in the biotite-sericite gneiss, which are interpreted to represent sedimentary beds of differing composition. A possible origin for such metamorphic fabrics is a period of extension during or after deposition and prior to any contractional deformation, such as has been proposed for the low angle S_1 fabrics observed in the Willyama Supergroup in the Curnamona Province (Gibson et al. 2004, Forbes et al. 2005) as well as other metamorphic regions (e.g. Lee et al. 1987, Fowler and Hassan 2008). The inference that the D_1 event may have been extensional is consistent with the stratigraphy being the right way up, as extension preserves the stratigraphic order (Hand et al. 1999, Tucker et al. 2015).

Metamorphic conditions calculated by Morrissey et al. (2013) for metapelites in the Houghton and Myponga inliers gave peak metamorphic conditions of 800-870° C and 8-9 kbar, which suggests that if D_1 was extensional it must have been produced by deep burial. While burial to supracrustal depths of >25km is traditionally considered to reflect crustal thickening, Tucker et al. (2015) showed that deep rift basins can accommodate >25km of sediment, meaning that deep burial is not necessarily related to crustal thickening. The S_1 fabric in the pelitic assemblages of the Houghton Inlier is defined by sillimanite, which indicates that peak metamorphism occurred during the formation of S_1 (M_1).

The D_2 folds mapped in the northern Houghton Inlier deform the S_1 fabric into a series of west verging folds (Figure 8). It is also possible that these folds represent parasitic folds on a larger fold structure (i.e. major antiform to the west) which is obscured by Neoproterozoic cover. In either case, D_2 shortening was oriented approximately E-W.

The D_3 folds in the Houghton Inlier preserve open upright folds with axial traces trending approximately NW-SE, indicating compression due to a NE-SW oriented primary stress. The calculated plunge of the larger F_3 fold in the central Houghton Inlier is 40° towards 95°. This plunge angle is comparable to the dip of the overlying Neoproterozoic sediments, which ranges from 40° to 70° towards the east-NE. This indicates that the original plunge of this fold was originally gently to moderately west plunging.

5.4 Metamorphic age constraints

Several works have investigated the timing of metamorphism in the Barossa Complex and identified a range of metamorphic zircon and monazite ages spanning c. 1630 Ma to 1550 Ma (Belousova et al. 2006, Szpunar et al. 2007, Morrissey et al. 2013, Jagodzinski et al. 2017) . The earliest stage of metamorphic mineral growth has been identified in zircon at c. 1630 Ma (Belousova et al. 2006, Jagodzinski et al. 2017), with two subsequent pulses at c. 1610 Ma and 1590 Ma (Szpunar et al. 2007, Jagodzinski et al. 2017). All three ages are recorded in zircon across all of the inliers in the Barossa Complex (Jagodzinski et al. 2017). The ages of monazite have been found to largely record a later stage of metamorphism between c. 1580 Ma and 1550 Ma (Szpunar et al. 2007, Morrissey et al. 2013). In the southern Myponga Inlier, Szpunar et al. (2007) identified metamorphic monazites aged 1579 ± 7 Ma in age from a coarse grained migmatitic garnet-sillimanite metapelite granulite. Essentially identical ages of 1581 ±13 Ma and 1578 ±9 Ma were also recorded in monazite in the southern Myponga Inlier by Morrissey et al. (2013). Younger ages of 1563 ±9 Ma and 1566 ±9 Ma were identified in the Myponga Inlier and were suggested to relate to retrograde shear zone development (Morrissey et al. 2013). In the southern Houghton Inlier, Morrissey et al. (2013) obtained monazite ages of 1547 ±18 Ma and 1555 ±10 Ma which overlap within error of the youngest ages from the Myponga Inlier, and attributed these ages to post peak metamorphism which produced (now weathered) cordierite during high-T

decompression.

A post deformation pegmatitic granite from the southern Myponga inlier preserves a magmatic crystallisation age of 1580 ±4 Ma (Jagodzinski et al. 2017), indicating deformation had ceased by this time. It is unclear which of the zircon and monazite ages relate to the peak granulite facies conditions modelled by Morrissey et al. (2013). However, as fabrics peak minerals in the Houghton and Myponga inliers define the S_1 fabrics, peak metamorphism must be older than 1580 Ma.

5.5 Tectonic relationships

The preceding sedimentary, metamorphic, and deformational framework builds a picture of the formation and development of the Barossa Complex. A summary of the following framework is provided in the timespace plot in Figure 9, which encompasses the geological regions highlighted in Figure 1.

The depositional timing constraints indicate that deposition of the sedimentary protoliths to the Barossa Complex initiated prior to 1717 ±7 Ma and continued until at least 1655 Ma (Jagodzinski et al. 2017). This is comparable to Palaeoproterozoic basins in the central and northern Gawler Craton, and in the Curnamona Province (Page et al. 2005a, Payne et al. 2006, Hand et al. 2007, Howard et al. 2011). The earliest of these occur in the eastern Gawler Craton with the Darke Peak group. This group was deposited synchronously with felsic volcanic rocks at ca. 1865 Ma, which were interpreted to be the result of rift related magmatism (Szpunar et al. 2011). At 1850 Ma a series of dominantly granitoid igneous bodies were intruded synchronous with the Cornian Orogeny (Schwarz 2003, Reid et al. 2008a). This magmatic suite is proposed to have formed in a back arc or far field back arc setting before a buoyant collider jammed the subduction zone, which switched the regime from extensional to compressive following the emplacement of the batholith (Reid et al. 2008a). Deposition continued through the period 1800-1730 Ma, in a series of extensional basins which get progressively younger to the east (Kositcin 2010). The Cleve Group was deposited between 1790-1730 Ma on the eastern Eyre Peninsula (Szpunar et al. 2011, Lane et al. 2015). During this interval the protolith to the Broadview Schist and the associated bimodal Myola Volcanics were deposited at approximately 1790 Ma on the northeastern Eyre Peninsula (Fanning et al. 1988, Parker et al. 1993, Szpunar and Fraser 2010). Further north in the Gawler Craton in the Peake and Denison block, deposition also occurred between 1800 – 1780 Ma in association with bimodal magmatism, which is interpreted to represent a rift or backarc setting (Ross 2011). Much of the Olympic Domain which makes up the eastern part of the Gawler Craton, including the Wallaroo Group and its equivalents, were similarly deposited in association with bimodal magmatism during the interval 1760-1740 Ma (Fanning et al. 1988, Conor 1995, Zang 2002, Cowley et al. 2003).

Between 1730-1690 Ma, the Kimban Orogeny occurred throughout the eastern and northern Gawler Craton (Hand et al. 2007, Payne et al. 2008). In the Eastern Gawler Craton the Kimban Orogeny strongly metamorphosed and deformed the Palaeoproterozoic basins in the eastern Gawler Craton and the Neoarchean basement which they overlie (e.g. Vassallo and Wilson 2002, Dutch et al. 2008, Reid et al. 2008b, Lane et al. 2015).

Further to the east, and northeast of the Barossa Complex, the Willyama Supergroup was deposited between 1720-1640 Ma (e.g. Raetz et al. 2002, Page et al. 2005a, Stevens et al. 2008). The onset of deposition in the Willyama Supergroup is synchronous with the Kimban Orogeny. The lower Willyama Supergroup (rift phase) is characterised by volcanism and relatively shallow water depositional environments (Conor and Preiss 2008). The lower Willyama Supergroup has been proposed by many workers to have been deposited in a continental or back arc rift (Willis

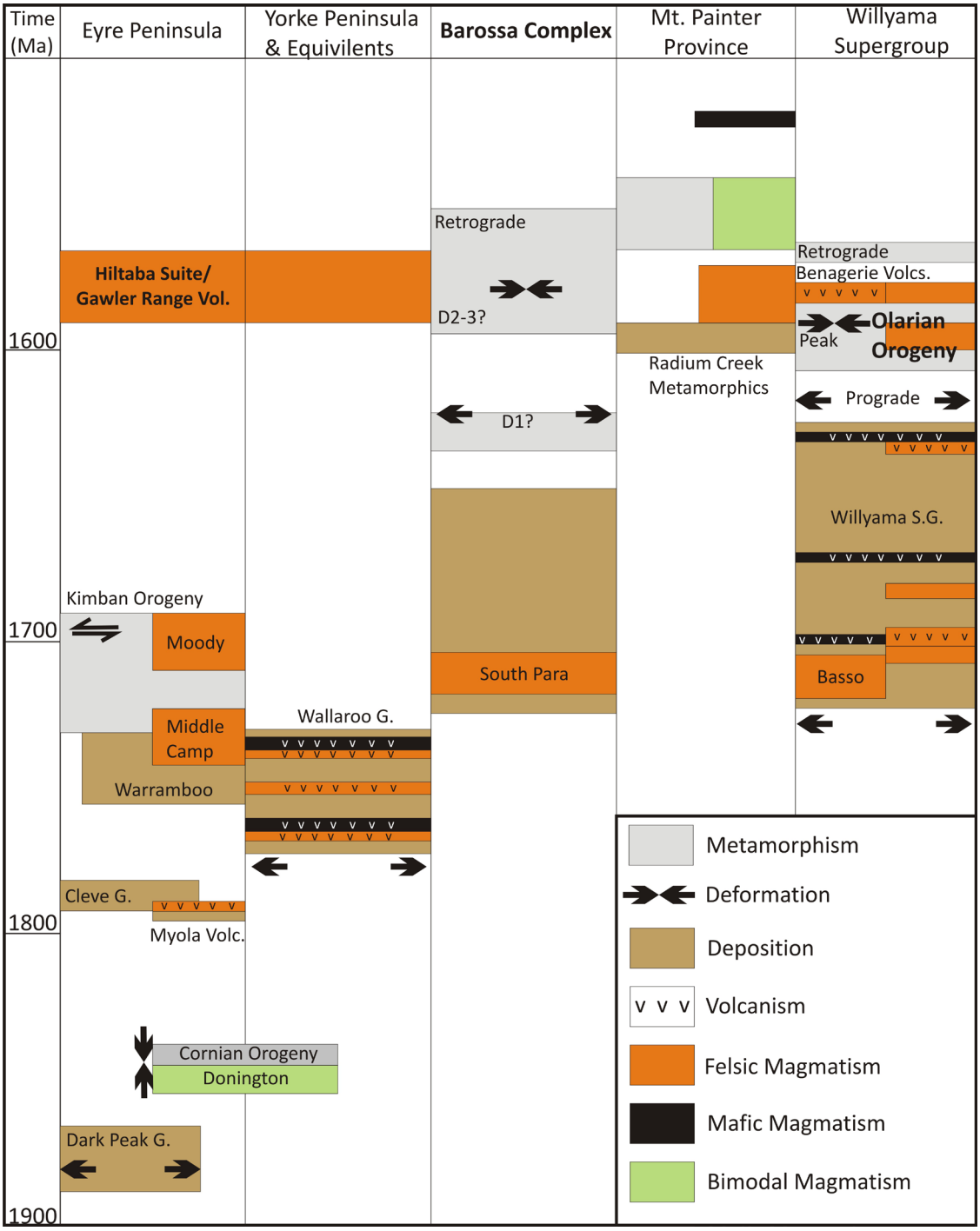

Figure 9: Time-Space plot of the Eastern South Australian Craton Provinces. Modified after Kositchin (2010) and references therein, Szpunar and Fraser (2010), Szpunar et al. (2011), Armit et al. (2012), Armit et al. (2014), Lane et al. (2015), Jagodzinski et al. (2017).

et al. 1983, Stevens et al. 1988, Rutherford et al. 2006, Conor and Preiss 2008, Forbes et al. 2008). The upper Willyama Supergroup represents the sag phase of deposition and contains no volcanics and an apparent switch to a more juvenile sediment source after 1655 Ma (Barovich and Hand 2008).

Although the driving mechanism behind the Kimban Orogeny remains ambiguous, the timing of deposition in the Barossa Complex

also coincides with the onset of the Kimban Orogeny. One possible interpretation is that the Barossa Complex was deposited into the foreland of the Kimban Orogen. However, the intrusion of the South Para Orthogneiss at 1717 ±7 Ma suggests that the Barossa Complex was located in a more active tectonic setting at this time, such as an extension of the Willyama rift system. Detrital zircons in the Barossa Complex contain age peaks corresponding to the c. 1760-1730 Ma Wallaroo Group volcanics, as well as volcanic ages found in syn-depositional Willyama Supergroup volcanic units from between 1710-1680 Ma (Jagodzinski et al. 2017). The Barossa Complex and Willyama Supergroup detrital zircon age spectra contain essentially the same age peaks, with the exception of the 1730 Ma and 1765 Ma peaks identified in the Barossa Complex (Jagodzinski et al. 2017). This, in addition to their similar depositional age constraints, has been interpreted to indicate that the Barossa Complex and Willyama Supergroup basins were contiguous during the late Palaeoproterozoic (Jagodzinski et al. 2017).

Several authors have previously suggested possible links between the Willyama Supergroup and the Mount Isa rift basins in northern Australia (e.g. Giles et al. 2004, Page et al. 2005b, Betts and Giles 2006). If this notion is valid, it indicates a continental scale system of rift basins developed on the eastern margin of Australia between 1720-1640 Ma (Giles et al. 2002, Forbes et al. 2008). This scenario could easily extend to accommodate rifting on the south-eastern margin of the Gawler Craton, including creating the setting for the proto-Barossa Complex. A rift related depositional setting for the Barossa Complex was also suggested by Kositcin (2010).

The timing and nature of metamorphism of the Barossa Complex was discussed in detail by Morrissey et al. (2013), who described the similarity between the high geothermal gradient metamorphic conditions in the Barossa Complex and other regions of eastern Proterozoic Australia during the period 1630-1550 Ma. It was suggested in that study that a common tectonic regime drove that period of metamorphism and orogenesis. The low angle S_1 fabrics in the Barossa Complex with no folds of the same structural generation are suggestive of an extensional setting. In the Willyama Supergroup, several authors have similarly suggested that metamorphism may have initiated prior to the ca. 1600 Ma Olarian Orogeny possibly as early as 1650 Ma (Forbes et al. 2005, McFarlane and Frost 2009). The generation of the low angle metamorphic fabrics in the Willyama Supergroup have also been attributed to extension (Forbes et al. 2005, Forbes et al. 2008, McFarlane and Frost 2009).

Between 1620-1580 Ma, deformation, metamorphism, and igneous activity were widespread across the Gawler Craton and Curnamona Province. In the Gawler Craton high grade metamorphism occurred in the north, with high and ultra-high temperature conditions recorded around Mt. Woods and the Coober Pedy Ridge between 1615 and 1590 Ma (Forbes et al. 2011, Cutts et al. 2011).

The Olarian Orogeny in the Curnamona Province caused widespread metamorphism and magmatism between 1610-1580 Ma (e.g. Raetz et al. 2002, Page et al. 2005a, Forbes et al. 2005, Rutherford et al. 2007, Clark and Hand 2010). This event is attributed to subduction leading to collision with another continental mass or island arc (Forbes et al. 2008).

Metamorphism and retrograde metamorphism is recorded in the northern Gawler Craton and Curnamona Province between 1570-1540 Ma (Rutherford et al. 2007, Forbes et al. 2012). In the Gawler Craton this event is termed the Kararan Orogeny (Hand et al. 2007). While higher grade metamorphism occurred in the northern Gawler Craton at approximately 1560 Ma

(Hand et al. 2007, Fanning et al. 2007). Exhumation is also identified in the Mt. Woods region in the northeast of the craton between 1590-1530 Ma (Forbes et al. 2012). In the northwestern Curnamona Province, the protoliths to the metasediments of the Mount Painter Inlier were deposited at 1590 Ma and were intruded and deformed during the interval 1585-1555 Ma (Armit et al. 2012). Retrograde metamorphism has also been identified in the Willyama Supergroup between 1570-1550 Ma (Rutherford et al. 2007). The suggested retrograde metamorphic ages in the Barossa Complex between 1560-1550 Ma (Morrissey et al. 2013) coincides with the timing of the Kararan Orogeny, metamorphism in the Mount Painter Province, and post peak retrogression in the Willyama supergroup, and may represent a widespread exhumation event driven by the Kararan Orogeny.

6. Conclusions

Deposition of calcsilicate, pelite, and psammopelite protoliths to the Barossa Complex occurred between 1720-1650 Ma, in one of a series of basins that developed on the eastern margin of the Gawler Craton through the Palaeoproterozoic. The depositional timing of the Barossa Complex protoliths correlates to the deposition of the Willyama Supergroup in the Curnamona Province, and it is likely that the two regions were once part of a contiguous basin on the eastern margin of the Gawler Craton.

High-grade metamorphism (800^{o}C, 8-9 kbar) was synchronous with the development of a low angle metamorphic fabric that likely formed between 1630-1600 Ma during extension. The S_1 fabric was deformed in two subsequent stages during the Palaeo-Mesoproterozoic; initially in an east-west compressional regime, and subsequently in a northeast-southwest directed compressional regime. These deformational events are interpreted to have occurred between 1590-1550 Ma, with the period of 1560-1550 Ma attributed to post peak retrogression. The timing of these events corresponds to the Kararan and Olarian orogenies in the Gawler Craton and Curnamona Province. The Barossa Complex was structurally reworked and retrogressed in during the ca. 500 Ma Delamerian Orogeny, and although the Warren Inlier is much more strongly retrogressed and overprinted, Palaeo-Mesoproterozoic structures are still largely preserved in the Houghton Inlier.

References

Aitken, A. R. A., Betts, P. G., Young, D. A., Blankenship, D. D., Roberts, J. L. & Siegert, M. J., 2016. The Australo-Antarctic Columbia to Gondwana transition. Gondwana Research, 29(1), 136-152.

Armit, R. J., Betts, P. G., Schaefer, B. F. & Ailleres, L., 2012. Constraints on long-lived Mesoproterozoic and Palaeozoic deformational events and crustal architecture in the northern Mount Painter Province, Australia. Gondwana Research, 22(1), 207-226.

Armit, R. J., Betts, P. G., Schaefer, B. F., Pankhurst, M. J. & Giles, D., 2014. Provenance of the Early Mesoproterozoic Radium Creek Group in the northern Mount Painter Inlier: Correlating isotopic signatures to inform tectonic reconstructions. Precambrian Research, 243, 63-87.

Barovich, K. & Hand, M., 2008. Tectonic setting and provenance of the Paleoproterozoic Willyama Supergroup, Curnamona Province, Australia: Geochemical and Nd isotopic constraints on contrasting source terrain components. Precambrian Research, 166(1–4), 318-337.

Belousova, E. A., Preiss, W. V., Schwarz, M. P. & Griffin, W. L., 2006. Tectonic affinities of the Houghton Inlier, South Australia: U - Pb and Hf-isotope data from zircons in modern stream sediments. Australian Journal of Earth Sciences, 53(6), 971-989.

Benson, W. N., 1909. Petrographical Notes on Certain Pre-Cambrian Rocks of the Mount Lofty Ranges, With Special Reference to the Geology of the Houghton District.

Transactions of the Royal Society of South Australia, 33, 101-140.

Betts, P. G., Armit, R. J., Stewart, J., Aitken, A. R. A., Ailleres, L., Donchak, P., Hutton, L., Withnall, I. & Giles, D., 2015. Australia and Nuna. Geological Society, London, Special Publications, 424.

Betts, P. G. & Giles, D., 2006. The 1800–1100 Ma tectonic evolution of Australia. Precambrian Research, 144(1–2), 92-125.

Brown, H. Y., 1885. Geological Map of Barossa and Para Wirra. Parliamentary Paper No. 178, South Australia.

Callen, R. A., 1966. A comparison of the genesis of copper orebodies at Kuitpo and Moonta in South Australia, with particular reference to the economic potential of each district. Unpub. BSc (Hons) Thesis, University of Adelaide.

Cawood, P. A. & Korsch, R. J., 2008. Assembling Australia: Proterozoic building of a continent. Precambrian Research, 166(1–4), 1-35.

Chappel, B. E. E., 1964. The geology of the Willunga Hill - Kuitpo area. Unpub. BSc (Hons) Thesis, University of Adelaide.

Clark, C. & Hand, M., 2010. Decoding Mesoproterozoic and Cambrian metamorphic events in Willyama Complex metapelites through the application of Sm–Nd garnet geochronology and P–T pseudosection analysis. Gondwana Research, 17(1), 59-74.

Conor, C., 1995. Moonta-Wallaroo Region: An interpretation of the geology of the Maitland and Wallaroo 1:100 000 sheet areas, South Australian Department of Primary Industries and Resources.

Conor, C. H. H. & Preiss, W. V., 2008. Understanding the 1720–1640 Ma Palaeoproterozoic Willyama Supergroup, Curnamona Province, Southeastern Australia: Implications for tectonics, basin evolution and ore genesis. Precambrian Research, 166(1–4), 297-317.

Cowley, W., Conor, C. & Zang, W., 2003. New and revised Proterozoic stratigraphic units on northern Yorke Peninsula. MESA Journal, 29, 46-58.

Crowhurst, P. V., 1988. The geology, petrology and geochemistry of the Proterozoic inlier, south of Myponga, Fleurieu Peninsula, South Australia. Unpub. BSc (Hons) Thesis, University of Adelaide.

Cutts, K., Hand, M. & Kelsey, D. E., 2011. Evidence for early Mesoproterozoic (ca. 1590 Ma) ultrahigh-temperature metamorphism in southern Australia. Lithos, 124(1–2), 1-16.

Davies, M. B., 1972. The geology and petrology of an Archaean inlier south of Normanville – the geochemistry of the Houghton granulite. Unpub. BSc (Hons) Thesis, University of Adelaide.

Dirks, P. H. G. M., 1990. Intertidal and subtidal sedimentation during a mid-Proterozoic marine transgression, reynolds range group, Arunta block, central Australia. Australian Journal of Earth Sciences, 37(4), 409-422.

Dutch, R., Hand, M. & Kinny, P. D., 2008. High-grade Paleoproterozoic reworking in the southeastern Gawler Craton, South Australia. Australian Journal of Earth Sciences, 55(8), 1063-1081.

Fanning, C. M., Flint, R. B., Parker, A. J., Ludwig, K. R. & Blissett, A. H., 1988. Refined Proterozoic evolution of the Gawler Craton, South Australia, through U-Pb zircon geochronology. Precambrian Research, 40–41(0), 363-386.

Fanning, C. M., Reid, A. J. & Teale, G., 2007. A geochronological framework for the Gawler Craton, South Australia. Geological Survey of South Australia.

Flottmann, T. & James, P., 1997. Influence of basin architecture on the style of inversion and fold-thrust belt tectonics—the southern Adelaide Fold-Thrust Belt, South Australia. Journal of Structural Geology, 19(8), 1093-1110.

Flöttmann, T., James, P., Rogers, J. & Johnson, T., 1994. Early Palaeozoic foreland thrust-

ing and basin reactivation at the Palaeo-Pacific margin of the southeastern Australian Precambrian Craton: a reappraisal of the structural evolution of the Southern Adelaide Fold-Thrust Belt. Tectonophysics, 234(1–2), 95-116.

Foden, J., Sandiford, M., Dougherty-Page, J. & Williams, I., 1999. Geochemistry and geochronology of the Rathjen Gneiss: Implications for the early tectonic evolution of the Delamerian Orogen. Australian Journal of Earth Sciences, 46(3), 377-389.

Forbes, C. J., Betts, P. G., Giles, D. & Weinberg, R., 2008. Reinterpretation of the tectonic context of high-temperature metamorphism in the Broken Hill Block, NSW, and implications on the Palaeo- to Meso-Proterozoic evolution. Precambrian Research, 166(1–4), 338-349.

Forbes, C. J., Betts, P. G., Weinberg, R. & Buick, I. S., 2005. A structural metamorphic study of the Broken Hill Block, NSW, Australia. Journal of Metamorphic Geology, 23(8), 745-770.

Forbes, C. J., Giles, D., Hand, M., Betts, P. G., Suzuki, K., Chalmers, N. & Dutch, R., 2011. Using P–T paths to interpret the tectonothermal setting of prograde metamorphism: An example from the northeastern Gawler Craton, South Australia. Precambrian Research, 185(1–2), 65-85.

Forbes, C. J., Giles, D., Jourdan, F., Sato, K., Omori, S. & Bunch, M., 2012. Cooling and exhumation history of the northeastern Gawler Craton, South Australia. Precambrian Research, 200–203(0), 209-238.

Fowler, A. & Hassan, I., 2008. Extensional tectonic origin of gneissosity and related structures of the Feiran–Solaf metamorphic belt, Sinai, Egypt. Precambrian Research, 164(3), 119-136.

Gibson, G. M., Peljo, M. & Chamberlain, T., 2004. Evidence and timing of crustal extension versus shortening in the early tectonothermal evolution of a Proterozoic continental rift sequence at Broken Hill, Australia. Tectonics, 23(5)

Giles, D., Betts, P. & Lister, G., 2002. Far-field continental backarc setting for the 1.80–1.67 Ga basins of northeastern Australia. Geology, 30(9), 823-826.

Giles, D., Betts, P. G. & Lister, G. S., 2004. 1.8-1.5-Ga links between the North and South Australian Cratons and the Early-Middle Proterozoic configuration of Australia. Tectonophysics, 380(1-2), 27-41.

Grotzinger, J., 1989. Facies and Evolution of Precambrian Carbonate Depositional Systems: Emergence of the Modern Platform Archetype. In: Controls on Carbonate Platform and Basin Development, The Society of Economic Paleontologists and Mineralogists.

Hand, M., Mawby, J., Kinny, P. & Foden, J., 1999. U–Pb ages from the Harts Range, central Australia: evidence for early Ordovician extension and constraints on Carboniferous metamorphism. Journal of the Geological Society, 156(4), 715-730.

Hand, M., Reid, A. & Jagodzinski, L., 2007. Tectonic framework and evolution of the Gawler craton, Southern Australia. Economic Geology, 102(8), 1377-1395.

Heaslip, J. E., 1972. Review of the Geology of the Mt. Magnificent Area, University of Adelaide.

Horsfall, C. L., 1973. Interpretation of aeromagnetic and ground magnetic data over the Houghton Inlier, South Australia, as an aid to geological mapping. Unpub. BSc (Hons) Thesis, University of Adelaide.

Howard, K. E., Hand, M., Barovich, K. M. & Belousova, E., 2011. Provenance of late Paleoproterozoic cover sequences in the central Gawler Craton: exploring stratigraphic correlations in eastern Proterozoic Australia using detrital zircon ages, Hf and Nd isotopic data. Australian Journal of Earth Sciences, 58(5), 475-500.

Jagodzinski, E.A., Meaney, K., Szpunar, M., and Fraser, G., 2017. SHRIMP U-Pb dating of the Barossa Complex, South Aus-

tralia: exploring tectonic links between the Gawler Craton and Curnamona Province. Report Book 2017/00017. Department of the Premier and Cabinet, South Australia, Adelaide.

Johnson, S.P., 2013. The Birth of supercontinents and the Proterozoic Assembly of Western Australia. Geological Survey of Western Australia, 72p

Kositcin, N., 2010. Geodynamic Synthesis of the Gawler Craton and Curnamona Province. Geoscience Australia, Record, 2010/27, 113p.

Lane, K., Jagodzinski, E. A., Dutch, R., Reid, A. J. & Hand, M., 2015. Age constraints on the timing of iron ore mineralisation in the southeastern Gawler Craton. Australian Journal of Earth Sciences, 62(1), 55-75.

Lee, J., Miller, E. L. & Sutter, J. F., 1987. Ductile strain and metamorphism in an extensional tectonic setting: a case study from the northern Snake Range, Nevada, USA. Geological Society, London, Special Publications, 28(1), 267-298.

Maidment, D. W., Hand, M. & Williams, I. S., 2013. High grade metamorphism of sedimentary rocks during Palaeozoic rift basin formation in central Australia. Gondwana Research, 24(3–4), 865-885.

Mancktelow, N. S., 1990. The structure of the southern Adelaide Fold Belt, South Australia. In: The evolution of a Late Precambrian-Early Paleozoic Rift Complex: The Adelaide Geosyncline (eds Jago, J. B. & Moore, P. J.), pp. 483-495, The Geological Society of Australia Special Publication

McEwin, A. J., 1972. Geology and petrology of part of the Archaean Inlier north-east of Yankalilla on the Fleurieu Peninsula, University of Adelaide.

McFarlane, C. R. M. & Frost, B. R., 2009. Constraints on the early metamorphic evolution of Broken Hill, Australia, from in situ U-Pb dating and REE geochemistry of monazite. Journal of Metamorphic Geology, 27(1), 3-17.

Mills, K. J., 1963. The geology of the Mount Crawford granite gneiss and adjacent metasediments. Transactions of the Royal Society of South Australia, 87, 167-183.

Mills, K. J., 1973. The structural geology of the Warren National Park and the western portion of the Mount Crawford State Forest, South Australia. Transactions of the Royal Society of South Australia, 97(Part 4), Pages: 281-315.

Morrissey, L., Payne, J. L., Kelsey, D. E. & Hand, M., 2011. Grenvillian-aged reworking in the North Australian Craton, central Australia: Constraints from geochronology and modelled phase equilibria. Precambrian Research, 191(3–4), 141-165.

Morrissey, L. J., Hand, M., Wade, B. P. & Szpunar, M., 2013. Early Mesoproterozoic metamorphism in the Barossa Complex, South Australia: links with the eastern margin of Proterozoic Australia. Australian Journal of Earth Sciences, 60(8), 769-795.

Offler, R. & Fleming, P. D., 1968. A synthesis of folding and metamorphism in the Mt Lofty Ranges, South Australia. Journal of the Geological Society of Australia, 15(2), 245-266.

Oliver, N. H. S. & Zakowski, S., 1995. Timing and geometry of deformation, low-pressure metamorphism and anatexis in the eastern Mt Lofty Ranges: The possible role of extension. Australian Journal of Earth Sciences, 42(5), 501-507.

Page, R. N., Stevens, B. P. J. & Gibson, G. M., 2005a. Geochronology of the sequence hosting the Broken Hill Pb-Zn-Ag orebody, Australia. Economic Geology, 100(4), 633-661.

Page, R. W., Conor, C. H. H., Stevens, B. P. J., Gibson, G. M., Preiss, W. V. & Southgate, P. N., 2005b. Correlation of Olary and Broken Hill Domains, Curnamona Province: Possible relationship to Mount Isa and other North Australian Pb-Zn-Ag-bearing successions. Economic Geology, 100(4), 663-676.

Parker, A. J., Daly, S. J., Flint, R. B., Flint, D. J., Preiss, W. V. & Teale, G. S., 1993. Paleoproterozoic. In: The Geology of South Australia, Volume 1: The Precambrian (eds Drexel, J. F., Preiss, W. V. & Parker, A. J.), pp. 51-106, Geological Survey of South Australia, Adelaide.

Parker, A. J. & Lemon, N. M., 1982. Reconstruction of the early Proterozoic stratigraphy of the Gawler Craton, South Australia. Journal of the Geological Society of Australia, 29(1-2), 221-238.

Paul, E. G., 1998. The Geometry and Controls on Basement-Involved Deformation in the Adelaide Fold Belt, South Australia. Unpub. Ph.D. Thesis, University of Adelaide.

Payne, J. L., Barovich, K. M. & Hand, M., 2006. Provenance of metasedimentary rocks in the northern Gawler Craton, Australia: Implications for Palaeoproterozoic reconstructions. Precambrian Research, 148(3–4), 275-291.

Payne, J. L., Hand, M., Barovich, K. M. & Wade, B. P., 2008. Temporal constraints on the timing of high-grade metamorphism in the northern Gawler Craton: implications for assembly of the Australian Proterozoic. Australian Journal of Earth Sciences, 55(5), 623-640.

Preiss, W. V., 1993. Basement Inliers of the Mount Lofty Ranges. In: The Geology of South Australia, Volume 1, The Precambrian (eds Drexel, J. F., Preiss, W. V. & Parker, A. J.), pp. 102-105, Geological Survey of South Australia, Adelaide.

Preiss, W. V., 2000. The Adelaide Geosyncline of South Australia and its significance in Neoproterozoic continental reconstruction. Precambrian Research, 100(1-3), 21-63.

Preiss, W. V., Fanning, C. A., Szpunar, M. A. & Burtt, A. C., 2008. Age and tectonic significance of the Mount Crawford Granite Gneiss and a related intrusive in the Oakbank Inlier, Mount Lofty Ranges, South Australia. MESA Journal, 49, 38-49.

Raetz, M., Krabbendam, M. & Donaghy, A. G., 2002. Compilation of Pb zircon data from the Willyama Supergroup, Broken Hill region, Australia: Evidence for three tectonostratigraphic successions and four magmatic events? Australian Journal of Earth Sciences, 49(6), 965-983.

Reid, A., Hand, M., Jagodzinski, E., Kelsey, D. & Pearson, N., 2008a. Paleoproterozoic orogenesis in the southeastern Gawler Craton, South Australia. Australian Journal of Earth Sciences, 55(4), 449-471.

Reid, A. J., Jourdan, F. & Jagodzinski, E. A., 2017. Mesoproterozoic fluid events affecting Archean crust in the northern Olympic Cu–Au Province, Gawler Craton: insights from 40Ar/39Ar thermochronology. Australian Journal of Earth Sciences, 64(1), 103-119.

Reid, A. J., McAvaney, S. O. & Fraser, G. L., 2008b. Nature of the Kimban Orogeny across northern Eyre Peninsula. MESA Journal, 51, 25-34.

Ross, G. B., 2011. Tectonothermal history and evolving geodynamic setting of the Peake and Denison Block and Northern Gawler Craton, South Australia, Monash University, Australia.

Rutherford, L., Barovich, K., Hand, M. & Foden, J., 2006. Continental ca 1.7 – 1.69 Ga Fe-rich metatholeiites in the Curnamona Province, Australia: a record of melting of a heterogeneous, subduction-modified lithospheric mantle. Australian Journal of Earth Sciences, 53(3), 501-519.

Rutherford, L., Hand, M. & Barovich, K., 2007. Timing of Proterozoic metamorphism in the southern Curnamona Province: implications for tectonic models and continental reconstructions. Australian Journal of Earth Sciences, 54(1), 65-81.

Schwarz, M. P., 2003. Lincoln, South Australia, 1:250 000 map sheet SI 53-11 - Second edition, South Australia. In: Geological Atlas 1:250 000 Series, Geological Survey of South Australia.

Smits, R. G., Collins, W. J., Hand, M., Dutch,

R. & Payne, J., 2014. A Proterozoic Wilson cycle identified by Hf isotopes in central Australia: Implications for the assembly of Proterozoic Australia and Rodinia. Geology, 42(3), 231-234.

Spry, A. H., 1951. The Archaean complex at Houghton, South Australia. Transactions of the Royal Society of South Australia, 74(1), 115-134.

Stevens, B. P. J., Barnes, R. G., Brown, R. E., Stroud, W. J. & Willis, I. L., 1988. The Willyama Supergroup in the Broken Hill and Euriowie Blocks, New South Wales. Precambrian Research, 40-41(0), 297-327.

Stevens, B. P. J., Page, R. W. & Crooks, A., 2008. Geochronology of Willyama Supergroup metavolcanics, metasediments and contemporaneous intrusions, Broken Hill, Australia. Australian Journal of Earth Sciences, 55(3), 301-330.

Szpunar, M., Hand, M., Barovich, K., Jagodzinski, E. & Belousova, E., 2011. Isotopic and geochemical constraints on the Paleoproterozoic Hutchison Group, southern Australia: Implications for Paleoproterozoic continental reconstructions. Precambrian Research, 187(1–2), 99-126.

Szpunar, M., Wade, B., Hand, M. P. & Barovich, K. M., 2007. Timing of Proterozoic high-grade metamorphism in the Barossa Complex, southern South Australia; exploring the extent of the 1590 Ma event. MESA Journal, 47, 21-27.

Szpunar, M. A. & Fraser, G. L., 2010. Age of deposition and provenance of Palaeoproterozoic basins on north-eastern Eyre Peninsula, PIRSA Geological Survey Branch.

Talbot, J. L., 1963. Retrograde metamorphism of the Houghton Complex, South Australia. Transactions of the Royal Society of South Australia, 87, 185-197.

Tucker, N. M., Hand, M. & Payne, J. L., 2015. A rift-related origin for regional medium-pressure, high-temperature metamorphism. Earth and Planetary Science Letters, 421, 75-88.

Vassallo, J. J. & Wilson, C. J. L., 2002. Palaeoproterozoic regional-scale non-coaxial deformation: an example from eastern Eyre Peninsula, South Australia. Journal of Structural Geology, 24(1), 1-24.

Wade, B. P., Barovich, K. M., Hand, M., Scrimgeour, I. R. & Close, D. F., 2006. Evidence for Early Mesoproterozoic Arc Magmatism in the Musgrave Block, Central Australia: Implications for Proterozoic Crustal Growth and Tectonic Reconstructions of Australia. The Journal of Geology, 114(1), 43-63.

Webb, P. B., 1953. Structure of the Archaean complex of the Mount Lofty Ranges. Unpub. MSc Thesis, University of Adelaide.

Wicks, S. P., 1972. Geology of part of basement inlier north-east of Mt. Compass. Unpub. BSc (Hons) Thesis, University of Adelaide.

Willis, I. L., Brown, R. E., Stroud, W. J. & Stevens, B. P. J., 1983. The early Proterozoic Willyama supergroup: Stratigraphic subdivision and interpretation of high to low-grade metamorphic rocks in the Broken Hill Block, New South Wales. Journal of the Geological Society of Australia, 30(1-2), 195-224.

Zang, W., 2002. Late Palaeoproterozoic Wallaroo Group and early Mesoproterozoic mineralisation in the Moonta Subdomain, eastern Gawler Craton, South Australia, Primary Industry and Resources South Australia.

CHAPTER 3

An Overview of the Stratigraphy of the Aldgate, Oakbank, and Myponga Inliers.

ABSTRACT

The Barossa Complex inliers in the Mt. Lofty Ranges, South Australia, make up the south eastern most exposure of the Gawler Craton. The stratigraphy of these inliers is still poorly understood. Mapping of the southern inliers; the Aldgate, Oakbank, and Myponga inliers lends context to previous geochronology and reveal similar stratigraphic assemblages across the five inliers. The three areas considered are largely dominated by psammopelitic to pelitic metasediments, with less common calcsilicate and quartzofeldspathic metasediments. Previously reported zircon maximum depositional ages (MDA) of c. 1700 Ma from psammopelitic units in the Oakbank Inlier and the Houghton Inlier represents a likely stratigraphic correlation. Pelitic gneisses in the Aldgate Inlier preserve a MDA of c. 1679 Ma. This age occurs between the upper and lower limits of the psammopelitic gneiss in the Houghton Inlier, and likely reflects a temporal equivalent of that unit. A quartzite-calcsilicate association in the southern Myponga inlier yields an MDA of c. 1655 Ma, which is comparable to pelitic gneisses in the northern Barossa Complex. It is unclear whether this represents a temporal equivalent of the northern Barossa Complex, or a temporally distinct unit of the same zircon provenance.

1. Introduction

The Barossa Complex in the Mount Lofty Ranges, South Australia, forms the eastern most exposure of the Gawler Craton (Figure 1), and is a likely correlative to the Willyama Supergroup in the Curnamona Province (Jagodzinski et al. 2017). This makes it a valuable region for addressing the development of the marginal areas of the Gawler Craton, and the larger scale events which affected eastern Australia during the Proterozoic.

Much of the work conducted in the Mount Lofty Ranges has focussed on the stratigraphy of the Neoproterozoic Adelaide Rift Complex (e.g. Preiss 2000 and references therein) or structural and metamorphic effects of the Cambro-Ordovician Delamerian Orogeny (e.g. Mancktelow 1990 and references therein, Flöttmann et al. 1994). The basement inliers of the Barossa Complex are often considered only in the context of being the basement involved in Neoproterozoic rifting or the Delamerian thrust-fold belt (Offler and Fleming 1968, Flottmann and James 1997). While the pre-Neoproterozoic history of the Barossa Complex is poorly understood, recent geochronology has begun to illuminate the depositional and metamorphic timing of the Barossa Complex (Szpunar et al. 2007, Morrissey et al. 2013, Jagodzinski et al. 2017). While studies such as these shed light on some of the broader scale events which affected the Barossa Complex, the lack of stratigraphic and structural understanding limits the amount of targeted work possible.

Early mapping efforts identified similar lithologies between the different inliers (e.g. Benson 1909, Howchin 1926, Sprigg et al. 1951). In Chapter 2 of this thesis, the stratigraphy of the northern most inliers, the Houghton and Warren Inliers is presented. However, the lithological relationships and overall stratigraphy have not been meaningfully addressed in the Aldgate, Oakbank, and Myponga Inliers (Figure 1). Comparison between the various inliers is made more difficult by the wide spread presence of regional thrust faults associated with the Delamerian Orogeny, many of which are reactivated normal faults, which separate all of the inliers from one another (Flottmann and James 1997). This means that there is no certainty as to whether the various inliers represent the parts of the same

stratigraphic succession without detailed field and geochemical analysis.

This chapter aims to outline the lithologies of the Aldgate and Oakbank inliers, and part of the Myponga Inlier, and briefly address the broad scale structures which control the exposures and lithostratigraphic relationships. This work will function as an aid to further work in these inliers, and to provide context for existing geochronology.

2. Background

The Aldgate, Oakbank, and Myponga Inliers are exposed in the central to southern Mt. Lofty Ranges in South Australia within the sub-greenschist facies zone of the Delamerian Orogen (Offler and Fleming 1968; Figure 1). The Aldgate Inlier occurs as two elongate exposures in the central Mt. Lofty Ranges, immediately north of the township of Aldgate (Figure 2). Both sections of the inlier are exposed in the hanging wall of thrust faults associated with the Delamerian Orogeny (Flottmann and James 1997), and are overlain by the Neoproterozoic Aldgate Sandstone on the eastern margins. The western exposure is also partially fault bound on its eastern side. Extensive urbanisation and the weathered character of the inlier limits outcrop to infrequent road cuttings, as well as a small amount of exposure in the Mt. George Conservation Park. A psammite unit from the northeastern Aldgate Inlier yielded a detrital zircon maximum depositional age of 1679 ±12 Ma with metamorphic overgrowths preserving ages of 1582 ±4 Ma (Jagodzinski et al. 2017).

The Oakbank Inlier is a small exposure in the core of a prominent anticline which is exposed in the eastern Mt. Lofty Ranges (Figure 2; Adshead-Bell and Bell 1999). On its western margin a small sliver of basal Neoproterozoic Aldgate Sandstone is present in between the basement exposure and the bounding fault, while the eastern margin is completely fault bound. The northern and southern most extents of the inlier are obscured by Palaeogene to recent alluvial sediment. The Oakbank Inlier lies within the lower amphibolite facies zone of the Delamerian Orogen (Offler and Fleming 1968). A sample of paragneiss from the eastern Oakbank Inlier has yielded a detrital zircon maximum depositional age of 1701 ±14 Ma with metamorphic overgrowths recording a spread of ages ranging between c. 1630 Ma and 1580 Ma (Jagodzinski et al. 2017).

The Myponga Inlier is the southernmost inlier of the Barossa Complex and occurs as a 70km long discontinuous exposure within the Southern Mt. Lofty Ranges on the Fleurieu Peninsula (Figure 1, 3). The Myponga Inlier is exposed in the core of an overturned anticline with a partially faulted western margin. This inlier is variably overlain by Permian to recent sedimentary sequences (Figure 3), which combined with an often deep weathering profile drastically limits exposure and obscures the relationships between lithologies. Much of the detailed mapping of much of this inlier is restricted to unpublished Honours theses which each mapped small and often isolated parts of the inlier in varying levels of detail (Davies 1972, McEwin 1972, Heaslip 1972, Wicks 1972, Anderson 1975, Crowhurst 1988; Figure 3). A further complication of investigating the stratigraphic relationships in the Myponga Inlier is the retrograde tectonism which variably obscures the primary metamorphic lithologies and obscures lithological relationships (e.g. Morrissey et al. 2013).

The best exposures of the Myponga Inlier occur in the southern part of the inlier and have been previously mapped by Davies (1972; Figure 3). The southernmost extent of this exposure has been structurally assessed by Anderson (1975) and Steinhardt (1991). This area has also been recently targeted for zircon and monazite U-Pb geochronology and metamorphic phase equilibria modelling (Szpunar et al. 2007, Morrissey et al. 2013, Jagodzinski et al. 2017). A quartzite sample from the southern part of the Myponga Inlier gives a detrital zircon maximum depositional age of 1653 ±11 Ma (Jagodzinski et al. 2017).

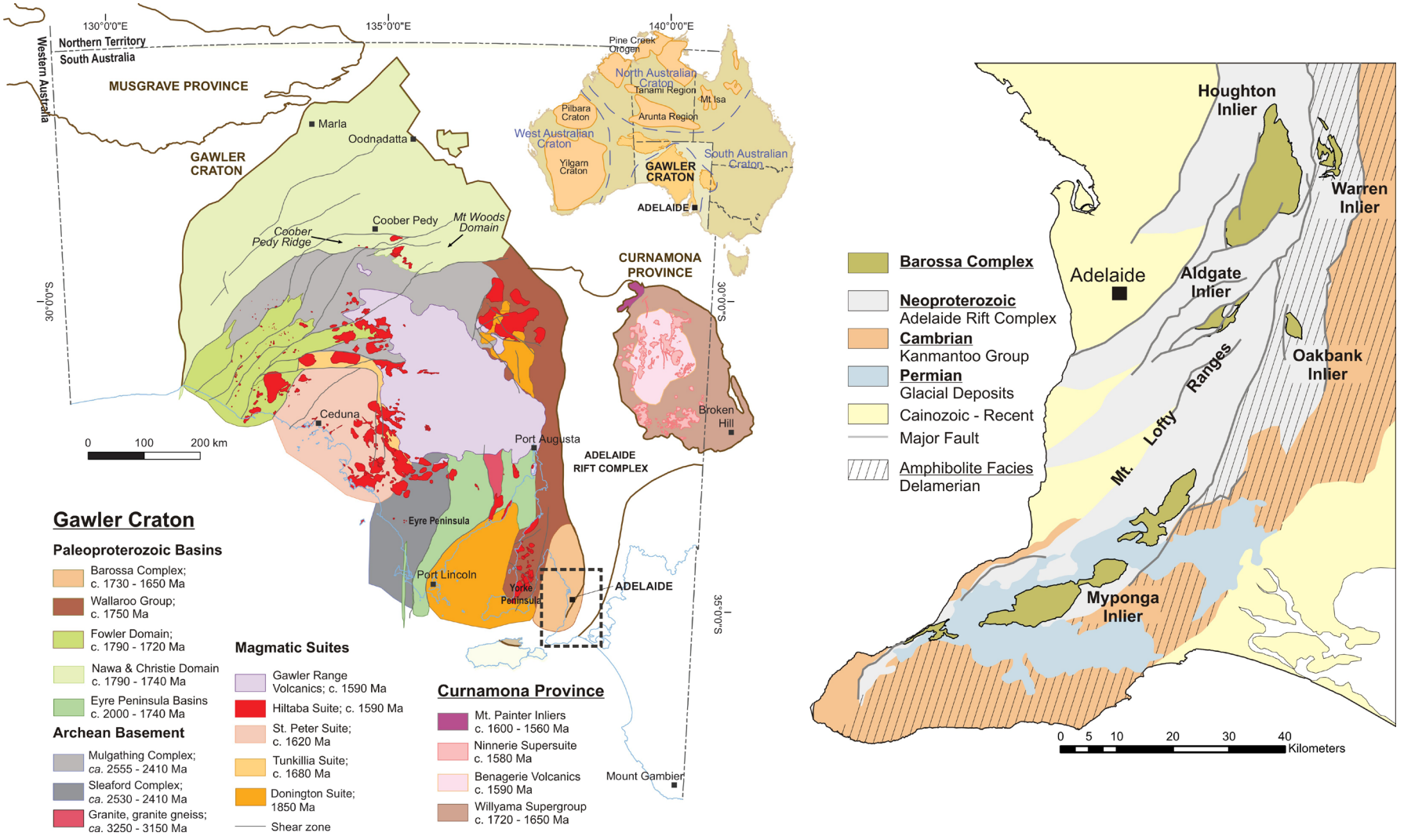

Figure 1: Left - The Barossa Complex and its position within the Gawler Craton in South Australia, adapted after Reid, et al., (2017). Right - simplified geology of the Mt. Lofty Ranges showing the positions of the Barossa Complex Inliers, adapted after Preiss, (1993). The Aldgate and Oakbank inliers occur in the central Mt. Lofty Ranges, and the Myponga Inlier occurs as a discontinuous exposure to the south.

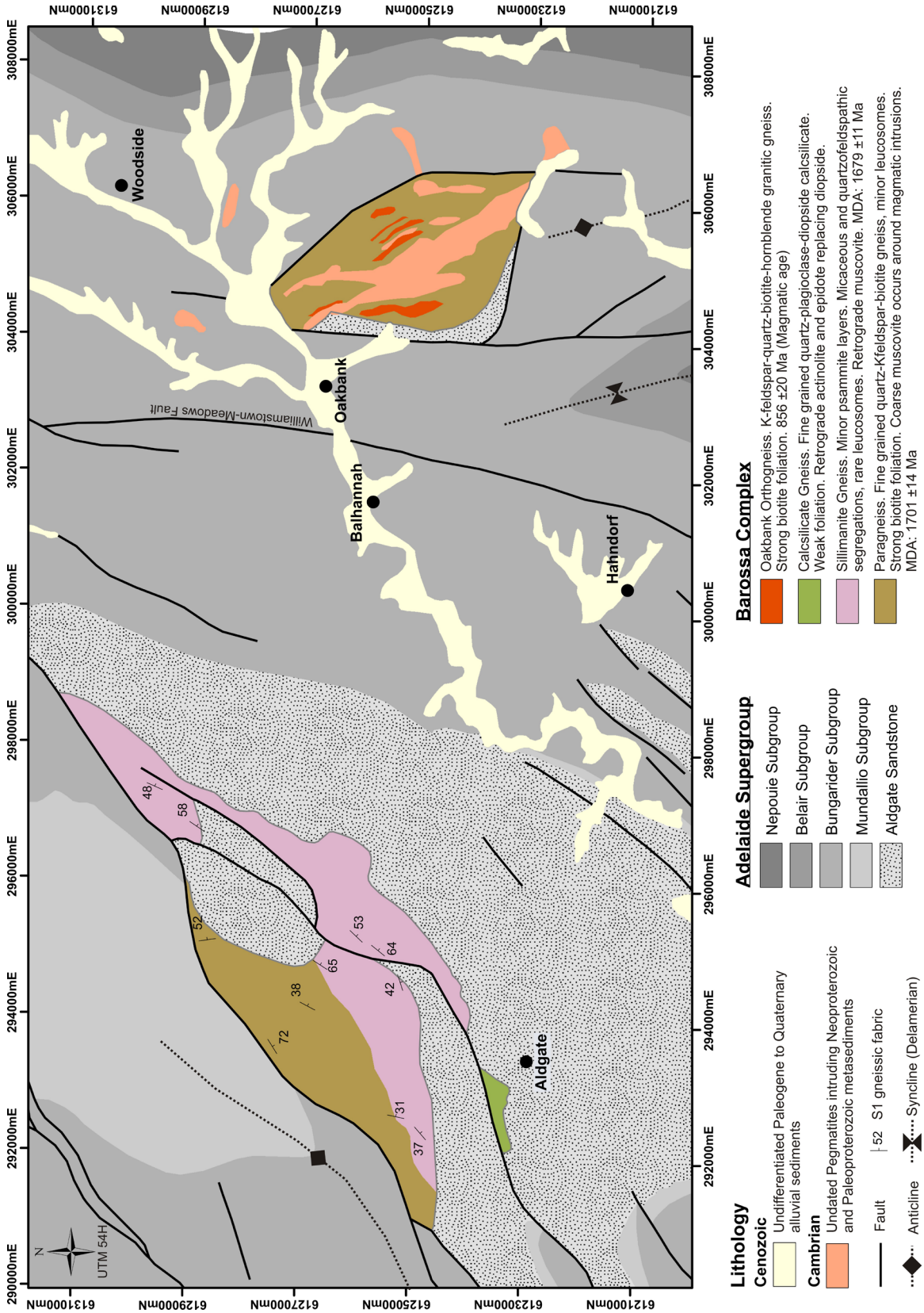

Figure 2: Lithology map of the Aldgate and Oakbank inliers.

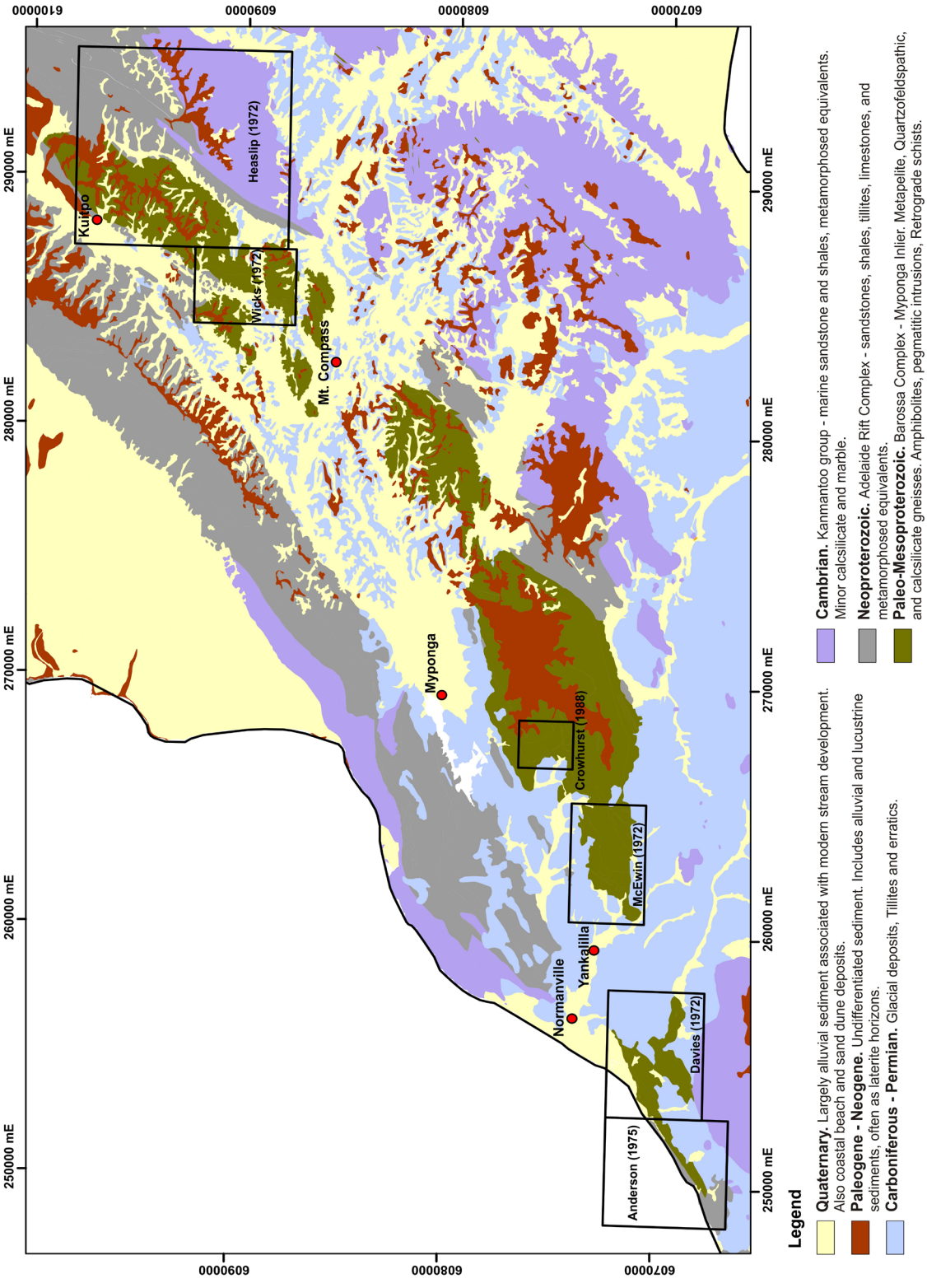

Figure 3: Simplified regional map of the Myponga Inlier illustrating the extent of Permian to recent cover. The locations of previous mapping studies noted in the text are marked.

Metamorphic zircon and monazite record ages between 1590-1580 Ma (Szpunar et al. 2007, Jagodzinski et al. 2017), with retrograde monazite recording ages of c. 1560 Ma from retrograde shear zones (Morrissey et al. 2013). Peak metamorphic conditions of 800-870^{o}C and 8-9 Kbar are interpreted to have occurred at c. 1590 Ma (Morrissey et al. 2013) prior to the emplacement of large undeformed pegmatite bodies at 1580 ±4 Ma (Jagodzinski et al. 2017).

3. Stratigraphy

3.1 Aldgate Inlier

Three distinguishable lithologies are present within the Aldgate Inlier (Figure 2). A retrogressed sillimanite bearing gneiss dominates the exposure. This unit is commonly extensively weathered and outcrops poorly. Fine grained sillimanite, biotite, and muscovite bands are weakly segregated from quartzofeldspathic material, defining a gneissocity (Figure 4). Sillimanite is commonly weathered to kaolinite but is still distinguishable as the primary crystal habit is preserved as white fibrous laths. Quartz-K-feldspar leucosomes frequently occur, typically paralleling the gneissic fabric. Psammitic layers up to 50 cm thick are frequently observed throughout this unit. Detrital zircons analysed from a psammite layer from the sillimanite gneiss yielded a maximum depositional age of 1679 ±12 Ma (Jagodzinski et al. 2017).

In the western extent of the Aldgate Inlier a quartzofeldspathic to psammopelitic gneiss is exposed. This gneiss typically contains between 20-40% mica that is dominantly biotite with minor muscovite, that define the foliation. The remainder of the rock is composed of quartz and K-feldspar. As in the sillimanite gneiss, small leucosomes occur which parallel the foliation. The contact between these two units was not identified in outcrop and it is unclear whether this is a conformable or tectonic boundary.

A small isolated exposure occurs to the south of the main inlier which contains a fine-grained calcsilicate gneiss. This lithology is composed primarily of plagioclase and diopside, with minor actinolite and epidote. In outcrop this gneiss appears massive, although trails of diopside are visible in thin section which define a weak layering.

The gneissic fabric in the lithologies of the Aldgate Inlier is typically planar and dominantly dips between 30^{o}-60^{o} to the east-southeast. A strong east dipping cleavage occurs in all exposures and often completely overprints the gneissic fabric. This cleavage is also present in the more pelitic units of the overlying Aldgate Sandstone and is attributed to the Delamerian Orogeny, which is the only major tectonic event to have affected the Neoproterozoic cover. Likewise, the growth of muscovite in the Neoproterozoic assemblages indicates that the muscovite present in the basement lithologies may be a retrograde feature.

3.2 Oakbank Inlier

The bulk of the Oakbank Inlier is a psammopelitic gneiss which in several areas becomes schistose. This lithology is often highly weathered and outcrops poorly. The psammopelitic gneiss is dominantly fine grained quartz, K-feldspar, muscovite, and biotite (Figure 4). A strong foliation is defined by micas, and in some places concentrations of the micas produce a gneissic layering. Coarser grained quartz-k-feldspar leucosomes are preserved which align with the foliation. In areas adjacent to pegmatite intrusions coarse-grained muscovite also occurs. This lithology rarely outcrops and is largely characterised by surface lag. The sparse outcrop inhibits any meaningful structural analysis. Detrital zircons sampled from this psammopelitic gneiss give a maximum depositional age of 1701 ±14 Ma (Jagodzinski et al. 2017).

Two generations of magmatism are exposed in the Oakbank Inlier. The earliest intrusive is a now gneissic granite containing K-feldspar, quartz, biotite, and hornblende.

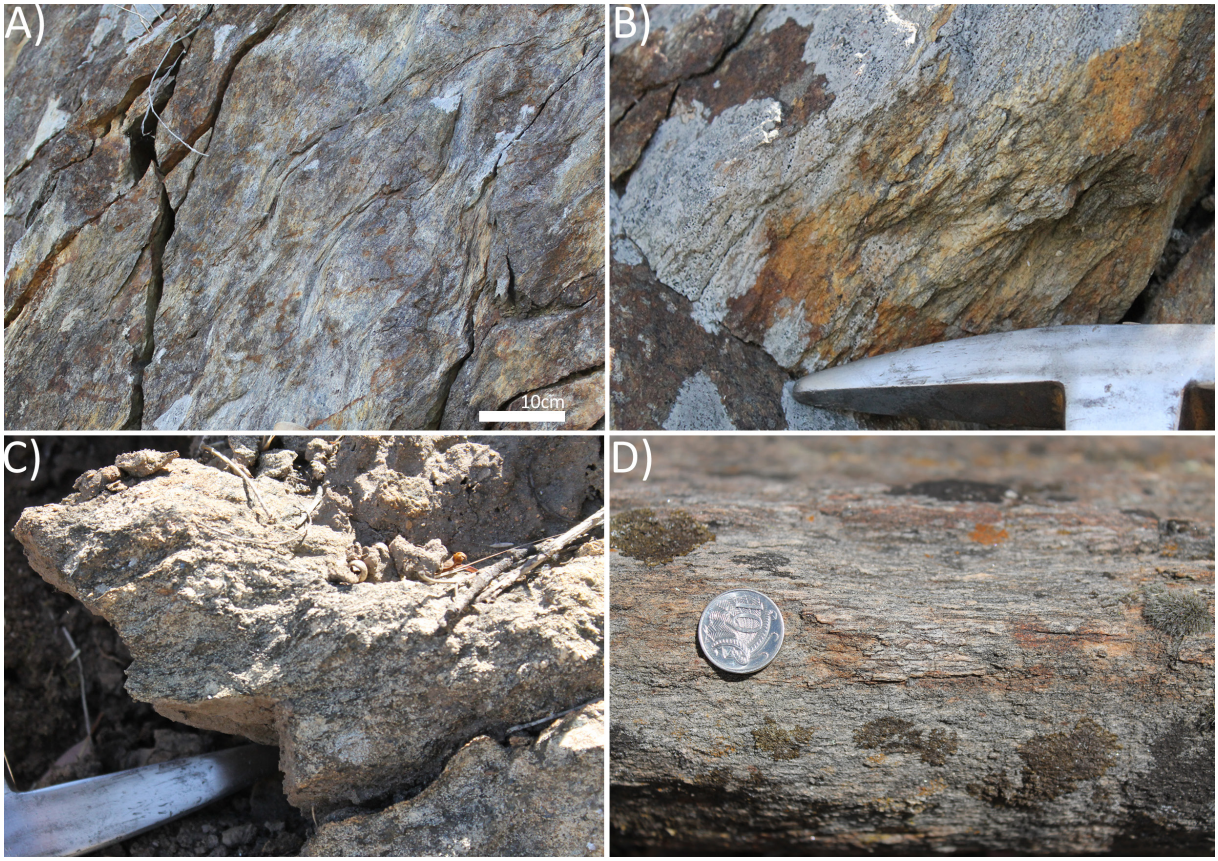

Figure 4: Field photographs from the Aldgate and Oakbank Inliers. A, B) Sillimanite gneiss from the Aldgate Inlier. C) Psammopelitic gneiss from the Oakbank Inlier. D) Strongly foliated Neoproterozoic granitic gneiss from the Oakbank Inlier.

Zircon U-Pb dating of magmatic zircon gives an age of 856 ±20 Ma (Preiss et al. 2008). The geochemical character of this granite is consistent with an A-type felsic magma, and is interpreted to have intruded during the onset of Neoproterozoic rifting (Preiss et al. 2008). A strong gneissic fabric defined by biotite is present within this lithology (Figure 4). It is unclear which structural generation this fabric correlates to.

A series of undeformed quartz-K-feldspar pegmatites make up the bulk of the outcrop in the Oakbank Inlier. In some areas these become quartz dominated. No geochronology currently exists for these pegmatites. As these pegmatites are undeformed, unlike the 856 ±20 Ma granite gneiss, and similar pegmatites occur in the Neoproterozoic sediments adjacent the Oakbank Inlier, they are most likely related to the Delamerian Orogeny.

The mapped extent of the Oakbank Granite Gneiss (Figure 2) is partially derived from the historical Echunga and Adelaide 1:1 Mile Geological Sheets (Sprigg et al. 1951, Sprigg and Wilson 1954) who mapped these intrusions in detail but did not recognise them as part of a basement exposure. Later maps which recognised the basement did not subdivide the basement lithologies, with the exception of the late pegmatites (e.g. Belperio 1985).

3.3 Myponga Inlier: Normanville Exposure

The exposure approximately 5km southwest of Normanville is one of the best exposures of the Myponga Inlier, although Permian and Cenozoic sediments still obscure much of the area (Figure 5). The exposed lithologies have been previously mapped by Davies (1972)

and Anderson (1975). The lithostratigraphic relationships were not discussed in any detail. This work builds upon these earlier maps and re-addresses some of the lithological relationships and interpretations made. The Normanville exposure offers more lithological variety than some other areas of the Myponga inlier (e.g. McEwin 1972) and is one of the best places to start assessing the stratigraphy of this inlier.

3.3.1 Quartzofelspathic gneiss

A quartzofeldspathic gneiss occurs in the middle of the Normanville exposure, and is largely bound by shear zones comprised of muscovite-biotite-chlorite shear fabrics (described below). This gneiss is dominated by quartz and pale grey K-feldspar. Biotite comprises up to 10% of the rock, and defines a weak foliation. This lithology is generally fine grained, with grain sizes rarely exceeding 2mm. Leucosomes occur as planar veins which follow the foliation. In addition to the leucosome layering, a subtle layering is present where quartz is the dominant mineral and biotite is absent. This lithology was interpreted to be a metamorphosed granite by Davies (1972) based on the presence of hornblende in one sample. However, the presence of biotite absent-quartz dominated layers are reminiscent of a primary sedimentary layering (Figure 6) and is more suggestive a sedimentary protolith rather than igneous.

3.3.2 Garnet-Sillimanite-Gneiss

One of the dominant lithologies in the Normanville exposure is a garnet-sillimanite-migmatitic gneiss. This unit was previously mapped by Davies (1972) as two sillimanite gneiss units which were subdivided based on leucosome abundance, and which did not describe the presence of garnet despite its abundance.

This unit is typically highly migmatised with garnet bearing quartz – K-feldspar leucosome making up to 40% of most outcrops. The restite is comprised of sillimanite, garnet, biotite, quartz, and K-feldspar. Garnet porphyroblasts occur up to 15cm in diameter in several areas (Figure 6). Rare minor folds are preserved by the leucosome layering, which generally occur as small (~20 cm) tight to isoclinal folds. The leucosome layering also appears boudinaged in some areas, with the restitic biotite-sillimanite foliation wrapping the leucosome pods. Garnet-absent sillimanite-biotite migmatites also locally occur within the extent of the garnet bearing assemblages.

Metamorphic phase equilibria modelling was undertaken on this unit by Morrissey et al. (2013), and predicted that now seriticised zones around garnet were likely to have been cordierite that formed during post-peak decompression from peak conditions of 800-870^{o}C and 8-9 kbar.

3.3.3 Calcsilicate and Quartzites

A coarse grained calcsilicate gneiss forms a prominent ridge running through the northern part of the Normanville exposure. This gneiss is dominated by coarse grained quartz and microcline feldspar with varying amounts of diopside which is commonly replaced by actinolite and epidote. Titanite and scapolite are common accessory minerals. A gneissic layering defined by calcsilicate minerals is present in some outcrops, although this lithology is also frequently unfoliated. Calcsilicate leucosomes and pegmatites also frequently occur (Figure 6), containing coarse grained diopside amongst a quartz – K-Feldspar groundmass. The calcsilicate is stratigraphically bound by layers of quartzite. Smaller isolated, potentially boudinaged, occurrences of calcsilicate-quartzite also occur in the south of the Normanville exposure within the garnet-sillimanite migmatite. A sample of quartzite from the calcsilicate quartzite association was sampled for detrital zircon geochronology and yielded a maximum depositional age of 1653 ±11 Ma (Jagodzinski et al. 2017).

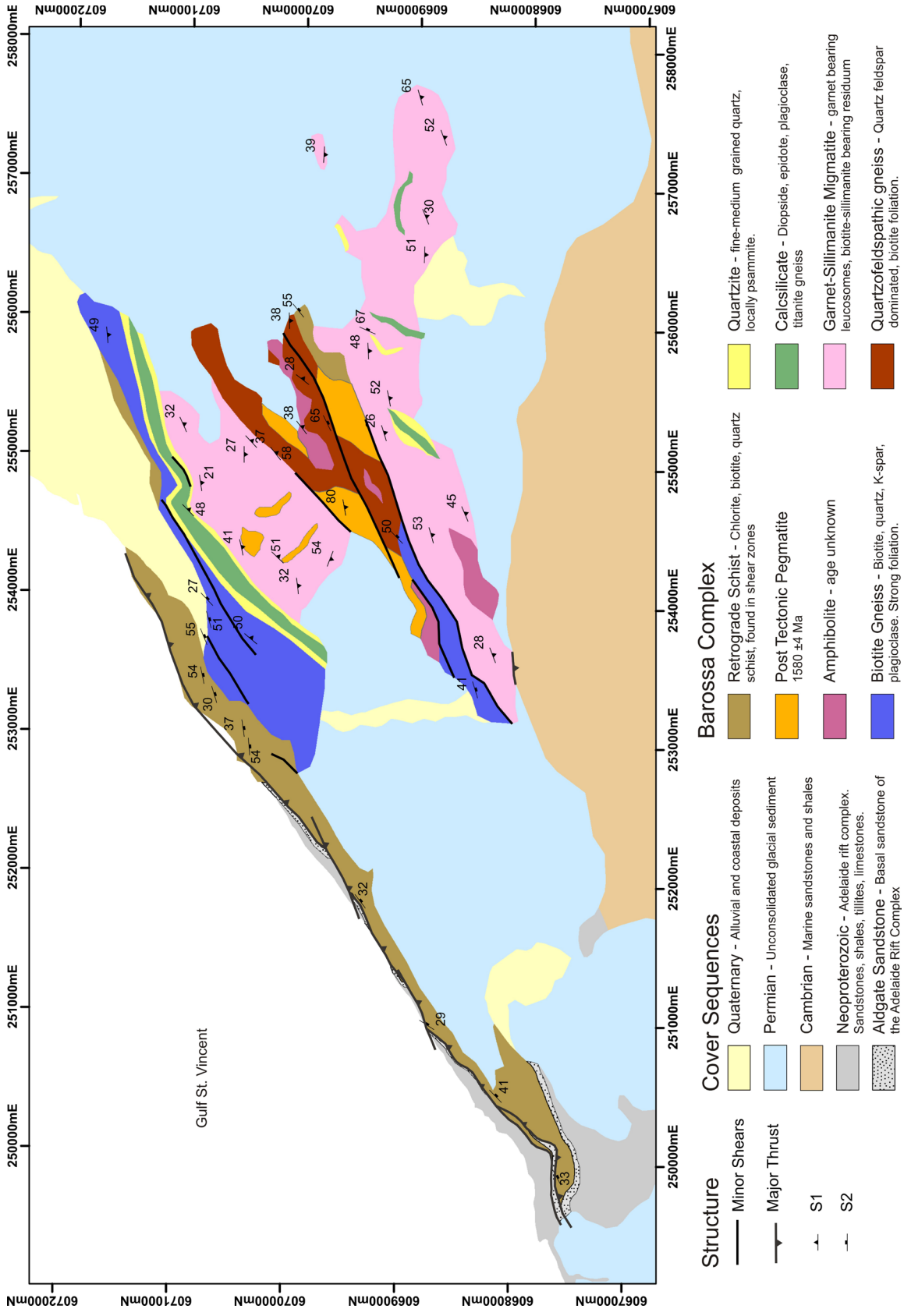

Figure 5: Geological map of the Normanville Exposure of the Myponga Inlier.

3.3.4 Biotite Gneiss

A biotite migmatite gneiss occurs in the northern extent of the Normanville exposure, with a similar shear-bound occurrence in the central part of the exposure. The gneiss is composed primarily of a psammopelitic quartz-plagioclase-biotite assemblage with leucosome material defining the gneissic layering. This lithology is similar to the quartzofeldspathic gneiss, but contains a larger abundance of biotite, which is about 30% of the groundmass in most instances. Muscovite occurs as traces in some occurrences and is likely a retrograde feature. In places where this unit is shear-bound, a strong retrograde fabric frequently overprints the gneissic layering and an increased abundance of muscovite occurs.

3.3.5 Amphibolites

Discrete occurrences of metamorphosed mafic rocks occur throughout the Normanville exposure, and are typically in association with the quartzofeldspathic gneiss and garnet-sillimanite-migmatite. These amphibolites are typically composed of coarse orthopyroxene, plagioclase, and hornblende, with minor alteration products including actinolite and epidote. Some instances of these amphibolites contain orthopyroxene and hornblende bearing leucosomes (Figure 6). Due to the lack of preserved sedimentary structures in the surrounding rocks, assessing whether these mafic bodies were emplaced syndeposition or post-deposition is difficult. The general trend of the amphibolites appears to follow the trends of lithological boundaries which indicates that they may have been syndepositional mafic lavas. However, these bodies are metamorphosed, and at the map scale appear boudinaged in the central Normanville exposure, so their distribution may be the result of tectonic reworking. The high grade metamorphic textures preserved indicates that they predate deformational metamorphism which occurred between c. 1590- 1580 Ma (Szpunar et al. 2007, Jagodzinski et al. 2017).

3.3.6 Pegmatites

A series of coarse grained granitic pegmatites intrude the various units throughout the Normanville exposure. These are dominated by large K-feldspar and quartz, with minor amounts of muscovite and biotite (Figure 6). These pegmatites do not preserve any deformation and are therefore interpreted to have intruded post deformation. In some pegmatites, coarse grained aggregates of ilmenite and rutile also occur. Jagodzinski et al. (2017) analysed zircon U-Pb magmatic crystallisation ages from one of these pegmatites, which yielded a crystallisation age of 1580 ±4 Ma.

3.3.7 Muscovite-Biotite-Chlorite Schists

Some of the best exposures of this part of the Myponga Inlier occur in the cliffs and shore platform along the coastline between 4 to 6km southwest of the Normanville township. In this the lithology is dominated by a muscovite-biotite-chlorite schist. Together the micas variably make up at least 70% of most outcrops, with quartz and seriticised feldspar forming the remainder in varying amounts. This lithology clearly displays high strain fabrics, with leucosome like layers frequently displaying boudinage, and are deformed into augen or sigma clast structures (Figure 6). These generally display top-to-the-west thrust kinematics, which have been described in detail by (Steinhardt 1991). Some discreet high strain zones also display top-to-the-east extensional kinematics (Steinhardt 1991, Morrissey et al. 2013). This lithology occurs at the boundaries of several units throughout this part of the inlier, and as it preserves a lower metamorphic grade than much of the inlier, this is considered to be a retrograde feature.

3.3.8 Structure

The structure of the Normanville exposure is largely controlled by features associated with low grade retrogression associated with the Cambro-Ordovician Delamerian

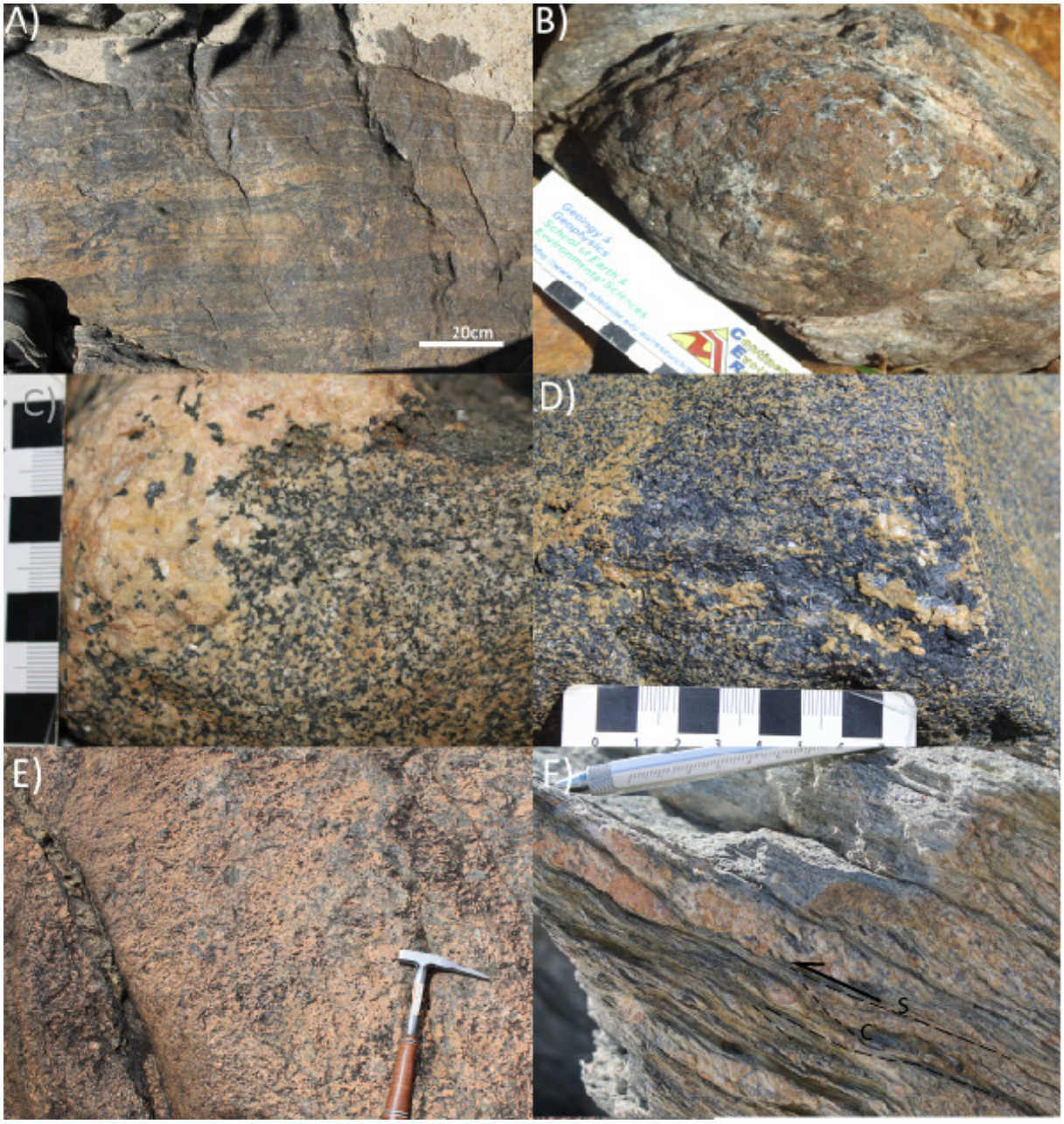

Figure 6: Field photographs from the Normanville exposure of the Myponga Inlier. A) Strongly layered quartzofeldspathic gneiss. B) Garnet sillimanite gneiss containing garnet porphyroblast approximately 10cm in diameter. C) Coarse grained calcsilicate with diopside bearing leucosome (top left of image). D) Amphibolite with coarse grained orthopyroxene bearing leucosome. E) Undeformed K-feldspar - quartz pegmatite. F) Retrograde fabrics displaying S-C fabrics and sigma clasts indicating top to the west thrust movement.

Orogeny. While the northern extent of the Myponga Inlier is exposed in the core of a Delamerian anticline (Offler and Fleming 1968), the southernmost extent of this structure is controlled by a thrust system which functions as the closure of the anticline in this area (Steinhardt 1991). Splays of this thrust system bound the western limit of the Normanville exposure (Figure 5). This system is expressed as muscovite-biotite-chlorite schists and display clear top-to-the-west thrust kinematics including S-C fabrics and

sigma clasts (Figure 6). Along the shorefront where these schists are best exposed, the basal conglomerates of the Aldgate Sandstone also occur. In some instances, cross bedding within the conglomerate indicate that it is the correct way up and effectively are younging towards the overthrust basement, indicating that some of these occurrences of the conglomerate are not conformable but rather thrust sheets associated with the development of the high strain zone. These conglomerates exhibit pebble stretching lineations which plunge 25°-45° to the southeast, down dip of the foliation planes. Detailed structural analysis of these features is given by Anderson (1975) and Steinhardt (1991). The central-southern margin of the Normanville exposure has also been previously recognised as a thrust contact (Steinhardt 1991), with Cambrian metasediments of the Kanmantoo Group thrust against the basement garnet-sillimanite gneiss. This boundary is largely obscured by Permian sediments.

Some areas within the inlier preserve retrograde shears that contain east side down S-C fabrics, which indicate an extensional history is also preserved (Steinhardt 1991, Morrissey et al. 2013). However these extensional kinematic indicators are much less frequent and the dominant preserved regime is undoubtedly compressional, as the basement has clearly been thrust atop the Neoproterozoic cover sequences on the western margin.

The intense retrogression in many areas hampers the identification of larger scale Palaeo-Mesoproterozoic structures. A strong gneissic fabric associated with peak metamorphic conditions, and the development of such features as garnet bearing leucosomes, is pervasive throughout many of the basement lithologies. This is layering is commonly planar and dips between 30°-50° towards the south-southeast (Davies 1972). No extensive Proterozoic folding is evident. Small scale (~20cm) tight to isoclinal folds are preserved in leucosome layering in some rare instances.

4. Discussion

4.1 Stratigraphic correlations

The lithologies across the various Barossa Complex inliers share a broad similarity. In every inlier, a quartzofeldspathic-rich psammopelite gneiss is exposed. This generally takes the form of a biotite-rich gneiss with quartzofeldspathic segregations. In the Warren and Oakbank inliers, where the retrogressive effects of the Delamerian Orogeny are stronger, muscovite is also a common constituent in this type of lithology. The psammopelite gneisses are commonly associated with a structurally overlying sillimanite bearing gneiss with similar quartzofeldspathic segregations, as is the case in the Houghton, Warren, and Aldgate inliers. In the Houghton and Myponga inliers,

Table 1: Summary of zirocn U-Pb depositional age constraints from Jagodzinski et al (2017)

Inlier	Lithology	Max. Dep. Age	Age type	Min. Dep. Age	Age Type
Houghton	Biotite- Sericite Gneiss (upper)	1655 ± 8 Ma	Youngest Detrital Zircon population	1609 ± 7 Ma	Metamorphic overgrowth
Houghton	Biotite- Sericite Gneiss (lower)	1707 ±5 Ma	Youngest Detrital Zircon population	1717 ± 7 Ma	Igneous Intrusion
Warren	Biotite Migmatite Gneiss	1658 ±11 Ma	Youngest Detrital Zircon population	1611 ± 5 Ma	Metamorphic overgrowth
Aldgate	Psammite - in SIllimanite Gneiss	1679 ± 12 Ma	Youngest Detrital Zircon population	1582 ± 4 Ma	Metamorphic overgrowth
Oakbank	Biotite Gneiss	1701 ± 14 Ma	Youngest Detrital Zircon population	1701 ± 14 Ma	Metamorphic overgrowth
Myponga	Quartzite	1653 ± 11 Ma	Youngest Detrital Zircon population	1590 ± 6 Ma	Metamorphic overgrowth

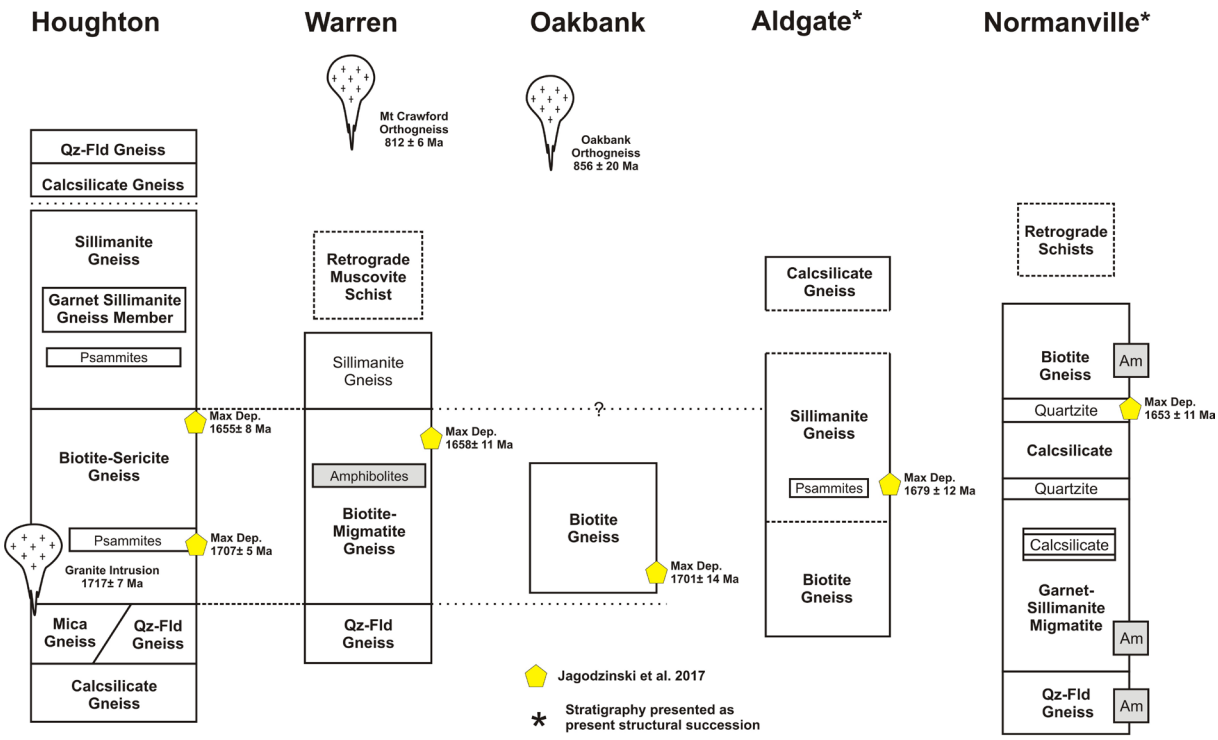

Figure 7: Proposed stratigraphic correlations between the Barossa Complex Inliers as discussed in text, with markers indicating the approximate stratigraphic position of samples analysed by Jagodzinski et al. (2017).

calcsilicate gneisses occur in association with quartzofeldspathic gneisses or quartzites. A small exposure of calcsilicate occurs in the southern extent of the Aldgate Inlier. Its relationship to other basement lithologies is completely obscured by the unconformably overlying Aldgate Sandstone.

Depositional timing constraints from these lithologies support some stratigraphic correlations. The psammopelitic unit of the Houghton Inlier (mapped as biotite-sericite gneiss, Chapter 1) records a minimum depositional age of 1717 ±7 Ma, given by the crystallisation age of an intruding magma, and a detrital zircon maximum depositional age from the upper extent of the sequence at 1655 ±8 Ma (Jagodzinski et al. 2017). The psammopelitic biotite gneiss from the Oakbank Inlier yields a detrital zircon MDA of 1701 ±14 Ma (Jagodzinski et al. 2017) which in combination with the similar lithofacies represents a likely stratigraphic correlation to the psammopelite in the Houghton Inlier (Figure 7). In the Aldgate Inlier, detrital zircon from a psammite layer within the sillimanite gneiss yielded a detrital zircon MDA of 1679 ±12 Ma. The lack of c. 1655 Ma zircon within this unit suggests that this unit is older than the upper psammopelitic unit in the Houghton and Warren inliers, but younger than the lower extent of this unit. As such it is reasonable to assume that the sillimanite gneiss in the Aldgate inlier is a temporal equivalent of the psammopelite units in the Houghton, Warren, and Oakbank inliers (Figure 7).

In the Normanville exposure of the Myponga Inlier, the stratigraphy is more cryptic than in the other inliers. This part of the Inlier is exposed in a high strain thrust zone which controls the closure of a regional anticline. The core of the Normanville exposure, where the regional fold trace should trend, is dominated by shear zones and no obvious fold hinge is exposed. In this part of the exposure, a quartzofeldspathic gneiss occurs which is largely mantled to the north

and south by garnet-sillimanite gneiss. The southern limit of this quartzofeldspathic gneiss is a retrograde shear and it is unclear if this is lithological repetition is the result of folding or thrusting. The garnet-sillimanite gneiss appears to largely have a conformable boundary with an interlayered quartzite-calcsilicate association in the northern extents of the Normanville exposure. Further south, the garnet sillimanite gneiss hosts smaller occurrences of quartzite and calcsilicate. The boundaries between these units are poorly exposed and it is unclear whether these are conformable or tectonic contacts. The final discernible metasedimentary unit in the Normanville exposure is a psammopelitic biotite-quartzofeldspathic gneiss. This gneiss is broadly similar in texture to the quartzofeldspathic gneiss but contains a greater abundance of biotite.

The proposed stratigraphic succession as described above is displayed in Figure 7. It must be noted that the depositional younging order of this succession is not known. A quartzite sample from the prominent quartzite-calcsilicate association in the northern extent of the Normanville exposure has a detrital zircon MDA of 1653 ±11 Ma, which is comparable to the c. 1655 Ma MDAs obtained from the Houghton and Warren Inlier psammopelites and may represent a temporal equivalent to these sequences. It may also be the case that no zircon younger than 1655 Ma exists in the sediment source regions. Further targeted geochronology is required in order to better establish the timing of the metasedimentary units in the Myponga Inlier, so that stratigraphic correlations can be identified and the nature of the basinal precursors to the Barossa Complex further refined.

One aspect which remains ambiguous in the Myponga Inlier is the relationship between the amphibolites and the metasedimentary units. In the Normanville exposure, the occurrences of amphibolites generally trend parallel to lithological boundaries, which may suggest that they were originally syn-depositional lava flows or sills. In other exposures, such as the Wild Dog locality mapped by Crowhurst (1988), the essentially linear occurrences of amphibolite do not appear to follow any of the metasedimentary lithological boundaries and are more suggestive of being intrusive. This may be the result of different levels of the stratigraphy being exposed, or of multiple generations of mafic magmatism. Addressing the relationship between the amphibolites and metasedimentary units may elucidate more of the basin conditions into which the Barossa Complex protoliths were deposited.

4.2 Structure and Metamorphic Timing

The Proterozoic metamorphic history of the Barossa Complex spans 80 m.y. from c. 1630 Ma to 1550 Ma (Szpunar et al. 2007, Morrissey et al. 2013, Jagodzinski et al. 2017). The earliest metamorphic phase is recorded in zircon growth at c. 1630 Ma which is best preserved in the Houghton and Oakbank inliers. This is followed by a second pulse of zircon growth at c. 1610 Ma (Jagodzinski et al. 2017). These first two pulses of zircon growth are not recorded by the Myponga Inlier, which only preserves metamorphic zircon ages of c. 1590 Ma (Szpunar et al. 2007, Jagodzinski et al. 2017). If the 1630-1610 Ma metamorphism recorded in zircon from the other four inliers did affect the Myponga Inlier, the record of these metamorphic periods has been obliterated by the 1590-1580 Ma stage of metamorphism.

The highest metamorphic grade in the Barossa Complex occurs in the southern Myponga Inlier (Preiss 1993) where granulite facies metamorphism is preserved. Phase equilibria modelling of a garnet-sillimanite migmatite sample from the Normanville exposure yielded peak metamorphic conditions of 800-870^{o}C and 8-9 Kbar (Morrissey et al. 2013). These peak conditions likely correspond to c. 1590 Ma, as the earlier 1630-1610 Ma periods are not recorded in this part of the Myponga Inlier. This period of peak metamorphism generated significant quantities of melt, as evidenced by the abundant occurrence of

garnet-bearing leucosome, which makes up to 40% of some outcrops. To the northeast of the Normanville exposure in the Myponga Inlier, monazite growth at c. 1580 Ma (Morrissey et al. 2013) coincides with the crystallisation of post deformational pegmatites at 1580 ±4 Ma (Jagodzinski et al. 2017). These pegmatites are offset in the core of the Normanville exposure by retrograde shear zones, demonstrating that the shears must be younger than c. 1580 Ma. Monazite from a shear zone displaying extensional kinematics yielded ages of 1563 ±9 Ma and 1566 ±9 Ma (Morrissey et al. 2013), which gives the probable age of extensional deformation. It is also possible that this monazite was inherited from the wall rocks (Morrissey et al. 2013), and that these shear zones developed during a later stage of extension, such as Neoproterozoic rifting.

Muscovite-biotite-chlorite shear zones with thrust movement senses are extensively developed, particularly on the northwestern margin of the inlier (Steinhardt 1991). The high strain zones here continue into the Neoproterozoic cover, and must have developed during the Delamerian Orogeny as this is the only major deformational event to have affected the Neoproterozoic sequences of the Adelaide Supergroup.

4.3 Future work in the Southern Barossa Complex

The tectonic reworking and limited exposure in the southern Barossa Complex inliers makes working in this region difficult. In the case of the Aldgate and Oakbank inliers, the limited lithological variety offers few unique opportunities to assess the development of the Barossa Complex. The Myponga Inlier offers the most promising prospects for further work of the three inliers discussed here. The extensive cover sequences and limited outcrop mean that any work conducted in the inlier will require extensive groundwork and mapping in order to establish the relationships between the sampled or addressed lithologies.

The stratigraphy is still largely cryptic in much of the Myponga Inlier, and it is unclear how the proposed stratigraphy from the Normanville exposure relates to the rest of the inlier, or the northern inliers. However, one of the more defining aspects of the Myponga Inlier is that mafic magmatism, preserved as amphibolites, occur with much greater frequency in the southern Myponga Inlier than anywhere else in the exposed Barossa Complex. The proposed links to the Barossa Complex to other Palaeoproterozoic basins in southeastern Australia rely largely on the timing of deposition and metamorphism. Characterising the geochemical character of intruding magmas could help further constrain the tectonic style of the basin hosting the protoliths to the Barossa Complex, such as has been done in other Palaeoproterozoic basins in eastern Australia (e.g. Rutherford et al. 2006, Raveggi et al. 2007, Baker et al. 2010). This could potentially help strengthen or redefine the proposed stratigraphic links between the Barossa Complex and areas such as the Willyama Supergroup in the Curnamona Province (Jagodzinski et al. 2017).

5. Conclusions

Broad lithostratigraphic similarities occur throughout the Barossa Complex inliers, from which probable stratigraphic correlations have been proposed based on lithological similarity and the available geochronology. The psammopelitic gneisses which occur in the Houghton Inliers yields minimum and maximum depositional ages from the lower and upper extents of this unit of 1717 ±7 Ma and 1655 ± 8 Ma (Jagodzinski et al. 2017). The lower age is within uncertainty of the maximum depositional age of the Oakbank Inlier psammopelite at 1701 ±14 Ma, and is a probable correlation. In the Aldgate Inlier, a psammitic layer from within sillimanite gneisses yields a maximum depositional age of 1679 ±12 Ma, which likely reflects

a deeper water temporal equivalent of the Houghton Inlier psammopelite gneiss. The Myponga Inlier records a sequence of quartzofeldspathic gneiss, pelitic gneiss, quartzite and calcsilicate, and psammopelitic gneiss. It is uncertain if this sequence is the correct way up. One of the quartzites which occurs in association with the calcsilicate has a detrital zircon MDA of 1653 ±11 Ma, which is comparable to MDAs obtained from the Houghton and Warren inliers in the northern Barossa Complex. Further refinement of the stratigraphy and depositional timing would be required to propose significant stratigraphic correlations.

References

Adshead-Bell, N. S. & Bell, T. H., 1999. The progressive development of a macroscopic upright fold pair during five near-orthogonal foliation-producing events: complex microstructures versus a simple macrostructure. Tectonophysics, 306(2), 121-147.

Anderson, J. A., 1975. Structural and strain analysis of the nose of the Myponga - Little Gorge Inlier, Fleurieu Peninsula, South Australia. Unpub. BSc (Hons) Thesis, University of Adelaide.

Baker, M. J., Crawford, A. J. & Withnall, I. W., 2010. Geochemical, Sm–Nd isotopic characteristics and petrogenesis of Paleoproterozoic mafic rocks from the Georgetown Inlier, north Queensland: Implications for relationship with the Broken Hill and Mount Isa Eastern Succession. Precambrian Research, 177(1–2), 39-54.

Belperio, A. P., 1985. Echunga 1:50000 Geological Sheet, South Australian Department of Mines and Energy.

Benson, W. N., 1909. Petrographical Notes on Certain Pre-Cambrian Rocks of the Mount Lofty Ranges, With Special Reference to the Geology of the Houghton District. Transactions of the Royal Society of South Australia, 33, 101-140.

Crowhurst, P. V., 1988. The geology, petrology and geochemistry of the Proterozoic inlier, south of Myponga, Fleurieu Peninsula, South Australia. Unpub. BSc (Hons) Thesis, University of Adelaide.

Davies, M. B., 1972. The geology and petrology of an Archaean inlier south of Normanville – the geochemistry of the Houghton granulite. Unpub. BSc (Hons) Thesis, University of Adelaide.

Flottmann, T. & James, P., 1997. Influence of basin architecture on the style of inversion and fold-thrust belt tectonics—the southern Adelaide Fold-Thrust Belt, South Australia. Journal of Structural Geology, 19(8), 1093-1110.

Flöttmann, T., James, P., Rogers, J. & Johnson, T., 1994. Early Palaeozoic foreland thrusting and basin reactivation at the Palaeo-Pacific margin of the southeastern Australian Precambrian Craton: a reappraisal of the structural evolution of the Southern Adelaide Fold-Thrust Belt. Tectonophysics, 234(1–2), 95-116.

Heaslip, J. E., 1972. Review of the Geology of the Mt. Magnificent Area. Unpub. BSc (Hons) Thesis, University of Adelaide.

Howchin, W., 1926. The geology of the Barossa Ranges and neighborhood in relation to the geological axis of the country. Transactions of the Royal Society of South Australia, 50, 1-16.

Jagodzinski, E.A., Meaney, K., Szpunar, M., and Fraser, G., 2017. SHRIMP U-Pb dating of the Barossa Complex, South Australia: exploring tectonic links between the Gawler Craton and Curnamona Province. Report Book 2017/00017. Department of the Premier and Cabinet, South Australia, Adelaide.

Mancktelow, N. S., 1990. The structure of the southern Adelaide Fold Belt, South Australia. In: The evolution of a Late Precambrian-Early Paleozoic Rift Complex: The Adelaide Geosyncline (eds Jago, J. B. & Moore, P. J.), pp. 483-495, The Geological

Society of Australia Special Publication

McEwin, A. J., 1972. Geology and petrology of part of the Archaean Inlier north-east of Yankalilla on the Fleurieu Peninsula. Unpub. BSc (Hons) Thesis, University of Adelaide.

Morrissey, L. J., Hand, M., Wade, B. P. & Szpunar, M., 2013. Early Mesoproterozoic metamorphism in the Barossa Complex, South Australia: links with the eastern margin of Proterozoic Australia. Australian Journal of Earth Sciences, 60(8), 769-795.

Offler, R. & Fleming, P. D., 1968. A synthesis of folding and metamorphism in the Mt Lofty Ranges, South Australia. Journal of the Geological Society of Australia, 15(2), 245-266.

Preiss, W. V., 1993. Basement Inliers of the Mount Lofty Ranges. In: The Geology of South Australia, Volume 1, The Precambrian (eds Drexel, J. F., Preiss, W. V. & Parker, A. J.), pp. 102-105, Geological Survey of South Australia, Adelaide.

Preiss, W. V., 2000. The Adelaide Geosyncline of South Australia and its significance in Neoproterozoic continental reconstruction. Precambrian Research, 100(1-3), 21-63.

Preiss, W. V., Fanning, C. A., Szpunar, M. A. & Burtt, A. C., 2008. Age and tectonic significance of the Mount Crawford Granite Gneiss and a related intrusive in the Oakbank Inlier, Mount Lofty Ranges, South Australia. MESA Journal, 49, 38-49.

Raveggi, M., Giles, D., Foden, J. & Raetz, M., 2007. High Fe–Ti mafic magmatism and tectonic setting of the Paleoproterozoic Broken Hill Block, NSW, Australia. Precambrian Research, 156(1–2), 55-84.

Reid, A. J., Jourdan, F. & Jagodzinski, E. A., 2017. Mesoproterozoic fluid events affecting Archean crust in the northern Olympic Cu–Au Province, Gawler Craton: insights from 40Ar/39Ar thermochronology. Australian Journal of Earth Sciences, 64(1), 103-119.

Rutherford, L., Barovich, K., Hand, M. & Foden, J., 2006. Continental ca 1.7 – 1.69 Ga Fe-rich metatholeiites in the Curnamona Province, Australia: a record of melting of a heterogeneous, subduction-modified lithospheric mantle. Australian Journal of Earth Sciences, 53(3), 501-519.

Sprigg, R. C., Whittle, A. W. G. & Campana, D., 1951. Adelaide 1:1 Mile Geological Sheet (ed Dickinson, S. B.), Department of Mines, Adelaide, Adelaide, South Australia.

Sprigg, R. C. & Wilson, B., 1954. Echunga 1:1 Mile Geological Sheet (ed Dickinson, S. B.), Departmen of Mines, Adelaide, Adelaide.

Steinhardt, C., 1991. The microstructural anatomy of a major thrust zone on Fleurieu Peninsula, South Australia. Australian Journal of Earth Sciences, 38(2), 139-150.

Szpunar, M., Wade, B., Hand, M. P. & Barovich, K. M., 2007. Timing of Proterozoic high-grade metamorphism in the Barossa Complex, southern South Australia; exploring the extent of the 1590 Ma event. MESA Journal, 47, 21-27.

Wicks, S. P., 1972. Geology of part of basement inlier north-east of Mt. Compass. Unpub. BSc (Hons) Thesis, University of Adelaide.

CHAPTER 4

This Chapter is written for submission to
The Australian Journal of Earth Sciences as;

Meaney, K., Hand, M., Payne, J.,
Timing constraints on the deposition of the Palaeoproterozoic Barossa Complex, south eastern Gawler Craton: Implications for Proterozoic reconstructions

Statement of Authorship

Title of Paper	Timing constraints on the deposition of the Paleoproterozoic Barossa Complex, South Eastern Gawler Craton: Implications for Proterozoic reconstructions
Publication Status	☐ Published ☐ Accepted for Publication ☐ Submitted for Publication ☑ Unpublished and Unsubmitted w ork w ritten in manuscript style
Publication Details	Written to be submitted to The Australian Journal of Earth Sciences

Principal Author

Name of Principal Author (Candidate)	Kieran Meaney		
Contribution to the Paper	Project design, Fieldwork, Sample Preparation, LA-ICP-MS Data Collection, MC-LA-ICP-MS Data Collection, Data interpretation, Manuscript design, Creation of figures		
Overall percentage (%)	80		
Certification:	This paper reports on original research I conducted during the period of my Higher Degree by Research candidature and is not subject to any obligations or contractual agreements with a third party that would constrain its inclusion in this thesis. I am the primary author of this paper.		
Signature		Date	21/12/17

Co-Author Contributions

By signing the Statement of Authorship, each author certifies that:

i. the candidate's stated contribution to the publication is accurate (as detailed above);
ii. permission is granted for the candidate in include the publication in the thesis; and
iii. the sum of all co-author contributions is equal to 100% less the candidate's stated contribution.

Name of Co-Author	Martin Hand		
Contribution to the Paper	Assistance with fieldwork, Guidance with data interpretation, Manuscript review		
Signature		Date	21/12/2017

Name of Co-Author	Justin Payne		
Contribution to the Paper	MC-LA-ICP-MS Data Collection, Data quality control, Manuscript Review		
Signature		Date	20/12/17

ABSTRACT

The Palaeo-Mesoproterozoic Barossa Complex lies on the eastern margin of the Gawler Craton and in this position it forms the south-eastern edge of Proterozoic Australia. As such it represents a valuable pinning point in paleogeographic reconstructions of Proterozoic supercontinents such as Columbia/Nuna or Rhodinia. U-Pb and Hf isotope analysis from detrital zircons and magmatic intrusives indicate that the protoliths to the Barossa Complex formed between ca. 1730 Ma and 1655 Ma. Detrital zircon $\varepsilon_{Hf}(t)$ values are consistent with sediment having been primarily sourced from the c. 1730-1690 Ma Kimban Orogen in the eastern and northern Gawler Craton. Metamorphic overgrowths on detrital and magmatic zircon yield ages of c. 1625 Ma. Together with previously reported c. 1590 Ma metamorphic ages in other parts of the Barossa Complex, these ages suggest either long lived metamorphism or a poly-metamorphic evolution. The depositional timing of the Barossa Complex correlates to the onset of deposition in the Willyama Supergroup in the Curnamona Province, and supports paleogeographic reconstructions that propose a basin extending along the eastern margin of Proterozoic Australia during the late Palaeoproterozoic.

1. Introduction

To create meaningful paleogeographic reconstructions of past supercontinents a variety of factors need to be considered. One crucial factor in aligning potentially displaced geological regions into their previous configurations is accurately recognising and correlating tectonic settings of depositional environments, metamorphic events, and magmatic events (e.g. Dalziel 1991, Zhao et al. 2002, Zhao et al. 2004, Goodge et al. 2008, Evans and Mitchell 2011, Zhang et al. 2012, Mulder et al. 2015). Two major supercontinents are proposed to have existed during the Proterozoic; the Palaeoproterozoic Nuna or Columbia supercontinent (e.g. Zhao et al. 2002, Zhao et al. 2004, Zhang et al. 2012, Betts et al. 2015), and the Meso-Neoproterozoic Rodinia supercontinent (e.g. Moores 1991, Dalziel 1991, Karlstrom et al. 1999, Li et al. 2008, Pisarevsky et al. 2014). The configuration of Australia within these reconstructions varies between the different models, however the North American craton, Laurentia, is commonly situated adjacent Australia's eastern margin during both time periods (e.g. Brookfield 1993, Giles et al. 2004, Zhao et al. 2004, Betts et al. 2008, Li et al. 2008, Zhang et al. 2012, Medig et al. 2014, Pisarevsky et al. 2014, Mulder et al. 2015). In order to test the validity of any of these reconstructions an accurate characterisation of the continental margins involved is needed before a meaningful comparison can be made.

In the case of eastern Proterozoic Australia, this involves studying the eastern regions of the North Australian Craton (NAC) and South Australian Craton (SAC). The Mawson Continent, which includes the SAC and the formerly attached Adèlie Craton of East Antarctica (Payne et al. 2009), make up the south-eastern portion of the proto-Australian continent during the Proterozoic (e.g. Giles et al. 2004, Zhao et al. 2004, Betts and Giles 2006, Betts et al. 2007, Li et al. 2008, Boger 2011, Zhang et al. 2012, Pisarevsky et al. 2014, Betts et al. 2015). The SAC consists of the Archean-Mesoproterozoic Gawler Craton and the Palaeo-Mesoproterozoic Curnamona Province (Figure 1; Myers et al. 1996). Throughout the Palaeoproterozoic, the Gawler Craton underwent widespread basin development (e.g. Payne et al. 2006, Hand et al. 2007, Howard et al. 2009, Payne et al. 2009, Kositcin 2010, Howard et al. 2011a, Szpunar et al. 2011, Reid and Hand

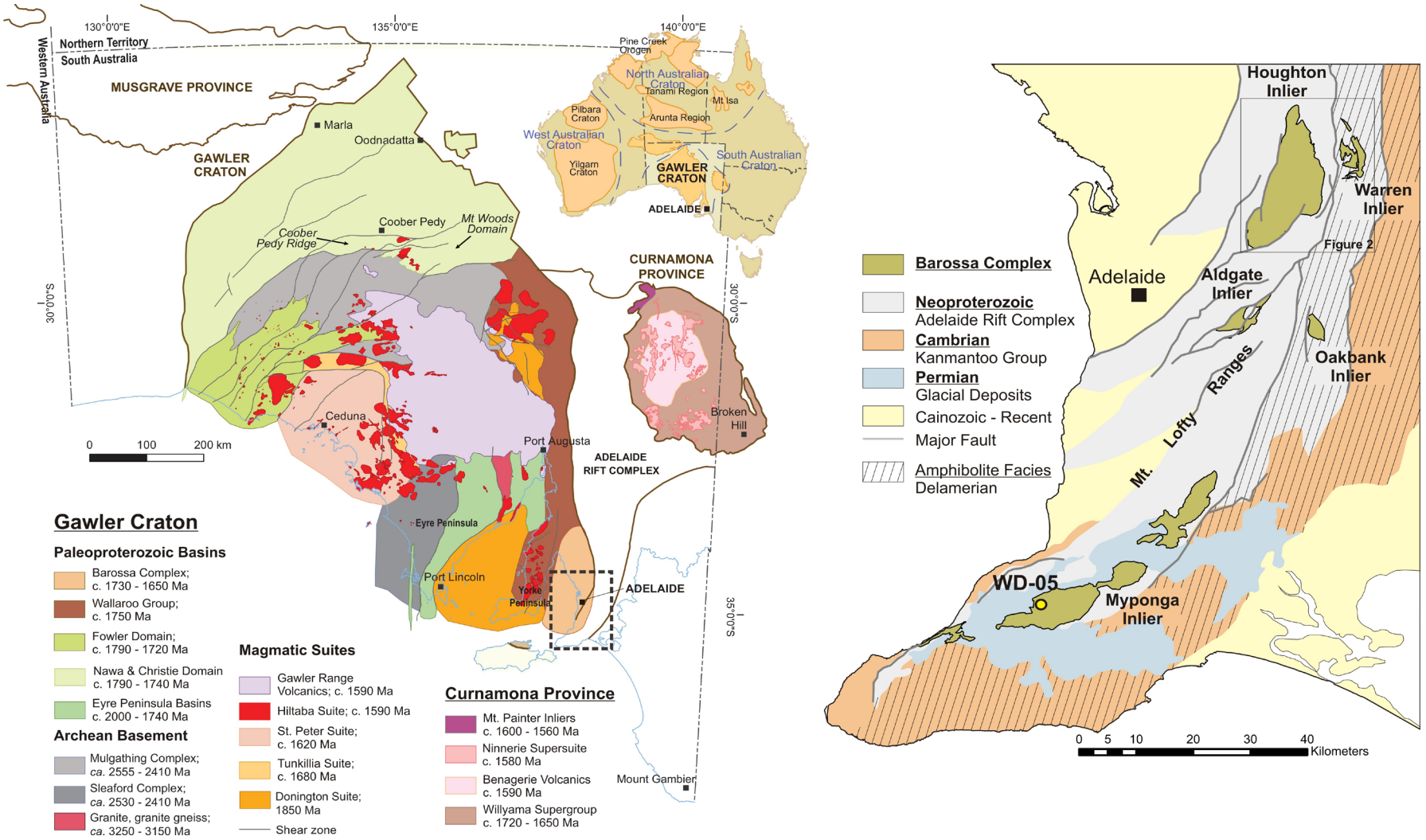

Figure 1: Left, geological domains of the Gawler Craton and Curnamona Province in South Australia and location of the Barossa Complex (after Reid et al. 2017). Right, simplified geology of the Mt. Lofty Ranges showing the locations of the 5 Barossa Complex Inliers (after Preiss 1993) and sampling location from the Myponga Inlier.

2012). In the eastern Gawler Craton and the Curnamona Province, these basins contain bimodal magmatism and sedimentation which is considered to represent either a continental rift or back arc extension (Willis et al. 1983, Zang 2002, Forbes et al. 2008, Reid et al. 2008a, Szpunar et al. 2011). When formulating Palaeogeographic reconstructions during the Palaeo-Mesoproterozoic it is these eastern Gawler Craton and Willyama Supergroup basins that are typically considered for comparison with potential adjacent continental blocks in paleogeographic reconstructions (e.g. Li et al. 2008, Zhang et al. 2012, Betts et al. 2015). While these are not likely a true representation of the Australian continental margin during the Palaeoproterozoic, they are the closest identifiable regions to that margin in south-eastern Australia.

One region which remains largely understudied is the Barossa Complex, which is exposed on the southeast margin of the Gawler Craton (Figure 1). Existing work on the Barossa Complex has focussed on the metamorphic characteristics (Szpunar et al. 2007, Morrissey et al. 2013), with limited work having been done on the depositional timing, setting, or provenance of the sedimentary protoliths to the Barossa Complex (Jagodzinski et al. 2017). This work aims to provide further insight into the provenance and depositional history of the Barossa Complex by building upon the existing detrital zircon U-Pb datasets, and providing the first Lu-Hf isotopic data to further assess sedimentary provenance.

2. Geological Setting

The Barossa Complex is the collective term for five basement inliers which are exposed in the Mt. Lofty Ranges in South Australia (Figure 1; Preiss 1993). These inliers are considered to represent the southeastern-most exposure of the Archean-Mesoproterozoic Gawler Craton (Szpunar et al. 2007). The generally poorly outcropping Barossa Complex forms the basement to the Neoproterozoic-Cambrian Adelaide Rift Complex (Preiss 2000) and is exposed as partially fault-bound anticlianal cores in folds associated with the Cambro-Ordovician Delamerian Orogeny (Offler and Fleming 1968, Mancktelow 1990).

The Barossa Complex consists primarily of metasedimentary and metaigneous gneisses (Preiss 1993 and references therin). A broad scale stratigraphy has been proposed for the Houghton and Warren Inliers (Figure 2; Chapter 2), which includes pelitic and psammopelitic gneisses, quartzofeldspathic gneisses, calcsilicate gneisses, and felsic orthogneisses. The depositional setting was interpreted to be either a marine shelf or rift basin setting (Chapter 2). Amphibolites are also present in the Warren Inlier, and occur more abundantly in the Myponga Inlier to the south (Davies 1972, Crowhurst 1988, Chapter 3). Whether these represent syn- or post-depositional magmatism remains unclear.

The depositional timing of the Barossa Complex is currently constrained to between approximately 1717 ±7 Ma when the protolith to the South Para Orthogneiss was intruded, and c. 1630 Ma during the onset of metamorphism (Jagodzinski et al. 2017). Maximum depositional ages defined by youngest detrital zircon across the five inliers range between 1707 ±5 Ma and 1653 ±11 Ma (Jagodzinski et al. 2017), all of which are younger than the South Para Orthogneiss, which indicates a syn-depositional magmatic event was occurring early in the depositional history of the Barossa Complex.

Three identified Proterozoic deformation events are preserved in the northern Barossa Complex (Chapter 2). An early high grade metamorphic event created a strong low angle metamorphic foliation (S_1) which was subsequently deformed by two folding phases. A multi-stage metamorphic history is recorded in the zircon and monazite of the Barossa Complex. Jagodzinski et al. (2017) identified multiple samples from across the Barossa Complex inliers with metamorphic zircon U-Pb ages at c. 1630 Ma, 1610 Ma, and 1590 Ma. Other studies on the metamorphism

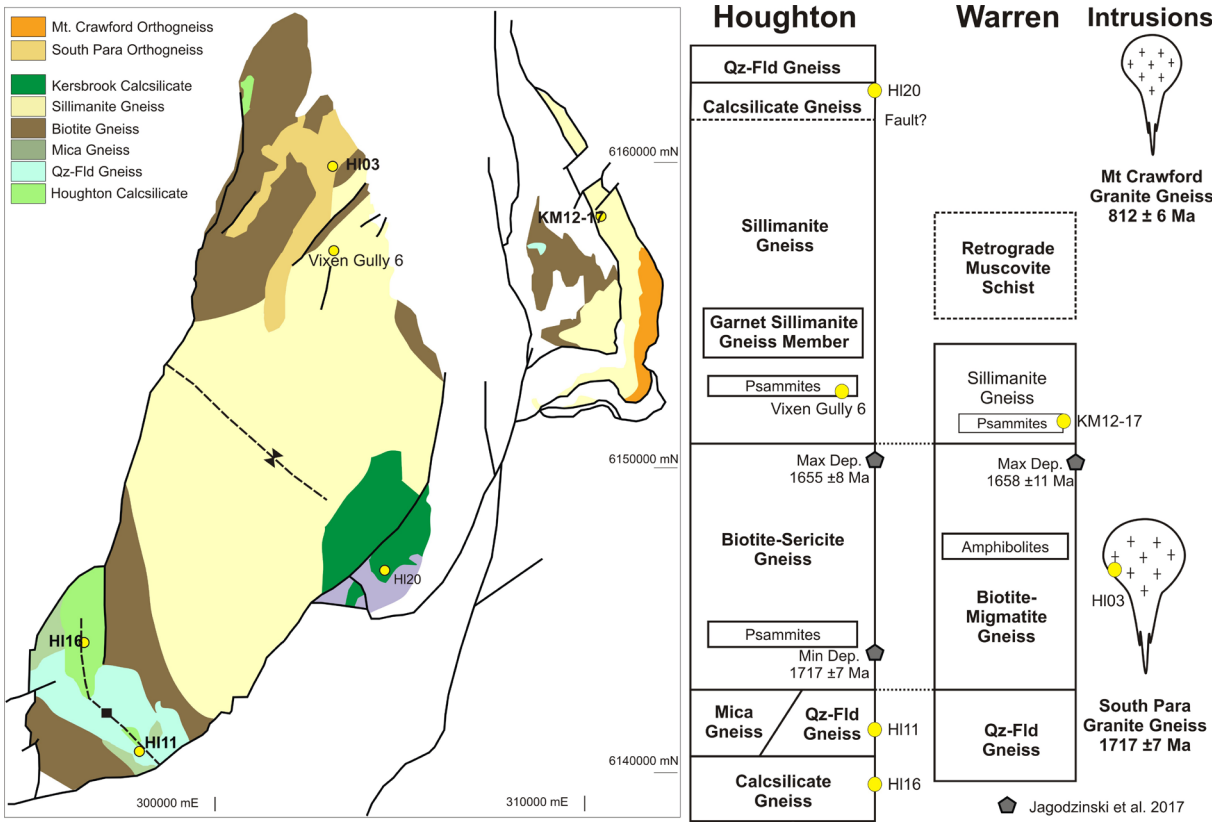

Figure 2: Left, simplified geological map of the Houghton and Warren Inliers with sampling locations indicated. Right, stratigraphic column for the Houghton and Warren Inliers (Chapter 2) with approximate positions of the stratigraphy sampled in this study and by Jagodzinski et al. (2017).

in the Barossa Complex have demonstrated metamorphic zircon and monazite U-Pb ages ranging between 1590-1580 Ma from the Myponga and Houghton Inliers (Szpunar et al. 2007, Morrissey et al. 2013). Calculated metamorphic conditions indicate that peak metamorphism occurred at 800-850°C and 8-9 kbar (Morrissey et al. 2013). Which period of metamorphism these conditions relate to is still uncertain. A further stage of monazite growth occurred between c. 1570-1550 Ma, which likely reflects a period of retrograde metamorphism (Morrissey et al. 2013).

During the Neoproterozoic the Barossa Complex was intruded by granites between 850-812 Ma, which are associated with the opening of the rift basin that hosts the Adelaide Rift Complex (Preiss et al. 2008). The Barossa Complex was retrogressed at greenschist facies and structurally reworked by the Cambro-Ordovician Delamerian Orogeny between 514-490 Ma (Talbot 1963, Foden et al. 2006, Chapter 2).

3. Methods

3.1 Sampling

Samples were collected from throughout the Barossa Complex for detrital zircon (Figure 1, 2). In the Houghton Inlier, samples were selected from across the stratigraphic profile proposed in Chapter 2 (Figure 2). In many cases metamorphic growth has completely destroyed the detrital grains. In some cases, particularly for the sillimanite gneiss in the Houghton Inlier, zircon was not recovered despite multiple attempts at sampling and separation. For this reason no detrital data are presented for the biotite-sericite gneiss and the bulk of the sillimanite gneiss of the Houghton Inlier, despite these units comprising the majority of the outcrop in the Houghton Inlier.

3.2 Analytical methods

3.2.1 Zircon U-Pb Analyses

Zircon separates were prepared from crushed samples using standard panning, Frantz magnetic, and heavy liquid techniques. Polished zircon mounts were imaged using backscatter secondary electron (BSE) and cathodoluminescence (CL) imaging on a Phillips XL-40 SEM with attached Gatan CL detector. Single-grain U–Pb zircon dating was undertaken by Laser Ablation Inductively Coupled Plasma Mass Spectrometry (LA-ICP-MS) using a NewWave 213 nm Nd-YAG laser in a He ablation atmosphere, coupled to an Agilent 7500cs ICP-MS at Adelaide Microscopy at the University of Adelaide. A 60 second gas blank was analysed followed by 60 seconds of measurement during zircon ablation. The laser was fired for 10 seconds with the shutter closed prior to ablation to allow for beam stabilisation. The Isotopes measured were ^{204}Pb, ^{206}Pb, ^{207}Pb, and 238U with dwell times of 10, 15, 30, and 15 ms, respectively. U-Pb isotope data and age estimates were exported into Microsoft Excel and age calculations and graphs were completed using Isoplot v4.11 (Ludwig 2003). All errors stated for age calculations are to the 2σ level.

For all analyses, the zircon standard GEMOC GJ-1 was used as a matrix-matched standard to correct for mass bias and fractionation (TIMS normalisation data ^{207}Pb/^{206}Pb = 608.3 Ma, ^{206}Pb/^{238}U = 600.7 Ma and ^{207}Pb/^{235}U = 602.2 Ma; Jackson et al. 2004). Accuracy was checked using the recognised zircon standard Plešovice (337.13 ± 0.37 Ma; Sláma et al. 2008). Over the duration of this study weighted ^{207}Pb/^{206}Pb, ^{206}Pb/^{238}U, and ^{206}Pb/^{235}U ages for GJ-1 yeilded 608.6 ±4 Ma, 600.5 ±0.97 Ma, and 602 ±0.96 Ma respectively (n=347). For Plešovice weighted ^{207}Pb/^{206}Pb, ^{206}Pb/^{238}U, and ^{206}Pb/^{235}U ages yielded 340 ±9 Ma, 334.2 ±1.9 Ma, and 334.6 ±1.9 Ma respectively. (n=71).

3.2.2 Zircon Lu-Hf analyses

The method for zircon Lu-Hf isotope analyses follow that of Payne et al. (2013). Analyses were conducted using a New Wave UP-193 ArF eximer laser with an attached Thermo-Scientific Neptune Multi Collector ICP-MS at the University of Adelaide. Analyses were undertaken using a 5 Hz repetition rate and an intensity of 6-8 J/cm^2. Beam sizes varied between 50 µm to 30 µm depending on the zircon or detrital core size. Data reduction was carried out using the macro-driven Hf isotope data reduction Excel spreadsheet HfTRAX of Payne et al. (2013). The data were normalised to ^{179}Hf/^{177}Hf = 0.7325 using an exponential correction for mass bias. Yb and Lu isobaric interferences were corrected for using the methods of Woodhead et al. (2004). The accuracy of the Yb and Lu corrections has been demonstrated by analysis of the natural zircon standards Mud Tank (Woodhead and Hergt 2005) and Plešovice (Sláma et al. 2008) before and during analysis to check instrument performance and stability. The mean ^{176}Hf/^{177}Hf ratio yielded from the Mud Tank standard was 0.282499 ± 0.000006 which is within uncertainty of the published value of 0.282506 ± 0.000026 (2σ; Woodhead and Hergt 2005). The mean ^{176}Hf/^{177}Hf ratio yielded from the Plešovice standard was 0.282468 ± 0.000008 which is within uncertainty of the published value of 0.28248 ± 0.000013 (2σ; Sláma et al. 2008). Values for $\varepsilon_{Hf}(t)$ and TDMc were calculated using the ^{176}Lu decay constant of 1.865 x 10^{-11} of Scherer et al. (2001). TDMc was calculated using the methods and average crustal composition of ^{176}Lu/^{177}Hf = 0.015 (Griffin et al. 2002).

4. Results

4.1 Houghton Inlier

4.1.1 HI20 – Kersbrook Calcsilicate

Sample HI20 was collected from an occurrence of calcsilicate east of the Kersbrook township (UTM 54H, 304708 mE, 6146708 mN), and is representative of the structural top of the exposed stratigraphy in the Houghton Inlier. This sample is composed largely of epidote, plagioclase, and actinolite. Zircons

from this sample range in size between 50-300 μm, but are most frequently around 100 μm. Grain shapes are typically tabular. Under CL imaging, bright oscillatory zoned cores occur frequently, however darker sector zoning is the most common texture which occurs in the rims and in homogeneous grains (Figure 3a).

A total of 70 analyses were obtained from 54 grains in this sample. Of these 33 analyses were within 5% of concordancy. Two clear populations are apparent (Figure 4a), with the older population corresponding to analyses from textural cores. The weighted mean of the $^{207}Pb/^{206}Pb$ age for this older population is 1728±17 Ma (n = 15, MSWD = 0.49, Probability = 0.94).

The weighted mean of the $^{207}Pb/^{206}Pb$ age for the younger population corresponding to textural rims or homogeneous unzoned grains is 1639 ±13 Ma (n =17, MSWD = 0.66, probability = 0.84).

4.1.2 Vixen Gully 6 – Psammite from sillimanite gneiss

Sample Vixen Gully 6 was collected from a psammite layer within the sillimanite gneiss which dominates the exposure of the Houghton Inlier (UTM 54H, 302969 mE, 6157147 mN). Of several samples collected from the sillimanite gneiss, this psammite was the only sample that yielded detrital zircon, and only relatively small quantities of zircon were recovered from this sample despite processing a large amount of material. Zircons from this sample have equant to tabular grain shapes ranging in size between 30-150 μm. Under CL imaging the grains present a range of textures including oscillatory zoned, dark sector zoned, and dark texturally homogeneous structures. Small texturally homogeneous rims occur on some grains (Figure 3b).

A total of 60 analyses were obtained from 57 grains in this sample. Of these analyses, 43 were within 5% of concordancy. Two major age groupings occur (Figure 4b). The first occurs at ca. 1600 Ma which relate to a group of zircons which are dark and texturally homogeneous under CL. The weighted mean $^{207}Pb/^{206}Pb$ age of this grouping gives 1610 ±26 Ma (n = 9, MSWD = 0.41, probability = 0.92). The second major grouping occurs as a broad range which plots between ca. 1700 and ca. 1900 Ma, and is reflected in the major peak in the probability density plot (Figure 5b). The weighted mean $^{207}Pb/^{206}Pb$ age of this population is 1799 ±24 Ma (n = 26, MSWD = 2.1, probability = 0.001). Given the MSWD value of 2.1, this age likely reflects the average of a series of age populations from between 1700 Ma and 1900 Ma. Several small peaks occur between ca. 2000 Ma and 3000 Ma, with the largest occurring at ca. 2600 Ma.

4.1.3 HI11 – Quartzofeldspathic gneiss

Sample HI11 was collected from an outcrop of quartzofeldspathic gneiss which structurally overlies the Houghton Calcsilicate in the southern Houghton Inlier (UTM 54H, 298040 mE, 6140808 mN). This gneiss is composed predominantly of quartz and plagioclase, with minor biotite and hematite. The zircon separated from this sample typically present tabular to equant grain shapes ranging in size between 50-200 μm.

Under CL imaging the majority of grains displayed oscillatory zoning, although this is typically dark and often only faintly visible (Figure 3c), which may be indicative of metamorphic disturbance. The zircons commonly have thin dark and textureless rims. Many grains appear to have broken or ragged edges which truncate the oscillatory zoning. Several grains presented as very dark with no visible texture, consistent with a metamorphic origin.

A total of 180 analyses were obtained from the cores of 180 grains. Of these analyses 64 were within 5% of concordancy. On a probability density plot this presents as a dominant peak at 1690 Ma with a subtle shoulder at 1600 Ma. Two concordant grains also occur at ca. 1840 Ma. The mean weighted $^{207}Pb/^{206}Pb$ age of the dominant grouping of data yields an age of 1693 ±5 Ma (n = 50,

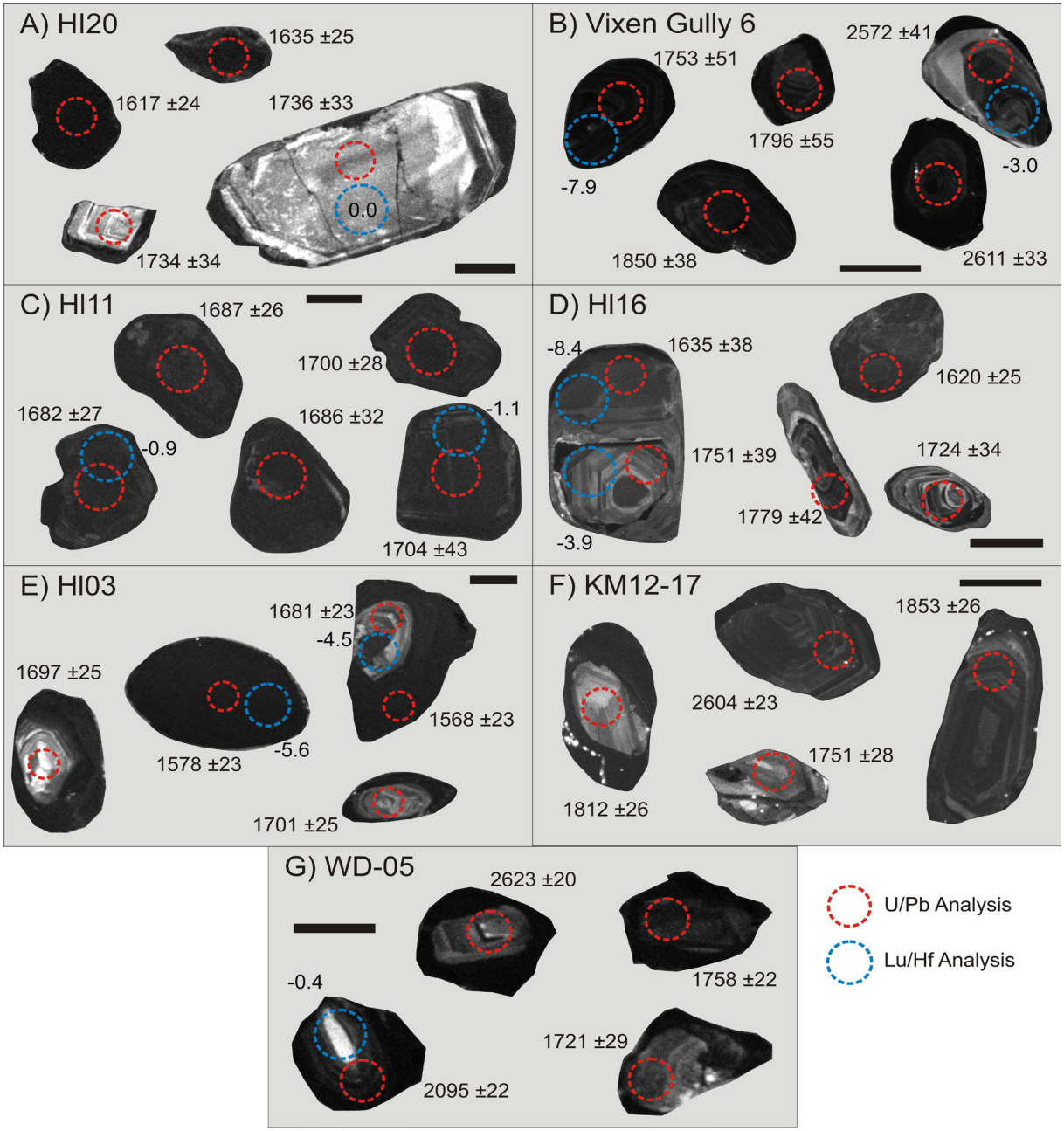

Figure 3: Representative zircon CL images of zircons analysed with locations of U-Pb and Lu-Hf isotopic analyses. Black scale bar in all frames is 50µm.

MSWD = 1.5, probability = 0.0015). The mean weighted $^{207}Pb/^{206}Pb$ age of the younger grouping is 1615 ±20 Ma (n = 8, MSWD = 0.39, probability = 0.91).

4.1.4 HI16 – Houghton Calcsilicate

Sample HI16 was collected from an outcrop of the Houghton Calcsilicate in the southern Houghton Inlier (UTM 54H, 296355 mE, 6144454 mN). This unit is structurally the lowest unit in the Houghton Inlier. The Houghton Calcsilicate is dominantly composed of plagioclase with minor quartz. Layers of diopside and actinolite define a strong gneissic layering. Epidote and hematite occur as common accessory minerals.

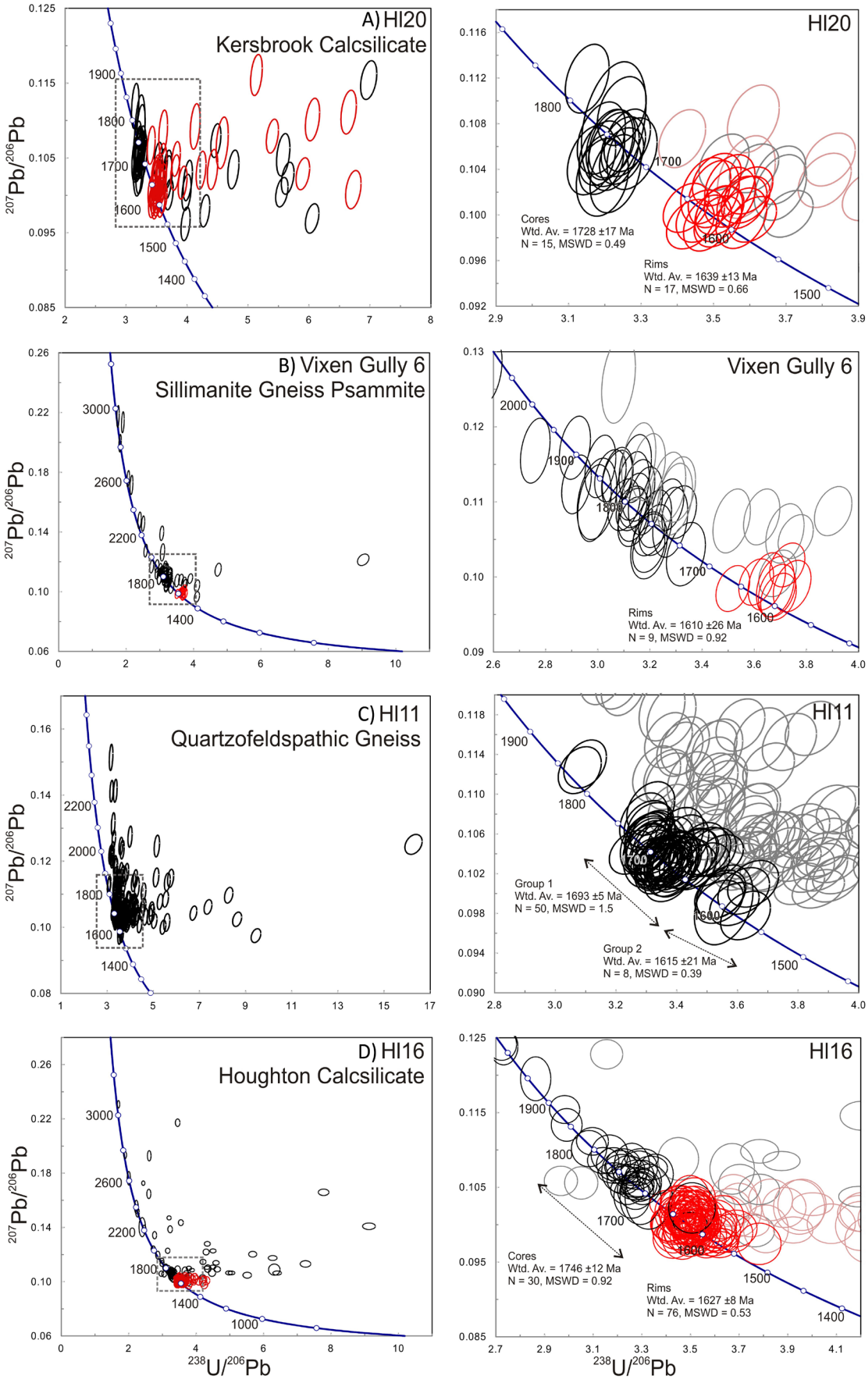
A) HI20
Kersbrook Calcsilicate
HI20
Cores
Wtd. Av. = 1728 ±17 Ma
N = 15, MSWD = 0.49
Rims
Wtd. Av. = 1639 ±13 Ma
N = 17, MSWD = 0.66
B) Vixen Gully 6
Sillimanite Gneiss Psammite
Vixen Gully 6
Rims
Wtd. Av. = 1610 ±26 Ma
N = 9, MSWD = 0.92
C) HI11
Quartzofeldspathic Gneiss
HI11
Group 1
Wtd. Av. = 1693 ±5 Ma
N = 50, MSWD = 1.5
Group 2
Wtd. Av. = 1615 ±21 Ma
N = 8, MSWD = 0.39
D) HI16
Houghton Calcsilicate
HI16
Cores
Wtd. Av. = 1746 ±12 Ma
N = 30, MSWD = 0.92
Rims
Wtd. Av. = 1627 ±8 Ma
N = 76, MSWD = 0.53
$^{207}Pb/^{206}Pb$
$^{238}U/^{206}Pb$

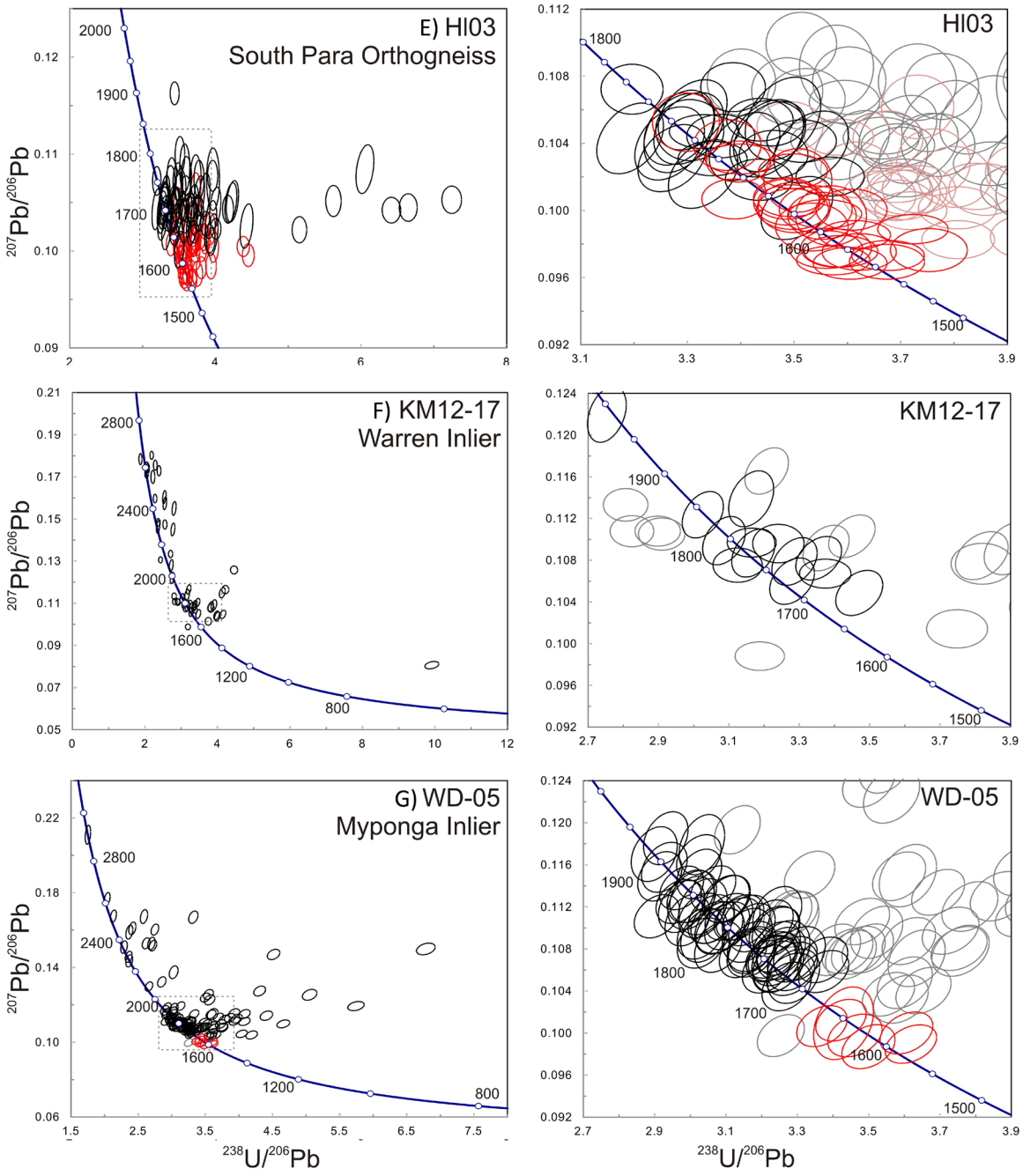

Figure 4: Concordia diagrams for all U-Pb samples analysed displaying all data With enlargements of dense areas on the right. Data greater than 5% discordant is semi-transparent in enlargement frames. Textural cores of detrital and magmatic zircon populations are represented by black data elipses, metamorphic populations are represented by red ellipses.

The zircon grains separated from this sample typically present elongate to tabular grain shapes ranging in size between 50-200 μm. Under CL imaging approximately two thirds of the zircons imaged displayed a textural core (Figure 3d). The rims and homogeneous zircons were typically patchy or sector zoned, or zoning absent, consistent with a metamorphic origin. The textural cores presented a range of morphologies but were most commonly either oscillatory zoned or very dark with zoning absent.

A total of 178 analyses were obtained from 143 grains, of which 83 corresponded to textural cores and 95 corresponded to rims or texturally homogeneous grains. Of these analyses, 44 of the cores and 76 of the rims and homogeneous grains were within 5% of concordancy. The rims and homogeneous grains form a single population (Figure 4d). The mean weighted $^{207}Pb/^{206}Pb$ age from this population is 1627 ±8 (n=76, MSWD = 0.53, probability = 1.000). The textural cores yield a range of ages from between ca. 1700 Ma to ca. 3000 Ma. On a probability density plot one major peak occurs at 1750 Ma (Figure 5). The average of the analyses contributing to this peak give a mean of 1746 ±12 Ma (n = 30, MSWD = 0.92, probability 0.59). This grouping of data shows some spread between ca. 1700-1850 Ma.

4.1.5 HI03 – South Para Orthogneiss (SPOG)

A sample of granite gneiss was collected from the South Para River in the northern Houghton Inlier (UTM 54H, 302842 mE, 6159981 mN), upstream from the modern sediment sample site of Beolusova et al (2006). The South Para Orthogneiss intrudes the biotite-retrograde sericite gneiss and the sillimanite gneiss units in the Houghton Inlier (Chapter 2). Zircons in this sample ranged in size from 50 to 250 μm, with grain shapes that range from equant to elongate. CL images show that the approximately half of the zircons are dark, homogeneous grains with almost no visible internal textures, indicative of a metamorphic origin. The other half of the zircons imaged show bright oscillatory zoned cores, indicative of a magmatic origin, with thick metamorphic rims (Figure 3g).

A total of 119 analyses were obtained from 99 zircons from this sample. Of these analyses, 53 were within 5% concordancy. Twenty four of these concordant analyses are from the oscillatory zoned cores and yield an older population than the rims and homogeneous grains. The weighted mean $^{207}Pb/^{206}Pb$ age for the oscillatory zoned cores is 1698 ±10 Ma (n = 24, MSWD = 0.99, probability = 0.47). 29 concordant analyses corresponded to textural rims or homogeneous grains. These analyses show a population at ca. 1600 Ma with some spread between ca. 1550 and 1700 Ma (Figure 4). The older spread of ages overlaps with the ages of magmatic cores and may represent metamorphic resetting of this initial magmatic age. The weighted mean $^{207}Pb/^{206}Pb$ age for the texturally-defined metamorphic population is 1612 ±14 Ma (n = 28, MSWD = 2.3, Probability = 0.00). Given the spread of data this age is not likely to be representative of the true metamorphic age.

4.2 Myponga and Warren Inliers

4.2.1 Warren Inlier: KM12-17 – Psammite from muscovite gneiss

Sample KM12-17 was collected from a psammite layer within the muscovite schist unit in the northeastern Warren Inlier (UTM 54H, 309753 mE, 6158424 mN). The host schist to this psammite is interpreted to be a retrogressed equivalent of the sillimanite

Figure 5 (Right): Probability density diagrams for detrital zircon samples from the Barossa Complex from this study and Jagodzinski et al. (2017). Data bins are 10 m.y. Houghton Inlier samples (A-F) are arranged by stratigraphic order. Other samples are grouped by inlier (G-L). Samples prefixed R are from Jagodzinski et al. (2017). The orange box represents the known timing of metamorphism in the Barossa Complex (Szpunar et al. 2007, Morrissey et al. 2013, Jagodzinski et al. 2017).

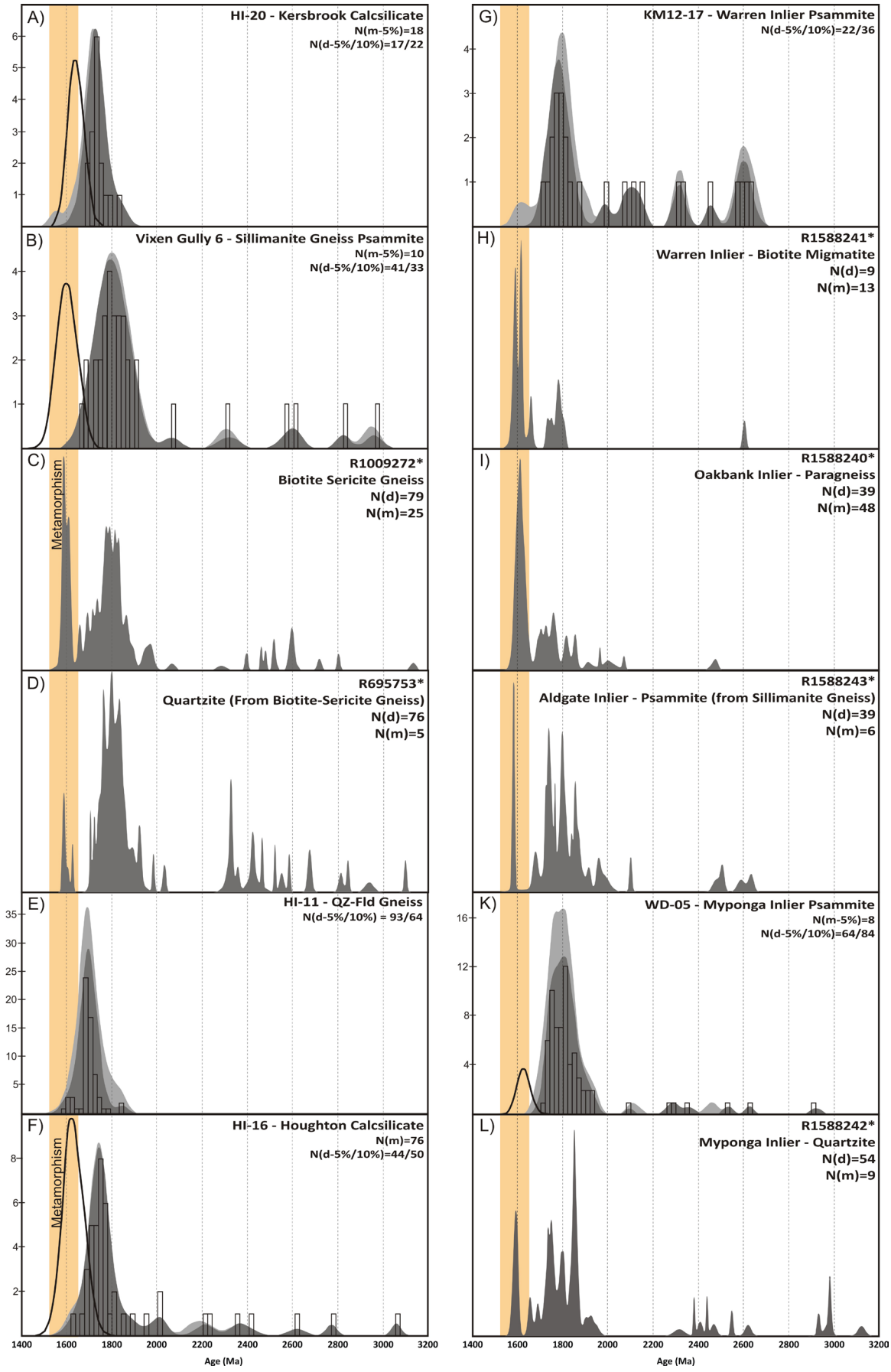
A)
HI-20 - Kersbrook Calcsilicate
N(m-5%)=18
N(d-5%/10%)=17/22
B)
Vixen Gully 6 - Sillimanite Gneiss Psammite
N(m-5%)=10
N(d-5%/10%)=41/33
C)
R1009272*
Biotite Sericite Gneiss
N(d)=79
N(m)=25
Metamorphism
D)
R695753*
Quartzite (From Biotite-Sericite Gneiss)
N(d)=76
N(m)=5
E)
HI-11 - QZ-Fld Gneiss
N(d-5%/10%) = 93/64
F)
HI-16 - Houghton Calcsilicate
N(m)=76
N(d-5%/10%)=44/50
Metamorphism
G)
KM12-17 - Warren Inlier Psammite
N(d-5%/10%)=22/36
H)
R1588241*
Warren Inlier - Biotite Migmatite
N(d)=9
N(m)=13
I)
R1588240*
Oakbank Inlier - Paragneiss
N(d)=39
N(m)=48
R1588243*
Aldgate Inlier - Psammite (from Sillimanite Gneiss)
N(d)=39
N(m)=6
K)
WD-05 - Myponga Inlier Psammite
N(m-5%)=8
N(d-5%/10%)=64/84
L)
R1588242*
Myponga Inlier - Quartzite
N(d)=54
N(m)=9
1400 1600 1800 2000 2200 2400 2600 2800 3000 3200
Age (Ma)
1400 1600 1800 2000 2200 2400 2600 2800 3000 3200
Age (Ma)

gneiss in the Houghton Inlier. Zircons in this sample range in size between 50-150 µm, although are typically around 100 µm. Grain shapes are typically rounded and equant and some larger grains are elongate. Under CL imaging a range of textures are observed. Oscillatory zoning is common in the larger grains, and many show dark sector zoning (Figure 3e).

A total of 52 analyses were obtained from 48 grains from this sample. Of these analyses 25 were within 5% of concordancy. These analyses show a scatter across a concordia diagram with one larger younger grouping and a smaller older grouping (Figure 4). The mean weighted $^{207}Pb/^{206}Pb$ age for the older group is 2602 ±43 Ma (n = 4, MSWD = 1.2, probability = 0.30). The younger grouping forms a peak at 1780 Ma (Figure 5), with some spread between between 1850 Ma to 1700 Ma. The analyses which comprise this group give a mean weighted $^{207}Pb/^{206}Pb$ age of 1782 ±23 Ma (n = 14, MSWD = 2.5, probability = 0.002). Smaller peaks also occur at ca. 2000 Ma, 2100 Ma, 2300 Ma, and 2450 Ma.

4.2.2 Myponga Inlier: WD-05 – Psammite from sillimanite gneiss

Sample WD-05 was collected from the southern Myponga Inlier in the vicinity of the Myponga Conservation Park (UTM 54H, 267551 mE, 6075600 mN). WD-05 comes from a psammitic layer from within a package of coarse grained sillimanite-garnet-biotite gneiss. Zircons separated from this sample range in size between 50 – 200 µm with equant to tabular grain shapes. Under CL imaging core and rim textures are common. Rims typically are dark and texture-less zones which are frequently too small to reliably analyse. Cores present a range of morphologies from light or dark oscillatory zoned to light sector zoned and textureless (Figure 3f).

A total of 129 analyses were obtained from 129 grains from this sample. Of these analyses, 75 were within 5% of concordancy. There is a scatter of data between ca. 1600 Ma and 2900 Ma, with a large grouping of data forming a spread between ca. 1700 Ma and 1900 Ma (Figure 4). A smaller grouping of data occurs between ca 1600 and 1650 Ma. This younger group corresponds to textural rims or homogeneous grains, and gives a weighted mean $^{207}Pb/^{206}Pb$ age of 1623 ±19 Ma (n = 7, MSWD = 0.48, probability = 0.82). On a probability density plot, a large grouping forms a peak centred on ca. 1800 Ma, with a minor peak at ca. 1760 Ma and a shoulder at ca. 1900 Ma (Figure 5). While these groupings show no clear separation, the minor peak at ca. 1760 Ma is tentatively considered to represent the youngest detrital population.

4.3 Discordant Analyses

Due to the significant number of discordant analyses obtained in many samples, the data was also assessed using the R code of Reimink et al. (2016). This program assesses the likelihood of additional populations which may be absent from the concordant analyses due to Pb loss. The program uses a series of tie lines across a concordia diagram in order to determine likely discordia lines and calculate the probable upper and lower intercepts of discordant trends. The results of this analysis are presented in Figure 6 as probability density plots of the upper and lower intercept likelihoods for the three inliers sampled. No additional zircon populations were identified by this method compared to those recorded in the concordant populations, suggesting that the concordant zircon analyses are a valid representation of the age structure of Barossa Complex zircons.

The lower intercept peaks identified by the method of Reimink et al. (2016) occur at approximately 0 Ma and 450 Ma, which are interpreted to be representative of Pb loss due to the extensive recent weathering, and the ca. 500 Ma Delamerian Orogeny respectively. Although the ca. 450 Ma peak does not perfectly coincide with the timing of the Delamerian Orogeny, this may be due to the combination of resetting towards ca. 500 Ma and subsequent Pb loss of already discordant

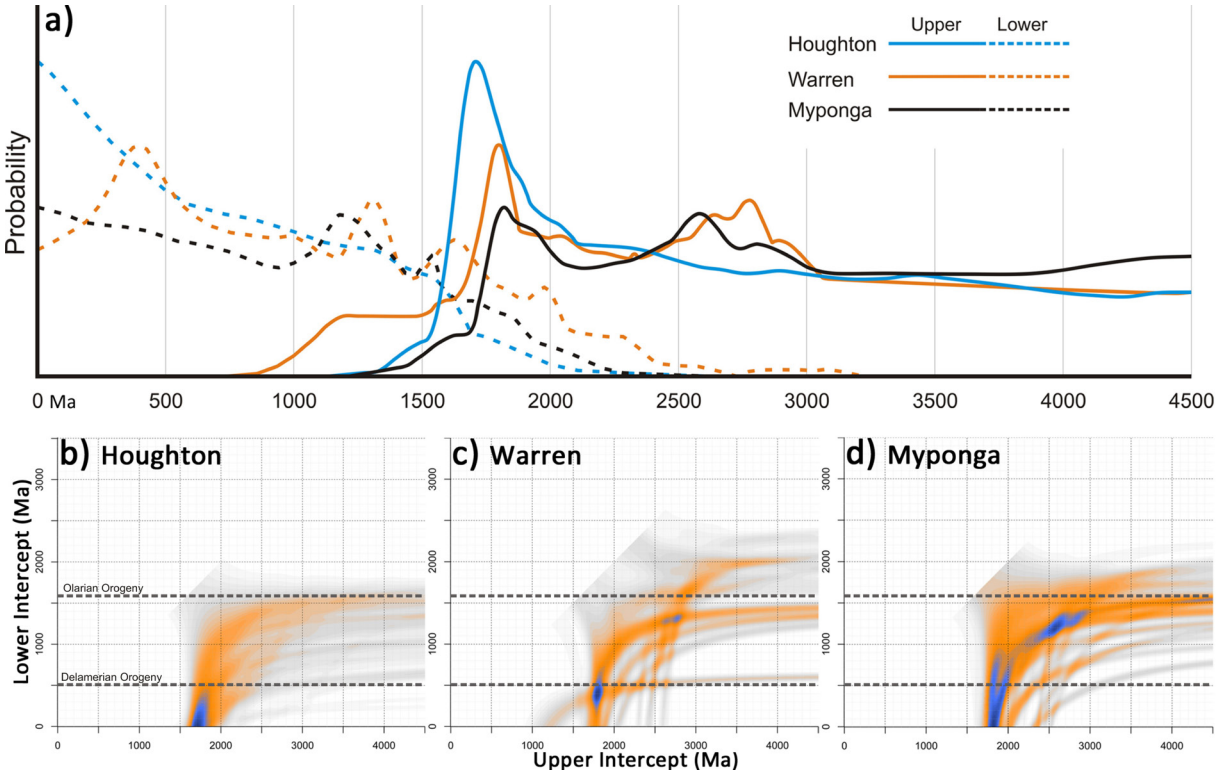

Figure 7: Results of the statistical analysis using the R code of Reminick et al. (2016). A) Probability density plots of upper and lower intercepts of discordance trends for the three inliers sampled in this study. Samples from the Houghton inlier were grouped in order to better identify discordance trends. B-D) 2D histograms for the three inliers sampled. Increasing probability density (Blue) indicates that one age population (X axis) is being reset towards a particular age (Y axis). B) Grouped detrital zircon discordance from the Houghton Inlier (Samples HI20, Vixen Gully 6, and HI16), showing resetting from 1600-1800 Ma to approximately 0 Ma. C) Detrital Zircon discordance from the Warren Inlier, showing resetting from 1700-1800 Ma to 500-400 Ma. D) Detrital zircon discordance from the Myponga Inlier 1700-1800 Ma populations being reset to 0-600 Ma, likely reflecting Delamerian resetting in combination with Pb loss.

grains due to modern weathering in the inliers.

In the samples from the Warren and Myponga inliers, grains with an upper intercept age of ca. 2500-2800 Ma yielded lower intercept ages of ca. 1200-1300 Ma. This is considered to be an artefact of the program's methods which was discussed by Reimink et al. (2016) as these lower intercept ages postdate the metamorphic ages obtained in the Barossa Complex, and does not appear to affect any other population of zircon.

4.4 Lu- Hf Isotope Results

Hf Isotopic results are presented in Figure 7 as $\varepsilon_{Hf}(t)$ vs. age. Only zircons with U-Pb ages within 10% concordancy were targeted for Hf isotope analysis.

4.4.1 Houghton Inlier

The majority of detrital zircon analyses fall between ca. 1700 Ma and ca. 1850 Ma. A small cluster of analyses around 1850 Ma give εHf values between +4 to -3. The main cluster of analyses lie between ca. 1800 Ma and ca. 1690 Ma and give $\varepsilon_{Hf}(t)$ values between +3 to -14 with the majority of analyses falling between 0 and -10. Samples HI20 and HI11, which yield largely unimodal U-Pb age spectra, show a more juvenile cluster with $\varepsilon_{Hf}(t)$ values between +3 to -4 for zircons aged between

1750 Ma and 1680 Ma. Zircons of this age range in samples HI16 and Vixen Gully 6 yield $\varepsilon_{Hf}(t)$ values between -4 and -14. 1580 Ma to 1650 Ma metamorphic grains from all samples yield $\varepsilon_{Hf}(t)$ values between -1 and -13.

Analyses from the magmatic cores of the South Para Orthogniess at ca. 1700 Ma yield εHf values between 0 and -6.5, which plots in a similar range to the more juvenile samples HI11 and HI20, with some overlap with the more evolved analyses. Ca. 1570 Ma to ca. 1630 Ma metamorphic analyses from the South Para Orthogneiss plot between -3 and -6.

4.4.2 Myponga Inlier

The bulk of zircon analysed from sample WD-05 is between 1700 Ma and 1950 Ma in age, with a few older analyses ranging between 2100 Ma and 2900 Ma. Samples from this older age range yield $\varepsilon_{Hf}(t)$ values between +1 and -0.5, with one grain at ca. 2350 Ma plotting at -9.8. Zircons aged between 1950 Ma and 1800 Ma yield $\varepsilon_{Hf}(t)$ values between +1.5 and -6. Zircons between 1800 and 1700 Ma show more scatter between juvenile and evolved, with $\varepsilon_{Hf}(t)$ values between +1 and -11. Two analyses of metamorphic zircon plot at -9 and -13..

5. Discussion

5.1 Age of the South Para Orthogneiss

The age of the South Para Orthogneiss (SPOG) has been assessed previously through zircon from modern stream sediment (Belousova et al. 2006) and an in situ sample (Jagodzinski et al. 2017) which yielded essentially identical magmatic crystallisation ages of 1718 ±8 Ma and 1717 ±7 Ma respectively. Both of these studies utilised analyses conducted by Sensitive High Resolution Ion Microprobe (SHRIMP). The magmatic crystallisation age obtained in this study was a significantly younger age of 1698 ±10 Ma, which does not overlap within uncertainty of the previously reported SHRIMP ages for this orthogneiss.

The reason for this discrepancy between ages may be due to a number of reasons. It is possible that the SPOG intruded during stages between c. 1717 Ma and c. 1698 Ma, although multiple intrusions have not been recognised in the field. Another option is that the subsequent multiple episodes of metamorphism (discussed below) have partially reset some grains. Another possibility is that the difference is due to the different analytical methods between this and past studies, as the SHRIMP method samples less material and is higher resolution than LA-ICP-MS. However it should still be expected that the ages would overlap within error.

Given the large zircon rims identified in the zircon from this sample, as well as wholly metamorphic zircon, a partial isotopic resetting of the primary magmatic age is considered the most likely explanation for the 1698 ±10 Ma magmatic zircon age. The true age of the SPOG is considered to be 1717 ±7 Ma (Jagodzinski et al. 2017).

5.2 Depositional Timing Constraints

Samples HI20 and HI16 in the Houghton Inlier represent the calcsilicate units which occur at the top and the bottom of the apparent stratigraphic column, as outlined in Chapter 2. Sample HI20 from the Kersbrook Calcsilicate yields an essentially unimodal zircon population at 1728 ±17 Ma. Sample HI16 from the Houghton Calcsilicate yields a multicomponent spectrum with the youngest peak at 1746 ±12 Ma. This suggests that the

Figure 7 (Right): Hf Isotopic data presented as age vs. $\varepsilon_{Hf}(t)$. A) All data collected from the Barossa Complex (this work). B) Enlargement of the Barossa Complex data for between 1550 Ma and 1900 Ma. C) South Para Orthogneiss data plotted against the data from modern sediment attributed to the same lithology (Belousova et al. 2006). D) Barossa Complex values plotted against values obtained from the Gawler Craton.

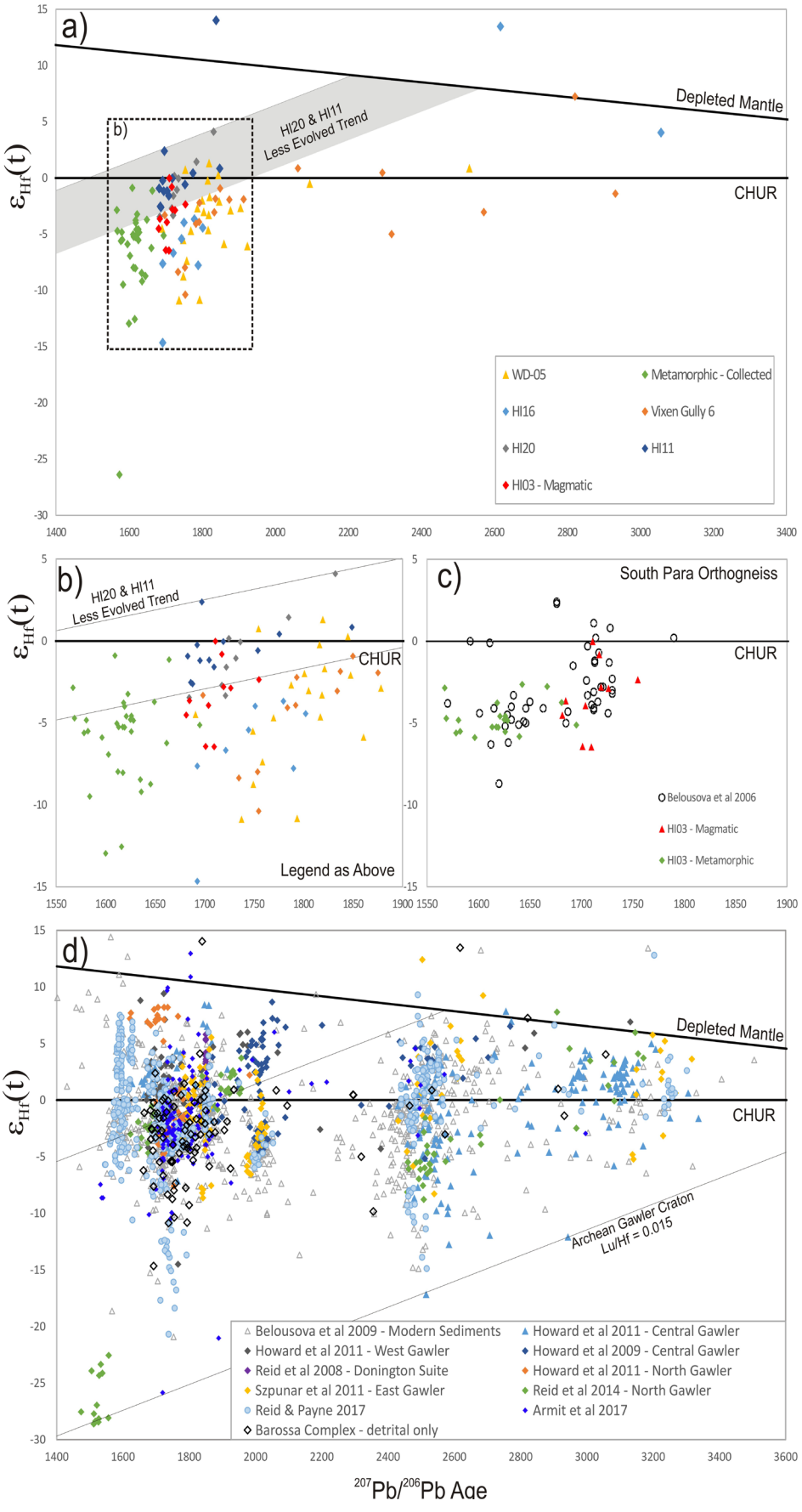
a)
b)
Depleted Mantle
CHUR
HI20 & HI11
Less Evolved Trend
WD-05
Metamorphic - Collected
HI16
Vixen Gully 6
HI20
HI11
HI03 - Magmatic
b)
HI20 & HI11
Less Evolved Trend
CHUR
Legend as Above
c)
South Para Orthogneiss
CHUR
Belousova et al 2006
HI03 - Magmatic
HI03 - Metamorphic
d)
Depleted Mantle
CHUR
Archean Gawler Craton
Lu/Hf = 0.015
Belousova et al 2009 - Modern Sediments
Howard et al 2011 - Central Gawler
Howard et al 2011 - West Gawler
Howard et al 2009 - Central Gawler
Reid et al 2008 - Donington Suite
Howard et al 2011 - North Gawler
Szpunar et al 2011 - East Gawler
Reid et al 2014 - North Gawler
Reid & Payne 2017
Armit et al 2017
Barossa Complex - detrital only
εHf(t)
207Pb/206Pb Age

maximum depositional ages for the Houghton Inlier is between approximately 1730 to 1750 Ma. These age constraints are somewhat older than the higher resolution detrital zircon spectra obtained by Jagodzinski et al. (2017), who obtained youngest detrital zircon populations of 1707 ±5 Ma and 1655 ±11 Ma from samples of the biotite-sericite gneiss in the Houghton Inlier. The older of these two samples, R695753, was taken from a quartzite layer to the west of a sheared boundary with the 1717 ±7 Ma SPOG, but the contact between these units is intrusive to the south of the sample location. This makes the interpretation of the detrital zircon data challenging, as based on zircon age data alone it appears that the SPOG is older than the sedimentary unit which it intrudes. Jagodzinski et al. (2017) propose that this apparent impossibility may be the result of some structural or sedimentary complexity that has not been recognised. This is certainly possible, as the quartzite layer sampled cannot be traced throughout the sequence, and high strain zones are present in the area sampled. However, as the youngest detrital population was calculated from only two analyses it is also possible that that some partial resetting of these zircon grains occurred either during the intrusion of the SPOG, or during the one subsequent metamorphic episodes. The next youngest age peak in this sample was approximately 1722 Ma, which is comparable to the 1728 ±17 Ma age obtained from sample HI20 in this study. 1722 Ma may represent a more accurate maximum depositional age constraint for the biotite-sericite gneiss that does not contradict the observed field relationships.

The second sample of biotite sericite gneiss by Jagodzinski et al. (2017), R1009272, was obtained from the southern Houghton Inlier in the transitional zone between biotite-sericite gneiss and sillimanite gneiss. It yielded a youngest detrital zircon population of 1655 ±11 Ma. This sample gives a similar spectrum of ages to that obtained in the samples collected in this study from psammitic layers in sillimanite gneiss units in the Houghton and Myponga Inliers, and the retrogressed equivalent from the Warren Inlier (Figure 5). Sample R1009272 was dominated by multiple closely spaced age peaks at approximately 1655 Ma, 1690 Ma, 1730 Ma, 1760 Ma, 1790 Ma, 1830 Ma, and 1850 Ma (Figure 5). These cover the age range given by the detrital zircon populations in samples Vixen Gully 6, KM12-17, and WD-05, and it is probable that these peaks represent similar populations to those in R1009272, but the lower age resolution LA-ICP-MS technique does not allow for their confident individual identification.

The sample of quartzofeldspathic gneiss from the southern Houghton Inlier, HI11, yields an essentially unimodal age peak at 1693 ±7 Ma. The zircon grains from this sample contain faint remnants of oscillatory zoning, but are dominantly dark under CL imaging and appear metamorphically disturbed. This casts some doubt onto whether the c. 1693 Ma age is valid, or whether it reflects a slightly older age which has been partially reset. As the quartzofeldspathic gneiss is one of the lowermost units of the proposed stratigraphy, the interpretation of this age will have significant effects on the interpretation of the deformational history of the area. The first option is that the age of 1693 ±7 Ma has not been partially reset by metamorphism and is a reliable age. The second option is that the 1693 ±7 Ma age has been metamorphically disturbed, and the true crystallisation age of the zircon is closer to 1750-1730 Ma as seen in other samples from this study, such as the unimodal population identified in sample HI20.

The quartzofeldspathic gneiss from which sample HI11 was obtained underlies the biotite-sericite gneiss which is intruded by the c. 1717 Ma SPOG in the north of the Houghton Inlier. For the 1693 Ma population to be a valid age, this would require the stratigraphy to have been completely overturned. However, the structurally-upper biotite sericite gneiss contains detrital zircon as young as 1655

Ma (Jagodzinski et al. 2017) and from a detrital zircon perspective is the youngest sedimentary unit in the Houghton Inlier. This is complicated by the Kersbrook Calcsilicate which appears to be the structural top of the exposed stratigraphy with a unimodal c. 1728 Ma detrital zircon population. The boundary between the Kersbrook calcsilicate and the sillimanite gneiss in the Houghton inlier is never exposed and is currently defined using regional magnetic maps (Chapter 2). It is therefore entirely possible that this boundary is tectonic rather than a change in lithofacies. If an older calcsilicate was thrust atop the sillimanite gneiss, the sillimanite gneiss could still be the stratigraphically youngest unit, which overlies the psammopelitic biotite-sericite gneiss and Houghton calcsilicates (Figure 1, 2).

In this interpretation, the apparent structural stratigraphy (excluding the Kersbrook calcsilicate) is the correct way up, and the 1693 ±7 Ma quartzofeldspathic gneiss still occurs stratigraphically below the biotite-sericite gneiss. As the biotite-sericite gneiss is intruded by the 1717 Ma SPOG, the c. 1693 Ma zircon population likely reflects a metamorphically disturbed age population which was originally 1730-1750 Ma, such as that seen in sample HI20.

5.3 Sediment Provenance

Detrital zircons in the Barossa Complex are dominated by zircon grains aged between 1655 to 1850 Ma, with very minor contributions of grains aged 2000 Ma to 3100 Ma (Jagodzinski et al. 2017). Many of these ages are similar to those obtained in the eastern Gawler Craton (e.g. Hand et al. 2007, Fanning et al. 2007).

In south-eastern Gawler Craton, the area most proximal to the Barossa Complex, the Archean Sleaford Complex and 2000 Ma Miltalie gneiss is overlain by Palaeoproterozoic volcano sedimentary basins aged between 1860 Ma to 1740 Ma (e.g. Hand et al. 2007, Kositcin 2010, Reid and Hand 2012). The earliest of these is the Darke Peak Group which was deposited synchronous to felsic volcanics at approximately 1865 Ma (Szpunar et al. 2011). Subsequent to this period of deposition a major magmatic event occurred during the Cornian Orogeny with the emplacement of the Donington Suite batholith which intruded at 1850 Ma (Reid et al. 2008a). Basin development continued subsequent to the Cornian Orogeny with the deposition of the Cleve Group and other basins on the Eyre Peninsula such as the Broadview Schist, which occurred coevally with bimodal volcanics such as the Myola Volcanics at 1790 Ma (Fanning et al. 1988, Szpunar and Fraser 2010, Szpunar et al. 2011). Further east, between 1760 Ma and 1740 Ma the Wallaroo Group and its equivalents were deposited and were associated with further bimodal magmatism (Fanning et al. 1988, Conor 1995, Zang 2002, Cowley et al. 2003). During this period, sedimentary successions were deposited across the southern Gawler Craton, including the protoliths to the Waramboo gneiss and Price metasediments (Lane et al. 2015).

The Gawler Craton was subsequently metamorphosed during the 1730 Ma to 1690 Ma Kimban Orogeny, which strongly affected these eastern successions (Vassallo and Wilson 2001, Swain et al. 2005, Hand et al. 2007, Reid et al. 2008b, Dutch et al. 2010). Metamorphic zircon and monazite ages from the northern and western Gawler Craton between 1740 Ma and 1690 Ma indicate that this was a craton wide event (Swain et al. 2005, Hand et al. 2007, Payne et al. 2008, Howard et al. 2011a). The Kimban Orogeny is a particularly significant as the depositional timing of the early Barossa Complex overlaps with the onset of the Kimban Orogeny. Given its proximity to the Barossa Complex, rocks uplifted by the Kimban Orogeny would be a likely source of sediment. However, the Barossa Complex does not record significant peaks of Archean (2600-2450 Ma, 2000 Ma) and only minor peaks of 1850 Ma detritus, despite the prevalence of those rock units in the exposed southeastern Gawler Craton

that was affected by the Kimban Orogeny. This indicates that elements of the currently exposed rocks of the southeast Gawler Craton such as the Darke Peak and Cleve groups, Donington Suite, and Archean Basement did not significantly contribute to the Barossa Complex (Fanning et al. 2007, Szpunar et al. 2011). Ar-Ar ages and Sm-Nd garnet ages from the eastern Eyre Peninsula indicate that large areas of the Kimban Orogen cooled through 500-350°C between 1610-1450 Ma (Foster and Ehlers 1998, Hand et al. 2007). Therefore, it is unlikely that the currently exposed rock system in the southeast Gawler Craton was exposed and contributing sediment to the Barossa Complex between 1730-1655 Ma.

The 1760 Ma metasedimentary sequences from the Waramboo Gneiss and Price Metasediments, as well as the sedimentary components of the Wallaroo Group, yield detrital zircon populations with essentially unimodal ca. 1760 Ma peaks and are similarly lacking in Archean and earlier Palaeoproterozoic zircon typical of that currently exposed in the Kimban Orogen (Figure 8; Jagodzinski 2005, Fanning et al. 2007, Lane et al. 2015). The lack of older detritus in these sequences suggests that this sedimentary cover may have been widespread across the southern Gawler Craton before being inverted and dissected by the Kimban Orogeny, and would erode in the early stages of uplift. The upper stratigraphic units in the Barossa Complex, the pelitic sillimanite gneiss units, show a more significant contributions of older zircons with significant peaks at 1790 Ma and 1850 Ma. This potentially represents a trend of younger (c. 1760 -1730 Ma) volcanic-dominated detritus being shed into the protolith of the calcsilicate units before older source rocks were exposed that contributed to the more pelitic deeper water successions of the Barossa Complex.

The Hf isotopic compositions of the

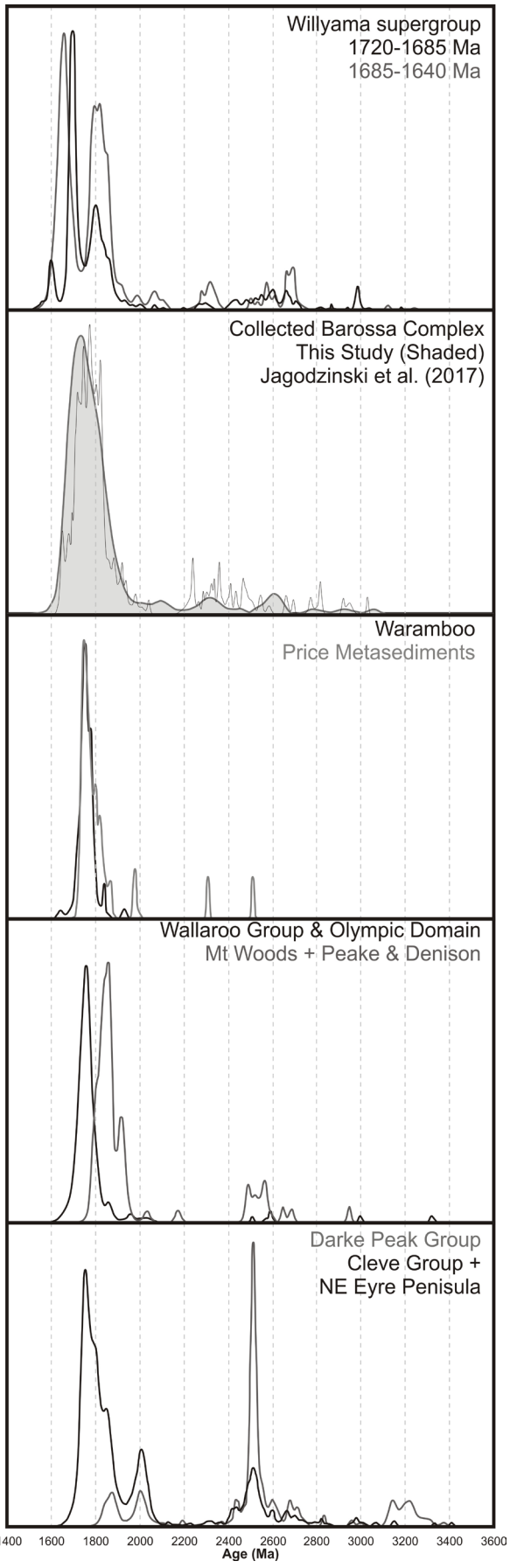

Figure 8 (Right): Comparison of detrital zircon spectra from the South Australian Craton to the Barossa Complex.

detrital zircons in the Barossa Complex is also similar to that recorded in the Gawler Craton (Figure 7d). Zircon from the Darke Peak and Cleve groups in the eastern Gawler Craton aged between 1780 Ma and 1865 Ma contain $\varepsilon_{Hf}(t)$ values dominantly between +4 and -4 (Szpunar et al. 2011), which is consistent with that recorded in the Barossa Complex for this age bracket.

In the northern Gawler Craton, metasedimentary and metaigneous sequences with protoliths aged between 1760-1720 Ma have been identified in the Nawa Domain, with subsequent metamorphism during the interval 1730-1710 Ma (Payne et al. 2006, Fanning et al. 2007, Howard et al. 2011b, Armit et al. 2017, Reid and Payne 2017). With the exception of one more juvenile mafic sample, the $\varepsilon_{Hf}(t)$ values from the Nawa Domain in the northern Gawler Craton for zircon aged between 1720-1780 Ma fall within the range of +1 to -5 (Howard et al. 2011b, Reid et al. 2014, Armit et al. 2017), and are consistent with the range recorded in the Barossa Complex (Figure 7d). 1720-1700 Ma volcano sedimentary units from the Nawa Domain have been suggested to be related to the lower units of the Willyama Supergroup (Payne et al. 2006), and these two regions have been suggested to be sourcing sediment from the North Australian Craton (Payne et al. 2006, Barovich and Hand 2008).

The two samples from the Barossa Complex which yield essentially unimodal detrital zircon age populations at c. 1730 Ma and 1690 Ma, had notably more juvenile $\varepsilon_{Hf}(t)$ values than the samples containing multiple zircon age populations from the Houghton Inlier (Figure 7b). This indicates that a magmatic source with a less evolved Hf signature was present at 1730 Ma, and which was likely reset to 1690 Ma in sample HI11. The unimodal detrital zircon signature in these samples requires a proximal magmatic source without contribution from additional lithologies.

5.4 Metamorphic Overprint

A metamorphic overprint between 1610 to 1640 Ma occurs in the majority of samples analysed in this study. However, the samples analysed in this study do not appear to preserve the c. 1590-1580 Ma event that has been widely reported in the Barossa Complex (Szpunar et al. 2007, Morrissey et al. 2013, Jagodzinski et al. 2017). The metamorphic zircon ages recorded in this study are consistent with the 1630 Ma and 1610 Ma metamorphic peaks identified by Jagodzinski et al. (2017). Only one sample in this study from the Houghton Inlier recorded any of the c.1590 Ma metamorphic growth, Sample HI03 from the SPOG, which yielded no coherent metamorphic population but rather a spread of ages between approximately 1630 and 1550 Ma.

The majority of existing metamorphic geochronology yields ages in the range of c. 1590-1580 Ma (Szpunar et al. 2007, Morrissey et al. 2013, Jagodzinski et al. 2017). In the Houghton and Warren Inliers the 1590 Ma age occurs with another metamorphic peak at 1630 Ma or 1610 Ma (Jagodzinski et al. 2017). In the Myponga and Aldgate inliers, only c.1590-1580 Ma metamorphism is recorded with no older metamorphic ages preserved (Szpunar et al. 2007, Morrissey et al. 2013, Jagodzinski et al. 2017).

The samples from this study preserve a much more pervasive c.1630-1600 Ma metamorphic zircon record. Sample HI16 is dominated by 1627 ±8 Ma metamorphic overgrowths, and sample WD-05 from the Myponga Inlier yields 1623 ±19 Ma from a small number of metamorphic overgrowths, indicating that this period of metamorphism was pervasive throughout the Barossa Complex and not just restricted to the northern area (Figure 1, 2).

Sample HI20 preserves metamorphic rims recording an age of 1639 ±13 Ma, which is particularly significant as it overlaps not only with the other c. 1630 Ma ages recorded in this study, but also with the youngest detrital zircon population recorded in the Houghton Inlier at

1655 ±8 Ma (Jagodzinski et al. 2017). This overlap indicates that metamorphism initiated very soon after deposition. Metamorphic pressure and temperature conditions previously calculated for the Barossa Complex indicated that metamorphism occurred at peak conditions of approximately 800-850oC and 8-9 kbar across the Houghton and Myponga inliers (Morrissey et al. 2013). Whether these conditions reflect the 1625 Ma, 1610 Ma, or the 1580 Ma metamorphic periods is uncertain. However a later period of metamorphism between c.1570-1550 Ma is recorded in monazite in texturally retrogressed rocks, and is more easily attributable to a late stage of decompression and possibly extension (Morrissey et al. 2013).

5.5 Tectonic Relationships

Numerous tectonic models for the Proterozoic evolution of Australia have been proposed (e.g. Giles et al. 2004, Betts and Giles 2006, Payne et al. 2009, Cawood and Korsch 2008, Betts et al. 2015, Aitken et al. 2016). One of the most widely accepted aspects of these models is the chronostratigraphic correlation between the Mt. Isa Domain and the Willyama Supergroup (Page et al. 2005b). This correlation is typically accompanied by an approximately 50^{o} rotation of the South Australian Craton (Figure 9a) such that the Curnamona Province sits adjacent the Mt. Isa Inlier in these reconstructions (e.g. Giles et al. 2004, Betts and Giles 2006, Betts et al. 2015, Aitken et al. 2016). In one of the most recent models, it is proposed that the rift basin accommodating the c. 1740-1640 Ma Calvert and Mt. Isa superbasins in the eastern North Australian Craton, as well as the Willyama Supergroup, is a back arc basin driven by west dipping subduction under the eastern margin of the Proterozoic continent (Aitken et al. 2016). In this model, a large basin exists along the eastern margin of proto-Australia reaching from Northern Australia, through the eastern Gawler Craton, and is inferred to continue into eastern Antarctica. Taking into account the rotation of the South Australian Craton, the position of the Barossa Complex falls within the proposed extent of this superbasin (Figure 9b). The depositional timing of the Barossa Complex at c. 1730 Ma to 1655 Ma coincides with the deposition of the Willyama Supergroup, and the Calvert and Isa Supergroups in the Mt. Isa Inlier (Page et al. 2000, Page et al. 2005a, Page et al. 2005b, Neumann et al. 2009). Lithological similarities also occur between the Barossa Complex and Willyama Supergroup, such as quartzofeldspathic and calcsilicate units overlain by psammopelitic to pelitic units in the Curnamona and Thackeringa groups, indicating similar depositional environments (Page et al. 2005a, Conor and Preiss 2008). Similarly, these areas are intruded by ca. 1710 Ma granitoids, such as the Basso Suite and Alma Gneiss in the Willyama Supergroup (Ashley et al. 1996, Page et al. 2005a), and the SPOG in the Barossa Complex.

The wider scale tectonic environment during the late Palaeoproterozoic in the Gawler Craton and eastern Australia is still poorly understood. While extension was developing on the eastern margin in the Curnamona Province, the inferred compressional to transpressional regime of the Kimban Orogeny was active in the Gawler Craton, further inland from the proposed subduction zone of Aitken et al. (2016). Exactly how these two regimes occur adjacent one another remains unclear. Some models proposed that the Kalinjala Shear Zone, which is a major Kimban aged crustal shear zone, represents a suture (Betts and Giles 2006, Betts et al. 2015). However, there is no evidence that the Kalinjala Shear Zone is a suture as pre-Kimban sequences on either side show similar provenance. For example, the c. 1790 Ma Cleve Group shows provenance from the c. 1850 Ma Donington Suite, and were evidently in proximity to one another prior to c. 1730-1690 Ma (Howard et al. 2006, Szpunar et al. 2011). Regardless of the driving force behind the Kimban Orogeny, structures including positive flower structures

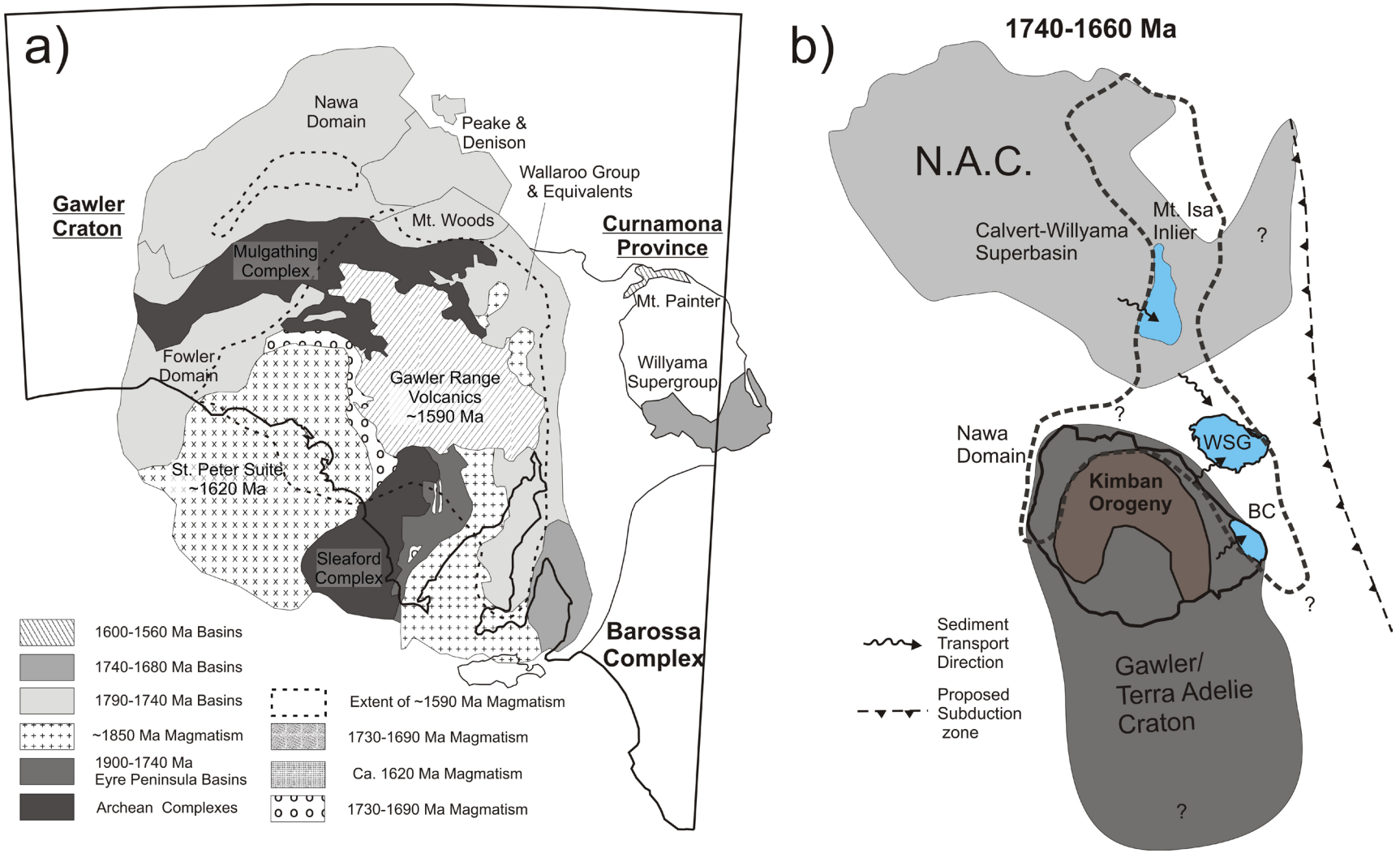

Figure 9: A) Significant elements of the Gawler Craton and Curnamona Province (South Australian Craton), and B) Schematic of Eastern Australian crustal elements at c. 1740-1660 Ma after Aitken et al. (2016). BC – Barossa Complex, WSG – Willyama Supergroup, N.A.C. – North Australian Craton

developed in splays of the Kalinjala Shear Zone (Vassallo and Wilson 2002), as well as granulite metamorphic conditions experienced by ca. 1760 Ma sedimentary units on the Eyre Peninsula (Lane et al. 2015, Morrissey et al. 2016) imply that crustal thickening and uplift must have occurred during the 1730 Ma to 1690 Ma interval that the Willyama-Calvert rift basins were developing.

Another key correlation in Palaeo-Mesoporoterozoic reconstruction models is the Isan-Olarian Orogeny at ca. 1600 Ma (e.g. Giles et al. 2004, Betts and Giles 2006, Aitken et al. 2016). Metamorphism in the Willyama Supergroup is considered to have initiated at ca. 1620 Ma (Forbes et al. 2005) with peak metamorphism at 1600 Ma (Page and Laing 1992, Raetz et al. 2002, Clark and Hand 2010), with retrogression between 1570 Ma to 1550 Ma (Rutherford et al. 2007). Similarly in the Isan Orogeny early metamorphism occurred at ca. 1630 Ma, followed by peak conditions at ca 1600-1580 Ma, and long lived retrogression (e.g. Page and Sun 1998, Sayab 2006, Rubenach et al. 2008).

This timing of these events closely matches the metamorphic history observed in the Barossa Complex (Szpunar et al. 2007, Morrissey et al. 2013, Jagodzinski et al. 2017, this study). Morrissey et al. (2013) discussed in detail the similarity in metamorphic timing and style along the eastern margin of Proterozoic Australia between 1630 Ma and 1550 Ma, and concluded a continental scale system was likely driving this metamorphism. Given the relatively High T-Low P metamorphic conditions across the Eastern Proterozoic margin (Morrissey et al. 2013), it appears likely that extension may have thermally primed the crust before a change in subduction angle or a buoyant collider drove a compressional system at ca. 1580 Ma (Morrissey et al. 2013). This scenario is consistent with reconstruction models which propose a back arc setting on the eastern margin of Australia during the late Palaeoproterozoic (Betts et al. 2015, Aitken et al. 2016).

6 Conclusions

The Barossa Complex on the eastern Gawler Craton records detrital zircons that give maximum depositional ages ranging from 1728 ±17 Ma to 1655 ±8 Ma. It is intruded by a syndepositional granite at 1717 ±7 Ma. The onset of deposition coincides with the onset of the Kimban Orogeny in the Gawler Craton. U-Pb and Hf isotopes in zircon show a strong similarity to that recorded in the eastern and northern Gawler Craton in areas affected by the Kimban Orogeny, and uplift associated with this event was probably a major source of sediment for the Barossa Complex. The depositional timing and lithological similarities indicate the Barossa Complex may be correlated with the Willyama Supergroup in the Curnamona Province to the present-day northeast.

A significant c. 1625 Ma metamorphic zircon population is preserved in the northern Barossa Complex, consistent with previous metamorphic zircon U-Pb studies. Little c. 1590 Ma metamorphism is identified in the northern Barossa Complex. These results contrast earlier studies which have identified extensive ca. 1580-1590 Ma metamorphism throughout the Barossa Complex and create further ambiguity as to the timing of peak metamorphic conditions.

These depositional and subsequent metamorphic age constraints support Palaeogeographic reconstructions which place a large basin on the eastern margin of Proterozoic Australia between 1730 Ma and 1640 Ma, such as that of Aitken et al. (2016) and Betts et al. (2015). Furthermore, the thermal style of metamorphism supports the existence of a long-lived extensional regime consistent with a back-arc setting.

References

Aitken, A. R. A., Betts, P. G., Young, D. A., Blankenship, D. D., Roberts, J. L. & Siegert, M. J., 2016. The Australo-Antarctic Columbia to Gondwana transition. Gond-

wana Research, 29(1), 136-152.

Armit, R., Betts, P. G., Schaefer, B. F., Yi, K., Kim, Y., Dutch, R. A., Reid, A., Jagodzinski, L., Giles, D. & Ailleres, L., 2017. Late Palaeoproterozoic evolution of the buried northern Gawler Craton. Precambrian Research, 291, 178-201.

Ashley, P. M., Cook, N. D. J. & Fanning, C. M., 1996. Geochemistry and age of metamorphosed felsic igneous rocks with A-type affinities in the Willyama Supergroup, Olary Block, South Australia, and implications for mineral exploration. Lithos, 38(3), 167-184.

Barovich, K. & Hand, M., 2008. Tectonic setting and provenance of the Paleoproterozoic Willyama Supergroup, Curnamona Province, Australia: Geochemical and Nd isotopic constraints on contrasting source terrain components. Precambrian Research, 166(1–4), 318-337.

Belousova, E. A., Preiss, W. V., Schwarz, M. P. & Griffin, W. L., 2006. Tectonic affinities of the Houghton Inlier, South Australia: U - Pb and Hf-isotope data from zircons in modern stream sediments. Australian Journal of Earth Sciences, 53(6), 971-989.

Betts, P. G., Armit, R. J., Stewart, J., Aitken, A. R. A., Ailleres, L., Donchak, P., Hutton, L., Withnall, I. & Giles, D., 2015. Australia and Nuna. Geological Society, London, Special Publications, 424.

Betts, P. G. & Giles, D., 2006. The 1800–1100 Ma tectonic evolution of Australia. Precambrian Research, 144(1–2), 92-125.

Betts, P. G., Giles, D. & Schaefer, B. F., 2008. Comparing 1800–1600 Ma accretionary and basin processes in Australia and Laurentia: Possible geographic connections in Columbia. Precambrian Research, 166(1–4), 81-92.

Betts, P. G., Giles, D., Schaefer, B. F. & Mark, G., 2007. 1600–1500 Ma hotspot track in eastern Australia: implications for Mesoproterozoic continental reconstructions. Terra Nova, 19(6), 496-501.

Boger, S. D., 2011. Antarctica — Before and after Gondwana. Gondwana Research, 19(2), 335-371.

Brookfield, M. E., 1993. Neoproterozoic Laurentia-Australia fit. Geology, 21(8), 683-686.

Cawood, P. A. & Korsch, R. J., 2008. Assembling Australia: Proterozoic building of a continent. Precambrian Research, 166(1–4), 1-35.

Clark, C. & Hand, M., 2010. Decoding Mesoproterozoic and Cambrian metamorphic events in Willyama Complex metapelites through the application of Sm–Nd garnet geochronology and P–T pseudosection analysis. Gondwana Research, 17(1), 59-74.

Conor, C., 1995. Moonta-Wallaroo Region: An interpretation of the geology of the Maitland and Wallaroo 1:100 000 sheet areas, South Australian Department of Primary Industries and Resources.

Conor, C. H. H. & Preiss, W. V., 2008. Understanding the 1720–1640 Ma Palaeoproterozoic Willyama Supergroup, Curnamona Province, Southeastern Australia: Implications for tectonics, basin evolution and ore genesis. Precambrian Research, 166(1–4), 297-317.

Cowley, W., Conor, C. & Zang, W., 2003. New and revised Proterozoic stratigraphic units on northern Yorke Peninsula. MESA Journal, 29, 46-58.

Crowhurst, P. V., 1988. The geology, petrology and geochemistry of the Proterozoic inlier, south of Myponga, Fleurieu Peninsula, South Australia. Unpub. BSc (Hons) Thesis, University of Adelaide.

Dalziel, I. W. D., 1991. Pacific margins of Laurentia and East Antarctica-Australia as a conjugate rift pair: Evidence and implications for an Eocambrian supercontinent. Geology, 19(6), 598-601.

Davies, M. B., 1972. The geology and petrology of an Archaean inlier south of Normanville – the geochemistry of the Houghton

granulite. Unpub. BSc (Hons) Thesis, University of Adelaide.

Dutch, R. A., Hand, M. & Kelsey, D. E., 2010. Unravelling the tectonothermal evolution of reworked Archean granulite facies metapelites using in situ geochronology: an example from the Gawler Craton, Australia. Journal of Metamorphic Geology, 28(3), 293-316.

Evans, D. A. D. & Mitchell, R. N., 2011. Assembly and breakup of the core of Paleoproterozoic–Mesoproterozoic supercontinent Nuna. Geology, 39(5), 443-446.

Fanning, C. M., Flint, R. B., Parker, A. J., Ludwig, K. R. & Blissett, A. H., 1988. Refined Proterozoic evolution of the Gawler Craton, South Australia, through U-Pb zircon geochronology. Precambrian Research, 40–41(0), 363-386.

Fanning, C. M., Reid, A. J. & Teale, G., 2007. A geochronological framework for the Gawler Craton, South Australia. Geological Survey of South Australia.

Foden, J., Elburg, M. A., Dougherty-Page, J. & Burtt, A., 2006. The timing and duration of the Delamerian orogeny: Correlation with the Ross Orogen and implications for Gondwana assembly. Journal of Geology, 114(2), 189-210.

Forbes, C. J., Betts, P. G., Giles, D. & Weinberg, R., 2008. Reinterpretation of the tectonic context of high-temperature metamorphism in the Broken Hill Block, NSW, and implications on the Palaeo- to Meso-Proterozoic evolution. Precambrian Research, 166(1–4), 338-349.

Forbes, C. J., Betts, P. G., Weinberg, R. & Buick, I. S., 2005. A structural metamorphic study of the Broken Hill Block, NSW, Australia. Journal of Metamorphic Geology, 23(8), 745-770.

Foster, D. A. & Ehlers, K., 1998. 40Ar-39Ar thermochronology of the southern Gawler Craton, Australia: Implications for Mesoproterozoic and Neoproterozoic tectonics of East Gondwana and Rodinia. Journal of Geophysical Research: Solid Earth, 103(B5), 10177-10193.

Giles, D., Betts, P. G. & Lister, G. S., 2004. 1.8-1.5-Ga links between the North and South Australian Cratons and the Early-Middle Proterozoic configuration of Australia. Tectonophysics, 380(1-2), 27-41.

Goodge, J. W., Vervoort, J. D., Fanning, C. M., Brecke, D. M., Farmer, G. L., Williams, I. S., Myrow, P. M. & DePaolo, D. J., 2008. A Positive Test of East Antarctica–Laurentia Juxtaposition Within the Rodinia Supercontinent. Science, 321(5886), 235-240.

Griffin, W. L., Wang, X., Jackson, S. E., Pearson, N. J., O'Reilly, S. Y., Xu, X. & Zhou, X., 2002. Zircon chemistry and magma mixing, SE China: In-situ analysis of Hf isotopes, Tonglu and Pingtan igneous complexes. Lithos, 61(3–4), 237-269.

Hand, M., Reid, A. & Jagodzinski, L., 2007. Tectonic framework and evolution of the Gawler craton, Southern Australia. Economic Geology, 102(8), 1377-1395.

Howard, K., Reid, A. J., Hand, M., Barovich, K. M. & Belousova, E. A., 2006. Does the Kalinjala Shear Zone represent a paleosuture zone? Implications for distribution of styles of Mesoproterozoic mineralisation in the Gawler Craton. MESA Journal, 43, 16-20.

Howard, K. E., Hand, M., Barovich, K. M., Payne, J. L. & Belousova, E. A., 2011a. U–Pb, Lu–Hf and Sm–Nd isotopic constraints on provenance and depositional timing of metasedimentary rocks in the western Gawler Craton: Implications for Proterozoic reconstruction models. Precambrian Research, 184(1–4), 43-62.

Howard, K. E., Hand, M., Barovich, K. M., Payne, J. L., Cutts, K. A. & Belousova, E. A., 2011b. U–Pb zircon, zircon Hf and whole-rock Sm–Nd isotopic constraints on the evolution of Paleoproterozoic rocks in the northern Gawler Craton. Australian Journal of Earth Sciences, 58(6), 615-638.

Howard, K. E., Hand, M., Barovich, K. M.,

Reid, A., Wade, B. P. & Belousova, E. A., 2009. Detrital zircon ages: Improving interpretation via Nd and Hf isotopic data. Chemical Geology, 262(3–4), 277-292.

Jackson, S. E., Pearson, N. J., Griffin, W. L. & Belousova, E. A., 2004. The application of laser ablation-inductively coupled plasma-mass spectrometry to in situ U–Pb zircon geochronology. Chemical Geology, 211(1–2), 47-69.

Jagodzinski, E.J. 2005. Compilation of SHRIMP U–Pb geochronological data, Olympic Domain, Gawler Craton, South Australia, 2001–2003. Geoscience Australia, Record 2005/20, 197 pp.

Jagodzinski, E.A., Meaney, K., Szpunar, M., and Fraser, G., 2017. SHRIMP U-Pb dating of the Barossa Complex, South Australia: exploring tectonic links between the Gawler Craton and Curnamona Province. Report Book 2017/00017. Department of the Premier and Cabinet, South Australia, Adelaide.

Karlstrom, K. E., Harlan, S. S., Williams, M. L., Geissman, J. W. & Åhäll, K., 1999. Refining Rodinia: Geologic Evidence for the Australia–Western U.S. connection in the Proterozoic GSA Today, 9(10), 1-7.

Kositcin, N., 2010. Geodynamic Synthesis of the Gawler Craton and Curnamona Province. Geoscience Australia, Record, 2010/27, 113p.

Lane, K., Jagodzinski, E. A., Dutch, R., Reid, A. J. & Hand, M., 2015. Age constraints on the timing of iron ore mineralisation in the southeastern Gawler Craton. Australian Journal of Earth Sciences, 62(1), 55-75.

Li, Z. X., Bogdanova, S. V., Collins, A. S., Davidson, A., De Waele, B., Ernst, R. E., Fitzsimons, I. C. W., Fuck, R. A., Gladkochub, D. P., Jacobs, J., Karlstrom, K. E., Lu, S., Natapov, L. M., Pease, V., Pisarevsky, S. A., Thrane, K. & Vernikovsky, V., 2008. Assembly, configuration, and break-up history of Rodinia: A synthesis. Precambrian Research, 160(1–2), 179-210.

Ludwig, K. R., 2003. Users Manual for Isoplot 3.75. In: Special Publication No. 5, Berkeley Geochronology Center

Mancktelow, N. S., 1990. The structure of the southern Adelaide Fold Belt, South Australia. In: The evolution of a Late Precambrian-Early Paleozoic Rift Complex: The Adelaide Geosyncline (eds Jago, J. B. & Moore, P. J.), pp. 483-495, The Geological Society of Australia Special Publication

Medig, K. P. R., Thorkelson, D. J., Davis, W. J., Rainbird, R. H., Gibson, H. D., Turner, E. C. & Marshall, D. D., 2014. Pinning northeastern Australia to northwestern Laurentia in the Mesoproterozoic. Precambrian Research, 249, 88-99.

Moores, E. M., 1991. Southwest U.S.-East Antarctic (SWEAT) connection: A hypothesis. Geology, 19(5), 425-428.

Morrissey, L. J., Hand, M., Lane, K., Kelsey, D. E. & Dutch, R. A., 2016. Upgrading iron-ore deposits by melt loss during granulite facies metamorphism. Ore Geology Reviews, 74, 101-121.

Morrissey, L. J., Hand, M., Wade, B. P. & Szpunar, M., 2013. Early Mesoproterozoic metamorphism in the Barossa Complex, South Australia: links with the eastern margin of Proterozoic Australia. Australian Journal of Earth Sciences, 60(8), 769-795.

Mulder, J. A., Halpin, J. A. & Daczko, N. R., 2015. Mesoproterozoic Tasmania: Witness to the East Antarctica–Laurentia connection within Nuna. Geology, 43(9), 759-762.

Myers, J. S., Shaw, R. D. & Tyler, I. M., 1996. Tectonic evolution of Proterozoic Australia. Tectonics, 15(6), 1431-1446.

Neumann, N. L., Southgate, P. N. & Gibson, G. M., 2009. Defining unconformities in Proterozoic sedimentary basins using detrital geochronology and basin analysis—An example from the Mount Isa Inlier, Australia. Precambrian Research, 168(3–4), 149-166.

Offler, R. & Fleming, P. D., 1968. A synthesis of folding and metamorphism in the Mt

Lofty Ranges, South Australia. Journal of the Geological Society of Australia, 15(2), 245-266.

Page, R. N., Stevens, B. P. J. & Gibson, G. M., 2005a. Geochronology of the sequence hosting the Broken Hill Pb-Zn-Ag orebody, Australia. Economic Geology, 100(4), 633-661.

Page, R. W., Conor, C. H. H., Stevens, B. P. J., Gibson, G. M., Preiss, W. V. & Southgate, P. N., 2005b. Correlation of Olary and Broken Hill Domains, Curnamona Province: Possible relationship to Mount Isa and other North Australian Pb-Zn-Ag-bearing successions. Economic Geology, 100(4), 663-676.

Page, R. W., Jackson, M. J. & Krassay, A. A., 2000. Constraining sequence stratigraphy in north Australian basins: SHRIMP U–Pb zircon geochronology between Mt Isa and McArthur River*. Australian Journal of Earth Sciences, 47(3), 431-459.

Page, R. W. & Laing, W. P., 1992. Felsic metavolcanic rocks related to the Broken Hill Pb-Zn-Ag orebody, Australia; geology, depositional age, and timing of high-grade metamorphism. Economic Geology, 87(8), 2138-2168.

Page, R. W. & Sun, S. S., 1998. Aspects of geochronology and crustal evolution in the Eastern Fold Belt, Mt Isa Inlier. Australian Journal of Earth Sciences, 45(3), 343-361.

Payne, J. L., Barovich, K. M. & Hand, M., 2006. Provenance of metasedimentary rocks in the northern Gawler Craton, Australia: Implications for Palaeoproterozoic reconstructions. Precambrian Research, 148(3–4), 275-291.

Payne, J. L., Hand, M., Barovich, K., Reid, A. & Evans, D. A. D., 2009. Correlations and Reconstruction Models for the 2500-1500 Ma evolution of the Mawson Continent. In: Paleoproterozoic Supercontinents and Global Evolution (eds Reddy, S. M., Mazumder, R., Evans, D. A. D. & Collins, A. S.), pp. 319-357, Geological Society, London.

Payne, J. L., Hand, M., Barovich, K. M. & Wade, B. P., 2008. Temporal constraints on the timing of high-grade metamorphism in the northern Gawler Craton: implications for assembly of the Australian Proterozoic. Australian Journal of Earth Sciences, 55(5), 623-640.

Payne, J. L., Pearson, N. J., Grant, K. J. & Halverson, G. P., 2013. Reassessment of relative oxide formation rates and molecular interferences on in situ lutetium-hafnium analysis with laser ablation MC-ICP-MS. Journal of Analytical Atomic Spectrometry, 28(7), 1068-1079.

Pisarevsky, S. A., Elming, S.-Å., Pesonen, L. J. & Li, Z.-X., 2014. Mesoproterozoic paleogeography: Supercontinent and beyond. Precambrian Research, 244, 207-225.

Preiss, W. V., 1993. Basement Inliers of the Mount Lofty Ranges. In: The Geology of South Australia, Volume 1, The Precambrian (eds Drexel, J. F., Preiss, W. V. & Parker, A. J.), pp. 102-105, Geological Survey of South Australia, Adelaide.

Preiss, W. V., 2000. The Adelaide Geosyncline of South Australia and its significance in Neoproterozoic continental reconstruction. Precambrian Research, 100(1-3), 21-63.

Preiss, W. V., Fanning, C. A., Szpunar, M. A. & Burtt, A. C., 2008. Age and tectonic significance of the Mount Crawford Granite Gneiss and a related intrusive in the Oakbank Inlier, Mount Lofty Ranges, South Australia. MESA Journal, 49, 38-49.

Raetz, M., Krabbendam, M. & Donaghy, A. G., 2002. Compilation of Pb zircon data from the Willyama Supergroup, Broken Hill region, Australia: Evidence for three tectonostratigraphic successions and four magmatic events? Australian Journal of Earth Sciences, 49(6), 965-983.

Reid, A., Hand, M., Jagodzinski, E., Kelsey, D. & Pearson, N., 2008a. Paleoproterozoic orogenesis in the southeastern Gawler Craton, South Australia. Australian Journal of

Earth Sciences, 55(4), 449-471.

Reid, A. J. & Hand, M., 2012. Mesoarchean to Mesoproterozoic Evolution of the Southern Gawler Craton, South Australia. Journal of International Geoscience, 35(1), 216-225.

Reid, A. J., Jagodzinski, E. A., Armit, R. J., Dutch, R. A., Kirkland, C. L., Betts, P. G. & Schaefer, B. F., 2014. U-Pb and Hf isotopic evidence for Neoarchean and Paleoproterozoic basement in the buried northern Gawler Craton, South Australia. Precambrian Research, 250, 127-142.

Reid, A. J., McAvaney, S. O. & Fraser, G. L., 2008b. Nature of the Kimban Orogeny across northern Eyre Peninsula. MESA Journal, 51, 25-34.

Reid, A. J. & Payne, J. L., 2017. Magmatic zircon Lu–Hf isotopic record of juvenile addition and crustal reworking in the Gawler Craton, Australia. Lithos, 292-293(Supplement C), 294-306.

Reimink, J. R., Davies, J. H. F. L., Waldron, J. W. F. & Rojas, X., 2016. Dealing with discordance: a novel approach for analysing U–Pb detrital zircon datasets. Journal of the Geological Society, 173(4), 577-585.

Rubenach, M. J., Foster, D. R. W., Evins, P. M., Blake, K. L. & Fanning, C. M., 2008. Age constraints on the tectonothermal evolution of the Selwyn Zone, Eastern Fold Belt, Mount Isa Inlier. Precambrian Research, 163(1–2), 81-107.

Rutherford, L., Hand, M. & Barovich, K., 2007. Timing of Proterozoic metamorphism in the southern Curnamona Province: implications for tectonic models and continental reconstructions. Australian Journal of Earth Sciences, 54(1), 65-81.

Sayab, M., 2006. Decompression through clockwise P–T path: implications for early N–S shortening orogenesis in the Mesoproterozoic Mt Isa Inlier (NE Australia). Journal of Metamorphic Geology, 24(2), 89-105.

Scherer, E., Munker, C. & Mezger, K., 2001. Calibration of the Lutetium-Hafnium Clock. Science, 293(5530), 683-687.

Sláma, J., Košler, J., Condon, D. J., Crowley, J. L., Gerdes, A., Hanchar, J. M., Horstwood, M. S. A., Morris, G. A., Nasdala, L., Norberg, N., Schaltegger, U., Schoene, B., Tubrett, M. N. & Whitehouse, M. J., 2008. Plešovice zircon — A new natural reference material for U–Pb and Hf isotopic microanalysis. Chemical Geology, 249(1–2), 1-35.

Swain, G. M., Hand, M., Teasdale, J., Rutherford, L. & Clark, C., 2005. Age constraints on terrane-scale shear zones in the Gawler Craton, southern Australia. Precambrian Research, 139(3–4), 164-180.

Szpunar, M., Hand, M., Barovich, K., Jagodzinski, E. & Belousova, E., 2011. Isotopic and geochemical constraints on the Paleoproterozoic Hutchison Group, southern Australia: Implications for Paleoproterozoic continental reconstructions. Precambrian Research, 187(1–2), 99-126.

Szpunar, M., Wade, B., Hand, M. P. & Barovich, K. M., 2007. Timing of Proterozoic high-grade metamorphism in the Barossa Complex, southern South Australia; exploring the extent of the 1590 Ma event. MESA Journal, 47, 21-27.

Szpunar, M. A. & Fraser, G. L., 2010. Age of deposition and provenance of Palaeoproterozoic basins on north-eastern Eyre Peninsula, PIRSA Geological Survey Branch.

Talbot, J. L., 1963. Retrograde metamorphism of the Houghton Complex, South Australia. Transactions of the Royal Society of South Australia, 87, 185-197.

Vassallo, J. J. & Wilson, C. J. L., 2002. Palaeoproterozoic regional-scale non-coaxial deformation: an example from eastern Eyre Peninsula, South Australia. Journal of Structural Geology, 24(1), 1-24.

Vassallo, J. J. & Wilson, J. L., 2001. Structural repetition of the Hutchison Group metasediments, Eyre Peninsula, South Australia. Australian Journal of Earth Sciences, 48(2), 331.

Willis, I. L., Brown, R. E., Stroud, W. J. & Stevens, B. P. J., 1983. The early Proterozoic Willyama supergroup: Stratigraphic subdivision and interpretation of high to low-grade metamorphic rocks in the Broken Hill Block, New South Wales. Journal of the Geological Society of Australia, 30(1-2), 195-224.

Woodhead, J., Hergt, J., Shelley, M., Eggins, S. & Kemp, R., 2004. Zircon Hf-isotope analysis with an excimer laser, depth profiling, ablation of complex geometries, and concomitant age estimation. Chemical Geology, 209(1–2), 121-135.

Woodhead, J. D. & Hergt, J. M., 2005. A Preliminary Appraisal of Seven Natural Zircon Reference Materials for In Situ Hf Isotope Determination. Geostandards and Geoanalytical Research, 29(2), 183-195.

Zang, W., 2002. Late Palaeoproterozoic Wallaroo Group and early Mesoproterozoic mineralisation in the Moonta Subdomain, eastern Gawler Craton, South Australia, Primary Industry and Resources South Australia.

Zhang, S., Li, Z.-X., Evans, D. A. D., Wu, H., Li, H. & Dong, J., 2012. Pre-Rodinia supercontinent Nuna shaping up: A global synthesis with new paleomagnetic results from North China. Earth and Planetary Science Letters, 353–354(0), 145-155.

Zhao, G., Cawood, P. A., Wilde, S. A. & Sun, M., 2002. Review of global 2.1–1.8 Ga orogens: implications for a pre-Rodinia supercontinent. Earth-Science Reviews, 59(1–4), 125-162.

Zhao, G., Sun, M., Wilde, S. A. & Li, S., 2004. A Paleo-Mesoproterozoic supercontinent: assembly, growth and breakup. Earth-Science Reviews, 67(1–2), 91-123.

Chapter 4 Supplementary Data Part 1: U-Pb isotopic data

SAMPLE: HI20 - Calcsilicate, Eastern Houghton Inlier

Analysis #	$^{207}Pb/^{235}U$ Ratio	1σ	$^{206}Pb/^{238}U$ Ratio	1σ	Rho	$^{207}Pb/^{206}Pb$ Age	2σ	$^{206}Pb/^{238}U$ Age	2σ	Conc. %	Comments
Detrital Zircon											
KERS_11	4.616	0.14888	0.3101	0.00566	0.2173482	1765.6	59.96	1741.2	27.84	99	Hf Analysis #2
KERS_18	4.63301	0.08705	0.30797	0.00421	0.4038232	1785	32.96	1730.7	20.73	97	Hf Analysis #4
KERS_20	4.43576	0.08887	0.30532	0.00426	0.3761371	1721.2	35.64	1717.6	21.06	100	Hf Analysis #5
KERS_27	4.56796	0.08923	0.3161	0.0044	0.3819181	1711.4	34.93	1770.7	21.54	103	
KERS_31	4.51389	0.09663	0.31012	0.00447	0.336914	1724.6	38.87	1741.3	21.98	101	Hf Analysis #8
KERS_32	4.61263	0.09104	0.31341	0.00431	0.3601334	1744.9	35.32	1757.5	21.16	101	
KERS_33	4.42334	0.09587	0.30961	0.00445	0.3223228	1690.3	39.63	1738.8	21.88	103	
KERS_43	4.4664	0.07215	0.30802	0.00382	0.4356248	1717.4	28.17	1731	18.84	101	Hf Analysis #10
KERS_45	4.46008	0.10514	0.31314	0.00465	0.4316363	1684.4	43.52	1756.1	22.83	104	Hf Analysis #11
KERS_47	4.55509	0.08862	0.31118	0.00415	0.3606816	1734.7	34.83	1746.5	20.41	101	
KERS_51	4.503	0.07827	0.30655	0.00396	0.4019021	1741.5	30.71	1723.7	19.56	99	
KERS_60	4.89765	0.08815	0.3173	0.00401	0.3692105	1832.1	31.86	1776.5	19.64	97	Hf Analysis #13
KERS_63	4.55346	0.08169	0.31327	0.00407	0.3848507	1721.9	32.06	1756.8	19.99	102	Hf Analysis #14
KERS_64	4.51393	0.07773	0.31341	0.00398	0.4051425	1705	30.58	1757.5	19.55	103	Hf Analysis #15
KERS_67	4.54912	0.08542	0.31055	0.00407	0.3668804	1736.1	33.55	1743.4	20.02	100	Hf Analysis #16
KERS_68	4.49439	0.07599	0.30756	0.00382	0.4136177	1731.6	29.68	1728.7	18.81	100	Hf Analysis #17
Metamorphic Zircon											
KERS_02	3.91495	0.05587	0.27797	0.00337	0.5013707	1664.1	24.35	1581.1	16.98	95	Hf Analysis #1
KERS_14	3.89334	0.05712	0.27866	0.00345	0.5189707	1649.3	24.62	1584.6	17.37	96	Hf Analysis #3
KERS_16	3.93502	0.0598	0.28428	0.00355	0.5072444	1632	25.74	1612.9	17.83	99	
KERS_19	4.05081	0.06456	0.28497	0.00361	0.4884003	1681.1	27.04	1616.3	18.1	96	
KERS_21	3.89517	0.06332	0.27944	0.00355	0.4834952	1644.8	27.72	1588.5	17.89	97	
KERS_22	3.94927	0.07074	0.28204	0.00372	0.4333458	1653.2	31.27	1601.6	18.71	97	
KERS_26	3.98026	0.06165	0.29103	0.00368	0.4902567	1609.4	26.54	1646.7	18.36	102	Hf Analysis #6
KERS_28	3.97633	0.06378	0.2887	0.00367	0.4671427	1622.5	27.81	1635	18.35	101	Hf Analysis #7
KERS_34	3.84341	0.06901	0.27955	0.00362	0.3917501	1619.1	32.24	1589.1	18.26	98	Hf Analysis #9
KERS_38	3.80622	0.05417	0.27712	0.00332	0.5001096	1617.1	24.45	1576.8	16.76	98	
KERS_39	4.05166	0.06046	0.29203	0.00355	0.4723445	1635.9	25.9	1651.7	17.71	101	
KERS_41	3.90345	0.06104	0.28473	0.0035	0.45291	1613.6	27.48	1615.1	17.58	100	
KERS_52	3.99002	0.07059	0.28208	0.00365	0.3921832	1672	31.76	1601.8	18.34	96	
KERS_55	3.93002	0.0661	0.28708	0.00359	0.4117891	1611.4	30.16	1626.9	18	101	Hf Analysis #12
KERS_56	3.92762	0.0655	0.28453	0.00353	0.4117454	1626.9	29.81	1614.1	17.74	99	
KERS_57	4.04742	0.07666	0.28745	0.00377	0.3573454	1663.7	34.46	1628.8	18.9	98	
KERS_65	4.01068	0.07705	0.28565	0.0038	0.3583353	1658	34.93	1619.8	19.06	98	
Discordant Analyses - Not used in age calculations											
KERS_01	2.49168	0.03475	0.17997	0.00217	0.5126021	1632.3	23.78	1066.8	11.83	65	
KERS_03	2.20717	0.03175	0.1652	0.002	0.4984729	1565.8	24.89	985.6	11.06	63	

Analysis #	$^{207}Pb/^{235}U$ Ratio	1σ	$^{206}Pb/^{238}U$ Ratio	1σ	Rho	$^{207}Pb/^{206}Pb$ Age	2σ	$^{206}Pb/^{238}U$ Age	2σ	Conc. %	Comments
KERS_04	3.7233	0.05405	0.26978	0.00327	0.4997698	1626.4	24.93	1539.7	16.6	95	
KERS_05	3.30679	0.04902	0.2235	0.00272	0.4854972	1754.7	25.12	1300.4	14.35	74	
KERS_06	3.56939	0.05403	0.25455	0.00312	0.4748529	1655.9	26.12	1461.9	16.01	88	
KERS_07	3.96793	0.09036	0.27851	0.0041	0.2992305	1685.3	41.99	1583.8	20.67	94	
KERS_08	2.99633	0.05129	0.21006	0.00268	0.4183148	1687.5	30.25	1229.1	14.25	73	
KERS_09	4.30921	0.07091	0.29294	0.00367	0.4363726	1744.1	28.46	1656.2	18.3	95	
KERS_10	3.87312	0.06569	0.27145	0.00343	0.4217119	1688	29.77	1548.2	17.39	92	
KERS_12	4.14111	0.07656	0.27701	0.00362	0.3848222	1773.4	32.63	1576.3	18.25	89	
KERS_13	3.97314	0.0586	0.27685	0.00343	0.5135365	1698.9	24.7	1575.5	17.33	93	
KERS_15	2.40382	0.0359	0.16947	0.00211	0.5118012	1677.3	25.09	1009.2	11.61	60	
KERS_17	4.08748	0.06752	0.28335	0.00365	0.4611338	1708.3	28.38	1608.2	18.33	94	
KERS_23	1.80195	0.03196	0.11726	0.00154	0.4349132	1823.5	30.25	714.8	8.87	39	
KERS_24	1.83756	0.03227	0.11599	0.00151	0.447315	1878.7	29.54	707.4	8.73	38	
KERS_25	3.22297	0.06879	0.21844	0.00315	0.3406716	1749.5	38.53	1273.6	16.69	73	
KERS_29	3.73174	0.06013	0.26268	0.00333	0.4608435	1679.9	27.82	1503.6	17.01	90	
KERS_30	2.27944	0.03601	0.14326	0.0018	0.4735139	1886.5	26.5	863.1	10.13	46	
KERS_35	1.84823	0.03229	0.12094	0.00154	0.4040787	1813.5	30.54	736	8.87	41	
KERS_36	2.6055	0.04715	0.17926	0.00231	0.3836643	1721.8	32.25	1063	12.62	62	
KERS_37	3.33452	0.05321	0.25145	0.00314	0.4361958	1551.5	28.54	1446	16.16	93	
KERS_40	1.6719	0.02582	0.10688	0.00131	0.4545615	1855.6	26.39	654.6	7.65	35	
KERS_42	3.14385	0.0483	0.23287	0.00284	0.4655821	1584.9	26.95	1349.5	14.84	85	
KERS_44	2.50613	0.04377	0.16505	0.00211	0.3964914	1801.6	30.74	984.8	11.67	55	
KERS_46	3.50325	0.05777	0.24915	0.00309	0.292239	1660.6	29.03	1434.1	15.96	86	
KERS_48	3.22751	0.0568	0.22626	0.00286	0.3974013	1687.1	31.18	1314.9	15.01	78	
KERS_49	2.49533	0.03654	0.17694	0.00214	0.4820157	1666.3	25.21	1050.2	11.74	63	
KERS_50	2.75466	0.04072	0.18515	0.00225	0.4816383	1764.8	25.19	1095	12.21	62	
KERS_53	3.36705	0.05641	0.2363	0.00297	0.4143912	1685.5	29.77	1367.5	15.51	81	
KERS_54	0.58954	0.00955	0.04097	0.00051	0.4230118	1703.7	28.58	258.8	3.13	15	
KERS_58	3.64221	0.06759	0.2419	0.00313	0.3608813	1786.8	33.24	1396.5	16.26	78	
KERS_59	3.83212	0.07159	0.2714	0.00351	0.3566142	1669	33.92	1547.9	17.77	93	
KERS_61	3.46695	0.05685	0.25046	0.00313	0.4253079	1631.7	29.21	1440.8	16.14	88	
KERS_62	3.784	0.0579	0.26173	0.00318	0.4542437	1712.1	26.53	1498.7	16.27	88	
KERS_66	3.11407	0.05058	0.19457	0.00239	0.4300708	1896.9	27.82	1146.1	12.92	60	
KERS_69	2.06479	0.03573	0.14863	0.00185	0.4017243	1638.2	30.86	893.3	10.39	55	
KERS_70	2.30338	0.04093	0.15034	0.00189	0.3853911	1817.9	31.13	902.9	10.59	50	

SAMPLE: Vixen Gully 6 - Psammitic Layer in Sillimanite Gneiss, Northern Houghton Inlier

	$^{207}Pb/^{235}U$		$^{206}Pb/^{238}U$			$^{207}Pb/^{206}Pb$		$^{206}Pb/^{238}U$		Conc.	
Analysis #	**Ratio**	**1σ**	**Ratio**	**1σ**	**Rho**	**Age**	**2σ**	**Age**	**2σ**	**%**	**Comments**
Detrital Zircon											
VIX6_001	5.13228	0.10499	0.32802	0.00429	0.3408334	1856	35.98	1828.8	20.84	99	
VIX6_002	4.87439	0.10217	0.32252	0.00424	0.3328458	1793.2	37.28	1802	20.69	100	Hf Analysis #1
VIX6_003	4.52168	0.09724	0.3019	0.004	0.3193582	1776.7	38.46	1700.7	19.79	96	
VIX6_005	17.01844	0.38108	0.56797	0.00762	0.3053728	2961.2	35.53	2899.5	31.31	98	
VIX6_006	4.25594	0.11369	0.29958	0.00443	0.2522031	1679.8	49.27	1689.2	21.96	101	
VIX6_007	5.54827	0.13151	0.34333	0.00464	0.2842578	1914.4	42	1902.7	22.26	99	Hf Analysis #3
VIX6_008	5.07822	0.16008	0.33363	0.00559	0.2113524	1806.2	57.85	1856	27.04	103	
VIX6_009	8.48242	0.21429	0.41662	0.00576	0.2595359	2319.4	43.04	2245.1	26.22	97	Hf Analysis #4
VIX6_010	4.48907	0.12153	0.31286	0.00451	0.238017	1698.3	49.78	1754.8	22.16	103	Hf Analysis #5
VIX6_011	4.80787	0.08797	0.31951	0.00399	0.3670728	1783.7	32.42	1787.3	19.51	100	Hf Analysis #6
VIX6_012	4.56095	0.08453	0.31282	0.00389	0.3568212	1725.9	33.14	1754.6	19.12	102	
VIX6_014	4.47841	0.09076	0.31294	0.004	0.3167108	1691.5	36.96	1755.2	19.66	104	
VIX6_015	11.74015	0.2404	0.48468	0.00628	0.3095482	2611.1	33.88	2547.6	27.25	98	
VIX6_016	4.54843	0.09507	0.31047	0.00395	0.2888254	1734.7	38.11	1743	19.42	100	Hf Analysis #7
VIX6_017	4.83558	0.10346	0.31826	0.00405	0.2728483	1801.2	38.94	1781.2	19.83	99	
VIX6_018	5.83456	0.13913	0.36225	0.00493	0.2431752	1906.8	43.28	1992.8	23.35	105	
VIX6_023	4.6217	0.09629	0.30593	0.00379	0.2844466	1792.1	37.81	1720.7	18.7	96	Hf Analysis #11
VIX6_024	5.07454	0.10808	0.32519	0.00405	0.2712078	1850.9	38.43	1815	19.68	98	
VIX6_025	4.61414	0.10623	0.31059	0.00403	0.2460072	1761.5	42.23	1743.6	19.81	99	
VIX6_027	5.07116	0.12026	0.32516	0.00421	0.2330268	1849.8	43.14	1814.9	20.47	98	Hf Analysis #12
VIX6_028	10.94114	0.26636	0.46274	0.00614	0.2299087	2572	41.05	2451.6	27.06	95	Hf Analysis #13
VIX6_030	5.01902	0.128	0.31809	0.00415	0.2069949	1870.8	46.46	1780.4	20.29	95	
VIX6_040	4.75961	0.10173	0.31882	0.00396	0.2787149	1770.4	38.89	1784	19.36	101	
VIX6_041	5.30633	0.12039	0.34263	0.0044	0.2609067	1837.2	41.06	1899.3	21.13	103	Hf Analysis #15
VIX6_042	4.87252	0.11641	0.31688	0.00419	0.2453292	1824.2	43.44	1774.5	20.49	97	
VIX6_046	4.76991	0.12691	0.31413	0.0043	0.2167756	1801.3	48.6	1761	21.1	98	
VIX6_047	4.71907	0.09531	0.31881	0.004	0.3016172	1754.7	36.62	1783.9	19.54	102	Hf Analysis #17
VIX6_048	15.0944	0.29574	0.54884	0.00676	0.313253	2821.5	31.64	2820.3	28.14	100	Hf Analysis #18
VIX6_049	6.80722	0.14984	0.38736	0.00511	0.2786899	2062.8	38.85	2110.6	23.76	102	Hf Analysis #19
VIX6_053	5.25461	0.12358	0.3322	0.00431	0.2402477	1875.2	42.56	1849.1	20.87	99	Hf Analysis #22
VIX6_057	4.93218	0.12902	0.31902	0.00423	0.2009143	1834	47.88	1784.9	20.65	97	Hf Analysis #23
VIX6_059	4.51249	0.12562	0.30506	0.00412	0.1768179	1753.6	51.62	1716.4	20.36	98	Hf Analysis #24
VIX6_060	5.06843	0.1506	0.3347	0.00475	0.1624756	1796.5	55.01	1861.1	22.96	104	
Metamorphic Zircon											
VIX6_019	3.63643	0.08132	0.267	0.0034	0.2425693	1600	42.08	1525.6	17.28	95	Hf Analysis #8
VIX6_020	3.67047	0.08446	0.27119	0.00347	0.2276209	1588.5	43.57	1546.8	17.58	97	Hf Analysis #9
VIX6_022	3.75737	0.09167	0.27413	0.00355	0.1898227	1612.5	46.49	1561.7	17.94	97	Hf Analysis #10
VIX6_031	3.69775	0.09663	0.27166	0.00354	0.1937716	1599.9	49.29	1549.2	17.96	97	Hf Analysis #14
VIX6_039	3.79582	0.07763	0.27719	0.00338	0.290865	1611.3	37.79	1577.2	17.04	98	

Analysis #	$^{207}Pb/^{235}U$ Ratio	1σ	$^{206}Pb/^{238}U$ Ratio	1σ	Rho	$^{207}Pb/^{206}Pb$ Age	2σ	$^{206}Pb/^{238}U$ Age	2σ	Conc. %	Comments
VIX6_050	3.85901	0.07878	0.28427	0.00346	0.2894145	1594.7	37.78	1612.8	17.38	101	Hf Analysis #20
VIX6_051	3.63537	0.07648	0.27078	0.00332	0.2815179	1574.1	39.14	1544.7	16.84	98	Hf Analysis #21
Discordant Analyses - Not used in age calculations											
VIX6_004	15.45878	0.34237	0.52527	0.00716	0.3139118	2932.2	~~35.25~~	2721.5	30.27	93	
VIX6_013	3.75444	0.07661	0.27102	0.00351	0.3161747	1631.4	37.47	1546	17.79	95	
VIX6_021	4.21705	0.10617	0.28462	0.00384	0.1935016	1756	47.02	1614.6	19.29	92	
VIX6_026	6.27186	0.14189	0.32697	0.00416	0.2510633	2216.1	39.36	1823.7	20.22	82	
VIX6_029	3.3438	0.08182	0.21139	0.00271	0.2185405	1875.3	44.46	1236.2	14.4	66	
VIX6_032	4.61687	0.12792	0.3034	0.00411	0.1816275	1805.1	51.1	1708.2	20.32	95	
VIX6_033	5.0386	0.14349	0.31672	0.00433	0.1659964	1885.6	52.1	1773.7	21.19	94	
VIX6_034	5.65405	0.16645	0.32469	0.00451	0.1590674	2046.8	52.95	1812.6	21.94	89	
VIX6_035	3.86495	0.0711	0.26602	0.00315	0.3287018	1720.9	33.3	1520.6	16.04	88	
VIX6_036	3.75881	0.07137	0.26833	0.00321	0.3142967	1653.5	34.76	1532.3	16.32	93	
VIX6_037	3.84278	0.07598	0.25624	0.00312	0.3008092	1778.8	35.81	1470.6	16	83	
VIX6_038	1.85232	0.03856	0.1107	0.00138	0.2770413	1976.3	37.02	676.8	8.01	34	
VIX6_043	8.01268	0.18596	0.39924	0.00508	0.2512875	2294.2	39.84	2165.5	23.41	94	
VIX6_044	3.92382	0.09548	0.26899	0.0035	0.2410155	1728	44.61	1535.7	17.78	89	
VIX6_045	4.94638	0.12512	0.31299	0.00416	0.2290063	1873.7	45.71	1755.4	20.42	94	
VIX6_052	4.10355	0.09202	0.27559	0.00349	0.253908	1765.5	41.04	1569.1	17.64	89	
VIX6_054	4.65446	0.1173	0.30237	0.00409	0.2236399	1826	46.1	1703.1	20.25	93	
VIX6_055	3.24416	0.07778	0.24397	0.0031	0.2253646	1556.1	45.16	1407.3	16.05	90	
VIX6_056	3.48928	0.0869	0.24361	0.00314	0.2186801	1694.4	46.2	1405.4	16.26	83	
VIX6_058	4.71805	0.12623	0.30565	0.00405	0.189454	1831.2	49.05	1719.3	20.01	94	
SAMPLE: HI11 - Quartzofeldspathic Gneiss, Southern Houghton Inlier											
Detrital Zircon											
HI11_28	4.15174	0.07794	0.29213	0.0045	0.5547725	1680.1	30.03	1652.2	22.45	98	
HI11_29	4.05868	0.06951	0.2861	0.00427	0.6156062	1676.8	25.96	1622	21.4	97	
HI11_31	4.39225	0.09244	0.3035	0.00489	0.4843396	1713.6	35.14	1708.7	24.17	100	
HI11_33	4.15769	0.07708	0.29666	0.00453	0.5647234	1654.4	29.43	1674.7	22.53	101	
HI11_34	4.19054	0.08341	0.29403	0.00461	0.5209653	1685.5	32.55	1661.6	22.97	99	
HI11_35	4.21723	0.07245	0.29773	0.00449	0.608022	1674.2	26.4	1680	22.33	100	
HI11_37	4.4159	0.07422	0.30753	0.0046	0.6213115	1699.3	25.41	1728.6	22.7	102	
HI11_45	4.26374	0.07249	0.29825	0.00443	0.605762	1691.2	26.02	1682.6	22.01	99	
HI11_49	4.04129	0.06632	0.2824	0.00415	0.6288682	1693	24.62	1603.5	20.87	95	
HI11_52	4.20944	0.07374	0.29505	0.00441	0.5841755	1687.4	27.38	1666.7	21.96	99	
HI11_54	4.4015	0.0826	0.30254	0.00463	0.5420237	1723.4	30.24	1703.9	22.9	99	
HI11_55	4.36581	0.08046	0.30291	0.00459	0.5513097	1706.2	29.48	1705.7	22.72	100	
HI11_57	4.38563	0.07757	0.30244	0.0045	0.5753326	1717.4	27.63	1703.4	22.29	99	
HI11_59	4.25473	0.06955	0.29881	0.00438	0.6279734	1683.9	24.62	1685.4	21.73	100	
HI11_60	4.35254	0.07647	0.30239	0.00453	0.5776128	1703.8	27.61	1703.2	22.45	100	

	$^{207}Pb/^{235}U$		$^{206}Pb/^{238}U$			$^{207}Pb/^{206}Pb$		$^{206}Pb/^{238}U$		Conc.	
Analysis #	**Ratio**	**1σ**	**Ratio**	**1σ**	**Rho**	**Age**	**2σ**	**Age**	**2σ**	**%**	**Comments**
HI11_63	4.36719	0.07857	0.30312	0.00457	0.5616439	1705.5	28.65	1706.8	22.63	100	
HI11_66	4.28708	0.08085	0.29603	0.00453	0.5299586	1715	30.7	1671.6	22.55	97	
HI11_67	4.36112	0.08108	0.30201	0.0046	0.5382282	1709.7	30.09	1701.3	22.75	100	
HI11_68	4.19504	0.0747	0.2961	0.00443	0.5658663	1674.5	28.33	1671.9	22.02	100	
HI11_69	4.17255	0.07644	0.29478	0.00445	0.5460707	1672.8	29.58	1665.4	22.15	100	
HI11_72	4.23917	0.07317	0.29925	0.00444	0.5842056	1674.4	27.12	1687.6	22.05	101	
HI11_75	4.23793	0.0744	0.29945	0.00446	0.5719049	1672.6	27.84	1688.6	22.12	101	
HI11_77	4.14941	0.07845	0.28963	0.00442	0.5258706	1695.1	30.98	1639.7	22.1	97	Hf Analysis #2
HI11_80	4.24384	0.08389	0.29948	0.00463	0.4945403	1674.9	33.02	1688.7	22.97	101	
HI11_81	4.19019	0.09397	0.29511	0.00481	0.4270547	1678.6	38.96	1667	23.95	99	
HI11_84	4.40926	0.07299	0.30294	0.00443	0.6018288	1724.4	25.47	1705.9	21.89	99	
HI11_86	4.23363	0.06775	0.29641	0.00427	0.6263252	1689.7	24.24	1673.5	21.24	99	
HI11_87	4.4052	0.07316	0.30118	0.00439	0.5956916	1733.5	25.65	1697.1	21.74	98	
HI11_88	4.21749	0.06858	0.29708	0.00429	0.6135118	1678.5	24.97	1676.8	21.32	100	
HI11_89	4.19666	0.06756	0.29629	0.00426	0.6166599	1674.3	24.6	1672.9	21.18	100	
HI11_93	4.22828	0.07234	0.29623	0.00432	0.5695375	1688.6	27.16	1672.6	21.46	99	
11B_004	4.19968	0.09435	0.29586	0.00496	0.4698667	1678.5	37.96	1670.8	24.66	100	
11B_005	4.49176	0.09002	0.30375	0.00487	0.5369047	1753.8	32	1709.9	24.07	97	Hf Analysis #1
11B_006	4.25171	0.08139	0.29679	0.00466	0.5693674	1695.4	30.06	1675.4	23.18	99	
11B_009	4.19926	0.0843	0.29462	0.00469	0.5422893	1686.1	32.22	1664.6	23.37	99	Hf Analysis #3
11B_010	4.30882	0.0899	0.29874	0.00483	0.5179496	1707.9	33.95	1685.1	23.96	99	
11B_011	4.34666	0.10961	0.30192	0.00529	0.4135284	1704.6	43.65	1700.8	26.19	100	Hf Analysis #4
11B_014	4.51584	0.08594	0.30169	0.00475	0.5694804	1775.5	29.67	1699.7	23.55	96	Hf Analysis #5
11B_018	4.10834	0.07611	0.28601	0.00444	0.5849127	1700.1	28.64	1621.5	22.24	95	
11B_025	5.03153	0.0863	0.32461	0.00493	0.6378031	1839	24.99	1812.2	24.01	99	Hf Analysis #6
11B_028	4.30998	0.08252	0.30126	0.00472	0.5568118	1692.5	30.39	1697.6	23.38	100	Hf Analysis #7
11B_035	4.28245	0.08458	0.29339	0.00459	0.5331655	1729.4	31.68	1658.5	22.88	96	
11B_037	4.4668	0.07818	0.3027	0.00463	0.6225047	1749.7	26.12	1704.7	22.89	97	
11B_040	4.27841	0.07499	0.29986	0.00457	0.6166454	1687.8	26.44	1690.6	22.65	100	Hf Analysis #12
11B_041	4.27732	0.07722	0.30059	0.00462	0.596173	1682.9	27.78	1694.2	22.88	101	Hf Analysis #9
11B_046	4.33207	0.08366	0.30007	0.00469	0.5493058	1709.5	30.69	1691.6	23.26	99	Hf Analysis #10
11B_048	4.1374	0.07903	0.28712	0.00445	0.5593058	1706.1	30.23	1627.1	22.31	95	
11B_056	4.12983	0.07727	0.29091	0.00444	0.5657606	1678.4	29.55	1646.1	22.19	98	
11B_059	4.23493	0.08094	0.29183	0.00446	0.5465334	1718.9	30.37	1650.7	22.26	96	Hf Analysis #13
11B_061	4.30213	0.07275	0.30155	0.00448	0.6284728	1687.8	25.35	1699	22.21	101	
11B_074	4.44556	0.07681	0.30181	0.00456	0.616293	1746.4	25.96	1700.3	22.56	97	
11B_075	4.1003	0.07134	0.28973	0.00438	0.6094483	1672.8	26.56	1640.2	21.88	98	
11B_076	4.14702	0.07572	0.28917	0.00444	0.5771982	1697.3	28.6	1637.4	22.18	96	Hf Analysis #11
11B_086	5.03047	0.08588	0.32276	0.00483	0.6165928	1848.9	25.34	1803.2	23.53	98	Hf Analysis #14
11B_087	4.08613	0.07376	0.28449	0.00432	0.579262	1699.8	28.23	1613.9	21.67	95	
11B_088	4.25634	0.07918	0.29898	0.00457	0.5593405	1683.4	29.6	1686.2	22.7	100	

Analysis #	$^{207}Pb/^{235}U$ Ratio	1σ	$^{206}Pb/^{238}U$ Ratio	1σ	Rho	$^{207}Pb/^{206}Pb$ Age	2σ	$^{206}Pb/^{238}U$ Age	2σ	Conc. %	Comments
Metamorphic Zircon											
HI11_26	3.81251	0.06839	0.27384	0.00415	0.580823	1642	28.17	1560.2	21	95	
HI11_32	3.79947	0.06589	0.27852	0.00416	0.6079315	1604.2	26.66	1583.9	20.99	99	
HI11_62	3.88452	0.07079	0.28196	0.00427	0.5527281	1622.7	29.49	1601.2	21.45	99	
HI11_70	3.86225	0.06566	0.28248	0.00415	0.5944186	1608.5	26.59	1603.8	20.85	100	
HI11_71	3.83394	0.10366	0.2813	0.00504	0.3442195	1602.7	49.23	1597.9	25.37	100	
HI11_91	3.7172	0.06818	0.27572	0.00412	0.5266826	1582.6	30.42	1569.8	20.8	99	
11B_001	3.81775	0.06995	0.27618	0.00428	0.5934383	1629.4	28.44	1572.1	21.63	96	
11B_019	3.8851	0.07014	0.28235	0.00433	0.6054538	1620.5	27.72	1603.2	21.79	99	
Discordant Analyses - Not used in age calculations											
HI11_23	1.63502	0.02779	0.11579	0.00172	0.6174618	1668.1	25.85	706.3	9.96	42	
HI11_24	3.6375	0.06197	0.25538	0.00381	0.6158513	1684.2	25.82	1466.2	19.56	87	
HI11_25	3.60084	0.06349	0.24297	0.00367	0.5907296	1757.1	27.04	1402.1	19.02	80	
HI11_27	3.91091	0.07893	0.27456	0.00435	0.5059807	1684.3	33.37	1563.9	21.98	93	
HI11_30	3.65305	0.06582	0.25812	0.00391	0.580984	1672.4	28.2	1480.2	20.05	89	
HI11_36	4.00646	0.06372	0.27861	0.00411	0.6614892	1702	23.05	1584.4	20.7	93	
HI11_38	3.93566	0.06446	0.27722	0.00411	0.6404623	1678.4	24.39	1577.4	20.75	94	
HI11_39	3.80341	0.0616	0.26985	0.00398	0.6447541	1665	23.98	1540	20.22	92	
HI11_40	3.58243	0.05727	0.25861	0.0038	0.658139	1632.9	23.53	1482.7	19.45	91	
HI11_41	2.70192	0.0469	0.1806	0.00272	0.5943358	1774.6	26.73	1070.2	14.84	60	
HI11_42	3.32894	0.05564	0.23227	0.00345	0.6204818	1695.9	25.27	1346.4	18.04	79	
HI11_43	2.54282	0.043	0.18435	0.00274	0.6132323	1625	26.02	1090.7	14.91	67	
HI11_44	4.29672	0.07479	0.2871	0.00431	0.5900359	1775.2	26.82	1627	21.59	92	
HI11_46	3.5708	0.06177	0.2554	0.00381	0.5927053	1650	26.93	1466.3	19.56	89	
HI11_47	3.69216	0.06289	0.25758	0.00384	0.6044214	1696.1	26.23	1477.5	19.68	87	
HI11_48	2.80471	0.04792	0.18882	0.00281	0.5972827	1761.5	26.15	1115	15.26	63	
HI11_50	3.83357	0.06665	0.25633	0.00384	0.5881703	1773.9	26.88	1471	19.69	83	
HI11_51	3.75907	0.06217	0.26376	0.00388	0.6244892	1685.5	24.95	1509	19.77	90	
HI11_53	4.30708	0.0729	0.28534	0.00422	0.6087382	1790.7	25.61	1618.2	21.15	90	
HI11_56	3.72601	0.06595	0.257	0.00383	0.5760253	1717.1	27.7	1474.5	19.66	86	
HI11_58	3.3892	0.05814	0.24077	0.00354	0.6009792	1662.6	26.49	1390.7	18.39	84	
HI11_61	3.78856	0.07002	0.25942	0.00396	0.5400732	1730.4	29.77	1486.9	20.25	86	
HI11_64	1.42173	0.02395	0.10579	0.00155	0.6036722	1576.4	26.34	648.3	9.06	41	
HI11_65	3.42408	0.06062	0.23955	0.00358	0.5698606	1690.9	28.06	1384.4	18.64	82	
HI11_73	2.95783	0.04805	0.20325	0.00296	0.6234615	1724	24.47	1192.7	15.85	69	
HI11_74	3.69203	0.05984	0.25864	0.00376	0.628962	1688.5	24.45	1482.9	19.25	88	
HI11_76	3.14619	0.05364	0.22686	0.00334	0.5911442	1635	26.75	1318	17.54	81	
HI11_78	3.34012	0.06309	0.23473	0.00357	0.5231798	1682.6	31.03	1359.3	18.64	81	
HI11_79	1.82865	0.03083	0.1209	0.00177	0.5951306	1794.5	25.82	735.7	10.16	41	
HI11_82	3.41383	0.06392	0.23997	0.00362	0.525786	1682.1	30.61	1386.6	18.82	82	
HI11_83	3.57191	0.05557	0.25422	0.00364	0.6494172	1659.3	23.11	1460.2	18.73	88	

Analysis #	$^{207}Pb/^{235}U$ Ratio	1σ	$^{206}Pb/^{238}U$ Ratio	1σ	Rho	$^{207}Pb/^{206}Pb$ Age	2σ	$^{206}Pb/^{238}U$ Age	2σ	Conc. %	Comments
HI11_85	3.65997	0.05967	0.26288	0.00381	0.6118164	1642.4	25.13	1504.6	19.45	92	
HI11_90	2.1324	0.03453	0.1483	0.00213	0.6087931	1702.2	24.83	891.4	11.96	52	
HI11_92	3.83331	0.0643	0.26641	0.00386	0.5858839	1703.4	26.28	1522.6	19.65	89	
HI11_94	3.92255	0.08763	0.2741	0.00444	0.4146468	1693.4	39.09	1561.6	22.44	92	
11B_002	2.78365	0.04858	0.19818	0.00303	0.6293351	1659.1	26.11	1165.5	16.28	70	
11B_003	5.32637	0.09789	0.31695	0.00494	0.5941403	1984.5	27.39	1774.8	24.19	89	
11B_007	4.15602	0.07738	0.28455	0.00442	0.5870171	1731	28.61	1614.2	22.2	93	
11B_008	4.32938	0.08805	0.27178	0.00438	0.5282915	1888.7	32.18	1549.8	22.18	82	
11B_012	2.5035	0.05022	0.17898	0.00283	0.5434518	1651.4	32.18	1061.4	15.48	64	
11B_013	3.91529	0.0704	0.26831	0.00415	0.6107096	1729	27.19	1532.2	21.07	89	
11B_015	3.20593	0.05639	0.21837	0.00334	0.6261329	1740.1	26.16	1273.3	17.68	73	
11B_016	4.49664	0.08299	0.28443	0.00443	0.5905891	1874.7	27.92	1613.6	22.23	86	
11B_017	5.53537	0.1093	0.30601	0.00492	0.5413768	2114.1	30.26	1721.1	24.28	81	
11B_020	3.76959	0.07042	0.24083	0.00374	0.5790476	1856.7	28.51	1391	19.44	75	
11B_021	6.57398	0.12918	0.31493	0.00504	0.5450631	2361.9	29.29	1764.9	24.73	75	
11B_022	3.843	0.07465	0.2622	0.00411	0.552332	1737.1	30.61	1501.1	21.01	86	
11B_023	4.21386	0.0806	0.26515	0.00414	0.5658047	1884.1	29.46	1516.1	21.07	80	
11B_024	4.54404	0.0881	0.2961	0.00463	0.5527308	1820.9	30.27	1671.9	23.03	92	
11B_026	3.44588	0.05998	0.23507	0.00358	0.6234279	1737.3	25.97	1361	18.68	78	
11B_027	1.9849	0.03377	0.13561	0.00205	0.639288	1734.5	24.97	819.8	11.61	47	
11B_029	5.79904	0.1087	0.29764	0.00468	0.5699604	2243.3	27.79	1679.6	23.24	75	
11B_030	4.32952	0.07783	0.28164	0.00431	0.6002972	1823.9	27.11	1599.6	21.67	88	
11B_031	4.08752	0.07815	0.27355	0.00427	0.5585141	1772.2	30.11	1558.8	21.59	88	
11B_032	3.95678	0.07549	0.27573	0.00428	0.5602627	1698.2	30.21	1569.8	21.64	92	
11B_033	4.71863	0.08771	0.29648	0.00456	0.5736791	1886.7	28.38	1673.8	22.69	89	
11B_034	3.60266	0.07379	0.23299	0.00371	0.5095816	1834.5	33.08	1350.2	19.41	74	
11B_036	2.90707	0.05667	0.20232	0.00314	0.5440181	1700.5	31.22	1187.8	16.82	70	
11B_038	3.44951	0.05773	0.24276	0.00365	0.6547483	1680.3	24.42	1401	18.94	83	
11B_039	4.17914	0.07592	0.25989	0.00402	0.5892738	1905.5	27.42	1489.3	20.59	78	
11B_042	3.98371	0.06914	0.27972	0.00424	0.6243785	1684.4	26.01	1590	21.34	94	
11B_043	4.43617	0.08144	0.28454	0.0044	0.5833851	1849.7	28.01	1614.2	22.06	87	
11B_044	3.91981	0.06965	0.26864	0.00409	0.6053499	1729.1	26.91	1533.9	20.78	89	
11B_045	4.63339	0.0885	0.29993	0.00469	0.5588734	1833.1	29.82	1691	23.24	92	
11B_047	3.83216	0.06866	0.27073	0.00411	0.600258	1673.2	27.44	1544.5	20.86	92	
11B_049	5.30172	0.08879	0.30336	0.00454	0.6475841	2053.6	23.54	1707.9	22.45	83	
11B_050	3.09595	0.05841	0.19511	0.00303	0.5588654	1881.4	29.36	1149	16.36	61	
11B_051	5.24326	0.09296	0.30881	0.0047	0.6025692	2002.4	26.14	1734.9	23.14	87	
11B_052	4.00102	0.07282	0.27538	0.0042	0.5847883	1721.1	28.16	1568.1	21.24	91	
11B_053	3.93736	0.07487	0.27744	0.00429	0.552212	1677.8	30.3	1578.5	21.64	94	
11B_054	6.0885	0.10993	0.31276	0.00477	0.5894287	2242	26.26	1754.3	23.44	78	
11B_055	4.57573	0.08432	0.29678	0.00453	0.5725594	1829.5	28.36	1675.3	22.51	92	

Analysis #	$^{207}Pb/^{235}U$ Ratio	1σ	$^{206}Pb/^{238}U$ Ratio	1σ	Rho	$^{207}Pb/^{206}Pb$ Age	2σ	$^{206}Pb/^{238}U$ Age	2σ	Conc. %	Comments
11B_057	4.46599	0.0897	0.28301	0.00445	0.5173848	1871.5	32.15	1606.5	22.36	86	
11B_058	4.62059	0.08839	0.29171	0.00448	0.5489874	1878.3	29.87	1650	22.38	88	
11B_060	3.05693	0.05742	0.21486	0.00325	0.5572682	1682.6	29.73	1254.6	17.26	75	
11B_062	3.9593	0.0678	0.27148	0.00405	0.6161082	1728.3	25.77	1548.3	20.53	90	
11B_063	5.21649	0.09169	0.3119	0.00471	0.5969478	1975.9	26.15	1750	23.12	89	
11B_064	4.2997	0.08027	0.28184	0.00433	0.5578834	1810.5	29.28	1600.6	21.77	88	
11B_065	3.93913	0.06999	0.26988	0.00406	0.5921237	1729.8	27.35	1540.2	20.63	89	
11B_066	4.80317	0.09505	0.2956	0.00465	0.5167055	1924.4	31.52	1669.4	23.15	87	
11B_067	3.78526	0.0659	0.25322	0.00378	0.6034173	1773.4	26.33	1455.1	19.43	82	
11B_068	3.64505	0.06834	0.24638	0.00377	0.5520633	1754.6	29.58	1419.8	19.48	81	
11B_069	2.79439	0.05091	0.17819	0.00269	0.5727143	1860.5	28	1057.1	14.73	57	
11B_070	1.0596	0.01947	0.06144	0.00093	0.5640331	2030.4	27.87	384.4	5.65	19	
11B_071	3.44196	0.06817	0.23687	0.00368	0.5183155	1721.7	32.21	1370.4	19.16	80	
11B_072	3.49853	0.06508	0.24533	0.00371	0.5584223	1687.1	29.43	1414.4	19.22	84	
11B_073	4.76995	0.08235	0.2778	0.00421	0.613848	2022.5	25.26	1580.3	21.24	78	
11B_077	4.33601	0.07917	0.28908	0.00444	0.5746497	1779.5	28.36	1636.9	22.2	92	
11B_078	3.55788	0.06167	0.23922	0.0036	0.6143787	1764.1	26.02	1382.6	18.74	78	
11B_079	3.93033	0.06837	0.27413	0.00413	0.6135537	1696.8	26.39	1561.7	20.88	92	
11B_080	3.82538	0.07314	0.26352	0.0041	0.5464974	1719.7	30.54	1507.8	20.9	88	
11B_081	2.93727	0.05453	0.20614	0.00316	0.5652182	1685.4	29.31	1208.2	16.9	72	
11B_082	4.19315	0.07459	0.27005	0.00409	0.600124	1842.4	26.83	1541.1	20.74	84	
11B_083	4.6572	0.08374	0.2735	0.00415	0.5899754	2007.8	26.76	1558.5	21.02	78	
11B_084	4.09484	0.0787	0.27422	0.00425	0.5442262	1771.4	30.52	1562.2	21.51	88	
11B_085	4.21755	0.08026	0.28231	0.00439	0.5437231	1771.9	30.41	1603	22.07	90	
11B_089	4.23983	0.07739	0.28215	0.00428	0.5674418	1782.5	28.48	1602.2	21.54	90	
11B_090	3.74423	0.06745	0.23665	0.00357	0.5780285	1876	27.59	1369.3	18.61	73	
11B_091	2.75084	0.04998	0.17377	0.00262	0.5688051	1876.9	27.98	1032.9	14.39	55	
11B_092	3.42746	0.06178	0.24093	0.00361	0.5775009	1682.1	28.21	1391.5	18.73	83	
11B_093	3.68449	0.06542	0.26082	0.00387	0.587411	1669.1	27.57	1494	19.8	90	
11B_094	3.64115	0.06508	0.24701	0.00367	0.5794528	1747.4	27.53	1423	18.95	81	
11B_095	4.36092	0.08133	0.28394	0.00427	0.5525326	1822.3	29.21	1611.2	21.44	88	
11B_096	5.18053	0.10397	0.30987	0.00481	0.5048792	1974.8	31.98	1740.1	23.66	88	
11B_097	3.19308	0.05583	0.2215	0.00325	0.5872061	1706.7	27.04	1289.8	17.16	76	
11B_098	4.46699	0.07828	0.27699	0.00407	0.5859417	1910.6	26.49	1576.2	20.55	82	
11B_099	4.42578	0.07795	0.29579	0.00434	0.5802969	1774.9	27.16	1670.4	21.59	94	
11B_100	4.0247	0.07313	0.27398	0.00405	0.5585808	1741.3	28.46	1561	20.51	90	
11B_101	3.21881	0.05773	0.2213	0.00325	0.5669017	1723.1	28.09	1288.8	17.15	75	
11B_102	4.63023	0.08408	0.29322	0.00432	0.5603841	1872.7	28.11	1657.6	21.53	89	
11B_103	3.3308	0.06099	0.21825	0.00321	0.5494656	1811	28.69	1272.6	17	70	
11B_104	4.45615	0.08481	0.29007	0.00433	0.5287753	1822.9	30.33	1641.9	21.61	90	
11B_105	4.39425	0.08259	0.25015	0.00371	0.5363988	2062.8	28.98	1439.2	19.11	70	

Analysis #	$^{207}Pb/^{235}U$ Ratio	1σ	$^{206}Pb/^{238}U$ Ratio	1σ	Rho	$^{207}Pb/^{206}Pb$ Age	2σ	$^{206}Pb/^{238}U$ Age	2σ	Conc. %	Comments
11B_106	3.3294	0.06456	0.19384	0.0029	0.5109828	2023	30.49	1142.1	15.65	56	
11B_107	4.05409	0.08029	0.27495	0.00412	0.5018879	1748.2	32.33	1565.9	20.84	90	
11B_108	4.87585	0.09553	0.29835	0.00444	0.5050697	1934.5	31.2	1683.1	22.07	87	
SAMPLE: HI16 - Calcsilicate Gneiss, Southern Houghton Inlier											
Detrital Zircon											
HI16_02	4.38883	0.10413	0.30677	0.00459	0.6306272	1692.7	42.79	1724.8	22.63	102	Hf Analysis #15
HI16_08	4.57144	0.10315	0.30678	0.00447	0.6457498	1768.7	38.31	1724.9	22.07	98	
HI16_23	4.29804	0.14501	0.30046	0.00578	0.5701822	1692.7	62.82	1693.6	28.63	100	Hf Analysis #17
HI16_45	4.76276	0.10582	0.31569	0.00499	0.7114275	1789.8	38.68	1768.7	24.45	99	Hf Analysis #13
HI16_48	4.61533	0.08165	0.31082	0.00444	0.8074592	1760.6	28.86	1744.7	21.85	99	
HI16_52	9.61038	0.25285	0.44927	0.00726	0.6141957	2403.6	43.66	2392	32.28	100	
HI16_56	8.05167	0.34158	0.41659	0.01103	0.6241087	2229.5	75.76	2245	50.21	101	
HI16_58	6.24888	0.12057	0.36599	0.00519	0.7349555	2012.2	31.8	2010.5	24.48	100	
HI16_60	4.54796	0.07293	0.3031	0.00418	0.8600046	1779.6	24.99	1706.7	20.69	96	Hf Analysis #10
HI16_63	4.38578	0.09718	0.29801	0.00435	0.6587617	1744.4	38.73	1681.4	21.62	96	Hf Analysis #16
HI16_64	3.95105	0.06331	0.28584	0.00376	0.820928	1628.9	26.83	1620.7	18.84	99	
HI16_76	4.3947	0.08289	0.30255	0.00424	0.7430119	1720.1	32	1704	20.97	99	
HI16_84	4.40492	0.09704	0.30539	0.00456	0.6777933	1707.6	38.88	1718	22.54	101	
HI16_87	4.5296	0.08281	0.31	0.00433	0.7640174	1731.5	31.87	1740.7	21.32	101	
HI16C_04	12.12404	0.29548	0.49904	0.0078	0.6413255	2617.5	39.3	2609.7	33.52	100	Hf Analysis #18
HI16C_07	4.40494	0.06579	0.30554	0.00392	0.8590098	1706.1	24.52	1718.7	19.33	101	
HI16C_12	4.59692	0.10762	0.3113	0.00491	0.6737152	1751.1	39.69	1747.1	24.12	100	Hf Analysis #1
HI16C_13	4.76584	0.08206	0.31833	0.00431	0.7863351	1775.9	29.05	1781.6	21.05	100	
HI16C_14	7.78393	0.158	0.40711	0.00594	0.718814	2210.4	33.1	2201.7	27.22	100	
HI16C_16	5.2242	0.09891	0.33427	0.00468	0.7394827	1854.5	31.86	1859	22.59	100	
HI16C_20	18.74722	0.29756	0.58929	0.00811	0.8670699	3057.2	21.44	2986.6	32.88	98	Hf Analysis #12
HI16C_28	4.33389	0.12234	0.30348	0.00513	0.5988206	1691	51.37	1708.5	25.35	101	
HI16C_31	4.68177	0.09241	0.31407	0.00455	0.7339662	1767.4	34.03	1760.7	22.3	100	
HI16C_33	4.44532	0.07469	0.29969	0.0041	0.8142395	1758.3	27.82	1689.8	20.33	96	
HI16C_34	5.3348	0.09288	0.33525	0.00461	0.7898199	1886.5	29.14	1863.8	22.25	99	
HI16C_40	4.41712	0.09026	0.30394	0.00442	0.7116694	1721.4	35.33	1710.8	21.86	99	Hf Analysis #14
HI16C_41	4.9268	0.10468	0.32432	0.00503	0.729954	1802.1	36.61	1810.8	24.5	100	Hf Analysis #9
HI16C_42	4.51404	0.07665	0.30746	0.00423	0.8102238	1739.8	27.9	1728.2	20.87	99	
HI16D_01	4.9474	0.08801	0.32283	0.00452	0.7870631	1818.2	29.4	1803.5	22.03	99	
HI16D_06	4.4096	0.10647	0.3027	0.00468	0.6403322	1726.3	43.24	1704.7	23.14	99	
HI16D_07	9.21076	0.19235	0.44233	0.00647	0.7004242	2357.7	33.98	2361.1	28.93	100	
HI16D_08	4.5625	0.08121	0.30815	0.00423	0.7712081	1756.2	30.79	1731.6	20.83	99	
HI16D_09	5.75364	0.12461	0.34916	0.005	0.6612038	1949.4	37	1930.6	23.9	99	
HI16D_12	6.28097	0.11673	0.36702	0.00541	0.7931435	2016	30.1	2015.4	25.53	100	
HI16D_21	4.42188	0.07359	0.30442	0.00405	0.7994108	1719.9	28.32	1713.2	20.03	100	

Analysis #	$^{207}Pb/^{235}U$ Ratio	1σ	$^{206}Pb/^{238}U$ Ratio	1σ	Rho	$^{207}Pb/^{206}Pb$ Age	2σ	$^{206}Pb/^{238}U$ Age	2σ	Conc. %	Comments
HI16D_22	4.02039	0.11364	0.2852	0.00514	0.6376033	1665.4	50.79	1617.5	25.76	97	
HI16D_23	4.41626	0.07019	0.30503	0.00406	0.8374577	1714.6	26.45	1716.2	20.05	100	
HI16D_26	4.45211	0.08265	0.30857	0.00431	0.7523962	1707.7	31.47	1733.7	21.22	102	
HI16D_28	4.61759	0.09149	0.31014	0.00457	0.7437041	1765.8	33.54	1741.4	22.49	99	
HI16D_30	14.0614	0.23161	0.52746	0.00734	0.8448465	2770.4	24.38	2730.7	30.99	99	
HI16D_31	4.48569	0.08395	0.30495	0.00433	0.758696	1743.1	31.9	1715.8	21.37	98	
HI16D_33	4.50837	0.09278	0.30398	0.00458	0.7321257	1759.1	34.37	1711	22.67	97	
HI16D_35	4.62596	0.07513	0.31381	0.00435	0.8535146	1747.3	25.47	1759.4	21.33	101	
HI16D_37	4.57544	0.06928	0.3108	0.004	0.8499707	1744.5	24.8	1744.6	19.69	100	
Metamorphic Zircon											
HI16_03	3.97181	0.11994	0.28551	0.00517	0.5996442	1641.2	55.12	1619.1	25.94	99	
HI16_05	3.91367	0.08262	0.28058	0.00424	0.7158271	1646.2	35.63	1594.3	21.33	97	
HI16_06	3.98046	0.08578	0.28469	0.00433	0.7057695	1650.6	36.43	1614.9	21.71	98	
HI16_07	3.9236	0.08868	0.28297	0.00438	0.6848457	1635.1	38.68	1606.3	22.01	98	Hf Analysis #2
HI16_09	3.90335	0.08929	0.28416	0.00439	0.6753614	1617.5	38.99	1612.3	22.06	100	Hf Analysis #3
HI16_10	3.98525	0.09657	0.28415	0.00451	0.6550014	1656.1	41.6	1612.2	22.63	97	
HI16_13	3.95224	0.11218	0.28535	0.00511	0.6309151	1633	51.05	1618.2	25.63	99	
HI16_14	4.10755	0.08441	0.28919	0.00446	0.7504825	1679.6	33.76	1637.5	22.29	97	
HI16_15	4.02922	0.09989	0.28894	0.00481	0.6714851	1645.5	43.24	1636.3	24.03	99	Hf Analysis #5
HI16_16	3.96958	0.0966	0.28773	0.00474	0.6769563	1625.6	42.34	1630.2	23.75	100	
HI16_17	4.0636	0.09486	0.2844	0.00459	0.6913706	1690.5	39.79	1613.5	23.06	95	
HI16_21	3.90289	0.11388	0.28432	0.00508	0.6123436	1616.1	52.39	1613.1	25.49	100	Hf Analysis #6
HI16_22	4.0731	0.10341	0.29072	0.00479	0.6489678	1654	43.97	1645.1	23.92	99	
HI16_24	3.81103	0.07868	0.27872	0.00428	0.7437957	1608.8	34.46	1584.9	21.6	99	
HI16_25	3.91095	0.08478	0.28312	0.00442	0.7201792	1627.8	36.74	1607.1	22.23	99	
HI16_28	3.90814	0.08338	0.28516	0.00436	0.7166484	1613.1	36.05	1617.3	21.86	100	
HI16_31	3.83615	0.09554	0.27544	0.00446	0.6501569	1643	43.83	1568.4	22.52	95	
HI16_32	3.7814	0.0968	0.27649	0.00451	0.637198	1609.2	45.52	1573.7	22.76	98	
HI16_33	3.9923	0.10919	0.28434	0.0048	0.6172251	1658	48.97	1613.2	24.07	97	
HI16_34	4.0304	0.09246	0.28649	0.00452	0.6877383	1661.7	39.77	1624	22.63	98	Hf Analysis #7
HI16_35	3.7151	0.08668	0.27258	0.0043	0.6761236	1602.9	40.95	1553.9	21.78	97	Hf Analysis #8
HI16_36	3.71981	0.08338	0.27117	0.00417	0.6860461	1614.9	38.91	1546.7	21.16	96	
HI16_37	3.9454	0.0924	0.29171	0.00456	0.6674713	1588.5	41.27	1650.1	22.73	104	
HI16_38	3.87358	0.08879	0.28579	0.00438	0.6686141	1592.6	40.21	1620.4	21.98	102	
HI16_40	3.55142	0.08677	0.26434	0.00413	0.6394692	1576.1	43.68	1512	21.03	96	
HI16_41	4.00418	0.11254	0.29151	0.00491	0.5992868	1617.5	51.23	1649.1	24.51	102	
HI16_46	3.95669	0.06069	0.28745	0.00371	0.8414465	1620.4	25.71	1628.8	18.58	101	
HI16_49	3.721	0.06442	0.27577	0.00371	0.7770802	1583.3	30.3	1570	18.75	99	
HI16_50	3.96801	0.07	0.28679	0.00389	0.7688831	1630	30.85	1625.5	19.51	100	
HI16_51	3.70939	0.06733	0.27638	0.00379	0.7554861	1573.2	32.18	1573.1	19.12	100	
HI16_53	3.97003	0.06703	0.28756	0.00384	0.7909105	1626	29.19	1629.3	19.22	100	

Analysis #	$^{207}Pb/^{235}U$ Ratio	1σ	$^{206}Pb/^{238}U$ Ratio	1σ	Rho	$^{207}Pb/^{206}Pb$ Age	2σ	$^{206}Pb/^{238}U$ Age	2σ	Conc. %	Comments
HI16_54	3.74017	0.05841	0.27618	0.00358	0.8300322	1590.1	26.45	1572.1	18.1	99	
HI16_57	3.96296	0.0701	0.28752	0.00409	0.8041868	1623.2	29.36	1629.1	20.49	100	
HI16_59	4.0859	0.07252	0.28989	0.00414	0.8046315	1664.7	29.36	1641	20.67	99	
HI16_61	4.00529	0.08703	0.28784	0.00446	0.7130971	1640.9	38.32	1630.7	22.31	99	
HI16_62	3.9425	0.07592	0.29015	0.00426	0.7624345	1596.6	33.03	1642.3	21.28	103	
HI16_65	3.93376	0.06915	0.28589	0.00406	0.8078724	1620.1	29.12	1620.9	20.35	100	
HI16_66	4.06816	0.08474	0.2901	0.00441	0.7297942	1655.3	36.31	1642	22.05	99	
HI16_67	4.15828	0.07731	0.29351	0.0042	0.7696698	1674.6	31.1	1659.1	20.91	99	
HI16_68	3.78521	0.06858	0.28052	0.00396	0.779155	1584	30.35	1594	19.95	101	Hf Analysis #11
HI16_69	3.92686	0.07855	0.2859	0.0042	0.7344029	1617.1	34.5	1621	21.07	100	
HI16_70	4.08786	0.08836	0.28926	0.00441	0.705327	1669.9	37.82	1637.9	22.07	98	
HI16_72	4.01227	0.08273	0.28928	0.00431	0.7225801	1635.3	35.79	1637.9	21.57	100	
HI16_73	3.94332	0.07749	0.28588	0.00417	0.7422815	1625	33.68	1620.9	20.92	100	
HI16_74	4.03718	0.0865	0.29259	0.00444	0.7082482	1625.6	37.59	1654.5	22.13	102	
HI16_77	3.75496	0.07462	0.27845	0.00408	0.7373319	1582.8	34.35	1583.6	20.56	100	
HI16_78	3.97145	0.06966	0.29124	0.00412	0.8065138	1603.6	28.98	1647.7	20.59	103	
HI16_79	3.97437	0.06796	0.28797	0.00404	0.8204442	1625.9	27.86	1631.4	20.24	100	
HI16_81	3.94299	0.06676	0.28245	0.00395	0.8259711	1647.2	27.39	1603.7	19.87	97	
HI16_82	3.93105	0.06515	0.28473	0.00396	0.8391819	1626.6	26.6	1615.2	19.85	99	
HI16_83	4.10904	0.08715	0.28936	0.00443	0.7218355	1678.8	36.95	1638.3	22.17	98	
HI16_85	3.93959	0.06753	0.28648	0.00403	0.8206633	1619.3	27.98	1623.9	20.17	100	
HI16_86	3.80727	0.09659	0.27789	0.00463	0.6567341	1612.4	46.14	1580.7	23.35	98	
HI16_88	3.96971	0.06726	0.29089	0.00407	0.825786	1605	27.56	1646	20.33	103	
HI16C_01	3.88118	0.07538	0.28154	0.00386	0.705919	1625.5	33.87	1599.1	19.4	98	
HI16C_03	4.034	0.08689	0.28808	0.00414	0.6671958	1654.7	37.85	1631.9	20.73	99	
HI16C_05	3.98724	0.08421	0.28291	0.00401	0.6711271	1666.6	36.29	1606	20.14	96	
HI16C_06	3.98994	0.09699	0.28467	0.00434	0.6271731	1656.3	42.91	1614.8	21.78	97	
HI16C_09	3.91921	0.09867	0.28205	0.00433	0.6097828	1639.8	43.71	1601.7	21.78	98	
HI16C_10	4.07296	0.10608	0.28591	0.00446	0.5989384	1685.6	44.88	1621.1	22.38	96	
HI16C_11	3.98477	0.12182	0.28543	0.00493	0.5649786	1648	54.27	1618.6	24.72	98	
HI16C_15	3.90792	0.09762	0.28849	0.00455	0.6313752	1591.2	45.68	1634	22.79	103	
HI16C_19	4.0133	0.1056	0.28754	0.0046	0.6079912	1647	48.32	1629.2	23.05	99	
HI16C_21	3.95524	0.09594	0.28857	0.00432	0.6171713	1613.3	44.38	1634.4	21.64	101	
HI16C_22	3.95819	0.11356	0.28778	0.00476	0.5765243	1619.8	53.46	1630.4	23.85	101	
HI16C_23	3.93075	0.0934	0.28296	0.00436	0.6484701	1638.1	43.01	1606.2	21.92	98	
HI16C_24	3.89947	0.0823	0.28321	0.00409	0.6842589	1621.5	37.38	1607.5	20.54	99	
HI16C_25	3.78715	0.07848	0.27714	0.00395	0.6877829	1607.4	36.57	1576.9	19.96	98	
HI16C_27	3.9295	0.09523	0.28529	0.00438	0.6335065	1622.2	43.84	1617.9	21.99	100	
HI16C_29	3.80871	0.09508	0.2805	0.00434	0.6197915	1595.6	45.36	1593.9	21.85	100	
HI16C_30	3.93353	0.10933	0.28344	0.00469	0.595326	1636.2	50.94	1608.7	23.54	98	
HI16C_32	3.85966	0.10158	0.28252	0.00445	0.5984828	1607.1	47.85	1604	22.37	100	

Analysis #	$^{207}Pb/^{235}U$ Ratio	1σ	$^{206}Pb/^{238}U$ Ratio	1σ	Rho	$^{207}Pb/^{206}Pb$ Age	2σ	$^{206}Pb/^{238}U$ Age	2σ	Conc. %	Comments
HI16C_36	3.84326	0.09226	0.2773	0.00431	0.6474612	1634.4	43.59	1577.7	21.77	97	
HI16C_38	4.04734	0.0841	0.29326	0.0042	0.6892395	1626.4	36.71	1657.8	20.93	102	
HI16C_43	3.89168	0.09547	0.28433	0.00433	0.6207767	1610.9	44.64	1613.1	21.74	100	
HI16C_44	3.9535	0.11203	0.28771	0.00478	0.5863006	1618.2	52.43	1630.1	23.94	101	
Discordant Analyses - Not used in age calculations											
HI16_01	3.23297	0.08425	0.23267	0.00388	0.6399162	1639	46.87	1348.5	20.27	82	
HI16_04	3.91921	0.08098	0.27775	0.00417	0.7266123	1667.6	34.69	1580	21.02	95	
HI16_11	3.71983	0.08811	0.26113	0.00408	0.6596313	1684.7	40.03	1495.6	20.84	89	
HI16_12	4.91834	0.09603	0.33696	0.00512	0.7782215	1729.8	31.29	1872	24.7	108	
HI16_18	8.74282	0.17988	0.38498	0.00586	0.7398235	2504.9	30.51	2099.5	27.29	84	
HI16_19	3.32425	0.07856	0.23711	0.00381	0.6799349	1655.4	40.45	1371.7	19.87	83	
HI16_20	3.38473	0.08005	0.24517	0.00392	0.6760541	1626.8	40.51	1413.5	20.32	87	
HI16_26	2.61933	0.05393	0.1813	0.00276	0.7393857	1710.7	33.95	1074.1	15.05	63	
HI16_27	3.85217	0.08777	0.27312	0.00433	0.6958149	1666.4	39.07	1556.6	21.91	93	
HI16_29	3.87309	0.10826	0.27195	0.00476	0.6261919	1684.4	50.09	1550.7	24.14	92	
HI16_30	3.81548	0.09275	0.2738	0.0044	0.6610807	1644.1	42.54	1560.1	22.29	95	
HI16_39	3.57613	0.10484	0.25337	0.00445	0.5990887	1667.9	53.4	1455.8	22.86	87	
HI16_42	3.5757	0.09858	0.25262	0.00417	0.5987432	1673.2	49.88	1452	21.48	87	
HI16_43	3.59869	0.09555	0.26246	0.00419	0.6012632	1614.2	48.16	1502.4	21.4	93	
HI16_44	3.27913	0.08818	0.23822	0.0038	0.5931901	1621.5	48.92	1377.4	19.78	85	
HI16_47	3.67675	0.06213	0.26681	0.00356	0.7896064	1622.5	29.25	1524.6	18.11	94	
HI16_55	3.49031	0.06253	0.25494	0.00347	0.7597436	1610.3	31.55	1463.9	17.85	91	
HI16_71	4.77142	0.09579	0.32774	0.00485	0.7371227	1724.7	34.2	1827.4	23.57	106	
HI16_75	3.81731	0.07407	0.26436	0.00384	0.7486013	1709.7	32.82	1512.1	19.59	88	
HI16_80	3.53949	0.06055	0.24984	0.00351	0.821243	1674.5	27.73	1437.6	18.1	86	
HI16C_02	10.18818	0.19323	0.38334	0.00526	0.7234752	2767.4	28.89	2091.9	24.51	76	
HI16C_08	3.80176	0.10833	0.27037	0.00452	0.5866997	1662	51.08	1542.7	22.94	93	
HI16C_17	3.47834	0.07726	0.23013	0.00339	0.6631989	1793.3	39.08	1335.2	17.78	74	
HI16C_18	2.37606	0.07291	0.15827	0.00282	0.5806585	1780.9	56.71	947.2	15.67	53	
HI16C_26	4.03559	0.10717	0.27236	0.00447	0.6180136	1756.9	48.02	1552.8	22.64	88	
HI16C_35	3.63045	0.08373	0.25739	0.00393	0.6620339	1666.9	41.5	1476.5	20.16	89	
HI16C_37	3.18387	0.08408	0.23588	0.00384	0.6164569	1585.1	48.88	1365.2	20.01	86	
HI16C_39	3.33535	0.07103	0.23829	0.00344	0.6778791	1652.6	37.71	1377.8	17.88	83	
HI16D_02	9.78608	0.14185	0.4112	0.00536	0.8992721	2583.2	21.11	2220.4	24.47	86	
HI16D_03	3.5206	0.05184	0.23159	0.00299	0.8768051	1803.8	23.44	1342.8	15.67	74	
HI16D_04	4.07073	0.06585	0.23085	0.0031	0.8301343	2069.4	26.06	1338.9	16.23	65	
HI16D_05	3.86203	0.05866	0.25811	0.00336	0.8570537	1774.8	24.59	1480.2	17.21	83	
HI16D_10	8.67549	0.13472	0.28975	0.00377	0.8378762	2959.9	22.32	1640.3	18.87	55	
HI16D_11	6.33963	0.09225	0.31276	0.00403	0.8855057	2311.6	22.06	1754.3	19.78	76	
HI16D_13	2.28958	0.03703	0.15615	0.00207	0.8196538	1738	27.35	935.3	11.54	54	
HI16D_14	3.75887	0.05797	0.2222	0.00291	0.8491862	1996	24.82	1293.5	15.34	65	

Analysis #	$^{207}Pb/^{235}U$ Ratio	1σ	$^{206}Pb/^{238}U$ Ratio	1σ	Rho	$^{207}Pb/^{206}Pb$ Age	2σ	$^{206}Pb/^{238}U$ Age	2σ	Conc. %	Comments
HI16D_15	2.90574	0.04495	0.19799	0.00258	0.8423712	1739.7	25.72	1164.5	13.9	67	
HI16D_16	3.41204	0.05384	0.23851	0.00313	0.8316619	1692.7	26.57	1379	16.29	81	
HI16D_17	3.9237	0.09015	0.27005	0.00421	0.6785283	1721.4	41.93	1541	21.35	90	
HI16D_18	2.95081	0.04751	0.20102	0.00265	0.8187717	1740.2	27.15	1180.8	14.23	68	
HI16D_19	3.3986	0.05346	0.22252	0.00291	0.8313713	1812.7	26.08	1295.2	15.34	71	
HI16D_20	3.6337	0.07393	0.26574	0.00385	0.7120855	1609.2	36.91	1519.1	19.62	94	
HI16D_24	3.42104	0.05686	0.21789	0.00296	0.8173456	1861.6	27.07	1270.7	15.66	68	
HI16D_25	4.34839	0.10249	0.28985	0.00463	0.6777268	1779	42.27	1640.8	23.15	92	
HI16D_27	2.93924	0.04837	0.12851	0.00173	0.8180279	2516.2	24.66	779.3	9.87	31	
HI16D_29	3.25346	0.06089	0.21626	0.00304	0.7510985	1784.2	31.7	1262.1	16.11	71	
HI16D_32	2.15217	0.04299	0.13804	0.00198	0.7180743	1849.2	33.98	833.6	11.2	45	
HI16D_34	3.28836	0.07668	0.22365	0.00354	0.678784	1742.5	41.79	1301.2	18.66	75	
HI16D_36	4.00097	0.06643	0.26423	0.0036	0.8205809	1796.3	26.85	1511.5	18.37	84	
HI16D_38	2.58192	0.0441	0.15947	0.00219	0.8040246	1917.3	27.52	953.9	12.17	50	
HI16D_39	5.36486	0.09343	0.31687	0.00439	0.7955279	1997.1	27.91	1774.4	21.49	89	
HI16D_40	5.57816	0.09434	0.28193	0.00385	0.8074479	2269.7	25.96	1601.1	19.36	71	
HI16D_41	3.75829	0.06686	0.2379	0.0033	0.7797285	1873.1	29.08	1375.8	17.16	73	
HI16D_42	2.91911	0.05303	0.17612	0.00246	0.7688742	1959.3	29.6	1045.7	13.46	53	
HI16D_43	2.12764	0.038	0.10956	0.00151	0.771684	2237.5	28.01	670.2	8.8	30	
HI16D_44	3.91118	0.07195	0.2328	0.00324	0.7565524	1983.4	29.9	1349.2	16.97	68	
HI16D_45	5.91892	0.1103	0.30968	0.00434	0.7520445	2210	29.6	1739.1	21.36	79	
HI16D_46	6.68646	0.13014	0.3612	0.00516	0.7339854	2154.3	31.48	1987.9	24.43	92	
SAMPLE: HI03 - South Para Othogneiss, Northern Houghton Inlier											
Igneous Zircon											
HI03_01	4.33302	0.06258	0.30016	0.00389	0.8973294	1709.7	22.99	1692.1	19.27	99	Hf Analysis #1
HI03_05	4.2466	0.06089	0.29875	0.00381	0.8894314	1681.5	23.12	1685.1	18.92	100	Hf Analysis #5
HI03_14	4.28182	0.06409	0.29737	0.00373	0.8380112	1704	25.35	1678.3	18.55	98	Hf Analysis #8
HI03_18	4.08556	0.05979	0.28455	0.00348	0.8356871	1698.8	24.89	1614.2	17.46	95	
HI03_19	4.19724	0.06254	0.28938	0.00354	0.8209953	1717.4	25.5	1638.4	17.71	95	Hf Analysis #9
HI03_20	4.11598	0.06305	0.28887	0.00355	0.802258	1684.7	26.6	1635.9	17.77	97	Hf Analysis #10
HI03_34	4.0884	0.0593	0.29119	0.00353	0.8357895	1642.4	25.67	1627.5	17.7	99	Hf Analysis #12
HI03_39	4.22971	0.06085	0.29103	0.00349	0.8335616	1701.1	25.39	1620.7	17.5	95	Hf Analysis #13
HI03_40	3.94254	0.05531	0.28028	0.00332	0.8443421	1639.7	24.79	1566.3	16.8	96	Hf Analysis #14
HI03_45	4.62532	0.0699	0.31286	0.00376	0.7952477	1726.4	27.12	1719.6	18.57	100	Hf Analysis #16
HI03_64	4.37203	0.07516	0.30261	0.00387	0.7439163	1710.9	30.5	1704.2	19.16	100	Hf Analysis #21
HI03_72	4.37167	0.06486	0.29536	0.00349	0.7964237	1754.9	25.6	1668.3	17.36	95	Hf Analysis #25
HI03A_01	4.20096	0.06112	0.29349	0.00376	0.561223	1693.5	23.58	1659	18.76	98	
HI03A_02	4.23083	0.06286	0.30034	0.00388	0.55499	1663.9	24.34	1693	19.22	102	
HI03A_03	4.50396	0.06725	0.31321	0.00405	0.5504126	1702	24.35	1756.5	19.89	103	
HI03A_04	4.16721	0.06198	0.28949	0.00374	0.5553661	1704	24.15	1639	18.69	96	

Analysis #	$^{207}Pb/^{235}U$ Ratio	1σ	$^{206}Pb/^{238}U$ Ratio	1σ	Rho	$^{207}Pb/^{206}Pb$ Age	2σ	$^{206}Pb/^{238}U$ Age	2σ	Conc. %	Comments
HI03A_07	4.16986	0.06674	0.28996	0.00383	0.51639	1702.3	26.6	1641.3	19.16	96	
HI03A_10	4.17958	0.07004	0.28741	0.00386	0.4941719	1722.9	28.05	1628.6	19.31	95	
HI03A_11	4.40125	0.06672	0.30447	0.00401	0.5571041	1711.8	24.56	1713.4	19.84	100	
HI03A_14	4.34552	0.06384	0.30564	0.00397	0.578333	1681.2	23.53	1719.2	19.62	102	
HI03A_16	4.38937	0.06793	0.30611	0.00404	0.5434795	1696.9	25.34	1721.6	19.92	101	
HI03A_17	4.37893	0.06628	0.3028	0.00396	0.5543443	1712.5	24.49	1705.2	19.57	100	
HI03A_20	4.05084	0.06225	0.28311	0.0037	0.5471381	1692.9	25.08	1607	18.57	95	
HI03A_24	4.40299	0.06462	0.30212	0.00389	0.5578228	1727	23.82	1701.8	19.26	99	
HI03A_26	3.93887	0.05566	0.28527	0.00361	0.5776287	1627.3	22.89	1617.8	18.13	99	
HI03A_27	4.39501	0.07256	0.30442	0.00406	0.4796282	1709.8	28.13	1713.2	20.08	100	
Metamorphic Zircon											
HI03_02	4.18043	0.05853	0.29418	0.00376	0.9128872	1680.8	22.08	1662.4	18.74	99	Hf Analysis #2
HI03_03	3.86645	0.05374	0.28102	0.00357	0.913999	1620.9	22.08	1596.5	17.99	98	Hf Analysis #3
HI03_04	3.74361	0.05246	0.27984	0.00356	0.9078258	1568.6	22.59	1590.6	17.92	101	Hf Analysis #4
HI03_06	3.70416	0.0528	0.27738	0.00352	0.8902733	1565.3	23.35	1578.2	17.77	101	
HI03_08	3.63789	0.0528	0.27217	0.00345	0.8733624	1567.1	24.12	1551.8	17.48	99	Hf Analysis #6
HI03_09	3.71221	0.05444	0.27607	0.0035	0.8644965	1578.4	24.52	1571.5	17.67	100	
HI03_12	3.75959	0.05082	0.27671	0.00339	0.9063181	1596.4	22.19	1574.8	17.11	99	Hf Analysis #7
HI03_13	3.65006	0.04986	0.27203	0.00333	0.8961386	1573	22.67	1551.1	16.86	99	
HI03_15	4.03388	0.056	0.28588	0.00348	0.8768603	1666.7	23.06	1620.9	17.47	97	Hf Analysis #30
HI03_31	4.24435	0.06628	0.29629	0.00365	0.7888684	1695.1	26.85	1672.9	18.17	99	Hf Analysis #11
HI03_35	3.66229	0.04794	0.26861	0.00315	0.895866	1586.7	22.6	1513.9	16.04	95	
HI03_36	3.96794	0.05271	0.28613	0.00336	0.8839912	1617.3	23	1600.1	16.91	99	Hf Analysis #29
HI03_42	4.09764	0.05819	0.29516	0.0035	0.8350183	1613.2	25.32	1637.3	17.48	101	Hf Analysis #15
HI03_43	3.98291	0.05715	0.28682	0.0034	0.8261402	1612.6	25.7	1595.1	17.11	99	
HI03_46	3.74922	0.05338	0.27871	0.00355	0.8946191	1578.2	23.09	1584.9	17.92	100	Hf Analysis #17
HI03_50	3.78229	0.05604	0.28086	0.00357	0.8578967	1580.5	24.71	1595.7	17.97	101	
HI03_51	3.94565	0.05931	0.28594	0.00364	0.8468707	1626	25.13	1621.2	18.23	100	Hf Analysis #18
HI03_53	3.58729	0.05512	0.26647	0.00338	0.8255163	1580	26.19	1522.9	17.22	96	Hf Analysis #28
HI03_54	3.89724	0.06111	0.28244	0.0036	0.8128701	1626.1	26.82	1603.7	18.07	99	Hf Analysis #27
HI03_56	3.86346	0.06135	0.28301	0.0036	0.8010554	1606.3	27.41	1606.5	18.1	100	
HI03_57	3.94615	0.06366	0.28569	0.00364	0.789793	1628.2	27.98	1619.9	18.25	99	Hf Analysis #19
HI03_60	3.76634	0.05438	0.27942	0.00341	0.8452345	1582.2	24.58	1588.4	17.2	100	Hf Analysis #26
HI03_61	3.82346	0.05594	0.27718	0.00338	0.8334679	1625.2	24.95	1577.1	17.08	97	
HI03_65	4.40145	0.07335	0.30328	0.00381	0.753836	1719.2	29.36	1707.6	18.82	99	Hf Analysis #22
HI03_69	3.85081	0.06564	0.28016	0.00345	0.7224312	1619.1	30.9	1592.1	17.38	98	Hf Analysis #23
HI03_70	4.17836	0.05882	0.29446	0.00344	0.8298756	1677.5	24.22	1663.8	17.13	99	
HI03_71	3.8688	0.05848	0.2815	0.00336	0.7896412	1618.2	26.7	1598.9	16.89	99	Hf Analysis #24
HI03_73	3.97479	0.05878	0.28685	0.00337	0.7944373	1633.3	25.95	1625.8	16.86	100	
HI03_80	4.00177	0.06865	0.28513	0.00342	0.6991893	1657.1	30.99	1617.1	17.15	98	

Analysis #	$^{207}Pb/^{235}U$ Ratio	1σ	$^{206}Pb/^{238}U$ Ratio	1σ	Rho	$^{207}Pb/^{206}Pb$ Age	2σ	$^{206}Pb/^{238}U$ Age	2σ	Conc. %	Comments
Discordant Analyses - Not used in age calculations											
HI03_07	3.16001	0.04559	0.22814	0.0029	0.8810802	1633.6	23.64	1324.8	15.2	81	
HI03_10	2.73362	0.04245	0.19402	0.00249	0.8264437	1665.2	26.34	1143.1	13.47	69	
HI03_11	3.75148	0.05801	0.2692	0.00344	0.8263864	1644.9	26.31	1536.7	17.5	93	
HI03_16	3.76285	0.05279	0.27089	0.0033	0.8683328	1637.5	23.56	1545.3	16.72	94	
HI03_17	3.87708	0.057	0.27064	0.00333	0.8369165	1694.6	24.99	1544	16.9	91	
HI03_21	3.44407	0.05179	0.25377	0.00308	0.807117	1594.4	26.37	1457.9	15.85	91	
HI03_22	3.73901	0.0569	0.2678	0.00325	0.7974751	1647.1	26.68	1529.6	16.52	93	
HI03_23	4.03585	0.05631	0.281	0.00338	0.8621044	1700	23.54	1596.4	17	94	
HI03_24	3.52119	0.0486	0.24967	0.00299	0.8676769	1666.4	23.26	1436.8	15.4	86	
HI03_25	4.01447	0.05515	0.27898	0.00333	0.8688681	1703.5	22.95	1586.2	16.77	93	
HI03_26	4.08413	0.05915	0.2782	0.00337	0.8364069	1740.2	24.53	1582.3	17.02	91	
HI03_27	3.70712	0.05241	0.2689	0.00323	0.8496385	1624.2	24	1535.2	16.39	95	
HI03_28	3.0835	0.04415	0.22464	0.0027	0.8394405	1616.1	24.38	1306.4	14.22	81	
HI03_29	3.66232	0.05384	0.25842	0.00313	0.8238904	1675.3	25	1481.8	16.04	88	
HI03_30	2.16691	0.03288	0.15042	0.00184	0.8061601	1705.6	25.93	903.3	10.3	53	
HI03_32	2.57893	0.04129	0.17788	0.00221	0.7759966	1717.3	27.61	1055.4	12.08	61	
HI03_33	3.80004	0.05962	0.27322	0.00336	0.783832	1640.5	27.06	1557.1	16.99	95	
HI03_37	3.79048	0.05071	0.27098	0.00319	0.879942	1632.4	23.2	1523.5	16.21	93	
HI03_38	4.65871	0.0631	0.29063	0.00342	0.8688043	1880.6	22.92	1619.9	17.17	86	
HI03_41	3.55811	0.05008	0.26263	0.00311	0.8413392	1568.6	25.16	1477.1	15.94	94	
HI03_44	3.44557	0.05209	0.23959	0.00289	0.7978769	1676.5	27.29	1357.1	15.08	81	
HI03_47	2.23917	0.03474	0.15584	0.00203	0.8396037	1700.7	25.83	933.6	11.33	55	
HI03_48	4.17352	0.07415	0.28387	0.00389	0.7712967	1742.8	30.64	1610.8	19.55	92	
HI03_49	3.92579	0.05907	0.27297	0.0035	0.8521444	1702.4	24.81	1555.8	17.74	91	
HI03_52	3.62761	0.05504	0.26269	0.00334	0.8380021	1627.5	25.52	1503.6	17.03	92	
HI03_58	3.79155	0.05424	0.26977	0.00332	0.8602834	1660	23.92	1539.6	16.85	93	
HI03_59	3.93148	0.05766	0.27254	0.00336	0.8406021	1708	24.66	1553.7	17.05	91	
HI03_62	2.00362	0.0304	0.13803	0.0017	0.8117405	1719.5	25.95	833.5	9.61	48	
HI03_63	3.55932	0.05544	0.25489	0.00315	0.7934171	1648	27.12	1463.6	16.16	89	
HI03_66	3.7593	0.06009	0.26988	0.0033	0.7649764	1643.5	28.25	1540.2	16.77	94	
HI03_67	3.90413	0.06351	0.27646	0.00339	0.7537886	1669.1	28.85	1573.5	17.1	94	
HI03_68	3.77676	0.06276	0.27089	0.00332	0.7375332	1645.4	29.79	1545.3	16.86	94	
HI03_74	4.12197	0.07269	0.2775	0.00349	0.7131692	1761.4	31.51	1578.8	17.61	90	
HI03_75	4.36315	0.07606	0.29399	0.00367	0.716106	1759.8	31.09	1661.4	18.27	94	
HI03_76	3.97767	0.07579	0.268	0.00347	0.6795345	1759.9	34.47	1530.6	17.66	87	
HI03_77	3.58904	0.05738	0.2545	0.00301	0.7397696	1665.9	28.45	1461.6	15.49	88	
HI03_78	3.92076	0.06718	0.26479	0.00322	0.7097159	1755.6	30.51	1514.3	16.4	86	
HI03_79	3.70092	0.0619	0.26316	0.00314	0.713393	1660.8	30.06	1506	16.02	91	
HI03_81	4.18212	0.08259	0.27936	0.00358	0.648915	1775.7	35.91	1588.1	18.06	89	
HI03_82	4.31312	0.07272	0.2846	0.00354	0.7377446	1798.7	29.96	1614.5	17.75	90	

Analysis #	$^{207}Pb/^{235}U$ Ratio	1σ	$^{206}Pb/^{238}U$ Ratio	1σ	Rho	$^{207}Pb/^{206}Pb$ Age	2σ	$^{206}Pb/^{238}U$ Age	2σ	Conc. %	Comments
HI03_83	4.23516	0.07443	0.28676	0.00362	0.7183098	1751.7	31.53	1625.3	18.12	93	
HI03_84	3.64183	0.05364	0.26039	0.00304	0.7926477	1651.4	25.93	1491.8	15.53	90	
HI03_85	4.14543	0.06192	0.28633	0.00335	0.7832792	1715.2	26.23	1623.2	16.77	95	
HI03_86	3.74881	0.05733	0.25233	0.00297	0.7696602	1762.6	26.74	1450.5	15.27	82	
HI03_87	3.61749	0.05596	0.25913	0.00305	0.7608723	1648	27.54	1485.4	15.6	90	
HI03_88	3.91118	0.06157	0.27202	0.00321	0.7496229	1702.6	27.93	1551	16.26	91	
HI03_89	3.4885	0.05601	0.25179	0.00298	0.7371416	1634	28.84	1447.7	15.35	89	
HI03_90	3.79994	0.06452	0.26525	0.00321	0.7127415	1695.9	30.55	1516.6	16.33	89	
HI03_91	3.92288	0.066	0.26797	0.00321	0.7119999	1735.7	29.99	1530.5	16.31	88	
HI03_92	3.73183	0.09203	0.252	0.00372	0.5985974	1756.9	45.82	1448.8	19.17	82	
HI03_93	3.77122	0.06621	0.26586	0.00321	0.6877179	1677.7	31.82	1519.7	16.37	91	
HI03A_05	3.60189	0.05455	0.25016	0.00325	0.5420134	1704.4	24.74	1439.3	16.75	84	
HI03A_06	3.19378	0.05128	0.22583	0.00299	0.5090103	1671.4	26.91	1312.6	15.71	79	
HI03A_08	3.54254	0.0553	0.25271	0.00331	0.5318526	1655.2	25.78	1452.4	17.02	88	
HI03A_09	3.85334	0.06059	0.27193	0.00357	0.5343381	1675.1	25.91	1550.6	18.07	93	
HI03A_12	3.61216	0.0521	0.25377	0.00329	0.5883011	1683.3	22.89	1457.9	16.91	87	
HI03A_13	3.85605	0.05771	0.26477	0.00347	0.5611093	1725.5	24.08	1514.2	17.67	88	
HI03A_15	3.82953	0.05758	0.26783	0.0035	0.5592944	1691.6	24.33	1529.8	17.8	90	
HI03A_18	3.42269	0.05178	0.23615	0.00308	0.555201	1716.6	24.5	1366.7	16.05	80	
HI03A_19	3.90659	0.06001	0.27067	0.00354	0.5421025	1708.9	25.03	1544.2	17.96	90	
HI03A_21	3.78517	0.06059	0.25972	0.00343	0.5165852	1726.7	26.46	1488.4	17.57	86	
HI03A_22	2.4698	0.04102	0.16519	0.00221	0.4962666	1773.4	27.77	985.6	12.21	56	
HI03A_23	3.43606	0.04993	0.23738	0.00305	0.5649732	1714.5	23.51	1373.1	15.89	80	
HI03A_25	3.96956	0.05823	0.27712	0.00356	0.5543891	1695.3	23.94	1576.8	17.97	93	
SAMPLE: KM12-17 - Psammite from Muscovite-Sillimanite Schist, Warren Inlier											
Detrital Zircon											
KM1701	11.55018	0.19826	0.48874	0.00744	0.886847	2571.5	24.07	2565.2	16.04	100	
KM1702	5.23738	0.09218	0.34374	0.00515	0.8512449	1807.9	27.2	1904.6	15.01	105	
KM1704	5.27094	0.08973	0.34506	0.00507	0.8631052	1812.5	25.92	1911	14.53	105	
KM1705	7.40809	0.11946	0.41138	0.00592	0.8924056	2106.3	23	2221.2	14.43	105	
KM1707	11.53827	0.19542	0.48081	0.00705	0.8657397	2597.1	23.79	2530.8	15.83	97	
KM1708	11.74433	0.19946	0.48725	0.00712	0.8604003	2604.4	23.93	2558.8	15.89	98	
KM1710	4.66297	0.0866	0.30858	0.00459	0.8009209	1792.8	29.96	1733.7	15.53	97	
KM1711	4.7783	0.08021	0.31595	0.0046	0.86733	1794.9	25.75	1769.9	14.1	99	
KM1715	4.36102	0.07289	0.2964	0.00425	0.8578885	1744.7	25.92	1673.4	13.8	96	
KM1716	8.63526	0.14006	0.42205	0.00598	0.8735717	2328.1	23.3	2269.8	14.76	97	
KM1717	9.65716	0.15929	0.43865	0.00624	0.862437	2452.8	23.67	2344.6	15.18	96	
KM1718	6.79041	0.11328	0.36926	0.00524	0.8506321	2143.4	24.96	2025.9	14.77	95	
KM1723	4.74449	0.08504	0.32001	0.00474	0.8263824	1757.8	28.15	1789.8	15.03	102	
KM1726	13.1079	0.23621	0.53283	0.008	0.8331749	2638.1	25.3	2753.4	17	104	

Analysis #	$^{207}Pb/^{235}U$ Ratio	1σ	$^{206}Pb/^{238}U$ Ratio	1σ	Rho	$^{207}Pb/^{206}Pb$ Age	2σ	$^{206}Pb/^{238}U$ Age	2σ	Conc. %	Comments
KM17b01	5.11985	0.07493	0.33048	0.00422	0.5516935	1838.5	23.53	1840.7	20.45	100	
KM17b03	4.52582	0.06927	0.30427	0.00393	0.5192872	1764.6	25.31	1712.5	19.41	97	
KM17b05	4.45627	0.06759	0.30492	0.0039	0.5192562	1732.4	25.19	1715.6	19.28	99	
KM17b06	4.16618	0.06256	0.28815	0.00366	0.5269771	1712.7	24.95	1632.3	18.34	95	
KM17b07	4.72807	0.07218	0.31551	0.00403	0.5148297	1778.3	25.38	1767.7	19.73	99	
KM17b13	6.46835	0.10354	0.36695	0.00488	0.5096716	2069.1	25.73	2015	23.02	97	
KM17b15	6.10802	0.0971	0.36317	0.00479	0.5157073	1985.9	25.59	1997.2	22.67	101	
KM17b16	4.90892	0.07592	0.32403	0.00421	0.5329489	1797.8	25.11	1809.4	20.52	101	
KM17b18	4.44573	0.06425	0.29804	0.00382	0.5679622	1769	23.09	1681.6	18.95	95	
KM17b19	8.52987	0.12875	0.42307	0.00552	0.5403812	2302.2	23.15	2274.4	25.02	99	
KM17b22	4.96408	0.08258	0.31612	0.00422	0.480406	1862.3	27.81	1770.8	20.68	95	
Discordant Analyses - Not used in age calculations											
KM1703	5.5661	0.09722	0.35628	0.00531	0.8532936	1853.3	26.8	1964.5	15.03	106	
KM1706	10.58721	0.18673	0.4375	0.00661	0.8566252	2611	25.29	2339.4	16.36	90	
KM1709	10.55686	0.214	0.45053	0.00731	0.800414	2557.3	31.06	2397.6	18.8	94	
KM1712	3.73053	0.07234	0.26678	0.00407	0.7867435	1650.9	32.38	1524.4	15.53	92	
KM1713	4.27323	0.07342	0.31369	0.00456	0.8460695	1602.3	27.42	1758.8	14.14	110	
KM1714	5.4073	0.09214	0.35401	0.00514	0.852079	1812.9	26.45	1953.7	14.6	108	
KM1719	7.96312	0.13971	0.39186	0.00569	0.8276317	2316.4	26.47	2131.5	15.83	92	
KM1720	9.97751	0.1695	0.41864	0.00594	0.8352148	2586	24.65	2254.3	15.68	87	
KM1721	11.36126	0.18024	0.45723	0.0065	0.8960948	2654.7	21.41	2427.3	14.81	91	
KM1722	298.0752	67.91415	2.16249	0.57322	1.16341	5236.8	273.96	7422.1	230.57	142	
KM1724	3.88625	0.0755	0.2618	0.004	0.7864555	1760.1	31.52	1499	15.69	85	
KM1725	3.89035	0.06938	0.2243	0.00332	0.8299715	2039.9	26.8	1304.6	14.4	64	
KM1727	3.80545	0.0716	0.237	0.00358	0.8028376	1902.4	29.07	1371.1	15.13	72	
KM17b02	3.91524	0.05989	0.26187	0.00339	0.5181349	1773.9	25.33	1499.4	17.3	85	
KM17b04	3.61628	0.05286	0.25165	0.00319	0.5442393	1701.4	23.99	1447	16.41	85	
KM17b08	4.40852	0.06156	0.28989	0.00366	0.5806178	1805.1	22.09	1641	18.29	91	
KM17b09	3.47757	0.04899	0.24083	0.00305	0.5741927	1710.4	22.59	1391	15.83	81	
KM17b10	5.01044	0.07161	0.31177	0.00397	0.5700022	1904.8	22.48	1749.4	19.49	92	
KM17b11	8.49938	0.12085	0.39172	0.00497	0.5768941	2428.2	20.99	2130.8	23.04	88	
KM17b12	8.7204	0.12578	0.39436	0.00503	0.5681195	2460.2	21.33	2143	23.26	87	
KM17b14	7.21131	0.11007	0.36068	0.0047	0.5393678	2288.4	23.46	1985.4	22.27	87	
KM17b17	7.61805	0.11832	0.35646	0.00465	0.5317533	2402.2	23.55	1965.4	22.1	82	
KM17b20	4.45852	0.06613	0.29621	0.0038	0.5532744	1785.5	23.97	1672.5	18.92	94	
KM17b21	3.57594	0.05447	0.25003	0.00323	0.530613	1691.8	25.16	1438.6	16.65	85	
KM17b23	1.12123	0.01766	0.10086	0.0013	0.5102714	1212.3	28.14	619.4	7.63	51	
KM17b24	3.83754	0.05967	0.24193	0.00312	0.5169595	1880.4	25.37	1396.7	16.19	74	
KM17b25	3.85592	0.0633	0.25623	0.00336	0.4815276	1785	27.66	1470.5	17.24	82	

SAMPLE: WD-05 - Psammite from Sillimanite Gneiss, Myponga Inlier

Analysis #	$^{207}Pb/^{235}U$ Ratio	1σ	$^{206}Pb/^{238}U$ Ratio	1σ	Rho	$^{207}Pb/^{206}Pb$ Age	2σ	$^{206}Pb/^{238}U$ Age	2σ	Conc. %	Comments
Detrital Zircon											
WD5_001	4.97634	0.06998	0.32655	0.00427	0.6151897	1809	21.54	1821.6	20.75	100.7	Hf Analysis #18
WD5_004	4.69053	0.07258	0.3153	0.00425	0.5650904	1765.3	24.65	1766.7	20.83	100.1	
WD5_005	4.89578	0.07581	0.32223	0.00434	0.5660461	1803.7	24.49	1800.6	21.17	99.8	Hf Analysis #19
WD5_006	4.78155	0.07528	0.31519	0.00427	0.5644254	1800.9	24.99	1766.2	20.92	98.1	
WD5_013	4.51983	0.07766	0.30838	0.00427	0.5414619	1737.3	27.49	1732.7	21.02	99.7	
WD5_014	5.27281	0.07804	0.33606	0.00459	0.6446284	1860.7	21.61	1867.7	22.16	100.4	
WD5_015	4.32541	0.0653	0.29638	0.00408	0.6299748	1728.8	22.65	1673.3	20.28	96.8	
WD5_017	4.99648	0.08061	0.32695	0.00461	0.5901279	1812.8	24.83	1823.6	22.37	100.6	
WD5_019	4.48998	0.07142	0.3043	0.00427	0.6076907	1748.8	24.25	1712.6	21.09	97.9	Hf Analysis #40
WD5_020	4.57443	0.07247	0.30996	0.00434	0.6108	1749.2	24	1740.5	21.37	99.5	
WD5_022	5.16056	0.08816	0.33305	0.00479	0.5652977	1837.9	26.65	1853.2	23.18	100.8	
WD5_023	5.17831	0.08708	0.33245	0.00476	0.5805627	1847.5	25.88	1850.2	23.01	100.1	
WD5_024	4.70393	0.07955	0.31519	0.00451	0.5791945	1769.7	26.3	1766.2	22.12	99.8	Hf Analysis #22
WD5_025	4.76925	0.08444	0.31649	0.00461	0.5554194	1787.5	28.03	1772.6	22.57	99.2	Hf Analysis #38
WD5_026	8.35939	0.14429	0.42252	0.0061	0.5738756	2269.7	25.39	2271.9	27.65	100.1	
WD5_028	5.32029	0.07915	0.3307	0.00451	0.6283638	1905.8	21.96	1841.8	21.84	96.6	Hf Analysis #25
WD5_030	4.72462	0.07508	0.31046	0.0043	0.584099	1805.2	24.75	1743	21.13	96.6	Hf Analysis #26
WD5_032	4.67048	0.07257	0.3086	0.00421	0.59097	1795.1	23.97	1733.8	20.74	96.6	
WD5_036	4.60229	0.07627	0.30853	0.00424	0.5431366	1768.6	26.61	1733.5	20.89	98.0	
WD5_039	5.3613	0.09418	0.32976	0.00459	0.5016273	1924.5	28.41	1837.2	22.25	95.5	Hf Analysis #27
WD5_040	5.05787	0.07708	0.32994	0.00454	0.6270766	1818.6	22.65	1838.1	22	101.1	
WD5_045	5.43607	0.08714	0.34311	0.0048	0.6034659	1878.2	24.15	1901.6	23.04	101.2	
WD5_046	4.46144	0.07409	0.30429	0.0043	0.5776647	1737.3	25.91	1712.5	21.27	98.6	Hf Analysis #35
WD5_047	4.67398	0.07859	0.30912	0.00439	0.5740137	1793.6	26.18	1736.4	21.62	96.8	Hf Analysis #30
WD5_048	4.67947	0.07733	0.31538	0.00445	0.5902095	1759.2	25.44	1767.1	21.8	100.4	
WD5_049	4.98345	0.08488	0.33017	0.0047	0.5700737	1790.5	26.56	1839.2	22.8	102.7	Hf Analysis #39
WD5_050	4.95788	0.08709	0.32902	0.00474	0.5528503	1787.5	27.77	1833.6	22.98	102.6	
WD5_051	4.41778	0.08053	0.30396	0.00443	0.5298451	1721.5	29.44	1710.9	21.91	99.4	
WD5_052	4.48542	0.08077	0.30246	0.00438	0.544863	1758.5	28.66	1703.5	21.7	96.9	Hf Analysis #32
WD5_053	4.92627	0.07751	0.32173	0.00456	0.612727	1817	23.76	1798.2	22.24	99.0	
WD5_054	4.87548	0.07516	0.31855	0.00448	0.6269275	1816.2	22.97	1782.7	21.9	98.2	
WD5_055	11.95249	0.18162	0.49039	0.00688	0.6400254	2623.1	20.56	2572.4	29.76	98.1	
WD5_056	6.72626	0.10346	0.37588	0.00528	0.630236	2095.4	22.17	2057	24.72	98.2	Hf Analysis #17
WD5_059	10.83359	0.16913	0.46929	0.0066	0.6195247	2532.4	21.71	2480.5	28.94	98.0	Hf Analysis #21
WD5_060	5.01673	0.07876	0.32265	0.00452	0.615061	1844.8	23.61	1802.6	22.04	97.7	
WD5_062	4.57724	0.0763	0.30937	0.00441	0.5733432	1754.5	26.18	1737.6	21.69	99.0	
WD5_063	4.84558	0.08202	0.32482	0.00464	0.5623421	1769.5	26.85	1813.2	22.6	102.5	Hf Analysis #28
WD5_065	4.52152	0.07994	0.30797	0.00445	0.5333923	1740.3	28.63	1730.7	21.95	99.4	
WD5_066	5.11814	0.07633	0.32631	0.00443	0.6197071	1860.5	22.38	1820.5	21.54	97.9	

Analysis #	$^{207}Pb/^{235}U$ Ratio	$^{207}Pb/^{235}U$ 1σ	$^{206}Pb/^{238}U$ Ratio	$^{206}Pb/^{238}U$ 1σ	Rho	$^{207}Pb/^{206}Pb$ Age	$^{207}Pb/^{206}Pb$ 2σ	$^{206}Pb/^{238}U$ Age	$^{206}Pb/^{238}U$ 2σ	Conc. %	Comments
WD5_068	4.4371	0.06679	0.30479	0.00414	0.6173684	1724.8	23.02	1715	20.45	99.4	
WD5_072	5.24696	0.08269	0.33056	0.00453	0.5847974	1882.1	24.15	1841.1	21.97	97.8	
WD5_074	4.4033	0.07331	0.30581	0.00426	0.5533478	1704.7	26.72	1720	21.01	100.9	
WD5_075	4.5652	0.07367	0.3072	0.00422	0.5762855	1762.6	25.23	1726.9	20.82	98.0	
WD5_077	5.1028	0.08523	0.33421	0.00463	0.5552771	1811.9	26.36	1858.7	22.37	102.6	Hf Analysis #29
WD5_078	4.73329	0.08134	0.30827	0.00431	0.5365513	1822.1	27.4	1732.2	21.22	95.1	
WD5_079	4.88128	0.07187	0.31936	0.00436	0.6449023	1813.7	21.68	1786.6	21.3	98.5	Hf Analysis #34
WD5_084	5.00761	0.07758	0.32218	0.00441	0.5957651	1843.9	23.73	1800.3	21.49	97.6	
WD5_093	4.5507	0.07878	0.30839	0.00438	0.5244759	1749.2	28.17	1732.8	21.57	99.1	Hf Analysis #33
WD5_094	4.71198	0.07673	0.31768	0.00442	0.5717659	1758.6	25.64	1778.4	21.61	101.1	
WD5_095	4.55224	0.07449	0.31119	0.00433	0.5682943	1733.2	25.87	1746.6	21.3	100.8	
WD5_096	4.37444	0.06888	0.29663	0.00408	0.5964275	1748	24.15	1674.6	20.28	95.8	
WD5_101	4.83518	0.08087	0.31677	0.00444	0.5756478	1810.9	25.89	1773.9	21.75	98.0	Hf Analysis #36
WD5_102	9.08673	0.15481	0.43681	0.00617	0.5677469	2355.8	24.93	2336.3	27.69	99.2	
WD5_105	5.27089	0.082	0.34407	0.00497	0.6694021	1817.6	22.05	1906.2	23.82	104.9	
WD5_106	4.58301	0.07204	0.30993	0.00448	0.6599995	1753.2	22.56	1740.4	22.05	99.3	
WD5_107	4.90643	0.0789	0.3243	0.00471	0.6466746	1794.9	23.44	1810.7	22.95	100.9	
WD5_111	8.51365	0.1404	0.42386	0.00617	0.630771	2295.8	22.98	2278	27.92	99.2	
WD5_113	16.60212	0.30361	0.57071	0.00856	0.5629547	2913.2	25.44	2910.8	35.14	99.9	Hf Analysis #24
WD5_114	5.56573	0.09677	0.34496	0.00507	0.5915082	1911.3	26.09	1910.5	24.3	100.0	
WD5_115	4.56319	0.088	0.30674	0.00467	0.527451	1764.3	31.03	1724.6	23.04	97.7	Hf Analysis #37
WD5_116	5.088	0.09257	0.32945	0.00489	0.5637415	1832.4	28.21	1835.7	23.73	100.2	
WD5_117	4.93852	0.08558	0.32992	0.00485	0.5978841	1775.5	26.45	1838	23.52	103.5	
WD5_118	5.22729	0.08092	0.33696	0.00479	0.6619885	1840.8	22.04	1872	23.1	101.7	
WD5_119	5.45283	0.08915	0.34162	0.00493	0.618259	1892.3	24.23	1894.4	23.71	100.1	
WD5_121	5.19179	0.08834	0.3332	0.00485	0.5820852	1848.9	26.18	1853.9	23.45	100.3	Hf Analysis #23
WD5_124	5.19161	0.08789	0.33607	0.00483	0.5733662	1833.3	26.31	1867.7	23.32	101.9	
WD5_125	4.92429	0.0846	0.32468	0.00468	0.5614022	1799.9	27.11	1812.5	22.75	100.7	
WD5_127	5.57509	0.09107	0.34113	0.00479	0.5841301	1934.6	24.89	1892.1	23.02	97.8	
Metamorphic Zircon											
WD5_003	3.77063	0.05428	0.27637	0.00364	0.6100916	1605.6	22.68	1573.1	18.37	98.0	
WD5_007	4.22685	0.0648	0.30732	0.00412	0.5835034	1620.6	24.4	1727.5	20.31	106.6	
WD5_018	4.11953	0.0636	0.29682	0.00412	0.6223157	1636	23.56	1675.5	20.48	102.4	
WD5_044	4.05745	0.09441	0.29157	0.00471	0.3883718	1641	41.37	1649.3	23.53	100.5	
WD5_064	3.88886	0.06342	0.28575	0.00402	0.5850668	1600.1	25.86	1620.3	20.16	101.3	
WD5_067	4.07762	0.06222	0.29217	0.00399	0.6043396	1646.9	23.8	1652.4	19.88	100.3	Hf Analysis #31
WD5_086	3.82382	0.05896	0.27731	0.00376	0.5916485	1624.2	24.29	1577.8	18.99	97.1	Hf Analysis #20
WD5_110	3.97345	0.06539	0.28887	0.0042	0.6307271	1619.7	24.8	1635.9	21.02	101.0	
95-90% discordant Analyses - Hf Isotopes analysed											
WD5_010	4.29379	0.06982	0.28983	0.00395	0.5586015	1757.4	25.7	1640.7	19.74	93.4	Hf Analysis #6
WD5_029	4.66666	0.07029	0.30397	0.00415	0.6203301	1821.2	22.66	1711	20.49	93.9	Hf Analysis #1

Analysis #	$^{207}Pb/^{235}U$ Ratio	1σ	$^{206}Pb/^{238}U$ Ratio	1σ	Rho	$^{207}Pb/^{206}Pb$ Age	2σ	$^{206}Pb/^{238}U$ Age	2σ	Conc. %	Comments
WD5_033	4.02079	0.06238	0.28124	0.00382	0.5944869	1690.8	24.22	1597.6	19.22	94.5	Hf Analysis #2
WD5_034	4.68587	0.07438	0.30549	0.00417	0.5747053	1819.5	24.72	1718.5	20.58	94.4	Hf Analysis #3
WD5_038	4.63934	0.08059	0.3038	0.00422	0.5134307	1811.5	28.32	1710.1	20.86	94.4	Hf Analysis #7
WD5_043	4.37102	0.07483	0.29376	0.0042	0.5557936	1764.3	27.21	1660.3	20.95	94.1	Hf Analysis #8
WD5_071	4.01197	0.06907	0.27768	0.00393	0.5289119	1710.9	28.17	1579.7	19.82	92.3	Hf Analysis #4
WD5_083	4.31959	0.06661	0.29062	0.00398	0.6019929	1762.6	23.7	1644.6	19.88	93.3	Hf Analysis #9
WD5_085	9.24807	0.15875	0.42217	0.00609	0.5271476	2443.7	26.05	2270.3	27.61	92.9	Hf Analysis #10
WD5_090	4.25949	0.06884	0.28591	0.00389	0.552943	1766.7	25.87	1621	19.49	91.8	Hf Analysis #11
WD5_092	5.25311	0.0796	0.31928	0.00433	0.611323	1946	22.64	1786.2	21.17	91.8	Hf Analysis #12
WD5_100	3.92602	0.0645	0.27368	0.00382	0.5838446	1697.3	25.68	1559.5	19.31	91.9	Hf Analysis #13
WD5_112	6.39375	0.10703	0.35062	0.00511	0.6172549	2128.2	23.97	1937.5	24.4	91.0	Hf Analysis #14
WD5_122	4.28494	0.07073	0.28809	0.00413	0.5962249	1764.4	25.27	1632	20.67	92.5	Hf Analysis #15
WD5_123	9.18928	0.15143	0.41429	0.00597	0.5937072	2465.3	23.5	2234.5	27.19	90.6	Hf Analysis #5
WD5_128	3.96413	0.06638	0.27852	0.00393	0.5620875	1683.4	26.77	1583.9	19.8	94.1	Hf Analysis #16
Discordant Analyses - Not used in age calculations											
WD5_002	4.23122	0.062	0.27065	0.00359	0.5905092	1855.4	22.75	1544.1	18.19	83.2	
WD5_008	4.05054	0.06405	0.25439	0.00344	0.569513	1888.4	24.62	1461.1	17.7	77.4	
WD5_009	3.04597	0.04837	0.14739	0.002	0.5702604	2345.5	23.42	886.3	11.22	37.8	
WD5_011	7.81046	0.12843	0.37069	0.00507	0.5565595	2378.3	24.27	2032.6	23.85	85.5	
WD5_012	6.25611	0.11297	0.33019	0.00471	0.5032183	2195.4	28.25	1839.3	22.83	83.8	
WD5_016	3.89462	0.0588	0.25395	0.0035	0.6341527	1819.3	22.33	1458.8	17.98	80.2	
WD5_021	4.05655	0.06516	0.26812	0.00377	0.6060035	1794.6	24.42	1531.2	19.18	85.3	
WD5_027	4.48472	0.06673	0.22137	0.00303	0.6308768	2310.4	21.04	1289.1	16	55.8	
WD5_031	6.92628	0.10668	0.30102	0.00413	0.5990147	2526.2	21.84	1696.4	20.44	67.2	
WD5_035	3.4166	0.05426	0.23859	0.00324	0.5725182	1693.8	25.15	1379.4	16.88	81.4	
WD5_037	8.91313	0.14764	0.38659	0.00532	0.5422957	2529.6	24.48	2107	24.74	83.3	
WD5_041	3.96866	0.06104	0.26641	0.00368	0.6217448	1766.4	23.14	1522.5	18.71	86.2	
WD5_042	4.87971	0.0754	0.28568	0.00395	0.6205802	2012.6	22.58	1619.9	19.81	80.5	
WD5_057	3.75118	0.05775	0.24498	0.00343	0.6306838	1817.1	22.93	1412.5	17.75	77.7	
WD5_058	4.75716	0.07371	0.29989	0.0042	0.6239548	1880.9	23.01	1690.8	20.83	89.9	
WD5_061	2.86338	0.04582	0.17407	0.00245	0.5990273	1946.1	24.09	1034.5	13.46	53.2	
WD5_069	3.24612	0.04876	0.21448	0.00291	0.6175697	1795.8	22.73	1252.6	15.43	69.8	
WD5_070	4.41871	0.06867	0.2789	0.00382	0.5916945	1878.7	23.73	1585.8	19.25	84.4	
WD5_073	4.15038	0.06576	0.27679	0.00379	0.5839796	1778.9	24.65	1575.2	19.16	88.5	
WD5_076	4.87852	0.07973	0.28191	0.00388	0.5678431	2036.3	24.9	1601	19.54	78.6	
WD5_080	8.03602	0.11956	0.36371	0.00498	0.6325713	2458.4	20.62	1999.7	23.54	81.3	
WD5_081	3.56256	0.05357	0.24736	0.00338	0.6218785	1704.8	22.87	1424.9	17.46	83.6	
WD5_082	7.68684	0.11496	0.36758	0.00501	0.6234126	2364.9	21.07	2018	23.6	85.3	
WD5_087	4.08247	0.06507	0.26428	0.00362	0.5674374	1832.7	24.98	1511.7	18.43	82.5	
WD5_088	3.88344	0.06106	0.24478	0.00332	0.5744045	1880.8	24.36	1411.5	17.2	75.0	
WD5_089	4.07451	0.06467	0.23204	0.00315	0.5690166	2061.7	24.24	1345.2	16.47	65.2	

Analysis #	$^{207}Pb/^{235}U$ Ratio	1σ	$^{206}Pb/^{238}U$ Ratio	1σ	Rho	$^{207}Pb/^{206}Pb$ Age	2σ	$^{206}Pb/^{238}U$ Age	2σ	Conc. %	Comments
WD5_091	4.28916	0.0714	0.28388	0.00389	0.528024	1792.4	26.96	1610.9	19.52	89.9	
WD5_097	4.03066	0.06467	0.25867	0.00358	0.5872872	1848.2	24.54	1483	18.33	80.2	
WD5_099	3.95649	0.06698	0.26612	0.00375	0.5553245	1762.9	26.77	1521.1	19.1	86.3	
WD5_103	4.06351	0.07533	0.27513	0.004	0.5174284	1750.9	30.05	1566.8	20.25	89.5	
WD5_104	4.39118	0.0831	0.27701	0.00407	0.5095717	1879.4	30.42	1576.3	20.55	83.9	
WD5_108	8.05163	0.12851	0.3819	0.00553	0.6529072	2378.7	21.61	2085.2	25.82	87.7	
WD5_109	4.37933	0.07113	0.28717	0.00417	0.6369247	1809.4	23.72	1627.4	20.89	89.9	
WD5_120	4.74428	0.08011	0.28056	0.00409	0.5879968	1995.5	25.34	1594.2	20.58	79.9	
WD5_126	3.91272	0.06324	0.25202	0.00354	0.592759	1842.3	24.65	1448.9	18.22	78.6	
WD5_129	3.56927	0.05935	0.22673	0.00318	0.5615253	1867.2	26.02	1317.4	16.7	70.6	
WD5_130	3.41962	0.05862	0.19786	0.0028	0.5350251	2034	26.84	1163.8	15.04	57.2	

Chapter 2 Supplementary Data 2: Barossa Complex Lu-Hf Isotopic Analyses

SAMPLE: HI20 - Calcsilicate, Eastern Houghton Inlier

Analysis #	$^{176}Hf/^{177}Hf$	2 S.E.	$^{176}Lu/^{177}Hf$	U/Pb AGE	Hf Chur (t)	Hf DM (t)	Hf NC(t)	Hf_i	epsilon	1s	T(DM) (crustal)	T(NC) (crustal)
Detrital Zircon												
Km_kersHF_04	0.281732651	6.45863E-05	0.001313017	1785	0.281648	0.281950	0.281878	0.281688	1.44	2.26052	2.35	2.1964054
Km_kersHF_05	0.281614213	2.89237E-05	0.00058583	1721.2	0.281689	0.281997	0.281925	0.281595	-3.33	1.01233	2.59	2.4337949
Km_kersHF_08	0.281726444	3.79068E-05	0.001074927	1724.6	0.281687	0.281995	0.281922	0.281691	0.16	1.32674	2.38	2.224927
KM_kersHF_10	0.281756442	0.000101589	0.004334736	1717.4	0.281691	0.282000	0.281928	0.281615	-2.70	3.55561	2.55	2.3925278
KM_kersHF_11	0.281665938	6.10057E-05	0.00157693	1684.4	0.281713	0.282025	0.281952	0.281616	-3.45	2.1352	2.57	2.411243
KM_kersHF_13	0.281810111	8.92037E-05	0.002228144	1832.1	0.281617	0.281915	0.281844	0.281733	4.10	3.12213	2.23	2.0731406
KM_kersHF_14	0.28169059	6.24335E-05	0.001438048	1721.9	0.281688	0.281997	0.281924	0.281644	-1.59	2.18517	2.48	2.3290683
KM_kersHF_16	0.281705464	4.20993E-05	0.000840371	1736.1	0.281679	0.281986	0.281914	0.281678	-0.05	1.47348	2.40	2.2472964
KM_kersHF_17	0.281767645	6.73625E-05	0.003506213	1731.6	0.281682	0.281990	0.281917	0.281653	-1.05	2.35769	2.46	2.3042517
Metamorphic Zircon												
Km_kersHF_03	0.281657783	5.59462E-05	0.00086177	1649.3	0.281735	0.282050	0.281977	0.281631	-3.71	1.95812	2.56	2.3989979
Km_kersHF_06	0.281763457	7.95244E-05	0.000893452	1609.4	0.281761	0.282080	0.282006	0.281736	-0.89	2.78335	2.35	2.1953843
Km_kersHF_07	0.281701595	6.88087E-05	0.001299603	1622.5	0.281753	0.282070	0.281997	0.281662	-3.23	2.40831	2.51	2.3484272
Km_kersHF_09	0.281656326	2.80122E-05	0.000451655	1619.1	0.281755	0.282073	0.281999	0.281642	-3.99	0.98043	2.55	2.3916973
KM_kersHF_12	0.281680958	6.9233E-05	0.002055684	1611.4	0.281760	0.282078	0.282005	0.281618	-5.03	2.42316	2.61	2.4483034
Km_kersHF_01	0.281710387	1.95155E-05	0.000527161	1664.1	0.281726	0.282040	0.281966	0.281694	-1.14	0.68304	2.41	2.2549589
Outlier												
KM_kersHF_15	0.279826544	0.002120576	0.001243308	1705	0.281699	0.282009	0.281937	0.279786	-67.91	74.2202	6.34	6.1912177

SAMPLE: Vixen Gully 6 - Psammitic Layer in Sillimanite Gneiss, Northern Houghton Inlier

Detrital Zircon												
km_VIX6_hf01	0.281629614	5.2748E-05	0.001462053	1793.2	0.281642	0.281944	0.281872	0.281580	-2.22	1.84618	2.58	2.4244566
km_VIX6_hf02	0.280939956	5.421E-05	0.001470044	2932.2	0.280896	0.281092	0.281033	0.280857	-1.39	1.89735	3.42	3.3001571
km_VIX6_hf03	0.281583348	4.9887E-05	0.00200701	1914.4	0.281564	0.281854	0.281784	0.281510	-1.89	1.74604	2.65	2.5028602
km_VIX6_hf04	0.281204187	3.08212E-05	0.001023265	2319.4	0.281300	0.281552	0.281487	0.281159	-5.00	1.07874	3.15	3.0157383
km_VIX6_hf05	0.281645496	4.19542E-05	0.001088335	1698.3	0.281704	0.282014	0.281942	0.281610	-3.31	1.4684	2.57	2.4141649
km_VIX6_hf06	0.28157401	7.89104E-05	0.001187554	1783.7	0.281648	0.281951	0.281879	0.281534	-4.07	2.76186	2.68	2.5286728
km_VIX6_hf07	0.28149241	4.86638E-05	0.0014478	1734.7	0.281680	0.281987	0.281915	0.281445	-8.36	1.70323	2.90	2.7475299
km_VIX6_hf11	0.281550306	4.90787E-05	0.000517519	1792.1	0.281643	0.281945	0.281873	0.281533	-3.92	1.71775	2.68	2.5261867
km_VIX6_hf12	0.281625651	8.23188E-05	0.001310039	1849.8	0.281606	0.281902	0.281831	0.281580	-0.92	2.88116	2.54	2.3920059
km_VIX6_hf13	0.281073206	3.18344E-05	0.000498623	2572	0.281134	0.281363	0.281301	0.281049	-3.03	1.11421	3.23	3.1035407
km_VIX6_hf15	0.28166783	0.000120386	0.003044735	1837.2	0.281614	0.281911	0.281840	0.281562	-1.85	4.2135	2.59	2.4378593
km_VIX6_hf16	0.281419458	5.23367E-05	0.002066726	2294.2	0.281316	0.281571	0.281506	0.281329	0.46	1.83178	2.81	2.670134
km_VIX6_hf17	0.281428057	0.000271837	0.001595983	1754.7	0.281667	0.281973	0.281901	0.281375	-10.38	9.51428	3.04	2.884653
km_VIX6_hf18	0.281255766	5.02173E-05	0.001528277	2821.5	0.280970	0.281175	0.281116	0.281173	7.25	1.75761	2.83	2.7002749
km_VIX6_hf19	0.281544146	7.82436E-05	0.001346292	2062.8	0.281467	0.281744	0.281675	0.281491	0.86	2.73852	2.60	2.4577041
km_VIX6_hf22	0.28160339	9.604E-05	0.001932888	1875.2	0.281589	0.281883	0.281813	0.281535	-1.94	3.3614	2.62	2.4738303

Analysis #	$^{176}Hf/^{177}Hf$	2 S.E.	$^{176}Lu/^{177}Hf$	U/Pb AGE	Hf Chur (t)	Hf DM (t)	Hf NC(t)	Hf_i	epsilon	1s	T(DM) (crustal)	T(NC) (crustal)
km_VIX6_hf23	0.281538975	3.80137E-05	0.000258595	1834	0.281616	0.281914	0.281843	0.281530	-3.05	1.33048	2.66	2.5076646
km_VIX6_hf24	0.281481809	4.98429E-05	0.001157834	1753.6	0.281668	0.281973	0.281901	0.281443	-7.98	1.7445	2.89	2.7396792
Metamorphic Zircon												
km_VIX6_hf10	0.281550306	4.90787E-05	0.000517519	1612.5	0.281759	0.282078	0.282004	0.281535	-7.97	1.71775	2.78	2.6272544
km_VIX6_hf21	0.288208802	0.010208762	0.240610157	1574.1	0.281784	0.282106	0.282032	0.281041	-26.38	357.307	3.85	3.6972138
Outliers												
km_VIX6_hf08	3.460196352	2.385828194	150.6558711	1600	0.281767	0.282087	0.282013	-1.103121	-49150.07	83504	218.75	218.75195
km_VIX6_hf09	-2.662914846	5.588166606	120.1563114	1588.5	0.281775	0.282095	0.282021	-6.275862	-232726.25	195586	301.39	301.38795
km_VIX6_hf14	0.120282721	4.014254019	56.19192868	1599.9	0.281767	0.282087	0.282013	-1.581645	-66133.00	140499	234.42	234.42279
km_VIX6_hf20	0.264517246	0.944702785	46.89443515	1594.7	0.281771	0.282091	0.282017	-1.151124	-50853.24	33064.6	220.55	220.55065
SAMPLE: HI11 - Quartzofeldspathic Gneiss, Southern Houghton Inlier												
Detrital Zircon												
KM_HI11_01	0.281760651	4.63474E-05	0.003286588	1753.8	0.281668	0.281973	0.281901	0.281651	-0.58	1.62216	2.45	2.293867
KM_HI11_02	0.281786652	4.49805E-05	0.0035618	1695.4	0.281706	0.282016	0.281944	0.281672	-1.19	1.57432	2.44	2.2830621
KM_HI11_03	0.281791745	5.55213E-05	0.004733416	1686.1	0.281712	0.282023	0.281950	0.281641	-2.52	1.94325	2.51	2.3566926
KM_HI11_04	0.281819928	4.46683E-05	0.0047358	1704.6	0.281700	0.282010	0.281937	0.281667	-1.16	1.56339	2.45	2.289048
KM_HI11_05	0.281793303	3.78063E-05	0.003783862	1775.5	0.281654	0.281957	0.281885	0.281666	0.43	1.32322	2.40	2.2499445
KM_HI11_06	0.282241956	8.44338E-05	0.006721062	1839	0.281613	0.281910	0.281839	0.282007	14.02	2.95518	1.63	1.4728387
KM_HI11_07	0.281879637	5.87816E-05	0.005577185	1692.5	0.281707	0.282019	0.281946	0.281701	-0.24	2.05735	2.38	2.2232469
KM_HI11_09	0.281775342	4.20131E-05	0.002749031	1682.9	0.281714	0.282026	0.281953	0.281688	-0.92	1.47046	2.41	2.2570655
KM_HI11_10	0.281757078	4.83655E-05	0.003252426	1709.5	0.281696	0.282006	0.281933	0.281652	-1.59	1.69279	2.47	2.3189841
KM_HI11_11	0.28195865	9.42567E-05	0.005816569	1697.3	0.281704	0.282015	0.281942	0.281772	2.39	3.29898	2.22	2.0676241
KM_HI11_12	0.281794605	7.09471E-05	0.004933853	1687.8	0.281711	0.282022	0.281949	0.281637	-2.62	2.48315	2.52	2.3636658
KM_HI11_13	0.281905277	7.79899E-05	0.006625166	1718.9	0.281690	0.281999	0.281927	0.281689	-0.03	2.72965	2.39	2.2322584
KM_HI11_14	0.281734106	3.50008E-05	0.002972553	1848.9	0.281606	0.281903	0.281832	0.281630	0.84	1.22503	2.44	2.2848572
SAMPLE: HI16 - Calcsilicate Gneiss, Southern Houghton Inlier												
Detrital Zircon												
HI16_hf01	0.281584406	4.55321E-05	0.00080383	1751.1	0.281670	0.281975	0.281903	0.281558	-3.97	1.59362	2.65	2.4965222
HI16_hf09	0.281532249	3.78731E-05	0.00059776	1802.1	0.281637	0.281937	0.281866	0.281512	-4.43	1.32556	2.72	2.5650879
HI16_hf10	0.281565013	4.38789E-05	0.000510633	1779.6	0.281651	0.281954	0.281882	0.281548	-3.67	1.53576	2.65	2.5012081
HI16_hf12	0.280984579	6.34617E-05	0.000984493	3057.2	0.280814	0.280997	0.280940	0.280927	4.03	2.22116	3.20	3.085042
HI16_hf13	0.281495628	8.12632E-05	0.002056379	1789.8	0.281645	0.281947	0.281875	0.281426	-7.76	2.84421	2.91	2.7558736
HI16_hf14	0.281519415	5.22202E-05	0.000565602	1721.4	0.281689	0.281997	0.281925	0.281501	-6.67	1.82771	2.79	2.6353489
HI16_hf15	0.281507725	3.88081E-05	0.000477762	1692.7	0.281707	0.282018	0.281946	0.281492	-7.63	1.35828	2.83	2.6704104
HI16_hf16	0.281538366	3.13648E-05	0.000520345	1744.4	0.281674	0.281980	0.281908	0.281521	-5.42	1.09777	2.73	2.5787266
HI16_hf17	0.28131178	4.83155E-05	0.00053875	1692.7	0.281707	0.282018	0.281946	0.281295	-14.66	1.69104	3.25	3.0917681
HI16_hf18	0.28149804	2.81947E-05	0.000307347	2617.5	0.281104	0.281329	0.281267	0.281483	13.47	0.98682	2.29	2.1587727

Analysis #	$^{176}Hf/^{177}Hf$	2 S.E.	$^{176}Lu/^{177}Hf$	U/Pb AGE	Hf Chur (t)	Hf DM (t)	Hf NC(t)	Hf_i	epsilon	1s	T(DM) (crustal)	T(NC) (crustal)
Metamorphic Zircon												
HI16_hf02	0.281518131	2.93223E-05	0.000377901	1635.1	0.281745	0.282061	0.281988	0.281506	-8.45	1.02628	2.83	2.6741034
HI16_hf03	0.281547311	2.86483E-05	0.000582408	1617.5	0.281756	0.282074	0.282000	0.281529	-8.04	1.00269	2.79	2.6350992
HI16_hf05	0.281507933	3.27053E-05	0.000509453	1645.5	0.281738	0.282053	0.281980	0.281492	-8.73	1.14469	2.86	2.6987505
HI16_hf06	0.281432424	4.5775E-05	0.000952193	1616.1	0.281757	0.282075	0.282001	0.281403	-12.55	1.60212	3.06	2.9053747
HI16_hf07	0.28157015	3.68571E-05	0.000577089	1661.7	0.281727	0.282041	0.281968	0.281552	-6.23	1.29	2.72	2.5610193
HI16_hf08	0.28160542	5.97979E-05	0.001159962	1602.9	0.281765	0.282085	0.282011	0.281570	-6.93	2.09293	2.71	2.5563525
HI16_hf11	0.281526123	3.78803E-05	0.000524322	1584	0.281778	0.282099	0.282025	0.281510	-9.48	1.32581	2.85	2.6955415
SAMPLE: HI03 - South Para Othogneiss, Northern Houghton Inlier												
Igneous Zircon												
HI03_hf01	0.281607385	4.69035E-05	0.002860634	1709.7	0.281696	0.282006	0.281933	0.281515	-6.45	1.64162	2.77	2.612796
HI03_hf05	0.281673347	3.43802E-05	0.002697211	1681.5	0.281715	0.282027	0.281954	0.281587	-4.51	1.20331	2.63	2.4734616
HI03_hf08	0.281667144	3.43536E-05	0.002408648	1704	0.281700	0.282010	0.281937	0.281589	-3.93	1.20238	2.61	2.4561402
HI03_hf09	0.281726561	3.94665E-05	0.001780489	1717.4	0.281691	0.282000	0.281928	0.281669	-0.81	1.38133	2.43	2.2780125
HI03_hf10	0.281683466	5.76913E-05	0.002296442	1684.7	0.281713	0.282024	0.281951	0.281610	-3.63	2.01919	2.58	2.4227685
HI03_hf12	0.281729224	3.17572E-05	0.002050986	1642.4	0.281740	0.282056	0.281982	0.281665	-2.64	1.1115	2.49	2.3286875
HI03_hf13	0.281606742	6.52785E-05	0.002661876	1701.1	0.281702	0.282012	0.281940	0.281521	-6.43	2.28475	2.76	2.6044725
HI03_hf14	0.281657333	5.31248E-05	0.002566195	1639.7	0.281742	0.282058	0.281984	0.281578	-5.82	1.85937	2.68	2.5188813
HI03_hf16	0.28170009	9.18625E-05	0.002917453	1726.4	0.281686	0.281994	0.281921	0.281605	-2.87	3.21519	2.57	2.4103145
HI03_hf21	0.281787034	3.12491E-05	0.002834539	1710.9	0.281696	0.282005	0.281932	0.281695	-0.02	1.09372	2.38	2.2246888
HI03_hf22	0.281700611	3.47086E-05	0.002734464	1719.2	0.281690	0.281999	0.281926	0.281612	-2.79	1.2148	2.56	2.3997251
HI03_hf25	0.281688225	3.24713E-05	0.002623942	1754.9	0.281667	0.281972	0.281900	0.281601	-2.35	1.13649	2.56	2.4016366
Metamorphic Zircon												
HI03_hf02	0.281711197	3.43449E-05	0.003189076	1680.8	0.281715	0.282027	0.281954	0.281610	-3.74	1.20207	2.58	2.4261658
HI03_hf03	0.281703765	3.13681E-05	0.002581416	1620.9	0.281754	0.282071	0.281998	0.281625	-4.59	1.09788	2.59	2.4292129
HI03_hf04	0.281735568	4.05212E-05	0.002720323	1568.6	0.281788	0.282110	0.282036	0.281655	-4.71	1.41824	2.55	2.3947651
HI03_hf06	0.281794234	3.35564E-05	0.002899416	1567.1	0.2817885	0.2821111	0.2820369	0.281708244	-2.85	1.17447	2.44	2.2805571
HI03_hf07	0.281675666	3.57377E-05	0.0023793	1596.4	0.2817696	0.2820895	0.282016	0.281604	-5.89	1.25082	2.65	2.4881896
HI03_hf11	0.281633776	7.49786E-05	0.002252416	1695.1	0.2817058	0.2820166	0.281944	0.281561	-5.13	2.62425	2.68	2.5212544
HI03_hf15	0.281703695	3.69671E-05	0.003031382	1613.2	0.2817587	0.2820771	0.282003	0.281611	-5.24	1.29385	2.62	2.4625773
HI03_hf17	0.281695959	3.59101E-05	0.002430648	1578.2	0.2817813	0.282103	0.282029	0.281623	-5.61	1.25686	2.62	2.4567764
HI03_hf18	0.281694816	6.35696E-05	0.003247615	1626	0.2817505	0.2820677	0.281994	0.281595	-5.52	2.22494	2.65	2.4900406
HI03_hf19	0.281694269	3.70523E-05	0.002650704	1628.2	0.2817491	0.2820661	0.281993	0.281613	-4.85	1.29683	2.61	2.4507078
HI03_hf20	0.28168609	2.94844E-05	0.00227819	1625.2	0.281751	0.2820683	0.281995	0.281616	-4.79	1.03196	2.60	2.445081
HI03_hf23	0.281676912	2.48305E-05	0.002291053	1619.1	0.2817549	0.2820728	0.281999	0.281607	-5.26	0.86907	2.63	2.4686369
HI03_hf24	0.28170988	4.05557E-05	0.001975573	1618.2	0.2817555	0.2820734	0.282000	0.281649	-3.77	1.41945	2.54	2.3774488
HI03_hf26	0.281697626	2.89696E-05	0.002468159	1582.2	0.2817788	0.2821	0.282026	0.281624	-5.50	1.01394	2.61	2.4536649
HI03_hf27	0.281704098	4.6938E-05	0.002675227	1626.1	0.2817504	0.2820676	0.281994	0.281622	-4.57	1.64283	2.59	2.4322152
HI03_hf28	0.281721159	5.78427E-05	0.002578451	1580.5	0.2817799	0.2821013	0.282027	0.281644	-4.82	2.02449	2.57	2.410991

Analysis #	$^{176}Hf/^{177}Hf$	2 S.E.	$^{176}Lu/^{177}Hf$	U/Pb AGE	Hf Chur (t)	Hf DM (t)	Hf NC(t)	Hf_i	epsilon	1s	T(DM) (crustal)	T(NC) (crustal)
HI03_hf29	0.281681979	3.31537E-05	0.002401028	1617.3	0.2817561	0.2820741	0.282000	0.281608	-5.24	1.16038	2.62	2.4658723
HI03_hf30	0.281722743	3.50264E-05	0.002427536	1666.7	0.2817242	0.2820376	0.281965	0.281646	-2.77	1.22592	2.51	2.3560604
SAMPLE: WD-05 - Psammite from Sillimanite Gneiss, Myponga Inlier												
Detrital Zircon												
WD_hf01	0.281621385	5.41059E-05	0.00116421	1800.9	0.2816373	0.2819384	0.281867	0.281582	-1.98	1.89371	2.57	2.4162674
WD_hf02	0.281487253	8.78988E-05	0.001525795	1860.7	0.2815985	0.2818941	0.281823	0.281433	-5.87	3.07646	2.85	2.6985262
WD_hf03	0.281437458	6.18764E-05	0.001972513	1737.3	0.2816785	0.2819854	0.281913	0.281373	-10.86	2.16567	3.05	2.9000467
WD_hf05	0.281578	6.12796E-05	0.001860071	1748.8	0.2816711	0.2819769	0.281905	0.281516	-5.49	2.14479	2.74	2.5864847
WD_hf06	0.281517353	6.48255E-05	0.00279595	1749.2	0.2816708	0.2819766	0.281905	0.281425	-8.74	2.26889	2.94	2.7820771
WD_hf07	0.281587577	4.89409E-05	0.001112114	1847.5	0.2816071	0.2819038	0.281833	0.281549	-2.08	1.71293	2.61	2.4599576
WD_hf08	0.28159646	6.62086E-05	0.002107093	1769.7	0.2816575	0.2819615	0.281890	0.281526	-4.68	2.3173	2.71	2.5541382
WD_hf09	0.281580239	6.47526E-05	0.002371302	1905.8	0.2815693	0.2818606	0.281790	0.281494	-2.66	2.26634	2.69	2.5419683
WD_hf10	0.281630161	7.08148E-05	0.001543824	1821.2	0.2816242	0.2819233	0.281852	0.281577	-1.68	2.47852	2.57	2.4147388
WD_hf11	0.281623355	6.92878E-05	0.002154459	1805.2	0.2816345	0.2819352	0.281864	0.281550	-3.02	2.42507	2.64	2.4824317
WD_hf12	0.281623941	5.26927E-05	0.001294235	1690.8	0.2817086	0.2820198	0.281947	0.281582	-4.48	1.84424	2.63	2.4786344
WD_hf13	0.281730618	6.61111E-05	0.001976719	1819.5	0.2816253	0.2819246	0.281853	0.281662	1.32	2.31389	2.39	2.2319063
WD_hf14	0.281466037	8.32018E-05	0.00216597	1924.5	0.2815571	0.2818467	0.281777	0.281387	-6.05	2.91206	2.91	2.7605246
WD_hf15	0.281573374	5.17182E-05	0.001159179	1818.6	0.2816258	0.281925	0.281854	0.28	-3.28	1.81	2.66	2.5093323
WD_hf16	0.281559483	5.18905E-05	0.001488167	1878.2	0.281587	0.281881	0.281810	0.281506	-2.87	1.81617	2.68	2.5323529
WD_hf17	0.281391034	7.1522E-05	0.001578963	1793.6	0.281642	0.281944	0.281872	0.281337	-10.82	2.50327	3.09	2.9419998
WD_hf18	0.281644458	6.14856E-05	0.002181284	1787.5	0.281646	0.281948	0.281877	0.281571	-2.68	2.152	2.60	2.4478843
WD_hf19	0.281536606	5.42008E-05	0.002373279	1758.5	0.281665	0.281970	0.281898	0.281457	-7.36	1.89703	2.86	2.7065949
WD_hf20	0.281566125	7.6405E-05	0.002014877	1817	0.281627	0.281926	0.281855	0.281497	-4.62	2.67418	2.74	2.5887918
WD_hf21	0.281671063	5.86603E-05	0.001440428	1816.2	0.281627	0.281927	0.281856	0.281621	-0.21	2.05311	2.47	2.3218836
WD_hf22	0.281490793	5.50068E-05	0.00147208	2095.4	0.281446	0.281720	0.281652	0.281432	-0.49	1.92524	2.71	2.5652901
WD_hf23	0.281213829	4.50459E-05	0.000602855	2532.4	0.281160	0.281393	0.281330	0.281185	0.88	1.57661	2.97	2.8398314
WD_hf24	0.281665709	5.70685E-05	0.001399827	1844.8	0.281609	0.281906	0.281835	0.281617	0.28	1.9974	2.47	2.3154072
WD_hf25	0.281723968	4.12364E-05	0.001063661	1754.5	0.281667	0.281973	0.281901	0.281689	0.75	1.44327	2.37	2.2133503
WD_hf27	0.281581189	0.000108137	0.001903872	1860.5	0.281599	0.281894	0.281823	0.281514	-3.01	3.78481	2.68	2.5265168
WD_hf28	0.281579439	5.92174E-05	0.001166802	1710.9	0.281696	0.282005	0.281932	0.281542	-5.47	2.07261	2.71	2.5544999
WD_hf29	0.28167986	5.42195E-05	0.001585727	1704.7	0.281700	0.282010	0.281937	0.281629	-2.52	1.89768	2.53	2.3714082
WD_hf30	0.281528637	4.50678E-05	0.001399484	1811.9	0.281630	0.281930	0.281859	0.281481	-5.31	1.57737	2.78	2.6262505
WD_hf31	0.281548109	6.77327E-05	0.001252642	1822.1	0.281624	0.281923	0.281851	0.281505	-4.22	2.37064	2.72	2.568434
WD_hf32	0.281568872	7.76883E-05	0.001466947	1748	0.281672	0.281978	0.281905	0.281520	-5.37	2.71909	2.73	2.5785484
WD_hf33	0.281096556	8.79442E-05	0.002175113	2355.8	0.281276	0.281525	0.281460	0.280999	-9.85	3.07805	3.47	3.3314418
WD_hf34	0.281549142	4.46829E-05	0.000793359	1794.9	0.281641	0.281943	0.281871	0.281522	-4.23	1.5639	2.70	2.5472043
WD_hf35	0.281388574	6.79601E-05	0.001386843	2295.8	0.281315	0.281570	0.281504	0.281328	0.45	2.3786	2.81	2.6717754
WD_hf36	0.28099309	3.86004E-05	0.001010348	2913.2	0.280909	0.281106	0.281047	0.280937	0.99	1.35101	3.27	3.1452526
WD_hf37	0.281489174	9.12582E-05	0.003301473	1799.9	0.281638	0.281939	0.281868	0.281376	-9.28	3.19404	3.01	2.8551101

Analysis #	$^{176}Hf/^{177}Hf$	2 S.E.	$^{176}Lu/^{177}Hf$	U/Pb AGE	Hf Chur (t)	Hf DM (t)	Hf NC(t)	Hf_i	epsilon	1s	T(DM) (crustal)	T(NC) (crustal)
WD_hf38	0.281629386	5.3199E-05	0.001437711	1934.6	0.281551	0.281839	0.281769	0.281577	0.92	1.86196	2.50	2.3494334
WD_hf39	0.281222612	3.83749E-05	0.000687032	2465.3	0.281204	0.281443	0.281379	0.281190	-0.49	1.34312	3.00	2.8662135
WD_hf40	0.281670339	5.01558E-05	0.001566785	1833.3	0.281616	0.281914	0.281843	0.281616	-0.02	1.75545	2.48	2.3239552
Metamorphic Zircon												
WD_hf04	0.281564514	7.35025E-05	0.00256999	1636	0.281744	0.282060	0.281987	0.281485	-9.20	2.57259	2.88	2.7196221
WD_hf26	0.281487898	6.37189E-05	0.002827215	1600.1	0.281767	0.282087	0.282013	0.281402	-12.95	2.23016	3.07	2.9169466

CHAPTER 5

Assessing the significance of U-Pb ages from metamorphic zircon in the Barossa Complex, southeast Gawler Craton: Insights from rare earth element partitioning

Statement of Authorship

Title of Paper	Assessing the significance of U-Pb ages from metamorphic zircon in the Barossa Complex, southeast Gawler Craton: Insights from rare earth element partitioning
Publication Status	☐ Published ☐ Accepted for Publication ☐ Submitted for Publication ☑ Unpublished and Unsubmitted w ork w ritten in manuscript style
Publication Details	Written to be submitted to The Australian Journal of Earth Sciences

Principal Author

Name of Principal Author (Candidate)	Kieran Meaney		
Contribution to the Paper	Project design, Fieldwork, Sample Preparation, LA-ICP-MS Data Collection, Data interpretation, Manuscript design, Creation of figures		
Overall percentage (%)	80		
Certification:	This paper reports on original research I conducted during the period of my Higher Degree by Research candidature and is not subject to any obligations or contractual agreements with a third party that would constrain its inclusion in this thesis. I am the primary author of this paper.		
Signature		Date	21/12/17

Co-Author Contributions

By signing the Statement of Authorship, each author certifies that:

i. the candidate's stated contribution to the publication is accurate (as detailed above);
ii. permission is granted for the candidate in include the publication in the thesis; and
iii. the sum of all co-author contributions is equal to 100% less the candidate's stated contribution.

Name of Co-Author	Martin Hand		
Contribution to the Paper	Assistance with fieldwork, Guidance with data interpretation, Manuscript review		
Signature		Date	21-12-17

ABSTRACT

The Barossa Complex of the southeast Gawler Craton, South Australia, preserves a polymetamorphic history spanning the late Palaeo- to Early Mesoproterozoic, recorded by U-Pb zircon ages spanning 1630 Ma to 1560 Ma. In the northern Barossa Complex, the Houghton Inlier records extensive 1630 Ma metamorphism. One metapelite sample from the Houghton Inlier yields a zircon U-Pb age of 1599 ±10 Ma, and records enriched, flat zircon REE patterns consistent with a hydrothermal origin. The origin of the hydrothermal fluid is not known. 1590 Ma to 1580 Ma metamorphism is extensively preserved throughout the other inliers of the Barossa Complex, in most cases obliterating the c. 1630 Ma signature. In the southern Myponga Inlier, REE distribution coefficients between zircon and garnet from garnet-bearing leucosomes indicate that these minerals grew in equilibrium during high grade metamorphism at 1581 ±12 Ma, and can be directly correlated to previously calculated peak metamorphic conditions of 8-9 kbar and 800-850°C. During the interval 1560 Ma to 1550 Ma, pegmatites intruded the northern Barossa Complex. These pegmatites temporally correspond to a previously recognised period of retrograde metamorphism in the Barossa Complex. The timing of metamorphism and associated structures in the Barossa Complex correlate with that found within the Olarian-Isan Orogen in Eastern Australia, making the Barossa Complex the southernmost exposure of this transcontinental orogenic system.

1. Introduction

Models for the development of the Australian continent frequently juxtapose the eastern margin of Australia with the western margin of the North American Craton, Laurentia (Giles et al. 2004, Betts and Giles 2006, Gibson et al. 2008, Betts et al. 2015). The relationship between these two crustal elements such as their timing of amalgamation, separation, and their relative position to one another throughout the Proterozoic varies widely between different reconstruction models (e.g. Dalziel 1991, Moores 1991, Brookfield 1993, Wingate et al. 2002, Betts et al. 2008, Gibson et al. 2008, Goodge et al. 2008, Li and Evans 2011, Zhang et al. 2012, Medig et al. 2014, Pisarevsky et al. 2014, Betts et al. 2015, Mulder et al. 2015, Aitken et al. 2016, Merdith et al. 2017). This inconsistency highlights the poor understanding of the relationship between these two crustal domains. In order to more accurately refine these models, a better understanding of the geological evolution of the Proterozoic continental margins, and the geodynamic drivers of the tectonic processes which affected these regions, is required.

The Barossa Complex, on the eastern margin of the Gawler Craton (Figure1), forms one of the eastern most exposures of pre-Neoproterozoic crust in Australia, making it a good place to assess any possible relationship between Australia and formerly contiguous crustal elements. The Barossa Complex records an 80 m.y. metamorphic history between 1630 Ma and 1550 Ma (Belousova et al. 2006, Szpunar et al. 2007, Morrissey et al. 2013, Jagodzinski et al. 2017).

One of the challenges of addressing a region which has experienced metamorphism over a long time frame is linking targeted geochronology to specific stages of metamorphism or deformation. One technique that is becoming widely used in directly linking zircon age to metamorphic mineral growth is assessing the partitioning of Rare Earth Elements (REE) between the potentially coeval metamorphic minerals zircon and garnet in order to determine whether these phases grew in equilibrium (e.g. Rubatto 2002, Hermann and Rubatto 2003, Whitehouse and Platt 2003, Rubatto and Hermann 2007, Taylor et al. 2015, Taylor et al.

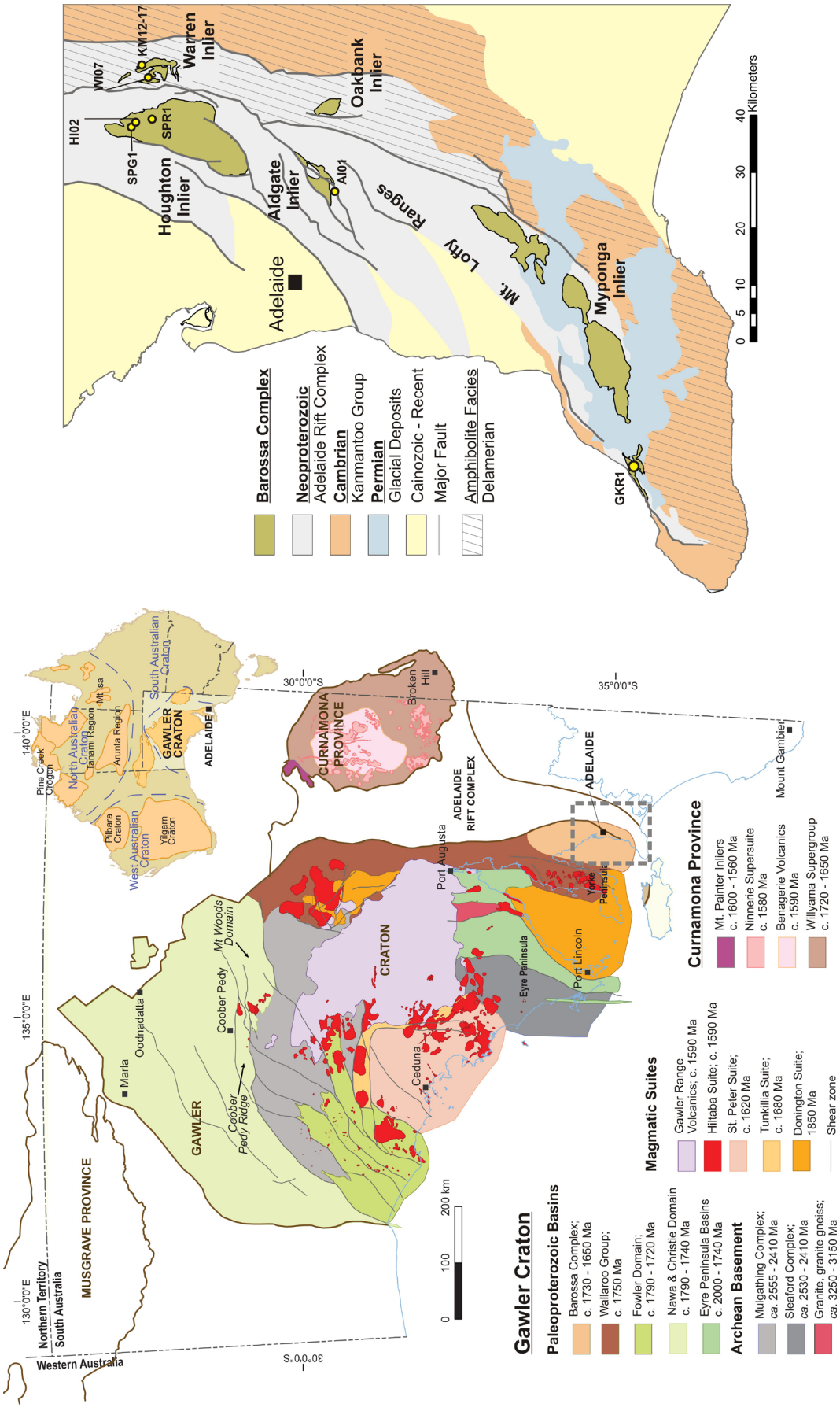

Figure 1: Location Map indicating Barossa Complexes position in the Gawler Craton modified after Reid et al (2017a), and right, simplified geology map of the Mount Lofty Ranges (after Preiss 1993) with locations for samples used in this study across four inliers.

2017). This study aims to interrogate the metamorphic history of the Barossa Complex with a combination of targeted U-Pb zircon geochronology and REE trace element analysis in order to better correlate specific metamorphic episodes with U-Pb ages, and therefore relate the metamorphic history of the Barossa Complex to regional tectonothermal events.

2. Geological Setting

Across the five exposures of the Barossa Complex in the Mt. Lofty Ranges (Figure 1), metamorphic geochronology has revealed an 80 m.y. history of events through the Late Palaeo- to Early Mesoproterozoic. In the Houghton and Myponga inliers (Figure 1) zircon U-Pb geochronology has yielded c. 1630 Ma metamorphic rims on detrital and igneous zircons (Belousova et al. 2006, Jagodzinski et al. 2017; Chapter 4). Detrital zircon geochronology has revealed that deposition of the protoliths to the Barossa Complex occurred from 1740 Ma until at least 1655 Ma (Jagodzinski et al. 2017; Chapter 4). This indicates that metamorphism initiated soon after deposition of the upper Barossa Complex. A second, minor, metamorphic zircon age peak is identified in several inliers at c. 1610 Ma (Jagodzinski et al. 2017). The most widely preserved metamorphic age population is c. 1590 Ma to 1580 Ma which is recorded in both zircon and monazite, and is recorded in every inlier (Szpunar et al. 2007, Morrissey et al. 2013, Jagodzinski et al. 2017). The Myponga Inlier records dominantly c. 1590-1580 Ma metamorphic ages, with only a single sample of metamorphic zircon from the central-southern Wild Dog locality recording c. 1623 Ma (Chapter 4). The Aldgate Inlier only records c. 1580 Ma metamorphism (Jagodzinski et al. 2017). The Oakbank Inlier preserves a range of metamorphic zircon ages spanning c. 1630 Ma to 1590 Ma with no clearly defined age populations (Jagodzinski et al. 2017). In the southern Myponga Inlier, retrograde shear zones displaying east side down extensional kinematics yielded monazite U-Pb ages at c. 1560 Ma, which occur within error of c. 1550 Ma monazite from the southern Houghton Inlier (Morrissey et al. 2013).

Metamorphic grades in the Barossa Complex range from upper amphibolite facies in the north to granulite facies in the south (Preiss 1993), with peak conditions calculated at 800-850^{o}C and 8-9 kbar for the southern Houghton and southern Myponga inliers (Morrissey et al. 2013). Ambiguity arises as to exactly which age bracket represents peak metamorphism. While monazite ages ranging between 1560-1550 Ma correspond to texturally retrogressed rocks and can be interpreted as the timing of long lived retrogression (Morrissey et al. 2013), the timing of peak metamorphism is still unclear. Garnet bearing upper amphibolite to granulite facies rocks reported in the Houghton and Myponga inliers offer an opportunity to assess the partitioning of REEs between zircon and garnet, and therefore to link the growth of peak metamorphic minerals to specific zircon U-Pb ages.

3. Methods

Seven samples were collected from across the exposed extent of the Barossa Complex (Figure 1; Table 1). Zircons were separated from each sample using standard crushing, panning, and heavy liquid techniques. Zircons were encased in epoxy resin mounts and polished to expose the core of each grain. Zircons were imaged using Backscatter Secondary Electron (BSE) and Cathodoluminescence (CL) using a Phillips XL-40 SEM with attached Gatan CL detector. U-Pb analysis was conducted using Laser Ablation Inductively Coupled Plasma Mass Spectrometry (LA-ICP-MS) using a New Wave 213 Nd-YAG laser in a Helium ablation atmosphere, with an attached Agilent 7500cs ICP-MS at Adelaide Microscopy at the University of Adelaide. For all analyses, a 60 second gas blank was analysed before 60 seconds of measurement during zircon ablation. Data was processed using the GLITTER software and U-Pb isotope data and age estimates were exported into Mi-

crosoft Excel and age calculations and graphs were completed using Isoplot v4.11 (Ludwig 2003). All errors stated for age calculations are to the 2σ level.

For all analyses, the zircon standard GEMOC GJ-1 was used as a matrix matched standard to correct for mass bias and fractionation (TIMS normalisation data $^{207}Pb/^{206}Pb$ = 608.3 Ma, $^{206}Pb/^{238}U$ = 600.7 Ma and $^{207}Pb/^{235}U$ = 602.2 Ma, Jackson et al. 2004). Accuracy was checked using the zircon standard Plešovice ($^{206}Pb/^{238}U$ = 337.13 ±0.37 Ma, Sláma et al. 2008). Over the duration of this study, $^{207}Pb/^{206}Pb$, $^{206}Pb/^{238}U$, and $^{206}Pb/^{235}U$ ages for standard GJ-1 yielded 605.3 ±5.6 Ma, 600.3 ±1.2 Ma, and 601.3 ±1.3 Ma respectively (n = 207). The $^{206}Pb/^{238}Ub$ age for Plešovice was 332 ±1.9 Ma (n= 25).

REE analyses were obtained using the same LA-ICP-MS instruments as described above. For all analyses a 60 second gas blank were analysed before 60 seconds of analysis during ablation. Zircon REE analyses were done on grains that yielded U-Pb ages within 10% of concordancy and large enough to accommodate a further 50μm analysis spot. Garnet REE analyses were obtained using single spot traverses across garnets in thin section. Calibration was performed against the NIST 612 and NIST 610 element glass standards (Pearce et al. 1997). Hf was used as the internal standard for zircon and Ca was used for garnet analyses, utilising previously determined values from electron microprobe analysis. These analyses were obtained using a Cameca SXFive electron microprobe at the University of Adelaide. Beam conditions of 20 nA and accelerating voltage of 15 kV were used for all analyses.

4. Results

4.1 U-Pb results

4.1.1 HI02

Sample HI02 is a sub-aluminous metapelitic gneiss from the northern Houghton Inlier, composed primarily of biotite, quartz, K-feldspar, with abundant retrograde sericite and minor retrograde muscovite (Figure 2a). Minor quartzofeldspathic segregations define the gneissic foliation, and small coarser grained leucosomes parallel this structural fabric. Zircons from this sample are typically small, ranging in size between 50 to 150 μm, and are rounded to ovoid in shape. Under CL imaging zircons are typically dark with patchy sector zones. Several grains contain distinct cores of various textures, but are frequently bright with faint oscillatory zoning (Figure 3a).

A total of 49 analyses were obtained from 48 grains. Of these, 13 analyses were on textural cores. The textural cores were mostly discordant (Figure 4a), with only 3 grains yielding ages within 5% of concordancy. These ages range between c. 1850 Ma and 1700 Ma. Of the rims and texturally metamorphic grains, 31 analyses were within 5% of concordancy. These gave a weighted mean $^{207}Pb/^{206}Pb$

Sample	Inlier	Easting	Northing	Age
HI02	Houghton	303139	6159773	1632 ±11
SPR1	Houghton	302695	6160183	1599 ±10
SPG1	Houghton	303214	6157194	a) 1561 ±13, b) 1577 ±11
KM12-11	Warren	309898	6158855	1584 ±15
WI07	Warren	309387	6157164	1548 ±12
AI-01	Aldgate	292927	6123321	1581 ±7
GKR-1	Myponga	255001	6070453	1581 ±12

Table 1: GPS locations for samples used in this chapter. Coordinates are in UTM 54H, GDA91

Figure 2: Photos of sampled lithologies. A) Biotite-sericite gneiss, with leucosomes paralleling the S_1 gneissic foliation. B) Weathered sillimanite-garnet gneiss, showing the sillimanite S_1 fabric wrapping large garnet porphyroblasts. C) Pegmatite from the northern Houghton Inlier, cross cutting the S_1 foliation. D) Weathered kyanite-tourmaline-chlorite schist from the Wartren Inlier. Kyanite is weakly foliated but commonly unoriented. E) Strongly deformed pegmatite from the northern Warren Inlier. F) Cut section of sample GKR1 from the southern Myponga Inlier showing large garnet in association with quartz - K-feldspar leucosome (orange/pink) and coarse biotite and sillimanite groundmass.

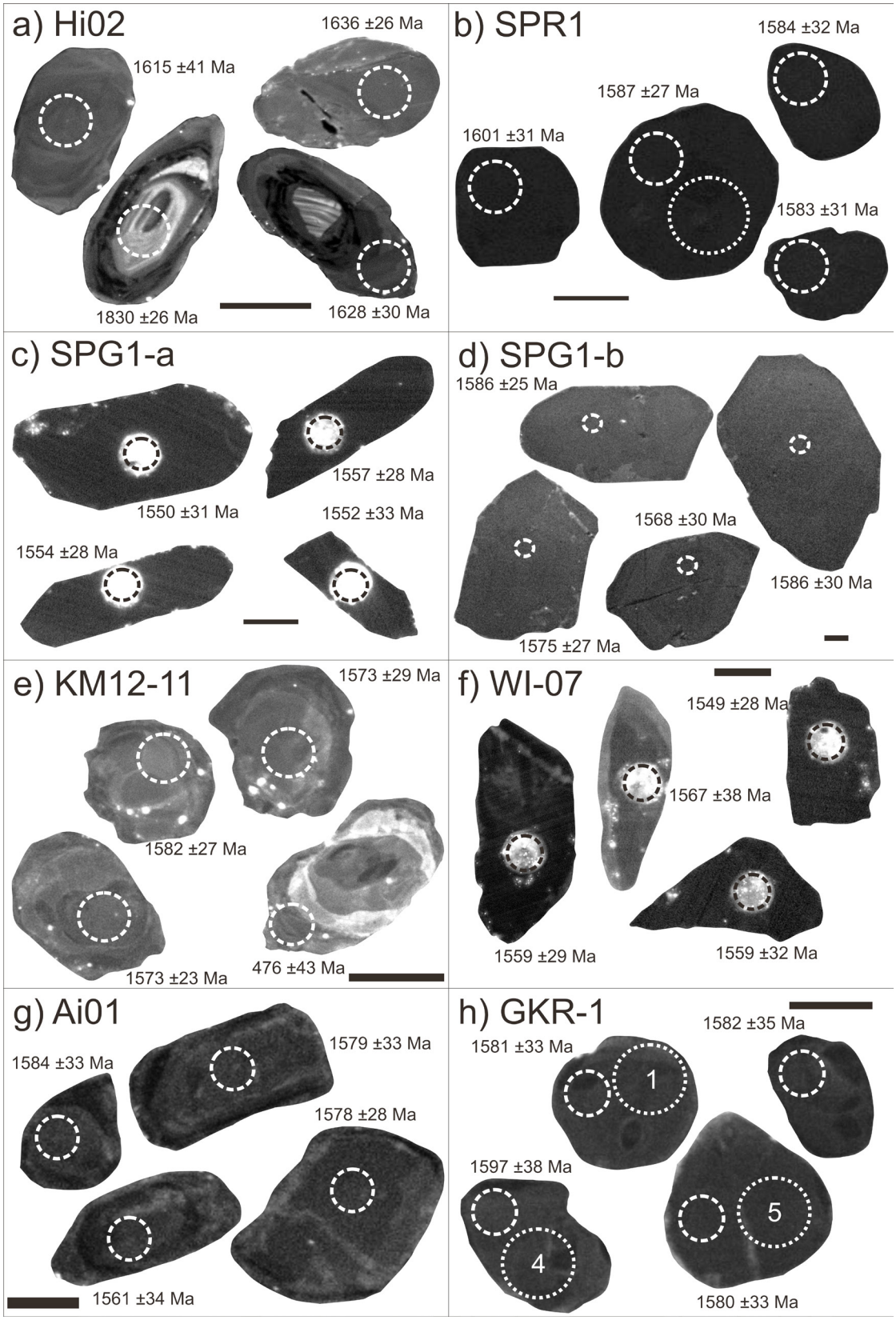

Figure 3: Representative zircon CL images for each analysed sample with locations of laser spots indicated by dashed circles. In sample b) SPR1 and h) GKR-1 the larger circles outlined with the finer dashed line represent location of REE analyses.

age of 1632 ±11 Ma (n=31, MSWD = 0.61, probability = 0.96).

4.1.2 SPR1

Sample SPR1 is a weathered sillimanite-garnet-bearing gneiss from the northern Houghton Inlier. This unit is dominated by sillimanite that wraps large garnet porphyroblasts (Figure 2b), which average approximately 2cm in size. Leucosomes occur but do not comprise more than 5% of any outcrop of this lithology. Zircons from this sample are typically round, equant grains with dark homogeneous patterns under CL imaging (Figure 3b). A total of 96 analyses were obtained from 94 grains, of which 11 are within 5% of concordancy. These concordant analyses give a weighted mean $^{207}Pb/^{206}Pb$ age of 1591 ±19 Ma (n=11, MSWD = 0.036, probability = 1.00). Due to the small number of concordant analyses, the intercept age was also calculated. Fifteen analyses were excluded as outliers to the discordia trend due to the presence of ^{204}Pb (Figure 4b). The intercept age of this sample is 1598.9 ±9.7 Ma (MSWD = 0.99, probability = 0.51), and is the preferred zircon age for this sample.

4.1.3 SPG1

Sample SPG1 is a pegmatite from the northern Houghton Inlier. This pegmatite intrudes the South Para Orthogneiss in the South Para Gorge, and cross cuts the S_1 metamorphic fabric (Figure 2c). Sample SPG1 yielded two distinct zircon morphologies. The first population (SPG1-a) is elongate, transparent, and frequently display prismatic terminations. These zircons range in size from 100 to 300 μm in length but rarely more than 50 μm in width. Under CL imaging this population did not display any zoning and were typically medium dark and homogeneous (Figure 3c). A total of 26 analyses were obtained from 26 grains of this population, of which 20 yielded ages within 5% of concordancy. These concordant analyses give a weighted mean $^{207}Pb/^{206}Pb$ age of 1561 ±13 Ma (n=20, MSWD = 0.35, probability = 0.996).

The second zircon population (SPG1-b) contained much larger zircons than group a, ranging in size between 200 μm to 400 μm with equant to tabular shapes. Few grains displayed prismatic terminations, and were opaque and honey coloured. Under CL several grains displayed faint oscillatory zoning, however most grains were dark and showed no visible texture (Figure 3d). A total of 26 analyses were conducted across 26 grains, with 25 analyses yielding ages within 5% of concordancy. These concordant analyses give a weighted mean $^{207}Pb/^{206}Pb$ age of 1577 ±11 Ma (n=25, MSWD = 0.19, probability = 1.00). This age is slightly older than that of population a, albeit within error.

4.1.4 KM12-11

Sample KM12-11 is a kyanite-tourmaline-chlorite schist from the northeastern Warren Inlier (Figure 2d). Kyanite is weakly aligned with the schistocity, which has been previously interpreted as a Delamerian aged fabric (S_4; see Chapter 2). Zircons separated from this sample were typically small and equant, ranging in size from 50 μm to 100 μm. Under CL imaging the zircon grains were frequently sector zoned and appeared to show textural cores and rims (Figure 3e). A total of 30 analyses were obtained from 29 grains, of which 13 yielded ages within 5% of concordancy. With the exception of a single young rim, which yielded a concordant $^{206}Pb/^{235}U$ age of 466 ±7 Ma, no distinguishable age difference was identified in any of the identified zones within the grains. The weighted mean $^{207}Pb/^{206}Pb$ age of the dominant population yielded 1584 ±15 Ma (n=12, MSWD = 0.56, probability = 0.86).

4.1.5 WI-07

Sample WI-07 was collected from a strongly deformed pegmatite in the northern Warren Inlier (Figure 2e). This pegmatite is composed primarily of quartz and K-feldspar, and preserves a strong biotite foliation. This pegmatite was tightly folded with axial

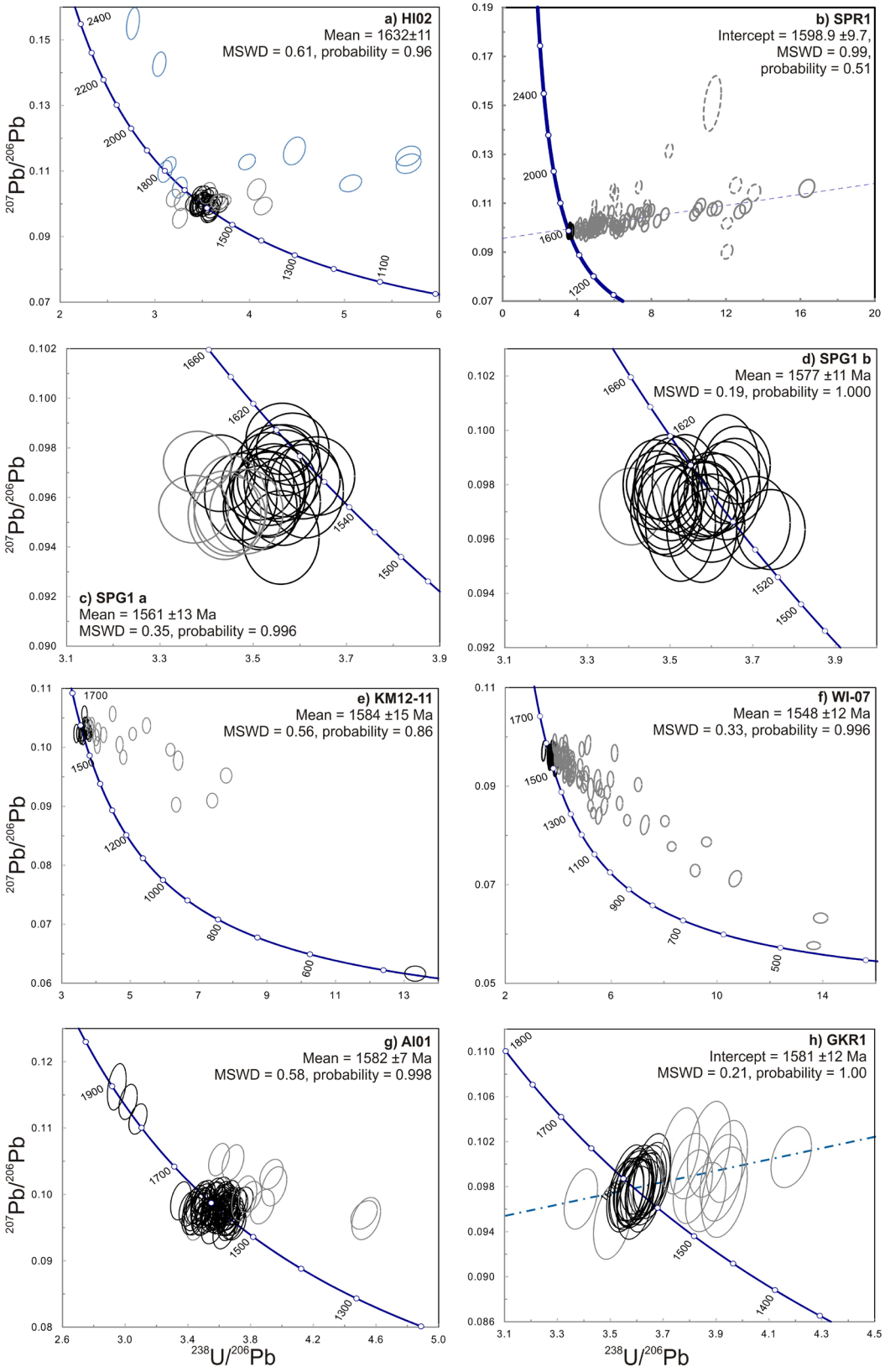

Figure 4: Terra-Wasserburg Concordia plots for each analysed sample. Ages and statistics presented with each sample are weighted mean or intercept age as indicated. Blue analyses in plot a) represent textural cores. Dashed ellipses in plot b) were excluded from the intercept calculation based on common Pb content.

planes that paralleled the local schistose foliation. These structures have previously been interpreted as being produced by the Cambrian-Ordovician Delamerian Orogeny (Chapter 2).

Zircons from this sample are typically elongate, often with prismatic terminations, and range in length from 100 µm to 400 µm. Under CL imaging many grains appeared metamict. Grains which did not appear metamict are largely dark and textureless (Figure 3f), with some grains displaying faint oscillatory zoning (Figure 3f). A total of 81 analyses were obtained from 80 grains, of which 19 yielded ages within 5% of concordancy. These concordant analyses give a weighted mean $^{207}Pb/^{206}Pb$ age of 1548 ±12 Ma (n=19, MSWD = 0.33, probability = 0.96).

4.1.6 AI-01

Sample AI-01 is a fine grained diopside-actinolite-microcline calcsilicate from the southern Aldgate Inlier. The zircons from this sample are typically tabular to equant grains ranging from 50 µm to 200 µm in size. Under CL imaging zircons display patchy and sector zones with some textural cores. Some grains also display faint oscillatory zoning, however the majority of grains displayed typically metamorphic textures (Figure 3g).

A total of 84 analyses were obtained from 82 grains, of which 73 were within 5% concordancy. Three analyses recorded ages ranging between 1850 Ma and 1750 Ma, and are likely detrital in origin. The remainder of the concordant analyses yielded a weighted mean $^{207}Pb/^{206}Pb$ age of 1581 ±7 Ma (n= 70, MSWD = 0.58, probability = 0.998).

4.1.7 GKR-1

Sample GKR-1 is a garnet-sillimanite-migmatite gneiss from the southern Myponga Inlier. This lithology is highly migmatised, containing 30 - 40% garnet bearing leucosome in many areas. The residuum is dominated by coarse grained garnet, sillimanite, biotite, quartz, and K-feldspar (Figure 2f). The zircons separated from this sample are typically round, equant grains which range in size between 50 µm to 200 µm. Under CL these grains are commonly sector zoned and many display lighter rims with dark cores (Figure 3h), however no age difference was identifiable between different textural zones.

A total of 31 analyses were obtained from 31 grains, of which 22 were within 5% concordancy. These concordant analyses give a weighted mean $^{207}Pb/^{206}Pb$ age of 1583 ±16 Ma (n=22, MSWD = 0.074, probability = 1.00). The Intercept age of this sample is 1581 ±12 Ma (MSWD = 0.21, probability = 1.000), and is the preferred age of this sample due to the more significant MSWD and smaller uncertainty.

4.2 REE Analyses

Two samples which contained garnet as a texturally peak metamorphic mineral were selected to assess the distribution of REE's between zircon and garnet; SPR1 from the northern Houghton Inlier, and GKR-1 from the southern Myponga Inlier. Chondrite normalised REE plots are presented in Figure 5.

4.2.1 SPR1

Elemental transects were taken across 6 garnets in thin section. Analysis by electron microprobe show no zoning in major elements, with garnet endmember proportions consistently flat across each garnet transect. Endmember proportions vary slightly between each garnet, but are consistently in the ranges of almandine 75-80%, pyrope 10-15%, grossular 2-5%, and spessartine 2-5% (Figure 6a). However, several garnet grains show a distinct zonation in REE across the garnet transects, with several grains showing HREE rich cores and relatively depleted rims (Figure 6c). The REE patterns in all of the analysed garnet from SPR1 yield steep LREE patterns (Figure 5a) with minor negative Ce anomalies (0.1 – 0.77, avg. 0.33) and strong negative Eu

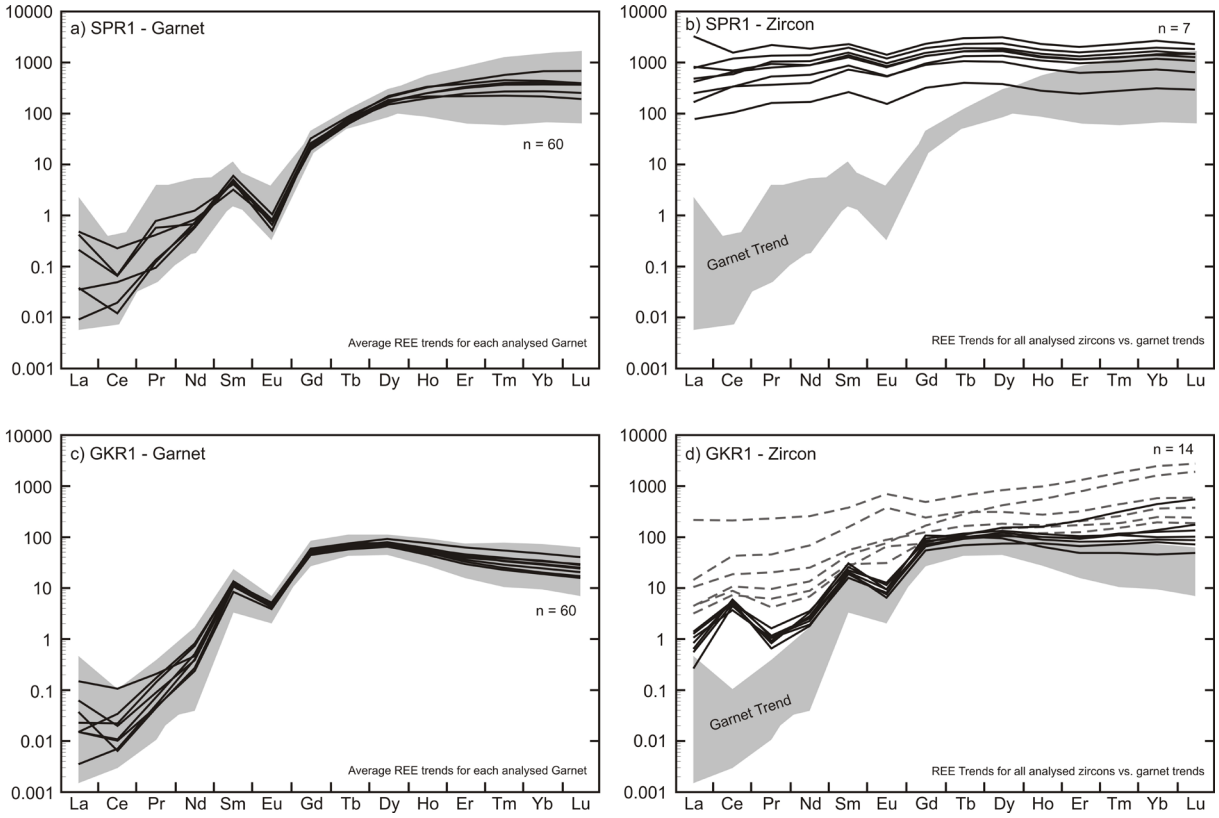

Figure 5: REE plots for garnet and zircon from SPR1 from the Houghton Inlier and GKR-1 from the Myponga Inlier. For the garnet analyses in a) and c) the range of garnet values are given by the grey shaded area, and the average values for each individual garnet analysed is given by the solid black lines. d) GKR-1 zircon REE trends, separated into two groups. Group 1 (solid black lines) are characterised by relatively low LREE trends, and large negative Eu anomalies. Group 2 (grey dashed) are characterised by relatively enriched LREE values and small negative to small positive Eu anomalies.

anomalies (0.03 – 0.06, avg. 0.053).

Of the 11 concordant zircons from SPR1, 7 were large enough to also analyse for REE. While the concentration of each element varied slightly between the analysed zircons, the trends are largely the same. All of the zircons are enriched in both LREE and HREE, with Chondrite normalised values ranging between 100 and 1600 (Figure 5b). The LREE, La to Sm, show a flat to weakly positive trend, with small to no Ce anomalies (0.83 – 1.2, avg. 0.9) and small negative Eu anomalies (0.53 – 0.62, avg. 0.61). The HREE have a flat to weakly negative trend.

4.2.2 GKR-1

Elemental analyses were obtained from 8 garnets in thin section. Major elements showed no zoning across the analysed garnets, consistently yielding approximately 75% almandine and approximately 20% pyrope (Figure 6b). REE concentrations also showed little to no zoning (Figure 6d). REE trends from the analysed garnets typically showed depletion in LREE giving a positive trend (Figure 5c), with minor negative Ce anomalies (0.21 – 0.85, avg. 0.39) and strong negative Eu anomalies (0.12 – 0.16, avg. 0.14). The MREE Gd, Tb, and Dy showed the most enrichment, with values typically approaching 100, followed by relative depletion in the HREE giving a weakly negative slope (Figure 5c).

14 REE analyses were acquired from concordant zircons from GKR-1. These

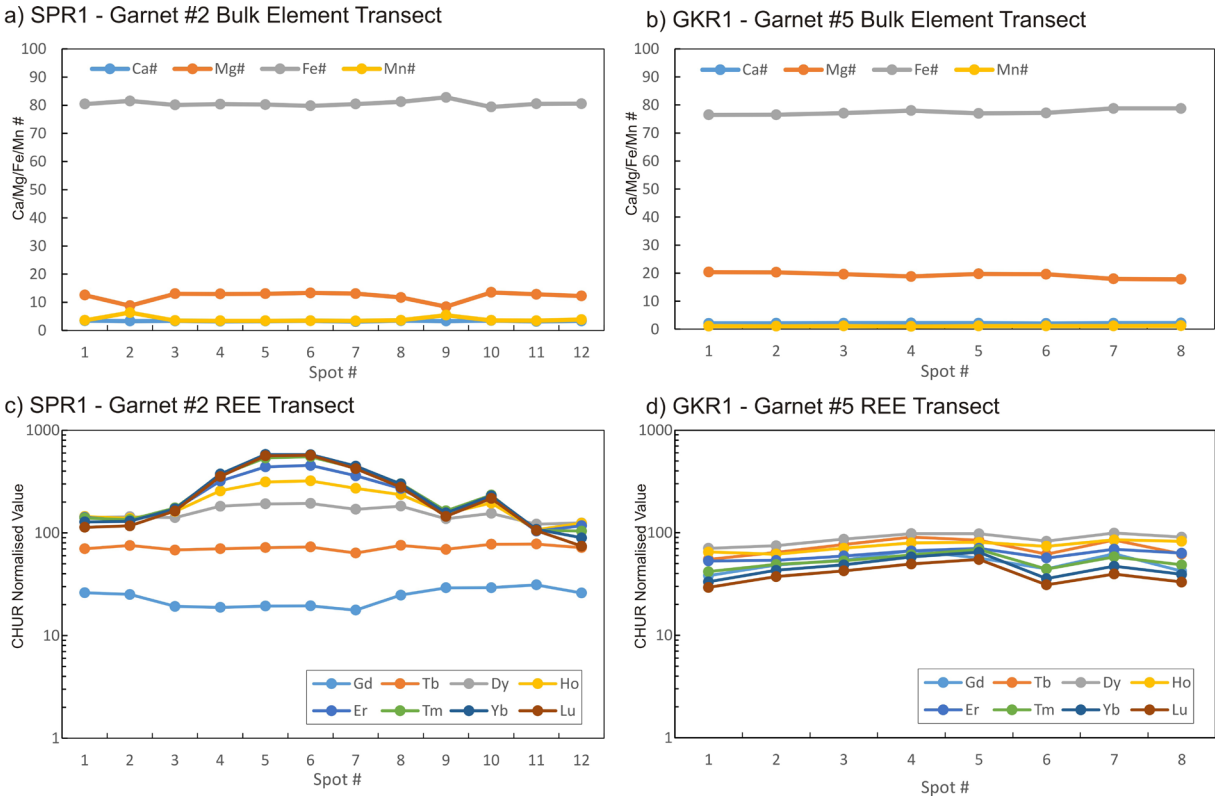

Figure 6: Transects across representative Garnets from SPR1 and GKR1. a) Garnet endmember proportions for a garnet from sample SPR1. b) Garnet endmember proportions for a typical garnet from sample GKR-1. c) Medium to heavy REE abundances from the same garnet represented in plot a. The core of the garnet shows an enrichment in M-HREE with a gradual decrease towards the rims. d) Medium to heavy REE abundances for the same garnet represented in plot b. The profiles appear relatively flat with no obvious zonation.

analyses displayed 2 groupings with characteristic LREE patterns (Figure 5d). In the first grouping, LREE are relatively depleted, with steeply positive trends, strongly positive Ce anomalies (3.47 – 7.16, avg. 5.27), and strong negative Eu anomalies (0.15 – 0.23, avg. 0.19). The second group yield relatively enriched LREE trends, which were shallowly positive to flat, had small positive to no Ce anomalies (0.97 – 1.78, avg. 1.40), and small negative to small positive positive Eu anomalies (0.77 – 2.00, avg. 1.20). These groupings do not correspond to any textural domains, and are only distinguishable by their REE pattern.

5. Discussion

5.1 U-Pb age constraints

The zircon U-Pb ages in this study are consistent with ages reported by previous authors (Crowhurst 1988, Belousova et al. 2006, Szpunar et al. 2007, Morrissey et al. 2013, Jagodzinski et al. 2017; Chapter 4), and show three stages of Palaeo-Mesoproterozoic metamorphism. In the Houghton Inlier, sample HI02 yields an age of 1632 ±11 Ma, which is comparable to several samples recording c. 1630 Ma metamorphism in this inlier (Belousova et al. 2006, Jagodzinski et al. 2017; Chapter 4). The other inliers largely do not record this period of metamorphism, and are dominated by c. 1590 Ma to 1580 Ma metamorphic ages. The 1590 Ma metamorphic period is recorded in two samples from the Houghton Inlier; sample SPG-1 and sample SPR1. Sample SPG-1 is a post S_1 pegmatite and contains zircons with two distinct morphologies. Population a is made up of

smaller and more prismatic zircon, and is interpreted to have grown during magmatic crystallisation. As such the crystallisation age of the pegmatite is interpreted to be 1561 ±13 Ma. Population b, with larger and more rounded zircon, is interpreted to have been inherited from the melt source which was metamorphosed at 1577 ±11 Ma. Sample SPG1 was collected less than a kilometre from the sample location of sample HI02, and suggests that at depth the U-Pb signatutre may be dominated by the influence of c. 1580 Ma metamorphism. Sample SPR1 was collected approximately 2 kilometers south of the sample location of HI02, but the zircons in SPR1 show no record of any c. 1630 Ma metamorphism. Zircon from sample SPR1 records an age of 1599 ±10 Ma, and is discussed in more detail below.

Metamorphic ages have also been recorded at c. 1580 Ma from the Warren and Aldgate inliers, with no indication of 1630 Ma metamorphism. Sample GKR 1 was collected from the same garnet-sillimanite-migmatite unit sampled by Szpunar et al. (2007) and yielded an age of 1581 ±12 Ma which is within uncertainty of the 1590 – 1580 Ma zircon and monazite ages obtained in that study. This age is consistent with metamorphic monazite as well as zircon from a pegmatite in the central Myponga Inlier (Crowhurst 1988, Morrissey et al. 2013). Sample AI01 from the southern Aldgate Inlier recorded a unimodal metamorphic age of 1581 ±7 Ma, which is consistent with the metamorphic age of 1582 ±4 Ma previously reported (Jagodzinski et al. 2017).

The 2 pegmatite samples analysed from the northern Barossa Complex yielded ages of 1561 ±13 Ma and 1548 ±12 Ma, which overlap within uncertainty. These ages also overlap within uncertainty of the ages obtained from monazites in the southern Houghton and southern Myponga inliers, from retrogressed rocks and retrograde shear zones (Morrissey et al. 2013). This demonstrates that during the interval 1560 Ma to 1550 Ma conditions occurred in the presently unexposed northern Barossa Complex sufficient to generate melt. Morrissey et al. (2013) interpreted this period to be a long lived retrogressive stage.

5.2 Zircon – Garnet REE distributions

The two garnet-bearing samples SPR-1 and SPG1 both yielded zircon U-Pb ages within error of 1590 Ma, but their REE distributions in zircon and garnet ($D_{REE}^{Zir/Gt}$) are distinctly different. The $D_{REE}^{Zir/Gt}$ for SPR1 and GKR1 were investigated using the D_{REE} trend method of Rubatto (2002) as well as the REE partitioning array plot of Taylor et al. (2017). These are presented in Figure 7.

5.2.1 SPR1 – Houghton Inlier

From the northern Barossa Complex, sample SPR1 yields garnet trends low in LREE and enriched in HREE, consistent with many previously reported compositions in metamorphic garnet (e.g. Bea 1996, Rubatto 2002, Whitehouse and Platt 2003, Taylor et al. 2017). The zircons analysed from this sample yield essentially flat REE trends with enriched values for all elements between 100 – 1000cn. This is highly unusual for metamorphic zircon, which typically preferentially incorporates HREE over LREE, leading to enriched values for the elements Gd to Lu and depleted values for La to Eu (Bea 1996, Rubatto 2002). As a result, the $D_{REE}^{Zir/Gt}$ values yield a negative to flat slope with increasing ionic radius (Figure 7a), which contrasts with equilibrium trends that have previously been published (Rubatto 2002, Whitehouse and Platt 2003, Hermann and Rubatto 2003, Rubatto and Hermann 2007).

The array plot (Figure 7b) also clearly shows the disequilibrium trend, with $Log(D_{REE})$ values far more negative than the experimental and modelled reference values used by Taylor et al. (2017). It is clear that the $D_{REE}^{Zir/Gt}$ trends recorded in SPR1 do not record equilibrium growth of zircon and garnet, and that zircon U-Pb age of 1599 ±10 Ma cannot be linked to peak metamorphism in

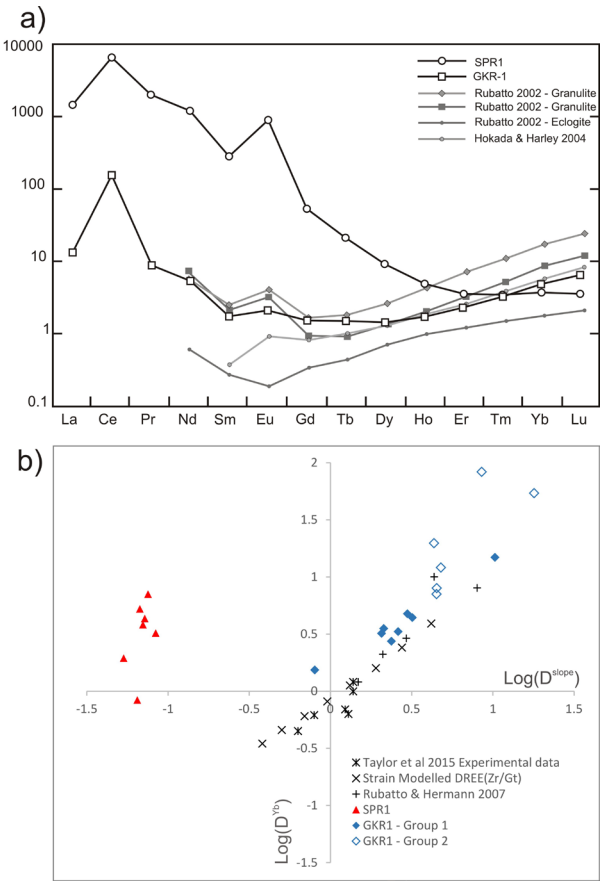

Figure 7: a) REE distribution coefficients between zircon and garnet, with selected published values for comparison. GKR1 $D_{REE}^{Zir/Gt}$ values calculated using zircon group 1 average values only. b) Array plot by the method of Taylor et al. (2017). Sample GKR1 group 1 zircons (LREE poor) plot close to the strain modelled data of Taylor et al. (2015) and the experimental data of Rubatto & Hermann (2007). GKR1 group 2 (LREE rich) show more variability and do not closely resemble the experimental data. Sample SPR1 does not plot near the experimental data and is clearly not representative of equilibrium growth.

the northern Houghton Inlier.

The flat REE patterns recorded in these zircons are consistent with those commonly recorded in hydrothermally grown or altered zircon (e.g. Geisler et al. 2003, Yang et al. 2014), and suggests that a hydrothermal fluid flow event affected the Houghton Inlier at 1600 Ma.

Small areas of apparent hydrothermal alteration and seritization have been previously recognised in the Houghton Inlier but are interpreted to be a product of retrogression and quartz veining during the Delamerian Orogeny (Chapter 2). It is possible that this is not the case for all such areas. Historically, some quartz veins in the northern Houghton Inlier have been found to be gold-bearing (Brown 1885). Hydrothermal activity has been identified as having been an influence in the generation of IOCG deposits in the eastern Gawler Craton between 1600 Ma and 1570 Ma (Skirrow et al. 2007, Reid et al. 2017b) and as such further characterisation of this hydrothermal activity may have economic implications. Given the intensity of weathering in the Houghton Inlier, coupled with greenschist retrograde metamorphism experienced during the Delamerian Orogeny, confidently identifying any Proterozoic hydrothermal activity would be difficult, and is beyond the scope of this work.

Given the disequilibrium $D_{REE}^{Zir/Gt}$ trend in SPR1, the timing of garnet growth and therefore peak metamorphic mineral growth, comes into question. There are two possible alternatives; peak metamorphism either predates or postdates the hydrothermal zircon growth at 1599 ±10 Ma. The $D_{REE}^{Zr/Gt}$ values for zircon and garnet in SPR1 for every REE is greater than 1, demonstrating a greater concentration of every REE in zircon. However the REE trends obtained from garnet do not appear to be affected by the growth of zircon. A common feature of garnet grown in equilibrium with zircon and melt is a depletion of HREE in garnet leading to a negative to flat slope in CHUR normalised values from GD to Lu (e.g. Hermann and Rubatto 2003, Clark et al. 2009). SPR1 shows positive slopes for the HREE in the garnet cores with a flattening of the slope towards the garnet rims. This is consistent with the progressive growth of garnet concentrating HREE without a major competitor for the HREE. Given this, it is most likely that the growth of garnet and other peak minerals occurred before the growth of

the 1599 ±10 Ma zircon population.

5.2.2 GKR1 – Myponga Inlier

Sample GKR1 from the southern Myponga Inlier records an age of 1581 ±12 Ma, which is consistent with previously reported geochronology from this lithology (Szpunar et al. 2007, Morrissey et al. 2013). The garnet REE trends from this sample are fairly consistent across the analysed grains and do not record any obvious zonation in either major or trace element composition (Figure 5, 6). However, the zircon analysed in this sample does record some variation in its REE composition. The bulk of analyses record REE trends consistent with what is typically expected from metamorphic zircon, with low concentrations of LREE, a positive Ce anomaly, and enrichment in HREE (e.g. Bea 1996, Rubatto 2002; Figure 5d). Several analyses also yield elevated LREE concentrations, little to no Ce anomaly, and present overall flat trends similar to that recorded in interpreted hydrothermal zircon in the Houghton Inlier. This suggests that both metamorphic and hydrothermal zircon formed at approximately the same time.

As some of the zircon in GKR-1 has a hydrothermal compositional signature, the $D_{REE}^{Zr/Gt}$ values for GKR1 have been calculated using the LREE depleted zircon which is consistent with metamorphic zircon that is unaltered by hydrothermal fluid. The resulting $D_{REE}^{Zr/Gt}$ values mimic values previously published as equilibrium partitioning trends in granulite facies rocks (e.g. Rubatto 2002, Hermann and Rubatto 2003, Buick et al. 2006, Rubatto and Hermann 2007; Figure 7). This is interpreted to represent the growth in equilibrium of garnet and zircon at 1581 ±12 Ma. This is also supported by the D_{REE} partitioning array plot (Figure 7b), where the compositionally metamorphic zircon plots very close to the experimental and modelled equilibrium partitioning data (Taylor et al. 2017). The group of zircons displaying elevated LREE compositions broadly follows the equilibrium trend but displays more scatter due to elevated $Log(D_{Yb})$ values outside the established range of equilibrium values, which may indicate hydrothermal modification of originally metamorphic zircon.

5.3 Metamorphic history of the Barossa Complex

The growing body of work on the Barossa Complex now allows for a much better understanding of the metamorphic history of this area. The first major metamorphic event occurred at 1630 Ma and is best recorded in the Houghton Inlier (Belousova et al. 2006, Jagodzinski et al. 2017; Chapter 4; this work). In many of the other inliers the c. 1630 Ma age is poorly preserved. Metamorphic overgrowths on detrital zircon in the Myponga Inlier at 1623 ±19 Ma (Chapter 4) demonstrate that this earlier stage of metamorphism likely affected the entire length of the exposed Barossa Complex.

In the Houghton Inlier, a pervasive low angle to layer parallel metamorphic fabric (S_1) is preserved. In metapelitic rocks this is characterised by sillimanite-garnet bearing assemblages that record relatively small volumes of leucosome material (Chapter 2). The formation of this fabric occurred during the growth of the garnet preserved in sample SPR1, and is interpreted to have occurred prior to 1599 ±10 Ma based on the REE distributions discussed above.

The dominant metamorphic U-Pb age preserved in both zircon and monazite throughout the Barossa Complex is that of the 1590-1580 Ma metamorphic stage. Metamorphic ages from the Warren, Aldgate, and Myponga inliers dominantly record ages between 1590 Ma to 1580 Ma in zircon and monazite (Szpunar et al. 2007, Morrissey et al. 2013, Jagodzinski et al. 2017, this study). This age bracket corresponds to the extensive migmatisation and development of garnet-bearing leucosomes in the southern Myponga Inlier, as demonstrated by the zircon-garnet REE partitioning in sample

GKR1. The lithology sampled for GKR1 was also sampled by Morrissey et al. (2013) for P-T phase equilibria modelling, which yielded peak conditions of 800-870°C and 8-9 kbar. Similar conditions of ~850°C and 7-8 Kbar were modelled for a garnet-sillimanite migmatite from the southern Houghton Inlier (Sample How-5, Morrissey et al. 2013). While samples from the Houghton Inlier dominantly preserve c. 1630 Ma metamorphic zircon ages in this work, Jagodzinski et al. (2017) obtained metamorphic zircon ages of 1585 ±8 Ma and 1609 ±7 Ma from a sample of biotite sericite gneiss from near the location of How-5 of Morrissey et al. (2013) in the southern Houghton Inlier. This may mean that the southern Houghton Inlier experienced similar metamorphic conditions to the Myponga Inlier at c. 1590 Ma. The monazite analysed from sample How-5 did not record c. 1590-1580 Ma metamorphic ages, but rather that of post peak metamorphism at c. 1550 Ma (Morrissey et al. 2013). The zircon in the Houghton Inlier within uncertainty of 1599 ±10 Ma may be the result of hydrothermal zircon growth. The apparent hydrothermal zircon growth at 1599 ±10 Ma identified in sample SPR1 means that c. 1600 Ma zircon ages from the Barossa Complex should be treated cautiously without trace element data to aid the interpretation of their origin. The uncertainty on the 1599 ±10 Ma age means that the 1610 Ma metamorphic zircon populations identified by Jagodzinski et al. (2017) overlap within error of this hydrothermal zircon age, and as such these populations may also have originated from hydrothermal growth. In the Myponga Inlier, several zircon grains from the c. 1581 Ma population also record a hydrothermal REE signature, indicating these fluids likely persisted throughout the system until 1580 Ma.

Given the comparatively lower metamorphic grades in the northern Houghton Inlier and the more prevalent preservation of c. 1630 Ma metamorphic zircon, it is likely that the Houghton Inlier was at a shallower crustal level at 1580 Ma than the rest of the exposed Barossa Complex, and did not undergo metamorphism of sufficient grade to extensively reset or grow new metamorphic zircon populations. The inherited zircon from a 1561 ±13 Ma pegmatite in the northern Houghton Inlier give a unimodal age of 1577 ±11 Ma, which suggests that at depth c. 1580 Ma metamorphic signatures are prevalent.

Given the interpretation that garnet growth occurred prior to hydrothermal zircon growth at 1599 ±10 Ma in the Houghton Inlier, and synchronous to metamorphic zircon growth at 1581 Ma in the Myponga Inlier, the metamorphic fabrics as defined by peak metamorphic minerals in these two inliers are of different generations. The S_1 metamorphic fabric is defined by sillimanite in the metapelites in the Houghton Inlier (Chapter 2), and developed synchronous to the extensive growth of 1630 Ma zircon, or alternatively at 1610 Ma (Jagodzinski et al. 2017; Chapter 4; this work). The 1623 Ma zircon population recorded in the central-southern Myponga Inlier (Chapter 4) demonstrates this earlier metamorphic stage also affected the Myponga Inlier. This makes it likely that the metamorphic fabric defined by high grade minerals in the southern Myponga Inlier is at least an S_2. The S_1 fabric in the Houghton inlier was deformed by D_2 and D_3 folding (Chapter 2). How these compare to the structures in the southern Myponga Inlier is unclear without further detailed structural work.

At c. 1560-1550 Ma, shear zones likely developed in the Myponga Inlier (Morrissey et al. 2013), coincident with the development of pegmatites in the Houghton and Warren inliers. These shear zones preserve east side down extensional kinematics, which are likely to reflect a late extensional stage in the early Mesoproterozoic, as these monazite ages have not been disturbed. Given the extensive rifting and extension that occurred in this area during the development of the Neoproterozoic Adelaide Rift Complex and Kanmantoo Trough (Preiss 2000), the possibility that these structures originated during the Neoproterozoic should not be ruled out.

5.4 Eastern Australia during the Paleo-Mesoproterozoic

The Barossa Complex is one of a number of metamorphosed sedimentary dominated rock systems in eastern Australia that were tectonised in the Late Palaeo- Early Mesoproterozoic. These include the eastern Gawler Craton, the Curnamona Province, the Mt. Isa Inlier, and the Georgetown and Coen inliers of the north-eastern North Australian Craton (NAC).

5.4.1 Eastern Gawler Craton

The geodynamic development of the Gawler Craton and its place within the development in Proterozoic Australia is still poorly understood, largely due to poor exposure limiting the extent to which different regions can be compared and related. The southern and eastern extents of the craton offer the best exposures and opportunities for study.

The Gawler Craton is characterised by an Archean core mantled by Palaeoproterozoic basins which extend outwards to the north and east (Hand et al. 2007; Figure 1). In the eastern Gawler Craton, the earliest of these is the c. 1865 Ma Darke Peak Group on the Eyre Peninsula (Szpunar et al. 2011) which was deposited shortly before the c. 1850 Ma intrusion of the Donington Suite during the Cornian Orogeny (Reid et al. 2008). This period was followed by widespread basin development between 1800-1740 Ma (Hand et al. 2007; Figure 8). Extensive volcano-sedimentary sequences were deposited as the Cleve Group (Szpunar et al. 2011), the Wallaroo Group and its equivalents in the Eastern Gawler Craton (Conor 1995, Cowley et al. 2003, Jagodzinski 2005), the Mt. Woods sequences (Chalmers 2007), and sedimentary sequences in the largely buried northern Gawler Craton (Payne et al. 2006, Reid et al. 2014, Armit et al. 2017).

This period of deposition continued until the onset of the craton-wide Kimban Event between 1730-1690 Ma (Payne et al. 2008, Hand et al. 2007, Swain et al. 2005). Metamorphism associated with the Kimban Event is recorded throughout most of the Gawler Craton and is associated with the development of terrane scale shear zones such as the Kalinjala Shear zone in the southeast Gawler Craton (Vassallo and Wilson 2002, Swain et al. 2005). The onset of deposition of the protoliths to the Barossa Complex on the eastern margin of the Gawler Craton and the Willyama Supergroup in the Curnamona Province occurred synchronous to the early stages of the Kimban Orogeny (Page et al. 2005b, Stevens et al. 2008; Chapter 4). The Peter Pan Supersuite occurred coevally with the Kimban Orogeny and is characterised by predominantly felsic magmas with minor mafics between 1740-1700 Ma (Wade and McAvaney 2017). These magmas are considered to be compositionally consistent with being produced by melting existing crust, with the mafic contributions suggested to be resultant of extensional phases within the Kimban Orogeny (Wade and McAvaney 2017). During the waning stages of the Kimban Event, the c. 1690-1670 Ma Tunkillia Suite was emplaced in the southwest Gawler Craton (Payne et al. 2010).

The next major period of tectonic activity was the development of the St. Peter Suite in an arc setting between 1620 Ma and 1608 Ma (Swain et al. 2008), which indicates subduction on the southwest margin of the craton. The period of 1590-1570 Ma was dominated by the extensive intrusion and eruption of the Hiltaba Suite I-A type granitoids and coeval Gawler Range Volcanics between 1590 Ma and 1570 Ma (Creaser and Cooper 1993, Fanning et al. 2007). This occurred synchronously with metamorphism in the northern regions of the craton which reached UHT conditions (Cutts et al. 2011, Forbes et al. 2011). The geodynamic setting of the Gawler Craton in the early Mesoproterozoic is still unclear (e.g. Hand et al. 2007, Betts et al. 2009, Reid and Hand 2012). The 1570-1540 Ma Kararan Orogeny reworked and metamorphosed the

northern Gawler Craton (Hand et al. 2007, Fanning et al. 2007), although this event is also poorly characterised.

5.4.2 Curnamona Province

The Willyama Supergroup (WSG) makes up a significant portion of the Curnamona Province (Conor and Preiss 2008). Deposition of the WSG occurred between c. 1720 Ma and 1640 Ma in an evolving rift basin (Figure 8; Page and Laing 1992, Raetz et al. 2002, Gibson et al. 2004, Page et al. 2005a, Page et al. 2005b, Stevens et al. 2008), and the stratigraphy is interpreted to represent rifting followed by a sag phase (Raetz et al. 2002, Page et al. 2005b). The lower WSG is dominated by psammitic to psammopelitic assemblages with calcsilicate and former evaporitic sequences (Willis et al. 1983, Stevens et al. 1988, Conor and Preiss 2008). In addition, syndepositional A-type and bimodal magmatism is associated with the rift phase of deposition (e.g. Ashley et al. 1996, Page et al. 2005a, Rutherford et al. 2006a, Raveggi et al. 2007). The sag phase of deposition between 1670-1640 Ma is characterised by a shift to dominantly pelitic compositions grading stratigraphically up to psammitic compositions, with no magmatism recorded over this interval (Page et al. 2005b, Conor and Preiss 2008).

The WSG underwent extensive metamorphism during the 1610-1580 Ma Olarian Orogeny, with exposed areas displaying greenschist to granulite facies metamorphism (Stevens et al. 1988, Page et al. 2005a, Stevens et al. 2008, Clark and Hand 2010). The onset of metamorphism has been suggested to have initiated at c. 1630 – 1620 Ma (Forbes et al. 2007, McFarlane and Frost 2009). This early metamorphic phase is associated with the development of a layer parallel metamorphic fabric (e.g. Marjoribanks et al. 1980, Forbes et al. 2005), which has been attributed to extension, as it is not accompanied by contractional deformation such as folding, and is largely absent in the uppermost units of the WSG (Forbes et al. 2005, Conor and Preiss 2008). Peak metamorphism is recorded in high grade metamorphic rocks by zircon and monazite at c. 1600 Ma (Page and Laing 1992, Raetz et al. 2002, Page et al. 2005a, White et al. 2005, Forbes et al. 2007, McFarlane and Frost 2009). The tectonic regime at this time was dominated by crustal thickening wherein isoclinal recumbent folds developed on a regional scale and were subsequently overprinted by upright folds (e.g. Marjoribanks et al. 1980, Clarke et al. 1986, Forbes et al. 2004, Conor and Preiss 2008). Peak metamorphic conditions were high-T low-P conditions of approximately 750^{o}C and 4-5 kbar (Wilson and Powell 2001, Forbes et al. 2005, White et al. 2005, Clark and Hand 2010). Anorogenic magmatism and volcanism occurred at c. 1580 Ma with the eruption of the Benagerie Volcanics. These cover much of the central Curnamona Province and have been linked to the Gawler Range Volcanics in the Gawler Craton (Wade 2011, Wade et al. 2012). The retrograde path of the Olarian Orogeny is obscured by the retrogressive effects of the Delamerian Orogeny at c. 500 Ma (Dutch et al. 2005, Rutherford et al. 2006b). Monazite attributed to a retrograde phase of the Olarian Orogeny has been identified recording ages between 1570 Ma and 1550 Ma (Rutherford et al. 2007).

5.4.3 Mt. Isa Inlier

The Mt. Isa Inlier in northeastern Australia contains an overlapping series of inverted Palaeoproterozoic basins which were deposited between c. 1890-1610 Ma (Figure 8; Betts et al. 2006, Foster and Austin 2008). The depositional environment of these sequences is considered to be a long lived extensional basin with multiple rift-sag phases and punctuated periods of contraction and inversion controlling the sedimentary facies and sediment flux (e.g. O'Dea et al. 1997, Betts et al. 1998, Southgate et al. 2000, Neumann et al. 2009).

The Mt. Isa Inlier sequences were deposited onto a basement recording metamorphic ages

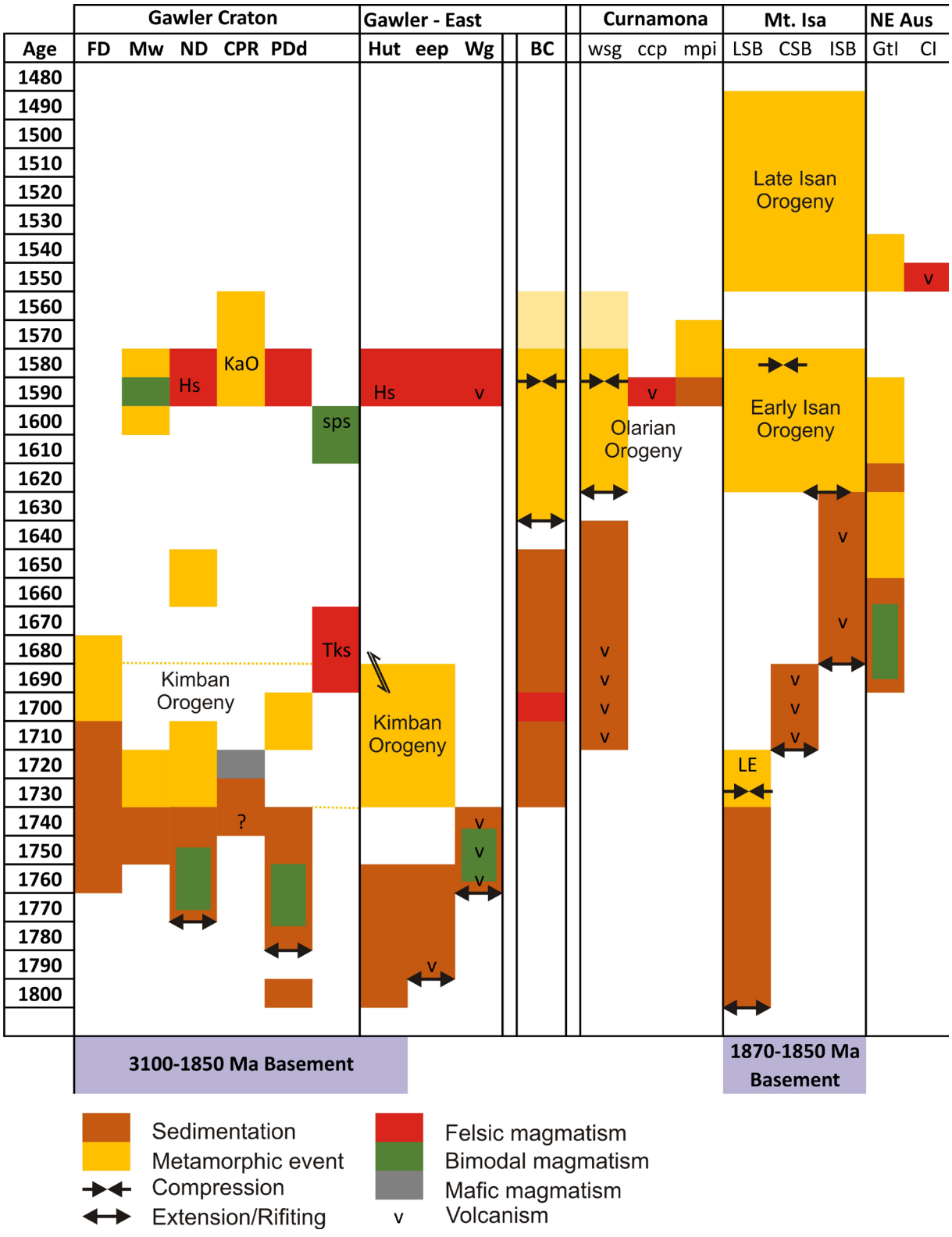

Figure 8: Time-space plot for Eastern Australia over the interval 1800 Ma to 1400 Ma focussing on events discussed in text. Abbreviations: Hs – Hiltaba Suite, KaO – Kararan Orogeny, sps – St. Peter Suite, Tks – Tunkillia Suite, Le - Leichhardt Event.

between 1870-1850 Ma (Page and Sweet 1998, Page and Williams 1988). The first major basin phase was the Leichhardt Superbasin which deposited between c. 1800-1740 Ma (Jackson et al. 2000) and included felsic to intermediate volcanism at 1740 Ma (Page and Sun 1998).

This period of deposition was terminated by the Leichhardt Event between c. 1740-1720 Ma, which included east-west compression and the intrusion of granites (Blaikie et al. 2017). This was followed by a renewed period of extension and the development of the c. 1710-1690 Ma Calvert Superbasin with the deposition of siliciclastic and volcanic sediment attributed to rifting (Southgate et al. 2000, Blake and Stewart 1992). A further period of deposition occurred between c. 1680 -1610 Ma and is termed the Isa Superbasin (Southgate et al. 2000, Foster and Austin 2008). This depositional phase is dominated by siliciclastic sediment with minor volcanics.

The major metamorphic event in the Mt. Isa Inlier is the Isan Orogeny (Blake and Stewart 1992, Betts et al. 2006). In the Eastern Fold Belt, early garnet and cordierite growth is dated by monazite at c. 1645-1630 Ma, with garnet compositions indicating high T-low P conditions of approximately 3 kbar and 550°C (Rubenach et al. 2008, Abu Sharib and Sanislav 2013). This period of metamorphism occured soon after the deposition of rift sequences at c. 1655 Ma (Page and Sun 1998, Foster and Austin 2008). An early low angle to layer parallel fabric is prevalent throughout the Mt. Isa Inlier (Adshead-Bell 1998, Rubenach and Lewthwaite 2002, Giles et al. 2006), and likely developed during this early metamorphic stage during extensional deformation (Giles et al. 2006).

Peak metamorphism occurred over the interval 1600-1580 Ma (e.g. Page and Sun 1998, Giles and Nutman 2002, Rubenach et al. 2008) with relatively high T-low P peak conditions of 600-650°C and 4-5 kbar (Rubenach 1992, Foster and Rubenach 2006, Rubenach et al. 2008, Abu Sharib and Sanislav 2013). The high temperature metamorphic conditions are considered to be a result of a combination of mafic intrusions emplacing heat into the upper crust (Abu Sharib and Sanislav 2013), thinned crust due to the overall extensional setting (Giles et al. 2006), and in some areas the burial and insulation of older high heat producing granites (McLaren et al. 1999). A second phase of deformation is considered to have occurred between 1550 Ma and 1500 Ma (Betts et al. 2006), and was associated with the intrusion of A-type granite batholiths between 1550 Ma to 1490 Ma (Page and Sun 1998, Mark 2001).

5.4.4 Georgetown & Coen inliers

In the northeastern NAC a series of Palaeo-Mesoproterozoic inliers are exposed (Figure 9a). These inliers are composed of variably metamorphosed sedimentary and igneous rocks (Withnall et al. 1988, Black and Withnall 1993). The dominant sedimentary facies are shallow water, fine grained clastic sediments, with some calcareous shales. Basalts and related dolerite intrusions also occur (Withnall et al. 1988). In the Georgetown Inlier, the Etheridge Group is the dominant sedimentary package. It is best constrained by syndepositional bimodal magmatic intrusions which range from 1695-1655 Ma, with the intrusion of felsic magmas between 1695-1684 Ma (Figure 8; Neumann and Kositcin 2011, Black et al. 1998). Mafic magmatism also occurred between 1675-1656 Ma (Black et al. 1998). The uppermost units of the Etheridge Group contain significant detrital zircon populations at c. 1655 Ma (Neumann and Kositcin 2011) which indicates a significant change in provenance in the upper units compared to the underlying sequences.

The growth of metamorphic monazite has been identified in three apparent pulses between 1650-1625 Ma, 1625-1585 Ma, and at 1550-1540 Ma (Cihan et al. 2006). The earliest of these metamorphic phases overlaps with the proposed timing of an unconformity that occurs between the Etheridge Group and the Langlovale Group, with the latter containing detrital zircon populations up to 1625 Ma in

age, demonstrating deposition occurred up to the onset of high grade metamorphism (Neumann and Kositcin 2011, Withnall and Henderson 2012). P-T conditions increase progressively from 3-4 kbar and 530-550°C to 6-7 kbar and 600-620°C (Black and Withnall 1993, Cihan et al. 2006).

Similarly in the Coen Inlier, metamorphic conditions of 6-7 kbar and 600-650oC occurred prior to a high T-low P overprint during the intrusion of the Forsayth Batholith at 1550 Ma (Boger and Hansen 2004). The widespread granite intrusions of the Forsayth Supersuite occurred at c. 1550 Ma and are typically S-type (Black and McCulloch 1990).

5.5.5 Evolution of Eastern Proterozoic Australia

Many reconstruction models have attempted to determine the Palaeogeographic history of the Proterozoic Australian continent (e.g. Myers et al. 1996, Betts and Giles 2006, Wade et al. 2006, Cawood and Korsch 2008, Payne et al. 2009, Smits et al. 2014, Betts et al. 2015, Aitken et al. 2016). In many of these reconstructions, special focus is given to the eastern margin of Australia during the Proterozoic as it is frequently proposed to have been connected with Laurentia. The timing of this connection and the relative position of each continent is debated (e.g. Moores 1991, Li et al. 1995, Karlstrom et al. 1999, Wingate et al. 2002, Li and Evans 2011, Smits et al. 2014, Mulder et al. 2015). While it is beyond the scope of this work to fully address the wider Proterozoic evolution of Australia, the Barossa Complex provides valuable insight into the development of eastern Australia during this time.

Many authors have proposed a link between the rift system accommodating the Willyama Supergroup in the Curnamona Province, the Calvert - Mt. Isa Groups in the Mt. Isa Inlier, and the Etheridge Group of the Georgetown Inlier based on similar depositional timing, sedimentary facies, base metal mineralisation, and igneous geochemistry (Giles et al. 2002, Page et al. 2005b, Payne et al. 2006, Betts and Giles 2006, Baker et al. 2010). This link is further strengthened by similarities in the timing, deformation style, and metamorphic histories of these regions (e.g. Giles et al. 2004, Betts and Giles 2006, Aitken et al. 2016). Based on this correlation, Giles et al. (2004) proposed a reconstruction wherein the Gawler Craton was rotated 52° counterclockwise from its present position such that the Curnamona Province and Mt. Isa Inlier were juxtaposed in a continuous rift basin. In reconstructions utilising this arrangement, the position of Barossa Complex falls within the proposed extent of this basin (Figure 9b; Aitken et al. 2016). The depositional timing of the Barossa Complex protoliths overlaps with that of the Willyama Supergroup (Raetz et al. 2002, Page et al. 2005a, Page et al. 2005b), the 1740-1655 Ma sequences in the Gawler Craton (Payne et al. 2006, Howard et al. 2011), and the deposition of the Calvert Superbasin in the Mt. Isa inlier (Page et al. 2000, Neumann et al. 2009). The low angle metamorphic fabric at 1630 Ma followed by peak metamorphism at 1590-1580 Ma with compressional deformation in the Curnamona Province, Mt. Isa and Georgetown Inliers, and the Barossa Complex indicates a shared metamorphic and deformational history across the entire eastern Proterozoic margin of Australia (Morrissey et al. 2013, Betts et al. 2015, Aitken et al. 2016).

Poor exposure of the Gawler Craton has hampered the understanding of the tectonic development, particularly for areas such as the Nawa Domain in the northern Gawler Craton which has largely been characterised by drill core (e.g. Payne et al. 2006, Howard et al. 2011, Armit et al. 2017). The model by Betts et al. (2015) proposes that the Gawler Craton is oroclinally bent, and restores the roughly semicircular domains into linear segments which align with the NAC. This model has many merits, such as explaining the presently highly arcuate extent of the St. Peter arc (Dutch et al. 2016), and the development of extensional basins with bimodal volcanism

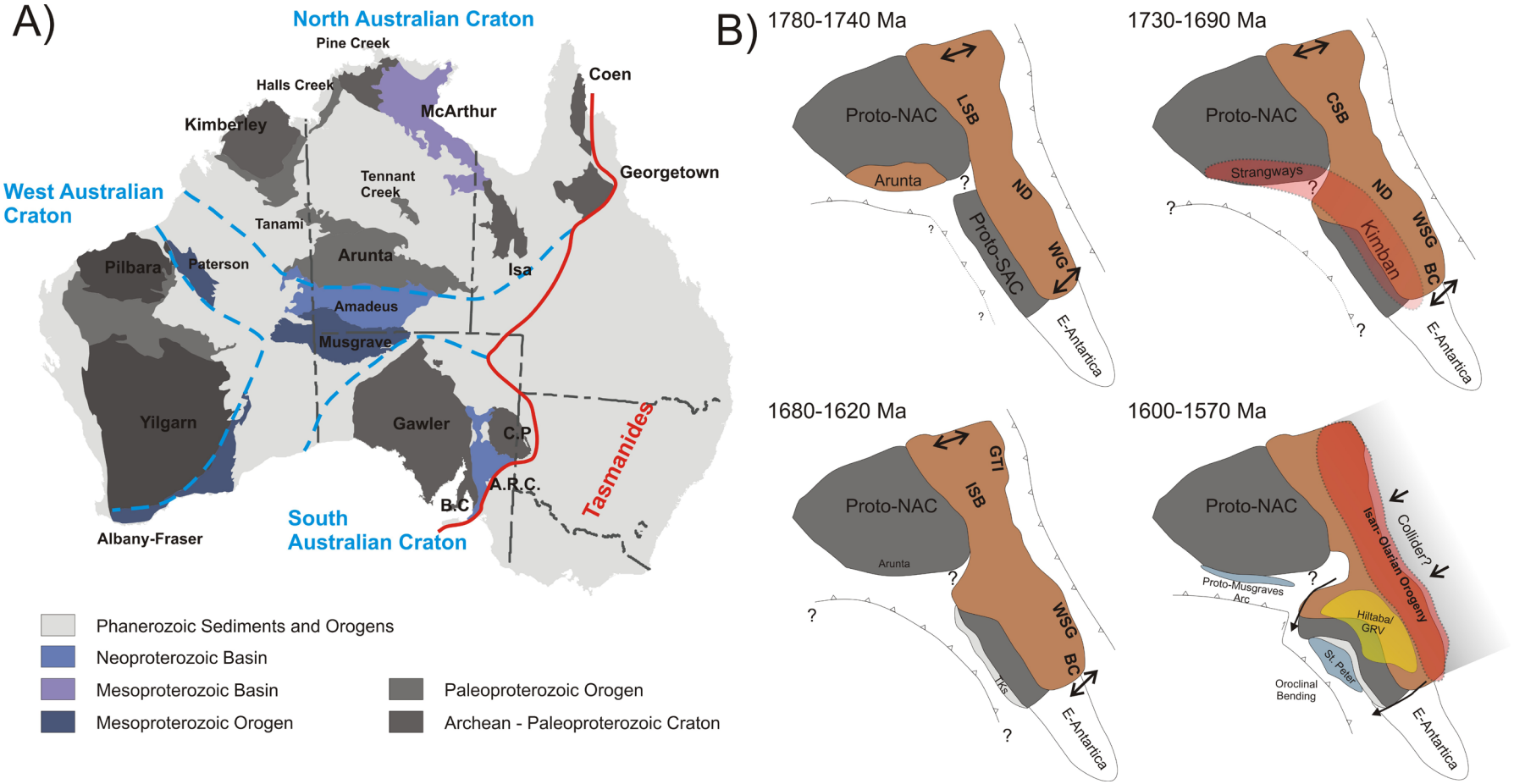

Figure 9: Proterozoic domains in Australia and schematic models of Australia during the interval 1780 Ma to 1570 Ma, showing proposed positions of subduction zones and orogenic events, modified after Betts et al. (2015) and Armit et al. (2016). Abbreviations: ARC – Adelaide Rift Complex, CP – Curnamona Province, LSB – Leichhardt Super Basin, Nd – Nawa Domain, WG – Wallaroo Group, CSB – Calvert Super Basin, WSB – Willyama Supergroup, BC – Barossa Complex, GTI – Georgetown Inlier, ISB – Isa Super Basin, GRV – Gawler Range Volcanics

in the west, north, and eastern extent of the craton between 1800 Ma and 1720 Ma (Hand et al. 2007, Payne et al. 2009).

In reconstructing the Palaeoproterozoic Gawler Craton, the unfolded orocline makes the 1800 Ma to 1720 Ma basins an essentially linear system of linked basins, or one large basin, which would align with the Leichhardt-Calvert Basins in the Mt. Isa Inlier (Figure 9b; Betts et al. 2015). This is consistent with detrital zircon provenance studies which suggested a North Australian Craton source for sediments in the northern Gawler Craton and Willyama supergroup (Payne et al. 2006, Barovich and Hand 2008, Howard et al. 2011, Reid et al. 2017a), and a possible link between these basins (Payne et al. 2006, Reid et al. 2017a).

The tectonic drivers of the 1800 Ma to 1600 Ma extensional basins in eastern Australia are currently debated. The largest school of thought proposes a back arc regime as the driving force behind the rift basin, but the position of the subduction zone is contested (Giles et al. 2002, Betts and Giles 2006, Cawood and Korsch 2008, Betts et al. 2015, Aitken et al. 2016). Some of these workers have argued for a subduction zone on the southern margin of the proto-Australian continent, as the Arunta region in the southern NAC experienced bimodal magmatism and sedimentation in a back-arc setting between c. 1810 Ma to 1770 Ma (Figure 9; Maidment et al. 2005, Wade et al. 2008, Howlett et al. 2015). The southwestern Gawler Craton, which has been interpreted to be contiguous to the southern NAC during the late Palaeoproterozoic (Cawood and Korsch 2008, Betts et al. 2015, Aitken et al. 2016), does not contain any unambiguous evidence of subduction related processes prior to 1620 Ma (Swain et al. 2008, Payne et al. 2010). Any link between the southern NAC and the western Gawler Craton remains ambiguous and requires further work to elucidate the processes involved.

Recent structural work has shown that the Leichardt Superbasin in the Mt. Isa Inlier underwent east-west compression at c. 1740 Ma, which is consistent with the eastern margin of Australia being active during the period 1800-1700 Ma (Blaikie et al. 2017). In both the Mt. Isa Inlier and the eastern Gawler Craton a progressive eastward migration of the locus of volcanism and basin development has been identified (Foster and Austin 2008, Kositcin 2010). This, in combination with punctuated periods of contraction, is consistent with a progressively retreating arc that is impacted on by changes in subduction angle (Kositcin 2010).

The driving force behind the Olarian-Isan Orogeny has been suggested to represent the collision of western Laurentia and eastern Australia between c. 1600 Ma and 1550 Ma (e.g. Betts et al. 2015, Aitken et al. 2016). This is based upon paleomagnetic evidence indicating Australia and Laurentia shared a similar apparent polar wander path after 1650 Ma (e.g. Pisarevsky et al. 2014), detrital zircon from Mesoproterozoic basins suggesting a connection between the two continents (e.g. Goodge et al. 2008, Mulder et al. 2015), and 1710 Ma volcanic arc material obducted onto the western margin of Laurentia at c. 1600 Ma (Nielsen et al. 2013, Thorkelson and Laughton 2016). Nonetheless, this evidence does not explicitly demonstrates a connection between eastern Australia and western Laurentia in the earliest Mesoproterozoic, and the driving force behind the Olarian-Isan Orogeny is still unclear.

While the Barossa Complex itself does not provide a direct link to a specific continental configuration, the transcontinental basin and metamorphic regime that it is a part of points towards a long lived plate margin environment during the Late Palaeoproterozoic, which should be considered in future paleogeographic reconstruction models.

6. Conclusions

The Barossa Complex in the southeastern Gawler Craton preserves an 80 m.y. period of Palaeo-Mesoproterozoic metamorphism.

The earliest metamorphic stage involved the development of a layer parallel metamorphic fabric at c. 1630-1625 Ma. This period of metamorphism is primarily recorded in the Houghton Inlier, which is interpreted to preserve this shallower crustal level than the other inliers. At c. 1600 Ma hydrothermal fluid infiltrated the northern Barossa Complex growing or resetting zircon at this time. The source and significance of this fluid is currently unknown, but may be linked to the wider scale hydrothermal events in the Gawler Craton at this time. Peak metamorphic conditions of 800-870°C and 8-9 kbar were reached during the interval 1590 Ma to 1580 Ma, which likely reflects a period of contractional deformation. During the period 1570 Ma to 1550 Ma retrograde shear zones developed, and in the northern inliers small volumes of melt intruded.

These metamorphic characteristics and timing correlates to those preserved in other eastern Australian Palaeo-Mesoproterozoic domains, specifically the Curnamona Province and Mt. Isa Inlier. When taking into account the depositional timing of the Barossa Complex and its position in Proterozoic reconstruction models it becomes apparent that the Barossa Complex is part of the Olarian - Isan system. Recent Proterozoic reconstruction models indicate that basins in the eastern NAC and SAC developed in response to west-dipping subduction on the eastern Australian margin between 1800 Ma and 1600 Ma. This period of basin development was terminated by the Olarian – Isan Orogeny. The tectonic driver of this event remains uncertain.

References

Abu Sharib, A. S. A. A. & Sanislav, I. V., 2013. Polymetamorphism accompanied switching in horizontal shortening during Isan Orogeny: Example from the Eastern Fold Belt, Mount Isa Inlier, Australia. Tectonophysics, 587, 146-167.

Adshead-Bell, N. S., 1998. Evolution of the Starra and Selwyn high-strain zones, Eastern fold belt, Mount Isa Inlier; implications for Au-Cu mineralization. Economic Geology, 93(8), 1450-1462.

Aitken, A. R. A., Betts, P. G., Young, D. A., Blankenship, D. D., Roberts, J. L. & Siegert, M. J., 2016. The Australo-Antarctic Columbia to Gondwana transition. Gondwana Research, 29(1), 136-152.

Armit, R., Betts, P. G., Schaefer, B. F., Yi, K., Kim, Y., Dutch, R. A., Reid, A., Jagodzinski, L., Giles, D. & Ailleres, L., 2017. Late Palaeoproterozoic evolution of the buried northern Gawler Craton. Precambrian Research, 291, 178-201.

Ashley, P. M., Cook, N. D. J. & Fanning, C. M., 1996. Geochemistry and age of metamorphosed felsic igneous rocks with A-type affinities in the Willyama Supergroup, Olary Block, South Australia, and implications for mineral exploration. Lithos, 38(3), 167-184.

Baker, M. J., Crawford, A. J. & Withnall, I. W., 2010. Geochemical, Sm–Nd isotopic characteristics and petrogenesis of Paleoproterozoic mafic rocks from the Georgetown Inlier, north Queensland: Implications for relationship with the Broken Hill and Mount Isa Eastern Succession. Precambrian Research, 177(1–2), 39-54.

Barovich, K. & Hand, M., 2008. Tectonic setting and provenance of the Paleoproterozoic Willyama Supergroup, Curnamona Province, Australia: Geochemical and Nd isotopic constraints on contrasting source terrain components. Precambrian Research, 166(1–4), 318-337.

Bea, F., 1996. Residence of REE, Y, Th and U in Granites and Crustal Protoliths; Implications for the Chemistry of Crustal Melts. Journal of Petrology, 37(3), 521-552.

Belousova, E. A., Preiss, W. V., Schwarz, M. P. & Griffin, W. L., 2006. Tectonic affinities of the Houghton Inlier, South Australia: U - Pb and Hf-isotope data from zircons in modern stream sediments. Australian Journal of Earth Sciences, 53(6), 971-989.

Betts, P. G., Armit, R. J., Stewart, J., Aitken, A. R. A., Ailleres, L., Donchak, P., Hutton,

L., Withnall, I. & Giles, D., 2015. Australia and Nuna. Geological Society, London, Special Publications, 424.

Betts, P. G. & Giles, D., 2006. The 1800–1100 Ma tectonic evolution of Australia. Precambrian Research, 144(1–2), 92-125.

Betts, P. G., Giles, D., Foden, J., Schaefer, B. F., Mark, G., Pankhurst, M. J., Forbes, C. J., Williams, H. A., Chalmers, N. C. & Hills, Q., 2009. Mesoproterozoic plume-modified orogenesis in eastern Precambrian Australia. Tectonics, 28(3), TC3006.

Betts, P. G., Giles, D., Mark, G., Lister, G. S., Goleby, B. R. & Aillères, L., 2006. Synthesis of the proterozoic evolution of the Mt Isa Inlier. Australian Journal of Earth Sciences, 53(1), 187-211.

Betts, P. G., Giles, D. & Schaefer, B. F., 2008. Comparing 1800–1600 Ma accretionary and basin processes in Australia and Laurentia: Possible geographic connections in Columbia. Precambrian Research, 166(1–4), 81-92.

Betts, P. G., Lister, G. S. & O'Dea, M. G., 1998. Asymmetric extension of the Middle Proterozoic lithosphere, Mount Isa terrane, Queensland, Australia. Tectonophysics, 296(3–4), 293-316.

Black, L. P., Gregory, P., Withnall, I. W. & Bain, J. H. C., 1998. U-Pb zircon age for the Etheridge Group, Georgetown region, north Queensland: Implications for relationship with the Broken Hill and Mt Isa sequences. Australian Journal of Earth Sciences, 45(6), 925-935.

Black, L. P. & McCulloch, M. T., 1990. Isotopic evidence for the dependence of recurrent felsic magmatism on new crust formation: An example from the Georgetown region of Northeastern Australia. Geochimica et Cosmochimica Acta, 54(1), 183-196.

Black, L. P. & Withnall, I., 1993. The ages of Proterozoic granites in the Georgetown Inlier of northeastern Australia, and their relevance to the dating of tectonothermal events. AGSO Journal of Australian Geology & Geophysics, 14(4), 331-341.

Blaikie, T. N., Betts, P. G., Armit, R. J. & Ailleres, L., 2017. The ca. 1740–1710 Ma Leichhardt Event: Inversion of a continental rift and revision of the tectonic evolution of the North Australian Craton. Precambrian Research, 292, 75-92.

Blake, D. H. & Stewart, A. J., 1992. Stratigraphic and tectonic framework, Mount Isa Inlier. In: Detailed Studies of the Mount Isa Inlier (eds Stewart, A. J. & Blake, D. H.), pp. 1-11, Australian Government Publishing Service, Canberra.

Boger, S. D. & Hansen, D., 2004. Metamorphic evolution of the Georgetown Inlier, northeast Queensland, Australia; evidence for an accreted Palaeoproterozoic terrane? Journal of Metamorphic Geology, 22(6), 511-527.

Brookfield, M. E., 1993. Neoproterozoic Laurentia-Australia fit. Geology, 21(8), 683-686.

Brown, H. Y., 1885. Geological Map of Barossa and Para Wirra. Parliamentary Paper No. 178, South Australia.

Buick, I. S., Hermann, J., Williams, I. S., Gibson, R. L. & Rubatto, D., 2006. A SHRIMP U–Pb and LA-ICP-MS trace element study of the petrogenesis of garnet–cordierite–orthoamphibole gneisses from the Central Zone of the Limpopo Belt, South Africa. Lithos, 88(1–4), 150-172.

Cawood, P. A. & Korsch, R. J., 2008. Assembling Australia: Proterozoic building of a continent. Precambrian Research, 166(1–4), 1-35.

Chalmers, N. C., 2007. Mount Woods Domain: Proterozoic metasediments and intrusives, Department of Primary Industries and Resources, South Australia.

Cihan, M., Evins, P., Lisowiec, N. & Blake, K., 2006. Time constraints on deformation and metamorphism from EPMA dating of monazite in the Proterozoic Robertson River Metamorphics, NE Australia. Precambrian Research, 145(1–2), 1-23.

Clark, C., Collins, A. S., Santosh, M., Taylor, R. & Wade, B. P., 2009. The P-T-t architecture of a Gondwanan suture: REE, U–Pb and Ti-in-zircon thermometric constraints

from the Palghat Cauvery shear system, South India. Precambrian Research, 174(1–2), 129-144.

Clark, C. & Hand, M., 2010. Decoding Mesoproterozoic and Cambrian metamorphic events in Willyama Complex metapelites through the application of Sm–Nd garnet geochronology and P–T pseudosection analysis. Gondwana Research, 17(1), 59-74.

Clarke, G. L., Burg, J. P. & Wilson, C. J. L., 1986. Stratigraphic and structural constraints on the proterozoic tectonic history of the Olary Block, South Australia. Precambrian Research, 34(2), 107-137.

Conor, C., 1995. Moonta-Wallaroo Region: An interpretation of the geology of the Maitland and Wallaroo 1:100 000 sheet areas, South Australian Department of Primary Industries and Resources.

Conor, C. H. H. & Preiss, W. V., 2008. Understanding the 1720–1640 Ma Palaeoproterozoic Willyama Supergroup, Curnamona Province, Southeastern Australia: Implications for tectonics, basin evolution and ore genesis. Precambrian Research, 166(1–4), 297-317.

Cowley, W., Conor, C. & Zang, W., 2003. New and revised Proterozoic stratigraphic units on northern Yorke Peninsula. MESA Journal, 29, 46-58.

Creaser, R. A. & Cooper, J. A., 1993. U-Pb geochronology of middle Proterozoic felsic magmatism surrounding the Olympic Dam Cu-U-Au-Ag and Moonta Cu-Au-Ag deposits, South Australia. Economic Geology, 88(1), 186-197.

Crowhurst, P. V., 1988. The geology, petrology and geochemistry of the Proterozoic inlier, south of Myponga, Fleurieu Peninsula, South Australia. Unpub. BSc (Hons) Thesis, University of Adelaide.

Cutts, K., Hand, M. & Kelsey, D. E., 2011. Evidence for early Mesoproterozoic (ca. 1590 Ma) ultrahigh-temperature metamorphism in southern Australia. Lithos, 124(1–2), 1-16.

Dalziel, I. W. D., 1991. Pacific margins of Laurentia and East Antarctica-Australia as a conjugate rift pair: Evidence and implications for an Eocambrian supercontinent. Geology, 19(6), 598-601.

Dutch, R., Reid, A., Smithies, H., Payne, J., Jagodzinski, E. A., Kirkland, C. L., Pawley, M., Spaggiari, C. & Preiss, W., 2016. Is Southern Australia bent?; recognition of a contiguous Palaeoproterozoic magmatic arc along the western margin of the Mawson Continent. In: Australian Earth Sciences Convention, Geological Society of Australia, Adelaide.

Dutch, R. A., Hand, M. & Clark, C., 2005. Cambrian reworking of the southern Australian Proterozoic Curnamona Province: constraints from regional shear-zone systems. Journal of the Geological Society, 162(5), 763-775.

Fanning, C. M., Reid, A. J. & Teale, G., 2007. A geochronological framework for the Gawler Craton, South Australia. Geological Survey of South Australia.

Forbes, C. J., Betts, P. G. & Lister, G. S., 2004. Synchronous development of Type 2 and Type 3 fold interference patterns: evidence for recumbent sheath folds in the Allendale Area, Broken Hill, NSW, Australia. Journal of Structural Geology, 26(1), 113-126.

Forbes, C. J., Betts, P. G., Weinberg, R. & Buick, I. S., 2005. A structural metamorphic study of the Broken Hill Block, NSW, Australia. Journal of Metamorphic Geology, 23(8), 745-770.

Forbes, C. J., Giles, D., Betts, P. G., Weinberg, R. & Kinny, P. D., 2007. Dating Prograde Amphibolite and Granulite Facies Metamorphism Using In Situ Monazite U-Pb SHRIMP Analysis. The Journal of Geology, 115(6), 691-705.

Forbes, C. J., Giles, D., Hand, M., Betts, P. G., Suzuki, K., Chalmers, N. & Dutch, R., 2011. Using P–T paths to interpret the tectonothermal setting of prograde metamorphism: An example from the northeastern Gawler Craton, South Australia. Precambrian Research, 185(1–2), 65-85.

Foster, D. R. W. & Austin, J. R., 2008. The

1800–1610 Ma stratigraphic and magmatic history of the Eastern Succession, Mount Isa Inlier, and correlations with adjacent Paleoproterozoic terranes. Precambrian Research, 163(1–2), 7-30.

Foster, D. R. W. & Rubenach, M. J., 2006. Isograd pattern and regional low-pressure, high-temperature metamorphism of pelitic, mafic and calc-silicate rocks along an east – west section through the Mt Isa Inlier. Australian Journal of Earth Sciences, 53(1), 167-186.

Geisler, T., Rashwan, A. A., Rahn, M. K. W., Poller, U., Zwingmann, H., Pidgeon, R. T., Schleicher, H. & Tomaschek, F., 2003. Low-temperature hydrothermal alteration of natural metamict zircons from the Eastern Desert, Egypt. Mineralogical Magazine, 67(3), 485-508.

Gibson, G. M., Peljo, M. & Chamberlain, T., 2004. Evidence and timing of crustal extension versus shortening in the early tectonothermal evolution of a Proterozoic continental rift sequence at Broken Hill, Australia. Tectonics, 23(5), n/a-n/a.

Gibson, G. M., Rubenach, M. J., Neumann, N. L., Southgate, P. N. & Hutton, L. J., 2008. Syn- and post-extensional tectonic activity in the Palaeoproterozoic sequences of Broken Hill and Mount Isa and its bearing on reconstructions of Rodinia. Precambrian Research, 166(1), 350-369.

Giles, D., Betts, P. & Lister, G., 2002. Far-field continental backarc setting for the 1.80–1.67 Ga basins of northeastern Australia. Geology, 30(9), 823-826.

Giles, D., Betts, P. G., Aillères, L., Hulscher, B., Hough, M. & Lister, G. S., 2006. Evolution of the Isan Orogeny at the southeastern margin of the Mt Isa Inlier. Australian Journal of Earth Sciences, 53(1), 91-108.

Giles, D., Betts, P. G. & Lister, G. S., 2004. 1.8-1.5-Ga links between the North and South Australian Cratons and the Early-Middle Proterozoic configuration of Australia. Tectonophysics, 380(1-2), 27-41.

Giles, D. & Nutman, A. P., 2002. SHRIMP U–Pb monazite dating of 1600–1580 Ma amphibolite facies metamorphism in the southeastern Mt Isa Block, Australia. Australian Journal of Earth Sciences, 49(3), 455-465.

Goodge, J. W., Vervoort, J. D., Fanning, C. M., Brecke, D. M., Farmer, G. L., Williams, I. S., Myrow, P. M. & DePaolo, D. J., 2008. A Positive Test of East Antarctica–Laurentia Juxtaposition Within the Rodinia Supercontinent. Science, 321(5886), 235-240.

Hand, M., Reid, A. & Jagodzinski, L., 2007. Tectonic framework and evolution of the Gawler craton, Southern Australia. Economic Geology, 102(8), 1377-1395.

Hermann, J. & Rubatto, D., 2003. Relating zircon and monazite domains to garnet growth zones: Age and duration of granulite facies metamorphism in the Val Malenco lower crust. Journal of Metamorphic Geology, 21(9), 833-852.

Howard, K. E., Hand, M., Barovich, K. M., Payne, J. L., Cutts, K. A. & Belousova, E. A., 2011. U–Pb zircon, zircon Hf and whole-rock Sm–Nd isotopic constraints on the evolution of Paleoproterozoic rocks in the northern Gawler Craton. Australian Journal of Earth Sciences, 58(6), 615-638.

Howlett, D., Raimondo, T. & Hand, M., 2015. Evidence for 1808–1770 Ma bimodal magmatism, sedimentation, high-temperature deformation and metamorphism in the Aileron Province, central Australia. Australian Journal of Earth Sciences, 62(7), 831-852.

Jackson, M. J., Scott, D. L. & Rawlings, D. J., 2000. Stratigraphic framework for the Leichhardt and Calvert Superbasins: Review and correlations of the pre- 1700 Ma successions between Mt Isa and McArthur River. Australian Journal of Earth Sciences, 47(3), 381-403.

Jackson, S. E., Pearson, N. J., Griffin, W. L. & Belousova, E. A., 2004. The application of laser ablation-inductively coupled plasma-mass spectrometry to in situ U–Pb zircon geochronology. Chemical Geology, 211(1–2), 47-69.

Jagodzinski, E.J. 2005. Compilation of

SHRIMP U–Pb geochronological data, Olympic Domain, Gawler Craton, South Australia, 2001–2003. Geoscience Australia, Record 2005/20, 197 pp.

Jagodzinski, E.A., Meaney, K., Szpunar, M., and Fraser, G., 2017. SHRIMP U-Pb dating of the Barossa Complex, South Australia: exploring tectonic links between the Gawler Craton and Curnamona Province. Report Book 2017/00017. Department of the Premier and Cabinet, South Australia, Adelaide.

Karlstrom, K. E., Harlan, S. S., Williams, M. L., Geissman, J. W. & Åhäll, K., 1999. Refining Rodinia: Geologic Evidence for the Australia–Western U.S. connection in the Proterozoic GSA Today, 9(10), 1-7.

Kositcin, N., 2010. Geodynamic Synthesis of the Gawler Craton and Curnamona Province. Geoscience Australia, Record, 2010/27, 113p.

Li, Z.-X. & Evans, D. A. D., 2011. Late Neoproterozoic 40° intraplate rotation within Australia allows for a tighter-fitting and longer-lasting Rodinia. Geology, 39(1), 39-42.

Li, Z.-X., Zhang, L. & Powell, C. M., 1995. South China in Rodinia: Part of the missing link between Australia–East Antarctica and Laurentia? Geology, 23(5), 407-410.

Ludwig, K. R., 2003. Users Manual for Isoplot 3.75. In: Special Publication No. 5, Berkeley Geochronology Center

Maidment, D. W., Hand, M. & Williams, I. S., 2005. Tectonic cycles in the Strangways Metamorphic Complex, Arunta Inlier, central Australia: geochronological evidence for exhumation and basin formation between two high-grade metamorphic events. Australian Journal of Earth Sciences, 52(2), 205-215.

Marjoribanks, R. W., Rutland, R. W. R., Glen, R. A. & Laing, W. P., 1980. The structure and tectonic evolution of the Broken Hill region, Australia. Precambrian Research, 13(2), 209-240.

Mark, G., 2001. Nd isotope and petrogenetic constraints for the origin of the Mount Angelay igneous complex: implications for the origin of intrusions in the Cloncurry district, NE Australia. Precambrian Research, 105(1), 17-35.

McFarlane, C. R. M. & Frost, B. R., 2009. Constraints on the early metamorphic evolution of Broken Hill, Australia, from in situ U-Pb dating and REE geochemistry of monazite. Journal of Metamorphic Geology, 27(1), 3-17.

McLaren, S., Sandiford, M. & Hand, M., 1999. High radiogenic heat–producing granites and metamorphism—An example from the western Mount Isa inlier, Australia. Geology, 27(8), 679-682.

Medig, K. P. R., Thorkelson, D. J., Davis, W. J., Rainbird, R. H., Gibson, H. D., Turner, E. C. & Marshall, D. D., 2014. Pinning northeastern Australia to northwestern Laurentia in the Mesoproterozoic. Precambrian Research, 249, 88-99.

Merdith, A. S., Collins, A. S., Williams, S. E., Pisarevsky, S., Foden, J. D., Archibald, D. B., Blades, M. L., Alessio, B. L., Armistead, S., Plavsa, D., Clark, C. & Müller, R. D., 2017. A full-plate global reconstruction of the Neoproterozoic. Gondwana Research, 50, 84-134.

Moores, E. M., 1991. Southwest U.S.-East Antarctic (SWEAT) connection: A hypothesis. Geology, 19(5), 425-428.

Morrissey, L. J., Hand, M., Wade, B. P. & Szpunar, M., 2013. Early Mesoproterozoic metamorphism in the Barossa Complex, South Australia: links with the eastern margin of Proterozoic Australia. Australian Journal of Earth Sciences, 60(8), 769-795.

Mulder, J. A., Halpin, J. A. & Daczko, N. R., 2015. Mesoproterozoic Tasmania: Witness to the East Antarctica–Laurentia connection within Nuna. Geology, 43(9), 759-762.

Myers, J. S., Shaw, R. D. & Tyler, I. M., 1996. Tectonic evolution of Proterozoic Australia. Tectonics, 15(6), 1431-1446.

Neumann, N. & Kositcin, N., 2011. New SHRIMP U-Pb zircon ages from north Queensland, 2007–2010. In: Record, pp. 82, Geoscience Australia.

Neumann, N. L., Southgate, P. N. & Gibson, G. M., 2009. Defining unconformities in Proterozoic sedimentary basins using detrital geochronology and basin analysis—An example from the Mount Isa Inlier, Australia. Precambrian Research, 168(3–4), 149-166.

Nielsen, A. B., Thorkelson, D. J., Gibson, H. D. & Marshall, D. D., 2013. The Wernecke igneous clasts in Yukon, Canada: Fragments of the Paleoproterozoic volcanic arc terrane Bonnetia. Precambrian Research, 238, 78-92.

O'Dea, M. G., Lister, G. S., Betts, P. G. & Pound, K. S., 1997. A shortened intraplate rift system in the Proterozoic Mount Isa terrane, NW Queensland, Australia. Tectonics, 16(3), 425-441.

Page, R. N., Stevens, B. P. J. & Gibson, G. M., 2005a. Geochronology of the sequence hosting the Broken Hill Pb-Zn-Ag orebody, Australia. Economic Geology, 100(4), 633-661.

Page, R. W., Conor, C. H. H., Stevens, B. P. J., Gibson, G. M., Preiss, W. V. & Southgate, P. N., 2005b. Correlation of Olary and Broken Hill Domains, Curnamona Province: Possible relationship to Mount Isa and other North Australian Pb-Zn-Ag-bearing successions. Economic Geology, 100(4), 663-676.

Page, R. W., Jackson, M. J. & Krassay, A. A., 2000. Constraining sequence stratigraphy in north Australian basins: SHRIMP U–Pb zircon geochronology between Mt Isa and McArthur River*. Australian Journal of Earth Sciences, 47(3), 431-459.

Page, R. W. & Laing, W. P., 1992. Felsic metavolcanic rocks related to the Broken Hill Pb-Zn-Ag orebody, Australia; geology, depositional age, and timing of high-grade metamorphism. Economic Geology, 87(8), 2138-2168.

Page, R. W. & Sun, S. S., 1998. Aspects of geochronology and crustal evolution in the Eastern Fold Belt, Mt Isa Inlier. Australian Journal of Earth Sciences, 45(3), 343-361.

Page, R. W. & Sweet, I. P., 1998. Geochronology of basin phases in the western Mt Isa Inlier, and correlation with the McArthur Basin. Australian Journal of Earth Sciences, 45(2), 219-232.

Page, R. W. & Williams, I. S., 1988. Age of the barramundi orogeny in northern Australia by means of ion microprobe and conventional U-Pb zircon studies. Precambrian Research, 40, 21-36.

Payne, J. L., Barovich, K. M. & Hand, M., 2006. Provenance of metasedimentary rocks in the northern Gawler Craton, Australia: Implications for Palaeoproterozoic reconstructions. Precambrian Research, 148(3–4), 275-291.

Payne, J. L., Ferris, G., Barovich, K. M. & Hand, M., 2010. Pitfalls of classifying ancient magmatic suites with tectonic discrimination diagrams: An example from the Paleoproterozoic Tunkillia Suite, southern Australia. Precambrian Research, 177(3–4), 227-240.

Payne, J. L., Hand, M., Barovich, K., Reid, A. & Evans, D. A. D., 2009. Correlations and Reconstruction Models for the 2500-1500 Ma evolution of the Mawson Continent. In: Paleoproterozoic Supercontinents and Global Evolution (eds Reddy, S. M., Mazumder, R., Evans, D. A. D. & Collins, A. S.), pp. 319-357, Geological Society, London.

Payne, J. L., Hand, M., Barovich, K. M. & Wade, B. P., 2008. Temporal constraints on the timing of high-grade metamorphism in the northern Gawler Craton: implications for assembly of the Australian Proterozoic. Australian Journal of Earth Sciences, 55(5), 623-640.

Pearce, N. J. G., Perkins, W. T., Westgate, J. A., Gorton, M. P., Jackson, S. E., Neal, C. R. & Chenery, S. P., 1997. A Compilation of New and Published Major and Trace Element Data for NIST SRM 610 and NIST SRM 612 Glass Reference Materials. Geostandards Newsletter, 21(1), 115-144.

Pisarevsky, S. A., Elming, S.-Å., Pesonen, L. J. & Li, Z.-X., 2014. Mesoproterozoic paleogeography: Supercontinent and beyond.

Precambrian Research, 244, 207-225.

Preiss, W. V., 1993. Basement Inliers of the Mount Lofty Ranges. In: The Geology of South Australia, Volume 1, The Precambrian (eds Drexel, J. F., Preiss, W. V. & Parker, A. J.), pp. 102-105, Geological Survey of South Australia, Adelaide.

Preiss, W. V., 2000. The Adelaide Geosyncline of South Australia and its significance in Neoproterozoic continental reconstruction. Precambrian Research, 100(1-3), 21-63.

Raetz, M., Krabbendam, M. & Donaghy, A. G., 2002. Compilation of Pb zircon data from the Willyama Supergroup, Broken Hill region, Australia: Evidence for three tectonostratigraphic successions and four magmatic events? Australian Journal of Earth Sciences, 49(6), 965-983.

Raveggi, M., Giles, D., Foden, J. & Raetz, M., 2007. High Fe–Ti mafic magmatism and tectonic setting of the Paleoproterozoic Broken Hill Block, NSW, Australia. Precambrian Research, 156(1–2), 55-84.

Reid, A., Hand, M., Jagodzinski, E., Kelsey, D. & Pearson, N., 2008. Paleoproterozoic orogenesis in the southeastern Gawler Craton, South Australia. Australian Journal of Earth Sciences, 55(4), 449-471.

Reid, A. J. & Hand, M., 2012. Mesoarchean to Mesoproterozoic Evolution of the Southern Gawler Craton, South Australia. Journal of International Geoscience, 35(1), 216-225.

Reid, A. J., Jagodzinski, E. A., Armit, R. J., Dutch, R. A., Kirkland, C. L., Betts, P. G. & Schaefer, B. F., 2014. U-Pb and Hf isotopic evidence for Neoarchean and Paleoproterozoic basement in the buried northern Gawler Craton, South Australia. Precambrian Research, 250, 127-142.

Reid, A. J., Jagodzinski, E. A., Wade, C. E., Payne, J. L. & Jourdan, F., 2017a. Recognition of c. 1780Ma magmatism and metamorphism in the buried northeastern Gawler Craton: Correlations with events of the Aileron Province. Precambrian Research, 302, 198-220.

Reid, A. J., Jourdan, F. & Jagodzinski, E. A., 2017b. Mesoproterozoic fluid events affecting Archean crust in the northern Olympic Cu–Au Province, Gawler Craton: insights from 40Ar/39Ar thermochronology. Australian Journal of Earth Sciences, 64(1), 103-119.

Rubatto, D., 2002. Zircon trace element geochemistry: partitioning with garnet and the link between U–Pb ages and metamorphism. Chemical Geology, 184(1–2), 123-138.

Rubatto, D. & Hermann, J., 2007. Experimental zircon/melt and zircon/garnet trace element partitioning and implications for the geochronology of crustal rocks. Chemical Geology, 241(1–2), 38-61.

Rubenach, M. J., 1992. Proterozoic low-pressure/high-temperature metamorphism and an anticlockwise P–T–t path for the Hazeldene area, Mount Isa Inlier, Queensland, Australia. Journal of Metamorphic Geology, 10(3), 333-346.

Rubenach, M. J., Foster, D. R. W., Evins, P. M., Blake, K. L. & Fanning, C. M., 2008. Age constraints on the tectonothermal evolution of the Selwyn Zone, Eastern Fold Belt, Mount Isa Inlier. Precambrian Research, 163(1–2), 81-107.

Rubenach, M. J. & Lewthwaite, K. A., 2002. Metasomatic albitites and related biotite-rich schists from a low-pressure polymetamorphic terrane, Snake Creek Anticline, Mount Isa Inlier, north-eastern Australia: microstructures and P–T–d paths. Journal of Metamorphic Geology, 20(1), 191-202.

Rutherford, L., Barovich, K., Hand, M. & Foden, J., 2006a. Continental ca 1.7 – 1.69 Ga Fe-rich metatholeiites in the Curnamona Province, Australia: a record of melting of a heterogeneous, subduction-modified lithospheric mantle. Australian Journal of Earth Sciences, 53(3), 501-519.

Rutherford, L., Hand, M. & Barovich, K., 2007. Timing of Proterozoic metamorphism in the southern Curnamona Province: implications for tectonic models and continental reconstructions. Australian Journal of Earth Sciences, 54(1), 65-81.

Rutherford, L., Hand, M. & Mawby, J., 2006b. Delamerian-aged metamorphism in the southern Curnamona Province, Australia: implications for the evolution of the Mesoproterozoic Olarian Orogeny. Terra Nova, 18(2), 138-146.

Skirrow, R. G., Bastrakov, E. N., Barovich, K., Fraser, G. L., Creaser, R. A., Fanning, C. M., Raymond, O. L. & Davidson, G. J., 2007. Timing of Iron Oxide Cu-Au-(U) Hydrothermal Activity and Nd Isotope Constraints on Metal Sources in the Gawler Craton, South Australia. Economic Geology, 102(8), 1441-1470.

Smits, R. G., Collins, W. J., Hand, M., Dutch, R. & Payne, J., 2014. A Proterozoic Wilson cycle identified by Hf isotopes in central Australia: Implications for the assembly of Proterozoic Australia and Rodinia. Geology, 42(3), 231-234.

Southgate, P. N., Bradshaw, B. E., Domagala, J., Jackson, M. J., Idnurm, M., Krassay, A. A., Page, R. W., Sami, T. T., Scott, D. L., Lindsay, J. F., McConachie, B. A. & Tarlowski, C., 2000. Chronostratigraphic basin framework for Palaeoproterozoic rocks (1730–1575 Ma) in northern Australia and implications for base-metal mineralisation. Australian Journal of Earth Sciences, 47(3), 461-483.

Stevens, B. P. J., Barnes, R. G., Brown, R. E., Stroud, W. J. & Willis, I. L., 1988. The Willyama Supergroup in the Broken Hill and Euriowie Blocks, New South Wales. Precambrian Research, 40-41(0), 297-327.

Stevens, B. P. J., Page, R. W. & Crooks, A., 2008. Geochronology of Willyama Supergroup metavolcanics, metasediments and contemporaneous intrusions, Broken Hill, Australia. Australian Journal of Earth Sciences, 55(3), 301-330.

Swain, G., Barovich, K., Hand, M., Ferris, G. & Schwarz, M., 2008. Petrogenesis of the St Peter Suite, southern Australia: Arc magmatism and Proterozoic crustal growth of the South Australian Craton. Precambrian Research, 166(1-4), 283-296.

Swain, G. M., Hand, M., Teasdale, J., Rutherford, L. & Clark, C., 2005. Age constraints on terrane-scale shear zones in the Gawler Craton, southern Australia. Precambrian Research, 139(3–4), 164-180.

Szpunar, M., Hand, M., Barovich, K., Jagodzinski, E. & Belousova, E., 2011. Isotopic and geochemical constraints on the Paleoproterozoic Hutchison Group, southern Australia: Implications for Paleoproterozoic continental reconstructions. Precambrian Research, 187(1–2), 99-126.

Szpunar, M., Wade, B., Hand, M. P. & Barovich, K. M., 2007. Timing of Proterozoic high-grade metamorphism in the Barossa Complex, southern South Australia; exploring the extent of the 1590 Ma event. MESA Journal, 47, 21-27.

Taylor, R. J. M., Clark, C., Harley, S. L., Kylander-Clark, A. R. C., Hacker, B. R. & Kinny, P. D., 2017. Interpreting granulite facies events through rare earth element partitioning arrays. Journal of Metamorphic Geology, 35(7), 759–775.

Taylor, R. J. M., Harley, S. L., Hinton, R. W., Elphick, S., Clark, C. & Kelly, N. M., 2015. Experimental determination of REE partition coefficients between zircon, garnet and melt: a key to understanding high-T crustal processes. Journal of Metamorphic Geology, 33(3), 231-248.

Thorkelson, D. J. & Laughton, J. R., 2016. Paleoproterozoic closure of an Australia–Laurentia seaway revealed by megaclasts of an obducted volcanic arc in Yukon, Canada. Gondwana Research, 33, 115-133.

Vassallo, J. J. & Wilson, C. J. L., 2002. Palaeoproterozoic regional-scale non-coaxial deformation: an example from eastern Eyre Peninsula, South Australia. Journal of Structural Geology, 24(1), 1-24.

Wade, B. P., Barovich, K. M., Hand, M., Scrimgeour, I. R. & Close, D. F., 2006. Evidence for Early Mesoproterozoic Arc Magmatism in the Musgrave Block, Central Australia: Implications for Proterozoic Crustal Growth and Tectonic Reconstructions of Australia. The Journal of Geology, 114(1), 43-63.

Wade, B. P., Hand, M., Maidment, D. W., Close, D. F. & Scrimgeour, I. R., 2008. Origin of metasedimentary and igneous rocks from the Entia Dome, eastern Arunta region, central Australia: a U – Pb LA-ICPMS, SHRIMP and Sm – Nd isotope study. Australian Journal of Earth Sciences, 55(5), 703-719.

Wade, C. E., 2011. Definition of the Mesoproterozoic Ninnerie Supersuite, Curnamona Province, South Australia. MESA Journal, 62, 25-42.

Wade CE and McAvaney SO 2017. Stratigraphy and geochemistry of the 1745–1700 Ma Peter Pan Supersuite, Report Book 2016/00026. Department of State Development, South Australia, Adelaide

Wade, C. E., Reid, A. J., Wingate, M. T. D., Jagodzinski, E. A. & Barovich, K., 2012. Geochemistry and geochronology of the c. 1585 Ma Benagerie Volcanic Suite, southern Australia: Relationship to the Gawler Range Volcanics and implications for the petrogenesis of a Mesoproterozoic silicic large igneous province. Precambrian Research, 206–207(0), 17-35.

White, R. W., Pomroy, N. E. & Powell, R., 2005. An in situ metatexite–diatexite transition in upper amphibolite facies rocks from Broken Hill, Australia. Journal of Metamorphic Geology, 23(7), 579-602.

Whitehouse, M. J. & Platt, J. P., 2003. Dating high-grade metamorphism—constraints from rare-earth elements in zircon and garnet. Contributions to Mineralogy and Petrology, 145(1), 61-74.

Willis, I. L., Brown, R. E., Stroud, W. J. & Stevens, B. P. J., 1983. The early Proterozoic Willyama supergroup: Stratigraphic subdivision and interpretation of high to low-grade metamorphic rocks in the Broken Hill Block, New South Wales. Journal of the Geological Society of Australia, 30(1-2), 195-224.

Wilson, C. J. L. & Powell, R., 2001. Strain localisation and high-grade metamorphism at Broken Hill, Australia: a view from the Southern Cross area. Tectonophysics, 335(1–2), 193-210.

Wingate, M. T. D., Pisarevsky, S. A. & Evans, D. A. D., 2002. Rodinia connections between Australia and Laurentia: no SWEAT, no AUSWUS? Terra Nova, 14(2), 121-128.

Withnall, I. & Henderson, B., 2012. Accretion on the long-lived continental margin of northeastern Australia. Journal of International Geoscience, 35(1), 166 - 176.

Withnall, I. W., Bain, J. H. C., Draper, J. J., MacKenzie, D. E. & Oversby, B. S., 1988. Proterozoic stratigraphy and tectonic history of the Georgetown Inlier, northeastern Queensland. Precambrian Research, 40, 429-446.

Yang, W.-B., Niu, H.-C., Shan, Q., Sun, W.-D., Zhang, H., Li, N.-B., Jiang, Y.-H. & Yu, X.-Y., 2014. Geochemistry of magmatic and hydrothermal zircon from the highly evolved Baerzhe alkaline granite: implications for Zr–REE–Nb mineralization. Mineralium Deposita, 49(4), 451-470.

Zhang, S., Li, Z.-X., Evans, D. A. D., Wu, H., Li, H. & Dong, J., 2012. Pre-Rodinia supercontinent Nuna shaping up: A global synthesis with new paleomagnetic results from North China. Earth and Planetary Science Letters, 353–354(0), 145-155.

Chapter 5 Supplementary Data 1: Barossa Complex U-Pb Isotopic Data

Sample HI02: Psammopelite Gneiss, Northern Houghton Inlier

Analysis #	$^{207}Pb/^{235}U$ Ratio	1σ	$^{206}Pb/^{238}U$ Ratio	1σ	Rho	$^{207}Pb/^{206}Pb$ Age	2σ	$^{206}Pb/^{238}U$ Age	2σ	Conc. %	Comments
HI02_01	3.87791	0.06362	0.2793	0.00406	0.6250613	1637.4	24.9	1587.8	20.5	97	
HI02_05	3.98642	0.06434	0.28243	0.00408	0.6443874	1668.0	23.8	1603.6	20.5	96	
HI02_07	3.91596	0.06644	0.28528	0.00418	0.6132272	1616.3	26.0	1617.9	21.0	100	
HI02_08	3.98848	0.06767	0.28561	0.00418	0.6153467	1648.3	25.8	1619.5	21.0	98	
HI02_10	3.8998	0.06866	0.28229	0.00417	0.5905814	1628.3	27.4	1602.9	21.0	98	
HI02_11	4.0512	0.07025	0.28808	0.00423	0.6062411	1661.3	26.5	1631.9	21.2	98	
HI02_12	3.80894	0.06812	0.27919	0.00413	0.5840151	1605.0	28.0	1587.3	20.8	99	
HI02_13	3.96467	0.07284	0.28473	0.00428	0.5771375	1642.6	28.8	1615.1	21.5	98	
HI02_14	3.82324	0.06742	0.27547	0.00408	0.6070693	1636.6	26.9	1568.5	20.6	96	
HI02_16	3.96471	0.07477	0.29002	0.00437	0.5614352	1608.4	29.9	1641.6	21.9	102	
HI02_17	4.0623	0.07775	0.29395	0.00444	0.553842	1628.6	30.5	1661.2	22.1	102	
HI02_18	4.07422	0.08238	0.28809	0.00443	0.5203117	1671.3	32.8	1632.0	22.2	98	
HI02_20	3.93171	0.08084	0.27936	0.0043	0.5121314	1662.4	33.5	1588.1	21.7	96	
HI02_23	4.02293	0.08984	0.28526	0.00449	0.4679791	1666.1	37.4	1617.8	22.5	97	
HI02_24	3.88182	0.087	0.28383	0.00445	0.4686487	1609.2	37.7	1610.6	22.4	100	
HI02_26	3.72643	0.07005	0.27105	0.00409	0.5761081	1618.9	29.5	1546.1	20.8	96	
HI02_31	3.89507	0.08374	0.28275	0.00441	0.489955	1622.7	35.8	1605.2	22.2	99	
HI02_34	3.97468	0.09226	0.28997	0.00461	0.4448454	1613.5	39.6	1641.4	23.0	102	
HI02_35	3.94788	0.09533	0.28732	0.00463	0.4222523	1618.0	41.7	1628.1	23.2	101	
HI02_36	3.95977	0.09516	0.28865	0.00462	0.4250546	1615.0	41.4	1634.8	23.1	101	
HI02_42	3.98609	0.0848	0.2898	0.00453	0.4967134	1619.7	35.2	1640.5	22.7	101	
HI02_43	3.99363	0.08614	0.28999	0.00455	0.4937984	1622.0	35.8	1641.5	22.8	101	
HI02_44	3.77303	0.08842	0.27899	0.00453	0.4484753	1588.1	40.1	1586.3	22.8	100	
HI02_46	3.78221	0.08699	0.27753	0.00444	0.4591599	1602.5	38.9	1578.9	22.4	99	
HI02_47	3.75649	0.08624	0.27995	0.00446	0.4669288	1573.5	38.8	1591.1	22.5	101	
HI02_48	3.95435	0.09654	0.28661	0.00469	0.4370822	1625.4	41.7	1624.5	23.5	100	
HI02_49	3.75251	0.0904	0.27861	0.0045	0.4469352	1580.5	41.1	1584.4	22.7	100	
Discordant Analyses - Not Used											
HI02_02	0.95907	0.01505	0.04662	0.00067	0.6557756	2337.2	21.3	293.7	4.1	13	
HI02_03	4.89163	0.08403	0.31713	0.0047	0.5941995	1830.4	26.1	1775.7	23.0	97	
HI02_04	3.79969	0.06206	0.27293	0.00396	0.635628	1642.5	24.5	1555.6	20.1	95	
HI02_06	3.91326	0.06554	0.25173	0.00368	0.6185315	1844.6	24.9	1447.4	19.0	78	
HI02_09	3.72935	0.06172	0.26873	0.0039	0.6343473	1636.7	24.7	1534.4	19.8	94	
HI02_15	3.76194	0.07302	0.27138	0.00414	0.5407829	1634.3	31.2	1547.8	21.0	95	
HI02_19	2.72563	0.05434	0.17614	0.00269	0.5298389	1836.0	31.5	1045.9	14.7	57	
HI02_21	4.23237	0.08709	0.30468	0.00467	0.5150335	1638.1	33.6	1714.5	23.1	105	
HI02_22	4.00131	0.09031	0.28112	0.00447	0.4577433	1683.2	37.9	1597.0	22.5	95	
HI02 25	2.89158	0.05442	0.19743	0.00299	0.5745296	1735.8	29.1	1161.5	16.1	67	

Analysis #	$^{207}Pb/^{235}U$ Ratio	1σ	$^{206}Pb/^{238}U$ Ratio	1σ	Rho	$^{207}Pb/^{206}Pb$ Age	2σ	$^{206}Pb/^{238}U$ Age	2σ	Conc. %	Comments
HI02_27	4.87541	0.10664	0.32186	0.00517	0.4775543	1797.3	36.0	1798.8	25.2	100	
HI02_28	6.45225	0.12739	0.3282	0.00503	0.5404916	2259.0	29.5	1829.7	24.4	81	
HI02_29	4.43443	0.09721	0.30649	0.00488	0.4780156	1713.4	36.4	1723.4	24.1	101	
HI02_30	7.71724	0.17278	0.36114	0.00589	0.463403	2401.9	34.8	1987.6	27.9	83	
HI02_32	3.53365	0.07872	0.24552	0.00387	0.467724	1703.8	37.2	1415.3	20.1	83	
HI02_33	2.32205	0.05351	0.15682	0.0025	0.4445855	1756.0	38.6	939.1	13.9	53	
HI02_37	2.49633	0.04853	0.15423	0.00235	0.5399497	1917.0	30.2	924.6	13.2	48	
HI02_38	4.39183	0.08648	0.313	0.00479	0.5356989	1656.7	31.7	1755.5	23.5	106	
HI02_39	2.78505	0.05515	0.1763	0.0027	0.5358807	1873.3	31.1	1046.7	14.8	56	
HI02_40	3.30682	0.06669	0.24146	0.00371	0.5248546	1611.6	32.8	1394.3	19.3	87	
HI02_41	3.5798	0.08973	0.2236	0.00383	0.3962393	1897.4	42.7	1300.8	20.2	69	
HI02_45	4.03657	0.09231	0.30622	0.0049	0.4605415	1540.1	39.0	1722.1	24.2	112	
Sample SPR-1: Garnet-Sillimanite Gneiss, Northern Houghton Inlier											
SPR1_05	3.79484	0.08052	0.28082	0.00471	0.5644555	1586.8	33.5	1595.5	23.7	101	REE Analysis #1
SPR1_20	3.81085	0.07715	0.28182	0.00469	0.5993391	1588.1	31.1	1600.5	23.6	101	REE Analysis #2
SPR1_27	3.79751	0.0801	0.28008	0.0047	0.5688274	1593.2	33.2	1591.8	23.7	100	
SPR1_36	3.77039	0.09386	0.27684	0.00482	0.460862	1601.5	42.1	1575.4	24.3	98	
SPR1_37	3.77603	0.07109	0.27935	0.00455	0.648906	1587.2	27.6	1588.1	22.9	100	REE Analysis #3
SPR1_43	3.76015	0.07674	0.27603	0.00455	0.5931603	1601.7	31.4	1571.3	23.0	98	REE Analysis #4
SPR1_64	3.79037	0.07148	0.28037	0.00436	0.587154	1587.5	29.5	1593.2	22.0	100	
SPR1_65	3.8089	0.07224	0.28059	0.00436	0.5774925	1595.2	29.8	1594.3	22.0	100	REE Analysis #5
SPR1_72	3.63737	0.08083	0.26819	0.00433	0.4696191	1593.5	37.8	1531.6	22.0	96	
SPR1_80	3.74924	0.07499	0.27776	0.00432	0.5242874	1584.8	32.9	1580.1	21.8	100	REE Analysis #6
SPR1_86	3.73015	0.07104	0.27657	0.00424	0.5424663	1583.4	31.0	1574.0	21.4	99	REE Analysis #7
Discordant Analyses - Not Used											
SPR1_01	2.74388	0.05656	0.19163	0.0032	0.5810923	1694.3	31.8	1130.2	17.3	67	
SPR1_02	2.58292	0.05405	0.16481	0.00277	0.5707877	1859.0	32.0	983.4	15.3	53	Excluded from Intercept
SPR1_03	1.41467	0.02936	0.09408	0.00157	0.5765881	1784.0	31.8	579.6	9.3	32	
SPR1_04	2.64413	0.05638	0.18006	0.00303	0.5610756	1740.6	33.2	1067.3	16.6	61	Excluded from Intercept
SPR1_06	3.08506	0.06576	0.22413	0.00376	0.5641746	1621.1	33.5	1303.6	19.8	80	
SPR1_07	2.53712	0.0555	0.18156	0.00307	0.5483079	1649.1	34.7	1075.5	16.8	65	
SPR1_08	2.70584	0.06106	0.19102	0.00326	0.5275017	1674.3	36.2	1126.9	17.7	67	
SPR1_09	2.81613	0.06334	0.20674	0.00352	0.5356007	1601.6	36.3	1211.4	18.8	76	
SPR1_10	2.53721	0.05755	0.18281	0.00311	0.5302365	1636.5	36.5	1082.3	17.0	66	
SPR1_11	2.94381	0.06807	0.21061	0.00361	0.5192142	1649.6	37.4	1232.1	19.2	75	
SPR1_12	2.73669	0.06434	0.20055	0.00345	0.508475	1605.0	38.4	1178.2	18.5	73	
SPR1_13	1.81237	0.03398	0.13065	0.00215	0.6579129	1635.6	27.1	791.6	12.3	48	
SPR1_14	2.67947	0.05145	0.19534	0.00324	0.6395291	1614.7	28.4	1150.2	17.5	71	
SPR1_15	2.51028	0.05037	0.17117	0.00288	0.6055498	1738.3	30.1	1018.5	15.8	59	

Analysis #	$^{207}Pb/^{235}U$ Ratio	1σ	$^{206}Pb/^{238}U$ Ratio	1σ	Rho	$^{207}Pb/^{206}Pb$ Age	2σ	$^{206}Pb/^{238}U$ Age	2σ	Conc. %	Comments
SPR1_16	1.66875	0.03229	0.1147	0.0019	0.630752	1723.6	28.4	700.0	11.0	41	
SPR1_17	2.14502	0.04178	0.14543	0.00241	0.6265762	1748.8	28.5	875.3	13.6	50	
SPR1_18	3.06264	0.0619	0.22569	0.00377	0.6020555	1594.7	31.0	1311.9	19.9	82	
SPR1_19	2.63096	0.05279	0.18651	0.00311	0.6046504	1666.7	30.4	1102.4	16.9	66	
SPR1_21	2.97508	0.06396	0.22223	0.00377	0.5571658	1569.4	34.3	1293.6	19.9	82	
SPR1_22	3.35662	0.06952	0.24764	0.00414	0.5810972	1592.5	32.2	1426.3	21.4	90	
SPR1_23	1.29299	0.02725	0.0869	0.00146	0.5695672	1764.8	32.4	537.2	8.6	30	
SPR1_24	2.84462	0.06115	0.20918	0.00352	0.5544877	1598.7	34.1	1224.4	18.8	77	
SPR1_25	2.77456	0.05543	0.19877	0.00329	0.6064755	1647.3	30.3	1168.7	17.7	71	
SPR1_26	2.29639	0.04642	0.16546	0.00274	0.5990856	1636.7	30.9	987.0	15.2	60	
SPR1_28	3.03697	0.06443	0.20265	0.0034	0.5616661	1777.9	32.9	1189.5	18.3	67	Excluded from Intercept
SPR1_29	2.74896	0.05791	0.19674	0.00328	0.5684006	1649.1	32.9	1157.8	17.7	70	
SPR1_30	1.29167	0.0276	0.07986	0.00134	0.5567237	1916.0	32.6	495.3	8.0	26	Excluded from Intercept
SPR1_31	2.21274	0.04881	0.16311	0.00275	0.5351867	1594.1	35.6	974.0	15.2	61	
SPR1_32	2.62311	0.05815	0.18573	0.00313	0.5328612	1669.0	35.5	1098.2	17.0	66	
SPR1_33	2.89707	0.06543	0.21317	0.0036	0.5190297	1597.5	36.8	1245.7	19.1	78	
SPR1_34	1.16543	0.0264	0.07401	0.00125	0.5180892	1867.6	35.8	460.3	7.5	25	Excluded from Intercept
SPR1_35	0.97921	0.02262	0.06118	0.00104	0.5078124	1897.1	36.6	382.8	6.3	20	Excluded from Intercept
SPR1_38	2.89878	0.05545	0.20622	0.00337	0.6379171	1660.0	28.1	1208.7	18.0	73	
SPR1_39	2.36353	0.0463	0.16859	0.00277	0.6212484	1655.1	29.3	1004.3	15.3	61	
SPR1_40	2.36643	0.04676	0.16915	0.00278	0.6148299	1651.2	29.7	1007.4	15.3	61	
SPR1_41	2.73927	0.05424	0.19456	0.00319	0.6157919	1663.0	29.7	1146.0	17.2	69	
SPR1_42	2.19363	0.0445	0.1552	0.00256	0.5959763	1670.2	30.9	930.0	14.3	56	
SPR1_44	2.80976	0.05936	0.20044	0.00333	0.5674812	1654.9	32.9	1177.7	17.9	71	
SPR1_45	1.95696	0.0424	0.13493	0.00226	0.5501529	1717.8	34.0	815.9	12.8	47	
SPR1_46	2.37339	0.05118	0.16016	0.00267	0.5565068	1757.2	33.5	957.7	14.8	55	Excluded from Intercept
SPR1_47	2.80302	0.06138	0.19812	0.00331	0.5483865	1672.1	34.6	1165.2	17.8	70	
SPR1_48	1.90301	0.04244	0.13339	0.00224	0.5367924	1687.5	35.5	807.2	12.7	48	
SPR1_49	1.1634	0.02217	0.08293	0.00133	0.6154841	1656.5	28.7	513.6	7.9	31	Excluded from Intercept
SPR1_50	3.44889	0.06722	0.25013	0.00402	0.5947276	1624.5	30.0	1439.2	20.7	89	
SPR1_51	3.29395	0.06552	0.24064	0.00388	0.575886	1611.0	31.1	1390.0	20.2	86	
SPR1_52	2.60929	0.05185	0.18932	0.00304	0.5750651	1623.7	31.1	1117.7	16.5	69	
SPR1_53	1.91245	0.03783	0.12972	0.00208	0.5755952	1748.1	30.5	786.3	11.9	45	
SPR1_54	3.14671	0.06701	0.2266	0.00371	0.5246286	1637.7	34.7	1316.7	19.5	80	
SPR1_55	1.03086	0.02422	0.08291	0.00139	0.458131	1429.6	41.0	513.5	8.3	36	Excluded from Intercept
SPR1_56	1.84409	0.08435	0.08872	0.00245	0.161076	2354.8	82.1	548.0	14.5	23	
SPR1_57	1.93251	0.04038	0.12901	0.00208	0.525949	1777.0	33.5	782.2	11.9	44	
SPR1_58	2.95265	0.06213	0.20801	0.00335	0.5176257	1678.3	34.2	1218.2	17.9	73	
SPR1_59	2.67531	0.057	0.19521	0.00314	0.5068121	1613.1	35.2	1149.6	17.0	71	
SPR1_60	2.12936	0.04581	0.14993	0.00241	0.4923771	1679.2	35.5	900.6	13.5	54	

Analysis #	$^{207}Pb/^{235}U$ Ratio	1σ	$^{206}Pb/^{238}U$ Ratio	1σ	Rho	$^{207}Pb/^{206}Pb$ Age	2σ	$^{206}Pb/^{238}U$ Age	2σ	Conc. %	Comments
SPR1_61	2.67157	0.04983	0.192	0.003	0.595284	1641.2	28.7	1132.2	16.2	69	
SPR1_62	3.18102	0.05853	0.23264	0.00361	0.603233	1608.7	28.2	1348.3	18.9	84	
SPR1_63	2.31037	0.04328	0.16875	0.00262	0.5879392	1611.1	29.1	1005.2	14.5	62	
SPR1_66	1.85942	0.03585	0.12952	0.00202	0.5635994	1699.0	30.2	785.1	11.5	46	
SPR1_67	2.13813	0.04194	0.1567	0.00245	0.5504448	1604.7	31.4	938.4	13.6	58	
SPR1_68	2.87402	0.05754	0.20911	0.00328	0.5392825	1618.3	32.4	1224.1	17.5	76	
SPR1_69	2.97747	0.06014	0.20393	0.0032	0.529563	1730.0	32.4	1196.4	17.2	69	Excluded from Intercept
SPR1_70	2.2712	0.04666	0.16403	0.00258	0.5164901	1632.1	33.6	979.1	14.3	60	
SPR1_71	1.1472	0.02361	0.07655	0.0012	0.5125228	1777.6	33.2	475.5	7.2	27	
SPR1_73	2.44886	0.04371	0.17298	0.00263	0.6038935	1673.3	27.2	1028.5	14.5	61	
SPR1_74	2.00669	0.03737	0.13797	0.00212	0.5701582	1723.0	29.1	833.2	12.0	48	
SPR1_75	2.61482	0.04758	0.18508	0.00282	0.5925256	1669.5	28.1	1094.7	15.3	66	
SPR1_76	1.84829	0.03378	0.12523	0.00191	0.5851692	1750.0	28.0	760.6	10.9	43	
SPR1_77	2.69148	0.04951	0.19591	0.00298	0.5802753	1617.7	28.8	1153.3	16.1	71	
SPR1_78	1.41105	0.0263	0.09709	0.00148	0.5680149	1721.7	29.1	597.4	8.7	35	
SPR1_79	1.31601	0.02495	0.08881	0.00136	0.5559107	1757.3	29.7	548.5	8.0	31	
SPR1_81	1.70299	0.03331	0.12022	0.00185	0.5360578	1674.6	31.5	731.8	10.6	44	
SPR1_82	2.10939	0.04172	0.15131	0.00233	0.5285871	1644.9	32.2	908.3	13.0	55	
SPR1_83	3.37075	0.06693	0.24105	0.00371	0.5231752	1650.7	32.3	1392.2	19.3	84	
SPR1_84	2.00728	0.04098	0.14261	0.00221	0.5025119	1662.9	33.6	859.4	12.5	52	
SPR1_85	1.88127	0.03278	0.12777	0.0019	0.600951	1745.7	26.4	775.1	10.9	44	
SPR1_87	2.19818	0.03913	0.13671	0.00205	0.5883384	1905.4	26.9	826.0	11.6	43	Excluded from Intercept
SPR1_88	2.02321	0.03627	0.11171	0.00167	0.5799178	2116.6	26.5	682.7	9.7	32	Excluded from Intercept
SPR1_89	2.02053	0.03679	0.14357	0.00215	0.5687582	1662.5	28.7	864.8	12.2	52	
SPR1_90	2.68299	0.05116	0.16893	0.00258	0.5379154	1883.2	30.0	1006.2	14.2	53	Excluded from Intercept
SPR1_91	3.39955	0.06497	0.25048	0.00381	0.5372651	1595.1	31.1	1441.0	19.6	90	
SPR1_92	2.1655	0.04144	0.15573	0.00236	0.5377217	1640.3	31.0	933.0	13.2	57	
SPR1_93	1.41393	0.02718	0.09549	0.00145	0.5308022	1756.1	30.7	587.9	8.5	33	
SPR1_94	1.15304	0.02279	0.07849	0.0012	0.5126374	1741.5	32.0	487.1	7.2	28	
SPR1_95	2.19892	0.04317	0.16005	0.00243	0.5219816	1617.9	32.2	957.0	13.5	59	
SPR1_96	3.16919	0.06572	0.23526	0.00364	0.4847842	1581.2	35.0	1362.0	19.0	86	
Sample SPG-1: Late Pegmatite, Northern Houghton Inlier											
SPG-1a: Magmatic Zircon											
SPPA_01	3.97355	0.06564	0.2958	0.00421	0.8615769	1576.2	26.0	1670.5	20.9	106	
SPPA_02	3.80744	0.0702	0.28987	0.00424	0.7933385	1534.1	30.5	1640.9	21.2	107	
SPPA_03	3.76723	0.06543	0.27896	0.004	0.8255878	1586.0	28.0	1586.1	20.2	100	
SPPA_04	3.7603	0.06671	0.28218	0.00407	0.8130172	1560.9	28.9	1602.4	20.5	103	
SPPA_05	3.74101	0.0664	0.28103	0.00404	0.8099337	1558.7	29.0	1596.5	20.3	102	
SPPA_06	3.81176	0.07272	0.28789	0.00424	0.7719887	1548.6	32.0	1631.0	21.2	105	

Analysis #	$^{207}Pb/^{235}U$ Ratio	1σ	$^{206}Pb/^{238}U$ Ratio	1σ	Rho	$^{207}Pb/^{206}Pb$ Age	2σ	$^{206}Pb/^{238}U$ Age	2σ	Conc. %	Comments
SPPA_07	3.79741	0.061	0.28163	0.00398	0.8797551	1582.6	24.7	1599.6	20.0	101	
SPPA_08	3.80681	0.06598	0.2807	0.00404	0.830401	1593.5	27.5	1594.9	20.4	100	
SPPA_09	3.77085	0.06554	0.2805	0.00405	0.8307206	1577.1	27.6	1593.9	20.4	101	
SPPA_10	3.67207	0.06684	0.27496	0.00403	0.8052116	1564.7	29.5	1565.9	20.4	100	
SPPA_11	3.69781	0.06733	0.27729	0.00406	0.8041328	1561.8	29.5	1577.7	20.5	101	
SPPA_12	3.74848	0.0712	0.28037	0.00414	0.777399	1566.6	31.3	1593.2	20.9	102	
SPPA_13	3.89965	0.06994	0.29165	0.00424	0.8105949	1565.9	28.9	1649.7	21.2	105	
SPPA_14	3.75781	0.06653	0.28287	0.00411	0.8206769	1554.0	28.4	1605.8	20.7	103	
SPPA_15	3.77496	0.07158	0.2869	0.00426	0.7830684	1536.2	31.1	1626.0	21.4	106	
SPPA_16	3.7512	0.07142	0.28303	0.0042	0.7794122	1550.0	31.2	1606.6	21.1	104	
SPPA_17	3.74915	0.07074	0.28449	0.00422	0.7861641	1539.5	30.7	1613.9	21.2	105	
SPPA_18	3.75067	0.07312	0.28404	0.00428	0.7729243	1543.3	32.1	1611.7	21.5	104	
SPPA_19	3.90544	0.06801	0.29652	0.00434	0.8404907	1538.3	27.8	1674.0	21.6	109	
SPPA_20	3.79192	0.06685	0.28493	0.00417	0.8301482	1557.8	28.3	1616.1	20.9	104	
SPPA_21	3.65633	0.0736	0.28096	0.00427	0.755007	1516.1	34.2	1596.2	21.5	105	
SPPA_22	3.82044	0.07415	0.29081	0.00435	0.7706943	1533.5	32.5	1645.6	21.8	107	
SPPA_23	3.70756	0.07116	0.2806	0.00417	0.7742846	1544.2	32.1	1594.4	21.0	103	
SPPA_24	3.67482	0.07284	0.2769	0.00415	0.756121	1552.5	33.5	1575.7	20.9	101	
SPPA_25	3.82482	0.07703	0.28973	0.00435	0.7454987	1542.6	34.3	1640.2	21.8	106	
SPPA_26	3.77044	0.07825	0.28328	0.00428	0.728007	1558.0	35.6	1607.8	21.5	103	
SPG-1b: Inherited Zircon											
SPPB_01	3.89468	0.06424	0.28826	0.00409	0.8602114	1586.7	25.7	1632.8	20.5	103	
SPPB_02	3.71422	0.06453	0.27776	0.00403	0.8351054	1567.4	27.6	1580.1	20.3	101	
SPPB_03	3.74189	0.06712	0.27792	0.00406	0.8144141	1580.3	28.7	1580.9	20.5	100	
SPPB_04	3.71634	0.06416	0.27304	0.00393	0.8337145	1600.5	27.1	1556.2	19.9	97	
SPPB_05	3.70091	0.066	0.27349	0.00395	0.8098792	1589.7	28.4	1558.5	20.0	98	
SPPB_06	3.73884	0.07464	0.2751	0.00407	0.7410868	1597.8	33.1	1566.6	20.6	98	
SPPB_08	3.696	0.06449	0.27779	0.00411	0.8479394	1557.3	27.2	1580.2	20.8	101	
SPPB_09	3.83596	0.06911	0.28559	0.00427	0.8298853	1575.0	28.4	1619.4	21.4	103	
SPPB_10	3.71587	0.077	0.27959	0.00437	0.7542748	1555.0	34.2	1589.3	22.0	102	
SPPB_11	3.7769	0.08109	0.28367	0.00449	0.7372268	1558.5	35.7	1609.8	22.6	103	
SPPB_12	3.84282	0.07251	0.28702	0.00432	0.7976709	1569.2	30.4	1626.6	21.6	104	
SPPB_13	3.74798	0.06543	0.27908	0.00408	0.8374363	1575.3	27.6	1586.7	20.6	101	
SPPB_14	3.72667	0.06555	0.27669	0.00404	0.830111	1581.2	27.8	1574.7	20.4	100	
SPPB_15	3.74929	0.06489	0.27897	0.00405	0.83882	1576.7	27.2	1586.1	20.4	101	
SPPB_16	3.54819	0.06296	0.2671	0.0039	0.8228731	1554.9	28.3	1526.1	19.9	98	
SPPB_17	3.8233	0.07076	0.28585	0.00421	0.7957826	1567.7	30.0	1620.7	21.1	103	
SPPB_18	3.70781	0.07149	0.27504	0.00411	0.7750293	1582.1	31.7	1566.3	20.8	99	
SPPB_19	3.87843	0.07052	0.28634	0.0042	0.8066979	1591.1	29.3	1623.2	21.0	102	
SPPB 20	3.85972	0.06718	0.28646	0.00418	0.8383553	1581.2	27.4	1623.8	20.9	103	

Analysis #	$^{207}Pb/^{235}U$ Ratio	1σ	$^{206}Pb/^{238}U$ Ratio	1σ	Rho	$^{207}Pb/^{206}Pb$ Age	2σ	$^{206}Pb/^{238}U$ Age	2σ	Conc. %	Comments
SPPB_21	3.76955	0.06716	0.28059	0.00411	0.8221451	1575.7	28.3	1594.3	20.7	101	
SPPB_22	3.90096	0.07203	0.2887	0.00426	0.7991364	1586.5	29.8	1635.0	21.3	103	
SPPB_23	3.84893	0.07331	0.28486	0.00425	0.7833111	1586.4	31.0	1615.8	21.3	102	
SPPB_24	3.59331	0.06785	0.26977	0.00402	0.7891821	1559.6	30.7	1539.6	20.4	99	
SPPB_25	3.81956	0.07464	0.28273	0.00424	0.7674245	1586.0	32.1	1605.1	21.3	101	
SPPB_26	3.85622	0.07707	0.28663	0.00429	0.7488798	1578.5	33.1	1624.6	21.5	103	
Discordant Analyses - Not Used											
SPPB_07	3.93504	0.06933	0.29364	0.00434	0.8388851	1570.9	27.7	1659.7	21.6	106	
Sample KM12-11: Kyanite Schist, Northern Warren Inlier											
KM11Z02	3.5479	0.0547	0.26451	0.00372	0.9121891	1573.0	23.2	1512.9	19.0	96	
KM11Z09	3.63274	0.06171	0.26789	0.00383	0.8416297	1593.4	26.9	1530.1	19.5	96	
KM11Z12	3.78484	0.06491	0.27273	0.00396	0.8466388	1636.3	27.0	1554.7	20.1	95	
KM11Z13	3.65479	0.06434	0.26884	0.00393	0.830386	1598.0	28.2	1534.9	20.0	96	
KM11Z14	3.69453	0.06433	0.27143	0.00395	0.8357664	1600.3	27.6	1548.0	20.0	97	
KM11Z17	0.58597	0.01245	0.07505	0.00113	0.7086532	476.7	43.2	466.5	6.8	98	
KM11Z18	3.59432	0.06327	0.26658	0.00388	0.826843	1582.6	27.9	1523.4	19.7	96	
KM11Z19	3.91208	0.07074	0.2915	0.00427	0.8100876	1573.9	29.1	1649.0	21.3	105	
KM11Z20	3.69124	0.06657	0.27611	0.00404	0.8113214	1566.6	28.9	1571.8	20.4	100	
KM11Z21	3.73949	0.06326	0.27994	0.00398	0.8404295	1565.2	26.4	1591.0	20.0	102	
KM11Z22	3.81994	0.06467	0.28464	0.00404	0.8383765	1573.8	26.5	1614.7	20.3	103	
KM11Z25	3.73962	0.06145	0.27866	0.00392	0.8560853	1573.8	25.4	1584.6	19.8	101	
KM11Z28	3.52578	0.05957	0.26259	0.00369	0.8317174	1574.8	26.6	1503.1	18.8	95	
Discordant Analyses - Not Used											
KM11Z01	2.48371	0.04209	0.18252	0.00264	0.8535234	1600.0	27.1	1080.7	14.4	68	
KM11Z03	3.6003	0.0584	0.26395	0.00376	0.8781971	1604.3	25.1	1510.0	19.2	94	
KM11Z04	3.17157	0.05379	0.23685	0.00341	0.8488946	1569.9	27.1	1370.3	17.8	87	
KM11Z05	3.51827	0.05569	0.25777	0.00364	0.8921152	1605.5	24.1	1478.4	18.6	92	
KM11Z06	1.60239	0.02764	0.13518	0.00194	0.8319926	1337.9	28.7	817.3	11.0	61	
KM11Z07	2.11154	0.03394	0.16191	0.00229	0.8799323	1520.1	24.9	967.4	12.7	64	
KM11Z08	3.32926	0.058	0.24973	0.00361	0.8297671	1561.6	28.1	1437.1	18.6	92	
KM11Z10	3.51367	0.06429	0.26	0.0038	0.7987811	1587.1	30.1	1489.8	19.5	94	
KM11Z11	2.64291	0.04238	0.19705	0.0028	0.8861414	1572.7	24.4	1159.5	15.1	74	
KM11Z15	2.68128	0.04489	0.20838	0.00299	0.8570531	1494.6	26.3	1220.2	16.0	82	
KM11Z16	2.80469	0.04882	0.21308	0.00309	0.833111	1537.5	27.7	1245.2	16.4	81	
KM11Z23	3.09276	0.05097	0.2228	0.00314	0.8551574	1636.8	25.2	1296.7	16.6	79	
KM11Z24	1.59383	0.02703	0.12813	0.00181	0.8329591	1430.2	27.1	777.2	10.3	54	
KM11Z26	1.85337	0.03167	0.15764	0.00222	0.8241393	1321.8	27.9	943.6	12.4	71	
KM11Z27	3.31016	0.05817	0.246	0.00348	0.8049966	1578.8	28.1	1417.8	18.0	90	
KM11Z29	3.25379	0.05594	0.24743	0.00348	0.8180766	1535.7	27.4	1425.2	18.0	93	

Analysis #	$^{207}Pb/^{235}U$ Ratio	1σ	$^{206}Pb/^{238}U$ Ratio	1σ	Rho	$^{207}Pb/^{206}Pb$ Age	2σ	$^{206}Pb/^{238}U$ Age	2σ	Conc. %	Comments
KM11Z30	1.99714	0.03668	0.15618	0.00222	0.773939	1482.7	30.5	935.5	12.4	63	
Sample WI-07: Deformed Pegmatite, Northern Warren Inlier											
KM0701	3.44279	0.05328	0.2581	0.00362	0.6385646	1562.4	23.5	1480.1	18.6	95	
KM0703	3.49585	0.05514	0.26309	0.00372	0.6287965	1555.0	24.1	1505.6	19.0	97	
KM0706	3.8713	0.06446	0.28906	0.00416	0.601576	1569.8	26.0	1636.8	20.8	104	
KM0707	3.49464	0.05864	0.26433	0.00381	0.5957297	1545.5	26.3	1511.9	19.4	98	
KM0712	3.6161	0.05765	0.27229	0.00392	0.6442331	1554.1	24.1	1552.4	19.9	100	
KM0715	3.60465	0.06017	0.27214	0.00396	0.6149898	1549.3	25.8	1551.6	20.1	100	
KM0716	3.53618	0.06	0.26579	0.00388	0.604472	1557.6	26.3	1519.4	19.8	98	
KM0721	3.48892	0.05636	0.26573	0.00388	0.6398766	1532.7	24.4	1519.1	19.8	99	
KM0723	3.40091	0.05549	0.25973	0.0038	0.6314685	1527.6	24.9	1488.5	19.4	97	
KM0724	3.3163	0.05504	0.25608	0.00376	0.6206043	1506.8	25.8	1469.7	19.3	98	
KM0727	3.54709	0.06191	0.26976	0.00399	0.5782868	1535.5	27.9	1539.6	20.2	100	
WI7_03	3.63782	0.05969	0.27311	0.0034	0.758719	1559.6	29.0	1556.6	17.2	100	
WI7_08	3.61895	0.066	0.27166	0.00353	0.7125046	1559.9	32.6	1549.2	17.9	99	
WI7_14	3.60742	0.05493	0.2727	0.00347	0.8356635	1547.2	25.8	1554.5	17.6	100	
WI7_17	3.45738	0.06137	0.2592	0.00344	0.7476777	1562.9	31.1	1485.7	17.6	95	
WI7_25	3.59717	0.06051	0.27146	0.00358	0.7839908	1549.9	28.9	1548.2	18.2	100	
WI7_35	3.52926	0.07677	0.26395	0.00378	0.6583582	1567.1	38.9	1510.0	19.3	96	
WI7_45	3.55861	0.05546	0.26927	0.00351	0.8364109	1545.5	26.0	1537.1	17.9	99	
WI7_50	3.43303	0.0557	0.25989	0.00345	0.8181858	1544.4	27.0	1489.3	17.6	96	
Discordant Analyses - Not Used											
KM0702	2.82203	0.04443	0.2226	0.00314	0.6289536	1466.2	24.5	1295.6	16.6	88	
KM0704	2.64839	0.04229	0.19534	0.00278	0.6220654	1592.7	24.4	1150.2	15.0	72	
KM0705	2.09168	0.03398	0.18056	0.00258	0.6117037	1292.8	26.1	1070.1	14.1	83	
KM0708	0.91829	0.01612	0.09351	0.00136	0.5675281	963.9	30.6	576.2	8.0	60	
KM0709	3.04542	0.05383	0.23239	0.0034	0.5679798	1529.0	28.4	1347.0	17.8	88	
KM0710	3.07493	0.05612	0.23213	0.00343	0.5522285	1549.2	29.6	1345.7	17.9	87	
KM0711	3.29854	0.05252	0.24933	0.00359	0.6408879	1547.0	24.1	1435.0	18.5	93	
KM0713	2.88569	0.04657	0.22206	0.00321	0.6351598	1513.3	24.6	1292.8	16.9	85	
KM0714	2.06316	0.03385	0.17415	0.00252	0.6241085	1336.7	25.9	1034.9	13.9	77	
KM0717	3.36229	0.05838	0.25348	0.00372	0.592728	1552.0	27.3	1456.4	19.2	94	
KM0718	3.15269	0.05613	0.23623	0.00349	0.5790744	1563.4	28.2	1367.1	18.2	87	
KM0719	1.55694	0.0284	0.1375	0.00204	0.5656174	1248.7	30.3	830.5	11.6	67	
KM0720	2.29326	0.04323	0.18261	0.00273	0.5458929	1448.4	31.0	1081.2	14.9	75	
KM0722	2.79712	0.04535	0.21946	0.00321	0.6381415	1476.5	24.9	1279.0	17.0	87	
KM0725	2.99052	0.05027	0.23424	0.00344	0.6099514	1479.7	26.5	1356.7	18.0	92	
KM0726	3.17829	0.05472	0.24212	0.00357	0.5923227	1532.3	27.3	1397.7	18.5	91	
KM0728	3.01434	0.05436	0.23257	0.00346	0.556682	1508.3	29.4	1348.0	18.1	89	

Analysis #	$^{207}Pb/^{235}U$ Ratio	1σ	$^{206}Pb/^{238}U$ Ratio	1σ	Rho	$^{207}Pb/^{206}Pb$ Age	2σ	$^{206}Pb/^{238}U$ Age	2σ	Conc. %	Comments
KM0729	3.1827	0.05867	0.24128	0.0036	0.5391889	1541.5	30.3	1393.3	18.7	90	
WI7_01	2.18924	0.03343	0.18776	0.00232	0.809174	1305.6	27.5	1109.2	12.6	85	
WI7_02	1.88716	0.03097	0.15818	0.00196	0.7550436	1350.1	30.0	946.6	10.9	70	
WI7_04	3.2272	0.06264	0.24793	0.00334	0.6940512	1515.9	35.3	1427.8	17.2	94	
WI7_05	1.10361	0.01796	0.07511	0.00095	0.7772042	1741.4	27.7	466.9	5.7	27	
WI7_06	2.107	0.03671	0.16724	0.00216	0.7412996	1454.0	31.1	996.9	11.9	69	
WI7_07	0.58215	0.00892	0.07324	0.00091	0.8108922	516.1	31.2	455.6	5.5	88	
WI7_09	1.73407	0.02709	0.15135	0.00192	0.8120381	1271.5	27.9	908.5	10.7	71	
WI7_10	0.62646	0.01042	0.07185	0.00092	0.7698156	716.1	32.9	447.3	5.6	62	
WI7_11	2.749	0.04539	0.20451	0.00263	0.7788535	1576.7	28.7	1199.5	14.1	76	
WI7_12	3.18701	0.0577	0.24135	0.00318	0.7277587	1543.4	32.1	1393.7	16.5	90	
WI7_13	2.35649	0.05121	0.19122	0.00268	0.6449296	1413.4	40.6	1128.0	14.5	80	
WI7_15	2.6095	0.0391	0.20804	0.00263	0.8437027	1446.3	25.7	1218.4	14.0	84	
WI7_16	1.12925	0.01713	0.10409	0.00133	0.8423166	1164.8	27.2	638.3	7.7	55	
WI7_18	2.49892	0.05014	0.19906	0.00274	0.6860165	1448.8	36.5	1170.3	14.7	81	
WI7_19	3.17042	0.06338	0.23406	0.00321	0.6860289	1591.9	35.7	1355.8	16.8	85	
WI7_20	3.07008	0.05857	0.23317	0.00315	0.7081289	1538.9	33.9	1351.1	16.5	88	
WI7_21	2.49392	0.03641	0.20189	0.00256	0.8685343	1417.1	24.5	1185.5	13.7	84	
WI7_22	3.29857	0.05516	0.24834	0.00328	0.7898209	1554.1	28.7	1429.9	17.0	92	
WI7_23	2.27048	0.03643	0.19146	0.0025	0.8138052	1338.4	28.1	1129.3	13.5	84	
WI7_24	2.84506	0.05025	0.22537	0.00303	0.7612054	1457.9	31.2	1310.2	15.9	90	
WI7_26	3.50916	0.06708	0.25826	0.00346	0.7008564	1597.1	33.7	1480.9	17.7	93	
WI7_27	2.62176	0.04984	0.2082	0.00285	0.7200772	1453.2	34.2	1219.2	15.2	84	
WI7_28	3.42463	0.05431	0.25441	0.00329	0.8154467	1580.1	26.8	1461.2	16.9	92	
WI7_29	1.09492	0.01908	0.10896	0.00144	0.7584019	1011.1	32.8	666.7	8.4	66	
WI7_30	1.42244	0.02245	0.12445	0.00162	0.8247792	1267.2	27.6	756.1	9.3	60	
WI7_31	2.98666	0.04601	0.23406	0.00306	0.8486484	1478.6	26.0	1355.8	16.0	92	
WI7_32	2.89723	0.04933	0.22793	0.00305	0.7859053	1471.7	29.6	1323.6	16.0	90	
WI7_33	2.95222	0.04959	0.22667	0.00299	0.785293	1517.7	28.9	1317.0	15.7	87	
WI7_34	2.91299	0.04878	0.22089	0.00295	0.7975229	1541.1	28.6	1286.6	15.6	83	
WI7_36	3.08278	0.04683	0.23688	0.00306	0.8503768	1516.1	25.7	1370.4	15.9	90	
WI7_37	1.23483	0.02087	0.07615	0.00101	0.7847588	1920.6	28.2	473.1	6.1	25	
WI7_38	2.686	0.04455	0.20699	0.00272	0.7922784	1510.9	29.1	1212.8	14.5	80	
WI7_39	1.77332	0.02947	0.14241	0.00185	0.7816966	1432.4	29.4	858.3	10.4	60	
WI7_40	2.96874	0.0496	0.22473	0.00291	0.775037	1544.5	29.3	1306.8	15.3	85	
WI7_41	2.22891	0.03923	0.18039	0.00236	0.7433165	1417.9	31.8	1069.1	12.9	75	
WI7_42	2.17412	0.03791	0.16303	0.00212	0.7457582	1562.5	30.9	973.6	11.7	62	
WI7_43	2.16868	0.03127	0.17742	0.00227	0.8873417	1397.1	24.0	1052.9	12.4	75	
WI7_44	2.58663	0.038	0.20381	0.00262	0.8750372	1468.7	24.5	1195.8	14.0	81	
WI7_46	1.2932	0.01997	0.12063	0.00158	0.8481827	1141.4	27.1	734.2	9.1	64	

Analysis #	$^{207}Pb/^{235}U$ Ratio	1σ	$^{206}Pb/^{238}U$ Ratio	1σ	Rho	$^{207}Pb/^{206}Pb$ Age	2σ	$^{206}Pb/^{238}U$ Age	2σ	Conc. %	Comments
WI7_47	3.30489	0.05148	0.251	0.00328	0.8389162	1538.6	25.8	1443.6	16.9	94	
WI7_48	2.52026	0.04446	0.19754	0.00269	0.7719215	1478.5	30.7	1162.1	14.5	79	
WI7_49	3.27397	0.05388	0.24129	0.0032	0.8058566	1595.0	27.4	1393.4	16.6	87	
WI7_51	2.09067	0.03507	0.17086	0.00229	0.7989964	1399.2	28.6	1016.8	12.6	73	
WI7_52	2.82335	0.0461	0.21816	0.00292	0.8197313	1505.7	27.2	1272.1	15.4	84	
SampleAI01: Calcsilicate, Southern Aldgate Inlier											
ALDGATE_02	3.68934	0.05589	0.27382	0.00342	0.4842331	1581.4	26.3	1560.2	17.3	99	
ALDGATE_03	3.91466	0.06177	0.28579	0.00362	0.469194	1612.2	27.6	1620.5	18.1	101	
ALDGATE_04	3.9038	0.0636	0.28685	0.00367	0.4531611	1600.1	28.7	1625.8	18.4	102	
ALDGATE_05	3.67013	0.05679	0.27666	0.00347	0.4767254	1552.2	27.0	1574.5	17.5	101	
ALDGATE_06	3.83962	0.0578	0.27717	0.00344	0.4917025	1633.0	25.8	1577.1	17.4	97	
ALDGATE_07	3.64134	0.05696	0.26703	0.00335	0.4768801	1603.6	27.2	1525.7	17.1	95	
ALDGATE_08	3.65368	0.0585	0.27154	0.00343	0.4596495	1578.6	28.0	1548.6	17.4	98	
ALDGATE_10	3.67857	0.06263	0.28117	0.00362	0.4385043	1525.9	30.4	1597.3	18.2	105	
ALDGATE_11	3.64781	0.06573	0.26965	0.00355	0.4094977	1588.6	32.2	1539.0	18.0	97	
ALDGATE_12	3.8676	0.06985	0.28469	0.00375	0.4097376	1596.5	32.3	1614.9	18.8	101	
ALDGATE_13	3.78853	0.05715	0.28182	0.00353	0.4950861	1577.2	26.1	1600.5	17.8	101	
ALDGATE_14	3.89586	0.05635	0.28512	0.00352	0.5159849	1607.6	24.6	1617.1	17.7	101	
ALDGATE_15	3.75684	0.05867	0.27732	0.0035	0.4704601	1591.6	27.2	1577.8	17.7	99	
ALDGATE_16	3.73487	0.05902	0.27757	0.00351	0.4651427	1578.9	27.7	1579.1	17.7	100	
ALDGATE_17	3.79047	0.06411	0.28168	0.00365	0.4303454	1579.0	30.1	1599.8	18.4	101	
ALDGATE_19	3.70862	0.05996	0.27296	0.00346	0.4493616	1596.9	28.5	1555.8	17.5	97	
ALDGATE_20	3.65763	0.05907	0.27413	0.00346	0.4491191	1563.1	28.5	1561.7	17.5	100	
ALDGATE_21	3.69172	0.06191	0.27444	0.00351	0.4333382	1578.3	29.8	1563.3	17.8	99	
ALDGATE_22	3.67298	0.06167	0.2702	0.00345	0.4312388	1597.9	29.8	1541.8	17.5	96	
ALDGATE_23	3.65215	0.06183	0.27314	0.00348	0.425394	1566.9	30.2	1556.7	17.6	99	
ALDGATE_24	3.75295	0.07483	0.27726	0.00378	0.3549748	1589.9	36.5	1577.5	19.1	99	
ALDGATE_25	3.72941	0.05681	0.27967	0.00348	0.4756019	1561.6	26.7	1589.7	17.5	102	
ALDGATE_27	3.69836	0.05907	0.27439	0.00345	0.4502621	1581.6	28.3	1563.0	17.5	99	
ALDGATE_28	3.71226	0.05834	0.27916	0.00348	0.4579312	1556.3	27.8	1587.1	17.5	102	
ALDGATE_30	3.71847	0.06187	0.27564	0.00348	0.4253223	1583.1	29.8	1569.3	17.6	99	
ALDGATE_33	3.78976	0.06387	0.2858	0.00358	0.4128582	1550.7	30.4	1620.5	18.0	105	
ALDGATE_34	3.7	0.06774	0.27405	0.00355	0.3712978	1584.5	33.4	1561.3	18.0	99	
ALDGATE_35	3.70107	0.06533	0.27789	0.0035	0.3822938	1558.9	32.2	1580.7	17.7	101	
ALDGATE_36	3.66266	0.06523	0.27325	0.00348	0.3849376	1570.9	32.4	1557.3	17.6	99	
ALDGATE_37	3.78409	0.05906	0.28122	0.00341	0.4243922	1578.5	28.1	1597.5	17.2	101	
ALDGATE_39	3.627	0.0592	0.27377	0.00335	0.4069606	1549.3	29.7	1559.9	17.0	101	
ALDGATE_40	3.76665	0.06591	0.28166	0.00354	0.3731369	1566.9	32.1	1599.7	17.8	102	
ALDGATE_41	3.75866	0.06438	0.27502	0.00341	0.3843567	1607.6	31.2	1566.2	17.3	97	

Analysis #	$^{207}Pb/^{235}U$ Ratio	1σ	$^{206}Pb/^{238}U$ Ratio	1σ	Rho	$^{207}Pb/^{206}Pb$ Age	2σ	$^{206}Pb/^{238}U$ Age	2σ	Conc. %	Comments
ALDGATE_44	3.73525	0.07221	0.27314	0.00354	0.3331431	1608.8	35.7	1556.7	17.9	97	
ALDGATE_45	3.75475	0.06937	0.27578	0.00348	0.3449091	1600.5	33.9	1570.1	17.6	98	
ALDGATE_46	3.76453	0.07429	0.27708	0.00359	0.3240476	1596.7	36.5	1576.6	18.1	99	
ALDGATE_47	3.59092	0.06971	0.27124	0.00346	0.3236628	1548.2	36.1	1547.1	17.6	100	
ALDGATE_48	3.91981	0.08385	0.2909	0.0039	0.2907516	1581.3	40.0	1646.0	19.5	104	
ALDGATE_49	3.7247	0.05883	0.27556	0.00337	0.418732	1587.1	28.5	1568.9	17.0	99	
ALDGATE_50	3.72565	0.05893	0.27815	0.00339	0.4157257	1570.0	28.6	1582.1	17.1	101	
ALDGATE_51	3.69239	0.0588	0.27277	0.00333	0.4190809	1589.7	28.7	1554.8	16.9	98	
ALDGATE_52	3.89048	0.07637	0.29143	0.00388	0.3317847	1563.7	36.6	1648.6	19.4	105	
ALDGATE_54	3.77962	0.06666	0.27603	0.00348	0.3665724	1611.1	32.2	1571.3	17.6	98	
ALDGATE_55	3.62147	0.06164	0.2731	0.00338	0.3859692	1551.0	31.1	1556.5	17.1	100	
ALDGATE_56	3.55985	0.06109	0.27016	0.00334	0.3852802	1539.2	31.5	1541.6	17.0	100	
ALDGATE_57	3.70735	0.06607	0.273	0.00342	0.363618	1595.6	32.6	1556.0	17.3	98	
ALDGATE_58	3.59108	0.06961	0.27537	0.00357	0.3288159	1519.6	36.2	1568.0	18.0	103	
ALDGATE_59	3.61016	0.06957	0.2732	0.00352	0.3316273	1544.4	35.8	1557.0	17.8	101	
ALDGATE_60	3.72763	0.06959	0.27659	0.0035	0.3425402	1581.3	34.4	1574.2	17.7	100	
ALDGATE_61	3.81379	0.05861	0.28468	0.0034	0.4255966	1570.9	27.7	1614.9	17.1	103	
ALDGATE_62	3.86637	0.05944	0.2799	0.00334	0.4217121	1628.1	27.5	1590.9	16.8	98	
ALDGATE_63	3.93176	0.06684	0.28678	0.00355	0.3810253	1614.2	31.0	1625.4	17.8	101	
ALDGATE_64	3.92693	0.07509	0.2892	0.00377	0.3282615	1596.2	35.5	1637.5	18.8	103	
ALDGATE_65	3.92433	0.06551	0.2905	0.00354	0.3784156	1586.6	30.5	1644.0	17.7	104	
ALDGATE_66	3.63058	0.06512	0.2728	0.00341	0.3500666	1558.7	33.3	1555.0	17.3	100	
ALDGATE_67	3.83184	0.06976	0.28027	0.00352	0.3416973	1609.1	33.6	1592.7	17.7	99	
ALDGATE_68	3.59737	0.06438	0.2705	0.00335	0.3434948	1557.4	33.3	1543.3	17.0	99	
ALDGATE_70	3.87519	0.06884	0.28679	0.00353	0.3477782	1587.2	32.9	1625.5	17.7	102	
ALDGATE_71	3.88758	0.07186	0.287	0.00358	0.3266435	1591.9	34.4	1626.5	18.0	102	
ALDGATE_73	3.7353	0.05812	0.27975	0.00337	0.4264728	1564.0	28.0	1590.1	17.0	102	
ALDGATE_74	3.72043	0.06281	0.27808	0.00346	0.3915822	1567.7	30.8	1581.7	17.5	101	
ALDGATE_75	3.78881	0.06259	0.27848	0.00343	0.4053019	1599.1	29.8	1583.7	17.3	99	
ALDGATE_76	3.85089	0.06467	0.28111	0.00349	0.4004416	1611.9	30.3	1597.0	17.5	99	
ALDGATE_77	3.91518	0.06559	0.28497	0.00352	0.4001716	1617.3	30.1	1616.4	17.7	100	
ALDGATE_78	3.95575	0.07019	0.2933	0.00371	0.3769146	1582.8	32.3	1658.0	18.5	105	
ALDGATE_79	3.861	0.07032	0.28678	0.00366	0.3729026	1579.5	33.2	1625.4	18.3	103	
ALDGATE_80	3.81833	0.07144	0.28644	0.00369	0.3593295	1560.9	34.3	1623.7	18.5	104	
ALDGATE_81	3.64494	0.08107	0.26598	0.00375	0.2958322	1612.6	41.3	1520.4	19.1	94	
ALDGATE_82	3.78876	0.07119	0.28375	0.00364	0.3649966	1564.1	34.3	1610.2	18.3	103	
ALDGATE_83	3.87136	0.07534	0.29038	0.00378	0.3515696	1561.3	35.6	1643.4	18.9	105	
ALDGATE_84	4.06883	0.07929	0.29799	0.00387	0.3562227	1606.0	35.4	1681.3	19.2	105	

Analysis #	$^{207}Pb/^{235}U$ Ratio	1σ	$^{206}Pb/^{238}U$ Ratio	1σ	Rho	$^{207}Pb/^{206}Pb$ Age	2σ	$^{206}Pb/^{238}U$ Age	2σ	Conc. %	Comments
Detrital Zircon											
ALDGATE_01	4.9822	0.07289	0.32448	0.00402	0.5069258	1822.2	24.4	1811.6	19.6	99	
ALDGATE_26	5.20337	0.08359	0.33124	0.00423	0.4513046	1862.9	27.5	1844.4	20.5	99	
ALDGATE_43	5.43701	0.10716	0.33934	0.00455	0.3274075	1898.6	35.3	1883.5	21.9	99	
Discordant Analyses - Not Used											
ALDGATE_09	3.61193	0.0556	0.25423	0.00316	0.4839378	1679.7	26.3	1460.3	16.3	87	
ALDGATE_18	3.61722	0.05878	0.26332	0.00336	0.4533538	1617.5	28.6	1506.8	17.1	93	
ALDGATE_29	3.49188	0.06235	0.25804	0.00337	0.3905889	1588.9	32.4	1479.8	17.3	93	
ALDGATE_31	2.95346	0.04567	0.22104	0.00271	0.4605696	1565.1	27.3	1287.4	14.3	82	
ALDGATE_32	3.53208	0.0682	0.25311	0.00339	0.3496606	1646.1	35.3	1454.5	17.5	88	
ALDGATE_38	4.03159	0.06328	0.27785	0.00337	0.4186218	1718.3	27.8	1580.5	17.0	92	
ALDGATE_42	3.81741	0.06731	0.28951	0.00362	0.3680414	1540.5	32.5	1639.1	18.1	106	
ALDGATE_53	3.91891	0.06628	0.27113	0.00338	0.3858872	1711.2	30.4	1546.6	17.2	90	
ALDGATE_72	2.92825	0.06236	0.22039	0.00294	0.2763584	1555.7	40.4	1283.9	15.5	83	
Sample GKR-1: Garnet-Sillimanite Gneiss, Southern Myponga Inlier											
GKR_01	3.71911	0.06741	0.27598	0.0034	0.333133	1581.8	33.6	1571.1	17.2	99	REE Analysis #1
GKR_02	3.76567	0.07126	0.27936	0.00351	0.3241017	1582.3	35.2	1588.1	17.7	100	
GKR_03	3.73241	0.07449	0.27803	0.00359	0.3022513	1574.6	37.3	1581.4	18.1	100	REE Analysis #2
GKR_04	3.46634	0.07156	0.259	0.00339	0.2965287	1568.8	38.7	1484.7	17.4	95	REE Analysis #3
GKR_06	3.73326	0.07693	0.27468	0.00357	0.3009412	1597.7	38.4	1564.5	18.1	98	REE Analysis #4
GKR_07	3.76832	0.07673	0.27713	0.00356	0.3063351	1598.5	37.8	1576.9	18.0	99	
GKR_13	3.75159	0.06757	0.27853	0.00344	0.3260743	1580.8	33.7	1583.9	17.4	100	REE Analysis #5
GKR_16	3.76027	0.0819	0.27868	0.00378	0.2592364	1584.1	41.5	1584.7	19.0	100	REE Analysis #6
GKR_17	3.75235	0.07156	0.27837	0.00347	0.2892331	1582.2	36.0	1583.2	17.5	100	REE Analysis #7
GKR_18	3.73719	0.07591	0.27832	0.00357	0.2739023	1574.9	38.6	1582.9	18.0	101	REE Analysis #8
GKR_19	3.72881	0.0714	0.2758	0.0034	0.2866608	1587.7	36.2	1570.2	17.2	99	REE Analysis #9
GKR_20	3.76938	0.08085	0.28113	0.00368	0.2459227	1572.1	41.0	1597.1	18.5	102	REE Analysis #10
GKR_22	3.54433	0.07538	0.26231	0.00337	0.2409555	1586.5	40.7	1501.6	17.2	95	REE Analysis #11
GKR_23	3.76422	0.08399	0.2788	0.00367	0.2197511	1585.1	42.8	1585.3	18.5	100	
GKR_24	3.77907	0.09167	0.27986	0.00388	0.1996146	1585.3	46.7	1590.7	19.5	100	REE Analysis #12
GKR_25	3.70967	0.07761	0.27509	0.00352	0.245672	1582.6	40.0	1566.6	17.8	99	REE Analysis #13
GKR_26	3.76763	0.074	0.2809	0.00343	0.2599556	1572.4	37.5	1595.9	17.3	101	
GKR_27	3.70349	0.07883	0.27816	0.00355	0.2296566	1558.6	40.9	1582.1	17.9	102	
GKR_28	3.73896	0.07685	0.27736	0.00344	0.2338547	1581.9	39.4	1578.0	17.4	100	
GKR_30	3.71644	0.08071	0.2735	0.00347	0.2187901	1596.8	41.7	1558.5	17.6	98	
GKR_32	3.73872	0.08406	0.2734	0.00349	0.2028658	1608.6	43.2	1558.0	17.7	97	REE Analysis #14
GKR_34	3.70818	0.08675	0.27556	0.00356	0.1811811	1578.7	45.3	1569.0	18.0	99	

Analysis #	$^{207}Pb/^{235}U$ Ratio	1σ	$^{206}Pb/^{238}U$ Ratio	1σ	Rho	$^{207}Pb/^{206}Pb$ Age	2σ	$^{206}Pb/^{238}U$ Age	2σ	Conc. %	Comments
Discordant Anlayses - Not Used											
GKR_05	3.62226	0.0694	0.26318	0.0033	0.3215189	1621.1	35.4	1506.1	16.8	93	
GKR_14	3.9429	0.07113	0.2951	0.00363	0.3227374	1565.7	33.9	1667.0	18.1	106	
GKR_15	3.31581	0.05832	0.23899	0.00289	0.3273226	1636.0	32.7	1381.5	15.0	84	
GKR_21	3.73355	0.08703	0.28495	0.00391	0.2282225	1528.8	45.0	1616.2	19.6	106	
GKR_29	3.41911	0.08846	0.25433	0.00368	0.1870028	1576.8	50.0	1460.7	18.9	93	
GKR_31	3.50697	0.08009	0.25375	0.00331	0.1986264	1628.4	43.8	1457.8	17.0	90	
GKR_33	3.47494	0.08497	0.25513	0.00344	0.1797351	1601.2	47.2	1464.9	17.7	91	
GKR_35	3.70621	0.08819	0.26568	0.00345	0.1771317	1645.8	45.8	1518.9	17.6	92	
GKR_36	3.60675	0.09451	0.25818	0.00359	0.1520615	1648.5	50.5	1480.5	18.4	90	

Chapter 5 Supplementary Data 2: Zircon and Garnet REE compositions

Sample SPR-1: Zircon REE Analyses

Analysis #	La	Ce	Pr	Nd	Sm	Eu	Gd	Tb	Dy	Ho	Er	Tm	Yb	Lu	Hf
Analyses in PPM															
SPRZ_01	63.87	314.64	49.88	284.46	172.17	45.64	291.08	77.24	546.41	96.1	241.97	37.69	301.4	43.33	13567.7
SPRZ_02	28.62	100.36	22.42	120.53	59.82	13.51	97.99	23.12	145.35	23.93	61.35	9.81	78.19	11.29	13567.7
SPRZ_03	1192.66	1499.98	302.88	1341.99	519.45	123.04	711.34	174.59	1192.79	198.08	506.13	82.78	660.43	86.4	13567.7
SPRZ_04	94.13	323.69	73.31	410.84	201.94	48.16	276.97	62.19	392.85	64.27	155.61	24.04	181.96	24.72	13567.7
SPRZ_05	175.99	585.24	134.34	749.71	336.89	80.48	456.5	106.38	719.19	125.98	321.03	51.75	404.65	53.66	13567.7
SPRZ_06	294.48	1163.6	189.25	995.8	455.84	106.04	593.48	135.44	897.49	152.89	396.68	63.12	490.94	70.11	13567.7
SPRZ_07	158.07	630.95	118.93	651.16	315.96	73.98	413.68	95.1	632.83	110.15	288.89	46.19	357.03	53.47	13567.7
AVERAGE	286.831	659.78	127.287	650.641	294.581	70.1214	405.863	96.2943	646.701	110.2	281.666	45.0543	353.514	48.9971	13567.7
Analyses Chondrite Normalised															
SPRZ_01	174.02	328.78	364.1	400.09	745.31	524.63	951.25	1331.64	1434.14	1129.26	971.75	1058.82	1215.31	1137.23	75797
SPRZ_02	77.99	104.87	163.66	169.53	258.94	155.24	320.22	398.61	381.49	281.15	246.4	275.48	315.29	296.36	75797
SPRZ_03	3249.77	1567.38	2210.78	1887.46	2248.7	1414.28	2324.65	3010.11	3130.67	2327.62	2032.66	2325.39	2663.03	2267.73	75797
SPRZ_04	256.48	338.23	535.1	577.84	874.21	553.6	905.14	1072.23	1031.1	755.25	624.94	675.39	733.71	648.85	75797
SPRZ_05	479.53	611.53	980.61	1054.44	1458.4	925.1	1491.82	1834.09	1887.63	1480.37	1289.29	1453.71	1631.65	1408.47	75797
SPRZ_06	802.41	1215.88	1381.42	1400.56	1973.35	1218.84	1939.48	2335.21	2355.62	1796.64	1593.09	1773.12	1979.6	1840.21	75797
SPRZ_07	430.7	659.3	868.1	915.84	1367.79	850.35	1351.89	1639.72	1660.98	1294.39	1160.2	1297.36	1439.65	1403.43	75797

Sample SPR-1: Garnet REE Analyses

Analysis #	La	Ce	Pr	Nd	Sm	Eu	Gd	Tb	Dy	Ho	Er	Tm	Yb	Lu	Hf
Analyses in PPM															
SPR2_01	<0.025	<0.022	0.022	0.493	1.09	0.062	8.01	4.07	53.91	12.32	35.43	4.97	31.8	4.33	0.207
SPR2_02	<0.028	0.037	0.03	0.48	1.23	0.063	7.7	4.38	54.83	11.81	32.75	4.8	32.29	4.47	<0.099
SPR2_03	<0.0164	0.024	0.0268	0.378	0.76	0.049	5.9	3.96	53.77	13.77	42.23	6.24	42.66	6.24	0.104
SPR2_04	0.0194	0.026	0.0262	0.351	0.455	0.098	5.76	4.08	69.38	21.89	79.76	12.91	92.85	13.49	0.153
SPR2_05	0.0189	<0.023	<0.0204	0.338	0.5	0.087	5.95	4.17	73.18	26.71	109.56	19.14	144.35	21.53	0.171
SPR2_06	<0.023	0.025	<0.0162	0.182	0.545	0.035	5.97	4.24	73.96	27.36	113.4	19.68	143.96	21.8	0.096
SPR2_07	<0.0225	0.024	<0.0202	0.225	0.485	<0.035	5.43	3.7	64.86	23.16	89.74	15.24	111.28	16.12	0.131
SPR2_08	<0.023	<0.025	0.046	0.587	1.33	0.088	7.59	4.39	69.63	20.13	67.5	10.76	74.36	10.66	0.176
SPR2_09	<0.0235	0.029	<0.0163	0.404	1.99	<0.033	8.96	4.02	52.44	13.13	39.55	5.85	38.88	5.53	0.144
SPR2_10	<0.024	<0.022	0.034	0.537	1.8	0.062	8.97	4.5	59.15	16.63	54.69	8.33	57.02	8.26	0.121
SPR2_11	<0.026	<0.022	0.022	0.519	1.48	0.07	9.57	4.52	46.38	9.14	25.91	3.76	26.95	4.03	<0.102
SPR2_12	<0.026	0.049	<0.0215	0.546	1.77	0.075	7.98	4.17	47.77	10.61	29.28	3.72	22.25	2.83	0.133
SPR3_01	<0.041	<0.031	<0.029	0.33	1.11	<0.063	7.29	4.97	80.25	28.09	102.14	17.01	107.63	14.63	<0.195
SPR3_02	<0.042	0.067	0.038	0.44	0.99	<0.059	7.64	4.78	78.46	28.81	102.5	16.67	111.24	14.96	<0.179
SPR3_03	<0.052	<0.045	<0.030	0.36	0.61	0.071	7.35	4.82	89.03	34.74	140.75	24.79	181.01	28.34	<0.161
SPR3_04	<0.050	<0.044	0.039	<0.28	0.86	0.123	8.67	5.13	94.52	36.1	149.92	27.04	202.06	31.62	0.26
SPR3_05	<0.053	<0.036	<0.046	0.32	1.22	<0.074	6.58	4.16	79	27.5	109.11	18.49	129.93	19.31	0.38
SPR3_06	<0.056	<0.042	0.041	0.41	0.76	<0.077	6.87	4.88	82.99	27.14	92.31	14.22	88.67	11.66	0.41

Analysis #	La	Ce	Pr	Nd	Sm	Eu	Gd	Tb	Dy	Ho	Er	Tm	Yb	Lu	Hf
SPR3_07	<0.056	<0.044	<0.041	0.61	0.98	<0.070	7.07	4.79	83.25	25.92	82.81	11.72	72.76	9	<0.166
SPR3_08	<0.040	<0.037	<0.039	0.68	0.62	<0.079	7.36	4.35	72.55	25.53	94.25	15.95	107.76	15.08	<0.21
SPR3_09	<0.050	<0.050	<0.042	0.48	0.85	<0.089	8.67	5.78	91.07	30.28	92.28	13.34	79.38	9.97	0.41
SPR3_10	<0.057	<0.038	<0.033	0.68	1.56	<0.070	9.38	5.48	92.35	27.22	79.62	11.67	67.26	8.14	<0.25
SPR3_11	0.156	0.067	0.078	0.96	1.06	0.073	7.05	4.58	73.05	22.58	69.8	10	58.61	7.46	<0.25
SPR3_12	<0.095	<0.056	<0.061	0.75	1.51	0.262	10.08	5.9	87.52	25.68	69.2	9.46	54.19	6.54	<0.29
SPR4_01	<0.028	<0.024	0.028	0.432	0.94	0.118	6.48	4.56	65.97	16.49	42.11	5.47	33.89	4.28	0.113
SPR4_02	<0.025	<0.031	<0.021	0.322	0.71	0.042	7.18	4.78	78.04	21.51	64.13	9.31	61.27	8.15	0.142
SPR4_03	<0.025	<0.025	0.024	0.286	0.88	0.046	7.04	4.67	72.18	19.45	55.93	7.96	50.96	6.61	0.161
SPR4_04	<0.0253	<0.022	<0.022	0.295	0.58	0.102	7.67	5.13	83.61	24.98	81.67	12.28	83.45	11.74	0.135
SPR4_05	<0.023	<0.031	<0.020	0.35	0.86	0.073	7.05	4.96	80.15	24.36	80.46	12.27	84.9	11.53	0.203
SPR4_06	<0.023	<0.034	<0.023	0.358	0.75	0.073	7.57	5.11	87.11	27.71	91.84	14.25	100.02	14.44	<0.107
SPR4_07	<0.025	<0.025	<0.018	0.239	0.6	0.059	7.05	4.78	78.03	23.78	75.86	11.39	75.48	10.45	0.227
SPR4_08	0.021	0.051	<0.0198	0.509	0.91	0.054	7.94	4.93	76.33	21.82	62.62	9.03	58.3	7.66	0.215
SPR4_09	<0.026	0.04	<0.021	0.495	1.31	0.08	7.45	4.5	67.49	17.15	47.59	6.22	40.75	5.33	0.209
SPR4_10	<0.0188	0.024	<0.0200	0.415	1.29	0.062	7.48	4.33	52.62	10.55	23.5	2.92	18.99	2.6	2.33
SPR4_11	0.126	0.411	0.071	0.76	2.24	0.07	9.81	4.38	46.11	8.59	19.52	2.55	17.92	2.59	0.129
SPR4_12	<0.0201	0.025	0.027	0.44	2.08	0.059	10.46	4.21	47.45	8.61	18.86	2.49	18.41	2.57	0.237
SPR-6_01	0.0172	0.0139	0.0389	0.58	0.99	0.07	7.63	3.84	41.52	8.02	19.6	2.78	18.65	2.61	0.132
SPR-6_02	1.29	1.61	0.299	1.93	0.34	0.055	0.233	0.0263	0.156	0.034	0.121	0.0175	0.151	0.024	0.74
SPR-6_03	<0.0053	0.0197	0.0199	0.267	0.64	0.045	6.91	4.69	75.83	22.58	75.81	11.96	81.08	11.4	0.111
SPR-6_04	0.0059	0.02	0.0166	0.314	0.427	0.067	5.47	3.89	65.98	21.84	77.7	12.54	89.21	12.95	0.144
SPR-6_05	<0.0131	0.0067	0.0227	0.402	0.66	0.053	6.49	4.43	79.12	28.92	114.94	20.27	150.26	22.51	0.142
SPR-6_06	0.0077	0.0135	0.0133	0.27	0.91	0.07	6.83	4.27	78.02	30.71	129.61	23.34	172.28	26.71	11.17
SPR-6_07	0.0021	0.0091	0.0244	0.54	1.03	0.103	7.91	5.2	91.08	33.15	129.65	21.8	156.5	22.88	0.162
SPR-6_08	<0.0077	0.0345	0.0144	0.374	0.78	0.078	7.07	4.49	80.46	28.49	107.09	17.69	121.53	17.4	0.115
SPR-7_01	<0.0067	0.0299	0.0231	0.285	0.529	0.041	5.32	3.52	58.83	18.93	67.51	10.96	75.16	10.01	0.074
SPR-7_02	<0.0080	0.0199	0.0193	0.147	0.49	0.056	6.87	4.37	70.46	20.42	62.16	9	56.73	6.98	0.193
SPR-7_03	0.03	0.038	0.0255	0.343	0.69	0.044	7.74	5.03	83.14	24.57	77.34	11.3	70.7	9.24	0.112
SPR-7_04	<0.0107	0.0232	0.0221	0.345	0.68	0.066	5.92	3.69	66.78	24.24	97.4	17.22	127.33	18.43	0.069
SPR-7_05	0.81	0.176	0.383	3.1	1.19	0.106	6.54	4.04	70.32	30.04	142.75	28.78	245.71	44.35	41.39
SPR-7_06	0.374	0.147	0.302	1.67	1.57	0.13	8.02	3.68	57.47	18.8	66.04	10.38	68.41	8.92	0.121
SPR-7_07	<0.0059	0.0161	0.0283	0.56	1.07	0.069	6.06	4.01	66.82	21.24	71.12	10.84	70.73	9.16	0.185
SPR-7_08	0.0089	0.033	0.0266	0.54	1.15	0.058	7.13	4.09	61.07	16.07	47.88	6.74	41.79	5.2	0.073
GKP-8_01	0.515	0.196	0.459	2.14	1.97	0.113	9.75	3.43	38.26	10.57	31.59	4.57	29.94	3.2	<0.039
GKP-8_02	<0.0113	<0.0096	0.0164	0.224	1.49	0.06	8.25	4.32	68.34	23.33	78.59	12.06	81.02	9.6	0.297
GKP-8_03	0.043	0.16	0.057	0.181	1.79	0.101	12.14	5.61	95.38	41.05	195	39.21	332.96	56.85	0.187
GKP-8_04	0.036	0.0211	0.0209	0.243	1.47	0.078	9.64	4.77	77.15	28.1	110.95	21.12	174.3	25.39	0.153
GKP-8_05	<0.0054	0.0195	0.0087	0.159	1	0.086	8.16	4.75	78.3	29.53	123.21	24.73	217.11	36.93	9.93
GKP-8_06	<0.0093	0.0206	0.0116	0.275	1	0.095	10.1	6.48	103.64	35.98	144.75	28.81	248.42	40.51	9.24
GKP-8_07	<0.0062	<0.0075	0.0073	0.215	0.97	0.091	10.11	6.14	93.83	30.05	114.88	21.93	186.29	27.6	0.195
GKP-8_08	0.016	0.073	0.029	0.38	1.09	0.099	10.72	6.24	88.13	23.48	70.38	11.01	82.54	9.96	1.49

Analysis #	La	Ce	Pr	Nd	Sm	Eu	Gd	Tb	Dy	Ho	Er	Tm	Yb	Lu	Hf
Analyses Chondrite Normalised															
SPR2_01	0	0	0.163	0.69	4.71	0.72	26.18	70.24	141.5	144.74	142.3	139.71	128.22	113.6	1.16
SPR2_02	0	0.039	0.219	0.67	5.32	0.72	25.17	75.56	143.9	138.82	131.53	134.78	130.22	117.23	0
SPR2_03	0	0.025	0.195	0.532	3.28	0.56	19.28	68.23	141.14	161.83	169.61	175.22	172	163.72	0.58
SPR2_04	0.053	0.027	0.191	0.493	1.97	1.13	18.82	70.28	182.11	257.19	320.32	362.58	374.41	354.2	0.86
SPR2_05	0.052	0	0	0.48	2.16	1	19.44	71.98	192.06	313.84	439.99	537.57	582.08	565.02	0.95
SPR2_06	0	0.027	0	0.255	2.36	0.4	19.51	73.14	194.11	321.54	455.4	552.77	580.49	572.15	0.54
SPR2_07	0	0.025	0	0.316	2.1	0	17.74	63.74	170.24	272.18	360.4	428.05	448.69	423.07	0.73
SPR2_08	0	0	0.333	0.83	5.76	1.01	24.82	75.76	182.76	236.49	271.09	302.23	299.85	279.72	0.98
SPR2_09	0	0.03	0	0.57	8.63	0	29.28	69.24	137.63	154.25	158.82	164.29	156.76	145.17	0.81
SPR2_10	0	0	0.25	0.75	7.8	0.71	29.32	77.65	155.26	195.46	219.62	233.96	229.93	216.68	0.68
SPR2_11	0	0	0.162	0.73	6.42	0.81	31.27	78.01	121.74	107.37	104.06	105.66	108.66	105.74	0
SPR2_12	0	0.051	0	0.77	7.65	0.86	26.06	71.97	125.37	124.73	117.6	104.41	89.73	74.36	0.74
SPR3_01	0	0	0	0.46	4.82	0	23.83	85.7	210.62	330.08	410.2	477.84	433.98	384.09	0
SPR3_02	0	0.07	0.28	0.62	4.28	0	24.95	82.41	205.93	338.54	411.64	468.36	448.53	392.74	0
SPR3_03	0	0	0	0.5	2.64	0.82	24.03	83.15	233.66	408.23	565.28	696.46	729.88	743.75	0
SPR3_04	0	0	0.28	0	3.7	1.42	28.35	88.41	248.08	424.2	602.07	759.64	814.77	829.96	1.46
SPR3_05	0	0	0	0.45	5.28	0	21.52	71.71	207.36	323.14	438.18	519.4	523.91	506.86	2.13
SPR3_06	0	0	0.3	0.58	3.3	0	22.45	84.11	217.82	318.89	370.73	399.38	357.53	306.12	2.3
SPR3_07	0	0	0	0.86	4.22	0	23.1	82.59	218.51	304.57	332.59	329.29	293.37	236.13	0
SPR3_08	0	0	0	0.95	2.68	0	24.05	75.05	190.43	300.01	378.52	447.95	434.53	395.84	0
SPR3_09	0	0	0	0.67	3.7	0	28.33	99.65	239.03	355.76	370.6	374.61	320.08	261.64	2.31
SPR3_10	0	0	0	0.95	6.73	0	30.67	94.55	242.39	319.86	319.74	327.74	271.22	213.69	0
SPR3_11	0.426	0.07	0.57	1.35	4.6	0.84	23.03	78.88	191.72	265.29	280.32	280.77	236.34	195.8	0
SPR3_12	0	0	0	1.05	6.55	3.01	32.93	101.8	229.72	301.82	277.92	265.85	218.5	171.62	0
SPR4_01	0	0	0.206	0.61	4.08	1.35	21.19	78.55	173.15	193.82	169.11	153.58	136.67	112.4	0.63
SPR4_02	0	0	0	0.45	3.05	0.49	23.45	82.43	204.83	252.71	257.54	261.42	247.07	213.82	0.79
SPR4_03	0	0	0.177	0.4	3.81	0.52	23.02	80.53	189.45	228.5	224.61	223.72	205.47	173.49	0.9
SPR4_04	0	0	0	0.42	2.51	1.17	25.05	88.42	219.46	293.56	328	344.9	336.49	308.14	0.75
SPR4_05	0	0	0	0.49	3.7	0.84	23.04	85.55	210.36	286.23	323.15	344.66	342.34	302.71	1.13
SPR4_06	0	0	0	0.5	3.23	0.84	24.74	88.09	228.63	325.68	368.82	400.15	403.29	378.93	0
SPR4_07	0	0	0	0.34	2.6	0.68	23.05	82.38	204.79	279.44	304.65	319.86	304.34	274.37	1.27
SPR4_08	0.056	0.053	0	0.72	3.92	0.62	25.94	85.01	200.34	256.43	251.49	253.55	235.1	201.01	1.2
SPR4_09	0	0.042	0	0.7	5.69	0.92	24.35	77.54	177.13	201.47	191.14	174.82	164.31	139.86	1.17
SPR4_10	0	0.025	0	0.58	5.57	0.71	24.43	74.63	138.1	123.97	94.37	81.91	76.59	68.2	13.02
SPR4_11	0.345	0.43	0.51	1.06	9.71	0.8	32.06	75.54	121.03	100.96	78.38	71.67	72.28	67.91	0.72
SPR4_12	0	0.026	0.195	0.62	8.99	0.68	34.19	72.58	124.55	101.21	75.74	69.89	74.23	67.56	1.32
SPR-6_01	0.047	0.0145	0.284	0.82	4.28	0.8	24.94	66.17	108.97	94.23	78.71	78.19	75.2	68.59	0.74
SPR-6_02	3.51	1.68	2.18	2.72	1.49	0.63	0.76	0.45	0.41	0.4	0.49	0.49	0.61	0.64	4.13
SPR-6_03	0	0.0206	0.145	0.375	2.77	0.52	22.58	80.86	199.02	265.29	304.47	335.81	326.94	299.33	0.62
SPR-6_04	0.016	0.0209	0.121	0.441	1.85	0.77	17.87	67.15	173.17	256.66	312.04	352.12	359.73	339.98	0.81
SPR-6_05	0	0.007	0.166	0.57	2.85	0.61	21.21	76.39	207.65	339.85	461.62	569.35	605.87	590.83	0.79
SPR-6_06	0.021	0.0141	0.097	0.379	3.93	0.8	22.33	73.58	204.78	360.91	520.52	655.62	694.69	700.93	62.39

Analysis #	La	Ce	Pr	Nd	Sm	Eu	Gd	Tb	Dy	Ho	Er	Tm	Yb	Lu	Hf
SPR-6_07	0.0058	0.0095	0.178	0.75	4.48	1.19	25.86	89.58	239.06	389.49	520.68	612.22	631.07	600.58	0.9
SPR-6_08	0	0.036	0.105	0.53	3.36	0.89	23.1	77.49	211.19	334.74	430.08	496.8	490.03	456.69	0.64
SPR-7_01	0	0.0312	0.168	0.401	2.29	0.47	17.39	60.76	154.42	222.4	271.12	307.74	303.08	262.84	0.41
SPR-7_02	0	0.0208	0.141	0.206	2.14	0.64	22.45	75.28	184.93	239.96	249.62	252.9	228.77	183.3	1.08
SPR-7_03	0.082	0.04	0.186	0.48	2.97	0.51	25.3	86.71	218.21	288.67	310.61	317.39	285.09	242.48	0.62
SPR-7_04	0	0.0243	0.161	0.485	2.96	0.76	19.36	63.61	175.29	284.9	391.17	483.81	513.43	483.74	0.38
SPR-7_05	2.2	0.184	2.79	4.36	5.16	1.22	21.37	69.58	184.57	353.03	573.29	808.42	990.77	1164.09	231.25
SPR-7_06	1.02	0.154	2.2	2.34	6.78	1.49	26.21	63.37	150.83	220.91	265.24	291.47	275.86	234.14	0.68
SPR-7_07	0	0.0169	0.207	0.79	4.65	0.8	19.81	69.16	175.37	249.64	285.64	304.49	285.21	240.31	1.03
SPR-7_08	0.024	0.0345	0.194	0.77	4.96	0.67	23.31	70.43	160.3	188.84	192.31	189.36	168.49	136.44	0.41
GKP-8_01	1.4	0.205	3.35	3	8.52	1.29	31.88	59.06	100.41	124.26	126.85	128.48	120.73	84.1	0
GKP-8_02	0	0	0.12	0.315	6.44	0.69	26.96	74.44	179.36	274.09	315.63	338.85	326.71	251.94	1.66
GKP-8_03	0.116	0.167	0.42	0.255	7.73	1.16	39.66	96.68	250.33	482.43	783.13	1101.48	1342.57	1492.19	1.05
GKP-8_04	0.097	0.022	0.152	0.341	6.38	0.89	31.5	82.31	202.51	330.2	445.57	593.24	702.82	666.35	0.86
GKP-8_05	0	0.0203	0.064	0.224	4.34	0.99	26.66	81.95	205.5	346.99	494.83	694.57	875.43	969.21	55.46
GKP-8_06	0	0.0216	0.085	0.387	4.31	1.09	33.01	111.73	272.03	422.81	581.34	809.26	1001.71	1063.19	51.59
GKP-8_07	0	0	0.053	0.303	4.21	1.05	33.03	105.79	246.28	353.13	461.37	616.06	751.17	724.47	1.09
GKP-8_08	0.044	0.076	0.212	0.54	4.7	1.14	35.04	107.59	231.31	275.9	282.66	309.34	332.82	261.43	8.31

Sample GKR-1: Zircon REE Analyses

Analysis #	La	Ce	Pr	Nd	Sm	Eu	Gd	Tb	Dy	Ho	Er	Tm	Yb	Lu	Hf
Analyses in PPM															
GKPZ_01	0.297	3.98	0.0964	1.318	3.94	0.816	21.95	6.22	50.99	13.21	50.13	10.75	106.57	20.52	14330.8
GKPZ_02	5.04	42.36	6.63	47.01	35.91	33.37	69.3	16.85	121.1	25.37	79.83	15.04	141.6	21.23	14330.8
GKPZ_03	0.478	4.5	0.154	1.77	4.51	0.931	23.65	5.63	34.49	6.24	17.25	2.81	23	4.12	14330.8
GKPZ_04	1.755	7.93	0.618	4.85	6.52	6.11	24.04	5.92	45.76	10.23	31.46	5.73	50.89	7.58	14330.8
GKPZ_05	0.486	5.11	0.1251	2.18	4.1	0.576	17.61	4.12	28.49	5.77	16.1	2.656	19.68	2.98	14330.8
GKPZ_06	1.276	7.49	0.864	6.71	6.84	2.78	26.99	7.05	55.13	13.64	43.64	7.14	57.33	9.77	14330.8
GKPZ_07	1.666	10.12	1.295	9.71	11.01	6.62	45.9	15.54	150.64	44.79	187.1	41.12	388.19	74.89	14330.8
GKPZ_08	0.428	4.58	0.204	2.32	5.21	1.056	24.42	6.02	38.67	7.73	23.45	3.99	34.23	6.24	14330.8
GKPZ_09	0.384	3.53	0.148	1.39	3.66	0.675	19.48	5.31	35.39	7.02	19.53	3.01	23.92	3.43	14330.8
GKPZ_10	3.86	16.88	2.8	17.31	12.61	7.43	38.57	9.53	69.21	14.72	46.5	9	86.86	14.31	14330.8
GKPZ_11	75.25	204.04	32.04	179.49	84.96	60.23	148.15	36.5	307.58	79.93	303.61	62.29	595.94	103.48	14330.8
GKPZ_12	0.21	4.9	0.114	2.11	6.34	0.847	29.22	6.28	34.11	5.44	12.16	1.629	11.01	1.756	14330.8
GKPZ_13	0.107	4.21	0.128	1.86	5.18	0.937	25.36	6.33	45.27	9.23	25.09	3.63	25.45	3.93	14330.8
GKPZ_14	0.238	5.34	0.145	1.72	4.4	0.749	21.08	5.6	39.84	8.39	23.71	3.99	31.71	5	14330.8
Analyses Chondrite Normalised															
GKPZ_01	0.808	4.16	0.704	1.85	17.07	9.38	71.73	107.16	133.82	155.18	201.33	301.86	429.71	538.67	80060.5
GKPZ_02	13.74	44.27	48.4	66.12	155.45	383.53	226.46	290.5	317.84	298.15	320.6	422.54	570.95	557.26	80060.5
GKPZ_03	1.303	4.7	1.123	2.48	19.54	10.7	77.3	97.12	90.52	73.35	69.29	79.05	92.75	108.05	80060.6
GKPZ_04	4.78	8.29	4.51	6.82	28.22	70.25	78.55	102	120.09	120.21	126.34	160.82	205.21	198.89	80060.6
GKPZ_05	1.325	5.34	0.913	3.07	17.76	6.62	57.56	71.04	74.79	67.76	64.65	74.6	79.34	78.34	80060.6

Analysis #	La	Ce	Pr	Nd	Sm	Eu	Gd	Tb	Dy	Ho	Er	Tm	Yb	Lu	Hf
GKPZ_06	3.48	7.83	6.31	9.44	29.63	31.95	88.21	121.63	144.69	160.26	175.26	200.56	231.17	256.32	80060.6
GKPZ_07	4.54	10.58	9.45	13.65	47.66	76.13	149.99	267.96	395.37	526.31	751.4	1154.93	1565.28	1965.53	80060.6
GKPZ_08	1.167	4.78	1.49	3.27	22.57	12.14	79.82	103.71	101.49	90.84	94.18	112.06	138.02	163.67	80060.6
GKPZ_09	1.045	3.69	1.079	1.95	15.86	7.76	63.66	91.61	92.89	82.47	78.42	84.58	96.45	89.97	80060.6
GKPZ_10	10.51	17.64	20.44	24.35	54.58	85.45	126.03	164.34	181.66	172.95	186.76	252.92	350.23	375.51	80060.6
GKPZ_11	205.03	213.21	233.9	252.45	367.81	692.32	484.14	629.24	807.29	939.2	1219.31	1749.72	2402.98	2716.05	80060.6
GKPZ_12	0.572	5.12	0.83	2.97	27.47	9.74	95.48	108.26	89.53	63.97	48.82	45.76	44.4	46.1	80060.6
GKPZ_13	0.291	4.4	0.937	2.62	22.41	10.77	82.88	109.11	118.82	108.42	100.76	101.86	102.63	103.19	80060.6
GKPZ_14	0.648	5.58	1.061	2.43	19.03	8.61	68.88	96.47	104.56	98.57	95.21	112.06	127.86	131.18	80060.6

Sample SPR-1: Garnet REE Analyses

Analysis #	La	Ce	Pr	Nd	Sm	Eu	Gd	Tb	Dy	Ho	Er	Tm	Yb	Lu	Hf
Analyses in PPM															
GKP-1_01	0.0006	0.0053	0.0069	0.234	2.59	0.317	12.98	2.97	19.1	3.01	6.13	0.708	4.06	0.541	0.207
GKP-1_02	0.00073	0.0064	0.0104	0.392	2.56	0.414	14.82	3.66	24.93	4.03	8.12	0.95	5.87	0.745	0.221
GKP-1_03	0.036	0.028	0.0156	0.089	1.09	0.265	11.8	3.53	26.95	5.04	12.33	1.57	9.54	1.26	0.201
GKP-1_04	<0.0027	0.0072	0.0043	0.067	1.52	0.292	14.66	4.16	30.73	5.69	14.24	1.77	11.32	1.55	0.309
GKP-1_05	<0.0031	0.003	<0.0021	0.109	2.42	0.42	16.58	4.35	31.2	5.98	13.67	1.57	9.23	1.26	0.383
GKP-1_06	0.0032	0.0133	0.0021	0.047	1.32	0.248	15.22	4.07	30.62	5.52	13.11	1.59	9.13	1.26	0.25
GKP-1_07	0.0032	0.0071	0.0048	0.027	0.82	0.205	14.34	4.22	31.76	5.62	13.36	1.68	10.2	1.38	0.16
GKP-1_08	<0.00243	0.0052	0.0076	0.357	3.05	0.439	15.58	3.65	23.09	3.6	7.78	0.86	5.38	0.68	0.3
GKP-2_01	<0.0036	0.0065	<0.0017	0.09	1.89	0.309	14.35	3.64	24.75	3.9	7.88	0.807	4.51	0.594	0.27
GKP-2_02	0.0227	0.0136	0.0106	0.249	3.36	0.517	21.51	5.26	36.19	5.45	10.34	1.09	5.95	0.79	0.447
GKP-2_03	0.0299	0.0485	0.0488	0.245	1.97	0.267	11.06	2.77	18.42	2.81	5.38	0.591	3.13	0.423	0.19
GKP-2_04	<0.0063	0.013	0.0094	0.43	3.96	0.56	22.88	5.63	37.18	5.54	10.63	1.24	6.33	0.81	0.46
GKP-2_05	0.358	0.69	0.133	0.73	2.95	0.519	17.11	4.07	26.75	3.97	8.05	0.84	4.73	0.646	0.364
GKP-2_06	0.0033	0.0164	<0.0027	0.315	2.51	0.405	14.39	3.47	23.25	3.48	6.71	0.69	4.29	0.537	0.219
GKP-2_07	0.0165	0.0191	0.0126	0.298	3.37	0.473	19.12	4.49	29.63	4.35	8.49	0.86	5.04	0.68	0.373
GKP-2_08	<0.0055	0.0071	0.0083	0.262	2.78	0.443	16.93	4.05	25.75	3.83	7.64	0.86	5.09	0.622	0.301
GKP-3_01	<0.00211	0.0035	0.0018	0.089	1.64	0.291	12.05	3.06	20.22	3.19	6.69	0.76	4.46	0.567	0.185
GKP-3_02	0.00138	0.0203	0.0285	0.713	3	0.367	12.85	3.04	19.74	3.31	7.84	0.99	5.73	0.753	0.318
GKP-3_03	0.0241	0.058	0.045	1.13	4.72	0.497	18.16	3.97	24.6	3.98	8.74	1.06	6.17	0.82	0.438
GKP-3_04	<0.0037	0.0294	0.0046	0.053	1.67	0.321	16.94	4.72	34.93	6.4	15.25	1.88	11.13	1.35	0.236
GKP-3_05	<0.28	0.0057	0.0051	0.201	2.37	0.376	15.93	4.37	31.96	5.64	13.86	1.72	10.82	1.49	0.373
GKP-3_06	0.0127	0.0205	0.0177	0.453	2.93	0.345	13.02	3.22	22.34	3.45	7.01	0.769	4.93	0.58	0.196
GKP-3_07	0.0032	0.086	0.0473	1.05	3.76	0.467	14.84	3.43	22.54	3.72	8.67	1.11	6.67	0.9	0.361
GKP-3_08	0.0032	0.0356	0.0354	0.86	3.55	0.433	15.19	3.4	21.87	3.69	9.01	1.22	7.73	1.01	0.323
GKP-4_01	<0.00300	0.0061	<0.0020	0.0117	0.86	0.186	14.33	4.19	30.31	5.12	11.85	1.44	8.6	1.09	0.233
GKP-4_02	<0.00	0.0063	0.0063	0.328	3.14	0.453	18.54	3.94	24.32	4.15	9.84	1.34	8.37	1.03	0.411
GKP-4_03	0.0204	0.0126	0.0106	0.24	2.4	0.358	14.91	3.67	24.46	4.2	9.78	1.24	7.74	0.98	0.323
GKP-4_04	0.0131	0.0318	0.0374	0.8	3.85	0.524	21.54	5.33	34.97	6.42	16.48	2.27	14.66	1.9	0.558
GKP-4_05	0.0144	0.0207	0.0308	0.67	3.42	0.421	17.78	4.15	26.86	4.64	11.68	1.53	9.92	1.33	0.462

Analysis #	La	Ce	Pr	Nd	Sm	Eu	Gd	Tb	Dy	Ho	Er	Tm	Yb	Lu	Hf
GKP-4_06	<0.0032	0.0272	0.0244	0.64	3.61	0.456	18.23	4.34	26.3	3.74	7.25	0.83	4.74	0.591	0.245
GKP-4_07	0.006	0.0251	0.0226	0.562	3.24	0.405	17.08	4.11	26.55	4.4	9.86	1.28	7.89	1.13	0.438
GKP-4_08	0.0131	0.0362	0.0218	0.77	3.58	0.398	17.66	4.37	26.29	3.72	7.04	0.79	4.63	0.545	0.205
GKP-5_01	<0.0022	0.0036	0.0047	0.244	2.25	0.329	11.68	3.18	26.86	5.51	13.22	1.49	8.23	1.11	0.267
GKP-5_02	<0.00	0.008	0.0068	0.214	2.39	0.358	14.79	3.72	28.49	5.26	13.4	1.75	10.66	1.42	0.353
GKP-5_03	0.0036	0.007	0.0068	0.211	2.59	0.405	16.55	4.45	32.96	6	14.78	1.9	12.03	1.62	0.384
GKP-5_04	0.0011	0.0068	0.0053	0.382	3.17	0.436	20.51	5.26	37.28	6.77	16.55	2.17	14.39	1.89	0.294
GKP-5_05	<0.0029	0.0106	0.0119	0.365	2.86	0.413	17.32	4.89	37.25	6.86	17.53	2.44	15.98	2.09	0.314
GKP-5_06	<0.0030	0.0031	0.0086	0.275	2.81	0.409	13.55	3.57	31.45	6.28	14.13	1.57	8.84	1.18	0.363
GKP-5_07	0.0057	0.0147	0.0015	0.168	3.03	0.398	19.05	4.91	37.82	7.26	17.18	2.07	11.68	1.51	0.398
GKP-5_08	<0.0030	<0.0045	0.0088	0.369	2.96	0.461	12.89	3.6	34.52	7.01	15.72	1.73	9.74	1.26	0.352
GKP-6_01	0.002	<0.0028	<0.0021	0.121	2.42	0.372	18.91	4.74	34.27	6.08	13.89	1.75	11.01	1.29	0.278
GKP-6_02	<0.0037	0.0093	0.0126	0.53	3.85	0.488	22.68	5.29	37.76	5.95	12.5	1.4	8.3	1.03	0.436
GKP-6_03	0.0063	0.0032	0.0066	0.099	2.19	0.337	13.66	3.14	23.15	3.96	8.1	0.89	5.12	0.638	0.254
GKP-6_04	0.0233	0.0144	0.0128	0.098	2.4	0.37	15.08	3.53	26.33	4.45	9.4	1.01	5.64	0.78	0.307
GKP-6_05	0.0119	0.0129	0.0025	0.183	2.1	0.332	11.52	2.96	23.19	4.2	8.51	0.89	5.38	0.7	0.213
GKP-6_06	0.0012	0.0096	0.0034	0.2	2.5	0.376	15.79	3.7	30.58	5.47	11.34	1.16	6.64	0.84	0.347
GKP-6_07	0.0098	<0.0024	<0.0019	0.176	2.05	0.322	13.09	3.15	25.02	4.7	9.79	1.07	6.13	0.82	0.296
GKP-6_08	0.053	<0.043	0.0119	0.109	1.96	0.347	15.36	3.73	28.36	5.26	12.11	1.4	8.3	1.08	0.28
GKP-7_01	0.0092	0.0087	0.004	0.22	2.65	0.384	12.64	3.2	27.98	5.16	11	1.12	6.37	0.88	0.344
GKP-7_02	0.0034	0.0089	0.0037	0.108	1.96	0.302	11.11	2.85	21.54	3.93	8.08	0.86	4.91	0.659	0.261
GKP-7_03	<0.0033	0.0101	0.015	0.466	3.75	0.516	18.37	4.36	32.05	5.48	11.76	1.33	7.78	0.97	0.403
GKP-7_04	0.0024	0.0113	0.0143	0.476	3.09	0.401	14.93	3.43	23.47	3.87	9	1.13	6.97	0.86	0.271
GKP-7_05	0.0286	0.0139	0.0109	0.209	2.05	0.274	10.4	2.66	18.75	3.18	7.66	0.99	5.8	0.757	0.282
GKP-7_06	<0.00	0.0044	0.0075	0.394	2.89	0.362	12.62	3.1	22.39	3.51	6.64	0.715	3.79	0.469	0.202
GKP-7_07	0.002	0.0162	0.0146	0.584	3.67	0.457	15.42	3.65	25.81	4.21	9	1.03	6.25	0.8	0.308
GKP-7_08	<0.0023	0.0055	0.0077	0.299	2.66	0.314	11.1	2.58	17.91	3.11	6.96	0.91	5.66	0.76	0.233
GKP-8_01	<0.0035	0.0047	0.0022	0.117	3.8	0.526	20.58	4.91	35.86	5.91	11.35	1.15	6.6	0.86	0.364
GKP-8_02	<0.0024	<0.0036	0.0035	0.097	2.23	0.301	13.29	3.17	22.11	3.45	6.27	0.628	3.24	0.412	0.204
GKP-8_03	0.0108	0.0085	0.0073	0.169	2.61	0.37	14.21	3.28	21.55	3.35	6.63	0.79	4.62	0.55	0.233
GKP-8_04	<0.0037	0.0061	0.0071	0.248	2.28	0.339	10.9	2.73	17.79	2.52	4.8	0.499	2.72	0.337	0.237
GKP-8_05	0.0022	0.0205	0.0227	0.67	3.57	0.456	16.98	4.33	31.54	5.28	11.7	1.47	9.57	1.23	0.277
GKP-8_06	0.0036	0.0134	0.0153	0.311	2.67	0.324	9.99	2.65	18.34	2.53	4.3	0.413	2.46	0.293	0.165
GKP-8_07	0.16	0.093	0.0359	0.382	2.33	0.336	11.49	2.73	18.89	2.83	5.18	0.548	2.97	0.361	0.22
GKP-8_08	0.0033	0.0064	0.0022	0.201	2.56	0.333	9.29	2.9	24.98	4.31	8.3	0.9	5.08	0.74	0.233
Analyses Chondrite Normalised															
GKP-1_01	0.0016	0.0055	0.051	0.329	11.2	3.65	42.43	51.26	50.14	35.31	24.61	19.89	16.37	14.21	1.15
GKP-1_02	0.002	0.0067	0.076	0.551	11.08	4.76	48.43	63.19	65.44	47.33	32.62	26.69	23.69	19.55	1.23
GKP-1_03	0.098	0.0293	0.114	0.125	4.74	3.04	38.56	60.92	70.74	59.18	49.54	44.17	38.47	33.13	1.12
GKP-1_04	0	0.0075	0.031	0.094	6.57	3.36	47.91	71.7	80.66	66.88	57.17	49.66	45.65	40.66	1.73
GKP-1_05	0	0.0031	0	0.154	10.48	4.83	54.18	75.06	81.89	70.23	54.89	44.01	37.23	33.09	2.14
GKP-1_06	0.0086	0.0139	0.016	0.066	5.72	2.86	49.74	70.22	80.37	64.92	52.64	44.74	36.81	32.97	1.4
GKP-1_07	0.0088	0.0075	0.035	0.039	3.57	2.36	46.86	72.75	83.37	66.01	53.67	47.3	41.14	36.25	0.89

Analysis #	La	Ce	Pr	Nd	Sm	Eu	Gd	Tb	Dy	Ho	Er	Tm	Yb	Lu	Hf
GKP-1_08	0	0.0055	0.055	0.502	13.2	5.05	50.91	62.85	60.61	42.35	31.26	24.2	21.7	17.84	1.67
GKP-2_01	0	0.0068	0	0.126	8.17	3.56	46.88	62.78	64.96	45.8	31.64	22.66	18.21	15.59	1.51
GKP-2_02	0.062	0.0142	0.077	0.35	14.54	5.94	70.28	90.71	94.98	64.08	41.53	30.51	23.98	20.61	2.5
GKP-2_03	0.082	0.0506	0.356	0.344	8.52	3.07	36.15	47.78	48.35	32.98	21.62	16.61	12.6	11.11	1.06
GKP-2_04	0	0.0136	0.069	0.61	17.13	6.45	74.76	97.14	97.57	65.05	42.7	34.91	25.52	21.19	2.56
GKP-2_05	0.98	0.72	0.97	1.03	12.78	5.96	55.92	70.19	70.22	46.7	32.33	23.66	19.06	16.95	2.04
GKP-2_06	0.0089	0.0171	0	0.443	10.88	4.65	47.03	59.85	61.03	40.93	26.95	19.34	17.28	14.09	1.22
GKP-2_07	0.045	0.02	0.092	0.419	14.57	5.43	62.48	77.5	77.77	51.15	34.1	24.13	20.33	17.79	2.08
GKP-2_08	0	0.0075	0.061	0.369	12.04	5.09	55.32	69.9	67.59	45.02	30.67	24.21	20.52	16.32	1.68
GKP-3_01	0	0.0037	0.0135	0.125	7.08	3.34	39.37	52.68	53.07	37.53	26.86	21.36	17.97	14.88	1.04
GKP-3_02	0.0038	0.0212	0.208	1	13	4.22	41.98	52.43	51.8	38.93	31.49	27.89	23.09	19.76	1.78
GKP-3_03	0.066	0.061	0.328	1.59	20.44	5.71	59.35	68.45	64.56	46.79	35.08	29.64	24.88	21.65	2.45
GKP-3_04	0	0.0307	0.034	0.074	7.23	3.69	55.36	81.41	91.68	75.17	61.25	52.71	44.89	35.38	1.32
GKP-3_05	0	0.006	0.038	0.283	10.24	4.32	52.06	75.27	83.88	66.24	55.68	48.32	43.65	39.18	2.08
GKP-3_06	0.0345	0.0214	0.129	0.638	12.7	3.96	42.54	55.53	58.63	40.49	28.16	21.6	19.89	15.22	1.09
GKP-3_07	0.0088	0.09	0.346	1.48	16.27	5.37	48.51	59.16	59.17	43.66	34.83	31.16	26.88	23.68	2.02
GKP-3_08	0.0086	0.0372	0.259	1.21	15.38	4.97	49.65	58.59	57.4	43.38	36.19	34.27	31.16	26.52	1.8
GKP-4_01	0	0.0063	0	0.0165	3.7	2.13	46.82	72.3	79.56	60.15	47.59	40.38	34.68	28.5	1.3
GKP-4_02	0	0.0066	0.046	0.462	13.58	5.21	60.6	67.9	63.84	48.73	39.51	37.73	33.76	27.16	2.3
GKP-4_03	0.055	0.0132	0.077	0.338	10.41	4.12	48.71	63.32	64.2	49.31	39.26	34.89	31.2	25.63	1.8
GKP-4_04	0.036	0.0332	0.273	1.13	16.67	6.02	70.39	91.85	91.8	75.49	66.17	63.88	59.11	49.9	3.12
GKP-4_05	0.039	0.0216	0.225	0.94	14.79	4.84	58.1	71.48	70.51	54.48	46.9	43.07	40.02	34.98	2.58
GKP-4_06	0	0.0285	0.178	0.9	15.64	5.24	59.59	74.84	69.04	43.92	29.13	23.38	19.12	15.51	1.37
GKP-4_07	0.0164	0.0262	0.165	0.79	14.04	4.65	55.83	70.94	69.68	51.65	39.6	36.04	31.83	29.63	2.45
GKP-4_08	0.036	0.0378	0.159	1.08	15.51	4.57	57.73	75.26	68.99	43.7	28.26	22.12	18.68	14.31	1.14
GKP-5_01	0	0.0038	0.035	0.343	9.72	3.78	38.18	54.91	70.51	64.76	53.09	41.72	33.18	29.23	1.49
GKP-5_02	0	0.0084	0.05	0.3	10.36	4.12	48.32	64.11	74.78	61.84	53.8	49.05	42.99	37.33	1.97
GKP-5_03	0.0099	0.0074	0.05	0.297	11.21	4.66	54.07	76.75	86.5	70.56	59.34	53.24	48.51	42.48	2.15
GKP-5_04	0.003	0.0071	0.039	0.54	13.72	5.01	67.04	90.73	97.85	79.61	66.47	60.85	58.03	49.5	1.64
GKP-5_05	0	0.011	0.087	0.513	12.4	4.75	56.6	84.25	97.76	80.63	70.42	68.51	64.43	54.86	1.75
GKP-5_06	0	0.0033	0.063	0.387	12.16	4.7	44.27	61.57	82.55	73.83	56.74	44.21	35.65	31.04	2.03
GKP-5_07	0.0155	0.0154	0.0113	0.236	13.11	4.58	62.25	84.67	99.25	85.28	69	58.06	47.1	39.51	2.22
GKP-5_08	0	0	0.064	0.519	12.8	5.3	42.13	61.99	90.6	82.43	63.14	48.57	39.28	33.06	1.97
GKP-6_01	0.0053	0	0	0.17	10.46	4.28	61.8	81.78	89.95	71.39	55.77	49.05	44.39	33.78	1.55
GKP-6_02	0	0.0097	0.092	0.74	16.67	5.61	74.12	91.25	99.1	69.88	50.21	39.26	33.46	27.07	2.44
GKP-6_03	0.0172	0.0033	0.048	0.14	9.49	3.87	44.65	54.19	60.75	46.49	32.51	25.09	20.64	16.73	1.42
GKP-6_04	0.064	0.015	0.094	0.138	10.4	4.25	49.28	60.79	69.12	52.31	37.74	28.24	22.75	20.58	1.71
GKP-6_05	0.032	0.0135	0.018	0.258	9.1	3.81	37.65	51.11	60.87	49.36	34.17	25.05	21.68	18.27	1.19
GKP-6_06	0.0033	0.01	0.025	0.281	10.82	4.32	51.61	63.85	80.25	64.24	45.55	32.47	26.76	22.04	1.94
GKP-6_07	0.0268	0	0	0.247	8.87	3.71	42.79	54.32	65.68	55.22	39.31	29.97	24.72	21.61	1.65
GKP-6_08	0.144	0	0.087	0.154	8.49	3.99	50.19	64.31	74.43	61.81	48.65	39.24	33.46	28.25	1.57
GKP-7_01	0.0252	0.0091	0.029	0.309	11.45	4.42	41.29	55.17	73.45	60.63	44.19	31.59	25.7	23.03	1.92
GKP-7_02	0.0093	0.0093	0.027	0.152	8.49	3.47	36.32	49.14	56.54	46.21	32.44	24.24	19.79	17.31	1.46

Analysis #	La	Ce	Pr	Nd	Sm	Eu	Gd	Tb	Dy	Ho	Er	Tm	Yb	Lu	Hf
GKP-7_03	0	0.0105	0.11	0.66	16.25	5.93	60.03	75.15	84.13	64.34	47.21	37.32	31.38	25.42	2.25
GKP-7_04	0.0066	0.0118	0.104	0.67	13.37	4.6	48.79	59.15	61.61	45.51	36.14	31.83	28.09	22.6	1.51
GKP-7_05	0.078	0.0146	0.079	0.293	8.86	3.15	33.99	45.8	49.22	37.33	30.75	27.67	23.39	19.88	1.58
GKP-7_06	0	0.0045	0.054	0.554	12.5	4.16	41.24	53.41	58.76	41.25	26.67	20.09	15.3	12.31	1.13
GKP-7_07	0.0054	0.0169	0.107	0.82	15.9	5.25	50.4	63.02	67.74	49.45	36.13	28.8	25.2	20.87	1.72
GKP-7_08	0	0.0057	0.056	0.42	11.5	3.61	36.28	44.55	47.01	36.58	27.95	25.62	22.84	19.87	1.3
GKP-8_01	0	0.0049	0.016	0.165	16.46	6.05	67.25	84.73	94.11	69.46	45.58	32.43	26.6	22.61	2.04
GKP-8_02	0	0	0.026	0.137	9.67	3.46	43.42	54.64	58.03	40.53	25.18	17.65	13.05	10.82	1.14
GKP-8_03	0.0294	0.0089	0.053	0.238	11.3	4.25	46.43	56.54	56.56	39.33	26.63	22.24	18.61	14.44	1.3
GKP-8_04	0	0.0064	0.052	0.349	9.87	3.9	35.61	47.02	46.69	29.6	19.28	14	10.97	8.86	1.32
GKP-8_05	0.0059	0.0214	0.166	0.94	15.45	5.24	55.48	74.65	82.79	62.05	47	41.23	38.59	32.23	1.55
GKP-8_06	0.0097	0.014	0.112	0.438	11.54	3.72	32.65	45.7	48.14	29.74	17.28	11.59	9.94	7.69	0.92
GKP-8_07	0.436	0.097	0.262	0.538	10.08	3.87	37.55	47.06	49.58	33.3	20.81	15.4	11.98	9.47	1.23
GKP-8_08	0.0091	0.0067	0.0163	0.283	11.1	3.82	30.34	49.93	65.55	50.62	33.34	25.36	20.49	19.32	1.3

Sample SPR-1: Zircon - Garnet REE Distribution Coefficients - D(Zr/Gt)

Analysis #	La	Ce	Pr	Nd	Sm	Eu	Gd	Tb	Dy	Ho	Er	Tm	Yb	Lu	Hf
Gt Av. ALL	0.19428	0.09999	0.06262	0.53297	1.04402	0.0778	7.59988	4.51944	70.8079	22.3566	78.7442	13.016	93.7049	13.7127	1.73796
Zr Av. All	286.831	659.78	127.287	650.641	294.581	70.1214	405.863	96.2943	646.701	110.2	281.666	45.0543	353.514	48.9971	13567.7
D(Zr/Gt)	1476.36	6598.35	2032.84	1220.79	282.162	901.304	53.4038	21.3067	9.13318	4.9292	3.57697	3.46147	3.77264	3.57311	7806.67

Sample GKR-1: Zircon - Garnet REE Distribution Coefficients - D(Zr/Gt)

Analysis #	La	Ce	Pr	Nd	Sm	Eu	Gd	Tb	Dy	Ho	Er	Tm	Yb	Lu	Hf
Garnet Av.	0.02323	0.02796	0.01538	0.33135	2.69063	0.38342	15.2833	3.80703	27.1064	4.61313	10.1795	1.20434	7.20078	0.93813	0.30208
All Zircon - Ungrouped															
Zircon Av. ALL	6.53393	23.2121	3.24011	19.982	13.9421	8.79479	38.2657	9.77857	75.4764	17.9793	62.8257	12.3418	114.027	19.9454	14330.8
D(zr/Gt - All)	281.298	830.262	210.727	60.304	5.18175	22.9376	2.50376	2.56856	2.78445	3.89742	6.17177	10.2477	15.8354	21.2609	47440.8
Zircon Population A - LREE Enriched (Hydrothermal)															
Zircon Av. A	14.8078	48.1367	7.3745	44.18	26.3083	19.4233	58.825	15.2317	124.903	31.4467	115.357	23.3867	220.135	38.5433	14330.8
D(Zr/Gt - a)	637.506	1721.77	479.615	133.331	9.77778	50.6579	3.84898	4.00093	4.60789	6.81678	11.3322	19.4186	30.571	41.0855	47440.8
Zircon Population B - LREE Depleated (Metamorphic)															
Zircon Av. B	0.3285	4.51875	0.13931	1.8335	4.6675	0.82338	22.8463	5.68875	38.4063	7.87875	23.4275	4.05813	34.4463	5.997	14330.8
D(Zr/Gt - b)	14.1426	161.629	9.06047	5.53335	1.73473	2.14744	1.49485	1.49427	1.41687	1.7079	2.30143	3.36957	4.78368	6.39254	47440.8

CHAPTER 6

This Chapter is written for submission to
Earth and Planetary Science Letters as;

Meaney, K., Hand, M., Payne, J.,
What you expect versus what you get:
How well can you trust zircons in modern stream systems?

Statement of Authorship

Title of Paper	What you expect versus what you get: How well can you trust zircons in modern stream systems?
Publication Status	☐ Published ☐ Accepted for Publication ☐ Submitted for Publication ☑ Unpublished and Unsubmitted w ork w ritten in manuscript style
Publication Details	Written to be submitted to Earth and Planetary Science Letters

Principal Author

Name of Principal Author (Candidate)	Kieran Meaney		
Contribution to the Paper	Project design, Fieldwork, Sample Preparation, LA-ICP-MS Data Collection, MC-LA-ICP-MS Data Collection, Data interpretation, Manuscript design, Creation of figures		
Overall percentage (%)	75		
Certification:	This paper reports on original research I conducted during the period of my Higher Degree by Research candidature and is not subject to any obligations or contractual agreements with a third party that would constrain its inclusion in this thesis. I am the primary author of this paper.		
Signature		Date	21/12/17

Co-Author Contributions

By signing the Statement of Authorship, each author certifies that:

i. the candidate's stated contribution to the publication is accurate (as detailed above);
ii. permission is granted for the candidate in include the publication in the thesis; and
iii. the sum of all co-author contributions is equal to 100% less the candidate's stated contribution.

Name of Co-Author	Martin Hand		
Contribution to the Paper	Guidance with Project Design, Guidance with data interpretation, Manuscript review		
Signature		Date	22/12/2017

Name of Co-Author	Justin Payne		
Contribution to the Paper	MC-LA-ICP-MS Data Collection, Data quality control, Manuscript Review		
Signature		Date	20/12/17

ABSTRACT

Detrital zircon sampling from modern drainage systems is used extensively as an efficient approach in determining the age and isotopic evolution of large regions of crust. This technique has been applied to the Broken Hill region in the eastern Curnamona Province in Southern Australia to compare stream-hosted detrital zircon age populations with those expected from erosion of the 1710-1640 Ma Willyama Supergroup which forms the bedrock geology. A large existing detrital zircon dataset obtained from in situ sampling of the Willyama Supergroup coupled with outcrop distribution and modern drainage patterns allows synthetic age histograms to be constructed for specific sample locations within the modern stream system. Comparison of these synthetic histograms with the actual stream-hosted zircon U-Pb age data shows significant differences. Despite that the youngest expected zircon age for the Willyama Supergroup is c. 1600 Ma, analysis of the modern stream-hosted detrital zircons shows significant proportions of 1300-1000 Ma and 600-100 Ma zircons in every sample. In order to identify the possible source of these younger zircons, samples of sand dunes from the Strzelecki Desert approximately 120 km north of Broken Hill were analysed, and also show significant proportions of 1300-1000 Ma and 600-100 Ma zircons. The aeolian deposited sediments of the Strzelecki Desert dunes are a likely source for the young zircons in the modern streams in the Broken Hill area. The dunes are sourced from successive reworking events that cover a widespread region of eastern Australia. They contain approximately 20% of grains older than 1600 Ma with ages are similar to that expected from erosion of the Willyama Supergroup. Therefore the presence of Palaeoproterozoic-aged zircons in the Strzelecki Desert dunes means that Palaeoproterozoic-aged grains in the Broken Hill area streams cannot be assumed to come from the Willyama Supergroup. The U-Pb-Hf compositions of modern stream-hosted Palaeoproterozoic-aged zircons in the eastern Curnamona Province are not a reliable source of information about the crustal evolution of the Willyama Supergroup and its source regions. More generally, in areas of long-lived aridity, U-Pb-Hf compositions of zircons in modern streams should not be assumed to reflect the crustal evolution of the underlying bedrock and its origins. Most significantly, sedimentary sequences in the geological record which are derived from fluvial systems, passive margins adjacent to regions of subdued topography, or any other environment where sediment deposition is not a direct result of rapid uplift and erosion, are at risk of being contaminated by aeolian detritus, and as such, interpretations regarding provenance should be treated with appropriate caution.

1. Introduction

Detrital zircons from sedimentary rocks have long been used to provide constraints on the depositional timing of sedimentary rock packages and the crustal evolution of source regions (e.g. Rainbird et al. 1992, Ireland et al. 1998, Fedo et al. 2003, Griffin et al. 2004, Andersen 2005, Moecher and Samson 2006, Carrapa 2010, Gehrels 2014, Andersen et al. 2016). In recent years a large number of studies have used the technique of sampling zircons and other minerals from modern sediments (e.g. Sircombe and Freeman 1999, Cawood et al. 2003, Griffin et al. 2004, Link et al. 2005, Griffin et al. 2006, Morton et al. 2008, Belousova et al. 2009, Cina et al. 2009, Howard et al. 2009, Alizai et al. 2011, Yi et al. 2014). The logic behind this practice is

that zircons taken from a sample of modern detritus will provide an efficient average zircon composition of the entire catchment area which can then be used to analyse terrain-scale events, evaluate underexplored terrains, or gain zircon concentrates from low yielding rocks such as mafic lithologies with greater ease.

While studies have shown strong links between underlying geology and modern detrital zircons (e.g. Cawood et al. 2003, Link et al. 2005, Malusà et al. 2016), a number of other studies have not seen such a clear relationship. Belousova et al. (2009) presented a study of modern stream sourced detrital zircons in the Gawler Craton in South Australia, which would be expected to contain zircons ranging from Mesoarchean to earliest Mesoproterozoic derived from the Gawler Craton (e.g. Hand et al. 2007, Fanning et al. 2007, Fraser et al. 2010). While this was the case, the zircon age populations also showed significant age peaks ranging between ca. 1200 Ma to 300 Ma, with a Late Mesoproterozoic grouping proposed to represent a phase of previously unrecorded Mesoproterozoic crustal growth in the Gawler Craton, despite the basement geology showing no evidence of any such event (e.g. Hand et al. 2007, Reid and Hand 2012). Andersen et al. (2016) showed that detrital zircons in Phanerozoic successions in the Cape Supergroup in Southern Africa lack specific ages and Hf isotopic characteristics expected from the bedrock sources within the adjacent Mesoproterozoic crust. Instead, the detrital zircons were interpreted to reflect long-lived multi-cycle reworking and homogenisation rather than fingerprinting any particular source system. A recent study by Bonich et al. (2017) directly compared the zircon of a granodiorite pluton in the Stepladder Mountains in southeastern California and the detritus shed by that outcropping pluton. In this instance, sediment was seemingly directly derived from a Cretaceous granodiorite, which also contained Mesoproterozoic xenoliths. The sediment contained a disproportionately large concentration of Mesoproterozoic zircon, such that the zircon age populations of the source and the sediment were statistically distinct. This departure from the expected zircon population is interpreted to be the result of aeolian input from nearby Mesoproterozoic lithologies.

The Palaeoproterozoic Broken Hill region in the eastern Curnamona Province, southern Australia (Figure 1), presents an interesting case study in apparent discrepancy between modern stream sediment and the outcropping basement lithologies. Condie et al. (2005) documented a dominant proportion of juvenile c. 1630 Ma zircons in modern stream sediments in catchments contained within the Palaeoproterozoic ca. 1710-1640 Ma Willyama Supergroup. This is despite extensive and detailed geological mapping and geochronology that has failed to identify any 1630 Ma magmatism in the areas drained by the catchments (e.g. Raetz et al. 2002, Page et al. 2005a, Page et al. 2005b, Stevens et al. 2008). This is another example which demonstrates that there may not be a simple relationship between the zircon signatures of rocks comprising the physiology of a catchment and the zircons contained within the modern sediment of the catchment.

Following on from the study of Condie et al. (2005), the Willyama Supergroup in the Broken Hill region of the Curnamona Province (Figure 1) represents an excellent natural laboratory to investigate the relationship between zircon in modern stream sediment and the basement lithologies. The province has been extensively mapped in detail and there is a large in situ zircon U-Pb dataset that covers the outcropping stratigraphy of the Willyama Supergroup (Page and Laing 1992, Ashley et al. 1996, Raetz et al. 2002, Page et al. 2005a, Page et al. 2005b, Stevens et al. 2008, McFarlane and Frost 2009). A number of stream systems have comparatively limited catchments that are contained entirely

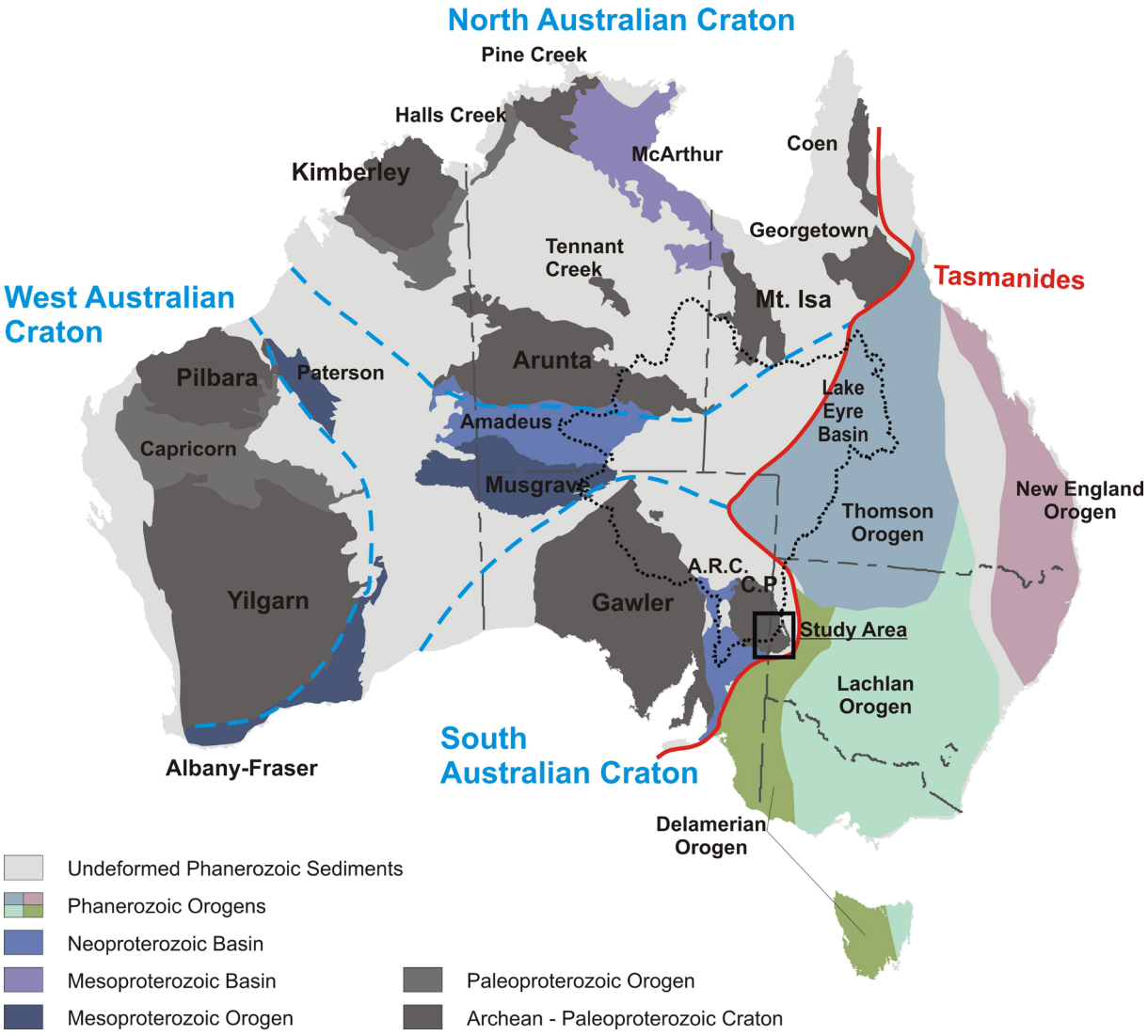

Figure 1: Geological regions within Australia. The Curnamona Province (C.P.) lies within the South Australian Craton, adjacent to the Tasman Line which indicates the change from Proterozoic dominated crustal domains to Phanerozoic crustal domains.

within outcropping Willyama Supergroup. This means that the expected age peaks for a given drainage system should be relatively predictable, and any exotic or unexpected zircon ages easily identifiable. This study investigates the relationships between drainage and host province geology using stream sediment samples from 8 catchments within the Curnamona Province and modelling of expected zircon distributions.

2. Geological Setting

The Curnamona Province is an area of Palaeo-Mesoproterozoic metasedimentary and metaigneous rocks in the eastern part of the South Australian Craton (Figure 1). The Broken Hill region is dominated by the 1720-1640 Ma Willyama Supergroup, which is interpreted to have been deposited in a continental rift or back-arc setting (e.g. Stevens et al. 1988, Rutherford et al. 2006a, Forbes et al. 2008). The lower units of the Willyama Supergroup (Figure 2) are comprised of quartzites, psammitic to psammopelitic metasedimentary

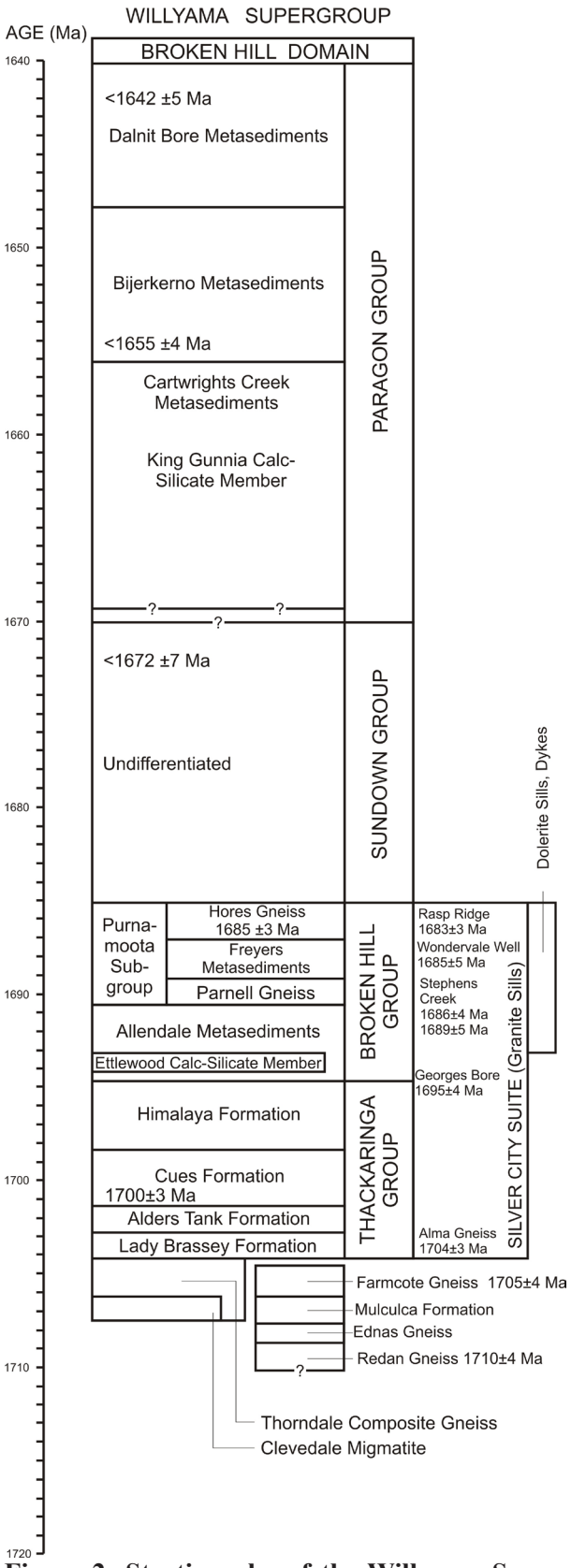

Figure 2: Stratigraphy of the Willyama Supergroup in the Broken Hill region, amended from Conor & Preiss (2008).

rocks, and calcsilicates (Conor and Preiss 2008). Syndepositional magmatism is associated with this early rifting phase, with bimodal magmatism occurring during the period 1720-1685 Ma (Page and Laing 1992, Ashley et al. 1996, Raetz et al. 2002, Page et al. 2005a, Stevens et al. 2008). After 1685 Ma, magmatism became less frequent and the sequences became predominantly psammopelitic and pelitic between 1685-1670 Ma (Stevens et al. 1988, Page et al. 2005a). The upper units of the Willyama Supergroup (Figure 2) were deposited between 1670-1640 Ma (Page et al. 2005a, Forbes et al. 2008).

Metamorphism of the Willyama Supergroup is predominantly recorded by the ca. 1620-1590 Ma Olarian Orogeny (e.g. Page and Laing 1992, Forbes et al. 2005, Page et al. 2005a, White et al. 2005, Conor and Preiss 2008, Clark and Hand 2010). This event produced greenschist to granulite facies metamorphism throughout the Willyama Supergroup, with the highest grades occurring in the southern Broken Hill Domain (White et al. 2005, Conor and Preiss 2008). Post peak magmatism included the eruption of the 1585 Ma Benagerie Volcanics in the central Curnamona Province (Raetz et al. 2002, Wade et al. 2012), and emplacement of S-type granites between 1580-1550 Ma (Jagodzinski and Fricke 2010, Wade 2011), coincident with retrograde metamorphism at the current exposure level (Rutherford et al. 2007).

The Curnamona Province was reworked during the Cambro-Ordovician Delamerian Orogeny at ca. 500 Ma, which generated large scale shear zones and greenschist to mid amphibolite-grade retrograde metamorphism (Dutch et al. 2005, Rutherford et al. 2006b, Clark and Hand 2010). No zircon growth associated with this event has been identified in the Willyama Supergroup, and the documented chronometric record of this event is typically recorded by monazite U-Pb and garnet Sm-Nd systems within the retrograde shear zones (Dutch et al. 2005, Rutherford et al. 2006b).

3. Methods

3.1. Sampling and Analytical Methods

Eight modern stream sediment samples were collected from rivers and creeks in the Broken Hill area, approximately replicating the sample sites of Condie et al. (2005; Figure 3, 4). Two samples of approximately 3-4 kilograms were collected from different sections of the stream at each location to check consistency (a & b samples). For all samples, areas where heavy minerals such as garnet were visibly concentrated in the stream bed were preferentially sampled to achieve the greatest concentration of zircon. Samples were sieved with a 1mm mesh at the sampling location to remove coarse fractions and organic material. With the exception of sample site KBH-5 south of Broken Hill (Figure 3, 4), the chosen drainage systems are dominated by Willyama Supergroup outcrop which consists of slightly weathered metasedimentary dominated mica schist and migmatitic gneiss (Hill, 2001). Sample site KBH-5 occurs within a catchment dominated by colluvial sheet wash and alluvial fans overlying the Willyama Supergroup. Sample locations and the lithologies sampled by the drainage systems are summarised in Table 1.

In order to interrogate the results obtained from the sampled streams within the Willyama Supergroup, a second set of samples were taken from sand dunes in the Strzelecki Desert around 120 km north of Broken Hill (Figure 5). The aim of this set of samples was to examine the zircon populations that accumulate from large-scale aeolian deposition in regions close to Broken Hill. Four sand dunes were sampled several kilometres apart (Table 1, Figure 5). The samples were dug from the top 30 cm of the surface of each sampled dune, from a point near the crest.

Zircons were separated using the standard mineral separation techniques of panning, Frantz magnetic separation, and heavy liquid separation. Zircons were mounted in epoxy resin and polished to expose the core of each grain. For the samples prefixed K-GB, zircon mounts were imaged using Backscatter Secondary Electron (BSE) and cathodoluminescence (CL) imaging on a Phillips XL-40 SEM with attached Gatan CL detector. For the samples prefixed K-BH and SDF, zircon mounts were imaged using BSE and CL imaging on a FEI Quanta 600 SEM with attached Gatan CL detector. Single-grain U–Pb zircon dating was done on all samples by Laser Ablation Inductively Coupled Plasma Mass Spectrometry (LA-ICP-MS) using a NewWave 213 nm Nd-YAG laser in a He ablation atmosphere, coupled to an Agilent 7500cs ICP-MS at Adelaide Microscopy at the University of Adelaide, following the method of Payne et al (2006). A 60 second gas blank was analysed followed by 60 seconds of measurement during zircon ablation. Prior to each ablation the laser is fired for 10 seconds with the shutter closed to allow crystal and beam stabilisation.

For all analyses, the zircon standard GEMOC GJ-1 was used as a matrix-matched standard to correct for mass bias and fractionation (TIMS normalisation data $^{207}Pb/^{206}Pb$ = 608.3 Ma, $^{206}Pb/^{238}U$ = 600.7 Ma and $^{207}Pb/^{235}U$ = 602.2 Ma; (Jackson et al. 2004). Accuracy was checked using the recognised zircon standard Plešovice (337.13 ±0.37Ma; (Sláma et al. 2008). Over the two year period of this study weighted $^{207}Pb/^{206}Pb$, $^{206}Pb/^{238}U$, and $^{206}Pb/^{235}U$ ages for GJ-1 yeilded 609.7 ±2 Ma, 599.3 ±0.5 Ma, and 601 ±0.5 Ma respectively (n=1118). For Plešovice weighted $^{207}Pb/^{206}Pb$, $^{206}Pb/^{238}U$, and $^{206}Pb/^{235}U$ ages yielded 340.0 ±4.2 Ma, 334.0 ±0.9 Ma, and 334.5 ±0.8 Ma respectively (N=259). These weighted mean Pb/U ages are slightly outside of uncertainty of the known published age and hence the true uncertainty of any reported weighted mean ages should include a propagated component to reflect this. However, in this study we are only concerned with single ages from detrital zircons and the typical uncertainty on each analysis (2%) exceeds they observed deviation of the Plesovice Pb/U ages from the known age.

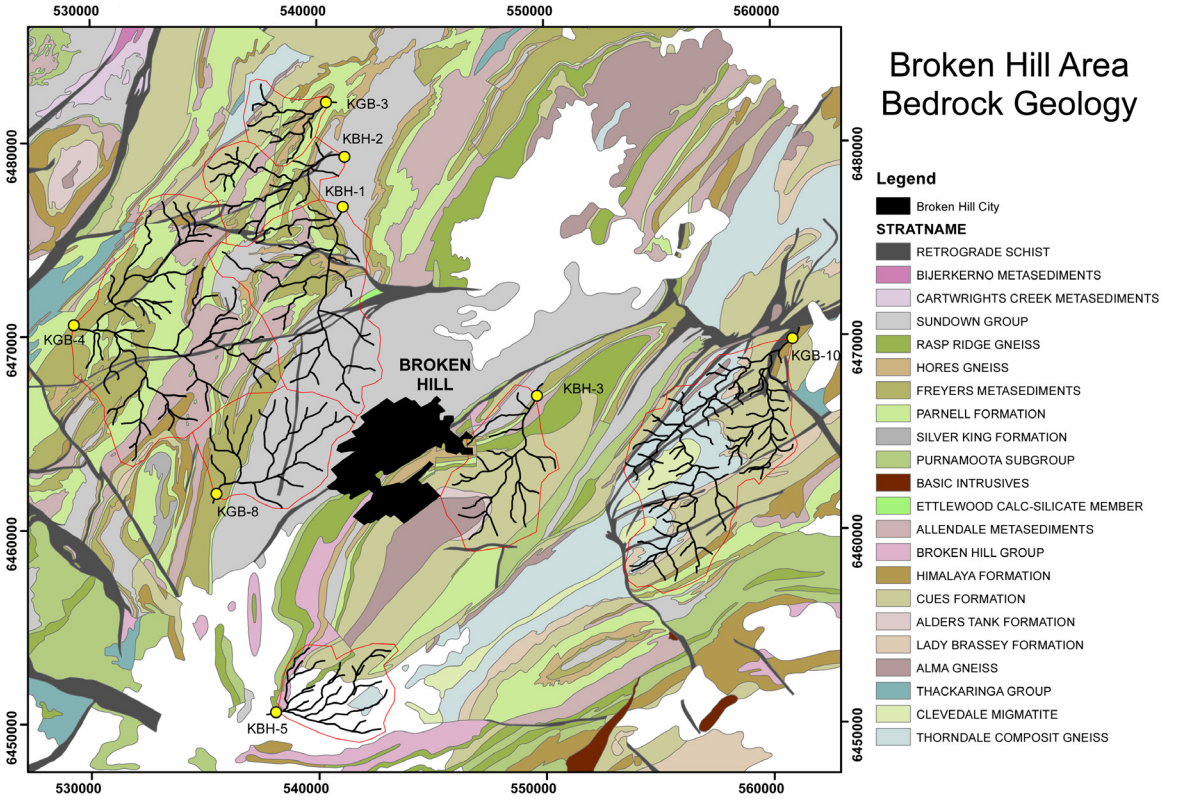

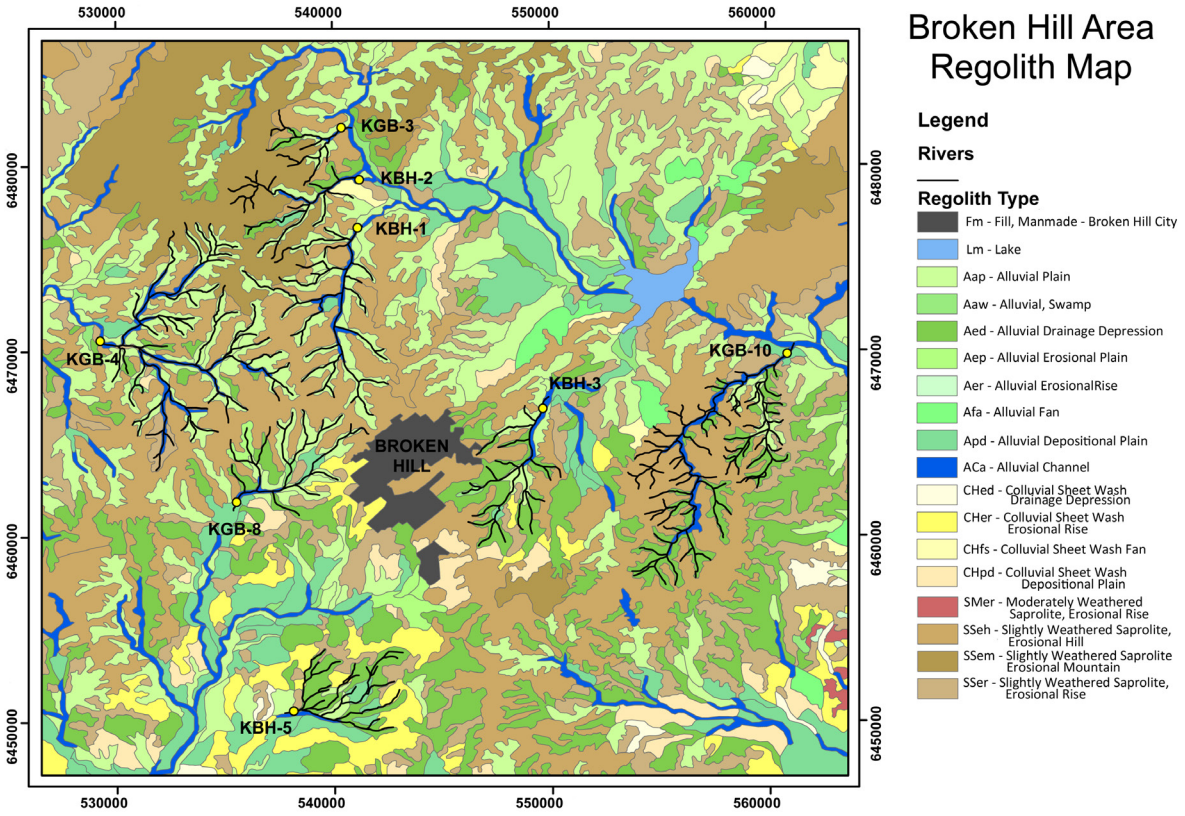

Figure 3 (Upper): Bedrock Geology map of Broken Hill, with streams sampled and catchment areas outlined in red.
Figure 4 (Lower): Simplified regolith landform map of the study area adapted from Hill (2001).

The method for zircon Lu-Hf isotope analyses follows that of Payne et al. (2013). Analyses were obtained using a New Wave UP-193 ArF eximer laser with an attached Thermo-Scientific Neptune Multi Collector ICP-MS at the University of Adelaide. Analyses were undertaken using a 5 Hz repetition rate and an intensity of 6-8 J/cm^2. Beam sizes varied between 50 µm to 30 µm depending on the zircon or detrital core size. Data reduction was carried out using the macro-driven Hf isotope data reduction Excel spreadsheet Hf-TRAX of Payne et al. (2013). The data were normalised to $^{179}Hf/^{177}Hf = 0.7325$ using an exponential correction for mass Bias. Yb and Lu isobaric interferences were corrected using the methods of Woodhead et al. (2004). The accuracy of the Yb and Lu corrections has been demonstrated by analysis of the natural zircon standards Mud Tank (Woodhead and Hergt 2005) and Plešovice (Sláma et al. 2008) before and during analysis to check instrument performance and stability. The mean $^{176}Hf/^{177}Hf$ ratio yielded from the Mud Tank standard was 0.282499 ± 0.000006 which is within uncertainty of the published value of 0.282506 ± 0.000026 (2σ; Woodhead and Hergt 2005). The mean $^{176}Hf/^{177}Hf$ ratio from the Plešovice standard was 0.282468 ± 0.000008 which is within uncertainty of the published value of 0.28248 ± 0.000013 (2σ; Sláma et al. 2008). Values for $\varepsilon_{Hf}(t)$, and $T_{DM}c$ were calculated using the ^{176}Lu decay constant of 1.865 x 10^{-11} of Scherer et al. (2001). $T_{DM}c$ was calculated using the methods and average crustal composition of $^{176}Lu/^{177}Hf = 0.015$ of Griffin et al. (2002).

3.2. Predicted zircon U-Pb age histograms

For each sample site, the drainage channels upstream from the sample location were traced out on 1:25,000 geological maps (Brown 1983, Stevens and Bradley 1983, Brown 1984, Bradley 1984, Willis 1984) and a list compiled of all the formations exposed in each catchment area. For each formation identified, the published zircon geochronology from in situ samples was collected and an age probability density plot was constructed for each catchment area. The sources and sample numbers for each stratigraphic unit used to construct these predicted age populations are presented in Appendix 1.

The purpose of these predictive plots is to identify the age peaks which would be expected to be derived from eroding the lithologies exposed within each catchment, to compare with the zircon age populations derived from the modern stream sediment. The proportions of each age population cannot be predicted without comprehensive models of zircon fertility and erodibility, which has not been previously assessed and is beyond the scope of the current work. The intention of these predicted age histograms was to identify which age peaks should be expected to be present in each sample, but not to identify the relative abundance of any given age peak. Furthermore, any age populations in the modern stream sediments that have not been identified from in situ samples of the Willyma Supergroup should be readily identifiable through comparison of the predicted and measured age populations. The dominant age peaks of in situ samples from units of the Willyama Supergroup range between approximately 1590-1620 Ma for metamorphic zircons generated during the Olarian Orogeny, 1710-1680 Ma for igneous zircons from felsic intrusive and extrusive rocks, and back to approximately 3000 Ma for detrital zircons.

4. Results

4.1. Broken Hill Stream Sediments

A total of 1400 zircons were analysed from the 8 stream samples from around the Broken Hill area. Of these, 730 analyses were less than 10% discordant and are summarised in Figure 6, plotted with reference to the predicted aged histograms derived for each sample site. Each zircon age population typically contains a variety of different grain morphologies and internal textures. Features common to age populations are summarised in Table 2. Hf data are plotted in Figure 7. The U-Pb data are presented in Supplementary Data 2 and Lu-Hf isotopic data in Supplementary Data 3.

4.1.1. 2000 Ma to 3300 Ma zircons

Of the 730 concordant zircons, 91 were older than 2000 Ma. Relatively small peaks occur at ca. 2100 Ma, 2300 Ma, 2480 Ma, 2650 Ma, 2890 Ma, as well as peaks at 3080 Ma and 3250 Ma which are only characterised by one or two analyses. $\varepsilon_{Hf}(t)$ values for grains between 2100 Ma and 2600 Ma were scattered between values of +8, to -6. The grains with ages older than 2600 Ma have $\varepsilon_{Hf}(t)$ values of approximately 0.

4.1.2. 1400 Ma to 2000 Ma zircons

Of the 730 concordant zircons, 420 range in age between 1400 Ma and 2000 Ma. The dominant age peaks which occur in this age bracket are ca. 1600 Ma, 1690 Ma, and 1780 Ma, with a minor population at approximately 1850 Ma. $\varepsilon_{Hf}(t)$ values for this age bracket show two trends. Zircons younger than 1800 Ma have a wider range of $\varepsilon_{Hf}(t)$ values, from near depleted mantle values of +11 to -8, with a small number of analyses ranging between -12 and -20. $\varepsilon_{Hf}(t)$ values for grains between 1800 Ma and 2000 Ma are less juvenile overall and range between +1.5 to -14.5.

4.1.3. 800 Ma to 1400 Ma zircons

Of the 730 concordant zircon analyses, 119 recorded ages between 800 Ma and 1400 Ma. This age range is dominated by a broad peak at ca. 1170 Ma, with a smaller peak at 1000 Ma. The $\varepsilon_{Hf}(t)$ values of this population are predominantly clustered between +7 and -7. Several more evolved $\varepsilon_{Hf}(t)$ values also occur between -10 and -23.

Table 1: Summarised sample locations (GDA 94) and bedrock lithologies sampled.

Sample	Easting	Northing	Stratigraphy intersected by stream
Broken Hill Streams			
KBH-1	541141	6476669	Sundown Group, Freyers Metasediments, Hores Gneiss, Allendale Metasediments, Parnell Formation
KBH-2	541234	6479241	Allendale Metasediments, Cues Formation, Freyers Metasediments, Hores Gneiss, Parnell Formation, Sundown Group
KBH-3	549652	6466886	Broken Hill group, Cues Formation, Freyers Metasediments, Hores Gneiss, Parnell Formatiion, Rasp Ridge Gneiss, Sundown Group, Thorndale Composite Gneiss
KBH-5	538116	6450583	Broken Hill Group, Cues Formation, Himalaya Formation, Thorndale Composite Gneiss
kGB3	540424	6482071	Parnell Formation, Freyers Metasediments, Hores Gneiss, Allendale Metasediments, Cues Formation, Thorndale Composite Gneiss, Alma Gneiss
kGB4	529276	6470589	Freyers Metasediments, Cues Formation, Himalaya Formation, Allendale Metasediments, Sundown Group, Hores Gneiss
kGB8	535532	6461873	Freyers Metasediments, Parnell Formation, Sundown Group, Himalaya Formation, Allendale Metasediments, Hores Gneiss
kGB10	560926	6469785	Himalaya Formation, Cues Formation, Thorndale Composite Gneiss, Lady Brassey Formation, Parnell Formation, Alma Gneiss
Sand Dunes			
SDF-1	507803	6596929	Sand Dune
SDF-2	507847	6591571	Sand Dune
SDF-3	508092	6586922	Sand Dune
SDF-5	530316	6592874	Sand Dune

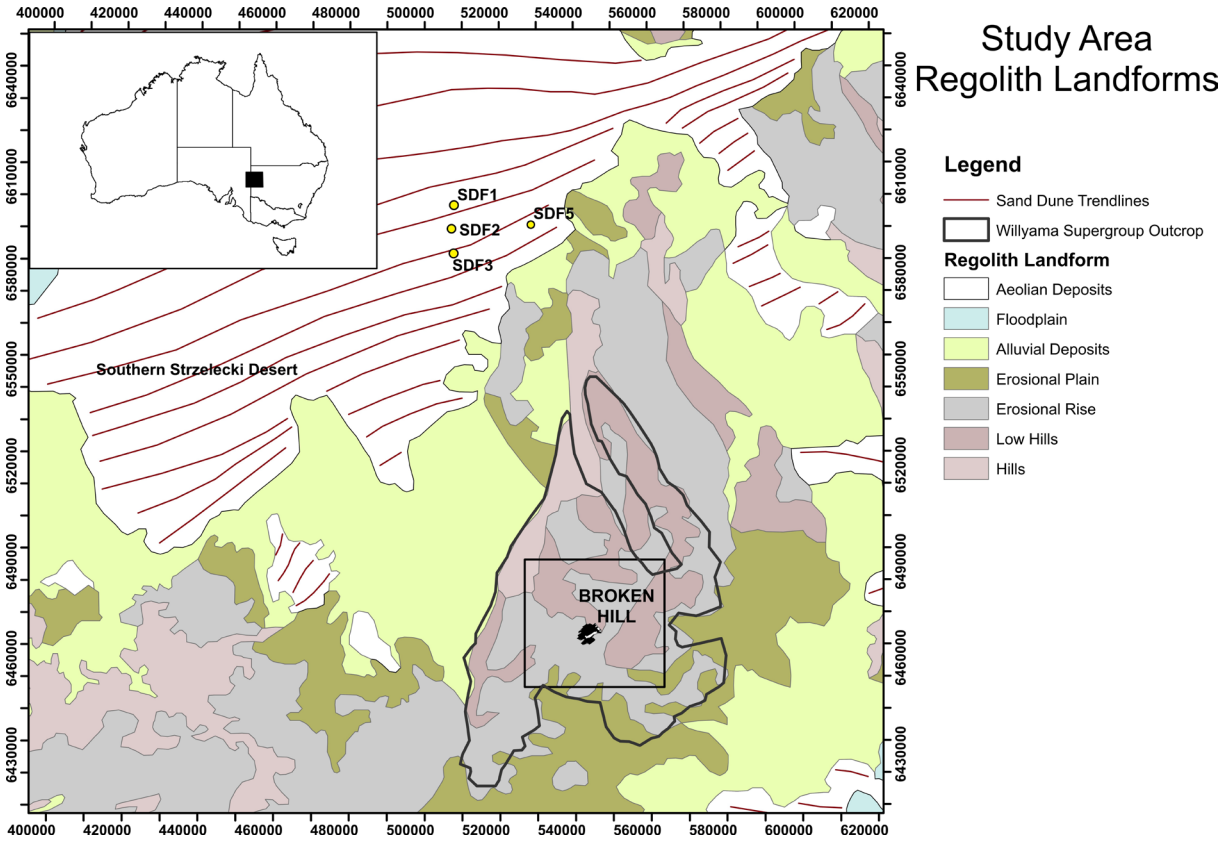

Figure 5: Regional Regolith Map of the Study area adapted after Gibson (1999), showing sand dune sample locations, relative to the Broken Hill study area.

4.1.4. 100 Ma to 800 Ma zircons

Of the 730 concordant zircon analyses, 99 recorded U-Pb ages between 100 Ma and 800 Ma. The dominant age peaks in this age bracket occur at 100 Ma, 130 Ma, 180 Ma, 250 Ma, 320 Ma, 420 Ma, 500 Ma, 550 Ma, and 600 Ma. The Hf isotope signatures of zircons in this age bracket form several groupings. Zircons aged between 100 Ma to 180 Ma form a relatively juvenile cluster with $\varepsilon_{Hf}(t)$ values between +7 and +12. Two grains aged 350 Ma have $\varepsilon_{Hf}(t)$ values of approximately -2. Zircons aged between 500 Ma and 630 Ma showed a much larger spread of $\varepsilon_{Hf}(t)$ values, with a weak grouping between +3 to -9, as well as an outlier with $\varepsilon_{Hf}(t)$ of -27.

4.2. Summary of zircon U-Pb ages from Broken Hill Stream Sediments

In most samples, the bulk of the analyses are older than 1600 Ma. However in all samples, a component ranging in age between 100 Ma and 1400 Ma occurs, making up between 8% - 35% of analyses. As outlined above, zircon grains derived from the Willyama Supergroup should not be significantly younger than ca. 1580 Ma. It is evident that with respect to the bedrock geology of the stream system, the modern stream sediments contain substantial zircon contamination. In order to explore the potential origins zircon populations younger than 1580 Ma, results from analysis of sand dunes in the Strzelecki Desert to the north of the Broken Hill region are described below, since the aeolian deposits of the Strzelecki Desert are an obvious potential source of zircon.

4.3. Strzelecki Desert sand dune samples

A total of 413 zircons contained within the aeolian sediments were analysed, of which 312 are less than 10% discordant. The U-Pb age spectra are shown in Figure 6, and Hf isotopic data are displayed in Figure 7. The dune-sourced zircon populations are described

Table 2: Summarised common zircon characteristics for the age divisions discussed in text. The majority of populations contained a variety of zircon morphologies and textures.

Broken Hill Streams Zircon Populations		
Age	**Physical Characteristics**	**CL characteristics**
100 Ma – 800 Ma	100 Ma to 250 Ma - subangular to subrounded, various aspect ratios. 300 Ma - 600 Ma: rounded to sub-rounded. Commonly elongate. 300 Ma - 600 Ma: oscillatory zoned to dark and homogenous for all ages	100 Ma - 250 Ma: typically bright oscillatory zoned CL patterns.
800 Ma – 1400 Ma	Grain shapes are typically well rounded to sub-rounded.	Dominantly dark homogeneous CL patterns, some oscillatory zoned grains.
1400 Ma – 2000 Ma	Typically well rounded to sub-rounded, various aspect ratios and sizes.	Various CL textures, no clear correlation between CL texture and age. Darker homogeneous common for all ages. Bright and oscillatory zoned textures, sometimes faint, less abundant but present in all ages.
2000 Ma – 3300 Ma	Well rounded and equant. 2800 Ma grains elongate and semi-prismatic	The zircon in this age bracket are most commonly very dark under CL, and show either no internal structure or very faint zoning.
Strzelecki Sand Dune Zircon Populations		
100 Ma – 800 Ma	100 Ma - 350 Ma: Typically angular to subrounded, various aspect ratios. 400 Ma - 650 Ma: Most grains elongate and angular	100 Ma - 350 Ma: Bright, oscillatory zoned. 400 Ma and 650 Ma: dark, unstructured or sector zoned. Few oscillatory zoned grains.
800 Ma – 1400 Ma	Generally rounded to subrounded, mostly equant grains.	Dark, sector zoned or unzoned. Few oscillatory zoned grains, not corresponding to one age.
1400 Ma – 2000 Ma	Commonly subangular to sub-rounded, generally equant with few elongate grains	Dark, structureless or sector zoned. Few oscillatory zoned grains
2000 Ma – 3300 Ma	Typically small, well rounded to subangular	Dark, little visible texture, faint oscillatory zoning in 2500 Ma grains.

in detail below in the same age groupings as above. The collected probability density of these samples is presented in Figure 8. The U-Pb data is shown in Supplementary Data 4 and Lu-Hf isotopic data in Supplementary Data 5.

4.3.1. 2000 Ma to 3300 Ma

Of the 312 concordant zircons analysed, 12 yielded ages older than 2000 Ma. These grains produce a spread of ages contributing to a series of minor peaks characterised by only one or two grains. The largest peaks in this age range occur at ca. 2500 Ma, 2600 Ma and 2700 Ma. Minor peaks also occur at 2150 Ma, 2280 Ma, 3080 Ma, and 3250 Ma. The $\varepsilon_{Hf}(t)$ values of zircon between 2500 Ma and 2700 Ma are between -0.5 and -3.5.

4.3.2. 1400 Ma to 2000 Ma

Of the 312 concordant zircon analyses, 49 yielded ages between 1400 Ma and 2000 Ma. These form two main peaks at 1600 Ma and 1780 Ma, with a small age shoulder at 1450 Ma. The $\varepsilon_{Hf}(t)$ of the two dominant age peaks give different trends. The 1600 Ma zircons yield relatively juvenile $\varepsilon_{Hf}(t)$ values which range from +10, which is close to the depleted

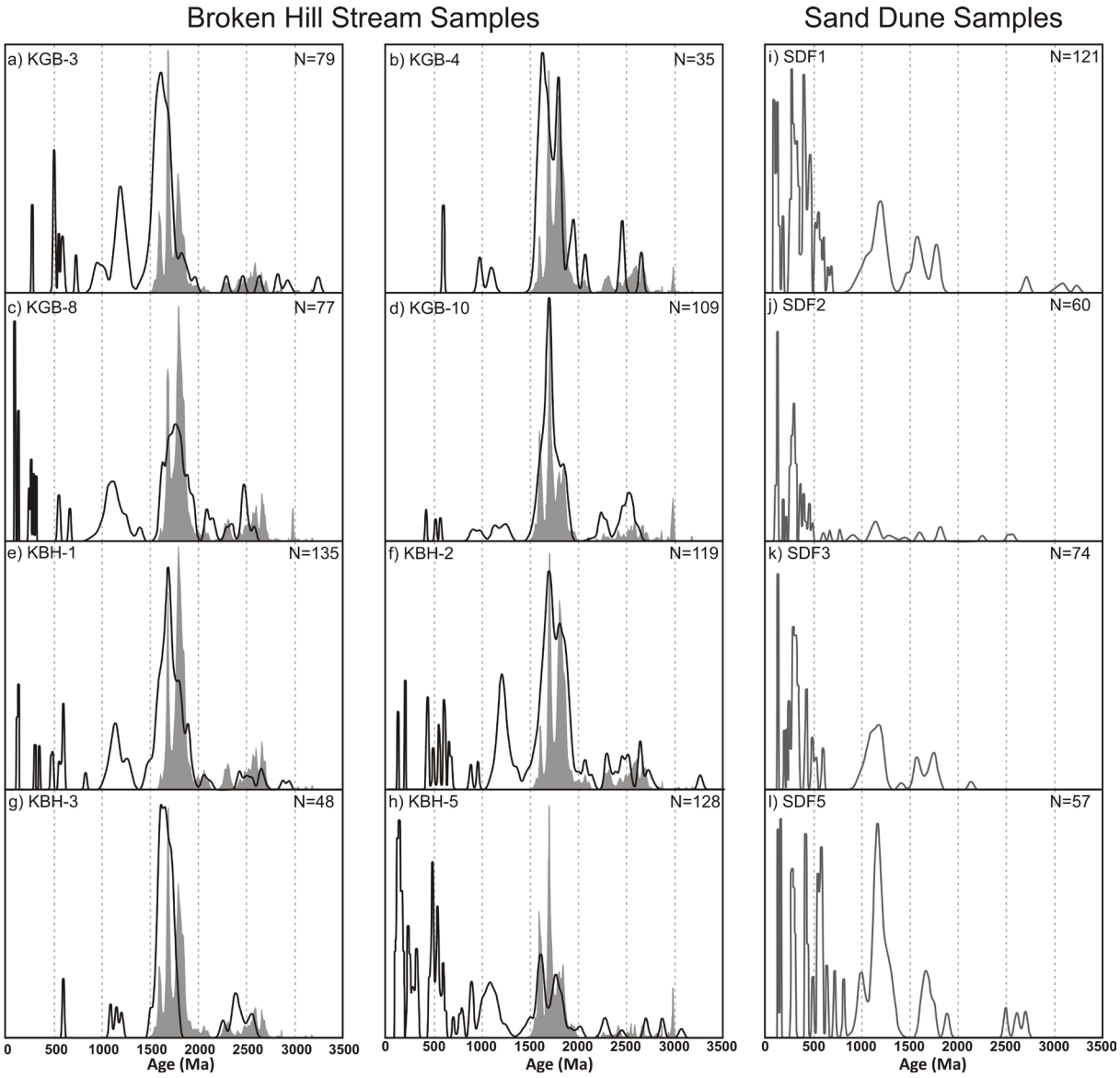

Figure 6: Predicted and measured probability density plots of each stream sediment sample. Predicted probabilities are shaded grey, measured probabilities represented by solid black line.

mantle value of this time, to -2. The 1780 Ma zircons have a less juvenile signature which ranges between -1 and -6.

4.3.3. 800 Ma to 1400 Ma

92 of the 312 concordant zircon ages are between 800 Ma and 1400 Ma. One major age peak occurs at 1170 Ma with a shoulder at 1000 Ma. The $\varepsilon_{Hf}(t)$ values for these age peaks are scattered between +6 to -7, with minor outliers with evolved values of -11 and -19.

4.3.4. 100 Ma to 800 Ma

159 of the 312 concordant zircons from the sand dune samples are aged between 100 Ma and 800 Ma. Major peaks occur at 100 Ma, 130 Ma, 180 Ma, 300 Ma with shoulders at 280 Ma and 330 Ma, 430 Ma, and 550 to 650 Ma. The $\varepsilon_{Hf}(t)$ values in this age bracket show several trends. For grains aged between 100 Ma and 180 Ma, $\varepsilon_{Hf}(t)$ values are relatively juvenile and range from +6 to +10. Grains aged approximately 250 Ma have $\varepsilon_{Hf}(t)$ values between +4 and +8. 300 Ma zircon shows more variability with $\varepsilon_{Hf}(t)$ values ranging from +7 to -6. Grains aged between 400 Ma and 650 Ma are more evolved with $\varepsilon_{Hf}(t)$ values be-

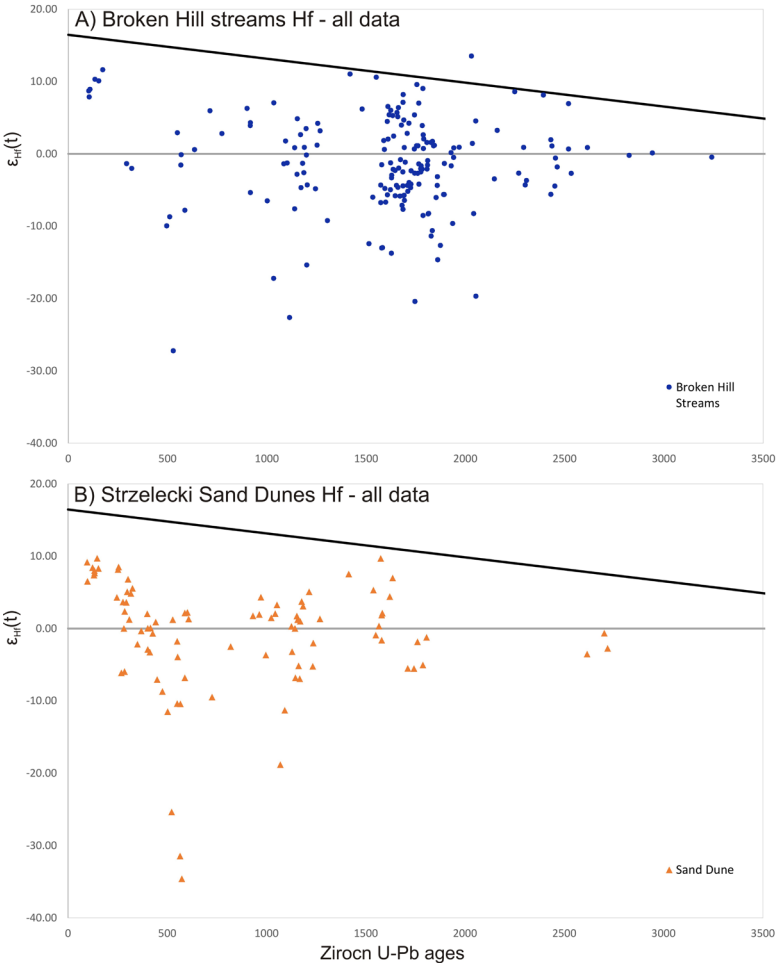

Figure 7: Lu-Hf isotopic compositions of modern detrital zircons for A) Broken Hill stream sediments, and B) Strzelecki sand dune sediments.

tween -12 and + 2. One 520 Ma grain also yields an $\varepsilon_{Hf}(t)$ value of -25.

5. Discussion:

5.1. Comparison with previous work on modern detrital zircons in the Broken Hill streams

In a study on the development of Late Palaeoproterozoic juvenile crust, Condie et al. (2005) presented data that showed that modern detrital zircons in Broken Hill streams were dominated by juvenile c. 1630 Ma zircons, producing essentially unimodal age populations with $\varepsilon_{Hf}(t)$ values ranging from +11 to -2. These results are surprising given that the stream catchments are dominated by the metasedimentary Willyama Supergroup, whose stratigraphic ages make it impossible to yield an essentially unimodal c. 1630 Ma-age population. The only way that zircons of this age could dominate the modern detrital age populations is if the Willyama Supergroup in its entirety was devoid of zircon and was intruded by granites c. 1630 Ma in age. Neither of these possibilities are the case (e.g. Stevens et al. 1988, Page et al. 2005a, Page et al. 2005b, Conor and Preiss 2008, Stevens et al. 2008). In the present study, zircon with a $^{207}Pb/^{206}Pb$ age within 1630 ±15 Ma makes up only 5.5% of the total concordant analyses (39 of 730). These include metamorphic-structured grains as well as zircons with magmatic-style CL textures. Furthermore, the $\varepsilon_{Hf}(t)$ signatures are not solely juvenile and range from -8 to +11. In addition to this, one of the Strzelecki sand dune age peaks occurs at ca. 1600 Ma and includes grains which overlap within

error of 1630 Ma. Given the likelihood of aeolian contamination on the Broken Hill area land surface (see below), only moderate significance can be attached to any of the zircons found in the modern stream sediments in terms of specific Palaeoproterozoic terrain evolutions. This study finds no evidence of significant juvenile crustal additions at around 1630 Ma in the eastern Curnamona Province, and have no explanation for the data presented by Condie et al. (2005).

5.2. Expectations vs. Reality

The stream sediment sample locations used in this study come from catchments that for the most part consist almost entirely of outcropping Willyama Supergroup (Fig 3, 4). The rock types consist of slightly to moderately weathered schists and gneisses and therefore should be amenable to erosion, providing zircons (and other detritus) directly into the stream sediments. Therefore unsurprisingly there is a strong similarity between the ages of zircons in the stream sediments and the predicted ages calculated from zircons analysed in situ within the rock units that define the physiology of the stream catchments (Figure 6). Based on the extensively characterised geology of the Willyama Supergroup (e.g. Page and Laing 1992, Raetz et al. 2002, Page et al. 2005a, Page et al. 2005b, Stevens et al. 2008, McFarlane and Frost 2009), the youngest zircons that could be realistically expected to be derived are 1580-1550 Ma in age. However, it is evident that in most samples of stream sediment, there is a significant (up to 30%) proportion of zircons younger than this age (Figure 6, Table 3), which must be derived from elsewhere. The age range of these younger zircons means they have to be derived from rocks that include sources as young as Jurassic. While not exclusively the only possibility, one logical possible source for such young zircons are the dune systems in the Strzelecki Desert to the north of Broken Hill. Figure 8 shows a comparison between the modern detrital zircons in the Broken Hill area with

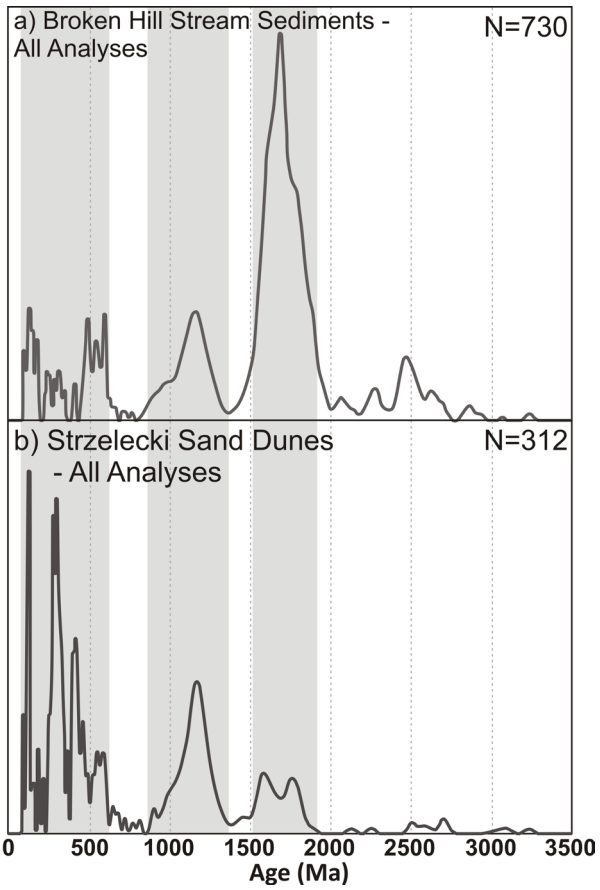

Figure 8: a) collected probability density plot for Broken Hill stream sediment samples. b) Collected probability density plot for Strzelecki sand dune samples. There is significant overlap in ages between 100-600 Ma, 900-1300 Ma, and minor overlap between 1500-1900 Ma.

zircons in the Strzelecki Desert dunes. While the proportions of the different age groups are different, it is evident that similar zircon age ranges occur in both sample sets, making it permissible that the stream sediments in the Broken Hill region have been contaminated by aeolian detritus similar to that in the Strzelecki Desert. The obvious correspondence in zircon ages between stream sediments and predicted stream sediment populations (Figure 6), makes it tempting to conclude that stream-hosted zircons older than 1600 Ma are derived from the Willyama Supergroup. However, the presence of zircons >1600 Ma in age in the Strzelecki Desert dunes forbids a simple age filter to remove non-Willyama Supergroup sourced zircons in the Broken Hill stream

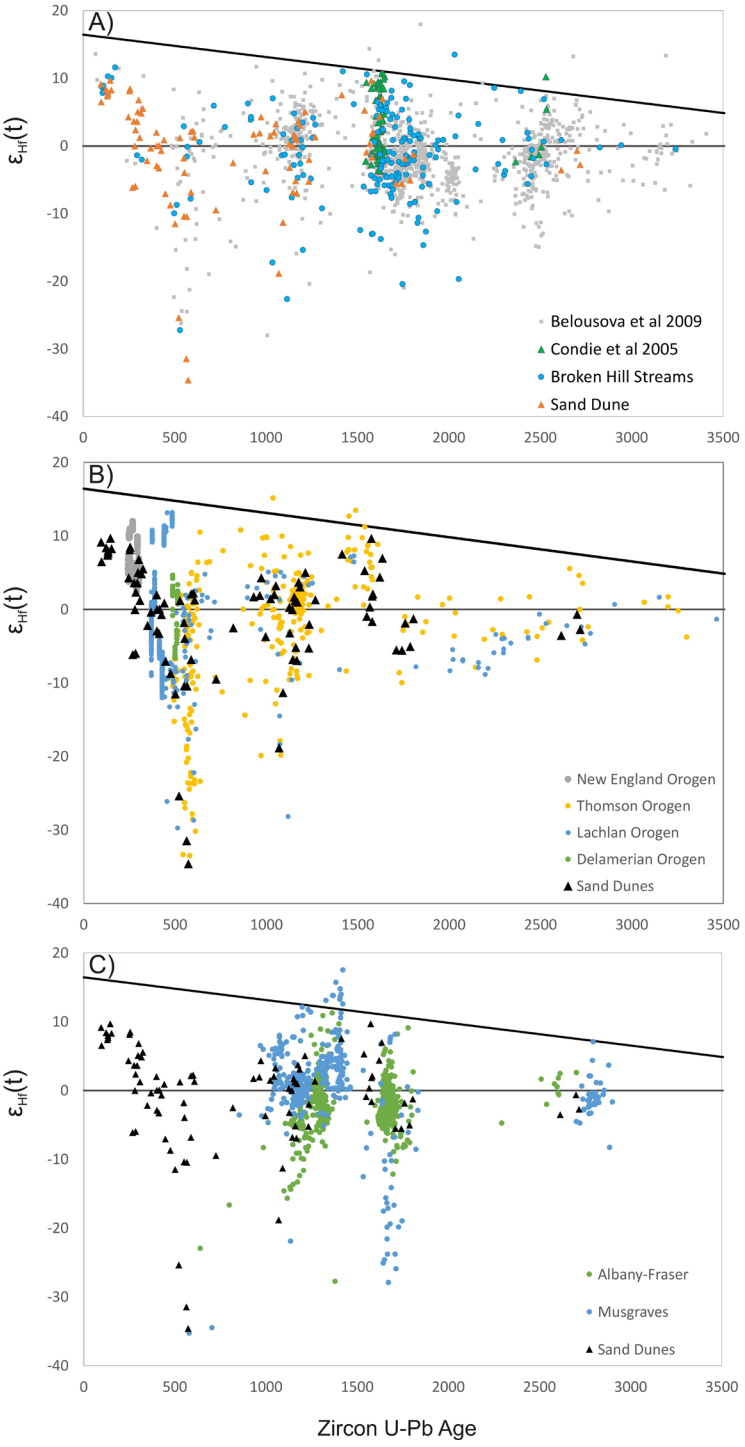

Figure 9: A) Age vs. $\varepsilon_{Hf}(t)$ values for Broken Hill stream sediment and Strzelecki sand dune samples. While the sand dune analyses are more numerous in for the Paleozoic, considerable overlap occurs between both sets of samples. The Broken Hill stream sediments show a strong similarity to the values obtained from the Gawler craton by Belousova et al (2009). The significant juvenile 1630 Ma presented by Condie et al (2005) is not apparent, and some values of this age overlap with sand dune values. B) Sand dune Analyses plotted with in situ $\varepsilon_{Hf}(t)$ values from the Tasminides (Delamerian, Lachlan, Thomson, and New England orogens). Significant overlap occurs for groups at ca. 1600 Ma, 1200-1000 Ma, and 600-250 Ma. C) $\varepsilon_{Hf}(t)$ values from in situ zircon analyses from the Albany Fraser Orogen (AFO) and the Musgrave Block (Smits et al. 2014 and references therein).

Table 3: Numerical breakdown of number of zircons and the percentage of the zircons in relevant age brackets from the Broken Hill stream sediments (BH) and the sand dune samples (SDF).

Broken Hill Streams										Sand Dunes				
Age Bracket	**BH1**	**BH2**	**BH3**	**BH5**	**GB3**	**GB4**	**GB8**	**GB10**	**BH Total**	**SDF1**	**SDF2**	**SDF3**	**SDF5**	**SDF Total**
0-800 Ma	11	12	1	54	7	1	10	3	99	63	40	35	19	157
800-1400 Ma	22	21	3	28	18	2	17	9	120	31	11	24	28	94
1400-2000 Ma	89	68	37	36	49	28	38	76	421	21	6	14	7	48
>2000 Ma	13	18	7	10	6	4	12	21	91	5	3	1	3	12
Total	135	119	48	128	80	35	77	109	731	120	60	74	57	311
Age Bracket	**BH1**	**BH2**	**BH3**	**BH5**	**GB3**	**GB4**	**GB8**	**GB10**	**BH Average**	**SDF1**	**SDF2**	**SDF3**	**SDF5**	**SDF Average**
0-800 Ma	8.1%	10.1%	2.1%	42.2%	8.8%	2.9%	13.0%	2.8%	11.2%	52.5%	66.7%	47.3%	33.3%	49.9%
800-1400 Ma	16.3%	17.6%	6.3%	21.9%	22.5%	5.7%	22.1%	8.3%	15.1%	25.8%	18.3%	32.4%	49.1%	31.5%
1400-2000 Ma	65.9%	57.1%	77.1%	28.1%	61.3%	80.0%	49.4%	69.7%	61.1%	17.5%	10.0%	18.9%	12.3%	14.7%
>2000 Ma	9.6%	15.1%	14.6%	7.8%	7.5%	11.4%	15.6%	19.3%	12.6%	4.2%	5.0%	1.4%	5.3%	3.9%
Total	100.0%	100.0%	100.0%	100.0%	100.0%	100.0%	100.0%	100.0%		100.0%	100.0%	100.0%	100.0%	

sediments. Thus, determining the origin of the dune sand and associated zircon becomes important before any meaningful assessment of the modern detrital zircons in the Broken Hill area can be made.

5.3. Detrital zircons in the Strzelecki Desert

The Strzelecki Desert overlaps with the central Curnamona Province (Figure 5). The dominant surface features of the Strzelecki Desert are linear sand dunes which trend east-northeast in the southern regions and progressively rotate to a north-south orientation in the northern regions (Figure 5; Wasson et al. 1988). These dunes are currently migrating eastward (Rubin 1990). The sand dunes developed during the Late Pleistocene and Holocene as increasing aridity on the Australian continent promoted aeolian activity (Alley 1998, Fujioka et al. 2009). Optical luminescence dating indicates that the existing dunefields developed episodically between 73 ka and 10 ka, and are built upon and likely recycle older dunes and fluvial to lacustrine deposits which were deposited between 100 ka to 200 ka (Lomax et al. 2003, Fitzsimmons et al. 2007b).

Pell et al. (2000) used zircon U-Pb ages in order to identify potential source regions for dune sands in the Strzelecki and other Australian deserts. Potential sources include the Tasmanides, (ca. 100-500 Ma), the Musgrave Province (900-1300 Ma), and the Gawler Craton, Curnamona Province, and North Australian Craton (1500 Ma and older). Comparisons of Hf isotopic data to these primary source regions show strong similarities to that in the sand dunes (Figure 9). Much like the trend in the sand dune samples, zircon from the Tasmanides, a large spread of $\varepsilon_{Hf}(t)$ values occurs in detrital zircon aged between 650-500 Ma (Figure 9) before developing a trend towards more positive values between 450 Ma and 250 Ma (Figure 9; Kemp et al. 2006, Kemp et al. 2007, Kemp et al. 2009, Jeon et al. 2014, Purdy et al. 2016, Regmi et al. 2016). For the age cluster at ca. 1000-1200 Ma, the sand dune samples show strong similarity to detrital zircons from the Tasmanides (Figure 9) as well as those from the Musgrave Province (Figure 9).

While these regions may potentially be the primary zircon source region, it is likely that these are not directly the sources for the aeolian sediments. In the northern Strzelecki Desert dunes have been proposed to be derived from alluvial and fluvial sediments (Lomax et al. 2003, Cohen et al. 2010), and in the eastern Strzelecki Desert, sediments are interpreted to be from the Lake Frome playa (Figure 10; Fitzsimmons et al. 2007a). Lake Frome forms one of the drainage centres for the Lake Eyre Basin (Alley 1998) which is a large internally drained basin which covers approximately 15% of the Australian continent (Figure 10; Habeck-Fardy and Nanson 2014). The dominant drainage systems in the Lake Eyre Basin are the Georgina River, Diamantia River, and Cooper Creek, all of which flow from the north and northeast to Lake Eyre in the southwest. The northeast extent of the basin is dominated by Mesozoic sediments of the Eromanga Basin. One of the upper units of the Eromanga Basin is the Winton Formation, which is extensively exposed in the north east of the Lake Eyre Basin (Tucker et al. 2013). Only limited detrital zircon geochronology has been undertaken on the sequences of the Eromanga Basin. Detrital zircon dating in the Winton Formation gives age peaks of 100 Ma to 600 Ma, with minor contributions of older material up to 3500 Ma (Tucker et al. 2013).

Another proximal source of sediment to the Lake Eyre Basin is the Neoproterozoic Adelaide Rift Complex, which outcrops in the Flinders Ranges (Figure 10). It contains a detrital zircon record that includes significant Meso-Palaeoproterozoic (1600-1800 Ma and older) peaks in the lower units, and an increasingly large component of Meso-Neoproterozoic (1300-1000 Ma) and late Neoproterozoic (ca. 600 Ma) zircon in the upper units (Ireland et al. 1998). The Mesoproterozoic Mount Painter

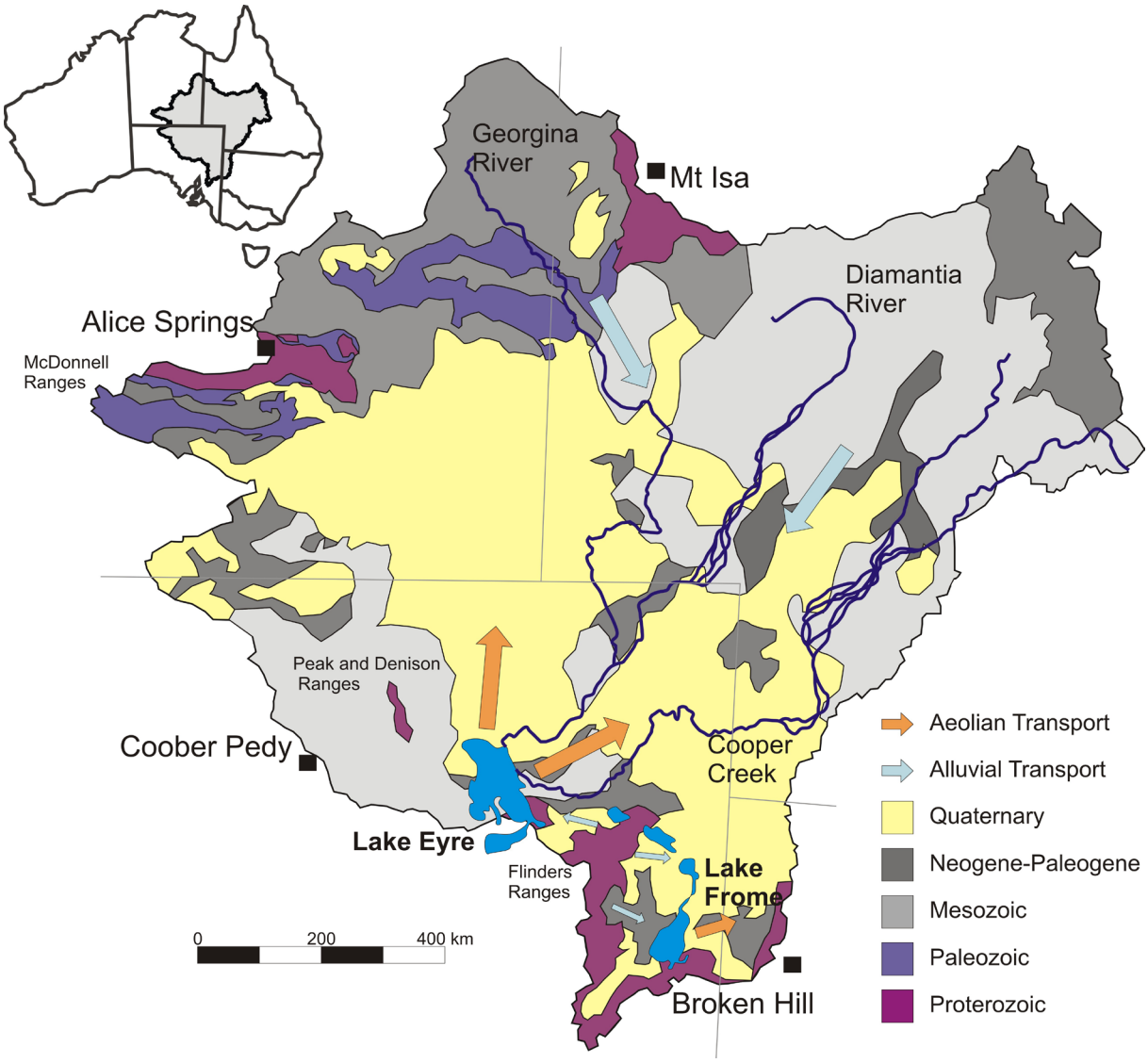

Figure 10: Surface geology of the Lake Eyre Basin. The most significant drainage pathways are the Georgina River, Diamantia River, and Cooper Creek, which predominantly sample the Mesozoic sediments of the Eromanga Basin in the North East of the Basin. Modified after Habeck-Fardy and Nanson (2014).

and Mount Babbage Inliers also outcrop in the northern Flinders Ranges and contain detrital zircon records dominated by 1590 Ma to 1750 Ma detrital zircon, and metamorphic and igneous zircon between 1590 Ma to 1550 Ma (Armit et al. 2012, Kromkhun et al. 2013, Elburg et al. 2001).

The most likely source of Phanerozoic zircon in the dune sands of the Southern Strzelecki Desert is Mesozoic sediments which contain zircon sourced from the Tasmanide orogens and the Whitsunday Volcanic Province (Tucker et al. 2013). Proterozoic sources are more varied and have had more opportunity for reworking. The wide variety of potential sources for Proterozoic-aged zircon in addition to the numerous reworking events makes assigning source regions for zircon obtained in the sand dunes difficult. This is emphasised by aeolian events such as the 2009 Canberra-Sydney dust storm which illustrate how sediments from these usually dry playa lakes can be transported great distances (> 1600 km) even in one event (e.g.

De Deckker et al. 2014). During the 2009 Canberra-Sydney dust storm, dust was sourced from the Lake Eyre sub-basin (Figure 10), and the transported particle sizes ranged between 0.4 to 2000 μm with a mode at around 40 μm but with a significant proportion around 100 μm (De Deckker et al. 2014). This grain size distribution means that zircons of the sizes typically analysed in detrital zircon studies can be transported large distances during single catastrophic sediment transport events. Dust storms and extreme aeolian events clearly have the potential to deposit zircons on the currently exposed Willyama Supergroup, obviating the link between modern detrital zircons and the geology defining the physiology of the drainage system.

5.4. Implications for Detrital Zircon Studies

It is apparent in the modern detrital zircons from the Broken Hill region that a source of zircon is present in addition to that from the bedrock. We attribute this to aeolian reworking that is part of a system that also deposited zircons in the dunes of the southern Strzelecki Desert. This transportation regime redistributed zircons from a wide range of sources that reflect both primary and reworked reservoirs. Such reworking must be considered whenever modern detrital zircons are sampled in areas of low rainfall.

While aeolian contamination of zircon populations can be verified with relative ease in modern environments by the in situ sampling of the sediment sources, this is not necessarily possible for detrital zircon in the geological record. The stream sediment aspect of this study used samples of what would be considered very immature sediment from a proximal and clearly identifiable source. Clasts of up to several centimetres in size of the rock types that define the physiology of the stream catchments was still present in all of the creeks. Excluding the large clasts, typical grain sizes of the sediment present in the streams ranged from silt to coarse sand. If this sediment was preserved in the geological record it would be correctly interpreted as an immature sediment with a proximal source. However, the detrital zircon record would be extremely misleading when considered in the context of proximal derivation, with an input of an "exotic" zircon component of up to 30%. If the zircon ages were interpreted to reflect a proximal source region, then the incorrect interpretation would be made that the proximal source contained zircons aged between ca. 100 Ma to 1400 Ma. Although it is not present in any of the sampled catchments, the Adelaide Supergroup which overlies parts of the Willyama Supergroup is a possible proximal source which could have contributed to the peaks between 1400 Ma to 550 Ma (Ireland et al. 1998). However, the 500 Ma to 100 Ma zircons must be exotic to the bedrock geology in the Broken Hill area. While it is possible in the present study to track back to the likely zircon source region for the exotic zircons in the Broken Hill streams, in ancient sedimentary rocks sampled from areas where drainage directions or aeolian activity are unknown, there is a high potential that the sediment source(s) and their characteristics may be misinterpreted. It therefore becomes essential that certain characteristics of sedimentary packages sampled for detrital zircon studies are recognised and considered.

Several instructive cases exist where modern stream sampling has proved reliable. Malusà et al. (2016) analysed stream sediments from a series of catchments in the European Alps and was able to successfully map the zircon and apatite fertility of the bedrock to those catchments. Similarly, numerous modern sediment zircon studies from areas including Scandanavia, the Himalayas, and China have demonstrated a reliable correlation between bedrock and modern detrital zircons (e.g. Morton et al. 2008, Cina et al. 2009, Zhang et al. 2012, Li et al. 2013). These studies were carried out in areas of ongoing uplift or orogenesis, with subsequent rapid erosion and deposition. In cases such as this, the rapid flux of sediment would minimise the contribution

of any aeolian material.

It is evident that certain environments promote the ad hoc accumulation of geodynamically unrelated zircon grains. Aeolian detritus deposited in settings dominated by slowly accumulating alluvial, fluvial, or lacustrine sedimentary processes has the potential to become a significant proportion of the sedimentary pile, given sufficient time. The reworking of this aeolian detritus in these systems makes this contribution virtually undetectable until aeolian deposition becomes the dominant sedimentary process and dunes begin to form. Furthermore, sediment sourced from catchments which contain non-trivial proportions of aeolian material have a significant chance of recording zircon age signatures which include geodynamically unrelated zircon.

Another impacting factor on the prevalence of aeolian material is vegetation which binds soil and prevents erosion. However, macroscopic vegetation has been influencing the terrestrial environment since the Mid-Ordovician (Davies and Gibling 2010). While some workers have proposed that prior to the appearance of plants, microbial mats may have inhabited terrestrial environments potentially binding soils (e.g. Dott 2003 and references therein), however the fossil record for this is scant. Therefore interpretations of detrital zircons in pre-Ordovician sequences need to be mindful of aeolian transport.

5.5. A Cautionary Tale: Southern Australia

Figure 9 presents a comparison of modern sediment zircon $\varepsilon_{Hf}(t)$ data from across southern Australia which includes data from this study and from the Gawler Craton (Belousova et al. 2009). The stream sediment and sand dune zircon age data obtained in this study bear a striking similarity to that obtained from stream sediments from the Gawler Craton in regard to both incongruous age populations and $\varepsilon_{Hf}(t)$ character. The Gawler Craton is an arid region of Mesoarchean to early Mesoproterozoic lithosphere overlain by Neoproterozoic to recent sedimentary sequences (Hand et al. 2007, Reid and Hand 2012). In addition to zircons that would logically be expected to be derived from the Gawler Craton, Belousova et al. (2009) identified a series of zircons ranging in age between 300 Ma to 1300 Ma. Zircons younger than c. 1000 Ma were discounted as not representative of the crustal evolution, for reasons not entirely made clear. However, zircons in the range ~ 1000-1200 Ma and their allied Lu-Hf isotopic compositions were interpreted as recording juvenile crustal additions into the Gawler Craton, despite evidence from low-temperature Ar-Ar and Rb-Sr systems indicating high-T crustal processes ceased in the Gawler Craton at around 1450 Ma (Webb et al. 1986, Fraser and Lyons 2006, Thomas et al. 2008). Obscuring the significance of any modern detrital zircon in the Gawler Craton is that the southwestern part of the craton hosts the Eocene to Miocene-aged world class zircon deposits Jacinth and Ambrosia within the Eucla Basin (Reid et al. 2013). The overwhelmingly dominant zircon age in the Eucla Basin deposits is 1200 ±100 Ma (Reid et al. 2013), and the heavy minerals include kyanite and staurolite (Iluka Resources, 2011), which are essentially unknown in the Gawler Craton (Hand et al. 2007). All the age and mineralogical evidence points to a sediment source for the zircon deposits ~ 1500 km to the west in the Albany Fraser Province in southwestern Australia (Reid et al. 2013).

A westerly sediment source in southern Australia during the Cainozoic is not surprising. During the Eocene-Miocene, Australia was located between 60°-50°S. Open marine conditions were not established over the whole of the Eucla Basin until accelerated spreading of the Southern Ocean in the Middle Eocene (McGowran et al. 1997). This constraint coupled with the southerly latitude and strong westerly prevailing winds (Hou et al. 2008), promoted the building of large sand barrier complexes on the southwestern margin of the Gawler Craton.

Aridity in southern Australia was imposed during the Pliocene (Fujioka et al. 2009, McLaren and Wallace 2010) with the consequence that aeolian deposits would have undergone west to east reworking, leading to the deposition of aeolian material, including zircons, across the Gawler Craton. Therefore, rather than a phase of crustal growth in the Gawler Craton, the comparatively juvenile 1300-1000 Ma zircons documented in modern streams in the Gawler Craton (Belousova et al. 2009) record reworked aeolian-transported contamination derived from the geodynamically unrelated Albany Fraser Province in Western Australia. The potential for these exotic zircons to contaminate even very local catchments in the Gawler Craton was shown by Howard et al. (2009), who sampled a small (~ 1 hectare) drainage system composed entirely of outcropping 2000 Ma orthogneiss in the eastern Gawler Craton, and found that 30% of the analysed zircons were between 1300-1100 Ma in age. This provides a good example of the risk of over-interpretation that is possible when using detrital zircons which lack sediment transport context.

Although it has been demonstrated that the geochemical signatures much of the Gawler Craton aged zircon (i.e. pre-1500 Ma) appears to accurately reflect zircon found in situ within the craton (e.g. Reid et al. 2014, Armit et al. 2017), the use of modern detritus without the context of in situ sampling for comparison may lead to erroneous conclusions. While the contemporary example from the Gawler Craton is readily decipherable, into the future sediment derived from Gawler Craton and deposited in new sedimentary successions will contain geodynamically unrelated zircon populations that hold no particular significance for the evolution of any one lithospheric system. By extension, in the ancient sedimentary record that is routinely sampled for detrital zircon studies, the potential also clearly exists for the ad hoc accumulation of geodynamically unrelated zircon populations.

6. Conclusions

Detrital zircon sampled from modern stream sediments in the Broken Hill area in the eastern Curnamona Province in southern Australia yield populations ranging in age from c. 3000-100 Ma. This includes populations of c. 1400-100 Ma zircon, which are exotic to the outcropping 1710-1580 Ma Willyama Supergroup which defines the physiology of the stream catchments. The presence of significant numbers of these young zircons indicates an additional source of zircon than the bedrock, despite the sedimentological evidence that the sediment was proximally derived. Zircons sampled from aeolian dune sands 120km north of the Broken Hill area contain ages and Hf isotope values consistent with the exotic young grains identified in the Broken Hill steam sediments, and therefore aeolian detritus is a plausible source of the young zircons in the stream sediments. However, the dune sands also contain zircons whose ages are similar to detrital zircons obtained from in situ sampling of the Willyama Supergroup. This means that little significance can be attached to any zircon found in the Broken Hill stream sediments in terms of the evolution of the Willyama Supergroup and its source regions. The sources of the dune sands are the dry inland lakes of the Lake Eyre Basin in southern Central Australia, which sample a wide area of eastern Australia. Sediment from the now arid Lake Eyre Basin can be transported large distances by strong westerly winds, including catastrophic dust storm events. Such events lead to widespread homogenisation of zircon populations and make identifying true zircon sources difficult.

In studies relying on the sampling of modern detrital zircons it is essential that the regolith evolution of the catchment area be given appropriate consideration, as well as the surrounding surface environments, especially in arid mid-latitude areas with strong and persistent prevailing wind systems. This study also has potential implications for the way in which detrital zircons are interpreted within

the rock record. The immature and source proximal sediments in the Broken Hill area contain zircon up to 1.5 Ga younger than what is known to exist in the bedrock, which if preserved in the rock record would incorrectly suggest a proximal source of young zircon. This highlights the extreme caution required when interpreting detrital zircon provenance.

References

Alizai, A., Carter, A., Clift, P. D., VanLaningham, S., Williams, J. C. & Kumar, R., 2011. Sediment provenance, reworking and transport processes in the Indus River by U–Pb dating of detrital zircon grains. Global and Planetary Change, 76(1–2), 33-55.

Alley, N. F., 1998. Cainozoic stratigraphy, palaeoenvironments and geological evolution of the Lake Eyre Basin. Palaeogeography, Palaeoclimatology, Palaeoecology, 144(3–4), 239-263.

Andersen, T., 2005. Detrital zircons as tracers of sedimentary provenance: limiting conditions from statistics and numerical simulation. Chemical Geology, 216(3–4), 249-270.

Andersen, T., Kristoffersen, M. & Elburg, M. A., 2016. How far can we trust provenance and crustal evolution information from detrital zircons? A South African case study. Gondwana Research, 34, 129-148.

Armit, R., Betts, P. G., Schaefer, B. F., Yi, K., Kim, Y., Dutch, R. A., Reid, A., Jagodzinski, L., Giles, D. & Ailleres, L., 2017. Late Palaeoproterozoic evolution of the buried northern Gawler Craton. Precambrian Research, 291, 178-201.

Armit, R. J., Betts, P. G., Schaefer, B. F. & Ailleres, L., 2012. Constraints on long-lived Mesoproterozoic and Palaeozoic deformational events and crustal architecture in the northern Mount Painter Province, Australia. Gondwana Research, 22(1), 207-226.

Ashley, P. M., Cook, N. D. J. & Fanning, C. M., 1996. Geochemistry and age of metamorphosed felsic igneous rocks with A-type affinities in the Willyama Supergroup, Olary Block, South Australia, and implications for mineral exploration. Lithos, 38(3), 167-184.

Belousova, E. A., Reid, A. J., Griffin, W. L. & O'Reilly, S. Y., 2009. Rejuvenation vs. recycling of Archean crust in the Gawler Craton, South Australia: Evidence from U–Pb and Hf isotopes in detrital zircon. Lithos, 113(3–4), 570-582.

Bonich, M. B., Samson, S. D. & Fedo, C. M., 2017. Incongruity of Detrital Zircon Ages of Granitic Bedrock and Its Derived Alluvium: An Example from the Stepladder Mountains, Southeastern California. The Journal of Geology, 125(3), 337-350.

Bradley, G. M., 1984. Mount Gipps 1:25,000 Geological Sheet, Geological Survey of New South Wales, Sydney.

Brown, R. E., 1983. Broken Hill 1:25,000 Geological Sheet, Geological Survey of New South Wales, Sydney.

Brown, R. E., 1984. Pinnacles 1:25,000 Geological Sheet, Geological Survey of New South Wales, Sydney.

Carrapa, B., 2010. Resolving tectonic problems by dating detrital minerals. Geology, 38(2), 191-192.

Cawood, P. A., Nemchin, A. A., Freeman, M. & Sircombe, K., 2003. Linking source and sedimentary basin: Detrital zircon record of sediment flux along a modern river system and implications for provenance studies. Earth and Planetary Science Letters, 210(1–2), 259-268.

Cina, S. E., Yin, A., Grove, M., Dubey, C. S., Shukla, D. P., Lovera, O. M., Kelty, T. K., Gehrels, G. E. & Foster, D. A., 2009. Gangdese arc detritus within the eastern Himalayan Neogene foreland basin: Implications for the Neogene evolution of the Yalu–Brahmaputra River system. Earth and Planetary Science Letters, 285(1–2), 150-162.

Clark, C. & Hand, M., 2010. Decoding Mesoproterozoic and Cambrian metamorphic

events in Willyama Complex metapelites through the application of Sm–Nd garnet geochronology and P–T pseudosection analysis. Gondwana Research, 17(1), 59-74.

Cohen, T. J., Nanson, G. C., Larsen, J. R., Jones, B. G., Price, D. M., Coleman, M. & Pietsch, T. J., 2010. Late Quaternary aeolian and fluvial interactions on the Cooper Creek Fan and the association between linear and source-bordering dunes, Strzelecki Desert, Australia. Quaternary Science Reviews, 29(3–4), 455-471.

Condie, K. C., Beyer, E., Belousova, E., Griffin, W. L. & O'Reilly, S. Y., 2005. U–Pb isotopic ages and Hf isotopic composition of single zircons: The search for juvenile Precambrian continental crust. Precambrian Research, 139(1–2), 42-100.

Conor, C. H. H. & Preiss, W. V., 2008. Understanding the 1720–1640 Ma Palaeoproterozoic Willyama Supergroup, Curnamona Province, Southeastern Australia: Implications for tectonics, basin evolution and ore genesis. Precambrian Research, 166(1–4), 297-317.

Davies, N. S. & Gibling, M. R., 2010. Cambrian to Devonian evolution of alluvial systems: The sedimentological impact of the earliest land plants. Earth-Science Reviews, 98(3–4), 171-200.

De Deckker, P., Munday, C. I., Brocks, J., O'Loingsigh, T., Allison, G. E., Hope, J., Norman, M., Stuut, J.-B. W., Tapper, N. J. & van der Kaars, S., 2014. Characterisation of the major dust storm that traversed over eastern Australia in September 2009; a multidisciplinary approach. Aeolian Research, 15, 133-149.

Dott, R. H. J., 2003. The Importance of Eolian Abrasion in Supermature Quartz Sandstones and the Paradox of Weathering on Vegetation-Free Landscapes. The Journal of Geology, 111(4), 387-405.

Dutch, R. A., Hand, M. & Clark, C., 2005. Cambrian reworking of the southern Australian Proterozoic Curnamona Province: constraints from regional shear-zone systems. Journal of the Geological Society, 162(5), 763-775.

Elburg, M. A., Bons, P. D., Dougherty-Page, J., Janka, C. E., Neumann, N. & Schaefer, B., 2001. Age and metasomatic alteration of the Mt Neill Granite at Nooldoonooldoona Waterhole, Mt Painter Inlier, South Australia. Australian Journal of Earth Sciences, 48(5), 721-730.

Fanning, C. M., Reid, A. J. & Teale, G., 2007. A geochronological framework for the Gawler Craton, South Australia. Geological Survey of South Australia.

Fedo, C. M., Sircombe, K. N. & Rainbird, R. H., 2003. Detrital Zircon Analysis of the Sedimentary Record. Reviews in Mineralogy and Geochemistry, 53(1), 277-303.

Fitzsimmons, K. E., Bowler, J. M., Rhodes, E. J. & Magee, J. M., 2007a. Relationships between desert dunes during the late Quaternary in the Lake Frome region, Strzelecki Desert, Australia. Journal of Quaternary Science, 22(5), 549-558.

Fitzsimmons, K. E., Rhodes, E. J., Magee, J. W. & Barrows, T. T., 2007b. The timing of linear dune activity in the Strzelecki and Tirari Deserts, Australia. Quaternary Science Reviews, 26(19–21), 2598-2616.

Forbes, C. J., Betts, P. G., Giles, D. & Weinberg, R., 2008. Reinterpretation of the tectonic context of high-temperature metamorphism in the Broken Hill Block, NSW, and implications on the Palaeo- to Meso-Proterozoic evolution. Precambrian Research, 166(1–4), 338-349.

Forbes, C. J., Betts, P. G., Weinberg, R. & Buick, I. S., 2005. A structural metamorphic study of the Broken Hill Block, NSW, Australia. Journal of Metamorphic Geology, 23(8), 745-770.

Fraser, G., McAvaney, S., Neumann, N., Szpunar, M. & Reid, A., 2010. Discovery of early Mesoarchean crust in the eastern Gawler Craton, South Australia. Precam-

brian Research, 179(1–4), 1-21.

Fraser, G. L. & Lyons, P., 2006. Timing of Mesoproterozoic tectonic activity in the northwestern Gawler Craton constrained by 40Ar/39Ar geochronology. Precambrian Research, 151(3–4), 160-184.

Fujioka, T., Chappell, J., Fifield, L. K. & Rhodes, E. J., 2009. Australian desert dune fields initiated with Pliocene–Pleistocene global climatic shift. Geology, 37(1), 51-54.

Gehrels, G., 2014. Detrital Zircon U-Pb Geochronology Applied to Tectonics. Annual Review of Earth and Planetary Sciences, 42(1), 127-149.

Gibson, D. L., 1999. Explanatory Notes for the Broken Hill and Curnamona Province 1:500 000 Regolith Landform Maps. In: CRC LEME Open File Report CRC LEME.

Griffin, W. L., Belousova, E. A., Shee, S. R., Pearson, N. J. & O'Reilly, S. Y., 2004. Archean crustal evolution in the northern Yilgarn Craton: U–Pb and Hf-isotope evidence from detrital zircons. Precambrian Research, 131(3–4), 231-282.

Griffin, W. L., Belousova, E. A., Walters, S. G. & O'Reilly, S. Y., 2006. Archaean and Proterozoic crustal evolution in the Eastern Succession of the Mt Isa district, Australia: U – Pb and Hf-isotope studies of detrital zircons. Australian Journal of Earth Sciences, 53(1), 125-149.

Griffin, W. L., Wang, X., Jackson, S. E., Pearson, N. J., O'Reilly, S. Y., Xu, X. & Zhou, X., 2002. Zircon chemistry and magma mixing, SE China: In-situ analysis of Hf isotopes, Tonglu and Pingtan igneous complexes. Lithos, 61(3–4), 237-269.

Habeck-Fardy, A. & Nanson, G. C., 2014. Environmental character and history of the Lake Eyre Basin, one seventh of the Australian continent. Earth-Science Reviews, 132, 39-66.

Hand, M., Reid, A. & Jagodzinski, L., 2007. Tectonic framework and evolution of the Gawler craton, Southern Australia. Economic Geology, 102(8), 1377-1395.

Hill, S. M., 2001. Broken Hill Regolith Landform Map (1:100 000 Scale), Cooperative Research Center for Landscape Evolution and Mineral Exploration (CRC LEME), Canberra, Australia.

Hou, B., Frakes, L. A., Sandiford, M., Worrall, L., Keeling, J. & Alley, N. F., 2008. Cenozoic Eucla Basin and associated palaeovalleys, southern Australia — Climatic and tectonic influences on landscape evolution, sedimentation and heavy mineral accumulation. Sedimentary Geology, 203(1–2), 112-130.

Howard, K. E., Hand, M., Barovich, K. M., Reid, A., Wade, B. P. & Belousova, E. A., 2009. Detrital zircon ages: Improving interpretation via Nd and Hf isotopic data. Chemical Geology, 262(3–4), 277-292.

Ireland, T. R., Flo¨ttmann, T., Fanning, C. A., Gibson, G. M. & Preiss, W. V., 1998. Development of the early Paleozoic Pacific margin of Gondwana from detrital-zircon ages across the Delamerian orogen. Geology, 26(3), 243-246.

Jackson, S. E., Pearson, N. J., Griffin, W. L. & Belousova, E. A., 2004. The application of laser ablation-inductively coupled plasma-mass spectrometry to in situ U–Pb zircon geochronology. Chemical Geology, 211(1–2), 47-69.

Jagodzinski, E. A. & Fricke, C. E., 2010. Compilation of new SHRIMP U-Pb geochronological data for the southern Curnamona Province, South Australia, South Australia. Department of Primary Industries and Resources.

Jeon, H., Williams, I. S. & Bennett, V. C., 2014. Uncoupled O and Hf isotopic systems in zircon from the contrasting granite suites of the New England Orogen, eastern Australia: Implications for studies of Phanerozoic magma genesis. Geochimica et Cosmochimica Acta, 146, 132-149.

Kemp, A. I. S., Hawkesworth, C. J., Collins, W. J., Gray, C. M. & Blevin, P. L., 2009. Iso-

topic evidence for rapid continental growth in an extensional accretionary orogen: The Tasmanides, eastern Australia. Earth and Planetary Science Letters, 284(3–4), 455-466.

Kemp, A. I. S., Hawkesworth, C. J., Foster, G. L., Paterson, B. A., Woodhead, J. D., Hergt, J. M., Gray, C. M. & Whitehouse, M. J., 2007. Magmatic and Crustal Differentiation History of Granitic Rocks from Hf-O Isotopes in Zircon. Science, 315(5814), 980-983.

Kemp, A. I. S., Hawkesworth, C. J., Paterson, B. A. & Kinny, P. D., 2006. Episodic growth of the Gondwana supercontinent from hafnium and oxygen isotopes in zircon. Nature, 439(7076), 580-583.

Kromkhun, K., Foden, J., Hore, S. & Baines, G., 2013. Geochronology and Hf isotopes of the bimodal mafic–felsic high heat producing igneous suite from Mt Painter Province, South Australia. Gondwana Research, 24(3–4), 1067-1079.

Li, W., Neubauer, F., Liu, Y., Genser, J., Ren, S., Han, G. & Liang, C., 2013. Paleozoic evolution of the Qimantagh magmatic arcs, Eastern Kunlun Mountains: Constraints from zircon dating of granitoids and modern river sands. Journal of Asian Earth Sciences, 77, 183-202.

Link, P. K., Fanning, C. M. & Beranek, L. P., 2005. Reliability and longitudinal change of detrital-zircon age spectra in the Snake River system, Idaho and Wyoming: An example of reproducing the bumpy barcode. Sedimentary Geology, 182(1–4), 101-142.

Lomax, J., Hilgers, A., Wopfner, H., Grün, R., Twidale, C. R. & Radtke, U., 2003. The onset of dune formation in the Strzelecki Desert, South Australia. Quaternary Science Reviews, 22(10–13), 1067-1076.

Malusà, M. G., Resentini, A. & Garzanti, E., 2016. Hydraulic sorting and mineral fertility bias in detrital geochronology. Gondwana Research, 31, 1-19.

McFarlane, C. R. M. & Frost, B. R., 2009. Constraints on the early metamorphic evolution of Broken Hill, Australia, from in situ U-Pb dating and REE geochemistry of monazite. Journal of Metamorphic Geology, 27(1), 3-17.

McGowran, B., Li, Q., Cann, J., Padley, D., McKirdy, D. M. & Shafik, S., 1997. Biogeographic impact of the Leeuwin Current in southern Australia since the late middle Eocene. Palaeogeography, Palaeoclimatology, Palaeoecology, 136(1–4), 19-40.

McLaren, S. & Wallace, M. W., 2010. Plio-Pleistocene climate change and the onset of aridity in southeastern Australia. Global and Planetary Change, 71(1–2), 55-72.

Moecher, D. P. & Samson, S. D., 2006. Differential zircon fertility of source terranes and natural bias in the detrital zircon record: Implications for sedimentary provenance analysis. Earth and Planetary Science Letters, 247(3–4), 252-266.

Morton, A., Fanning, M. & Milner, P., 2008. Provenance characteristics of Scandinavian basement terrains: Constraints from detrital zircon ages in modern river sediments. Sedimentary Geology, 210(1–2), 61-85.

Page, R. N., Stevens, B. P. J. & Gibson, G. M., 2005a. Geochronology of the sequence hosting the Broken Hill Pb-Zn-Ag orebody, Australia. Economic Geology, 100(4), 633-661.

Page, R. W., Conor, C. H. H., Stevens, B. P. J., Gibson, G. M., Preiss, W. V. & Southgate, P. N., 2005b. Correlation of Olary and Broken Hill Domains, Curnamona Province: Possible relationship to Mount Isa and other North Australian Pb-Zn-Ag-bearing successions. Economic Geology, 100(4), 663-676.

Page, R. W. & Laing, W. P., 1992. Felsic metavolcanic rocks related to the Broken Hill Pb-Zn-Ag orebody, Australia; geology, depositional age, and timing of high-grade metamorphism. Economic Geology, 87(8), 2138-2168.

Payne, J. L., Pearson, N. J., Grant, K. J. & Halverson, G. P., 2013. Reassessment of relative oxide formation rates and molecular interferences on in situ lutetium-hafnium analysis with laser ablation MC-ICP-MS. Journal of Analytical Atomic Spectrometry, 28(7), 1068-1079.

Pell, S. D., Chivas, A. R. & Williams, I. S., 2000. The Simpson, Strzelecki and Tirari Deserts: development and sand provenance. Sedimentary Geology, 130(1–2), 107-130.

Purdy, D. J., Cross, A. J., Brown, D. D., Carr, P. A. & Armstrong, R. A., 2016. New constraints on the origin and evolution of the Thomson Orogen and links with central Australia from isotopic studies of detrital zircons. Gondwana Research, 39, 41-56.

Raetz, M., Krabbendam, M. & Donaghy, A. G., 2002. Compilation of Pb zircon data from the Willyama Supergroup, Broken Hill region, Australia: Evidence for three tectonostratigraphic successions and four magmatic events? Australian Journal of Earth Sciences, 49(6), 965-983.

Rainbird, R. H., Hearnan, L. M. & Young, G., 1992. Sampling Laurentia: Detrital zircon geochronology offers evidence for an extensive Neoproterozoic river system originating from the Grenville orogen. Geology, 20(4), 351-354.

Regmi, K. R., Weinberg, R. F., Nicholls, I. A., Maas, R. & Raveggi, M., 2016. Evidence for hybridisation in the Tynong Province granitoids, Lachlan Fold Belt, eastern Australia. Australian Journal of Earth Sciences, 63(3), 235-255.

Reid, A., Keeling, J., Boyd, D., Belousova, E. & Hou, B., 2013. Source of zircon in world-class heavy mineral placer deposits of the Cenozoic Eucla Basin, southern Australia from LA-ICPMS U–Pb geochronology. Sedimentary Geology, 286–287, 1-19.

Reid, A. J. & Hand, M., 2012. Mesoarchean to Mesoproterozoic Evolution of the Southern Gawler Craton, South Australia. Journal of International Geoscience, 35(1), 216-225.

Reid, A. J., Jagodzinski, E. A., Armit, R. J., Dutch, R. A., Kirkland, C. L., Betts, P. G. & Schaefer, B. F., 2014. U-Pb and Hf isotopic evidence for Neoarchean and Paleoproterozoic basement in the buried northern Gawler Craton, South Australia. Precambrian Research, 250, 127-142.

Rubin, D. M., 1990. Lateral migration of linear dunes in the Strzelecki desert, Australia. Earth Surface Processes and Landforms, 15(1), 1-14.

Rutherford, L., Barovich, K., Hand, M. & Foden, J., 2006a. Continental ca 1.7 – 1.69 Ga Fe-rich metatholeiites in the Curnamona Province, Australia: a record of melting of a heterogeneous, subduction-modified lithospheric mantle. Australian Journal of Earth Sciences, 53(3), 501-519.

Rutherford, L., Hand, M. & Barovich, K., 2007. Timing of Proterozoic metamorphism in the southern Curnamona Province: implications for tectonic models and continental reconstructions. Australian Journal of Earth Sciences, 54(1), 65-81.

Rutherford, L., Hand, M. & Mawby, J., 2006b. Delamerian-aged metamorphism in the southern Curnamona Province, Australia: implications for the evolution of the Mesoproterozoic Olarian Orogeny. Terra Nova, 18(2), 138-146.

Scherer, E., Munker, C. & Mezger, K., 2001. Calibration of the Lutetium-Hafnium Clock. Science, 293(5530), 683-687.

Sircombe, K. N. & Freeman, M. J., 1999. Provenance of detrital zircons on the Western Australia coastline—Implications for the geologic history of the Perth basin and denudation of the Yilgarn craton. Geology, 27(10), 879-882.

Sláma, J., Košler, J., Condon, D. J., Crowley, J. L., Gerdes, A., Hanchar, J. M., Horstwood, M. S. A., Morris, G. A., Nasdala, L., Norberg, N., Schaltegger, U., Schoene, B., Tubrett, M. N. & Whitehouse, M. J., 2008. Plešovice zircon — A new natural refer-

ence material for U–Pb and Hf isotopic microanalysis. Chemical Geology, 249(1–2), 1-35.

Smits, R. G., Collins, W. J., Hand, M., Dutch, R. & Payne, J., 2014. A Proterozoic Wilson cycle identified by Hf isotopes in central Australia: Implications for the assembly of Proterozoic Australia and Rodinia. Geology, 42(3), 231-234.

Stevens, B. P. J., Barnes, R. G., Brown, R. E., Stroud, W. J. & Willis, I. L., 1988. The Willyama Supergroup in the Broken Hill and Euriowie Blocks, New South Wales. Precambrian Research, 40-41(0), 297-327.

Stevens, B. P. J. & Bradley, G. M., 1983. Lakes Creek 1:25,000 Geological Sheet, Geological Survey of New South Wales, Sydney.

Stevens, B. P. J., Page, R. W. & Crooks, A., 2008. Geochronology of Willyama Supergroup metavolcanics, metasediments and contemporaneous intrusions, Broken Hill, Australia. Australian Journal of Earth Sciences, 55(3), 301-330.

Thomas, J. L., Direen, N. G. & Hand, M., 2008. Blind orogen: Integrated appraisal of multiple episodes of Mesoproterozoic deformation and reworking in the Fowler Domain, western Gawler Craton, Australia. Precambrian Research, 166(1–4), 263-282.

Tucker, R. T., Roberts, E. M., Hu, Y., Kemp, A. I. S. & Salisbury, S. W., 2013. Detrital zircon age constraints for the Winton Formation, Queensland: Contextualizing Australia's Late Cretaceous dinosaur faunas. Gondwana Research, 24(2), 767-779.

Wade, C. E., 2011. Definition of the Mesoproterozoic Ninnerie Supersuite, Curnamona Province, South Australia. MESA Journal, 62, 25-42.

Wade, C. E., Reid, A. J., Wingate, M. T. D., Jagodzinski, E. A. & Barovich, K., 2012. Geochemistry and geochronology of the c. 1585 Ma Benagerie Volcanic Suite, southern Australia: Relationship to the Gawler Range Volcanics and implications for the petrogenesis of a Mesoproterozoic silicic large igneous province. Precambrian Research, 206–207(0), 17-35.

Wasson, R. J., Fitchett, K., Mackey, B. & Hyde, R., 1988. Large-scale patterns of dune type, spacing and orientation in the Australian continental dunefield. Australian Geographer, 19(1), 89-104.

Webb, A. W., Thomson, B. P., Blissett, A. H., Daly, S. J., Flint, R. B. & Parker, A. J., 1986. Geochronology of the Gawler Craton, South Australia. Australian Journal of Earth Sciences, 33(2), 119-143.

White, R. W., Pomroy, N. E. & Powell, R., 2005. An in situ metatexite–diatexite transition in upper amphibolite facies rocks from Broken Hill, Australia. Journal of Metamorphic Geology, 23(7), 579-602.

Willis, I. L., 1984. Silverton 1:25,000 Geological sheet, Geological Survey of New South Wales, Sydney.

Woodhead, J., Hergt, J., Shelley, M., Eggins, S. & Kemp, R., 2004. Zircon Hf-isotope analysis with an excimer laser, depth profiling, ablation of complex geometries, and concomitant age estimation. Chemical Geology, 209(1–2), 121-135.

Woodhead, J. D. & Hergt, J. M., 2005. A Preliminary Appraisal of Seven Natural Zircon Reference Materials for In Situ Hf Isotope Determination. Geostandards and Geoanalytical Research, 29(2), 183-195.

Yi, K., Bennett, V. C., Nutman, A. P. & Lee, S. R., 2014. Tracing Archaean terranes under Greenland's Icecap: U–Th–Pb–Hf isotopic study of zircons from melt-water rivers in the Isua area. Precambrian Research, 255, Part 3, 900-921.

Zhang, J. Y., Yin, A., Liu, W. C., Wu, F. Y., Lin, D. & Grove, M., 2012. Coupled U-Pb dating and Hf isotopic analysis of detrital zircon of modern river sand from the Yalu River (Yarlung Tsangpo) drainage system in southern Tibet: Constraints on the transport processes and evolution of Himalayan rivers. Geological Society of America Bulletin.

Chapter 6 Supplementary Data 1: Data sources for predicted histograms

Formation	**Reference**	**Sample Numbers**
Cues Formation	Stephens et al. 2008	200218.5804, 200218.5815, 200218.5 200218.5803, 200218.5812
Himalaya Formation	Page et al. 2005a	9918.5516,
Allendale Metasediment	Page et al. 2005a	9918.5519,
Parnell Formation	Stephens et al. 2008	200218.2005,
Freyers Metasediments	Page et al. 2005a	9918.5517,
Thorndale Composite Gneiss	Page et al. 2005a	9918.5525,
Hores Gneiss	Page et al. 2005a	8618.2001,
Sundown Group	Page et al. 2005a	9918.5506, 9918.5510, 9918.5511, 9918.5520, 9918.5521
Rasp Ridge Gneiss	Page et al. 2005a	9918.5523,
Alma Gneiss	Page et al. 2005a	9918.5526,
Lady Brassey Formation	Raetz et al. 2002*	TDBH03096

*While the data used in this study was collected from Raetz et al. 2002,
that study sourced data collected from a variety of unpublished sources,
further details of which can be obtained from Appendix 1 of Raetz et al. 2002.

Chapter 6 Supplementary Data 2: Broken Hill Streams U-Pb isotopic data

Sample KBH-1: GDA 94, 541141 mE, 6476669 mN

Analysis #	$^{207}Pb/^{235}U$ Ratio	1σ	$^{206}Pb/^{238}U$ Ratio	1σ	Rho	$^{207}Pb/^{206}Pb$ Age	2σ	$^{206}Pb/^{238}U$ Age	2σ	Conc. %	Comments
Concordant Zircon Analyses											
BH1B_003	3.2345	0.05296	0.25345	0.00341	0.5081453	1480	28	1456	18	98	Hf Isotope Analysis #1
BH1B_004	3.61693	0.0546	0.26962	0.00353	0.5590133	1574	25	1539	18	98	Hf Isotope Analysis #2
BH1B_005	4.22351	0.06418	0.29586	0.00389	0.5599985	1690	25	1671	19	99	Hf Isotope Analysis #3
BH1B_009	6.62927	0.11783	0.37521	0.00525	0.4842345	2074	29	2054	25	99	
BH1B_010	3.90714	0.06453	0.28352	0.00381	0.5278822	1624	27	1609	19	99	
BH1B_011	5.51087	0.07634	0.34234	0.00445	0.630882	1907	21	1898	21	100	
BH1B_016	3.64982	0.05578	0.27168	0.0036	0.5571909	1576	25	1549	18	98	
BH1B_017	4.77826	0.069	0.31696	0.00413	0.5942446	1789	23	1775	20	99	
BH1B_018	3.90754	0.06097	0.28205	0.00376	0.5391633	1633	26	1602	19	98	
BH1B_019	4.93376	0.07571	0.32083	0.00426	0.5487635	1825	25	1794	21	98	
BH1B_020	5.60769	0.10432	0.34188	0.00493	0.4407614	1941	32	1896	24	98	Hf Isotope Analysis #4
BH1B_021	2.09942	0.05232	0.19192	0.00298	0.3092909	1181	49	1132	16	96	Hf Isotope Analysis #5
BH1B_023	3.44064	0.05708	0.2649	0.00359	0.5008406	1512	29	1515	18	100	
BH1B_025	4.23748	0.06348	0.29535	0.00388	0.5618117	1698	24	1668	19	98	Hf Isotope Analysis #6
BH1B_026	4.60804	0.06675	0.31025	0.00404	0.583235	1761	23	1742	20	99	Hf Isotope Analysis #7
BH1B_027	4.2365	0.0619	0.29567	0.00385	0.5761774	1695	23	1670	19	98	
BH1B_028	5.39827	0.07711	0.33659	0.00435	0.5899233	1900	22	1870	21	98	
BH1B_029	4.22292	0.06303	0.29608	0.00387	0.5658724	1687	24	1672	19	99	Hf Isotope Analysis #8
BH1B_030	4.27818	0.06313	0.29932	0.0039	0.5732759	1691	24	1688	19	100	
BH1B_031	10.89446	0.15747	0.47546	0.00616	0.58372	2520	21	2508	27	100	Hf Isotope Analysis #9
BH1B_032	1.69273	0.02876	0.16645	0.00223	0.4850776	1035	31	993	12	96	Hf Isotope Analysis #10
BH1B_037	2.13692	0.03105	0.19906	0.00257	0.5761893	1144	25	1170	14	102	
BH1B_040	4.87872	0.07192	0.3203	0.00417	0.5651368	1807	23	1791	20	99	Hf Isotope Analysis #11
BH1B_042	4.18813	0.06189	0.29329	0.00381	0.5658734	1689	24	1658	19	98	
BH1B_046	2.15427	0.03346	0.19776	0.00258	0.52823	1173	28	1163	14	99	Hf Isotope Analysis #12
BH1B_047	11.40516	0.15681	0.48535	0.00626	0.6058175	2562	20	2551	27	100	
BH1B_052	4.27957	0.06419	0.29956	0.00391	0.5430213	1689	25	1689	19	100	Hf Isotope Analysis #13
BH1B_053	4.75995	0.06655	0.31963	0.00408	0.5915651	1765	22	1788	20	101	
BH1B_055	4.80971	0.07031	0.31885	0.00412	0.5611652	1788	24	1784	20	100	Hf Isotope Analysis #14
BH1B_056	4.5788	0.06721	0.30929	0.00399	0.5523949	1754	24	1737	20	99	Hf Isotope Analysis #15
BH1B_058	0.63339	0.01016	0.08004	0.00104	0.4952971	504	32	496	6	98	Hf Isotope Analysis #16
BH1B_059	4.37343	0.06111	0.30304	0.00386	0.5972766	1709	22	1706	19	100	Hf Isotope Analysis #17
BH1B_061	3.76544	0.05257	0.27799	0.00354	0.5985638	1591	22	1581	18	99	
BH1B_065	5.32804	0.09734	0.33347	0.00471	0.4388552	1894	31	1855	23	98	Hf Isotope Analysis #18

BH1B_069	2.51801	0.04109	0.21921	0.00289	0.4998747	1277	29	1278	15	100	

Analysis #	$^{207}Pb/^{235}U$ Ratio	1σ	$^{206}Pb/^{238}U$ Ratio	1σ	Rho	$^{207}Pb/^{206}Pb$ Age	2σ	$^{206}Pb/^{238}U$ Age	2σ	Conc. %	Comments
BH1B_071	6.38742	0.10691	0.3655	0.00519	0.5507977	2054	26	2008	25	98	Hf Isotope Analysis #20
BH1B_075	4.52875	0.07721	0.30129	0.00427	0.5489262	1783	27	1698	21	95	
BH1B_080	4.90369	0.08524	0.32138	0.00457	0.5542702	1811	27	1797	22	99	Hf Isotope Analysis #21
BH1B_090	5.64642	0.09674	0.34404	0.00484	0.5240304	1942	27	1906	23	98	Hf Isotope Analysis #22
BH1B_092	3.82346	0.06993	0.27935	0.00399	0.4826571	1611	31	1588	20	99	Hf Isotope Analysis #23
BH1B_095	3.70568	0.06649	0.27335	0.00393	0.5114538	1593	30	1558	20	98	Hf Isotope Analysis #24
BH1B_100	1.3073	0.0344	0.13848	0.0022	0.3217046	883	53	836	12	95	
BH1B_101	15.96336	0.25923	0.56101	0.00782	0.5695426	2877	23	2871	32	100	
BH1B_102	9.44717	0.16574	0.43647	0.0063	0.5223748	2424	27	2335	28	96	
BH1B_103	4.46435	0.08239	0.30345	0.00439	0.4909916	1744	31	1708	22	98	
BH1B_104	3.59265	0.06104	0.26698	0.00373	0.5413684	1579	28	1526	19	97	Hf Isotope Analysis #25
BH1B_105	2.21019	0.04255	0.19936	0.00286	0.4548793	1207	35	1172	15	97	
BH1B_106	3.54599	0.07274	0.26353	0.00395	0.4201844	1579	36	1508	20	96	Hf Isotope Analysis #26
BH1B_107	2.54328	0.04715	0.21812	0.0031	0.4699507	1306	33	1272	16	97	Hf Isotope Analysis #27
BH1B_108	4.0439	0.06123	0.28753	0.00386	0.5953747	1661	24	1629	19	98	Hf Isotope Analysis #28
BH1B_109	3.92531	0.06873	0.28324	0.00398	0.5028597	1634	29	1608	20	98	Hf Isotope Analysis #29
BH1B_111	3.79125	0.06004	0.27736	0.00375	0.5600625	1608	26	1578	19	98	Hf Isotope Analysis #30
BH1B_113	3.92727	0.06316	0.28507	0.00386	0.5511165	1623	26	1617	19	100	Hf Isotope Analysis #31
BH1B_116	1.81937	0.03281	0.17511	0.00242	0.4747824	1078	33	1040	13	96	
BH1B_117	5.00491	0.08103	0.32361	0.00444	0.5326525	1835	26	1807	22	98	
BH1B_118	4.01931	0.06117	0.28795	0.00385	0.5714768	1647	24	1631	19	99	Hf Isotope Analysis #32
BH1B_119	2.12511	0.03216	0.19782	0.00263	0.5741627	1145	26	1164	14	102	
BH1B_120	4.37468	0.06859	0.30055	0.00405	0.5527281	1724	25	1694	20	98	Hf Isotope Analysis #33
BH1B_123	0.15087	0.0038	0.02236	0.00033	0.310077	144	57	143	2	99	
BH1B_125	4.25168	0.07069	0.29509	0.00402	0.5152715	1706	28	1667	20	98	
BH1B_131	0.82228	0.01798	0.09816	0.00139	0.3564193	631	45	604	8	96	
BH1B_135	16.37442	0.26365	0.55275	0.00743	0.5166372	2943	24	2837	31	96	Hf Isotope Analysis #34
BH1B_136	3.92746	0.06705	0.28119	0.00378	0.4783651	1648	29	1597	19	97	
Discordant Analyses - Not used in calculations											
BH1B_001	0.8044	0.01418	0.09927	0.00133	0.4617539	560	35	610	8	109	
BH1B_002	183.96837	14.10084	1.74109	0.14461	0.6277194	4861	95	6500	340	134	
BH1B_006	4.36537	0.06705	0.25473	0.00336	0.5559154	2020	24	1463	17	72	
BH1B_007	3.6512	0.05651	0.15308	0.00202	0.5538085	2588	23	918	11	35	
BH1B_008	3.0079	0.04788	0.20506	0.00273	0.5412649	1740	26	1202	15	69	
BH1B_012	27.16084	1.4177	0.47995	0.02264	0.2693142	3948	87	2527	99	64	
BH1B_013	9.22781	0.13152	0.42458	0.00558	0.611475	2431	20	2281	25	94	

BH1B_022	0.73263	0.01538	0.09151	0.00128	0.3804624	532	44	565	8	106	
BH1B_024	4.07229	0.05869	0.27216	0.00354	0.5863521	1775	23	1552	18	87	
BH1B_033	3.96461	0.05852	0.24157	0.00313	0.5709626	1942	23	1395	16	72	
	$^{207}Pb/^{235}U$		$^{206}Pb/^{238}U$			$^{207}Pb/^{206}Pb$		$^{206}Pb/^{238}U$		Conc.	
Analysis #	**Ratio**	**1σ**	**Ratio**	**1σ**	**Rho**	**Age**	**2σ**	**Age**	**2σ**	**%**	**Comments**
BH1B_034	4.73386	0.07371	0.30547	0.00403	0.5328097	1839	25	1718	20	93	
BH1B_035	1.27855	0.0203	0.13189	0.00174	0.5247786	938	29	799	10	85	
BH1B_036	5.85188	0.08062	0.25914	0.00332	0.6134202	2495	20	1485	17	60	
BH1B_038	1.1895	0.03022	0.11111	0.00172	0.2902443	1138	50	679	10	60	
BH1B_039	2.08219	0.02917	0.10816	0.00139	0.5969439	2223	21	662	8	30	
BH1B_041	3.37951	0.05012	0.23414	0.00305	0.5587965	1709	24	1356	16	79	
BH1B_043	3.80672	0.05499	0.2533	0.00326	0.5756717	1783	23	1456	17	82	
BH1B_044	0.42634	0.00932	0.057	0.0008	0.3547	381	47	357	5	94	
BH1B_045	5.01805	0.07387	0.305	0.00394	0.5650067	1946	23	1716	19	88	
BH1B_048	4.64336	0.06398	0.23017	0.00295	0.602019	2303	20	1335	15	58	
BH1B_049	0.20263	0.0086	0.0265	0.00048	0.1358838	430	95	169	3	39	
BH1B_050	4.06153	0.05553	0.24729	0.00315	0.6056733	1943	21	1425	16	73	
BH1B_051	-	81.27217	22.34041	0.60138	-	5204	18	-	166	-	
BH1B_054	4.62219	0.06533	0.30167	0.00386	0.5780864	1817	22	1700	19	94	
BH1B_057	3.8159	0.0541	0.24785	0.00316	0.5763717	1825	22	1427	16	78	
BH1B_060	4.09513	0.05816	0.26215	0.00336	0.5859521	1853	22	1501	17	81	
BH1B_062	5.15533	0.07335	0.30535	0.00391	0.5828155	1993	22	1718	19	86	
BH1B_063	6.67456	0.09444	0.31729	0.00406	0.5858494	2375	21	1777	20	75	
BH1B_064	2.86627	0.04991	0.17134	0.00237	0.4513029	1976	29	1020	13	52	
BH1B_066	5.21562	0.07522	0.30402	0.0039	0.5712498	2021	22	1711	19	85	
BH1B_070	4.53392	0.07003	0.29539	0.00386	0.5277003	1821	25	1668	19	92	
BH1B_072	3.43878	0.05285	0.24427	0.00334	0.6092228	1663	24	1409	17	85	
BH1B_073	6.96769	0.10721	0.21935	0.00301	0.613096	3055	21	1278	16	42	
BH1B_074	4.23254	0.06696	0.26778	0.0037	0.5964853	1874	24	1530	19	82	
BH1B_076	4.6616	0.07526	0.19396	0.0027	0.5858696	2600	23	1143	15	44	
BH1B_077	4.98643	0.08709	0.31459	0.0045	0.540354	1880	28	1763	22	94	
BH1B_078	3.50967	0.05948	0.24384	0.00344	0.5619971	1704	27	1407	18	83	
BH1B_079	6.58202	0.111	0.34167	0.00482	0.5681345	2224	25	1895	23	85	
BH1B_081	2.81866	0.04775	0.19127	0.0027	0.542684	1748	27	1128	15	65	
BH1B_082	7.60751	0.1175	0.34856	0.00479	0.6082614	2438	22	1928	23	79	
BH1B_083	1.76293	0.02911	0.13704	0.00191	0.559929	1495	27	828	11	55	
BH1B_084	1.79795	0.03086	0.17086	0.00239	0.5319618	1104	30	1017	13	92	
BH1B_085	0.13039	0.00556	0.01903	0.00035	0.160478	182	98	122	2	67	
BH1B_086	3.73537	0.06035	0.26804	0.0037	0.5702131	1645	26	1531	19	93	
BH1B 087	4.18799	0.06711	0.28569	0.00393	0.5723919	1738	25	1620	20	93	

BH1B_091	4.08555	0.06864	0.27995	0.00389	0.5349948	1729	27	1591	20	92	
BH1B_093	5.08217	0.07736	0.30801	0.00421	0.6181586	1951	23	1731	21	89	
BH1B_094	4.13409	0.06346	0.21497	0.00295	0.6110443	2221	22	1255	16	57	
BH1B_096	4.1135	0.07113	0.26476	0.00378	0.5299862	1843	28	1514	19	82	
	$^{207}Pb/^{235}U$		$^{206}Pb/^{238}U$			$^{207}Pb/^{206}Pb$		$^{206}Pb/^{238}U$		Conc.	
Analysis #	**Ratio**	**1σ**	**Ratio**	**1σ**	**Rho**	**Age**	**2σ**	**Age**	**2σ**	**%**	**Comments**
BH1B_097	2.6705	0.04163	0.14918	0.00205	0.5983696	2096	23	896	11	43	
BH1B_098	2.9076	0.04587	0.15379	0.00212	0.5906598	2191	23	922	12	42	
BH1B_099	2.89878	0.05422	0.20521	0.00299	0.4838452	1669	32	1203	16	72	
BH1B_110	2.13038	0.03575	0.18481	0.00253	0.5265103	1283	29	1093	14	85	
BH1B_112	4.04201	0.06738	0.27985	0.00385	0.5288182	1710	27	1591	19	93	
BH1B_114	0.63823	0.01319	0.07167	0.00102	0.4027667	761	41	446	6	59	
BH1B_115	3.58411	0.06139	0.23441	0.00323	0.502252	1814	28	1358	17	75	
BH1B_121	3.73886	0.06142	0.26086	0.00356	0.5214616	1696	27	1494	18	88	
BH1B_122	3.39488	0.0554	0.21838	0.00298	0.5234549	1844	27	1273	16	69	
BH1B_124	2.98272	0.04592	0.19058	0.00254	0.5618813	1856	24	1125	14	61	
BH1B_126	4.49326	0.0719	0.29694	0.00399	0.5394252	1795	26	1676	20	93	
BH1B_127	3.30062	0.052	0.1869	0.00249	0.543595	2072	24	1105	14	53	
BH1B_128	0.61602	0.01335	0.07752	0.0011	0.374241	515	46	481	7	93	
BH1B_129	11.22026	0.16605	0.42611	0.00559	0.5764861	2751	21	2288	25	83	
BH1B_130	2.59315	0.04618	0.18205	0.00252	0.4565347	1684	31	1078	14	64	
BH1B_132	3.67967	0.05542	0.18933	0.00247	0.5576873	2239	23	1118	13	50	
BH1B_133	3.86545	0.06013	0.24239	0.00318	0.5398077	1890	25	1399	17	74	
BH1B_134	3.06231	0.04736	0.19633	0.00256	0.5370679	1850	25	1156	14	62	
BH1B_137	4.44976	0.07198	0.28988	0.00381	0.5113921	1821	27	1641	19	90	
BH1B_138	15.91363	2.64833	0.22535	0.03304	0.0927045	4277	280	1310	174	31	
BH1B_139	1.1313	0.02005	0.10103	0.00135	0.4481732	1227	32	620	8	51	
BH1B_140	0.40101	0.02192	0.03783	0.00087	0.0900526	1118	110	239	5	21	
Sample KBH-2: GDA 94, 541234 mE, 6479241 mN											
Concordant Zircon Analyses											
BH2A_001	10.66178	0.14914	0.46807	0.0057	0.5033515	2510	22	2475	25	99	
BH2A_003	2.18557	0.04161	0.19801	0.00261	0.359586	1199	37	1165	14	97	Hf Isotope Analysis #1
BH2A_004	0.87911	0.01585	0.10374	0.00131	0.3735491	656	37	636	8	97	Hf Isotope Analysis #2
BH2A_005	2.14483	0.03629	0.19407	0.00246	0.409822	1201	32	1143	13	95	
BH2A_009	3.50022	0.05236	0.26642	0.00326	0.4800808	1534	26	1523	17	99	Hf Isotope Analysis #3
BH2A_011	2.38	0.0386	0.20904	0.00265	0.4462313	1259	30	1224	14	97	
BH2A_013	4.75411	0.06428	0.31654	0.00384	0.551539	1782	22	1773	19	100	
BH2A_014	4.07649	0.05556	0.29062	0.00353	0.5507293	1656	23	1645	18	99	Hf Isotope Analysis #4
BH2A_016	4.06096	0.05862	0.28844	0.00357	0.5154945	1663	24	1634	18	98	Hf Isotope Analysis #5

BH2A_023	4.90895	0.07203	0.3179	0.00401	0.5139867	1832	24	1780	20	97	
BH2A_024	5.08568	0.06903	0.32893	0.00404	0.5639553	1835	22	1833	20	100	Hf Isotope Analysis #7
BH2A_028	4.72153	0.06695	0.3143	0.00388	0.5245762	1782	24	1762	19	99	
BH2A_029	4.52755	0.06587	0.30123	0.00374	0.5094229	1783	24	1697	19	95	Hf Isotope Analysis #8
BH2A_030	3.85842	0.05653	0.27921	0.00346	0.5072207	1629	25	1587	17	97	Hf Isotope Analysis #9
	$^{207}Pb/^{235}U$		$^{206}Pb/^{238}U$			$^{207}Pb/^{206}Pb$		$^{206}Pb/^{238}U$		Conc.	
Analysis #	**Ratio**	**1σ**	**Ratio**	**1σ**	**Rho**	**Age**	**2σ**	**Age**	**2σ**	**%**	**Comments**
BH2A_031	2.15066	0.03608	0.19576	0.0025	0.4260482	1190	32	1153	13	97	Hf Isotope Analysis #10
BH2A_032	0.78348	0.0154	0.09537	0.00124	0.3582195	589	41	587	7	100	Hf Isotope Analysis #11
BH2A_034	4.73004	0.06941	0.31356	0.00386	0.4955011	1790	25	1758	19	98	Hf Isotope Analysis #12
BH2A_035	5.05711	0.09066	0.32539	0.00442	0.4054319	1844	32	1816	21	98	Hf Isotope Analysis #13
BH2A_041	4.79023	0.09336	0.31145	0.00438	0.3699741	1825	35	1748	22	96	
BH2A_043	3.94723	0.05623	0.2802	0.00342	0.517508	1664	24	1592	17	96	Hf Isotope Analysis #14
BH2A_044	8.57463	0.12566	0.42398	0.00527	0.5085678	2308	23	2279	24	99	Hf Isotope Analysis #15
BH2A_046	3.97128	0.06434	0.28048	0.00358	0.4491326	1674	28	1594	18	95	
BH2A_047	4.16477	0.05573	0.2942	0.00354	0.5529448	1674	22	1663	18	99	Hf Isotope Analysis #16
BH2A_049	4.83431	0.06785	0.31765	0.00388	0.5204193	1806	23	1778	19	98	Hf Isotope Analysis #17
BH2A_051	4.21245	0.06343	0.29216	0.00363	0.4762364	1707	26	1652	18	97	
BH2A_052	4.01472	0.05985	0.28592	0.00353	0.4824037	1658	26	1621	18	98	
BH2A_055	23.27383	0.35947	0.65156	0.0087	0.478177	3241	23	3234	34	100	Hf Isotope Analysis #18
BH2A_059	5.379	0.0788	0.33699	0.00454	0.6170456	1892	22	1872	22	99	
BH2A_062	8.36597	0.1219	0.42301	0.00569	0.6235904	2269	21	2274	26	100	Hf Isotope Analysis #19
BH2A_063	4.55225	0.06953	0.31	0.00422	0.5912331	1741	24	1741	21	100	
BH2A_065	4.64038	0.09506	0.30884	0.00472	0.4217529	1783	36	1735	23	97	
BH2A_066	4.57923	0.07131	0.31116	0.00425	0.580855	1745	24	1746	21	100	Hf Isotope Analysis #20
BH2A_067	0.68213	0.01395	0.08552	0.00122	0.4233913	524	42	529	7	101	Hf Isotope Analysis #21
BH2A_070	2.02741	0.03426	0.18757	0.00263	0.539305	1157	30	1108	14	96	
BH2A_073	2.71594	0.04093	0.22828	0.00311	0.6092556	1345	24	1326	16	99	
BH2A_074	1.53977	0.02533	0.15654	0.00217	0.5487194	967	29	938	12	97	
BH2A_075	4.71248	0.07346	0.31652	0.00438	0.5832685	1766	24	1773	21	100	Hf Isotope Analysis #22
BH2A_078	8.36479	0.1241	0.42256	0.00575	0.6186913	2271	21	2272	26	100	
BH2A_079	4.07808	0.06343	0.29371	0.00404	0.5874519	1637	25	1660	20	101	Hf Isotope Analysis #23
BH2A_080	3.92005	0.06424	0.28421	0.00397	0.5474631	1625	27	1613	20	99	Hf Isotope Analysis #24
BH2A_083	2.25347	0.04268	0.20208	0.00292	0.4655701	1218	34	1187	16	97	
BH2A_087	0.11454	0.01471	0.01719	0.0007	0.0272949	115	288	110	4	95	Hf Isotope Analysis #25
BH2A_091	6.52786	0.10111	0.3748	0.00512	0.5849336	2047	23	2052	24	100	
BH2A_092	3.79135	0.05845	0.27929	0.00379	0.5849872	1595	25	1588	19	100	Hf Isotope Analysis #26
BH2A_093	0.51408	0.01147	0.06713	0.00097	0.3718749	434	47	419	6	97	
BH2A_097	4.22118	0.06086	0.29538	0.0039	0.6157316	1691	22	1668	19	99	Hf Isotope Analysis #28
BH2A_099	4.77084	0.08942	0.31539	0.00458	0.4524914	1795	32	1767	22	98	

BH2A_105	12.04887	0.17096	0.49677	0.00649	0.6007566	2615	20	2600	28	99	Hf Isotope Analysis #30
BH2A_109	12.06863	0.17398	0.49647	0.00647	0.5757939	2619	21	2599	28	99	
BH2A_113	5.73487	0.08891	0.35067	0.00463	0.5172767	1936	25	1938	22	100	
BH2B_001	12.04108	0.1947	0.49259	0.00775	0.7131726	2625	20	2582	33	98	
BH2B_005	2.14504	0.03833	0.1972	0.00311	0.6368499	1168	28	1160	17	99	
BH2B_013	4.28782	0.07526	0.29711	0.00486	0.6757506	1704	25	1677	24	98	
Analysis #	$^{207}Pb/^{235}U$ Ratio	1σ	$^{206}Pb/^{238}U$ Ratio	1σ	Rho	$^{207}Pb/^{206}Pb$ Age	2σ	$^{206}Pb/^{238}U$ Age	2σ	Conc. %	Comments
BH2B_016	0.91458	0.01893	0.1078	0.00183	0.4398977	654	43	660	11	101	
BH2B_020	0.19995	0.00504	0.0291	0.0005	0.4596897	187	53	185	3	99	
BH2B_021	3.61979	0.06599	0.27011	0.00435	0.6594915	1571	27	1541	22	98	
BH2B_024	5.19855	0.09466	0.33245	0.0054	0.6574431	1855	26	1850	26	100	
BH2B_031	3.09167	0.06641	0.2439	0.00428	0.5626452	1468	35	1407	22	96	
BH2B_033	4.09058	0.08909	0.2865	0.0049	0.5680481	1689	34	1624	25	96	
BH2B_034	6.1501	0.11112	0.36571	0.00615	0.7052608	1986	24	2009	29	101	
BH2B_035	12.82342	0.24074	0.50382	0.00846	0.6644766	2695	24	2630	36	98	
BH2B_039	1.36688	0.02734	0.14372	0.00244	0.6392563	899	33	866	14	96	
BH2B_045	10.32474	0.2222	0.46335	0.0084	0.5434955	2473	32	2454	37	99	
BH2B_052	4.83034	0.09276	0.31137	0.00532	0.6752808	1841	26	1748	26	95	
BH2B_053	3.98888	0.08504	0.28558	0.00501	0.6018046	1648	32	1619	25	98	
BH2B_054	3.36214	0.06543	0.25881	0.00441	0.6713763	1513	28	1484	23	98	
BH2B_058	4.11406	0.07725	0.29108	0.005	0.6981879	1670	26	1647	25	99	
BH2B_059	2.14068	0.04633	0.19517	0.00344	0.5857783	1186	35	1149	19	97	
BH2B_061	3.82603	0.07846	0.28014	0.00486	0.6240172	1606	31	1592	24	99	
BH2B_066	2.26939	0.05926	0.20113	0.00371	0.4714013	1241	46	1181	20	95	
BH2B_070	2.07858	0.04086	0.19064	0.00325	0.6547888	1173	30	1125	18	96	
BH2B_076	2.14987	0.04418	0.20026	0.00354	0.6621621	1143	31	1177	19	103	
BH2B_077	3.65476	0.08277	0.27365	0.00508	0.618188	1564	34	1559	26	100	
BH2B_079	6.69536	0.10082	0.36936	0.00462	0.4917743	2118	24	2026	22	96	
BH2B_080	3.7802	0.06667	0.27896	0.00367	0.4138404	1592	32	1586	18	100	
BH2B_082	13.44108	0.28721	0.51545	0.0083	0.3576038	2735	35	2680	35	98	
BH2B_083	5.29412	0.08668	0.33358	0.00425	0.4457237	1882	28	1856	21	99	
BH2B_084	4.18144	0.07523	0.29257	0.00385	0.3984183	1691	32	1654	19	98	
BH2B_085	3.62237	0.07387	0.27214	0.00376	0.3454284	1559	38	1552	19	100	
BH2B_086	4.69044	0.08845	0.31179	0.0042	0.3759069	1785	34	1750	21	98	
BH2B_090	3.95752	0.05833	0.28278	0.00348	0.4921841	1652	25	1605	18	97	
BH2B_091	3.77427	0.05607	0.27744	0.00341	0.4903211	1600	26	1579	17	99	
BH2B_095	5.09302	0.08335	0.32395	0.0041	0.431917	1865	28	1809	20	97	
BH2B_096	9.70922	0.17282	0.44857	0.00605	0.3998922	2424	29	2389	27	99	
BH2B_097	4.53219	0.08917	0.30416	0.00416	0.3520684	1767	36	1712	21	97	

BH2B_105	4.29642	0.06925	0.29816	0.0037	0.4338504	1706	28	1682	18	99	
BH2B_111	4.39443	0.07831	0.29875	0.00379	0.3788441	1744	32	1685	19	97	
BH2B_113	0.80192	0.01372	0.09722	0.0012	0.3923474	597	36	598	7	100	
BH2B_115	4.38535	0.08045	0.30453	0.004	0.3697202	1705	33	1714	20	101	
BH2B_116	2.23913	0.03627	0.20209	0.00249	0.4219124	1206	31	1187	13	98	
BH2B_117	10.51183	0.15925	0.46765	0.00568	0.45524	2488	24	2473	25	99	
BH2B_123	4.78197	0.10035	0.31464	0.00439	0.3151803	1804	38	1764	22	98	
	$^{207}Pb/^{235}U$		$^{206}Pb/^{238}U$			$^{207}Pb/^{206}Pb$		$^{206}Pb/^{238}U$		Conc.	
Analysis #	**Ratio**	**1σ**	**Ratio**	**1σ**	**Rho**	**Age**	**2σ**	**Age**	**2σ**	**%**	**Comments**
Discordant Analyses - Not used											
BH2A_002	4.06917	0.05824	0.24743	0.00301	0.4902315	1946	24	1425	16	73	
BH2A_006	4.03289	0.05724	0.26765	0.00323	0.5064098	1788	24	1529	16	86	
BH2A_007	3.74479	0.05788	0.23981	0.00299	0.4591779	1853	26	1386	16	75	
BH2A_008	3.43994	0.04979	0.24533	0.00297	0.4982896	1656	25	1414	15	85	
BH2A_010	2.79483	0.04266	0.16812	0.00208	0.4708147	1965	25	1002	11	51	
BH2A_012	3.90095	0.05641	0.25507	0.00316	0.5084435	1815	24	1465	16	81	
BH2A_015	0.74003	0.01189	0.07789	0.00098	0.4557829	896	31	484	6	54	
BH2A_017	4.21542	0.06139	0.27818	0.00346	0.511958	1798	24	1582	17	88	
BH2A_018	0.94939	0.01491	0.05939	0.00076	0.4671003	1895	27	372	5	20	
BH2A_019	3.86435	0.05517	0.26855	0.00331	0.5283516	1703	24	1533	17	90	
BH2A_021	3.52639	0.05177	0.16597	0.00207	0.5158092	2392	23	990	11	41	
BH2A_025	4.26113	0.05864	0.28053	0.00345	0.5495583	1802	22	1594	17	88	
BH2A_026	0.45722	0.00967	0.05232	0.0007	0.3288312	721	44	329	4	46	
BH2A_027	456.14056	39.45488	3.54252	0.32224	0.8170413	5141	74	9757	457	190	
BH2A_033	3.53131	0.04972	0.24656	0.003	0.5253056	1695	24	1421	16	84	
BH2A_036	3.85801	0.06802	0.24876	0.00334	0.4027418	1840	31	1432	17	78	
BH2A_037	3.61386	0.04844	0.24703	0.00298	0.5556783	1734	22	1423	15	82	
BH2A_038	1.74891	0.02795	0.16777	0.0021	0.4519362	1085	30	1000	12	92	
BH2A_039	0.94134	0.01487	0.10539	0.00131	0.4582676	768	31	646	8	84	
BH2A_040	0.45713	0.00868	0.03908	0.00052	0.3603736	1312	36	247	3	19	
BH2A_042	0.41386	0.00811	0.0481	0.00063	0.3620495	688	41	303	4	44	
BH2A_045	5.04446	0.07463	0.28404	0.00352	0.5009535	2082	24	1612	18	77	
BH2A_048	144.48222	5.21661	1.02072	0.04248	0.5443075	5275	51	4535	136	86	
BH2A_050	2.40162	0.04505	0.11332	0.00161	0.3480857	2388	32	692	9	29	
BH2A_053	7.70848	0.10278	0.31815	0.00379	0.5396837	2613	20	1781	19	68	
BH2A_054	4.96903	0.06895	0.31154	0.00375	0.5136506	1891	23	1748	18	92	
BH2A_056	3.47015	0.05072	0.22864	0.00279	0.4820121	1801	25	1327	15	74	
BH2A_057	0.79059	0.01537	0.09416	0.00121	0.3482388	636	41	580	7	91	
BH2A_058	16.97559	0.2356	0.52863	0.00634	0.505776	3072	21	2736	27	89	
BH2A_060	1.90882	0.03138	0.15579	0.00215	0.5365868	1402	28	933	12	67	

BH2A_068	5.52757	0.08541	0.31147	0.00424	0.5885887	2081	23	1748	21	84	
BH2A_069	7.43089	0.1061	0.36573	0.00495	0.6488916	2315	20	2009	23	87	
BH2A_071	3.96841	0.05779	0.27075	0.00367	0.6352979	1737	22	1545	19	89	
BH2A_072	4.00702	0.06457	0.27435	0.00384	0.5653485	1730	26	1563	19	90	
BH2A_076	5.13305	0.07522	0.27474	0.00373	0.6256703	2170	21	1565	19	72	
BH2A_077	2.26655	0.03537	0.18358	0.00252	0.5819869	1416	26	1087	14	77	
BH2A_081	6.86384	0.09628	0.33832	0.00455	0.6553185	2313	19	1879	22	81	
BH2A_082	4.05514	0.06141	0.2721	0.00373	0.6008328	1767	24	1552	19	88	
Analysis #	$^{207}Pb/^{235}U$ Ratio	1σ	$^{206}Pb/^{238}U$ Ratio	1σ	Rho	$^{207}Pb/^{206}Pb$ Age	2σ	$^{206}Pb/^{238}U$ Age	2σ	Conc. %	Comments
BH2A_084	2.03396	0.02916	0.13525	0.00182	0.6393975	1784	21	818	10	46	
BH2A_085	2.84664	0.04164	0.19216	0.0026	0.6274013	1756	22	1133	14	65	
BH2A_086	1.19395	0.02842	0.08097	0.00131	0.331317	1748	43	502	8	29	
BH2A_088	5.90776	0.08753	0.21636	0.00294	0.6142434	2810	20	1263	16	45	
BH2A_089	3.40771	0.05168	0.21735	0.00295	0.6002027	1860	23	1268	16	68	
BH2A_090	4.33867	0.06585	0.28448	0.00386	0.6004783	1809	23	1614	19	89	
BH2A_094	1.88183	0.04259	0.16411	0.00249	0.360596	1273	43	980	14	77	
BH2A_095	2.77586	0.04061	0.18381	0.00245	0.6090899	1792	23	1088	13	61	
BH2A_096	3.47083	0.05265	0.25365	0.00341	0.5801636	1610	24	1457	18	91	
BH2A_098	0.44338	0.00943	0.05302	0.00076	0.3933049	627	44	333	5	53	
BH2A_101	5.26366	0.07779	0.28989	0.00384	0.5903895	2121	22	1641	19	77	
BH2A_102	0.55804	0.0134	0.06867	0.00101	0.3351841	565	51	428	6	76	
BH2A_104	2.86608	0.04322	0.15996	0.00211	0.5687463	2098	23	957	12	46	
BH2A_106	3.06287	0.04649	0.19415	0.00257	0.5471206	1871	24	1144	14	61	
BH2A_107	4.35253	0.08013	0.28928	0.00413	0.4378322	1786	32	1638	21	92	
BH2A_108	2.1411	0.03138	0.12829	0.00167	0.566469	1972	23	778	10	39	
BH2A_110	8.3178	0.11862	0.24169	0.00312	0.5781768	3183	20	1396	16	44	
BH2A_111	3.50777	0.05137	0.23377	0.00303	0.5592566	1780	24	1354	16	76	
BH2A_112	2.32749	0.03385	0.09292	0.0012	0.5581164	2669	21	573	7	21	
BH2A_114	2.34266	0.03497	0.15757	0.00204	0.536027	1764	24	943	11	53	
BH2B_002	0.69448	0.01208	0.08757	0.00137	0.6579494	508	30	541	8	107	
BH2B_003	2.94531	0.07506	0.29498	0.00556	0.3582273	974	52	1666	28	171	
BH2B_004	2.63856	0.04478	0.1629	0.00262	0.6883064	1911	23	973	15	51	
BH2B_006	3.07754	0.05241	0.23449	0.00366	0.6794313	1532	24	1358	19	89	
BH2B_007	0.42788	0.01023	0.0516	0.0009	0.4556545	594	48	324	6	55	
BH2B_008	4.58927	0.07614	0.29039	0.00458	0.6853398	1869	23	1644	23	88	
BH2B_009	3.59689	0.06524	0.26131	0.00415	0.6375057	1621	27	1497	21	92	
BH2B_010	0.6221	0.01407	0.07269	0.00121	0.490997	676	43	452	7	67	
BH2B_011	1.14357	0.02484	0.09748	0.00162	0.5153606	1318	37	600	10	46	
BH2B 012	2.14971	0.03682	0.16635	0.00265	0.6866537	1502	25	992	15	66	

Analysis #	$^{207}Pb/^{235}U$ Ratio	1σ	$^{206}Pb/^{238}U$ Ratio	1σ	Rho	$^{207}Pb/^{206}Pb$ Age	2σ	$^{206}Pb/^{238}U$ Age	2σ	Conc. %	Comments
BH2B_017	3.48882	0.07029	0.24975	0.00414	0.5877265	1649	31	1437	21	87	
BH2B_018	4.27016	0.07472	0.26632	0.00426	0.6826207	1900	24	1522	22	80	
BH2B_019	3.10913	0.06006	0.20028	0.00335	0.6098254	1840	29	1177	18	64	
BH2B_022	1.81489	0.03315	0.10789	0.00176	0.6652284	1986	25	661	10	33	
BH2B_023	0.86747	0.02928	0.09011	0.00176	0.3090089	923	67	556	10	60	
BH2B_025	1.79365	0.03461	0.1621	0.00266	0.6177726	1203	31	969	15	80	
BH2B_026	0.17329	0.00463	0.01899	0.00034	0.4237853	812	52	121	2	15	
BH2B_027	0.5107	0.01773	0.06601	0.00127	0.3037537	458	74	412	8	90	
BH2B_028	2.17135	0.04714	0.19024	0.00328	0.5526263	1265	36	1123	18	89	
BH2B_029	4.73834	0.09588	0.30406	0.00523	0.6246954	1850	29	1711	26	93	
BH2B_030	4.31374	0.08265	0.2647	0.00442	0.6431885	1930	27	1514	23	78	
BH2B_032	3.33897	0.06816	0.08775	0.00151	0.6231817	3342	26	542	9	16	
BH2B_036	4.13311	0.07328	0.25829	0.00429	0.7223831	1897	23	1481	22	78	
BH2B_037	2.34811	0.04452	0.19306	0.00325	0.6722751	1388	28	1138	18	82	
BH2B_038	2.0104	0.05083	0.18543	0.00338	0.4795687	1164	45	1097	18	94	
BH2B_040	0.82845	0.01938	0.08782	0.00156	0.5418127	882	42	543	9	62	
BH2B_041	1.76007	0.03832	0.16519	0.00283	0.5634229	1129	37	986	16	87	
BH2B_042	3.0732	0.0613	0.20997	0.00361	0.6503957	1735	29	1229	19	71	
BH2B_043	3.70565	0.06943	0.26057	0.00435	0.6820766	1682	26	1493	22	89	
BH2B_044	4.17648	0.08191	0.28682	0.00485	0.6475108	1725	28	1626	24	94	
BH2B_046	2.82637	0.06056	0.22595	0.00398	0.5756933	1441	34	1313	21	91	
BH2B_047	0.69027	0.01241	0.06995	0.00116	0.7016126	974	27	436	7	45	
BH2B_048	3.53022	0.06207	0.09037	0.00149	0.7237933	3382	20	558	9	16	
BH2B_049	8.82794	0.15874	0.33937	0.00566	0.712651	2731	22	1884	27	69	
BH2B_050	4.26373	0.08356	0.2568	0.00437	0.6407893	1963	28	1474	22	75	
BH2B_051	2.04968	0.03797	0.18546	0.00311	0.6964871	1202	27	1097	17	91	
BH2B_055	3.62518	0.07312	0.20582	0.00352	0.6406292	2068	28	1207	19	58	
BH2B_056	9.26019	0.16286	0.42617	0.0072	0.7484425	2430	21	2288	33	94	
BH2B_057	2.22298	0.05918	0.19377	0.00361	0.4584582	1274	47	1142	19	90	
BH2B_060	0.60695	0.01471	0.07658	0.00137	0.5183854	510	47	476	8	93	
BH2B_062	5.28067	0.09785	0.30941	0.00528	0.7121105	2011	24	1738	26	86	
BH2B_063	2.80328	0.06176	0.18858	0.00337	0.5806322	1763	34	1114	18	63	
BH2B_064	4.65532	0.10548	0.26529	0.00478	0.5650665	2061	34	1517	24	74	
BH2B_065	2.43977	0.06728	0.16482	0.00325	0.4312133	1755	47	984	18	56	
BH2B_067	3.33663	0.0676	0.22301	0.00379	0.6237059	1772	30	1298	20	73	
BH2B_068	3.67183	0.06998	0.24395	0.00413	0.669618	1785	27	1407	21	79	
BH2B_069	8.63354	0.15767	0.41315	0.007	0.7211994	2363	22	2229	32	94	
BH2B 071	3.56263	0.06529	0.16504	0.00281	0.7196873	2418	22	985	16	41	

BH2B_074	1.93619	0.04498	0.17223	0.00316	0.5816097	1234	38	1024	17	83
BH2B_075	1.89524	0.04369	0.17581	0.00318	0.5701784	1151	38	1044	17	91
BH2B_077	2.64599	0.03922	0.16426	0.00204	0.5000454	1909	24	980	11	51
BH2B_078	0.40661	0.02038	0.05028	0.00098	0.1056118	555	109	316	6	57
BH2B_081	0.67112	0.01777	0.0811	0.00116	0.2460465	605	57	503	7	83
BH2B_087	3.94466	0.06545	0.25097	0.00316	0.4284067	1864	29	1444	16	77
BH2B_088	1.90153	0.03349	0.09794	0.00127	0.3954042	2237	30	602	7	27
BH2B_089	4.70445	0.06778	0.27045	0.00332	0.5058791	2046	23	1543	17	75
BH2B_092	4.65965	0.07287	0.24054	0.00304	0.4578503	2234	26	1390	16	62
BH2B_093	0.37395	0.00915	0.01928	0.0003	0.2346557	2236	44	123	2	6
Analysis #	$^{207}Pb/^{235}U$ Ratio	1σ	$^{206}Pb/^{238}U$ Ratio	1σ	Rho	$^{207}Pb/^{206}Pb$ Age	2σ	$^{206}Pb/^{238}U$ Age	2σ	Conc. %	Comments
BH2B_094	1.9759	0.04593	0.1702	0.00243	0.2800223	1298	45	1013	13	78	
BH2B_098	0.20901	0.0204	0.02064	0.00054	0.0380816	1026	190	132	3	13	
BH2B_099	2.81581	0.04577	0.16604	0.00205	0.4247378	2000	28	990	11	50	
BH2B_101	1.29382	0.02228	0.11127	0.00141	0.3978769	1300	32	680	8	52	
BH2B_102	2.97366	0.04727	0.14155	0.00178	0.432766	2373	26	853	10	36	
BH2B_104	2.82568	0.04711	0.20863	0.00262	0.4148527	1591	30	1222	14	77	
BH2B_106	1.94056	0.0367	0.16028	0.00209	0.3541955	1379	36	958	12	70	
BH2B_107	3.58074	0.07093	0.22207	0.00303	0.336127	1910	35	1293	16	68	
BH2B_108	1.55484	0.02797	0.13262	0.00169	0.3723317	1316	34	803	10	61	
BH2B_109	3.68689	0.063	0.2276	0.00286	0.3996732	1919	30	1322	15	69	
BH2B_110	1.02019	0.02043	0.07621	0.00101	0.3187986	1569	37	474	6	30	
BH2B_112	2.29882	0.05464	0.19806	0.00282	0.2667366	1297	46	1165	15	90	
BH2B_114	1.70068	0.02909	0.11512	0.00147	0.3899401	1752	31	702	8	40	
BH2B_118	1.32013	0.02129	0.1009	0.00124	0.4153884	1526	29	620	7	41	
BH2B_119	0.40192	0.0135	0.03811	0.00061	0.1633869	1108	68	241	4	22	
BH2B_120	1.79085	0.02854	0.08959	0.00109	0.4213216	2288	26	553	6	24	
BH2B_121	3.47381	0.05779	0.24005	0.00297	0.3994974	1714	30	1387	15	81	
BH2B_122	1.5429	0.02778	0.1415	0.00178	0.3635321	1175	35	853	10	73	
BH2B_124	1.65552	0.0294	0.13927	0.00174	0.3714309	1343	34	841	10	63	
Sample KBH-3: GDA 94, 549652 mE, 6466886 mN											
Concordant Zircon Analyses											
BH3A_09	4.27218	0.09063	0.29486	0.00401	0.3809985	1715	37	1666	20	97	
BH3A_13	4.19281	0.06694	0.29118	0.0038	0.5052827	1704	27	1647	19	97	
BH3A_18	4.37208	0.07303	0.29817	0.0039	0.4859444	1738	28	1682	19	97	
BH3A_24	3.65473	0.05162	0.2711	0.00345	0.5867281	1583	23	1546	17	98	
BH3A_36	3.51865	0.05257	0.2632	0.00339	0.5509147	1566	25	1506	17	96	
BH3A 41	9.94625	0.15499	0.4419	0.00586	0.5615466	2490	23	2359	26	95	

BH3A_56	4.63145	0.08194	0.3052	0.00406	0.4473654	1801	30	1717	20	95
BH3A_67	3.89112	0.07123	0.28371	0.00382	0.4485126	1615	32	1610	19	100
BH3A_73	4.13736	0.08767	0.29199	0.00413	0.3802725	1676	37	1651	21	99
BH3A_78	4.05039	0.1236	0.28816	0.00453	0.2271992	1660	56	1632	23	98
BH3A_81	4.39149	0.10891	0.30385	0.00449	0.3112903	1712	45	1710	22	100
BH3A_84	4.2426	0.09895	0.29345	0.00419	0.3300388	1712	42	1659	21	97
BH3A_85	10.36919	0.25314	0.45063	0.00666	0.3171029	2527	40	2398	30	95
BH3A_88	4.31234	0.10175	0.29609	0.00423	0.3244905	1726	42	1672	21	97
BH3B_03	4.38329	0.06623	0.29658	0.00406	0.6215854	1753	23	1674	20	96
BH3B_04	4.4394	0.06734	0.30244	0.00415	0.6188906	1740	23	1703	21	98
BH3B_21	4.498	0.07068	0.30745	0.00431	0.6226065	1734	24	1728	21	100

Analysis #	$^{207}Pb/^{235}U$ Ratio	1σ	$^{206}Pb/^{238}U$ Ratio	1σ	Rho	$^{207}Pb/^{206}Pb$ Age	2σ	$^{206}Pb/^{238}U$ Age	2σ	Conc. %	Comments
BH3B_30	4.0525	0.06613	0.28404	0.00401	0.5903896	1688	25	1612	20	95	
BH3B_31	2.28285	0.06199	0.20582	0.00347	0.3213527	1208	52	1207	19	100	
BH3B_35	3.83017	0.06545	0.28036	0.00401	0.5718408	1607	27	1593	20	99	
BH3B_41	4.03925	0.06314	0.2858	0.00402	0.6227746	1670	24	1621	20	97	
BH3B_50	3.93173	0.05928	0.28596	0.00398	0.6466397	1619	23	1621	20	100	
BH3B_56	10.25417	0.15971	0.46198	0.00648	0.6198559	2466	22	2448	29	99	
BH3B_57	11.18676	0.18039	0.47901	0.00682	0.595799	2552	23	2523	30	99	
BH3B_63	4.79544	0.07487	0.31868	0.00445	0.6125857	1785	24	1783	22	100	
BH3B_66	3.80415	0.05822	0.28045	0.00388	0.6239477	1594	23	1594	20	100	
BH3B_70	2.16275	0.04071	0.19566	0.00284	0.4918608	1201	34	1152	15	96	
BH3B_73	4.31527	0.0677	0.29875	0.00415	0.6093648	1710	24	1685	21	99	
BH3B_74	4.33262	0.06659	0.29959	0.00414	0.6215133	1713	23	1689	21	99	
BH3B_80	3.85647	0.06376	0.27981	0.00393	0.5788988	1624	26	1590	20	98	
BH3B_84	4.59324	0.07948	0.30868	0.0044	0.5508027	1765	28	1734	22	98	
Discordant Analyses - Not used											
BH3A_01	5.4408	0.07081	0.25021	0.00296	0.547978	2431	20	1440	15	59	
BH3A_02	5.26288	0.06849	0.25468	0.00301	0.5511504	2344	20	1463	15	62	
BH3A_03	7.55289	0.10251	0.30681	0.00368	0.5326188	2639	21	1725	18	65	
BH3A_04	5.2543	0.07028	0.23814	0.00285	0.5471043	2456	20	1377	15	56	
BH3A_05	4.68674	0.06413	0.25303	0.00307	0.5473861	2156	21	1454	16	67	
BH3A_06	6.85945	0.09705	0.24362	0.00298	0.531407	2860	21	1406	15	49	
BH3A_07	4.15335	0.06	0.27051	0.00333	0.5295437	1822	24	1543	17	85	
BH3A_08	4.06994	0.06023	0.26339	0.00327	0.5214121	1833	24	1507	17	82	
BH3A_10	3.82406	0.06339	0.25948	0.00337	0.4961553	1747	27	1487	17	85	
BH3A_11	3.76435	0.06634	0.26371	0.00348	0.4556022	1688	30	1509	18	89	
BH3A_12	9.98436	0.14655	0.33978	0.00434	0.5492071	2929	21	1886	21	64	
BH3A 14	11.20344	0.16964	0.44902	0.00576	0.5341443	2662	22	2391	26	90	

BH3A_17	6.14096	0.09885	0.23738	0.00308	0.5053788	2722	24	1373	16	50	
BH3A_19	17.45181	0.2923	0.28123	0.00368	0.4867338	4086	23	1598	19	39	
BH3A_20	14.5121	0.24973	0.16134	0.00214	0.4710765	4629	23	964	12	21	
BH3A_21	9.90639	0.14179	0.3094	0.00393	0.545631	3068	21	1738	19	57	
BH3A_22	8.70132	0.12759	0.28833	0.00363	0.5369322	2974	21	1633	18	55	
BH3A_23	5.107	0.07366	0.25728	0.00329	0.5745097	2276	22	1476	17	65	
BH3A_25	15.90965	0.3042	0.38468	0.0053	0.4287054	3471	28	2098	25	60	
BH3A_26	3.30629	0.05302	0.21886	0.00284	0.5235015	1793	26	1276	15	71	
BH3A_27	2.03142	0.03717	0.18469	0.00254	0.4554119	1192	33	1093	14	92	
BH3A_28	4.23793	0.07049	0.26989	0.00356	0.5196923	1863	27	1540	18	83	
BH3A_29	3.33346	0.05013	0.09969	0.00132	0.5900661	3137	20	613	8	20	
BH3A_30	3.90145	0.06139	0.25337	0.00335	0.5700721	1827	25	1456	17	80	
	$^{207}Pb/^{235}U$		$^{206}Pb/^{238}U$			$^{207}Pb/^{206}Pb$		$^{206}Pb/^{238}U$		Conc.	
Analysis #	Ratio	1σ	Ratio	1σ	Rho	Age	2σ	Age	2σ	%	Comments
BH3A_31	4.46943	0.0745	0.28311	0.0038	0.5425267	1872	26	1607	19	86	
BH3A_34	22.73507	0.32443	0.25293	0.00334	0.5495999	4628	19	1454	17	31	
BH3A_35	17.48257	0.25001	0.36731	0.00473	0.5661307	3686	19	2017	22	55	
BH3A_37	5.0265	0.07405	0.26386	0.00339	0.5657551	2204	22	1510	17	68	
BH3A_38	7.21639	0.10712	0.27494	0.00356	0.5676804	2745	21	1566	18	57	
BH3A_39	56.47859	1.1873	0.58762	0.00819	0.4104898	4725	28	2980	33	63	
BH3A_40	0.34781	0.01141	0.04355	0.00068	0.2266207	526	71	275	4	52	
BH3A_42	5.22458	0.08925	0.28263	0.00381	0.5154216	2152	27	1605	19	75	
BH3A_43	4.94674	0.08045	0.16951	0.00227	0.5546441	2918	23	1009	13	35	
BH3A_44	14.31523	0.20729	0.31062	0.00385	0.5362737	3637	20	1744	19	48	
BH3A_45	13.69691	0.21727	0.48962	0.00616	0.4835582	2851	24	2569	27	90	
BH3A_46	15.29233	0.23203	0.38272	0.00484	0.5230242	3417	21	2089	23	61	
BH3A_47	4.56959	0.09107	0.2735	0.00379	0.4031577	1974	34	1559	19	79	
BH3A_48	4.52297	0.08353	0.27922	0.00378	0.4510733	1918	31	1588	19	83	
BH3A_49	4.29347	0.06948	0.25321	0.00327	0.5132698	2000	26	1455	17	73	
BH3A_50	4.28993	0.07685	0.22811	0.00306	0.4760509	2182	28	1325	16	61	
BH3A_51	7.97972	0.13479	0.1499	0.00197	0.5094965	3856	23	900	11	23	
BH3A_52	5.26097	0.11114	0.28404	0.00395	0.4219211	2156	34	1612	20	75	
BH3A_54	3.93478	0.06309	0.27585	0.00367	0.5181818	1687	27	1570	19	93	
BH3A_55	3.659	0.06104	0.21283	0.00281	0.4836944	2025	27	1244	15	61	
BH3A_57	5.04439	0.09297	0.31186	0.00422	0.4302002	1916	31	1750	21	91	
BH3A_58	4.82156	0.08604	0.3059	0.0041	0.445622	1870	30	1721	20	92	
BH3A_59	6.37508	0.09839	0.13562	0.00177	0.5443899	3667	21	820	10	22	
BH3A_60	6.82985	0.11972	0.28756	0.00391	0.4742039	2580	27	1629	20	63	
BH3A_61	4.99644	0.2508	0.18046	0.00394	-0.012438	2844	87	1070	21	38	
BH3A_62	4.53985	0.08567	0.28928	0.00401	0.4462327	1862	32	1638	20	88	

BH3A_65	5.13796	0.09332	0.30966	0.00419	0.4534471	1962	30	1739	21	89
BH3A_66	32.81395	0.68019	0.50578	0.00709	0.3765053	4152	30	2639	30	64
BH3A_68	6.75538	0.12348	0.29409	0.00397	0.4495529	2524	29	1662	20	66
BH3A_69	10.46819	0.26457	0.27886	0.00408	0.2385082	3319	40	1586	21	48
BH3A_70	3.69202	0.06918	0.22776	0.00308	0.4364693	1920	31	1323	16	69
BH3A_71	4.35795	0.09679	0.28703	0.00403	0.346233	1802	39	1627	20	90
BH3A_72	4.9673	0.09708	0.30415	0.00418	0.4151645	1934	33	1712	21	89
BH3A_74	7.65848	0.1908	0.27893	0.00419	0.3086593	2819	40	1586	21	56
BH3A_75	5.78367	0.11159	0.14229	0.00194	0.4188798	3444	28	858	11	25
BH3A_76	10.43764	0.25883	0.30315	0.0044	0.302474	3184	38	1707	22	54
BH3A_77	3.68751	0.09055	0.16133	0.00236	0.3033428	2517	41	964	13	38
BH3A_79	5.67307	0.16144	0.3162	0.00492	0.2612158	2101	49	1771	24	84
BH3A_80	15.95894	0.33457	0.43581	0.00606	0.3792621	3280	32	2332	27	71

Analysis #	$^{207}Pb/^{235}U$ Ratio	1σ	$^{206}Pb/^{238}U$ Ratio	1σ	Rho	$^{207}Pb/^{206}Pb$ Age	2σ	$^{206}Pb/^{238}U$ Age	2σ	Conc. %	Comments
BH3A_82	85.77028	2.64227	0.78006	0.01244	0.240977	4918	44	3717	45	76	
BH3A_83	6.70623	0.24697	0.29901	0.00535	0.1769717	2484	63	1686	27	68	
BH3A_86	8.71668	0.19358	0.30984	0.00436	0.3485996	2859	35	1740	21	61	
BH3A_87	5.85333	0.13208	0.2677	0.00378	0.3434035	2441	37	1529	19	63	
BH3A_89	7.8998	0.18483	0.26225	0.00375	0.3286738	2970	37	1501	19	51	
BH3A_90	8.8091	0.19999	0.28141	0.00398	0.3408221	3032	35	1599	20	53	
BH3B_01	15.51869	0.24081	0.34044	0.00491	0.5852103	3620	21	1889	24	52	
BH3B_02	6.16024	0.0896	0.29245	0.00396	0.6423387	2377	20	1654	20	70	
BH3B_05	23.69084	0.37409	0.43264	0.00629	0.5933744	3899	21	2318	28	59	
BH3B_06	0.71683	0.01472	0.07717	0.00113	0.4387485	850	40	479	7	56	
BH3B_07	15.44293	0.24008	0.32931	0.00464	0.6141477	3663	20	1835	22	50	
BH3B_08	3.73824	0.06282	0.25889	0.00368	0.5673108	1710	27	1484	19	87	
BH3B_09	9.13631	0.14312	0.24177	0.00338	0.6191263	3330	20	1396	18	42	
BH3B_10	10.98905	0.1873	0.39756	0.00582	0.565815	2830	24	2158	27	76	
BH3B_11	4.04889	0.06883	0.25778	0.00369	0.5731832	1863	26	1479	19	79	
BH3B_12	3.84222	0.06495	0.2612	0.00373	0.5826308	1743	26	1496	19	86	
BH3B_13	4.37206	0.06683	0.2917	0.0041	0.6445621	1778	23	1650	20	93	
BH3B_14	4.31992	0.06423	0.26349	0.00367	0.6626583	1940	21	1508	19	78	
BH3B_15	5.93329	0.08808	0.13999	0.00195	0.6629686	3508	18	845	11	24	
BH3B_16	4.64889	0.07021	0.23441	0.00327	0.6518632	2274	21	1358	17	60	
BH3B_17	4.661	0.07087	0.2502	0.0035	0.6486771	2166	21	1440	18	66	
BH3B_18	5.74093	0.08822	0.29289	0.0041	0.6399932	2254	22	1656	20	73	
BH3B_19	4.76852	0.07373	0.27555	0.00386	0.6344598	2036	22	1569	20	77	
BH3B_20	1.40059	0.02288	0.04948	0.00071	0.5828482	2869	23	311	4	11	
BH3B 22	9.33771	0.14995	0.32478	0.00462	0.607109	2894	22	1813	22	63	

BH3B_25	0.90554	0.02449	0.09481	0.00154	0.3126247	907	54	584	9	64
BH3B_26	5.78034	0.08671	0.23812	0.00328	0.6395441	2616	20	1377	17	53
BH3B_27	4.40793	0.07151	0.29149	0.00411	0.5846563	1794	25	1649	21	92
BH3B_28	6.4549	0.09941	0.30138	0.00419	0.6259899	2406	22	1698	21	71
BH3B_29	5.12959	0.07957	0.28249	0.00393	0.6245863	2121	22	1604	20	76
BH3B_32	5.6816	0.09191	0.315	0.00444	0.5990793	2109	24	1765	22	84
BH3B_33	5.59685	0.08992	0.26553	0.00373	0.6108321	2379	23	1518	19	64
BH3B_34	2.62313	0.04357	0.18759	0.00266	0.5906611	1651	26	1108	14	67
BH3B_36	4.0371	0.06826	0.27817	0.00396	0.5818379	1719	26	1582	20	92
BH3B_37	17.92808	0.28184	0.42011	0.00614	0.6171303	3519	20	2261	28	64
BH3B_38	8.55276	0.1296	0.24703	0.00348	0.6434359	3192	19	1423	18	45
BH3B_39	5.60769	0.08623	0.30383	0.00427	0.6353235	2149	22	1710	21	80
BH3B_40	7.15553	0.11462	0.27752	0.004	0.6029638	2716	22	1579	20	58
BH3B_42	6.54562	0.09951	0.23551	0.00329	0.6443851	2839	20	1363	17	48

Analysis #	$^{207}Pb/^{235}U$ Ratio	1σ	$^{206}Pb/^{238}U$ Ratio	1σ	Rho	$^{207}Pb/^{206}Pb$ Age	2σ	$^{206}Pb/^{238}U$ Age	2σ	Conc. %	Comments
BH3B_43	5.28861	0.08134	0.15052	0.00211	0.6340234	3215	20	904	12	28	
BH3B_44	4.74266	0.07698	0.30525	0.00434	0.5988891	1843	25	1717	21	93	
BH3B_45	5.00081	0.08004	0.23902	0.00339	0.605351	2366	23	1382	18	58	
BH3B_46	5.12726	0.0829	0.29136	0.00413	0.5985125	2066	24	1648	21	80	
BH3B_47	9.60003	0.15428	0.41906	0.00594	0.6053724	2519	23	2256	27	90	
BH3B_48	3.82349	0.06189	0.20374	0.00288	0.6010592	2178	24	1195	15	55	
BH3B_49	5.11503	0.07742	0.31779	0.00444	0.6435109	1907	22	1779	22	93	
BH3B_51	4.39919	0.06605	0.22792	0.00317	0.6457639	2227	21	1324	17	59	
BH3B_52	4.0482	0.06389	0.27985	0.00395	0.6123677	1713	24	1591	20	93	
BH3B_53	4.87065	0.07609	0.31077	0.00437	0.6198267	1859	23	1745	21	94	
BH3B_54	3.95188	0.05986	0.18838	0.00262	0.6413779	2370	21	1113	14	47	
BH3B_55	6.74872	0.1077	0.28014	0.00399	0.5984403	2604	22	1592	20	61	
BH3B_58	6.42153	0.10358	0.26814	0.00381	0.5917173	2594	23	1531	19	59	
BH3B_59	7.16639	0.11603	0.27848	0.00395	0.5896834	2713	23	1584	20	58	
BH3B_60	5.77612	0.09261	0.29663	0.00416	0.5981719	2243	23	1675	21	75	
BH3B_61	5.15246	0.0764	0.18612	0.00257	0.6507343	2833	19	1100	14	39	
BH3B_62	4.46002	0.06778	0.28197	0.00391	0.630432	1876	22	1601	20	85	
BH3B_64	5.7019	0.09113	0.31032	0.00438	0.5943609	2142	24	1742	22	81	
BH3B_65	5.01786	0.07594	0.26035	0.0036	0.6339453	2225	21	1492	18	67	
BH3B_67	4.62875	0.07169	0.28109	0.0039	0.6192468	1948	23	1597	20	82	
BH3B_68	6.09936	0.094	0.25773	0.00357	0.6209909	2574	21	1478	18	57	
BH3B_69	5.92556	0.09552	0.27897	0.00393	0.5882784	2392	23	1586	20	66	
BH3B_71	2.62274	0.0418	0.10835	0.00151	0.5918617	2612	22	663	9	25	
BH3B 72	6.72552	0.10851	0.28793	0.00402	0.5834104	2552	23	1631	20	64	

BH3B_77	9.71276	0.15026	0.2983	0.00413	0.6193806	3094	20	1683	21	54	
BH3B_78	0.67996	0.01696	0.07819	0.00121	0.3440483	711	51	485	7	68	
BH3B_79	14.04997	0.22103	0.28925	0.00403	0.6083041	3717	20	1638	20	44	
BH3B_81	8.98038	0.14327	0.17795	0.00248	0.5995574	3775	20	1056	14	28	
BH3B_82	7.49567	0.12144	0.30606	0.00428	0.5910587	2631	23	1721	21	65	
BH3B_83	6.13994	0.10053	0.26871	0.00376	0.5847478	2515	23	1534	19	61	

Sample KBH-5: GDA 94, 538116 mE, 6450583 mN

Concordant Zircon Analyses

BH5A_01	0.6475	0.01166	0.08174	0.00115	0.5024482	509	36	507	7	100	
BH5A_05	3.90754	0.07297	0.28373	0.00418	0.4956331	1622	32	1610	21	99	
BH5A_06	0.82019	0.01379	0.09892	0.00139	0.5630027	609	31	608	8	100	
BH5A_07	3.00227	0.06886	0.24093	0.00383	0.3898474	1434	42	1392	20	97	
BH5A_08	0.27518	0.00967	0.03894	0.00067	0.2235135	252	80	246	4	98	
BH5A_09	4.57057	0.07591	0.30783	0.00437	0.5786682	1761	26	1730	22	98	

Analysis #	$^{207}Pb/^{235}U$ Ratio	1σ	$^{206}Pb/^{238}U$ Ratio	1σ	Rho	$^{207}Pb/^{206}Pb$ Age	2σ	$^{206}Pb/^{238}U$ Age	2σ	Conc. %	Comments
BH5A_100	3.67432	0.05997	0.27243	0.00377	0.5472474	1583	27	1553	19	98	Hf Isotope Analysis #20
BH5A_101	2.09677	0.03556	0.19431	0.00269	0.5283996	1154	30	1145	15	99	Hf Isotope Analysis #21
BH5A_102	3.93945	0.06105	0.28372	0.00386	0.5823575	1637	25	1610	19	98	
BH5A_104	4.7448	0.07751	0.31669	0.00437	0.5453768	1777	26	1774	21	100	
BH5A_106	0.60167	0.01508	0.07732	0.00117	0.3304106	469	54	480	7	102	
BH5A_107	3.83101	0.06117	0.28085	0.00382	0.5584791	1604	26	1596	19	99	
BH5A_108	3.25204	0.06103	0.2559	0.00366	0.4617797	1471	33	1469	19	100	
BH5A_11	4.15964	0.07154	0.28964	0.00416	0.5681328	1700	27	1640	21	96	
BH5A_13	2.0449	0.03927	0.18982	0.00282	0.4944012	1150	34	1120	15	97	
BH5A_15	14.9539	0.23313	0.5279	0.00757	0.6314297	2870	21	2733	32	95	
BH5A_17	0.1644	0.00587	0.0242	0.00042	0.2303828	161	82	154	3	96	Hf Isotope Analysis #1
BH5A_18	4.34561	0.07476	0.29551	0.0043	0.5645914	1743	27	1669	21	96	Hf Isotope Analysis #2
BH5A_20	1.94972	0.03565	0.18584	0.00271	0.5278206	1098	32	1099	15	100	
BH5A_21	1.49519	0.0318	0.15321	0.00232	0.4335554	951	40	919	13	97	
BH5A_22	18.77345	0.3256	0.58488	0.00882	0.5602633	3072	24	2969	36	97	
BH5A_23	1.89965	0.03395	0.18164	0.00263	0.5387386	1091	31	1076	14	99	
BH5A_24	3.83111	0.06773	0.28043	0.00407	0.5427148	1607	29	1594	21	99	Hf Isotope Analysis #3
BH5A_25	0.75857	0.01963	0.0923	0.00146	0.3504102	590	54	569	9	97	Hf Isotope Analysis #4
BH5A_27	0.18616	0.01399	0.02728	0.00074	0.0742101	172	172	174	5	101	Hf Isotope Analysis #5
BH5A_28	4.93913	0.0755	0.31711	0.00445	0.6406168	1848	22	1776	22	96	
BH5A_29	0.16708	0.00507	0.02465	0.0004	0.2820488	155	69	157	3	101	
BH5A_30	0.62292	0.01287	0.07944	0.00117	0.4544253	486	42	493	7	101	
BH5A_32	2.33934	0.0391	0.20631	0.00294	0.5806745	1252	28	1209	16	97	

BH5A_36	0.20005	0.00709	0.02913	0.0005	0.2253374	187	81	185	3	99	
BH5A_37	4.68615	0.07236	0.3129	0.00428	0.591297	1776	24	1755	21	99	Hf Isotope Analysis #8
BH5A_38	0.27404	0.00759	0.0387	0.0006	0.2955181	257	62	245	4	95	
BH5A_39	0.57746	0.01106	0.0739	0.00104	0.4586379	478	39	460	6	96	
BH5A_40	0.70299	0.01724	0.08759	0.00133	0.3404324	537	52	541	8	101	
BH5A_41	4.60537	0.07069	0.30646	0.0042	0.6086275	1783	23	1723	21	97	Hf Isotope Analysis #9
BH5A_43	5.05169	0.08478	0.32345	0.00458	0.5571125	1853	26	1807	22	98	
BH5A_46	1.64974	0.02821	0.16445	0.00232	0.5534019	1007	30	982	13	97	
BH5A_49	0.20711	0.00505	0.0302	0.00046	0.3678619	183	54	192	3	105	
BH5A_50	0.7084	0.01876	0.0874	0.00138	0.3268319	559	56	540	8	97	
BH5A_51	0.86146	0.01403	0.10311	0.00144	0.5792036	625	30	633	8	101	
BH5A_52	1.92658	0.03032	0.18358	0.00255	0.6050214	1102	26	1087	14	99	Hf Isotope Analysis #10
BH5A_53	1.45826	0.02665	0.15185	0.00218	0.509728	918	34	911	12	99	Hf Isotope Analysis #11
BH5A_57	13.33599	0.20936	0.52042	0.00725	0.6033262	2706	22	2701	31	100	
BH5A_60	4.90891	0.08373	0.31898	0.00453	0.5435603	1826	27	1785	22	98	
BH5A_61	5.07468	0.07739	0.32906	0.00454	0.6220711	1830	23	1834	22	100	
	$^{207}Pb/^{235}U$		$^{206}Pb/^{238}U$			$^{207}Pb/^{206}Pb$		$^{206}Pb/^{238}U$		Conc.	
Analysis #	**Ratio**	**1σ**	**Ratio**	**1σ**	**Rho**	**Age**	**2σ**	**Age**	**2σ**	**%**	**Comments**
BH5A_63	4.19475	0.06833	0.29424	0.00414	0.5758031	1686	26	1663	21	99	Hf Isotope Analysis #12
BH5A_64	3.40855	0.06182	0.2619	0.0038	0.5061196	1516	31	1500	19	99	
BH5A_65	6.11233	0.09823	0.35429	0.00498	0.5859614	2031	24	1955	24	96	Hf Isotope Analysis #13
BH5A_67	3.42123	0.05386	0.26308	0.00364	0.5987026	1515	25	1506	19	99	Hf Isotope Analysis #14
BH5A_69	5.52576	0.09267	0.3414	0.00484	0.5521878	1917	26	1893	23	99	
BH5A_70	1.44128	0.03185	0.15015	0.00227	0.3965815	917	43	902	13	98	Hf Isotope Analysis #15
BH5A_72	1.85344	0.032	0.18029	0.00254	0.5317319	1057	31	1069	14	101	
BH5A_74	3.77905	0.05596	0.27926	0.00381	0.6334097	1589	23	1588	19	100	
BH5A_76	0.6256	0.0164	0.0802	0.00125	0.3234168	474	56	497	7	105	
BH5A_77	0.71272	0.0121	0.08903	0.00124	0.5450342	532	33	550	7	103	
BH5A_78	0.14164	0.00934	0.02115	0.00051	0.0809341	127	153	135	3	105	Hf Isotope Analysis #16
BH5A_79	1.01874	0.02253	0.11716	0.00174	0.3931539	711	45	714	10	101	Hf Isotope Analysis #17
BH5A_80	2.23788	0.04028	0.20429	0.0029	0.5045235	1184	32	1198	16	101	
BH5A_82	0.6321	0.01857	0.07988	0.00129	0.2708673	507	64	495	8	98	
BH5A_84	3.72959	0.06641	0.27572	0.00392	0.5068079	1589	30	1570	20	99	
BH5A_88	4.07647	0.12767	0.29041	0.00553	0.2616308	1658	58	1644	28	99	
BH5A_89	1.84193	0.04202	0.17797	0.0027	0.3694267	1070	44	1056	15	99	
BH5A_90	2.01596	0.03421	0.18819	0.00261	0.5304462	1139	30	1112	14	98	
BH5A_92	3.82806	0.06067	0.27933	0.00381	0.5654732	1613	26	1588	19	98	
BH5A_93	1.72135	0.02951	0.17086	0.00236	0.5185841	1016	31	1017	13	100	
BH5A_94	4.70308	0.07484	0.31475	0.00429	0.5645273	1772	25	1764	21	100	
BH5A_96	1.14613	0.02233	0.12764	0.00181	0.446719	779	38	774	10	99	Hf Isotope Analysis #18

BH5B_04	2.08283	0.03769	0.19141	0.00296	0.6061248	1170	30	1129	16	96
BH5B_05	0.41576	0.01005	0.05611	0.00091	0.4233893	360	50	352	6	98
BH5B_06	4.52487	0.07797	0.30927	0.00472	0.6375709	1734	25	1737	23	100
BH5B_07	0.16063	0.01	0.02375	0.00058	0.1149442	151	144	151	4	101
BH5B_10	0.73232	0.03055	0.09038	0.00183	0.2102389	559	90	558	11	100
BH5B_13	0.14567	0.01055	0.02162	0.00056	0.0900498	142	167	138	4	97
BH5B_15	1.41743	0.02659	0.14692	0.00226	0.5679694	928	33	884	13	95
BH5B_17	0.81903	0.0155	0.09831	0.00151	0.5694819	619	35	605	9	98
BH5B_18	0.62103	0.01482	0.07951	0.00128	0.4348473	477	49	493	8	103
BH5B_25	0.57871	0.0102	0.07504	0.00113	0.6174357	450	32	467	7	104
BH5B_26	0.33477	0.00662	0.0464	0.00071	0.5442949	300	39	292	4	97
BH5B_32	0.3847	0.01032	0.05296	0.00087	0.366788	316	57	333	5	105
BH5B_34	8.6144	0.15259	0.42695	0.00659	0.6111262	2304	25	2292	30	99
BH5B_37	0.63296	0.01341	0.08054	0.00124	0.4805123	491	42	499	7	102
BH5B_38	0.2897	0.00851	0.04072	0.00068	0.3255797	268	65	257	4	96
BH5B_42	0.40148	0.01234	0.05435	0.00092	0.3047264	353	67	341	6	97
BH5B_44	0.17516	0.00929	0.0257	0.00054	0.1319347	169	122	164	3	97

Analysis #	$^{207}Pb/^{235}U$ Ratio	1σ	$^{206}Pb/^{238}U$ Ratio	1σ	Rho	$^{207}Pb/^{206}Pb$ Age	2σ	$^{206}Pb/^{238}U$ Age	2σ	Conc. %	Comments
BH5B_48	10.21073	0.19437	0.46244	0.00724	0.5280735	2457	29	2450	32	100	
BH5B_49	3.96912	0.06394	0.28503	0.00414	0.6403705	1643	24	1617	21	98	
BH5B_51	4.82529	0.08169	0.31593	0.00467	0.602783	1812	26	1770	23	98	
BH5B_53	0.63658	0.0151	0.08096	0.00127	0.4098236	492	49	502	8	102	
BH5B_54	0.60355	0.0132	0.07728	0.00118	0.4482416	477	45	480	7	101	
BH5B_56	0.13176	0.00508	0.0197	0.00036	0.2146487	124	89	126	2	101	
BH5B_58	0.72492	0.01343	0.0893	0.00132	0.5402362	563	35	551	8	98	
BH5B_60	1.79594	0.03228	0.17557	0.00259	0.5664861	1047	31	1043	14	100	
BH5B_62	0.14267	0.00544	0.02124	0.00038	0.2084067	134	88	136	2	101	
BH5B_64	0.26199	0.00587	0.03727	0.00057	0.4312594	240	48	236	4	98	
BH5B_65	1.61818	0.0317	0.16208	0.00245	0.4978975	998	36	968	14	97	
BH5B_66	0.35385	0.00924	0.04855	0.00077	0.351074	323	56	306	5	95	
BH5B_70	0.38375	0.01162	0.05237	0.00087	0.284578	335	67	329	5	98	
BH5B_73	0.68378	0.01349	0.08522	0.00127	0.5069592	537	39	527	8	98	
BH5B_75	3.9699	0.06289	0.28732	0.00414	0.6471865	1628	24	1628	21	100	
BH5B_76	0.16058	0.01059	0.02375	0.00058	0.0952884	150	152	151	4	101	
BH5B_78	2.00357	0.04681	0.18662	0.003	0.4136188	1144	44	1103	16	96	
BH5B_84	3.98169	0.07792	0.28611	0.00438	0.5113066	1642	32	1622	22	99	
Discordant Analyses - Not used											
BH5A_02	2.38772	0.03683	0.16952	0.00233	0.6009807	1664	24	1010	13	61	
BH5A_03	0.36884	0.01141	0.03509	0.00061	0.2493653	1101	62	222	4	20	

BH5A_103	8.40746	0.13037	0.3325	0.00456	0.5776776	2684	22	1851	22	69
BH5A_105	4.11417	0.06628	0.27991	0.00384	0.5530548	1742	26	1591	19	91
BH5A_12	4.50929	0.0784	0.28978	0.00419	0.565773	1846	27	1641	21	89
BH5A_14	3.4247	0.05352	0.24516	0.00347	0.6270332	1649	24	1414	18	86
BH5A_16	1.75357	0.0268	0.0995	0.0014	0.6436853	2068	22	612	8	30
BH5A_19	1.58814	0.03045	0.14558	0.00215	0.4892668	1175	34	876	12	75
BH5A_26	4.2144	0.06368	0.22679	0.00318	0.6534881	2161	21	1318	17	61
BH5A_31	0.20129	0.00888	0.02647	0.00052	0.1599291	418	98	168	3	40
BH5A_34	5.96844	0.18196	0.1297	0.00338	0.2245997	3635	53	786	19	22
BH5A_42	0.31944	0.00798	0.0401	0.00061	0.3417736	521	53	254	4	49
BH5A_44	1.64582	0.03093	0.15954	0.0023	0.4867471	1064	34	954	13	90
BH5A_45	1.47991	0.02463	0.14598	0.00204	0.5685346	1029	29	878	11	85
BH5A_47	1.8112	0.03317	0.17221	0.00248	0.5199331	1102	32	1024	14	93
BH5A_48	0.707	0.01962	0.0782	0.00127	0.3109499	793	57	485	8	61
BH5A_54	0.16969	0.00423	0.02411	0.00037	0.3485482	243	55	154	2	63
BH5A_55	1.2333	0.02307	0.13168	0.0019	0.4936927	866	35	798	11	92
BH5A_56	0.50998	0.01237	0.06179	0.00095	0.3618555	598	50	387	6	65
BH5A_58	1.32876	0.02432	0.10918	0.00157	0.4951705	1388	32	668	9	48
Analysis #	$^{207}Pb/^{235}U$ Ratio	1σ	$^{206}Pb/^{238}U$ Ratio	1σ	Rho	$^{207}Pb/^{206}Pb$ Age	2σ	$^{206}Pb/^{238}U$ Age	2σ	Conc. %	Comments
BH5A_59	7.73493	0.12739	0.30036	0.00426	0.567159	2714	24	1693	21	62	
BH5A_62	1.55327	0.02748	0.15552	0.00221	0.5228783	998	32	932	12	93	
BH5A_66	0.69962	0.01303	0.08322	0.00119	0.4890329	638	36	515	7	81	
BH5A_68	0.93391	0.02093	0.10497	0.00158	0.3925413	759	45	644	9	85	
BH5A_71	1.47448	0.02767	0.14837	0.00214	0.4881393	988	35	892	12	90	
BH5A_73	2.28514	0.03522	0.14363	0.00199	0.6047186	1886	23	865	11	46	
BH5A_75	0.38473	0.00777	0.0518	0.00074	0.4392249	365	42	326	5	89	
BH5A_81	0.20227	0.00578	0.02635	0.00042	0.2801272	439	62	168	3	38	
BH5A_83	3.90359	0.06613	0.25748	0.00361	0.5325776	1799	27	1477	19	82	
BH5A_85	0.29281	0.00903	0.03838	0.00062	0.2469046	426	67	243	4	57	
BH5A_86	2.23433	0.05342	0.19554	0.00307	0.352392	1266	45	1151	17	91	
BH5A_87	1.23016	0.02485	0.12206	0.00177	0.4293729	1017	38	742	10	73	
BH5A_91	0.94219	0.03672	0.10652	0.00202	0.1853837	747	83	653	12	87	
BH5A_95	10.60409	0.18139	0.39983	0.00573	0.5163469	2763	25	2168	26	78	
BH5A_97	0.29547	0.00801	0.04089	0.00063	0.2978233	304	60	258	4	85	
BH5A_98	3.68225	0.05625	0.26662	0.00363	0.5955525	1627	24	1524	18	94	
BH5A_99	3.48623	0.06539	0.25685	0.00374	0.4669209	1595	32	1474	19	92	
BH5B_03	5.89851	0.09885	0.30995	0.00472	0.6602056	2203	23	1741	23	79	
BH5B_08	1.75498	0.0462	0.1682	0.0029	0.3818618	1087	50	1002	16	92	
BH5B 09	0.52547	0.01535	0.06542	0.00113	0.336762	539	62	409	7	76	

BH5B_14	3.18597	0.05009	0.15554	0.00232	0.6987651	2330	20	932	13	40
BH5B_16	0.55023	0.01082	0.05444	0.00085	0.5379964	1023	34	342	5	33
BH5B_19	1.27172	0.03007	0.13452	0.0022	0.4333802	886	45	814	12	92
BH5B_20	3.32288	0.05713	0.235	0.00357	0.6302795	1671	26	1361	19	81
BH5B_21	0.48487	0.01177	0.0606	0.00098	0.4248202	531	50	379	6	71
BH5B_22	0.29686	0.00964	0.04059	0.00071	0.2936354	331	71	257	4	77
BH5B_23	14.86757	0.25483	0.52147	0.00797	0.6338565	2881	22	2705	34	94
BH5B_24	4.37833	0.07861	0.28908	0.00444	0.6032112	1797	27	1637	22	91
BH5B_27	5.28029	0.08742	0.31191	0.00471	0.6604005	1997	23	1750	23	88
BH5B_28	9.30757	0.17705	0.40596	0.00661	0.5609922	2521	28	2196	30	87
BH5B_29	1.40511	0.02992	0.1372	0.00218	0.4877751	1049	39	829	12	79
BH5B_30	0.81675	0.01553	0.09519	0.00146	0.5625723	682	35	586	9	86
BH5B_31	0.82072	0.01608	0.09554	0.00147	0.5402448	685	36	588	9	86
BH5B_33	0.36755	0.00984	0.05089	0.00084	0.3790254	302	57	320	5	106
BH5B_35	4.48882	0.09042	0.282	0.00453	0.5194047	1887	32	1601	23	85
BH5B_36	11.81825	0.20414	0.46161	0.00704	0.6270603	2705	23	2447	31	90
BH5B_39	0.29838	0.01155	0.04156	0.00077	0.2247219	289	87	263	5	91
BH5B_40	0.16611	0.00538	0.02499	0.00042	0.2861183	110	74	159	3	145
BH5B_41	2.15428	0.05767	0.15399	0.00273	0.3457011	1651	48	923	15	56

Analysis #	$^{207}Pb/^{235}U$ Ratio	1σ	$^{206}Pb/^{238}U$ Ratio	1σ	Rho	$^{207}Pb/^{206}Pb$ Age	2σ	$^{206}Pb/^{238}U$ Age	2σ	Conc. %	Comments
BH5B_43	0.12773	0.00568	0.01718	0.00034	0.1738999	369	99	110	2	30	
BH5B_45	3.00217	0.06139	0.19852	0.00313	0.4816954	1794	34	1167	17	65	
BH5B_46	7.36118	0.12481	0.33298	0.00493	0.6029214	2459	24	1853	24	75	
BH5B_47	0.14122	0.00438	0.01965	0.00033	0.2895167	291	69	126	2	43	
BH5B_50	0.22045	0.00586	0.03149	0.0005	0.3473366	231	58	200	3	87	
BH5B_52	0.18941	0.00705	0.02785	0.0005	0.2254234	164	85	177	3	108	
BH5B_55	0.1187	0.00662	0.01788	0.00039	0.1240617	107	130	114	3	107	
BH5B_57	0.40054	0.01443	0.04974	0.00091	0.2297165	545	78	313	6	57	
BH5B_59	7.68439	0.14925	0.39017	0.00613	0.5126535	2262	30	2124	28	94	
BH5B_61	7.24469	0.11003	0.31682	0.00455	0.6748815	2516	20	1774	22	71	
BH5B_63	0.19724	0.00601	0.02856	0.00047	0.2896702	199	69	182	3	91	
BH5B_67	0.48382	0.01133	0.04896	0.00077	0.3952016	977	45	308	5	32	
BH5B_68	1.46939	0.0258	0.1472	0.00216	0.5681747	997	31	885	12	89	
BH5B_69	0.17816	0.01409	0.02591	0.00074	0.0688935	189	181	165	5	87	
BH5B_71	0.67965	0.01599	0.08357	0.0013	0.4024948	566	48	517	8	91	
BH5B_72	0.47529	0.01009	0.06435	0.00097	0.4589252	353	44	402	6	114	
BH5B_74	0.17094	0.00367	0.02453	0.00037	0.4584968	220	45	156	2	71	
BH5B_77	1.03451	0.01717	0.10404	0.00151	0.6178851	989	28	638	9	65	
BH5B_79	0.83163	0.02015	0.09743	0.00154	0.3960899	671	49	599	9	89	

BH5B_82	0.10604	0.00553	0.01533	0.00033	0.14625	202	120	98	2	48	
BH5B_83	2.29055	0.03875	0.15694	0.00229	0.6043513	1729	26	940	13	54	
Sample kGB-3: GDA 94, 540424 mE, 6482071 mN											
Concordant Zircon Analyses											
GB32_09	0.73819	0.01443	0.09071	0.0012	0.3816288	569	41	560	7	98	
GB32_15	4.42618	0.06279	0.30346	0.00388	0.5827848	1728	23	1709	19	99	
GB32_18	4.12562	0.08783	0.29351	0.00438	0.3769295	1660	38	1659	22	100	
GB32_23	3.30547	0.05708	0.25399	0.00343	0.4671514	1516	30	1459	18	96	
GB32_45	0.32458	0.01596	0.04503	0.00079	0.1246551	298	110	284	5	95	
GB32_48	2.08428	0.04065	0.19018	0.00262	0.3983759	1184	37	1122	14	95	
GB32_52	1.66414	0.03172	0.16677	0.00228	0.417583	997	37	994	13	100	
GB32_55	4.19054	0.06842	0.29679	0.00393	0.499056	1668	28	1675	20	100	
GB32_56	1.69809	0.02841	0.16691	0.0022	0.487401	1036	31	995	12	96	
GB32_58	1.49464	0.0345	0.15328	0.00223	0.3273629	950	46	919	12	97	
GB3A_03	0.82705	0.04754	0.09893	0.00218	0.1196774	626	122	608	13	97	
GB3A_05	3.846	0.06384	0.27472	0.00397	0.6078458	1653	26	1565	20	95	
GB3A_06	3.61905	0.05729	0.27127	0.00375	0.590223	1562	25	1547	19	99	
GB3A_08	4.26433	0.07814	0.30119	0.00449	0.5374732	1674	30	1697	22	101	
GB3A_09	4.12476	0.07001	0.28948	0.00418	0.5834304	1685	27	1639	21	97	
	$^{207}Pb/^{235}U$		**$^{206}Pb/^{238}U$**			**$^{207}Pb/^{206}Pb$**		**$^{206}Pb/^{238}U$**		**Conc.**	
Analysis #	**Ratio**	**1σ**	**Ratio**	**1σ**	**Rho**	**Age**	**2σ**	**Age**	**2σ**	**%**	**Comments**
GB3A_10	3.645	0.06992	0.27476	0.00413	0.5077365	1553	32	1565	21	101	
GB3A_11	3.92252	0.07511	0.28898	0.0044	0.5221603	1597	32	1636	22	102	
GB3A_12	4.18299	0.0903	0.29719	0.00476	0.4391633	1663	37	1677	24	101	
GB3A_13	3.95146	0.06905	0.29053	0.00428	0.5777181	1599	28	1644	21	103	
GB3A_19	3.51044	0.0581	0.26725	0.00379	0.5905214	1533	26	1527	19	100	
GB3A_22	0.64222	0.02405	0.08188	0.00145	0.2176863	487	82	507	9	104	
GB3A_26	3.37297	0.05477	0.26262	0.00372	0.599138	1492	26	1503	19	101	
GB3A_27	3.50866	0.05345	0.26594	0.0037	0.6394248	1542	23	1520	19	99	
GB3A_29	3.15198	0.05687	0.24801	0.00356	0.522067	1472	31	1428	18	97	
GB3A_37	4.2356	0.0655	0.29645	0.00408	0.613998	1690	24	1674	20	99	
GB3A_40	3.9232	0.06533	0.29216	0.00416	0.5828089	1575	26	1652	21	105	
GB3A_42	3.85307	0.08031	0.28093	0.0043	0.4458545	1615	36	1596	22	99	
GB3A_43	3.92912	0.06622	0.28703	0.0041	0.5767725	1611	27	1627	21	101	
GB3B_01	4.05992	0.07046	0.29207	0.00463	0.6878317	1639	24	1652	23	101	Hf Isotope Analysis #1
GB3B_05	9.65175	0.17634	0.43541	0.00707	0.6560373	2464	24	2330	32	95	Hf Isotope Analysis #4
GB3B_06	4.12399	0.07549	0.28882	0.00465	0.6570443	1689	26	1636	23	97	
GB3B_09	3.53028	0.07036	0.26561	0.00438	0.6041339	1556	31	1519	22	98	
GB3B 18	3.73304	0.06991	0.27885	0.00452	0.6381339	1569	28	1586	23	101	

GB3B_25	2.15985	0.04228	0.19538	0.00319	0.6115621	1202	31	1150	17	96	Hf Isotope Analysis #11
GB3B_26	4.42657	0.0802	0.30089	0.00482	0.6716437	1744	25	1696	24	97	Hf Isotope Analysis #13
GB3B_32	3.88639	0.0798	0.28047	0.00462	0.5812546	1633	32	1594	23	98	
GB3B_33	23.35589	0.46521	0.65366	0.01074	0.6037723	3242	26	3243	42	100	
GB3B_34	2.23399	0.04838	0.20187	0.00335	0.5431859	1203	37	1185	18	99	
GB3B_38	4.17696	0.0794	0.29194	0.0047	0.6159492	1693	29	1651	23	98	
GB3B_39	4.00262	0.07396	0.28699	0.00457	0.6426455	1646	27	1627	23	99	
GB3B_41	2.18689	0.04909	0.19935	0.00334	0.5125072	1187	39	1172	18	99	
GB3B_42	2.36675	0.05124	0.20818	0.00346	0.5444234	1257	36	1219	18	97	
GB3B_43	5.11715	0.11306	0.32968	0.00561	0.5313077	1842	35	1837	27	100	
GB3B_44	4.98145	0.10078	0.32334	0.00529	0.595245	1828	30	1806	26	99	
GB3B_47	3.95169	0.0719	0.28581	0.00461	0.655951	1629	26	1621	23	99	
GB3B_49	3.89964	0.07617	0.28399	0.00468	0.6035389	1617	30	1611	23	100	
GB3B_50	2.31675	0.04161	0.21022	0.00337	0.6715612	1195	27	1230	18	103	
GB3B_53	2.11851	0.1171	0.1947	0.0051	0.1642773	1170	109	1147	28	98	
GB3B_60	2.15717	0.04845	0.19492	0.00329	0.5104864	1204	39	1148	18	95	
GB3B_61	5.69154	0.10397	0.34146	0.00549	0.6555422	1970	25	1894	26	96	
GB3B_69	4.9314	0.10701	0.32021	0.00543	0.5548513	1827	34	1791	27	98	
GB3B_70	2.41821	0.05533	0.213	0.00364	0.523287	1254	39	1245	19	99	
GB3B_72	8.57532	0.15542	0.42741	0.00689	0.6606809	2294	24	2294	31	100	
GB3B_76	4.36259	0.08256	0.3028	0.00489	0.6339227	1706	28	1705	24	100	
	$^{207}Pb/^{235}U$		$^{206}Pb/^{238}U$			$^{207}Pb/^{206}Pb$		$^{206}Pb/^{238}U$		Conc.	
Analysis #	**Ratio**	**1σ**	**Ratio**	**1σ**	**Rho**	**Age**	**2σ**	**Age**	**2σ**	**%**	**Comments**
GB3B_77	17.01234	0.38114	0.57933	0.01063	0.5220366	2929	32	2946	43	101	
GB3B_79	2.28342	0.0581	0.20203	0.00356	0.4437498	1245	46	1186	19	95	
GB3B_80	3.81161	0.07634	0.28174	0.00459	0.5933935	1589	31	1600	23	101	
GB3B_81	2.90037	0.06056	0.23447	0.00386	0.5658945	1420	34	1358	20	96	
Discordant Analyses - Not Used											
GB32_01	2.94053	0.05199	0.17026	0.00224	0.4180978	2035	30	1014	12	50	
GB32_02	5.20665	0.08801	0.31233	0.00399	0.4246884	1970	29	1752	20	89	
GB32_03	2.54479	0.04428	0.15683	0.00205	0.4325185	1923	30	939	11	49	
GB32_04	4.58025	0.072	0.27523	0.00345	0.4740588	1967	26	1567	17	80	
GB32_05	3.21818	0.05161	0.243	0.00309	0.4769798	1551	28	1402	16	90	
GB32_06	1.63903	0.03416	0.14949	0.00204	0.3436404	1186	40	898	11	76	
GB32_07	12.39235	0.70543	0.22625	0.01071	0.145403	3901	99	1315	56	34	
GB32_08	2.72727	0.04391	0.12994	0.00165	0.4753848	2372	25	788	9	33	
GB32_10	1.58048	0.07499	0.11924	0.00268	0.1306826	1552	91	726	15	47	
GB32_11	3.23395	0.04358	0.19384	0.00244	0.6079222	1972	20	1142	13	58	
GB32_12	2.72571	0.03897	0.17129	0.0022	0.5702188	1887	23	1019	12	54	
GB32_13	4.73292	0.06914	0.28457	0.00369	0.5601426	1966	23	1614	19	82	

GB32_17	4.24588	0.0707	0.28094	0.0038	0.4878745	1793	28	1596	19	89
GB32_19	4.50447	0.06774	0.28871	0.00376	0.5558651	1851	24	1635	19	88
GB32_20	0.89556	0.01808	0.07004	0.00099	0.3895414	1483	37	436	6	29
GB32_21	5.64646	0.10021	0.31861	0.00446	0.4652217	2078	29	1783	22	86
GB32_22	3.98562	0.06216	0.27893	0.00367	0.5441046	1690	25	1586	18	94
GB32_24	2.72268	0.04057	0.17362	0.00224	0.5459056	1860	24	1032	12	55
GB32_25	2.73963	0.04585	0.18172	0.00243	0.4725151	1789	28	1076	13	60
GB32_26	3.606	0.05283	0.25684	0.00327	0.552591	1658	24	1474	17	89
GB32_27	3.34817	0.13655	0.23916	0.00533	0.173964	1653	78	1382	28	84
GB32_28	3.71797	0.05881	0.25982	0.00336	0.5029855	1693	27	1489	17	88
GB32_29	2.13027	0.04581	0.12362	0.00183	0.3321623	2029	38	751	11	37
GB32_30	6.9136	0.10802	0.21448	0.00275	0.5010485	3078	23	1253	15	41
GB32_31	4.16625	0.06685	0.26147	0.00336	0.4813829	1889	27	1497	17	79
GB32_41	3.14339	0.04661	0.19271	0.00249	0.5557574	1931	23	1136	13	59
GB32_42	3.38097	0.05053	0.24947	0.00322	0.5504458	1592	25	1436	17	90
GB32_43	0.38786	0.00701	0.04115	0.00055	0.4397319	880	35	260	3	30
GB32_44	1.13613	0.04192	0.06349	0.00126	0.1606965	2095	67	397	8	19
GB32_46	3.52667	0.05299	0.25509	0.00327	0.5421755	1629	25	1465	17	90
GB32_47	0.61426	0.01631	0.05758	0.00088	0.2661944	1131	53	361	5	32
GB32_49	4.27822	0.06879	0.26984	0.00351	0.5001446	1880	26	1540	18	82
GB32_50	3.58675	0.05798	0.25626	0.00333	0.4973267	1652	27	1471	17	89
GB32_51	3.43028	0.05558	0.24822	0.00321	0.491192	1629	28	1429	17	88

Analysis #	$^{207}Pb/^{235}U$ Ratio	1σ	$^{206}Pb/^{238}U$ Ratio	1σ	Rho	$^{207}Pb/^{206}Pb$ Age	2σ	$^{206}Pb/^{238}U$ Age	2σ	Conc. %	Comments
GB32_53	2.61444	0.04242	0.20781	0.00274	0.5024358	1452	28	1217	15	84	
GB32_54	5.85441	0.09313	0.25838	0.00346	0.5100942	2501	24	1482	18	59	
GB32_57	3.37327	0.06011	0.20603	0.00283	0.4488129	1938	30	1208	15	62	
GB32_59	3.18489	0.05031	0.1625	0.00212	0.5186697	2254	25	971	12	43	
GB32_60	3.34769	0.05414	0.21938	0.00287	0.5036915	1811	27	1279	15	71	
GB32_61	3.57136	0.0568	0.26099	0.00338	0.5172435	1610	27	1495	17	93	
GB32_62	1.10442	0.01802	0.0437	0.00057	0.4964738	2683	25	276	4	10	
GB32_63	1.844	0.0309	0.11251	0.00148	0.4860404	1939	27	687	9	35	
GB3A_01	3.92472	0.09706	0.12539	0.00242	0.3232752	3031	41	762	14	25	
GB3A_02	0.80734	0.03373	0.0962	0.00184	0.1787324	634	89	592	11	93	
GB3A_04	0.663	0.0303	0.08204	0.00164	0.166069	553	99	508	10	92	
GB3A_07	1.17596	0.02081	0.1157	0.00168	0.5462334	1034	31	706	10	68	
GB3A_14	3.91048	0.06061	0.30016	0.00427	0.6440856	1518	24	1692	21	111	
GB3A_15	0.76406	0.01707	0.09057	0.00138	0.4215359	646	45	559	8	86	
GB3A_16	1.69638	0.03925	0.1454	0.0023	0.3916789	1307	43	875	13	67	
GB3A_17	4.05444	0.06227	0.30334	0.0043	0.6513699	1566	23	1708	21	109	

GB3A_21	2.52956	0.04145	0.20584	0.00295	0.5905056	1408	27	1207	16	86	
GB3A_23	1.49505	0.02178	0.05759	0.0008	0.6760551	2728	19	361	5	13	
GB3A_24	1.14829	0.06565	0.09132	0.00228	0.1126734	1451	110	563	13	39	
GB3A_25	1.25155	0.02626	0.1211	0.00183	0.439785	1068	39	737	11	69	
GB3A_28	1.40003	0.0461	0.12118	0.00218	0.2462347	1288	64	737	13	57	
GB3A_30	1.51222	0.0445	0.1304	0.00221	0.2849382	1295	56	790	13	61	
GB3A_31	4.79212	0.08001	0.24423	0.00345	0.5656507	2256	25	1409	18	62	
GB3A_32	0.7412	0.01573	0.08836	0.00131	0.4366594	634	42	546	8	86	
GB3A_32	75.56327	1.40307	0.76435	0.01388	0.5549933	4766	25	3660	51	77	
GB3A_33	6.83631	0.18906	0.1519	0.00356	0.2715893	3601	47	912	20	25	
GB3A_35	4.23	0.06603	0.10015	0.00141	0.6274703	3503	20	615	8	18	
GB3A_36	1.35825	0.03081	0.1129	0.00175	0.392212	1367	42	690	10	50	
GB3A_38	4.20179	0.06578	0.28159	0.00393	0.6237654	1770	24	1599	20	90	
GB3A_39	8.86299	0.18727	0.15764	0.00306	0.3763226	3938	34	944	17	24	
GB3A_41	4.15711	0.06891	0.3038	0.00431	0.5890958	1610	26	1710	21	106	
GB3B_02	1.99148	0.03515	0.17268	0.00274	0.6798842	1284	26	1027	15	80	
GB3B_03	0.84082	0.01865	0.07977	0.00134	0.5153629	1107	39	495	8	45	
GB3B_04	0.67157	0.01416	0.08252	0.00135	0.5561033	568	39	511	8	90	
GB3B_07	4.82001	0.08924	0.30142	0.00487	0.6501761	1895	26	1698	24	90	
GB3B_08	8.64401	0.16155	0.39918	0.0065	0.6448112	2424	25	2165	30	89	
GB3B_10	4.28203	0.08028	0.25095	0.00406	0.6504592	2011	26	1443	21	72	
GB3B_15	3.50131	0.06109	0.19382	0.0031	0.6914523	2112	23	1142	17	54	
GB3B_16	2.83157	0.04971	0.17607	0.00281	0.689462	1906	24	1046	15	55	
Analysis #	$^{207}Pb/^{235}U$ Ratio	1σ	$^{206}Pb/^{238}U$ Ratio	1σ	Rho	$^{207}Pb/^{206}Pb$ Age	2σ	$^{206}Pb/^{238}U$ Age	2σ	Conc. %	Comments
GB3B_17	0.12321	0.00303	0.01692	0.00029	0.4740823	322	50	108	2	34	
GB3B_19	12.44279	0.22548	0.42188	0.0068	0.663499	2936	23	2269	31	77	
GB3B_22	1.11894	0.02242	0.09435	0.00155	0.5882737	1339	32	581	9	43	
GB3B_23	5.80894	0.10107	0.31284	0.00499	0.7030621	2160	22	1755	24	81	
GB3B_24	14.00632	0.24748	0.50822	0.00816	0.6901645	2825	22	2649	35	94	Hf Isotope Analysis #10
GB3B_27	3.6729	0.06868	0.22809	0.00369	0.6479007	1908	26	1325	19	69	
GB3B_28	1.67617	0.03769	0.15909	0.00268	0.5197804	1106	39	952	15	86	
GB3B_29	1.94588	0.03724	0.18153	0.00293	0.6289578	1140	30	1075	16	94	
GB3B_30	3.86583	0.07416	0.19341	0.00314	0.6272333	2287	26	1140	17	50	
GB3B_31	3.84326	0.07548	0.23468	0.00382	0.6132613	1938	29	1359	20	70	
GB3B_35	7.67069	0.13008	0.35683	0.00556	0.692483	2413	22	1967	26	82	
GB3B_36	1.1006	0.02014	0.12106	0.00191	0.6365947	805	30	737	11	91	
GB3B_37	4.11521	0.07229	0.27041	0.00425	0.6719973	1806	25	1543	22	85	
GB3B_40	0.71529	0.01394	0.06162	0.00099	0.602292	1298	31	386	6	30	
GB3B 45	8.14135	0.13637	0.37573	0.00593	0.7224193	2425	21	2056	28	85	

GB3B_51	0.43386	0.01343	0.02373	0.00048	0.3134701	2133	54	151	3	7
GB3B_52	4.2897	0.07577	0.26388	0.00421	0.6825431	1925	24	1510	22	78
GB3B_54	3.85804	0.08134	0.20394	0.00349	0.5469424	2192	32	1197	19	55
GB3B_55	4.67992	0.08568	0.26356	0.00425	0.6548192	2082	25	1508	22	72
GB3B_56	4.36285	0.11254	0.18828	0.00364	0.4127684	2539	41	1112	20	44
GB3B_57	1.10089	0.02396	0.11126	0.00186	0.5342632	979	38	680	11	69
GB3B_58	4.14419	0.07101	0.28589	0.0045	0.6979665	1717	23	1621	23	94
GB3B_59	2.39104	0.04147	0.1584	0.0025	0.6885045	1791	24	948	14	53
GB3B_62	2.23328	0.04416	0.1784	0.00292	0.5963147	1442	31	1058	16	73
GB3B_63	4.44614	0.0815	0.26612	0.00427	0.6584398	1974	25	1521	22	77
GB3B_64	2.86051	0.0537	0.18007	0.00291	0.6439758	1883	27	1067	16	57
GB3B_65	3.57849	0.06772	0.20715	0.00336	0.641298	2033	27	1214	18	60
GB3B_66	5.6233	0.10748	0.26368	0.00429	0.6355808	2398	26	1509	22	63
GB3B_67	3.32612	0.06659	0.19653	0.00324	0.6046743	1997	29	1157	17	58
GB3B_68	5.37369	0.1077	0.31537	0.0052	0.6068776	2009	29	1767	25	88
GB3B_71	0.58363	0.01514	0.0525	0.00092	0.4215044	1213	47	330	6	27
GB3B_73	0.7701	0.01594	0.09017	0.00147	0.5699193	672	37	557	9	83
GB3B_74	0.553	0.01052	0.06999	0.00112	0.6277328	503	33	436	7	87
GB3B_75	4.90779	0.09043	0.2447	0.00393	0.650655	2294	25	1411	20	62
GB3B_78	3.21526	0.06742	0.20758	0.00346	0.5595017	1838	32	1216	18	66
GB3B_82	3.61449	0.07891	0.1999	0.00337	0.5320283	2114	33	1175	18	56

Sample kGB-4: GDA94, 529276 mE, 6470589 mN

Analysis #	$^{207}Pb/^{235}U$ Ratio	1σ	$^{206}Pb/^{238}U$ Ratio	1σ	Rho	$^{207}Pb/^{206}Pb$ Age	2σ	$^{206}Pb/^{238}U$ Age	2σ	Conc. %	Comments
Concordant Zircon Analyses											
GB4_001	1.58964	0.02215	0.16033	0.00208	0.6337567	983	23	959	12	98	
GB4_002	3.6545	0.05214	0.27248	0.00358	0.6237392	1572	22	1553	18	99	
GB4_004	3.90862	0.06009	0.28252	0.00383	0.592323	1630	24	1604	19	98	
GB4_005	3.68135	0.05601	0.27043	0.00367	0.6117359	1599	24	1543	19	96	
GB4_009	3.92615	0.05988	0.28222	0.00392	0.6534283	1640	22	1603	20	98	
GB4_011	12.62839	0.19975	0.50759	0.00752	0.6704562	2657	21	2646	32	100	
GB4_012	3.86589	0.05832	0.27988	0.00404	0.708894	1628	21	1591	20	98	
GB4_013	3.7953	0.05893	0.2804	0.00407	0.6818072	1590	22	1593	21	100	
GB4_014	4.44434	0.07433	0.30384	0.00452	0.6263311	1733	25	1710	22	99	
GB4_015	4.77613	0.07523	0.31495	0.0046	0.6754966	1799	22	1765	23	98	
GB4_017	4.42358	0.0693	0.30351	0.00442	0.6763597	1727	22	1709	22	99	
GB4_020	10.2386	0.1629	0.46146	0.00676	0.6654631	2466	21	2446	30	99	

GB4_25	6.64484	0.10702	0.37557	0.00561	0.6878395	2075	22	2056	26	99
GB4_26	4.87673	0.08064	0.31982	0.00481	0.673082	1809	23	1789	24	99
GB42_03	4.22807	0.07303	0.29658	0.00473	0.6939637	1687	24	1674	24	99
GB42_05	4.26075	0.07446	0.29961	0.0048	0.6888735	1682	24	1689	24	100
GB42_06	3.69864	0.07272	0.2696	0.00447	0.6031037	1615	30	1539	23	95
GB42_08	5.86044	0.10404	0.35326	0.0057	0.6843275	1961	24	1950	27	99
GB42_09	4.22203	0.07579	0.29754	0.00481	0.6775675	1678	25	1679	24	100
GB42_11	0.82158	0.01604	0.09829	0.00161	0.6234654	626	34	604	9	97
GB42_12	4.19772	0.08074	0.29625	0.00489	0.6348237	1675	28	1673	24	100
GB42_14	4.67438	0.08754	0.31456	0.00521	0.6523842	1762	27	1763	26	100
GB42_15	4.10329	0.07201	0.29275	0.00475	0.7025874	1655	24	1655	24	100
GB42_16	4.92285	0.08806	0.32317	0.00527	0.6883722	1808	24	1805	26	100
GB42_17	9.81571	0.17735	0.44602	0.00733	0.6788169	2452	23	2378	33	97
GB42_18	4.70446	0.0868	0.31224	0.00513	0.6663519	1788	26	1752	25	98
GB42_20	5.68637	0.10301	0.34455	0.00562	0.6801231	1952	25	1909	27	98
GB42_21	3.58546	0.08077	0.26876	0.00469	0.5267455	1563	37	1535	24	98
GB42_22	4.21892	0.07849	0.29392	0.00482	0.6586357	1699	27	1661	24	98
GB42_23	1.86455	0.0371	0.17719	0.00294	0.6102835	1104	32	1052	16	95
GB42_24	5.5721	0.10436	0.34627	0.00568	0.6553853	1907	26	1917	27	101
Discordant Analyses - Not used										
GB4_003	4.71103	0.06879	0.26015	0.00347	0.6179893	2115	21	1491	18	70
GB4_006	3.62525	0.05278	0.19259	0.0026	0.6531257	2183	20	1135	14	52
GB4_007	3.79792	0.06154	0.24151	0.00339	0.5880446	1864	25	1395	18	75
GB4_008	2.57058	0.0398	0.13601	0.00189	0.6267681	2190	22	822	11	38
GB4_010	3.90089	0.06155	0.2269	0.00321	0.6415631	2024	22	1318	17	65

Analysis #	$^{207}Pb/^{235}U$ Ratio	1σ	$^{206}Pb/^{238}U$ Ratio	1σ	Rho	$^{207}Pb/^{206}Pb$ Age	2σ	$^{206}Pb/^{238}U$ Age	2σ	Conc. %	Comments
GB4_016	4.25577	0.06495	0.24573	0.00355	0.6993596	2038	20	1416	18	70	
GB4_018	4.54257	0.07094	0.26374	0.00384	0.6812046	2028	21	1509	20	74	
GB4_019	0.28912	0.00757	0.03529	0.00057	0.365529	583	54	224	4	38	
GB4_22	1.23701	0.01929	0.07043	0.00104	0.7004786	2062	21	439	6	21	
GB4_23	1.38606	0.02192	0.08359	0.00124	0.692311	1960	21	518	7	26	
GB4_27	4.52816	0.07617	0.29692	0.00449	0.6632728	1810	24	1676	22	93	
GB4_28	2.60079	0.04308	0.1319	0.00199	0.6768437	2264	22	799	11	35	
GB42_01	4.14384	0.06848	0.27206	0.00428	0.7225944	1808	22	1551	22	86	
GB42_02	7.15256	0.12021	0.3028	0.00481	0.7095387	2571	21	1705	24	66	
GB42_04	3.83504	0.06538	0.26598	0.00423	0.7042602	1707	23	1520	22	89	
GB42_07	4.93191	0.08717	0.29302	0.00472	0.6836019	1987	24	1657	24	83	
GB42_10	3.68692	0.10195	0.23071	0.00448	0.3971753	1894	47	1338	23	71	
GB42_13	3.54602	0.06087	0.2192	0.00354	0.7187961	1916	22	1278	19	67	

Sample kGB-8: GDA94, 535532 mE, 6461873 mN

Concordant Zircon Analyses

Analysis #	$^{207}Pb/^{235}U$ Ratio	1σ	$^{206}Pb/^{238}U$ Ratio	1σ	Rho	$^{207}Pb/^{206}Pb$ Age	2σ	$^{206}Pb/^{238}U$ Age	2σ	Conc. %	Comments
GB8A_03	6.60987	0.08065	0.36919	0.00427	0.5657642	2096	19	2026	20	97	
GB8A_04	6.61521	0.08201	0.3732	0.00434	0.5548217	2079	20	2044	20	98	
GB8A_09	4.19276	0.06263	0.2922	0.0036	0.4543073	1698	26	1653	18	97	
GB8A_19	4.37128	0.05472	0.29586	0.00347	0.5607116	1752	21	1671	17	95	
GB8A_21	3.90319	0.04914	0.28217	0.00331	0.5576037	1630	21	1602	17	98	
GB8A_22	4.40833	0.0602	0.30294	0.00364	0.509807	1724	23	1706	18	99	
GB8A_24	4.52056	0.05663	0.29987	0.00351	0.5567265	1789	21	1691	17	95	
GB8A_25	0.30858	0.01057	0.04302	0.00067	0.1548733	287	79	272	4	95	
GB8A_27	10.31619	0.13336	0.462	0.00555	0.5408493	2476	20	2448	24	99	
GB8A_32	4.95985	0.06361	0.32296	0.00379	0.5374171	1822	21	1804	18	99	
GB8A_33	4.94669	0.0609	0.32193	0.00373	0.5679283	1823	20	1799	18	99	
GB8A_36	1.97432	0.0262	0.18479	0.00217	0.5252473	1134	24	1093	12	96	
GB8A_39	5.39324	0.07185	0.33721	0.00402	0.5210279	1896	22	1873	19	99	
GB8B_002	4.85512	0.07949	0.31304	0.00471	0.6710806	1840	23	1756	23	95	Hf Isotope Analysis #2
GB8B_003	8.54534	0.15148	0.42461	0.00665	0.6170713	2300	25	2281	30	99	
GB8B_005	5.45862	0.08752	0.33116	0.00496	0.6961289	1950	21	1844	24	95	
GB8B_006	4.80597	0.08336	0.31801	0.00488	0.6416318	1793	25	1780	24	99	
GB8B_007	4.22323	0.06899	0.29635	0.00446	0.6866951	1686	23	1673	22	99	Hf Isotope Analysis #3
GB8B_009	10.2839	0.17736	0.46116	0.00712	0.6524542	2474	23	2445	31	99	
GB8B_011	4.21883	0.07178	0.29719	0.00452	0.669233	1678	24	1677	22	100	Hf Isotope Analysis #4
GB8B_012	5.73023	0.09945	0.35025	0.00537	0.657515	1936	24	1936	26	100	Hf Isotope Analysis #5
GB8B_014	5.22674	0.09068	0.33345	0.00514	0.6413131	1859	25	1855	25	100	Hf Isotope Analysis #6
GB8B_016	2.13346	0.03521	0.19787	0.00298	0.6818626	1152	25	1164	16	101	Hf Isotope Analysis #7
GB8B_019	4.59363	0.07647	0.30955	0.00468	0.6733546	1760	23	1739	23	99	Hf Isotope Analysis #9
GB8B_020	7.17516	0.12952	0.38944	0.00609	0.6096274	2146	26	2120	28	99	Hf Isotope Analysis #10
GB8B_022	2.18175	0.03915	0.19924	0.00305	0.6177168	1183	29	1171	16	99	
GB8B_024	10.13141	0.17253	0.45945	0.00696	0.6501125	2455	23	2437	31	99	
GB8B_025	3.90988	0.06286	0.28213	0.0042	0.6850556	1634	23	1602	21	98	Hf Isotope Analysis #12
GB8B_026	5.71446	0.09582	0.34555	0.00522	0.654297	1956	24	1913	25	98	
GB8B_029	0.37194	0.0094	0.05084	0.00082	0.4111249	332	53	320	5	96	Hf Isotope Analysis #13
GB8B_031	1.95405	0.04665	0.18656	0.00308	0.4337256	1095	44	1103	17	101	Hf Isotope Analysis #14
GB8B_035	4.30414	0.07466	0.29499	0.00447	0.6422712	1729	25	1666	22	96	
GB8B_038	5.28282	0.08709	0.33298	0.00501	0.6573003	1882	23	1853	24	98	
GB8B_039	2.15075	0.03678	0.19479	0.00293	0.6283065	1200	27	1147	16	96	Hf Isotope Analysis #15
GB8B_040	0.93821	0.01891	0.1097	0.00169	0.5210271	676	38	671	10	99	
GB8B_041	0.10947	0.00748	0.01651	0.00042	0.1015361	105	159	106	3	100	Hf Isotope Analysis #16

GB8B_046	4.44664	0.07786	0.30345	0.00462	0.6160705	1737	26	1708	23	98	
GB8B_047	1.8245	0.03056	0.17524	0.00261	0.6484178	1082	27	1041	14	96	
GB8B_049	1.48129	0.04101	0.15234	0.00262	0.353421	944	54	914	15	97	Hf Isotope Analysis #18
GB8B_050	5.45493	0.08795	0.33905	0.00505	0.6772048	1906	22	1882	24	99	
GB8B_051	4.4042	0.0728	0.30125	0.00451	0.6577357	1732	24	1698	22	98	Hf Isotope Analysis #19
GB8B_052	4.20093	0.06978	0.29197	0.00437	0.6537643	1703	24	1651	22	97	
GB8B_058	1.68962	0.02808	0.16813	0.0025	0.662495	1011	26	1002	14	99	Hf Isotope Analysis #20
GB8B_059	4.76055	0.07901	0.31432	0.0047	0.6640851	1797	24	1762	23	98	Hf Isotope Analysis #21
GB8B_060	7.29544	0.12373	0.39097	0.00589	0.6453716	2169	23	2127	27	98	Hf Isotope Analysis #22
GB8B_061	2.92977	0.04962	0.23946	0.00367	0.670148	1399	25	1384	19	99	
GB8B_062	0.33586	0.00976	0.04669	0.0008	0.3563512	293	63	294	5	100	Hf Isotope Analysis #23
GB8B_064	10.98242	0.17684	0.47961	0.00725	0.7071077	2519	20	2526	32	100	
GB8B_066	11.5618	0.19393	0.48626	0.00746	0.6703106	2582	22	2555	32	99	Hf Isotope Analysis #24
GB8B_068	4.64555	0.08957	0.30852	0.00491	0.5659984	1786	30	1733	24	97	Hf Isotope Analysis #25
GB8B_069	4.31342	0.07326	0.30136	0.00458	0.6589556	1694	25	1698	23	100	
GB8B_070	4.38164	0.07481	0.29586	0.0045	0.6510097	1756	25	1671	22	95	Hf Isotope Analysis #26
GB8B_071	4.59513	0.07866	0.30817	0.00468	0.6469893	1768	25	1732	23	98	
GB8B_075	4.25684	0.07089	0.29705	0.0045	0.6652358	1696	24	1677	22	99	
GB8B_076	10.4914	0.16705	0.46785	0.00701	0.6975524	2484	20	2474	31	100	
GB8B_077	5.41942	0.08722	0.33973	0.00509	0.690272	1891	22	1885	24	100	Hf Isotope Analysis #30
GB8B_078	0.7498	0.01635	0.09194	0.00145	0.4842909	573	42	567	9	99	Hf Isotope Analysis #29
GB8B_079	1.76567	0.03323	0.17358	0.00268	0.5796332	1036	32	1032	15	100	Hf Isotope Analysis #28
GB8B_081	3.81931	0.0675	0.27658	0.00424	0.6180876	1627	27	1574	21	97	
GB8B_083	4.78818	0.08101	0.31718	0.0048	0.649542	1791	24	1776	23	99	
GB8B_084	3.93109	0.06606	0.28526	0.0043	0.6565451	1624	25	1618	22	100	Hf Isotope Analysis #31
Discordant Analyses - Not used											
GB8A_01	3.75501	0.0451	0.17472	0.00201	0.575581	2412	18	1038	11	43	

Analysis #	$^{207}Pb/^{235}U$ Ratio	1σ	$^{206}Pb/^{238}U$ Ratio	1σ	Rho	$^{207}Pb/^{206}Pb$ Age	2σ	$^{206}Pb/^{238}U$ Age	2σ	Conc. %	Comments
GB8A_02	4.27633	0.0566	0.25583	0.00304	0.5126838	1975	22	1469	16	74	
GB8A_05	3.45026	0.04294	0.15715	0.00183	0.546629	2448	19	941	10	38	
GB8A_06	9.39835	0.11382	0.38681	0.00448	0.5690627	2618	18	2108	21	81	
GB8A_07	1.92103	0.02475	0.16202	0.00189	0.5277253	1338	23	968	10	72	
GB8A_08	1.7359	0.02188	0.16831	0.00195	0.5404879	1063	23	1003	11	94	
GB8A_10	3.22559	0.05286	0.20277	0.0026	0.3985083	1886	29	1190	14	63	
GB8A_11	4.73293	0.05799	0.28347	0.00331	0.5731827	1972	20	1609	17	82	
GB8A_12	3.3553	0.04067	0.2144	0.00249	0.5837844	1856	20	1252	13	67	
GB8A_13	2.53447	0.0351	0.17172	0.00207	0.4973935	1750	24	1022	11	58	
GB8A_14	2.99082	0.036	0.18301	0.00212	0.5825581	1934	19	1083	12	56	
GB8A_15	8.70327	0.10648	0.40068	0.00469	0.5750604	2429	19	2172	22	89	

GB8A_18	4.24483	0.05454	0.27037	0.0032	0.5480557	1862	21	1543	16	83	
GB8A_20	3.49146	0.04372	0.23183	0.00272	0.5635315	1787	21	1344	14	75	
GB8A_23	2.30711	0.06477	0.20134	0.00321	0.2252888	1272	56	1183	17	93	
GB8A_26	3.24411	0.03882	0.23204	0.00268	0.5827552	1650	20	1345	14	82	
GB8A_28	10.63481	0.12665	0.42888	0.00496	0.586779	2652	18	2301	22	87	
GB8A_29	10.64042	0.12796	0.41985	0.00488	0.5814439	2688	18	2260	22	84	
GB8A_30	260.65839	30.39972	2.61715	0.31878	0.7392107	4776	118	8288	568	174	
GB8A_31	2.86244	0.03438	0.14379	0.00167	0.5822834	2281	18	866	9	38	
GB8A_34	4.41488	0.05357	0.27851	0.00322	0.5730886	1880	20	1584	16	84	
GB8A_35	26.44465	0.34248	0.39605	0.00499	0.5331477	4194	18	2151	23	51	
GB8A_37	3.98933	0.04964	0.25623	0.00298	0.5583378	1847	20	1471	15	80	
GB8A_38	4.55391	0.05476	0.26162	0.00301	0.581593	2046	19	1498	15	73	
GB8B_001	0.10718	0.00598	0.0161	0.00036	0.1382443	113	130	103	2	91	
GB8B_004	8.88223	0.14238	0.38457	0.00578	0.6943849	2533	20	2098	27	83	
GB8B_008	4.5047	0.0797	0.2923	0.00451	0.6294766	1829	26	1653	23	90	
GB8B_010	8.27977	0.141	0.33156	0.00508	0.6635558	2663	22	1846	25	69	
GB8B_013	0.14559	0.00569	0.02171	0.0004	0.2367935	131	90	139	3	106	
GB8B_015	1.90871	0.03217	0.10718	0.00164	0.6569012	2087	23	656	10	31	
GB8B_017	6.35105	0.10134	0.21308	0.00319	0.7039653	2953	19	1245	17	42	
GB8B_018	2.25407	0.03681	0.19856	0.00298	0.6843404	1254	24	1168	16	93	Hf Isotope Analysis #8
GB8B_021	2.26968	0.05389	0.19605	0.00328	0.4376614	1292	43	1154	18	89	
GB8B_023	0.72968	0.01496	0.08906	0.00139	0.5309179	583	39	550	8	94	Hf Isotope Analysis #11
GB8B_027	4.50196	0.07241	0.28207	0.0042	0.6888792	1892	22	1602	21	85	
GB8B_028	0.64016	0.01327	0.06795	0.00106	0.506699	879	38	424	6	48	
GB8B_030	8.5325	0.13846	0.41132	0.00615	0.6851144	2351	21	2221	28	94	
GB8B_032	9.39137	0.15245	0.20255	0.00302	0.6860665	3646	19	1189	16	33	
GB8B_033	3.31981	0.05478	0.20915	0.00313	0.6747419	1882	23	1224	17	65	
GB8B_034	2.8047	0.04693	0.09301	0.0014	0.6639138	2972	21	573	8	19	
Analysis #	**$^{207}Pb/^{235}U$ Ratio**	**1σ**	**$^{206}Pb/^{238}U$ Ratio**	**1σ**	**Rho**	**$^{207}Pb/^{206}Pb$ Age**	**2σ**	**$^{206}Pb/^{238}U$ Age**	**2σ**	**Conc. %**	**Comments**
GB8B_036	389.98587	14.90314	2.55851	0.10537	0.6994213	5378	42	8183	191	152	
GB8B_037	2.62954	0.0426	0.19691	0.00294	0.670204	1565	24	1159	16	74	
GB8B_042	1.69275	0.02823	0.13209	0.00198	0.6498869	1487	25	800	11	54	
GB8B_044	1.91253	0.03132	0.12611	0.00188	0.6632388	1800	23	766	11	43	
GB8B_048	1.81262	0.03388	0.17042	0.00261	0.568692	1125	32	1014	14	90	
GB8B_053	4.71804	0.08117	0.30649	0.00465	0.6292054	1827	25	1723	23	94	
GB8B_054	1.3709	0.0255	0.083	0.00129	0.5627188	1953	29	514	8	26	
GB8B_055	3.80575	0.06243	0.27213	0.00406	0.6689707	1651	24	1552	21	94	
GB8B_056	7.99069	0.12815	0.37473	0.00556	0.6859421	2398	21	2052	26	86	
GB8B 057	6.61833	0.10732	0.31129	0.00463	0.6756805	2393	21	1747	23	73	

GB8B_067	0.28294	0.0178	0.04032	0.001	0.1184322	236	143	255	6	108	
GB8B_072	3.63295	0.06226	0.23856	0.00361	0.6473945	1807	25	1379	19	76	
GB8B_073	1.81312	0.03128	0.17133	0.0026	0.6371389	1115	28	1020	14	91	Hf Isotope Analysis #27
GB8B_074	7.73895	0.12145	0.3668	0.00547	0.7090261	2380	20	2014	26	85	
GB8B_080	4.53309	0.0784	0.28966	0.00443	0.6320549	1857	25	1640	22	88	
GB8B_082	1.88045	0.03189	0.13915	0.0021	0.6472047	1587	25	840	12	53	

Sample kGB-10: GDA 94, 560926 mE, 6469785 mN

Concordant Zircon Analyses

GB10A_06	5.31788	0.08902	0.3373	0.00425	0.4600547	1870	28	1874	21	100	
GB10A_13	1.97061	0.03628	0.18427	0.00244	0.4056616	1136	35	1090	13	96	
GB10A_14	4.2268	0.0717	0.30108	0.00395	0.4505566	1658	30	1697	20	102	
GB10A_15	1.53975	0.03624	0.1581	0.00223	0.2924419	947	48	946	12	100	
GB10A_23	3.88015	0.06659	0.28232	0.00364	0.4370545	1618	30	1603	18	99	
GB10A_27	3.93674	0.05956	0.28573	0.00357	0.4993054	1623	26	1620	18	100	
GB10A_36	3.39611	0.06044	0.26126	0.00343	0.3996601	1515	32	1496	18	99	
GB10A_37	4.02604	0.06014	0.29388	0.00364	0.4967154	1613	26	1661	18	103	
GB10A_38	1.64908	0.02746	0.16638	0.00212	0.4331663	983	32	992	12	101	
GB10A_39	4.18602	0.06561	0.28805	0.00363	0.4696621	1722	27	1632	18	95	
GB10A_41	3.94519	0.06263	0.28529	0.00359	0.4526363	1630	28	1618	18	99	
GB10A_45	8.01975	0.13212	0.41169	0.00517	0.424436	2244	27	2223	24	99	
GB10A_49	3.7842	0.06975	0.27468	0.00358	0.3778347	1623	33	1565	18	96	
GB10A_50	3.75445	0.0617	0.27631	0.00345	0.419542	1597	29	1573	17	98	
GB10A_54	8.45911	0.14839	0.42316	0.00548	0.3919555	2288	29	2275	25	99	
GB10A_59	2.10771	0.05041	0.19164	0.00272	0.2685261	1192	47	1130	15	95	
GB10A_62	4.1863	0.0639	0.2972	0.0036	0.451938	1664	27	1677	18	101	
GB10A_64	10.0637	0.36152	0.45607	0.00838	0.1753994	2456	62	2422	37	99	
GB10A_68	4.20505	0.07558	0.29218	0.00371	0.3805872	1704	32	1652	19	97	
GB10A_69	7.61957	0.30281	0.40345	0.00792	0.1722023	2189	70	2185	36	100	

Analysis #	$^{207}Pb/^{235}U$ Ratio	1σ	$^{206}Pb/^{238}U$ Ratio	1σ	Rho	$^{207}Pb/^{206}Pb$ Age	2σ	$^{206}Pb/^{238}U$ Age	2σ	Conc. %	Comments
GB10A_73	4.38596	0.07167	0.30467	0.00379	0.4227931	1703	29	1714	19	101	
GB10A_82	0.74318	0.02668	0.09203	0.00153	0.1722361	552	79	568	9	103	
GB10A_84	4.01837	0.06041	0.28747	0.00358	0.5012789	1650	26	1629	18	99	
GB10A_92	0.50887	0.02021	0.06718	0.0011	0.1516964	409	88	419	7	102	
GB10A_95	4.14859	0.06244	0.29243	0.00367	0.5054387	1677	26	1654	18	99	
GB10A_96	4.13025	0.06422	0.29174	0.0037	0.4871234	1674	27	1650	18	99	
GB10A_99	4.80278	0.07848	0.31794	0.00409	0.4562671	1793	28	1780	20	99	
GB10A104	3.83864	0.06569	0.28123	0.00361	0.4323871	1606	30	1598	18	99	
GB10A106	3.79252	0.07016	0.27846	0.00367	0.3925462	1602	33	1584	19	99	

GB10B_016	4.70434	0.08317	0.30742	0.00487	0.6711399	1816	25	1728	24	95	Hf Isotope Analysis #8
GB10B_017	3.76395	0.06546	0.27666	0.00435	0.6876842	1599	24	1575	22	98	Hf Isotope Analysis #9
GB10B_019	11.67344	0.20593	0.48784	0.00772	0.6803013	2592	22	2561	33	99	Hf Isotope Analysis #11
GB10B_020	9.66961	0.17838	0.43966	0.00709	0.6473936	2451	25	2349	32	96	Hf Isotope Analysis #12
GB10B_022	3.63804	0.06156	0.27111	0.0043	0.723658	1574	23	1546	22	98	Hf Isotope Analysis #13
GB10B_025	10.38836	0.18049	0.45329	0.00727	0.7002362	2520	22	2410	32	96	Hf Isotope Analysis #15
GB10B_027	4.75664	0.08246	0.3133	0.00498	0.702101	1802	23	1757	24	98	
GB10B_028	3.94598	0.06859	0.28267	0.00449	0.7009789	1647	24	1605	23	97	
GB10B_029	3.59812	0.06642	0.27163	0.00438	0.6525081	1549	27	1549	22	100	
GB10B_030	5.09714	0.09024	0.3217	0.00513	0.6874861	1879	24	1798	25	96	
GB10B_032	3.98302	0.07139	0.28597	0.00456	0.67569	1643	25	1621	23	99	
GB10B_034	4.33666	0.07424	0.29504	0.00465	0.6975077	1743	23	1667	23	96	
GB10B_036	4.10423	0.07981	0.29029	0.00475	0.5983767	1671	30	1643	24	98	Hf Isotope Analysis #16
GB10B_039	10.80114	0.18823	0.4677	0.0074	0.6718193	2533	23	2474	33	98	Hf Isotope Analysis #19
GB10B_040	4.24766	0.07687	0.29163	0.00463	0.6437499	1726	26	1650	23	96	Hf Isotope Analysis #20
GB10B_041	4.30108	0.0824	0.29446	0.00476	0.5989603	1731	29	1664	24	96	
GB10B_042	4.19792	0.07458	0.29405	0.00462	0.6516016	1689	26	1662	23	98	
GB10B_045	4.17429	0.06111	0.29195	0.00414	0.7146299	1692	20	1651	21	98	
GB10B_049	5.12132	0.07817	0.32889	0.00474	0.6959067	1847	21	1833	23	99	
GB10B_051	4.30392	0.06658	0.30062	0.00436	0.6945217	1694	22	1694	22	100	
GB10B_053	4.66203	0.07353	0.31135	0.00455	0.6873222	1776	22	1747	22	98	
GB10B_056	11.3194	0.17634	0.48316	0.00724	0.7244627	2557	19	2541	31	99	
GB10B_066	4.31733	0.07322	0.30249	0.00467	0.6796534	1688	24	1704	23	101	
GB10B_070	4.09874	0.06603	0.28739	0.00439	0.7233922	1687	21	1629	22	97	Hf Isotope Analysis #25
GB10B_078	4.18864	0.07148	0.29457	0.00454	0.6842488	1681	24	1664	23	99	Hf Isotope Analysis #32
GB10B_079	4.36705	0.07804	0.30209	0.00471	0.6468467	1712	26	1702	23	99	
GB10B_082	1.36476	0.02312	0.14335	0.00224	0.7034176	900	26	864	13	96	Hf Isotope Analysis #34
GB10B_084	5.16046	0.08424	0.33049	0.00514	0.7295998	1852	21	1841	25	99	
GB10B_085	4.36676	0.07331	0.30286	0.00475	0.7089426	1707	23	1706	23	100	Hf Isotope Analysis #36
GB10B_086	5.06872	0.08611	0.32775	0.00516	0.6991239	1835	23	1828	25	100	

Analysis #	$^{207}Pb/^{235}U$ Ratio	1σ	$^{206}Pb/^{238}U$ Ratio	1σ	Rho	$^{207}Pb/^{206}Pb$ Age	2σ	$^{206}Pb/^{238}U$ Age	2σ	Conc. %	Comments
GB10B_089	4.1958	0.06916	0.29334	0.00457	0.723512	1692	22	1658	23	98	Hf Isotope Analysis #39
GB10B_091	5.47696	0.09421	0.34098	0.00538	0.6902253	1904	23	1891	26	99	
GB10B_092	9.45945	0.16076	0.44497	0.007	0.6978146	2393	22	2373	31	99	Hf Isotope Analysis #40
GB10B_098	4.60976	0.07839	0.30792	0.00491	0.7169735	1776	22	1730	24	97	Hf Isotope Analysis #45
GB10B_099	4.25615	0.07171	0.29843	0.00475	0.7292971	1687	22	1684	24	100	Hf Isotope Analysis #44
GB10B_102	5.02778	0.08675	0.31836	0.00511	0.7172088	1873	23	1782	25	95	
GB10B_103	10.45298	0.18153	0.46528	0.0075	0.7116437	2486	21	2463	33	99	
GB10B 104	8.50807	0.14906	0.42416	0.00685	0.7081241	2293	22	2279	31	99	

GB10B_111	8.02625	0.14327	0.41394	0.00673	0.6931812	2235	23	2233	31	100
GB10B_114	0.67132	0.02248	0.08389	0.00158	0.3206093	531	70	519	9	98
GB10B_115	4.31842	0.07822	0.29813	0.00483	0.6861296	1715	25	1682	24	98
GB10B_116	12.22517	0.21828	0.49976	0.00808	0.6984662	2629	22	2613	35	99
GB10B_117	4.474	0.07491	0.31106	0.00498	0.745944	1703	21	1746	24	103
GB10B_120	3.88207	0.07452	0.29006	0.00481	0.6356531	1569	29	1642	24	105
GB10B_121	10.55328	0.18088	0.47826	0.00773	0.7226956	2456	21	2520	34	103
GB10B_122	4.09012	0.07167	0.29697	0.00479	0.7038613	1622	24	1676	24	103
GB10B_125	10.95451	0.18656	0.46943	0.00752	0.727728	2550	20	2481	33	97
GB10B_126	10.6239	0.18051	0.46855	0.00749	0.7295789	2502	20	2477	33	99
GB10B_132	4.19604	0.07117	0.29366	0.0047	0.7337524	1690	22	1660	23	98
GB10B_133	10.48163	0.17792	0.45883	0.00737	0.7316854	2515	20	2434	33	97
GB10B_134	5.0045	0.08549	0.32352	0.00519	0.7259667	1835	22	1807	25	98
GB10B_135	4.1987	0.07407	0.29783	0.00481	0.7024976	1665	24	1681	24	101
GB10B_138	4.07944	0.0701	0.2876	0.0046	0.7210221	1677	23	1630	23	97
GB10B_139	4.24676	0.0752	0.29336	0.00473	0.6975503	1714	24	1658	24	97
GB10B_141	4.6741	0.07918	0.31294	0.005	0.7316718	1772	22	1755	25	99
GB10B_148	4.48929	0.07927	0.30801	0.00496	0.6958835	1727	24	1731	24	100
Discordant Analyses - Not used										
GB10A_01	0.8456	0.01817	0.09505	0.00126	0.3169043	760	44	585	7	77
GB10A_02	3.62045	0.05284	0.24658	0.00292	0.4785402	1741	25	1421	15	82
GB10A_03	4.10297	0.0695	0.26832	0.00337	0.4400525	1815	29	1532	17	84
GB10A_04	6.69997	0.10215	0.31597	0.00381	0.4815108	2389	24	1770	19	74
GB10A_05	2.51166	0.0468	0.1553	0.00203	0.4187759	1917	31	931	11	49
GB10A_07	4.45818	0.07362	0.28157	0.00355	0.4792505	1878	27	1599	18	85
GB10A_08	3.56144	0.06192	0.24543	0.00313	0.4740806	1719	29	1415	16	82
GB10A_09	3.94842	0.087	0.21736	0.00296	0.4190556	2122	36	1268	16	60
GB10A_10	4.22477	0.09101	0.27802	0.00391	0.4107748	1803	37	1581	20	88
GB10A_11	3.42468	0.05864	0.22171	0.00292	0.4564072	1833	29	1291	15	70
GB10A_12	3.80058	0.05722	0.25208	0.00319	0.5148887	1789	25	1449	16	81
GB10A_16	10.59975	0.20771	0.42292	0.00599	0.3894819	2670	31	2274	27	85

Analysis #	$^{207}Pb/^{235}U$ Ratio	1σ	$^{206}Pb/^{238}U$ Ratio	1σ	Rho	$^{207}Pb/^{206}Pb$ Age	2σ	$^{206}Pb/^{238}U$ Age	2σ	Conc. %	Comments
GB10A_17	2.05911	0.03803	0.11545	0.00153	0.4101159	2090	31	704	9	34	
GB10A_18	3.93463	0.06618	0.27399	0.00351	0.4480401	1700	29	1561	18	92	
GB10A_19	4.80501	0.08223	0.285	0.0037	0.4484395	1990	29	1617	19	81	
GB10A_20	11.04676	0.24094	0.43702	0.00624	0.3461019	2684	35	2337	28	87	
GB10A_21	1.60702	0.02524	0.057	0.00072	0.4741916	2862	24	357	4	12	
GB10A_22	3.95723	0.07716	0.27469	0.00369	0.3918222	1706	34	1565	19	92	
GB10A_24	3.46869	0.05625	0.22	0.00282	0.4774091	1870	27	1282	15	69	

GB10A_28	0.14121	0.01326	0.02072	0.00051	0.040933	168	210	132	3	79
GB10A_29	1.28599	0.02392	0.12368	0.00163	0.396718	1080	36	752	9	70
GB10A_30	3.21304	0.06471	0.20313	0.00278	0.36592	1876	35	1192	15	64
GB10A_31	3.13413	0.04995	0.173	0.00218	0.4681904	2117	26	1029	12	49
GB10A_32	39.48819	3.0278	0.64288	0.04227	0.3006171	4071	121	3200	166	79
GB10A_33	3.70286	0.08389	0.2582	0.00372	0.3228308	1698	41	1481	19	87
GB10A_34	4.33261	0.09138	0.29099	0.00397	0.3287496	1766	38	1647	20	93
GB10A_35	1.44834	0.02697	0.08392	0.00108	0.3767662	2031	32	520	6	26
GB10A_40	2.12286	0.04169	0.19094	0.00252	0.3489764	1213	38	1127	14	93
GB10A_42	4.47986	0.09302	0.26774	0.00373	0.3178265	1977	37	1529	19	77
GB10A_43	4.23912	0.06247	0.2543	0.00312	0.483115	1970	25	1461	16	74
GB10A_44	3.80417	0.08448	0.25891	0.00361	0.3056579	1742	40	1484	18	85
GB10A_46	1.66688	0.03755	0.15195	0.0021	0.281745	1187	44	912	12	77
GB10A_47	3.35298	0.05296	0.22994	0.00285	0.4378774	1728	28	1334	15	77
GB10A_48	7.6616	0.16059	0.22232	0.0031	0.2943915	3184	34	1294	16	41
GB10A_51	3.6725	0.06252	0.25881	0.00332	0.4082633	1678	30	1484	17	88
GB10A_52	9.05571	0.13143	0.41301	0.00499	0.4859494	2445	23	2229	23	91
GB10A_53	3.52876	0.05831	0.24151	0.00298	0.4118508	1731	29	1395	15	81
GB10A_55	4.96507	0.09566	0.30493	0.004	0.3572082	1928	34	1716	20	89
GB10A_56	3.93357	0.06164	0.27785	0.0034	0.4443155	1673	27	1581	17	94
GB10A_57	5.66809	0.09894	0.32678	0.00408	0.3867756	2040	30	1823	20	89
GB10A_58	3.38303	0.07026	0.2535	0.00336	0.3119107	1564	39	1457	17	93
GB10A_60	3.9841	0.0618	0.27806	0.0034	0.4498509	1696	27	1582	17	93
GB10A_61	7.08624	0.10231	0.36788	0.00446	0.487138	2224	23	2019	21	91
GB10A_63	202.85368	38.16893	1.80021	0.26487	0.466157	4948	230	6638	610	134
GB10A_65	5.64761	0.0824	0.29364	0.00354	0.4743098	2221	24	1660	18	75
GB10A_66	3.76358	0.07616	0.25103	0.0034	0.3355221	1779	36	1444	18	81
GB10A_67	3.631	0.06486	0.18547	0.00232	0.3651851	2252	30	1097	13	49
GB10A_70	4.53937	0.08225	0.28839	0.00367	0.377779	1867	32	1634	18	87
GB10A_71	10.27235	0.18374	0.43844	0.0056	0.3845056	2557	29	2344	25	92
GB10A_72	3.96861	0.06148	0.2642	0.00322	0.442868	1781	27	1511	16	85
GB10A_74	3.81379	0.06056	0.25468	0.00313	0.4414732	1776	27	1463	16	82

Analysis #	$^{207}Pb/^{235}U$ Ratio	1σ	$^{206}Pb/^{238}U$ Ratio	1σ	Rho	$^{207}Pb/^{206}Pb$ Age	2σ	$^{206}Pb/^{238}U$ Age	2σ	Conc. %	Comments
GB10A_75	3.90481	0.06355	0.26586	0.0033	0.4357075	1741	28	1520	17	87	
GB10A_76	3.67154	0.06155	0.25452	0.00319	0.4289578	1708	29	1462	16	86	
GB10A_77	2.89047	0.04988	0.18888	0.00239	0.4260262	1816	30	1115	13	61	
GB10A_78	4.45799	0.07763	0.2162	0.00276	0.4251465	2341	28	1262	15	54	
GB10A_79	3.90779	0.0688	0.23369	0.00297	0.433886	1975	29	1354	16	69	
GB10A_80	7.14867	0.14418	0.3594	0.00499	0.3787977	2279	33	1979	24	87	

GB10A_85	2.36797	0.08185	0.18829	0.00338	0.1869303	1451	67	1112	18	77	
GB10A_86	3.58697	0.05996	0.25466	0.00328	0.4429725	1664	29	1463	17	88	
GB10A_87	9.34539	0.14643	0.39586	0.00499	0.4797314	2570	24	2150	23	84	
GB10A_88	10.12943	0.16066	0.42603	0.00537	0.4709892	2582	25	2288	24	89	
GB10A_89	2.16749	0.04066	0.19117	0.00253	0.3913089	1251	35	1128	14	90	
GB10A_90	0.14018	0.01545	0.0171	0.00045	0.0304468	583	227	109	3	19	
GB10A_91	3.18948	0.0534	0.18468	0.00234	0.4440995	2032	28	1093	13	54	
GB10A_93	1.97664	0.03445	0.12076	0.00155	0.4252434	1937	30	735	9	38	
GB10A_94	3.79208	0.07071	0.257	0.00338	0.3913405	1749	33	1475	17	84	
GB10A_97	5.73353	0.08678	0.30346	0.00382	0.5020479	2190	24	1709	19	78	
GB10A_98	5.55912	0.0899	0.29525	0.00382	0.4601208	2184	26	1668	19	76	
GB10A100	2.86472	0.04549	0.17779	0.00225	0.4681849	1909	27	1055	12	55	
GB10A101	4.13258	0.0771	0.27756	0.00376	0.3935312	1766	33	1579	19	89	
GB10A102	3.71767	0.06025	0.2486	0.00315	0.4603864	1774	28	1431	16	81	
GB10A103	4.11588	0.06988	0.27144	0.00349	0.4323693	1799	29	1548	18	86	
GB10A105	1.07144	0.02475	0.11791	0.00164	0.304043	804	48	719	9	89	
GB10B_001	3.94467	0.05863	0.25755	0.00363	0.6845942	1818	21	1477	19	81	
GB10B_002	5.37824	0.08001	0.3068	0.00435	0.697215	2059	20	1725	21	84	
GB10B_003	3.93148	0.05968	0.26018	0.00373	0.6931968	1793	21	1491	19	83	
GB10B_005	1.88345	0.03205	0.17735	0.00263	0.6272649	1122	27	1053	14	94	
GB10B_006	4.06883	0.0726	0.26054	0.00399	0.5996788	1853	27	1493	20	81	Hf Isotope Analysis #2
GB10B_007	3.99277	0.0634	0.27925	0.00413	0.6982151	1692	22	1588	21	94	Hf Isotope Analysis #3
GB10B_008	1.90196	0.03525	0.17533	0.0027	0.5961066	1164	30	1041	15	89	
GB10B_009	3.95711	0.06775	0.26405	0.00403	0.6614148	1778	24	1511	21	85	Hf Isotope Analysis #4
GB10B_010	3.45348	0.0655	0.24563	0.00389	0.5962376	1661	29	1416	20	85	
GB10B_011	4.24707	0.07575	0.28189	0.00447	0.6557099	1787	26	1601	22	90	Hf Isotope Analysis #7
GB10B_012	4.67978	0.07725	0.25986	0.00403	0.7196919	2106	21	1489	21	71	
GB10B_014	2.6936	0.04804	0.18364	0.00291	0.6598535	1738	25	1087	16	63	
GB10B_015	3.8072	0.06822	0.26036	0.00413	0.6601884	1733	26	1492	21	86	
GB10B_018	4.63452	0.08342	0.29985	0.00477	0.6607492	1834	25	1691	24	92	Hf Isotope Analysis #10
GB10B_021	4.42637	0.07501	0.27243	0.00433	0.7210795	1924	22	1553	22	81	
GB10B_023	4.43245	0.07641	0.28504	0.00454	0.7063078	1845	23	1617	23	88	
GB10B_024	4.01437	0.06949	0.27704	0.00441	0.7041874	1716	23	1576	22	92	Hf Isotope Analysis #14

Analysis #	$^{207}Pb/^{235}U$ Ratio	1σ	$^{206}Pb/^{238}U$ Ratio	1σ	Rho	$^{207}Pb/^{206}Pb$ Age	2σ	$^{206}Pb/^{238}U$ Age	2σ	Conc. %	Comments
GB10B_026	0.17509	0.0052	0.01987	0.00036	0.3627509	739	59	127	2	17	
GB10B_031	4.72839	0.08381	0.25437	0.00405	0.6864727	2162	23	1461	21	68	
GB10B_033	4.96445	0.08194	0.26124	0.00409	0.7275708	2201	21	1496	21	68	
GB10B_035	3.99406	0.06669	0.23821	0.00373	0.7151214	1980	22	1377	19	70	
GB10B_037	3.29046	0.05542	0.21582	0.00337	0.7026299	1810	23	1260	18	70	Hf Isotope Analysis #17

GB10B_044	3.50769	0.06323	0.20277	0.00319	0.6343953	2036	26	1190	17	58	Hf Isotope Analysis #21
GB10B_046	3.42932	0.05065	0.18591	0.00265	0.7100939	2149	19	1099	14	51	
GB10B_047	7.3448	0.10914	0.36448	0.00521	0.7080663	2302	19	2003	25	87	Hf Isotope Analysis #22
GB10B_048	0.622	0.00996	0.06192	0.0009	0.6547815	1010	26	387	5	38	
GB10B_050	4.38449	0.06947	0.28701	0.00419	0.6729406	1813	22	1627	21	90	
GB10B_052	4.30835	0.06703	0.27934	0.00406	0.6944679	1830	21	1588	20	87	
GB10B_054	4.13477	0.06566	0.27871	0.00408	0.6893525	1759	22	1585	21	90	
GB10B_055	4.25619	0.06548	0.26926	0.00401	0.7327538	1874	20	1537	20	82	Hf Isotope Analysis #23
GB10B_057	3.26495	0.0507	0.21693	0.00324	0.7270943	1786	20	1266	17	71	
GB10B_058	6.26048	0.09744	0.32467	0.00486	0.7303282	2226	19	1813	24	81	
GB10B_059	2.55149	0.04016	0.16398	0.00246	0.720201	1846	21	979	14	53	
GB10B_060	2.90649	0.04596	0.19276	0.0029	0.7222421	1789	21	1136	16	64	
GB10B_061	3.93623	0.07714	0.26723	0.00431	0.5599072	1746	31	1527	22	87	Hf Isotope Analysis #26
GB10B_062	2.72118	0.04319	0.14853	0.00225	0.7253864	2136	20	893	13	42	
GB10B_063	3.7382	0.0599	0.20381	0.00309	0.7185077	2138	20	1196	17	56	
GB10B_064	5.75445	0.09244	0.26466	0.00402	0.7195635	2431	20	1514	21	62	Hf Isotope Analysis #24
GB10B_065	3.54706	0.05794	0.2488	0.0038	0.7093667	1686	22	1432	20	85	
GB10B_067	3.74457	0.05939	0.2451	0.00373	0.7372955	1813	20	1413	19	78	Hf Isotope Analysis #27
GB10B_068	4.76	0.07618	0.28374	0.00433	0.7301218	1981	20	1610	22	81	
GB10B_069	3.79463	0.06077	0.25466	0.00388	0.727143	1767	21	1462	20	83	
GB10B_071	4.71612	0.10931	0.21396	0.00389	0.4511407	2454	37	1250	21	51	Hf Isotope Analysis #28
GB10B_072	2.40675	0.03946	0.14779	0.00226	0.7101444	1928	22	889	13	46	Hf Isotope Analysis #29
GB10B_073	4.14282	0.08313	0.25422	0.00418	0.5595203	1929	31	1460	21	76	
GB10B_074	4.08908	0.06705	0.27084	0.00414	0.7125776	1791	22	1545	21	86	
GB10B_075	3.35146	0.05548	0.19444	0.00298	0.7038905	2029	22	1145	16	56	
GB10B_076	3.70533	0.06158	0.21338	0.00327	0.7020691	2042	22	1247	17	61	Hf Isotope Analysis #31
GB10B_077	3.57186	0.06015	0.24217	0.00372	0.691792	1749	23	1398	19	80	
GB10B_080	1.67994	0.02676	0.08595	0.00133	0.7484682	2249	19	532	8	24	Hf Isotope Analysis #33
GB10B_081	0.8532	0.01688	0.09787	0.00157	0.5876269	716	35	602	9	84	
GB10B_083	5.68226	0.09211	0.26049	0.00405	0.7355049	2437	20	1492	21	61	Hf Isotope Analysis #35
GB10B_087	3.095	0.05122	0.20785	0.00324	0.7166815	1766	22	1217	17	69	Hf Isotope Analysis #38
GB10B_088	4.09152	0.06704	0.25602	0.00398	0.7272505	1894	21	1470	20	78	Hf Isotope Analysis #37
GB10B_090	2.01411	0.03462	0.16814	0.00264	0.6908354	1358	25	1002	15	74	
GB10B_093	1.8867	0.03412	0.14225	0.00229	0.6583874	1551	27	857	13	55	Hf Isotope Analysis #41
	$^{207}Pb/^{235}U$		$^{206}Pb/^{238}U$			$^{207}Pb/^{206}Pb$		$^{206}Pb/^{238}U$		Conc.	
Analysis #	**Ratio**	**1σ**	**Ratio**	**1σ**	**Rho**	**Age**	**2σ**	**Age**	**2σ**	**%**	**Comments**
GB10B_094	4.82168	0.08179	0.22182	0.00354	0.7104798	2431	21	1292	19	53	Hf Isotope Analysis #42
GB10B_095	3.32801	0.05528	0.21241	0.00336	0.7325952	1858	21	1242	18	67	Hf Isotope Analysis #43
GB10B_096	1.40063	0.02373	0.08576	0.00136	0.7155193	1933	22	530	8	27	
GB10B_097	2.4838	0.04275	0.17332	0.00277	0.7050739	1695	23	1030	15	61	

Chapter 6 Supplementary Data 3: Broken Hill Stream Sediment Lu-Hf Isotopic Analyses

Sample: KBH-1: GDA 94, 541141 mE, 6476669 mN

Analysis #	$^{176}Hf/^{177}Hf$	2 S.E.	$^{176}Lu/^{177}Hf$	U/Pb AGE	Hf Chur (t)	Hf DM (t)	Hf NC(t)	Hf_i	epsilon	1s	T(DM) (crustal)	T(NC) (crustal)
BH1_01	0.2820918	3.541E-05	0.00262	1480	0.281845	0.282175	0.282100	0.282019	6.17	1.2394303	1.82	1.6585453
BH1_02	0.2817379	3.251E-05	0.0025455	1574	0.281784	0.282106	0.282032	0.281662	-4.33	1.1378702	2.54	2.3759032
BH1_03	0.281617	2.545E-05	0.0022159	1690	0.281709	0.282021	0.281948	0.281546	-5.80	0.890821	2.71	2.5574078
BH1_04	0.2815793	2.402E-05	0.0012698	1941	0.281547	0.281835	0.281765	0.281532	-0.50	0.8405881	2.59	2.4403418
BH1_05	0.2820087	1.605E-05	0.0004054	1181	0.282037	0.282395	0.282316	0.282000	-1.32	0.5619123	2.05	1.8763819
BH1_06	0.2817466	3.452E-05	0.0023411	1698	0.281704	0.282015	0.281942	0.281671	-1.16	1.2081986	2.44	2.2836928
BH1_07	0.2817671	3.597E-05	0.0021868	1761	0.281663	0.281968	0.281896	0.281694	1.10	1.2588346	2.35	2.1976205
BH1_08	0.2820054	3.455E-05	0.001994	1687	0.281711	0.282023	0.281950	0.281942	8.18	1.2090876	1.86	1.7047826
BH1_09	0.2812387	2.31E-05	0.0010771	2520	0.281168	0.281402	0.281339	0.281187	0.66	0.8085444	2.98	2.8424506
BH1_10	0.2816622	1.746E-05	0.0009344	1035	0.282130	0.282502	0.282421	0.281644	-17.23	0.6109548	2.91	2.7338179
BH1_11	0.2816257	1.819E-05	0.0015227	1807	0.281633	0.281934	0.281862	0.281573	-2.12	0.6367467	2.58	2.4299979
BH1_12	0.2819179	1.63E-05	0.0003542	1173	0.282042	0.282401	0.282322	0.281910	-4.68	0.5704127	2.25	2.0763971
BH1_13	0.2816541	2.491E-05	0.0009961	1765	0.281660	0.281965	0.281893	0.281621	-1.41	0.8717828	2.51	2.3531367
BH1_14	0.2817406	1.842E-05	0.0006398	1788	0.281645	0.281948	0.281876	0.281719	2.61	0.6448506	2.28	2.1283307
BH1_15	0.2817465	2.228E-05	0.0014461	1754	0.281668	0.281973	0.281901	0.281698	1.09	0.7796656	2.35	2.1924861
BH1_16	0.2821958	1.692E-05	0.0005176	496	0.282472	0.282893	0.282806	0.282191	-9.96	0.5920268	2.06	1.8676485
BH1_17	0.2816359	2.516E-05	0.0019316	1709	0.281697	0.282007	0.281934	0.281573	-4.39	0.8806936	2.64	2.4878149
BH1_18	0.2814448	1.938E-05	0.0007398	1894	0.281577	0.281869	0.281799	0.281418	-5.64	0.6783825	2.86	2.711558
BH1_19	0.2816535	2.16E-05	0.0014191	1654	0.281733	0.282047	0.281974	0.281609	-4.38	0.7561063	2.60	2.4432096
BH1_20	0.2809485	1.76E-05	0.0007557	2054	0.281473	0.281751	0.281682	0.280919	-19.69	0.6161405	3.82	3.6725075
BH1_21	0.281641	2.153E-05	0.0010694	1811	0.281631	0.281931	0.281860	0.281604	-0.95	0.7535283	2.52	2.3619574
BH1_22	0.2816217	2.647E-05	0.0014467	1942	0.281546	0.281834	0.281764	0.281568	0.81	0.9263029	2.51	2.3627068
BH1_23	0.2818599	2.365E-05	0.0013978	1611	0.281760	0.282079	0.282005	0.281817	2.02	0.827698	2.18	2.0194137
BH1_24	0.2818329	2.77E-05	0.0014628	1593	0.281772	0.282092	0.282018	0.281789	0.59	0.9696372	2.25	2.0916633
BH1_25	0.2818077	2.653E-05	0.0023243	1579	0.281781	0.282103	0.282028	0.281738	-1.51	0.9284427	2.37	2.2088773
BH1_26	0.2814304	1.795E-05	0.0005534	1579	0.281781	0.282103	0.282029	0.281414	-13.03	0.6280915	3.06	2.9047954
BH1_27	0.2817165	1.701E-05	0.0008174	1306	0.281957	0.282304	0.282226	0.281696	-9.24	0.5952828	2.63	2.4601584
BH1_28	0.2816988	3.699E-05	0.0032273	1661	0.281728	0.282042	0.281969	0.281597	-4.64	1.2946982	2.62	2.4643879
BH1_29	0.2816233	1.473E-05	0.0006971	1608	0.281762	0.282081	0.282007	0.281602	-5.68	0.5154139	2.64	2.4850442
BH1_30	0.2816192	2.68E-05	0.0002088	1623	0.281753	0.282070	0.281997	0.281613	-4.97	0.9381267	2.61	2.4535365
BH1_31	0.2816237	2.881E-05	0.001623	1647	0.281737	0.282052	0.281979	0.281573	-5.81	1.0084727	2.68	2.5243585
BH1_32	0.2816068	2.135E-05	0.0015862	1724	0.281687	0.281995	0.281923	0.281555	-4.68	0.7473002	2.67	2.5179758
BH1_33	0.2809814	2.766E-05	0.0015765	2943	0.280890	0.281084	0.281026	0.280892	0.10	0.9682282	3.34	3.2210965
Sample KBH-2: GDA 94, 541234 mE, 6479241 mN												
BH2_01	0.2821125	2.144E-05	0.0008537	1199	0.2819951	0.2823524	0.282304	0.282093	3.48	0.7505059	1.77	1.6613149
BH2_02	0.2823841	1.937E-05	0.0005124	636	0.2823618	0.2827765	0.282707	0.282378	0.57	0.6780794	1.52	1.3701143
BH2_03	0.2816999	4.119E-05	0.0032631	1534	0.2817744	0.2820972	0.282061	0.281605	-6.00	1.4415699	2.60	2.5216753

Analysis #	$^{176}Hf/^{177}Hf$	2 S.E.	$^{176}Lu/^{177}Hf$	U/Pb AGE	Hf Chur (t)	Hf DM (t)	Hf NC(t)	Hf_i	epsilon	1s	T(DM) (crustal)	T(NC) (crustal)
BH2_04	0.2820071	4.209E-05	0.0048871	1656	0.2816937	0.2820038	0.281972	0.281854	5.68	1.4732341	1.98	1.9137408
BH2_05	0.2819225	2.713E-05	0.0017015	1663	0.2816891	0.2819985	0.281967	0.281869	6.38	0.949657	1.94	1.8768523
BH2_06	0.2818742	2.706E-05	0.0012436	1660	0.2816911	0.2820007	0.281969	0.281835	5.11	0.9470763	2.02	1.9518189
BH2_07	0.2816792	2.46E-05	0.0015985	1835	0.2815755	0.2818671	0.281842	0.281624	1.71	0.860977	2.36	2.3065889
BH2_08	0.2817462	3.885E-05	0.0008108	1783	0.2816095	0.2819064	0.281880	0.281719	3.88	1.3597956	2.19	2.1315001
BH2_09	0.2816476	2.372E-05	0.0009453	1629	0.2817119	0.2820248	0.281992	0.281618	-3.32	0.8302234	2.51	2.4378256
BH2_10	0.2820435	2.04E-05	0.0007855	1190	0.282001	0.2823592	0.282310	0.282026	0.88	0.7140311	1.92	1.8140027
BH2_11	0.2821753	1.611E-05	0.0002398	587	0.2823936	0.2828133	0.282742	0.282173	-7.82	0.5638672	2.01	1.8530428
BH2_12	0.2816878	2.151E-05	0.0007489	1790	0.2816049	0.2819011	0.281875	0.281662	2.04	0.7527685	2.31	2.2490499
BH2_13	0.2816352	1.773E-05	0.000957	1844	0.2815691	0.2818597	0.281835	0.281602	1.16	0.6205294	2.40	2.347943
BH2_14	0.2817129	2.761E-05	0.0025509	1664	0.2816883	0.2819975	0.281966	0.281632	-1.98	0.9663018	2.45	2.3867575
BH2_15	0.281182	2.108E-05	0.0005947	2308	0.2812598	0.2815019	0.281495	0.281156	-3.69	0.7379568	3.04	3.0288344
BH2_16	0.2817422	3.589E-05	0.0026268	1674	0.2816822	0.2819905	0.281960	0.281659	-0.82	1.256002	2.39	2.3244125
BH2_17	0.2816662	2.026E-05	0.0008177	1806	0.2815943	0.2818889	0.281863	0.281638	1.56	0.7090503	2.35	2.2916835
BH2_18	0.2807032	3.242E-05	0.0014038	3241	0.2806288	0.2807721	0.280803	0.280616	-0.46	1.1347633	3.57	3.628122
BH2_19	0.2812361	2.203E-05	0.0005983	2269	0.2812856	0.2815318	0.281524	0.281210	-2.68	0.7709083	2.95	2.9362941
BH2_20	0.2816001	2.179E-05	0.0012262	1745	0.281635	0.281936	0.281908	0.281560	-2.68	0.7627929	2.56	2.4962819
BH2_21	0.2816648	1.674E-05	0.0002701	529	0.2824313	0.2828569	0.282783	0.281662	-27.24	0.5860065	3.16	2.999076
BH2_22	0.2818233	1.745E-05	0.0001626	1766	0.2816212	0.28192	0.281893	0.281818	6.98	0.6107582	1.99	1.9276226
BH2_23	0.2817039	2.389E-05	0.0018902	1637	0.2817064	0.2820185	0.281986	0.281645	-2.17	0.8360513	2.44	2.3752991
BH2_24	0.2819239	2.88E-05	0.0013092	1625	0.2817145	0.2820279	0.281995	0.281884	6.00	1.0080856	1.94	1.8674658
BH2_25	0.2829546	2.243E-05	0.0007998	110	0.2827015	0.2831695	0.283080	0.282953	8.90	0.7851111	0.60	0.4002147
BH2_26	0.2816196	2.443E-05	0.0006794	1595	0.2817341	0.2820505	0.282017	0.281599	-4.79	0.8551047	2.57	2.4989761
BH2_27	0.2819312	1.933E-05	0.000768	1610	0.2817241	0.282039	0.282006	0.281908	6.52	0.6766909	1.90	1.823318
BH2_28	0.2819124	4.044E-05	0.0034364	1691	0.2816709	0.2819775	0.281947	0.281802	4.67	1.4155084	2.07	2.0050566
BH2_29	0.2815918	2.289E-05	0.0008778	2053	0.2814304	0.2816992	0.281683	0.281558	4.52	0.8011896	2.36	2.3219097
BH2_30	0.2810913	1.582E-05	0.0002758	2615	0.2810533	0.2812631	0.281269	0.281078	0.86	0.5536994	3.01	3.0184718
Sample KBH-5: GDA 94, 538116 mE, 6450583 mN												
BH5_01	0.282975	1.609E-05	0.0006448	154	0.282688	0.283139	0.283049	0.282973	10.08	0.5631342	0.53	0.3272719
BH5_02	0.2817356	2.218E-05	0.0012834	1743	0.281675	0.281981	0.281909	0.281693	0.66	0.7764066	2.37	2.210012
BH5_03	0.2819321	2.403E-05	0.0014275	1607	0.281763	0.282082	0.282008	0.281889	4.47	0.840896	2.03	1.8667829
BH5_04	0.2824263	1.632E-05	0.0003518	569	0.282426	0.282840	0.282755	0.282423	-0.14	0.5712084	1.50	1.3118166
BH5_05	0.2830067	1.826E-05	0.0007092	174	0.282676	0.283126	0.283035	0.283004	11.61	0.638933	0.45	0.2443821
BH5_08	0.2816015	1.74E-05	0.0005726	1776	0.281653	0.281957	0.281885	0.281582	-2.52	0.6089783	2.58	2.4293294
BH5_09	0.2816416	2.195E-05	0.0015633	1783	0.281649	0.281952	0.281880	0.281589	-2.14	0.768104	2.57	2.4115445
BH5_10	0.2820651	1.856E-05	0.000675	1102	0.282087	0.282452	0.282373	0.282051	-1.27	0.6497033	1.98	1.8105905
BH5_11	0.2820651	1.856E-05	0.000675	918	0.282205	0.282587	0.282505	0.282053	-5.36	0.6497033	2.09	1.9154461
BH5_12	0.2816263	1.906E-05	0.0012608	1686	0.281712	0.282023	0.281950	0.281586	-4.46	0.6672069	2.63	2.4736726
BH5_13	0.2819097	2.148E-05	0.0010786	2031	0.281488	0.281768	0.281699	0.281868	13.50	0.7516961	1.81	1.6651414

Analysis #	$^{176}Hf/^{177}Hf$	2 S.E.	$^{176}Lu/^{177}Hf$	U/Pb AGE	Hf Chur (t)	Hf DM (t)	Hf NC(t)	Hf_i	epsilon	1s	T(DM) (crustal)	T(NC) (crustal)
BH5_14	0.2814895	2.131E-05	0.0006138	1515	0.281822	0.282150	0.282075	0.281472	-12.43	0.7459926	2.98	2.8184627
BH5_15	0.2823455	2.285E-05	0.0011189	917	0.282205	0.282587	0.282506	0.282326	4.28	0.7997895	1.50	1.3160561
BH5_16	0.2829937	2.146E-05	0.0008672	135	0.282700	0.283153	0.283063	0.282992	10.30	0.7509571	0.50	0.297286
BH5_17	0.2825227	2.386E-05	0.0015377	714	0.282334	0.282735	0.282651	0.282502	5.94	0.8351546	1.23	1.0473422
BH5_18	0.2823945	2.273E-05	0.0013353	774	0.282296	0.282691	0.282608	0.282375	2.79	0.7956845	1.48	1.2934185
BH5_19	0.2813944	2.508E-05	0.0010493	1627	0.281750	0.282067	0.281993	0.281362	-13.75	0.8779592	3.14	2.9863881
BH5_20	0.2814236	1.486E-05	0.0003675	1583	0.281778	0.282099	0.282025	0.281413	-12.97	0.5202735	3.06	2.9049006
BH5_21	0.2822019	1.924E-05	0.0005316	1154	0.282054	0.282415	0.282336	0.282190	4.83	0.6732721	1.65	1.474663
Sample kGB-3: GDA 94, 540424 mE, 6482071 mN												
GB3a_hf01	0.2818173	3.001E-05	0.0002212	1639	0.281742	0.282058	0.281985	0.281810	2.43	1.0504983	2.18	2.017567
GB3a_hf03	0.2822231	3.743E-05	0.0006563	511	0.282463	0.282882	0.282796	0.282217	-8.73	1.3101598	1.99	1.8020692
GB3a_hf04	0.2812002	3.816E-05	0.0009773	2463	0.281206	0.281445	0.281381	0.281154	-1.82	1.3354733	3.08	2.9434935
GB3a_hf08	0.2818573	3.625E-05	0.0004484	1141	0.282063	0.282424	0.282345	0.281848	-7.62	1.2686743	2.40	2.2308408
GB3a_hf10	0.2810115	3.874E-05	0.0009441	2825	0.280967	0.281172	0.281113	0.280960	-0.23	1.3557873	3.27	3.1450574
GB3a_hf11	0.2815959	3.168E-05	0.0002588	1202	0.282024	0.282380	0.282301	0.281590	-15.37	1.1087376	2.92	2.7504635
GB3a_hf13	0.2818749	6.123E-05	0.0015071	1744	0.281674	0.281981	0.281908	0.281825	5.36	2.142897	2.08	1.9246336
GB3a_hf14	0.2821029	5.222E-05	0.0007876	1140	0.282063	0.282425	0.282345	0.282086	0.82	1.8278162	1.88	1.7117245
GB3a_hf20	0.2816784	2.842E-05	0.0002013	1646	0.281737	0.282053	0.281980	0.281672	-2.32	0.9947039	2.47	2.3121943
GB3a_hf21	0.2816032	7.793E-05	0.0024286	1693	0.281707	0.282018	0.281945	0.281525	-6.45	2.7275694	2.76	2.5996134
GB3a_hf23	0.2819692	3.731E-05	0.0004574	1187	0.282033	0.282391	0.282312	0.281959	-2.62	1.3059441	2.13	1.9614076
GB3a_hf24	0.2821206	5.142E-05	0.0006006	1257	0.281988	0.282339	0.282261	0.282106	4.20	1.7998002	1.77	1.5979343
GB3a_hf25	0.2813109	2.696E-05	0.0003417	1828	0.281619	0.281918	0.281847	0.281299	-11.38	0.9437381	3.15	3.0029315
GB3a_hf27	0.2816784	3.089E-05	0.0004462	1629	0.281748	0.282065	0.281992	0.281665	-2.97	1.0811312	2.50	2.3380992
GB3a_hf28	0.2819601	5.788E-05	0.0016847	1617	0.281757	0.282075	0.282001	0.281909	5.40	2.0256669	1.98	1.8178475
GB3a_hf31	0.2821286	3.078E-05	0.0004759	1170	0.282044	0.282403	0.282324	0.282118	2.64	1.0773835	1.80	1.6235395
GB3a_hf36	0.2816811	0.0001047	0.0031166	1717	0.281692	0.282001	0.281928	0.281580	-3.98	3.6648485	2.62	2.4695342
GB3a_hf38	0.2819121	3.131E-05	0.0005063	1204	0.282022	0.282378	0.282300	0.281901	-4.31	1.0959295	2.25	2.0785436
GB3a_hf39	0.2815911	4.454E-05	0.0010094	1970	0.281528	0.281813	0.281744	0.281553	0.91	1.5588657	2.53	2.37891
GB3a_hf46	0.2817183	3.777E-05	0.0015654	1827	0.281620	0.281919	0.281848	0.281664	1.56	1.321991	2.38	2.2238468
GB3a_hf48	0.2813664	3.775E-05	0.0005788	2294	0.281316	0.281571	0.281506	0.281341	0.88	1.321171	2.78	2.6447214
GB3a_hf52	0.2818675	3.072E-05	0.0003555	1245	0.281996	0.282348	0.282270	0.281859	-4.84	1.0751159	2.31	2.144036
GB3a_hf53	0.2818553	3.99E-05	0.0009794	1589	0.281774	0.282095	0.282021	0.281826	1.82	1.3963318	2.17	2.013584
GB3a_hf54	0.2822223	5.616E-05	0.0010459	1420	0.281884	0.282220	0.282144	0.282194	11.02	1.965512	1.48	1.3088282
Sample kGB-8: GDA94, 535532 mE, 6461873 mN												
GB8_hf01	0.2829675	5.152E-05	0.0007177	103	0.282720	0.283176	0.283085	0.282966	8.69	1.8030711	0.58	0.3744724
GB8_hf02	0.2816639	3.846E-05	0.0006031	1840	0.281612	0.281909	0.281838	0.281643	1.10	1.3459746	2.41	2.2618943
GB8_hf03	0.2816947	5.244E-05	0.0016779	1686	0.281712	0.282024	0.281951	0.281641	-2.51	1.8353932	2.51	2.3557129
GB8_hf04	0.2818972	5.351E-05	0.0021706	1678	0.281717	0.282029	0.281956	0.281828	3.96	1.8728537	2.11	1.9562418

Analysis #	$^{176}Hf/^{177}Hf$	2 S.E.	$^{176}Lu/^{177}Hf$	U/Pb AGE	Hf Chur (t)	Hf DM (t)	Hf NC(t)	Hf_i	epsilon	1s	T(DM) (crustal)	T(NC) (crustal)
GB8_hf05	0.2812924	2.927E-05	0.0003884	1936	0.281550	0.281838	0.281768	0.281278	-9.64	1.024346	3.13	2.9848261
GB8_hf06	0.2815831	4.532E-05	0.002078	1859	0.281599	0.281895	0.281824	0.281510	-3.18	1.5861265	2.69	2.536107
GB8_hf07	0.2820048	5.362E-05	0.0013685	1152	0.282055	0.282416	0.282337	0.281975	-2.84	1.876646	2.12	1.9470129
GB8_hf08	0.2820411	3.679E-05	0.0007437	1254	0.281990	0.282342	0.282264	0.282023	1.18	1.2877225	1.95	1.7811741
GB8_hf09	0.2816136	3.807E-05	0.0007717	1760	0.281664	0.281969	0.281897	0.281588	-2.70	1.3325999	2.58	2.4268658
GB8_hf10	0.2813346	4.079E-05	0.0004825	2146	0.281413	0.281682	0.281614	0.281315	-3.48	1.4277415	2.93	2.7853366
GB8_hf11	0.2825305	4.369E-05	0.0009619	550	0.282439	0.282854	0.282768	0.282521	2.90	1.529041	1.30	1.10533
GB8_hf12	0.281916	3.908E-05	0.0007158	1634	0.281745	0.282062	0.281988	0.281894	5.27	1.3679393	2.00	1.839743
GB8_hf13	0.2825317	4.889E-05	0.0008636	320	0.282584	0.283020	0.282932	0.282527	-2.04	1.711297	1.43	1.2318528
GB8_hf14	0.2821564	3.547E-05	0.0007233	1095	0.282092	0.282458	0.282378	0.282141	1.75	1.2415025	1.79	1.6173328
GB8_hf15	0.2820403	3.839E-05	0.0009084	1200	0.282025	0.282381	0.282303	0.282020	-0.18	1.3436657	1.99	1.8213397
GB8_hf16	0.2829424	3.431E-05	0.0007171	106	0.282719	0.283174	0.283084	0.282941	7.86	1.2007822	0.64	0.4300548
GB8_hf17	0.2820691	3.144E-05	0.0005207	1086	0.282098	0.282465	0.282385	0.282058	-1.40	1.1003546	1.98	1.8045548
GB8_hf18	0.2823241	3.362E-05	0.0005009	917	0.282206	0.282588	0.282506	0.282315	3.89	1.1766222	1.52	1.3400753
GB8_hf19	0.2816448	3.688E-05	0.0007883	1727	0.281685	0.281993	0.281921	0.281619	-2.35	1.2908296	2.53	2.3791698
GB8_hf20	0.281971	2.819E-05	0.0002112	1003	0.282151	0.282525	0.282445	0.281967	-6.52	0.9866928	2.23	2.0536933
GB8_hf21	0.2816928	3.908E-05	0.0008163	1789	0.281645	0.281947	0.281875	0.281665	0.72	1.3678729	2.40	2.2436894
GB8_hf22	0.2815099	3.995E-05	0.0003728	2161	0.281403	0.281671	0.281604	0.281495	3.24	1.3981425	2.54	2.3944337
GB8_hf23	0.2825655	3.395E-05	0.0007933	294	0.282600	0.283039	0.282950	0.282561	-1.38	1.1882021	1.37	1.1700497
GB8_hf24	0.2828666	4.195E-05	0.0014161	2582	0.281128	0.281356	0.281293	0.282797	59.37	1.4683891	-0.56	-0.703731
GB8_hf25	0.2819514	3.377E-05	0.0014928	1786	0.281647	0.281949	0.281878	0.281901	9.02	1.1819993	1.89	1.7355783
GB8_hf26	0.2819669	3.339E-05	0.0009402	1756	0.281666	0.281972	0.281900	0.281936	9.56	1.1687317	1.83	1.677723
GB8_hf27	0.281483	6.45E-05	0.0020248	1115	0.282079	0.282443	0.282364	0.281440	-22.64	2.2575882	3.29	3.121981
GB8_hf28	0.2823425	4.316E-05	0.0007185	1036	0.282130	0.282501	0.282421	0.282328	7.05	1.5104789	1.42	1.24025
GB8_hf29	0.2824013	5.484E-05	0.0016486	567	0.282428	0.282842	0.282756	0.282384	-1.56	1.9194845	1.59	1.3992483
GB8_hf30	0.2814437	3.957E-05	0.0006535	1891	0.281579	0.281872	0.281801	0.281420	-5.63	1.3849564	2.86	2.7088384
GB8_hf31	0.2817207	3.266E-05	0.000134	1624	0.281752	0.282070	0.281996	0.281717	-1.26	1.1430304	2.39	2.2296284
Sample kGB-10: GDA 94, 560926 mE, 6469785 mN												
GB10_hf01	0.2820764	2.118E-05	0.00028	1269	0.281981	0.282331	0.282253	0.282070	3.16	0.7414439	1.84	1.6711982
GB10_hf02	0.2814977	0.0001009	0.0018368	1853	0.281604	0.281900	0.281829	0.281433	-6.06	3.5307446	2.85	2.7036008
GB10_hf03	0.2816261	6.35E-05	0.0024893	1692	0.281708	0.282019	0.281946	0.281546	-5.74	2.2224953	2.71	2.5556052
GB10_hf04	0.2816312	3.532E-05	0.0007772	1778	0.281652	0.281956	0.281884	0.281605	-1.68	1.2362032	2.53	2.3795747
GB10_hf06	0.2816157	4.688E-05	0.002044	1711	0.281696	0.282005	0.281933	0.281549	-5.20	1.6406863	2.69	2.5379174
GB10_hf07	0.2814373	5.979E-05	0.0009313	1787	0.281646	0.281949	0.281877	0.281406	-8.54	2.0928107	2.95	2.8003641
GB10_hf08	0.2814916	9.198E-05	0.0028013	1816	0.281628	0.281928	0.281856	0.281395	-8.26	3.2191296	2.96	2.8063325
GB10_hf09	0.2816166	4.799E-05	0.0012373	1599	0.281768	0.282088	0.282014	0.281579	-6.70	1.6797949	2.70	2.5393721
GB10_hf10	0.2813333	3.907E-05	0.0004727	1834	0.281616	0.281914	0.281843	0.281317	-10.63	1.3675822	3.11	2.9621894
GB10_hf11	0.2825276	4.101E-05	0.0009828	2592	0.281121	0.281348	0.281286	0.282479	48.31	1.4353076	0.14	0.0019466
GB10_hf12	0.2811292	3.204E-05	0.0008853	2451	0.281214	0.281454	0.281390	0.281088	-4.48	1.1212784	3.22	3.090628

Analysis #	$^{176}Hf/^{177}Hf$	2 S.E.	$^{176}Lu/^{177}Hf$	U/Pb AGE	Hf Chur (t)	Hf DM (t)	Hf NC(t)	Hf_i	epsilon	1s	T(DM) (crustal)	T(NC) (crustal)
GB10_hf13	0.2816157	3.764E-05	0.0007317	1574	0.281784	0.282106	0.282032	0.281594	-6.75	1.3173799	2.68	2.5226109
GB10_hf14	0.2818483	4.312E-05	0.0011558	1716	0.281692	0.282001	0.281929	0.281811	4.21	1.5091121	2.13	1.9719313
GB10_hf15	0.2814173	4.656E-05	0.0011375	2520	0.281168	0.281402	0.281339	0.281363	6.92	1.629584	2.60	2.4700298
GB10_hf16	0.2816372	9.077E-05	0.0025453	1671	0.281721	0.282034	0.281961	0.281557	-5.85	3.1770822	2.70	2.5455731
GB10_hf17	0.281642	5.673E-05	0.0015795	1810	0.281632	0.281932	0.281861	0.281588	-1.56	1.9853842	2.55	2.3981094
GB10_hf18	0.2811971	3.004E-05	0.0003211	1861	0.281599	0.281894	0.281823	0.281186	-14.66	1.0515134	3.37	3.2239688
GB10_hf19	0.2811281	3.845E-05	0.0009315	2533	0.281159	0.281392	0.281329	0.281083	-2.72	1.3457695	3.19	3.0534599
GB10_hf20	0.2815996	4.191E-05	0.0009907	1726	0.281686	0.281994	0.281921	0.281567	-4.21	1.4668702	2.65	2.4908343
GB10_hf21	0.281594	6.526E-05	0.0017851	2036	0.281485	0.281764	0.281695	0.281525	1.43	2.2839497	2.55	2.401536
GB10_hf22	0.2812178	4.259E-05	0.0006429	2302	0.281311	0.281566	0.281500	0.281190	-4.32	1.4905633	3.10	2.9611465
GB10_hf23	0.2812632	4.869E-05	0.0008509	1874	0.281590	0.281884	0.281813	0.281233	-12.67	1.7040618	3.27	3.1163232
GB10_hf24	0.281149	4.067E-05	0.0017333	2431	0.281226	0.281469	0.281405	0.281069	-5.61	1.4235292	3.28	3.1419911
GB10_hf25	0.2819871	6.3E-05	0.0023676	1686	0.281712	0.282023	0.281950	0.281912	7.10	2.205092	1.93	1.7708359
GB10_hf26	0.2811538	4.239E-05	0.0016873	1746	0.281673	0.281979	0.281907	0.281098	-20.41	1.483798	3.63	3.4758315
GB10_hf27	0.2814666	5.981E-05	0.0020777	1813	0.281630	0.281930	0.281858	0.281395	-8.32	2.0934756	2.96	2.8078315
GB10_hf28	0.2812369	3.472E-05	0.0009006	2454	0.281211	0.281451	0.281388	0.281195	-0.59	1.2151037	3.00	2.8632096
GB10_hf29	0.2816132	4.876E-05	0.0014821	1928	0.281555	0.281844	0.281774	0.281559	0.15	1.7066391	2.54	2.3910051
GB10_hf30	0.2815892	6.572E-05	0.0022545	1929	0.281554	0.281843	0.281773	0.281507	-1.69	2.3001734	2.65	2.5023303
GB10_hf31	0.2812992	7.394E-05	0.0013345	2042	0.281481	0.281759	0.281691	0.281247	-8.29	2.5877975	3.13	2.9883836
GB10_hf32	0.2815631	3.611E-05	0.0015393	1681	0.281715	0.282027	0.281954	0.281514	-7.12	1.2637051	2.79	2.6306973
GB10_hf33	0.2816554	6.193E-05	0.0015976	2249	0.281346	0.281605	0.281539	0.281587	8.57	2.167425	2.29	2.1459345
GB10_hf34	0.2824014	3.622E-05	0.0005058	900	0.282216	0.282600	0.282518	0.282393	6.26	1.2677038	1.36	1.1785535
GB10_hf35	0.2813691	9.569E-05	0.0024973	2437	0.281223	0.281465	0.281400	0.281253	1.07	3.3493186	2.89	2.750011
GB10_hf36	0.2818052	4.507E-05	0.0008735	1707	0.281698	0.282008	0.281935	0.281777	2.80	1.5773733	2.21	2.050255
GB10_hf37	0.2816688	8.783E-05	0.003622	1894	0.281577	0.281869	0.281799	0.281539	-1.36	3.0739017	2.60	2.4542237
GB10_hf38	0.281584	3.975E-05	0.0012763	1766	0.281660	0.281964	0.281892	0.281541	-4.21	1.3913744	2.68	2.5229339
GB10_hf39	0.2818092	7.686E-05	0.0024091	1692	0.281708	0.282019	0.281946	0.281732	0.86	2.6901255	2.31	2.1561902
GB10_hf40	0.2815874	5.518E-05	0.0023639	2393	0.281251	0.281497	0.281433	0.281480	8.11	1.9312751	2.43	2.293179
GB10_hf41	0.2821338	4.305E-05	0.0012663	1551	0.281799	0.282123	0.282048	0.282097	10.58	1.5068558	1.61	1.4456622
GB10_hf42	0.2813992	0.0001127	0.0025414	2431	0.281227	0.281469	0.281405	0.281281	1.93	3.9455875	2.83	2.6935552
GB10_hf43	0.2816007	8.691E-05	0.0035132	1858	0.281600	0.281896	0.281825	0.281477	-4.38	3.041892	2.76	2.6073258
GB10_hf44	0.2815536	6.568E-05	0.001827	1687	0.281711	0.282023	0.281950	0.281495	-7.67	2.2989275	2.82	2.6679605
GB10_hf45	0.2816443	5.641E-05	0.0014499	1776	0.281654	0.281957	0.281885	0.281596	-2.07	1.9743373	2.56	2.4012609

Chapter 6 Supplementary Data 4: Strzelecki Sand Dunes U-Pb isotopic data

Sample SDF-1: GDA 94, 507803 mE, 6596929 mN

Analysis #	$^{207}Pb/^{235}U$ Ratio	1σ	$^{206}Pb/^{238}U$ Ratio	1σ	Rho	$^{207}Pb/^{206}Pb$ Age	2σ	$^{206}Pb/^{238}U$ Age	2σ	Conc. %	Comments
SDF1_004	2.09492	0.04304	0.19274	0.00268	0.3843255	1169.9	38.96	1136.2	14.47	97	
SDF1_008	3.20114	0.06779	0.24914	0.00357	0.4002368	1492.8	37.9	1434	18.41	96	
SDF1_009	0.50076	0.0179	0.06538	0.00107	0.2146974	435.6	78.26	408.3	6.48	94	
SDF1_011	0.92241	0.02065	0.10729	0.00156	0.3413803	685.1	46.57	657	9.11	96	
SDF1_013	1.85251	0.07601	0.17821	0.00347	0.1782832	1079.7	82.48	1057.2	18.96	98	
SDF1_026	0.34706	0.00762	0.04795	0.00067	0.3621248	307.3	47.66	301.9	4.15	98	
SDF1_027	0.32769	0.01144	0.0458	0.00071	0.2114751	280.6	78.28	288.7	4.4	103	
SDF1_030	2.15147	0.03737	0.19768	0.00266	0.4790601	1170.6	31.56	1162.8	14.31	99	
SDF1_034	3.82697	0.07953	0.27592	0.00395	0.3859139	1635.2	37.08	1570.8	19.94	96	Hf Isotope Analysis #1
SDF1_035	12.52447	0.23763	0.49074	0.00682	0.4278753	2699.3	29.56	2573.9	29.48	95	
SDF1_037	0.67534	0.02447	0.08531	0.00136	0.1990248	507.5	78.99	527.7	8.08	104	Hf Isotope Analysis #2
SDF1_041	2.00529	0.04048	0.18582	0.00261	0.3926663	1153.8	38.26	1098.7	14.16	95	
SDF1_042	0.32353	0.0127	0.04535	0.00073	0.1704829	274.5	88.74	285.9	4.53	104	
SDF1_044	0.96838	0.01936	0.11251	0.00153	0.3845288	689.1	40.73	687.3	8.88	100	
SDF1_045	2.45518	0.0408	0.21201	0.00278	0.478612	1292.5	29.81	1239.5	14.77	96	
SDF1_050	0.51308	0.01081	0.06689	0.00091	0.351462	437.1	44.83	417.4	5.47	95	
SDF1_051	0.52285	0.01616	0.06832	0.00102	0.2234089	431.9	67.7	426.1	6.17	99	Hf Isotope Analysis #3
SDF1_053	2.31375	0.03883	0.20574	0.00269	0.4699416	1234.8	30.55	1206.1	14.37	98	Hf Isotope Analysis #4
SDF1_056	0.50427	0.0183	0.06603	0.00107	0.1779611	427.3	80.46	412.2	6.46	96	Hf Isotope Analysis #5
SDF1_057	0.28537	0.01823	0.04032	0.00086	0.0821144	255.4	144.73	254.8	5.34	100	Hf Isotope Analysis #6
SDF1_058	0.40254	0.00972	0.05534	0.00077	0.2931978	317.9	53.6	347.2	4.72	109	
SDF1_059	1.87531	0.03975	0.17988	0.0025	0.3490626	1084.5	41.3	1066.3	13.67	98	
SDF1_060	0.54446	0.01211	0.07028	0.00096	0.3326459	458.9	48.26	437.9	5.79	95	
SDF1_062	1.68717	0.03263	0.16685	0.00226	0.3883154	1023.3	37.57	994.7	12.48	97	Hf Isotope Analysis #7
SDF1_067	1.43754	0.05286	0.14695	0.0026	0.1756083	956.4	75.63	883.8	14.6	92	
SDF1_068	3.61726	0.05991	0.27004	0.00349	0.4592238	1570.2	28.97	1541	17.7	98	
SDF1_069	0.52651	0.01433	0.06889	0.001	0.2528365	429.6	59.74	429.5	6.02	100	
SDF1_070	0.39304	0.02119	0.05318	0.00107	0.0941602	355.8	120.68	334	6.56	94	
SDF1_071	3.17538	0.07329	0.2514	0.00365	0.3032937	1459.8	43.7	1445.7	18.82	99	
SDF1_082	0.59336	0.01538	0.07616	0.00109	0.2577774	472.4	57.11	473.2	6.54	100	
SDF1_083	3.87854	0.06225	0.27795	0.00356	0.4628744	1647.2	27.99	1581	17.97	96	
SDF1_084	0.82925	0.01574	0.09966	0.00129	0.3737217	616.9	39.67	612.4	7.56	99	
SDF1_087	4.08582	0.08699	0.28484	0.00387	0.3103147	1699.5	38.89	1615.7	19.42	95	
SDF1_088	2.039	0.03614	0.18913	0.00243	0.3980243	1152.3	33.88	1116.6	13.18	97	
SDF1_089	0.10105	0.00441	0.0153	0.00027	0.1307169	93.4	104.14	97.9	1.69	105	Hf Isotope Analysis #8
SDF1_090	2.17641	0.05455	0.1959	0.00286	0.2657047	1211.6	49.19	1153.2	15.43	95	
SDF1_091	0.77462	0.01558	0.0946	0.00124	0.3446389	581.8	42.57	582.7	7.3	100	

Analysis #	$^{207}Pb/^{235}U$ Ratio	1σ	$^{206}Pb/^{238}U$ Ratio	1σ	Rho	$^{207}Pb/^{206}Pb$ Age	2σ	$^{206}Pb/^{238}U$ Age	2σ	Conc. %	Comments
SDF1_092	0.50592	0.01747	0.06679	0.00103	0.1725675	410.2	76.45	416.8	6.2	102	
SDF1_095	0.58594	0.01705	0.07438	0.00112	0.2267375	496.4	64.51	462.5	6.75	93	
SDF1_096	4.61589	0.06923	0.3064	0.00382	0.4929741	1787.4	25.31	1723	18.84	96	Hf Isotope Analysis #9
SDF1_097	0.8172	0.02942	0.09887	0.00158	0.1676853	602.1	77.66	607.8	9.25	101	Hf Isotope Analysis #10
SDF1_098	0.29339	0.02039	0.04164	0.00097	0.060061	247.3	157.88	263	6.03	106	
SDF1_099	13.20604	0.2248	0.51185	0.00667	0.4137917	2717.7	27.12	2664.5	28.43	98	Hf Isotope Analysis #11
SDF1_100	3.74253	0.05728	0.27197	0.00335	0.4717251	1620.8	26.64	1550.8	17	96	
SDF1_102	0.35316	0.01313	0.04874	0.00076	0.1535251	310.1	84.19	306.8	4.69	99	
SDF1_104	0.31903	0.00879	0.04458	0.00063	0.2293315	281.4	62.61	281.2	3.88	100	Hf Isotope Analysis #12
SDF1_105	0.48744	0.01258	0.06428	0.00089	0.2417658	412.9	56.6	401.6	5.36	97	Hf Isotope Analysis #13
SDF1_107	0.51478	0.01721	0.0673	0.001	0.1799561	432.1	73.92	419.9	6.04	97	
SDF1_108	0.44068	0.01291	0.05891	0.00084	0.2175801	382.4	65.25	369	5.09	96	Hf Isotope Analysis #14
SDF1_111	0.39128	0.01132	0.05357	0.00078	0.2171654	329.2	65.46	336.4	4.78	102	
SDF1_112	0.68593	0.02086	0.08682	0.00126	0.2061126	503.4	67.13	536.7	7.44	107	
SDF1_113	0.49804	0.01216	0.06527	0.00089	0.2681489	426.6	53.58	407.6	5.39	96	
SDF1_114	0.48213	0.01723	0.06348	0.00099	0.1577861	415.6	79.53	396.8	5.99	95	
SDF1_117	0.67865	0.0163	0.08432	0.00114	0.2590508	544.6	52.21	521.8	6.77	96	Hf Isotope Analysis #15
SDF1_118	0.75226	0.06129	0.0929	0.00237	0.061772	559.3	173.16	572.7	13.96	102	Hf Isotope Analysis #16
SDF1_119	0.73705	0.03639	0.09141	0.00162	0.1089506	548	106.85	563.9	9.55	103	Hf Isotope Analysis #17
SDF1_120	0.60103	0.01882	0.07653	0.00116	0.1756539	489.2	70.2	475.3	6.94	97	Hf Isotope Analysis #18
SDF1_121	1.51402	0.03098	0.154	0.00203	0.3212001	966.3	41.24	923.4	11.34	96	
SDF1_123	3.58641	0.07367	0.26585	0.00345	0.2995393	1583	38.22	1519.7	17.56	96	Hf Isotope Analysis #19
SDF1_125	0.57188	0.01509	0.07395	0.00103	0.2248221	455.4	58.6	459.9	6.16	101	
SDF1_127	4.7931	0.09978	0.31493	0.00435	0.3103656	1805.5	37.82	1764.9	21.34	98	Hf Isotope Analysis #20
SDF1_128	0.20503	0.00968	0.02978	0.0005	0.1014601	191.4	108.92	189.2	3.13	99	
SDF1_130	4.64788	0.0789	0.31143	0.00387	0.393314	1769.6	30.16	1747.7	19.02	99	
SDF1_131	0.15491	0.01856	0.02294	0.00056	0.0320962	146.4	262.67	146.2	3.54	100	Hf Isotope Analysis #21
SDF1_132	0.72773	0.01691	0.09045	0.0012	0.2674186	543.2	50.56	558.2	7.09	103	
SDF1_133	4.3602	0.06419	0.29663	0.00359	0.4563838	1742.5	25.56	1674.6	17.83	96	Hf Isotope Analysis #22
SDF1_134	2.17018	0.03793	0.19804	0.00249	0.3787085	1184.2	33.69	1164.8	13.37	98	
SDF1_135	0.56542	0.01485	0.07212	0.00101	0.2331901	485.9	58.63	448.9	6.06	92	
SDF1_138	0.14072	0.00981	0.02093	0.0004	0.0720191	136.6	158.93	133.6	2.51	98	Hf Isotope Analysis #23
SDF1_139	2.20841	0.03854	0.19855	0.00248	0.3757667	1213.8	33.47	1167.6	13.32	96	
SDF1_140	0.413	0.01345	0.05569	0.00081	0.1738934	362.3	73.13	349.4	4.96	96	
SDF1_145	1.77685	0.03282	0.17253	0.00213	0.3465291	1062.8	36.41	1026	11.7	97	
SDF1_146	2.32394	0.04105	0.20451	0.00251	0.3830905	1256.5	33.2	1199.5	13.43	95	
SDF1_147	0.30451	0.01144	0.04253	0.00067	0.1633435	284	85.29	268.5	4.13	95	Hf Isotope Analysis #24
SDF1_149	4.63728	0.08064	0.30623	0.00379	0.4420734	1797.7	29.41	1722.1	18.73	96	
SDF1_151	0.31963	0.01211	0.04435	0.00071	0.1886335	297.9	84.86	279.8	4.39	94	
SDF1_154	2.27912	0.03321	0.20516	0.00246	0.476173	1211.4	26.81	1203	13.18	99	

Analysis #	$^{207}Pb/^{235}U$ Ratio	1σ	$^{206}Pb/^{238}U$ Ratio	1σ	Rho	$^{207}Pb/^{206}Pb$ Age	2σ	$^{206}Pb/^{238}U$ Age	2σ	Conc. %	Comments
SDF1_155	3.66303	0.05835	0.27209	0.00336	0.4328226	1579.7	28.38	1551.4	17.02	98	Hf Isotope Analysis #25
SDF1_157	0.36125	0.00716	0.04984	0.00063	0.3370382	310.7	44	313.6	3.87	101	
SDF1_158	0.49924	0.01843	0.06609	0.00101	0.1502153	404.1	81.65	412.5	6.13	102	
SDF1_160	0.48705	0.01238	0.0642	0.00087	0.2514493	413.6	55.72	401.1	5.29	97	Hf Isotope Analysis #26
SDF1_161	0.36716	0.00905	0.05045	0.00067	0.2571608	320.3	55.37	317.3	4.13	99	
SDF1_167	0.34948	0.00911	0.04851	0.00066	0.2231056	298.4	59.34	305.4	4.08	102	
SDF1_168	3.64858	0.05956	0.27019	0.00332	0.4085909	1585.8	29.4	1541.8	16.86	97	
SDF1_169	0.39616	0.01049	0.05326	0.00073	0.2295918	369	59.32	334.5	4.49	91	
SDF1_171	0.48514	0.01815	0.06388	0.00102	0.1453922	415.8	83.24	399.2	6.19	96	Hf Isotope Analysis #27
SDF1_172	0.315	0.01432	0.04405	0.00073	0.1097831	279.9	103.14	277.9	4.5	99	
SDF1_175	3.47817	0.06099	0.26422	0.00332	0.3702604	1537.8	32.29	1511.4	16.91	98	Hf Isotope Analysis #28
SDF1_176	0.09916	0.01194	0.01498	0.00042	0.0213535	101	267.5	95.8	2.68	95	Hf Isotope Analysis #29
SDF1_178	0.57042	0.02293	0.07452	0.00122	0.1392532	433.2	89.53	463.3	7.33	107	
SDF1_180	2.05888	0.04821	0.18889	0.00266	0.2659627	1174	46.48	1115.3	14.4	95	
SDF1_181	0.5954	0.01295	0.07645	0.00099	0.2824242	471.3	48.2	474.9	5.93	101	
SDF1_182	1.56787	0.03406	0.1591	0.00212	0.2890125	971.7	44.24	951.8	11.8	98	Hf Isotope Analysis #30
SDF1_183	0.71848	0.02231	0.08901	0.00131	0.1885227	551.1	67.96	549.7	7.75	100	Hf Isotope Analysis #31
SDF1_185	18.51897	0.51513	0.5919	0.00878	0.215562	3032.5	45.08	2997.1	35.55	99	
SDF1_186	3.62105	0.05786	0.26955	0.00328	0.4122225	1576.6	28.85	1538.5	16.66	98	
SDF1_187	0.12838	0.00566	0.01926	0.00031	0.1208876	117.5	103.1	123	1.94	105	
SDF1_188	0.38164	0.02157	0.05252	0.00105	0.0818119	318.1	127.4	330	6.45	104	
SDF1_190	0.55066	0.01736	0.07209	0.00108	0.1849741	428.5	70.29	448.7	6.51	105	Hf Isotope Analysis #33
SDF1_193	0.13979	0.0065	0.02085	0.00034	0.1131651	130.1	108.28	133.1	2.14	102	Hf Isotope Analysis #34
SDF1_194	2.12418	0.04106	0.19263	0.0025	0.3320325	1196.7	37.68	1135.6	13.5	95	
SDF1_196	3.60058	0.05717	0.27182	0.00331	0.4136278	1549.6	28.88	1550	16.76	100	Hf Isotope Analysis #35
SDF1_199	0.32302	0.01047	0.04529	0.00066	0.1675461	274.1	74.35	285.5	4.07	104	
SDF1_200	4.69682	0.07786	0.31351	0.00385	0.3864908	1777.3	29.57	1758	18.87	99	
SDF1_201	0.33936	0.01319	0.04756	0.00077	0.1377817	274.6	89.02	299.5	4.71	109	
Discordant Analyses - Not used											
SDF1_001	0.3175	0.0112	0.04348	0.00067	0.1813423	329.3	79.18	274.4	4.12	83	
SDF1_002	2.15879	0.04395	0.19253	0.00267	0.3735137	1231.5	38.49	1135	14.41	92	
SDF1_003	0.32764	0.01511	0.04379	0.00073	0.1307249	384.4	101.42	276.3	4.54	72	
SDF1_005	2.16009	0.03955	0.19287	0.0026	0.4465303	1228.8	33.55	1136.9	14.03	93	
SDF1_006	0.25096	0.01169	0.03795	0.00065	0.141464	97.6	109.29	240.1	4.06	246	
SDF1_007	0.45252	0.00968	0.04187	0.00059	0.3719337	1157.9	40.56	264.4	3.66	23	
SDF1_010	0.32032	0.01304	0.04677	0.00075	0.1753356	180.7	92.77	294.7	4.64	163	
SDF1_012	0.13413	0.01832	0.02016	0.00054	0.0348335	111.2	297.53	128.7	3.43	116	
SDF1_014	1.93405	0.04497	0.17949	0.00267	0.3432297	1150.9	44.88	1064.2	14.57	92	
SDF1_015	0.66396	0.01428	0.07074	0.00101	0.3767293	870.9	42.73	440.6	6.06	51	
SDF1_016	1.00261	0.01715	0.07955	0.00107	0.4897248	1455	29.66	493.4	6.42	34	

Analysis #	$^{207}Pb/^{235}U$ Ratio	1σ	$^{206}Pb/^{238}U$ Ratio	1σ	Rho	$^{207}Pb/^{206}Pb$ Age	2σ	$^{206}Pb/^{238}U$ Age	2σ	Conc. %	Comments
SDF1_017	2.23287	0.05776	0.19728	0.00305	0.2935014	1247.5	49.8	1160.7	16.4	93	
SDF1_024	0.40347	0.01002	0.05331	0.00078	0.3234798	408	53.14	334.8	4.77	82	
SDF1_025	2.92757	0.0473	0.23114	0.00308	0.5244258	1464.4	27.57	1340.5	16.13	92	
SDF1_028	0.65039	0.01549	0.07687	0.00114	0.3351741	652.5	49.54	477.4	6.82	73	
SDF1_029	0.35109	0.01665	0.04653	0.00082	0.1392722	401.2	104.23	293.2	5.08	73	
SDF1_031	0.49677	0.01464	0.06746	0.00101	0.259027	346.2	65.26	420.8	6.1	122	
SDF1_032	2.8139	0.05139	0.17478	0.00241	0.4573778	1907.5	30.49	1038.4	13.21	54	
SDF1_033	0.77864	0.02394	0.08987	0.0014	0.2349379	702.9	64.57	554.8	8.27	79	
SDF1_036	0.60331	0.01426	0.05436	0.0008	0.3222139	1209.5	45.63	341.2	4.87	28	
SDF1_038	0.15698	0.0113	0.02059	0.00044	0.0720178	424.2	156.67	131.4	2.81	31	
SDF1_039	0.31331	0.00798	0.042	0.00062	0.3000015	375.6	55.73	265.2	3.81	71	
SDF1_040	0.33321	0.01391	0.04491	0.00077	0.1575542	363.2	93.04	283.2	4.75	78	
SDF1_043	0.61577	0.01656	0.08034	0.00122	0.276706	436.1	58.6	498.2	7.27	114	
SDF1_046	0.19889	0.00758	0.02687	0.00043	0.1698359	357.6	84.85	171	2.69	48	
SDF1_047	0.15039	0.0044	0.02163	0.00032	0.2463197	214.6	66.74	138	2	64	
SDF1_048	0.57652	0.00976	0.04661	0.00062	0.4727796	1419.1	29.83	293.7	3.81	21	
SDF1_049	0.11053	0.00433	0.01615	0.00025	0.1638344	177.6	90.04	103.3	1.62	58	
SDF1_052	0.13599	0.00776	0.01585	0.00031	0.0958828	681.1	120.43	101.4	1.98	15	
SDF1_054	21.22595	0.42577	0.59776	0.00837	0.3751821	3231.5	30.71	3020.8	33.77	93	
SDF1_055	0.66427	0.01786	0.05174	0.0008	0.254687	1489.9	51.06	325.2	4.9	22	
SDF1_061	9.03958	0.12875	0.34904	0.0044	0.5566794	2723.4	20.84	1930	21.01	71	
SDF1_063	3.36106	0.0506	0.17431	0.00221	0.5159601	2225.4	23.74	1035.8	12.12	47	
SDF1_064	3.52127	0.06025	0.24517	0.00323	0.4574457	1699.6	29.5	1413.5	16.7	83	
SDF1_065	0.54093	0.01484	0.06618	0.00098	0.2542127	577.6	59.09	413.1	5.93	72	
SDF1_066	3.6555	0.05876	0.24964	0.00322	0.483871	1735.3	27.29	1436.6	16.62	83	
SDF1_072	14.72098	0.21026	0.47851	0.00581	0.4761057	3005.8	21.77	2520.8	25.35	84	
SDF1_073	5.10129	0.07679	0.3098	0.00375	0.4498976	1950.6	25.56	1739.7	18.45	89	
SDF1_074	2.02071	0.06467	0.17905	0.00291	0.1872752	1244.4	63.29	1061.8	15.92	85	
SDF1_075	2.73436	0.05227	0.18108	0.00241	0.3929177	1793.9	33.28	1072.9	13.14	60	
SDF1_076	1.60733	0.02425	0.09615	0.00117	0.482753	1976.7	24.86	591.8	6.88	30	
SDF1_077	1.97719	0.04242	0.18352	0.00252	0.3553496	1152.7	40.99	1086.2	13.75	94	
SDF1_078	1.76493	0.05444	0.16833	0.0027	0.2340974	1098.7	61.42	1002.9	14.92	91	
SDF1_079	0.32501	0.01902	0.0459	0.00083	0.0980602	258.6	131.19	289.3	5.1	112	
SDF1_080	0.13267	0.01775	0.01994	0.00059	0.0344385	113.9	293.06	127.3	3.7	112	
SDF1_081	0.38166	0.00913	0.05136	0.00073	0.3488783	368.4	51.21	322.8	4.45	88	
SDF1_085	4.02961	0.06668	0.25604	0.0033	0.4357317	1867	28.47	1469.5	16.95	79	
SDF1_086	1.50547	0.04662	0.14768	0.00238	0.2094925	1040.3	62.79	887.9	13.35	85	
SDF1_093	0.36539	0.01177	0.04949	0.00076	0.1853538	354.5	72.91	311.4	4.65	88	
SDF1_094	2.71473	0.04982	0.17179	0.00224	0.3904663	1873.7	31.99	1022	12.34	55	
SDF1 101	2.02458	0.04412	0.18582	0.00255	0.307887	1173.2	42.77	1098.7	13.85	94	

Analysis #	$^{207}Pb/^{235}U$ Ratio	1σ	$^{206}Pb/^{238}U$ Ratio	1σ	Rho	$^{207}Pb/^{206}Pb$ Age	2σ	$^{206}Pb/^{238}U$ Age	2σ	Conc. %	Comments
SDF1_103	0.56637	0.01545	0.07105	0.001	0.230189	523	59.71	442.5	6.04	85	
SDF1_106	1.25097	0.02114	0.08425	0.00105	0.4057338	1761.3	29.73	521.4	6.25	30	
SDF1_109	2.0652	0.04971	0.18751	0.00266	0.2711013	1194.9	47.36	1107.8	14.46	93	
SDF1_110	1.89618	0.03154	0.14401	0.00182	0.4278536	1538.6	29.9	867.3	10.23	56	
SDF1_115	0.36259	0.02928	0.04891	0.00118	0.0506199	362.2	176.79	307.8	7.24	85	
SDF1_116	2.19914	0.05346	0.19585	0.0028	0.2683197	1232.5	47.59	1153	15.12	94	
SDF1_122	1.7219	0.03418	0.16515	0.00214	0.3170472	1084.6	39.49	985.3	11.83	91	
SDF1_124	62.96395	1.77954	0.62907	0.0186	0.3960536	4782.7	44.82	3145.9	73.61	66	
SDF1_126	1.77205	0.03472	0.16303	0.00212	0.3362534	1167.8	38.33	973.6	11.76	83	
SDF1_129	1.93976	0.03411	0.17305	0.00217	0.3756779	1228.7	33.63	1028.9	11.94	84	
SDF1_136	4.44093	0.07568	0.28674	0.00362	0.3943589	1837.5	29.97	1625.2	18.16	88	
SDF1_137	1.07734	0.02287	0.11682	0.00156	0.3039686	835.3	43.78	712.2	9	85	
SDF1_141	0.15531	0.01074	0.01938	0.00039	0.0675379	534.3	148.36	123.8	2.44	23	
SDF1_142	0.47866	0.01713	0.04509	0.00078	0.1534596	1120.8	72.62	284.3	4.82	25	
SDF1_143	17.76887	0.37101	0.54592	0.0071	0.358665	3096.4	31.95	2808.2	29.6	91	
SDF1_144	2.27734	0.03167	0.15	0.00169	0.4486277	1805.7	24.15	901	9.47	50	
SDF1_148	2.52728	0.04664	0.17869	0.00225	0.4172444	1669.2	31.94	1059.8	12.3	63	
SDF1_150	1.51399	0.03529	0.1491	0.00203	0.3583759	1033.2	44.69	895.9	11.39	87	
SDF1_152	9.98805	0.1712	0.4163	0.00519	0.4879674	2596.9	25.63	2243.7	23.6	86	
SDF1_153	0.36838	0.02037	0.04454	0.00082	0.0911067	603.4	118.22	280.9	5.08	47	
SDF1_156	4.20716	0.0692	0.28086	0.00356	0.4192826	1777.1	28.93	1595.7	17.9	90	
SDF1_159	0.91479	0.02181	0.09944	0.00136	0.2655519	828.9	49.57	611.1	7.99	74	
SDF1_162	0.75323	0.01615	0.08724	0.00116	0.3137498	695.9	45.01	539.2	6.86	77	
SDF1_163	0.39484	0.00982	0.0502	0.0007	0.267253	494	55.04	315.8	4.32	64	
SDF1_164	0.47729	0.01423	0.05722	0.00083	0.2022564	622.1	64.39	358.7	5.05	58	
SDF1_165	0.33646	0.01104	0.04487	0.00067	0.1840087	387.6	72.85	283	4.13	73	
SDF1_166	5.89394	0.09597	0.32947	0.00406	0.4173178	2095	27.52	1835.8	19.71	88	
SDF1_170	9.26198	0.14116	0.40321	0.00499	0.4486764	2524.1	24.46	2183.8	22.91	87	
SDF1_173	3.63295	0.08077	0.2642	0.00372	0.2931692	1619.1	41.36	1511.3	18.99	93	
SDF1_174	0.30432	0.00899	0.02356	0.00037	0.1815227	1502.4	57.11	150.1	2.31	10	
SDF1_177	0.15266	0.01062	0.0218	0.00046	0.0601728	231.5	157.11	139	2.91	60	
SDF1_179	0.42293	0.01148	0.05446	0.00075	0.2137006	465.1	60.59	341.8	4.59	73	
SDF1_184	0.66092	0.01658	0.07709	0.00106	0.2396865	681.5	53.79	478.7	6.34	70	
SDF1_189	0.56509	0.03211	0.06476	0.00137	0.0849034	718.3	120.45	404.5	8.27	56	
SDF1_191	0.2634	0.02648	0.01583	0.00062	0.0224549	1966.2	179.46	101.3	3.94	5	
SDF1_192	0.56359	0.01907	0.06759	0.00109	0.1618992	621.1	73.75	421.6	6.56	68	
SDF1_195	0.76771	0.0135	0.07023	0.00087	0.3567779	1179.6	34.26	437.6	5.25	37	
SDF1_197	0.3877	0.00868	0.04584	0.0006	0.272255	652.1	48.04	288.9	3.7	44	
SDF1_198	1.69529	0.03048	0.16496	0.00205	0.3461734	1056.4	35.94	984.3	11.35	93	

Sample SDF-2: GDA 94, 507847 mE, 6591571 mN

Analysis #	$^{207}Pb/^{235}U$ Ratio	1σ	$^{206}Pb/^{238}U$ Ratio	1σ	Rho	$^{207}Pb/^{206}Pb$ Age	2σ	$^{206}Pb/^{238}U$ Age	2σ	Conc. %	Comments
SDF2_01	11.01138	0.16926	0.4657	0.00653	0.6293938	2572	21	2465	29	96	
SDF2_02	3.80329	0.0581	0.28097	0.00389	0.6337974	1590	23	1596	20	100	
SDF2_03	0.32173	0.00783	0.04469	0.00068	0.3632371	295	53	282	4	95	
SDF2_04	4.97169	0.07679	0.32393	0.00449	0.625913	1821	23	1809	22	99	
SDF2_05	0.39499	0.02347	0.05275	0.00124	0.0996741	384	133	331	8	86	
SDF2_06	0.43686	0.01793	0.05855	0.0011	0.1803943	376	91	367	7	98	
SDF2_07	0.43022	0.0295	0.0585	0.00153	0.0865739	343	153	367	9	107	
SDF2_08	0.19521	0.00588	0.02796	0.00045	0.2733425	224	68	178	3	79	
SDF2_09	2.07908	0.03688	0.19374	0.00276	0.5300939	1143	31	1142	15	100	
SDF2_10	0.30106	0.01448	0.0419	0.00085	0.140169	290	110	265	5	91	
SDF2_11	2.76529	0.04801	0.18837	0.00268	0.5397021	1740	28	1113	15	64	
SDF2_12	1.4525	0.02767	0.15166	0.00218	0.4859724	913	36	910	12	100	
SDF2_13	0.13631	0.00762	0.02036	0.00044	0.1112032	127	130	130	3	102	
SDF2_14	1.43324	0.03737	0.14993	0.00241	0.3333592	909	52	901	14	99	
SDF2_15	0.37513	0.01266	0.05176	0.00088	0.2344566	311	75	325	5	105	
SDF2_16	0.31486	0.00801	0.04414	0.00068	0.3479483	275	56	278	4	101	
SDF2_17	0.37857	0.01125	0.05213	0.00084	0.2779273	315	66	328	5	104	
SDF2_18	0.24031	0.01733	0.03447	0.00091	0.0743037	222	164	219	6	99	
SDF2_19	0.13845	0.01141	0.0206	0.00058	0.0589786	137	189	131	4	96	
SDF2_20	0.82706	0.05418	0.09842	0.00264	0.0943692	638	141	605	15	95	
SDF2_21	0.3028	0.01337	0.04255	0.00082	0.1671157	269	100	269	5	100	
SDF2_22	0.5201	0.01834	0.06835	0.0012	0.2245349	420	77	426	7	101	
SDF2_23	0.37264	0.00871	0.05074	0.00077	0.3915647	341	50	319	5	94	
SDF2_24	2.43858	0.0423	0.21207	0.00303	0.5513878	1279	29	1240	16	97	
SDF2_25	0.57398	0.01301	0.07391	0.00119	0.4580586	465	46	460	7	99	
SDF2_26	0.13514	0.00765	0.0202	0.00045	0.1285226	125	131	129	3	103	
SDF2_27	0.61528	0.01308	0.07667	0.00122	0.4952412	537	42	476	7	89	
SDF2_28	4.83105	0.08015	0.31834	0.00486	0.6610052	1801	24	1782	24	99	
SDF2_29	1.88786	0.0353	0.1772	0.00277	0.575787	1129	32	1052	15	93	
SDF2_30	1.90672	0.03345	0.18206	0.0028	0.6271831	1094	29	1078	15	99	
SDF2_31	0.40191	0.00961	0.04802	0.00079	0.4330713	629	48	302	5	48	
SDF2_32	2.99291	0.04987	0.22468	0.00343	0.6643037	1560	24	1307	18	84	
SDF2_33	0.15703	0.0049	0.01756	0.00032	0.3039848	770	64	112	2	15	
SDF2_34	0.17097	0.00722	0.01597	0.00035	0.1874199	1138	85	102	2	9	
SDF2_35	0.14543	0.00537	0.01836	0.00035	0.2505504	509	80	117	2	23	
SDF2_36	0.34595	0.01065	0.04786	0.00084	0.3216714	304	67	301	5	99	
SDF2_37	2.11292	0.04127	0.19726	0.00315	0.5575862	1139	33	1161	17	102	
SDF2_38	0.34	0.00757	0.04692	0.00076	0.4871357	310	45	296	5	95	
SDF2_39	0.33565	0.0085	0.04645	0.00077	0.4136049	304	53	293	5	96	

Analysis #	$^{207}Pb/^{235}U$ Ratio	1σ	$^{206}Pb/^{238}U$ Ratio	1σ	Rho	$^{207}Pb/^{206}Pb$ Age	2σ	$^{206}Pb/^{238}U$ Age	2σ	Conc. %	Comments
SDF2_40	2.88947	0.05178	0.21346	0.00336	0.6217928	1590	27	1247	18	78	
SDF2_41	5.05051	0.08751	0.32658	0.0051	0.6480002	1835	25	1822	25	99	
SDF2_42	0.20299	0.00707	0.02974	0.00054	0.2762311	172	79	189	3	110	
SDF2_43	3.86489	0.06771	0.28039	0.00438	0.6380355	1624	26	1593	22	98	
SDF2_44	0.14152	0.01446	0.04683	0.00094	0.0975571	0	0	295	6	295000	
SDF2_45	0.47502	0.00982	0.06325	0.00101	0.5331816	391	40	395	6	101	
SDF2_46	0.28841	0.00807	0.04052	0.00069	0.3652829	269	60	256	4	95	
SDF2_47	0.48154	0.01581	0.06389	0.00116	0.3014461	399	70	399	7	100	
SDF2_48	0.35113	0.0126	0.04831	0.0009	0.2614252	317	79	304	6	96	
SDF2_49	0.32785	0.01061	0.04548	0.00081	0.2985384	298	71	287	5	96	
SDF2_50	0.35004	0.01833	0.04479	0.00103	0.1479551	479	116	283	6	59	
SDF2_51	2.11027	0.03914	0.19289	0.00304	0.5955791	1181	30	1137	16	96	
SDF2_52	0.63345	0.0128	0.07965	0.00126	0.5409673	517	39	494	8	95	
SDF2_53	873.1795	46.71245	10.88875	0.58424	0.8701564	4463	39	-	-	-	
SDF2_54	0.34748	0.00701	0.04749	0.00075	0.5481841	332	39	299	5	90	
SDF2_55	0.77588	0.01455	0.05301	0.00084	0.5827419	1735	29	333	5	19	
SDF2_56	8.15941	0.14126	0.41591	0.00644	0.645122	2255	24	2242	29	99	
SDF2_57	0.13615	0.00914	0.02023	0.00052	0.1078186	139	155	129	3	93	
SDF2_58	0.13341	0.00734	0.01986	0.00044	0.1355784	134	127	127	3	95	
SDF2_59	0.2926	0.01157	0.04125	0.00079	0.2263125	261	89	261	5	100	
SDF2_60	0.14091	0.00736	0.02081	0.00045	0.1547614	153	121	133	3	87	
SDF2_61	0.44043	0.01101	0.0592	0.00098	0.4168574	369	52	371	6	100	
SDF2_62	0.14515	0.00362	0.0193	0.00032	0.4187384	394	52	123	2	31	
SDF2_63	0.45853	0.01423	0.06268	0.0011	0.3219978	332	68	392	7	118	
SDF2_64	0.34943	0.00886	0.04818	0.00079	0.4066949	312	53	303	5	97	
SDF2_65	10.93726	0.18279	0.47681	0.00728	0.6646807	2522	22	2513	32	100	
SDF2_66	2.09717	0.03753	0.19335	0.00299	0.6112598	1164	29	1140	16	98	
SDF2_67	3.11036	0.05381	0.22614	0.00347	0.6364088	1620	26	1314	18	81	
SDF2_68	2.58221	0.059	0.21791	0.00364	0.4557227	1337	41	1271	19	95	
SDF2_69	200.3591	13.25868	2.24697	0.15526	0.6338366	4617	81	7592	308	164	
SDF2_70	3.62275	0.06286	0.21245	0.00325	0.6310037	2010	25	1242	17	62	
SDF2_71	0.36431	0.01004	0.05023	0.00085	0.3623658	312	59	316	5	101	
SDF2_72	1.18646	0.02762	0.12778	0.00209	0.4460346	849	45	775	12	91	
SDF2_73	1.95442	0.03584	0.18348	0.00285	0.5904553	1128	31	1086	16	96	
SDF2_74	0.32474	0.01429	0.04526	0.00091	0.1898827	287	99	285	6	99	
SDF2_75	10.77735	0.19062	0.47358	0.00749	0.6189117	2508	25	2499	33	100	
SDF2_76	9.27065	0.15777	0.4354	0.00673	0.6465156	2396	23	2330	30	97	
SDF2_77	0.13822	0.01164	0.02061	0.00061	0.0674797	131	193	132	4	100	
SDF2_78	0.39077	0.00922	0.05336	0.00086	0.4465031	334	49	335	5	100	
SDF2_79	0.3584	0.01263	0.04971	0.00091	0.2629188	299	78	313	6	105	

Analysis #	$^{207}Pb/^{235}U$ Ratio	1σ	$^{206}Pb/^{238}U$ Ratio	1σ	Rho	$^{207}Pb/^{206}Pb$ Age	2σ	$^{206}Pb/^{238}U$ Age	2σ	Conc. %	Comments
SDF2_80	3.46076	0.06591	0.23371	0.0037	0.5668016	1756	30	1354	19	77	
SDF2_81	1.88331	0.03672	0.18704	0.00293	0.552223	1015	34	1105	16	109	
SDF2_82	5.56471	0.0967	0.33128	0.00508	0.6338972	1983	25	1845	25	93	
SDF2_83	2.70471	0.04849	0.22535	0.00347	0.6077445	1362	28	1310	18	96	
SDF2_84	1.82576	0.0329	0.15488	0.00239	0.6090507	1327	29	928	13	70	
SDF2_85	0.11958	0.00689	0.01794	0.00041	0.1215669	117	134	115	3	98	
SDF2_86	0.35382	0.0088	0.04891	0.00079	0.3995014	306	53	308	5	101	
SDF2_87	33.78668	1.17676	0.40982	0.01509	0.3185681	4503	60	2214	69	49	
SDF2_88	0.6403	0.01198	0.05882	0.00091	0.5571919	1171	32	368	6	31	
SDF2_89	0.4912	0.01117	0.06528	0.00103	0.4491189	395	46	408	6	103	
SDF2_90	23.08756	0.37204	0.58751	0.00876	0.6618369	3391	20	2979	36	88	
SDF2_91	0.55354	0.0114	0.06896	0.00107	0.5021078	538	41	430	6	80	
SDF2_92	0.94468	0.03467	0.10985	0.00211	0.2359466	687	77	672	12	98	
SDF2_93	0.57745	0.01107	0.07477	0.00114	0.5343873	453	37	465	7	103	
SDF2_94	0.31506	0.01033	0.0441	0.00077	0.276234	278	73	278	5	100	
SDF2_95	3.11967	0.06311	0.24746	0.0039	0.502066	1456	35	1425	20	98	
SDF2_96	0.11104	0.00971	0.01669	0.0005	0.0651535	112	201	107	3	96	
Sample SDF-3: GDA 94, 508092 mE, 6586922 mN											
SDF3_001	0.53704	0.01137	0.06911	0.0011	0.5259808	466	41	431	7	92	
SDF3_007	1.62128	0.03201	0.1617	0.00257	0.5677685	1006	34	966	14	96	
SDF3_009	2.19125	0.05441	0.19774	0.0034	0.4344415	1206	45	1163	18	96	
SDF3_010	1.87736	0.03802	0.17927	0.00288	0.5557935	1094	35	1063	16	97	
SDF3_011	0.63793	0.01297	0.07967	0.00127	0.553922	532	38	494	8	93	
SDF3_013	2.11224	0.04108	0.19353	0.00311	0.5867975	1176	32	1140	17	97	Hf Isotope Analysis #1
SDF3_014	1.46762	0.02821	0.1488	0.00237	0.5957028	973	32	894	13	92	
SDF3_015	2.07329	0.04182	0.19297	0.00313	0.5652363	1145	34	1138	17	99	Hf Isotope Analysis #2
SDF3_016	0.35415	0.00902	0.04902	0.00082	0.4324886	303	53	309	5	102	Hf Isotope Analysis #3
SDF3_017	1.94145	0.03476	0.18413	0.0029	0.6479718	1108	28	1090	16	98	
SDF3_018	1.85492	0.03609	0.17929	0.00287	0.5877673	1070	33	1063	16	99	Hf Isotope Analysis #4
SDF3_020	0.50511	0.01409	0.06648	0.00115	0.3791034	417	58	415	7	100	Hf Isotope Analysis #5
SDF3_022	0.40118	0.00893	0.05412	0.00088	0.502473	361	44	340	5	94	
SDF3_023	0.68905	0.01541	0.08587	0.0014	0.4961776	537	44	531	8	99	
SDF3_026	0.53876	0.0131	0.06926	0.00115	0.4461285	468	49	432	7	92	
SDF3_027	4.31781	0.08796	0.30012	0.00497	0.5556813	1703	32	1692	25	99	
SDF3_028	4.28066	0.07662	0.29153	0.00462	0.6436193	1740	26	1649	23	95	
SDF3_029	4.63218	0.08329	0.31208	0.00495	0.6397769	1760	26	1751	24	99	Hf Isotope Analysis #6
SDF3_031	2.05158	0.03911	0.19119	0.00305	0.5985733	1143	31	1128	17	99	Hf Isotope Analysis #7
SDF3_032	3.59557	0.06994	0.27066	0.00438	0.5844083	1555	31	1544	22	99	
SDF3_034	1.8253	0.09251	0.17655	0.0044	0.1754775	1068	102	1048	24	98	

Analysis #	$^{207}Pb/^{235}U$ Ratio	1σ	$^{206}Pb/^{238}U$ Ratio	1σ	Rho	$^{207}Pb/^{206}Pb$ Age	2σ	$^{206}Pb/^{238}U$ Age	2σ	Conc. %	Comments
SDF3_035	0.21825	0.00906	0.03156	0.00062	0.2287333	203	94	200	4	99	
SDF3_038	3.63643	0.05982	0.27206	0.00422	0.7162862	1566	22	1551	21	99	Hf Isotope Analysis #8
SDF3_040	0.34776	0.01502	0.04768	0.00097	0.2119573	325	96	300	6	92	
SDF3_041	0.35788	0.00972	0.04958	0.00084	0.4014986	301	57	312	5	104	
SDF3_042	0.33365	0.00732	0.04672	0.00076	0.5124469	277	44	294	5	106	
SDF3_044	3.68803	0.09293	0.27469	0.00492	0.4300074	1575	44	1565	25	99	Hf Isotope Analysis #9
SDF3_045	4.34051	0.07704	0.30088	0.00475	0.6546473	1708	26	1696	24	99	
SDF3_046	2.24296	0.04973	0.20227	0.00338	0.5061887	1208	39	1188	18	98	
SDF3_047	3.69889	0.06492	0.27475	0.00431	0.664341	1580	25	1565	22	99	Hf Isotope Analysis #10
SDF3_048	0.14336	0.00394	0.02136	0.00036	0.3872639	132	60	136	2	103	
SDF3_050	0.38681	0.01102	0.05263	0.00091	0.365982	342	61	331	6	97	
SDF3_051	0.28237	0.00914	0.03984	0.00071	0.311766	259	71	252	4	97	Hf Isotope Analysis #11
SDF3_052	0.37138	0.01351	0.05071	0.00095	0.2699027	334	80	319	6	96	
SDF3_053	4.65671	0.08138	0.31313	0.00489	0.6567116	1764	25	1756	24	100	
SDF3_054	4.60519	0.08331	0.31079	0.00489	0.6300731	1757	27	1745	24	99	
SDF3_055	0.13738	0.00582	0.02047	0.0004	0.2119323	132	97	131	3	99	
SDF3_056	4.12392	0.08283	0.29365	0.00477	0.5546244	1658	32	1660	24	100	
SDF3_057	2.01751	0.06309	0.18962	0.00357	0.3237235	1126	60	1119	19	99	Hf Isotope Analysis #12
SDF3_058	0.37849	0.01102	0.05182	0.00089	0.3514106	328	62	326	5	99	
SDF3_059	2.13046	0.04902	0.19724	0.00328	0.4734992	1156	41	1161	18	100	
SDF3_061	0.37758	0.01076	0.05164	0.00089	0.3680087	330	61	325	5	98	Hf Isotope Analysis #13
SDF3_063	0.62072	0.01765	0.07799	0.00135	0.3744065	519	59	484	8	93	
SDF3_064	4.92919	0.08805	0.32307	0.00506	0.6489876	1810	26	1805	25	100	
SDF3_066	1.90109	0.03536	0.18178	0.00286	0.6213853	1091	30	1077	16	99	Hf Isotope Analysis #14
SDF3_067	3.02169	0.05899	0.245	0.00392	0.5876449	1414	31	1413	20	100	Hf Isotope Analysis #15
SDF3_069	1.71055	0.03619	0.16751	0.00272	0.5373138	1043	37	998	15	96	Hf Isotope Analysis #16
SDF3_070	0.41174	0.01566	0.05564	0.00107	0.2544095	357	83	349	7	98	Hf Isotope Analysis #17
SDF3_071	2.24384	0.04743	0.203	0.00331	0.5396031	1201	36	1191	18	99	
SDF3_072	0.30789	0.01197	0.04322	0.00083	0.2461657	271	86	273	5	101	
SDF3_074	0.36501	0.0081	0.05037	0.00082	0.5066939	310	44	317	5	102	Hf Isotope Analysis #18
SDF3_076	0.8137	0.02585	0.09695	0.00177	0.3177199	635	66	597	10	94	
SDF3_077	0.53523	0.01238	0.06968	0.00114	0.4779906	441	46	434	7	99	
SDF3_079	0.14127	0.00791	0.02106	0.00048	0.1432991	131	129	134	3	103	
SDF3_080	2.26505	0.04362	0.20363	0.00326	0.5896591	1214	32	1195	17	98	Hf Isotope Analysis #19
SDF3_081	0.81871	0.01639	0.09843	0.00157	0.5606067	615	37	605	9	98	
SDF3_082	2.23228	0.04326	0.20251	0.00324	0.5855809	1196	32	1189	17	99	
SDF3_084	0.40561	0.01272	0.05457	0.00097	0.325293	367	67	343	6	93	
SDF3_085	2.29636	0.04197	0.20538	0.00326	0.6327118	1224	29	1204	17	98	
SDF3_086	0.32475	0.01112	0.04513	0.00083	0.2968918	294	75	285	5	97	Hf Isotope Analysis #20
SDF3_088	0.33754	0.00979	0.04659	0.00081	0.3684592	310	62	294	5	95	Hf Isotope Analysis #21

Analysis #	$^{207}Pb/^{235}U$ Ratio	1σ	$^{206}Pb/^{238}U$ Ratio	1σ	Rho	$^{207}Pb/^{206}Pb$ Age	2σ	$^{206}Pb/^{238}U$ Age	2σ	Conc. %	Comments
SDF3_090	2.11118	0.03956	0.19507	0.00311	0.6155297	1160	30	1149	17	99	
SDF3_092	0.24644	0.00711	0.03515	0.00061	0.3753155	235	63	223	4	95	
SDF3_095	0.65796	0.04323	0.08253	0.00223	0.1207488	523	143	511	13	98	
SDF3_096	1.89336	0.04205	0.18032	0.003	0.5102175	1100	39	1069	16	97	
SDF3_097	2.16211	0.0455	0.19568	0.0032	0.5298625	1201	36	1152	17	96	
SDF3_098	0.33262	0.00802	0.04568	0.00075	0.4550456	321	50	288	5	90	
SDF3_100	0.34607	0.01204	0.04793	0.00088	0.2869469	302	76	302	5	100	Hf Isotope Analysis #22
SDF3_105	0.2758	0.00626	0.03893	0.00063	0.4892812	258	46	246	4	95	Hf Isotope Analysis #23
SDF3_106	0.13734	0.01136	0.02049	0.0006	0.0708351	130	190	131	4	101	Hf Isotope Analysis #24
Discordant Analyses - Not used											
SDF3_002	1.94646	0.03551	0.16913	0.00264	0.6184143	1280	29	1007	15	79	
SDF3_003	3.01918	0.17101	0.13126	0.00469	0.127394	2526	102	795	27	31	
SDF3_004	0.65334	0.01259	0.06957	0.0011	0.583782	872	33	434	7	50	
SDF3_005	1.89851	0.03474	0.1707	0.00267	0.6192094	1213	29	1016	15	84	
SDF3_006	0.17441	0.00832	0.02005	0.00044	0.1711877	711	101	128	3	18	
SDF3_008	1.60835	0.03049	0.15728	0.00248	0.6007867	1046	32	942	14	90	
SDF3_012	2.09571	0.04425	0.17238	0.00282	0.5321521	1387	35	1025	15	74	
SDF3_019	1.86479	0.0454	0.17627	0.00302	0.4459378	1114	45	1047	17	94	
SDF3_021	2.05998	0.04019	0.18183	0.00292	0.588242	1250	32	1077	16	86	
SDF3_024	0.37008	0.00813	0.04914	0.0008	0.5087165	397	43	309	5	78	
SDF3_025	3.58305	0.06222	0.26164	0.00411	0.666381	1611	25	1498	21	93	
SDF3_030	1.53314	0.0288	0.14126	0.00225	0.6122686	1165	30	852	13	73	
SDF3_033	0.60471	0.01203	0.07075	0.00113	0.5727306	674	36	441	7	65	
SDF3_036	0.79576	0.02071	0.09401	0.00161	0.4101492	653	52	579	9	89	
SDF3_037	1.03919	0.01717	0.04768	0.00074	0.7082591	2435	21	300	5	12	
SDF3_039	2.25115	0.04276	0.12434	0.00203	0.5951676	2116	28	756	12	36	
SDF3_043	0.48522	0.00961	0.06238	0.00099	0.5830757	468	37	390	6	83	
SDF3_049	5.45363	0.08961	0.25615	0.00395	0.7095294	2396	21	1470	20	61	
SDF3_060	2.55767	0.04802	0.21022	0.0033	0.6012224	1388	30	1230	18	89	
SDF3_062	1.10669	0.01955	0.0622	0.00097	0.6507467	2085	25	389	6	19	
SDF3_065	0.35554	0.01922	0.04578	0.00106	0.1486124	465	119	289	7	62	
SDF3_068	0.54545	0.0148	0.06875	0.00118	0.3966716	512	56	429	7	84	
SDF3_073	0.49572	0.01114	0.03308	0.00056	0.4720417	1777	38	210	4	12	
SDF3_075	2.97061	0.06175	0.21406	0.00355	0.5357105	1636	34	1250	19	76	
SDF3_078	0.36927	0.01086	0.04778	0.00084	0.3576607	455	62	301	5	66	
SDF3_083	6.41344	0.12168	0.35	0.00566	0.5942473	2137	28	1935	27	91	
SDF3_087	0.66234	0.02262	0.06019	0.00118	0.2782633	1193	66	377	7	32	
SDF3_089	0.46437	0.01071	0.04684	0.00078	0.4796286	984	42	295	5	30	
SDF3_091	0.47021	0.01767	0.04844	0.00097	0.2495611	941	76	305	6	32	
SDF3_093	0.23638	0.00984	0.02143	0.00047	0.2064675	1198	82	137	3	11	

Analysis #	$^{207}Pb/^{235}U$ Ratio	1σ	$^{206}Pb/^{238}U$ Ratio	1σ	Rho	$^{207}Pb/^{206}Pb$ Age	2σ	$^{206}Pb/^{238}U$ Age	2σ	Conc. %	Comments
SDF3_094	0.87452	0.04247	0.0903	0.00212	0.1752633	936	99	557	13	60	
SDF3_099	0.31908	0.0091	0.04376	0.00075	0.363942	324	61	276	5	85	
SDF3_101	0.58252	0.01051	0.04336	0.00068	0.6293283	1576	27	274	4	17	
SDF3_102	0.13399	0.00776	0.01735	0.00042	0.1298439	453	128	111	3	24	
SDF3_103	0.79966	0.02905	0.07562	0.00152	0.2549385	1114	72	470	9	42	
SDF3_104	2.61319	0.05108	0.1883	0.00302	0.5753744	1636	31	1112	16	68	
SDF3_107	0.32684	0.01442	0.04145	0.00086	0.2038857	498	96	262	5	53	
SDF3_108	0.82588	0.01658	0.08799	0.00139	0.5552206	871	36	544	8	62	
Sample SDF-5: GDA 94, 530316 mE, 6592874 mN											
SDF5_002	0.52028	0.01404	0.06803	0.001	0.2558644	431	59	424	6	98	
SDF5_003	2.11982	0.03158	0.19527	0.00249	0.5348829	1165	26	1150	13	99	
SDF5_004	0.34172	0.00965	0.04727	0.0007	0.2496775	304	63	298	4	98	Hf Isotope Analysis #1
SDF5_005	2.50212	0.04673	0.21572	0.00297	0.4201249	1295	35	1259	16	97	
SDF5_006	0.51911	0.0115	0.06772	0.00094	0.3409096	436	47	422	6	97	
SDF5_013	2.46477	0.04204	0.21545	0.00289	0.4758529	1269	31	1258	15	99	Hf Isotope Analysis #2
SDF5_014	4.64286	0.06713	0.31355	0.00405	0.5706505	1756	23	1758	20	100	
SDF5_015	2.22026	0.04206	0.20181	0.00279	0.4195292	1192	35	1185	15	99	
SDF5_017	1.75114	0.03343	0.17071	0.00234	0.4074882	1052	37	1016	13	97	Hf Isotope Analysis #3
SDF5_018	1.62311	0.02754	0.16223	0.00215	0.47215	1002	32	969	12	97	
SDF5_019	2.22501	0.0341	0.20143	0.0026	0.5295226	1200	27	1183	14	99	
SDF5_020	2.064	0.04974	0.19056	0.00287	0.3065226	1161	47	1124	16	97	Hf Isotope Analysis #4
SDF5_022	4.39144	0.08161	0.30389	0.00424	0.4208131	1711	33	1711	21	100	Hf Isotope Analysis #5
SDF5_023	1.66653	0.0273	0.167	0.00217	0.48427	997	31	996	12	100	
SDF5_026	0.36256	0.01696	0.04934	0.00095	0.1198421	342	106	311	6	91	
SDF5_027	2.1645	0.0386	0.19763	0.00266	0.4384101	1183	33	1163	14	98	Hf Isotope Analysis #6
SDF5_028	0.54546	0.01621	0.07092	0.00109	0.2327238	444	65	442	7	100	
SDF5_029	4.31996	0.06429	0.3014	0.00389	0.5448816	1696	24	1698	19	100	
SDF5_032	0.16278	0.00999	0.02401	0.00051	0.0838751	156	142	153	3	98	
SDF5_035	2.10611	0.04655	0.19387	0.00281	0.338069	1167	43	1142	15	98	Hf Isotope Analysis #7
SDF5_036	0.71941	0.01355	0.08906	0.00118	0.4067031	552	39	550	7	100	Hf Isotope Analysis #8
SDF5_038	2.22034	0.15452	0.20264	0.00627	0.1015102	1184	138	1190	34	100	
SDF5_039	1.53991	0.02928	0.15538	0.00211	0.4041522	983	37	931	12	95	Hf Isotope Analysis #10
SDF5_040	3.90586	0.063	0.28387	0.00375	0.4969456	1620	28	1611	19	99	Hf Isotope Analysis #11
SDF5_041	2.15277	0.03958	0.19796	0.00268	0.4234252	1169	35	1164	14	100	
SDF5_042	2.29825	0.04182	0.20375	0.00276	0.42425	1241	34	1195	15	96	
SDF5_045	0.17815	0.00647	0.02629	0.00042	0.1754324	155	85	167	3	108	
SDF5_047	0.64466	0.03789	0.08092	0.00159	0.101831	522	127	502	9	96	Hf Isotope Analysis #12
SDF5_051	1.99088	0.05868	0.18627	0.0027	0.2933756	1134	56	1101	15	97	
SDF5_053	0.6789	0.01171	0.08577	0.00117	0.5165884	506	34	531	7	105	

Analysis #	$^{207}Pb/^{235}U$ Ratio	1σ	$^{206}Pb/^{238}U$ Ratio	1σ	Rho	$^{207}Pb/^{206}Pb$ Age	2σ	$^{206}Pb/^{238}U$ Age	2σ	Conc. %	Comments
SDF5_054	2.24164	0.03632	0.20279	0.00276	0.5484526	1201	28	1190	15	99	
SDF5_058	4.9493	0.07	0.31661	0.00416	0.6323477	1854	21	1773	20	96	
SDF5_062	2.39289	0.04348	0.20849	0.00284	0.4289711	1275	34	1221	15	96	
SDF5_067	0.76287	0.01269	0.09431	0.00122	0.4727894	555	34	581	7	105	Hf Isotope Analysis #13
SDF5_069	12.95382	0.17872	0.51199	0.00659	0.586724	2685	20	2665	28	99	Hf Isotope Analysis #14
SDF5_070	2.16771	0.04529	0.20057	0.00286	0.3572708	1157	40	1178	15	102	
SDF5_072	2.07529	0.03265	0.19367	0.00252	0.5018956	1140	29	1141	14	100	Hf Isotope Analysis #15
SDF5_073	0.3247	0.00687	0.04528	0.00061	0.3475345	287	47	285	4	100	Hf Isotope Analysis #16
SDF5_074	0.72071	0.02958	0.08949	0.00165	0.146922	546	90	553	10	101	
SDF5_075	2.654	0.04602	0.22373	0.003	0.4476261	1339	32	1302	16	97	
SDF5_076	1.08372	0.01811	0.11903	0.00155	0.4725133	808	32	725	9	90	
SDF5_079	0.7823	0.01844	0.09552	0.00136	0.3142445	582	50	588	8	101	Hf Isotope Analysis #17
SDF5_081	0.3132	0.00776	0.04377	0.00062	0.294196	281	56	276	4	98	Hf Isotope Analysis #18
SDF5_083	0.74735	0.02471	0.09178	0.0015	0.1979463	570	72	566	9	99	Hf Isotope Analysis #19
SDF5_084	2.0837	0.03577	0.19327	0.00255	0.4527442	1152	32	1139	14	99	Hf Isotope Analysis #20
SDF5_086	10.60232	0.14304	0.46879	0.0059	0.5992064	2498	20	2478	26	99	
SDF5_089	1.95599	0.03041	0.18364	0.00237	0.5123735	1128	28	1087	13	96	Hf Isotope Analysis #21
SDF5_090	2.02427	0.0351	0.18688	0.00249	0.4516525	1162	32	1105	14	95	
SDF5_091	0.80782	0.01413	0.09767	0.00128	0.4481335	604	35	601	8	100	Hf Isotope Analysis #22
SDF5_092	1.25367	0.0226	0.13543	0.0018	0.4347529	843	35	819	10	97	Hf Isotope Analysis #23
SDF5_093	12.05794	0.18682	0.49742	0.00664	0.5225007	2614	23	2603	29	100	Hf Isotope Analysis #24
SDF5_094	0.14606	0.00826	0.02174	0.00046	0.094139	135	132	139	3	103	
SDF5_095	0.88772	0.01671	0.10521	0.00141	0.4181614	647	38	645	8	100	Hf Isotope Analysis #25
SDF5_096	0.75766	0.01621	0.09304	0.00129	0.3528036	570	45	574	8	101	
Discordant Analyses - Not Used											
SDF5_001	1.47978	0.02071	0.13435	0.00168	0.5675051	1194	24	813	10	68	
SDF5_007	0.43965	0.01155	0.04588	0.00069	0.2629539	914	54	289	4	32	
SDF5_008	3.32746	0.04892	0.23691	0.00305	0.5651961	1658	24	1371	16	83	
SDF5_009	3.64772	0.06282	0.25976	0.00353	0.4741454	1658	30	1489	18	90	
SDF5_010	1.50052	0.02915	0.1473	0.00204	0.4093983	1038	37	886	11	85	
SDF5_011	4.83513	0.07389	0.30306	0.00396	0.5513056	1891	24	1707	20	90	
SDF5_012	3.7262	0.05636	0.23445	0.00305	0.55783	1884	24	1358	16	72	
SDF5_016	1.73567	0.03381	0.16271	0.00226	0.399692	1131	37	972	13	86	
SDF5_021	2.04193	0.03347	0.18718	0.00245	0.4893244	1175	30	1106	13	94	
SDF5_024	0.43481	0.00736	0.0518	0.00067	0.4685461	635	34	326	4	51	
SDF5_025	9.96573	0.13646	0.3727	0.00473	0.59835	2776	19	2042	22	74	
SDF5_030	0.78909	0.01842	0.09319	0.00133	0.3213044	654	49	574	8	88	
SDF5_031	4.73175	0.07109	0.28832	0.00374	0.5357364	1942	24	1633	19	84	
SDF5_033	7.47841	0.10786	0.30377	0.00388	0.5610288	2640	21	1710	19	65	
SDF5_034	1.63072	0.08992	0.16122	0.00399	0.1148483	1024	113	964	22	94	

Analysis #	$^{207}Pb/^{235}U$ Ratio	1σ	$^{206}Pb/^{238}U$ Ratio	1σ	Rho	$^{207}Pb/^{206}Pb$ Age	2σ	$^{206}Pb/^{238}U$ Age	2σ	Conc. %	Comments
SDF5_037	2.99416	0.05441	0.21021	0.00291	0.4271462	1685	32	1230	16	73	
SDF5_043	3.81337	0.05816	0.27132	0.0035	0.5210283	1660	25	1548	18	93	
SDF5_044	3.16452	0.04786	0.23106	0.00296	0.5301209	1612	25	1340	16	83	
SDF5_046	0.53017	0.01084	0.06524	0.00089	0.3766264	565	43	407	5	72	
SDF5_048	0.59915	0.01597	0.07404	0.0011	0.2609653	556	58	460	7	83	
SDF5_049	2.14346	0.03627	0.20221	0.00279	0.5412104	1117	30	1187	15	106	
SDF5_050	0.6708	0.01203	0.06604	0.00092	0.5004858	1031	33	412	6	40	
SDF5_052	0.15542	0.13009	0.08816	0.00278	0.0117502	-	-	545	17	-	
SDF5_055	0.33232	0.02302	0.04787	0.00072	0.1169965	211	153	301	4	143	
SDF5_056	2.35183	0.03591	0.19582	0.00261	0.5882813	1362	25	1153	14	85	
SDF5_057	9.48927	0.13779	0.4249	0.00566	0.6172854	2476	21	2283	26	92	
SDF5_059	0.39097	0.01186	0.04662	0.0007	0.2529156	633	64	294	4	46	
SDF5_060	0.25084	0.00937	0.02529	0.00056	0.1439763	984	81	161	4	16	
SDF5_061	6.57066	0.08997	0.30828	0.0039	0.589813	2398	20	1732	19	72	
SDF5_063	7.76392	0.1042	0.3718	0.00467	0.6017468	2363	20	2038	22	86	
SDF5_064	2.19223	0.0963	0.1943	0.00426	0.1496854	1242	88	1145	23	92	
SDF5_065	1.81479	0.02608	0.16782	0.00213	0.5532385	1158	25	1000	12	86	
SDF5_066	0.67884	0.00937	0.05157	0.00065	0.5800165	1538	23	324	4	21	
SDF5_068	3.2933	0.05614	0.24275	0.00328	0.4533046	1594	30	1401	17	88	
SDF5_071	0.15819	0.00555	0.01841	0.00031	0.1792515	686	75	118	2	17	
SDF5_077	1.16847	0.02181	0.10829	0.00147	0.4107424	1154	35	663	9	57	
SDF5_078	1.89996	0.02707	0.17412	0.0022	0.563982	1176	25	1035	12	88	
SDF5_080	0.27235	0.00674	0.03933	0.00056	0.2919623	206	56	249	3	121	
SDF5_082	0.18901	0.00342	0.01523	0.00021	0.4196463	1426	33	98	1	7	
SDF5_085	0.40584	0.00651	0.04997	0.00064	0.4948167	564	32	314	4	56	
SDF5_087	2.21356	0.041	0.19711	0.00269	0.4204323	1233	35	1160	15	94	
SDF5_088	0.95328	0.0154	0.08706	0.00113	0.4888179	1183	29	538	7	45	

Chapter 6 Supplementary Data 5: Strzelecki Sand Dune Lu-Hf Isotopic Analyses

Sample SDF-1: GDA 94, 507803 mE, 6596929 mN

Analysis #	$^{176}Hf/^{177}Hf$	2 S.E.	$^{176}Lu/^{177}Hf$	U/Pb AGE	Hf Chur (t)	Hf DM (t)	Hf NC(t)	Hf_i	epsilon	1s	T(DM) (crustal)	T(NC) (crustal)
KM_SDF1_01	0.281924009	1.88273E-05	0.000624306	1635.2	0.28170752	0.2820198	0.281987	0.281905	7.00	0.65896	1.89	1.8154478
KM_SDF1_02	0.28246983	1.71765E-05	0.000288222	527.7	0.28243214	0.2828579	0.282784	0.282467	1.23	0.60118	1.40	1.2381393
KM_SDF1_03	0.28248321	1.95397E-05	0.000513728	426.1	0.28249785	0.2829339	0.282856	0.282479	-0.66	0.68389	1.45	1.2727699
KM_SDF1_04	0.281927646	1.85115E-05	0.000555619	1234.8	0.28197129	0.2823249	0.282277	0.281915	-2.01	0.6479	2.13	2.0293804
KM_SDF1_05	0.28241965	1.80224E-05	0.00063072	412.2	0.28250683	0.2829443	0.282866	0.282415	-3.26	0.63078	1.60	1.4242479
KM_SDF1_06	0.282852436	2.12523E-05	0.000800735	254.8	0.28260833	0.2830617	0.282978	0.282849	8.50	0.74383	0.74	0.5480343
KM_SDF1_07	0.282167903	1.88891E-05	0.000836463	1023.3	0.28210979	0.2824851	0.282430	0.282152	1.49	0.66112	1.76	1.6370207
KM_SDF1_08	0.282895538	1.77283E-05	0.000901862	97.9	0.28270921	0.2831784	0.283089	0.282894	6.53	0.62049	0.74	0.5416199
KM_SDF1_09	0.281493833	2.35026E-05	0.000851413	1787.4	0.28160672	0.2819032	0.281877	0.281465	-5.03	0.82259	2.73	2.6737598
KM_SDF1_10	0.282422353	2.24872E-05	0.000418111	607.8	0.28238025	0.2827979	0.282727	0.282418	1.32	0.78705	1.46	1.2994799
KM_SDF1_11	0.28094552	2.23623E-05	0.000731325	2717.7	0.28098413	0.2811831	0.281193	0.280907	-2.73	0.78268	3.30	3.3165285
KM_SDF1_12	0.282594726	1.82154E-05	0.000592959	281.2	0.28259133	0.283042	0.282959	0.282592	0.01	0.63754	1.29	1.1099591
KM_SDF1_13	0.282518818	1.82556E-05	0.000516607	401.6	0.28251367	0.2829522	0.282874	0.282515	0.04	0.63894	1.38	1.2078485
KM_SDF1_14	0.282532396	2.08738E-05	0.001035478	369	0.28253472	0.2829766	0.282897	0.282525	-0.34	0.73058	1.38	1.2046858
KM_SDF1_15	0.28172178	1.33632E-05	0.000202749	521.8	0.28243596	0.2828623	0.282788	0.281720	-25.36	0.46771	3.04	2.8790529
KM_SDF1_16	0.281431905	1.84934E-05	0.000544672	572.7	0.282403	0.2828242	0.282752	0.281426	-34.59	0.64727	3.63	3.4784345
KM_SDF1_17	0.281523596	1.91234E-05	0.000281177	563.9	0.2824087	0.2828308	0.282758	0.281521	-31.45	0.66932	3.44	3.2816776
KM_SDF1_18	0.282229275	2.13607E-05	0.001012635	475.3	0.28246605	0.2828971	0.282821	0.282220	-8.70	0.74762	1.98	1.8161127
KM_SDF1_19	0.281851005	2.5098E-05	0.00163869	1583	0.28174202	0.2820597	0.282025	0.281802	2.13	0.87843	2.14	2.0689039
KM_SDF1_20	0.281579245	1.83179E-05	0.000552476	1805.5	0.28159472	0.2818893	0.281864	0.281560	-1.22	0.64113	2.51	2.459246
KM_SDF1_21	0.282954971	2.06937E-05	0.000805544	146.2	0.28267819	0.2831425	0.283055	0.282953	9.71	0.72428	0.58	0.3784264
KM_SDF1_22	0.281528654	2.4322E-05	0.001455035	1742.5	0.28163649	0.2819376	0.281909	0.281481	-5.54	0.85127	2.73	2.6665752
KM_SDF1_23	0.282905436	2.19153E-05	0.000676661	133.6	0.28268628	0.2831519	0.283064	0.282904	7.69	0.76704	0.70	0.4973839
KM_SDF1_24	0.282434448	1.94596E-05	0.001529404	268.5	0.28259951	0.2830515	0.282968	0.282427	-6.11	0.68109	1.67	1.4851922
KM_SDF1_25	0.281700146	1.40578E-05	4.97676E-05	1579.7	0.2817442	0.2820622	0.282028	0.281699	-1.62	0.49202	2.37	2.2938331
KM_SDF1_26	0.282437144	1.90109E-05	0.000626002	401.1	0.28251399	0.2829526	0.282874	0.282432	-2.89	0.66538	1.57	1.3917685
KM_SDF1_27	0.282576975	2.03387E-05	0.000571667	399.2	0.28251522	0.282954	0.282876	0.282573	2.03	0.71186	1.26	1.0803451
KM_SDF1_28	0.281947074	2.04075E-05	0.000877178	1537.8	0.28177187	0.2820942	0.282058	0.281922	5.31	0.71426	1.91	1.8358225
KM_SDF1_29	0.282974269	3.22064E-05	0.002425274	95.8	0.28271056	0.2831799	0.283090	0.282970	9.17	1.12722	0.57	0.3703395
KM_SDF1_30	0.282277666	2.29682E-05	0.000669081	971.7	0.2821435	0.2825241	0.282467	0.282265	4.32	0.80389	1.54	1.4176762
KM_SDF1_31	0.282373814	1.8788E-05	0.000534959	549.7	0.2824179	0.2828414	0.282768	0.282368	-1.76	0.65758	1.61	1.4439417
KM_SDF1_32	0.282932699	1.51757E-05	0.000645383	123	0.28269309	0.2831597	0.283071	0.282931	8.42	0.53115	0.64	0.4415839
KM_SDF1_33	0.282289524	1.89241E-05	0.000634751	448.7	0.28248324	0.282917	0.282840	0.282284	-7.05	0.66234	1.86	1.6912591
KM_SDF1_34	0.282916171	2.61432E-05	0.001385595	133.1	0.28268661	0.2831522	0.283064	0.282913	8.00	0.91501	0.68	0.477334
KM_SDF1_35	0.281751483	1.65263E-05	0.000435228	1549.6	0.28176408	0.2820852	0.282050	0.281739	-0.90	0.57842	2.30	2.2250662

Sample SDF-3: GDA 94, 508092 mE, 6586922 mN

Analysis #	$^{176}Hf/^{177}Hf$	2 S.E.	$^{176}Lu/^{177}Hf$	U/Pb AGE	Hf Chur (t)	Hf DM (t)	Hf NC(t)	Hf_i	epsilon	1s	T(DM) (crustal)	T(NC) (crustal)
KM_SDF3_01	0.282164715	2.02354E-05	0.000874909	1176.2	0.282040	0.282398	0.282320	0.282145	3.74	0.70824	1.73	1.5602844
KM_SDF3_02	0.281875113	1.63066E-05	0.000336238	1145	0.282060	0.282421	0.282342	0.281868	-6.80	0.57073	2.36	2.1844438
KM_SDF3_03	0.282631839	1.8879E-05	0.000908325	308.5	0.282591	0.283028	0.282940	0.282627	1.26	0.66076	1.21	1.014976
KM_SDF3_04	0.281589916	2.18449E-05	0.000636215	1069.5	0.282108	0.282476	0.282396	0.281577	-18.82	0.76457	3.03	2.8568083
KM_SDF3_05	0.282529576	1.84221E-05	0.000450428	414.9	0.282524	0.282952	0.282864	0.282526	0.07	0.64477	1.37	1.1749109
KM_SDF3_06	0.281634135	1.84525E-05	0.000659463	1760.1	0.281664	0.281969	0.281897	0.281612	-1.83	0.64584	2.53	2.3745518
KM_SDF3_07	0.282082701	2.02221E-05	0.00097189	1142.5	0.282061	0.282423	0.282344	0.282062	0.01	0.70777	1.94	1.7633686
KM_SDF3_08	0.281851195	2.26623E-05	0.001761603	1566.1	0.281789	0.282112	0.282038	0.281799	0.35	0.79318	2.25	2.0851327
KM_SDF3_09	0.282078806	2.01799E-05	0.000735659	1574.6	0.281784	0.282106	0.282031	0.282057	9.70	0.7063	1.68	1.5191098
KM_SDF3_10	0.281849375	1.86236E-05	0.000558121	1579.7	0.281780	0.282102	0.282028	0.281833	1.86	0.65183	2.16	2.0041725
KM_SDF3_11	0.282865807	2.83989E-05	0.001806167	251.9	0.282627	0.283069	0.282980	0.282857	8.16	0.99396	0.73	0.5301756
KM_SDF3_12	0.282097506	2.47964E-05	0.000784954	1125.6	0.282072	0.282435	0.282356	0.282081	0.31	0.86788	1.90	1.7316452
KM_SDF3_13	0.282745473	2.07385E-05	0.001235472	324.6	0.282581	0.283017	0.282928	0.282738	5.56	0.72585	0.95	0.7550795
KM_SDF3_14	0.281802378	2.38184E-05	0.001315577	1091.4	0.282094	0.282460	0.282381	0.281775	-11.30	0.83365	2.59	2.4167974
KM_SDF3_15	0.282120246	2.00412E-05	0.000765401	1414	0.281887	0.282224	0.282148	0.282100	7.54	0.70144	1.69	1.519525
KM_SDF3_16	0.282195676	1.76013E-05	0.000652616	1043.4	0.282125	0.282495	0.282415	0.282183	2.06	0.61604	1.73	1.5567786
KM_SDF3_17	0.282515703	2.31734E-05	0.001722631	349.1	0.282566	0.282999	0.282911	0.282504	-2.16	0.81107	1.46	1.263169
KM_SDF3_18	0.282729745	1.82386E-05	0.001132222	316.8	0.282586	0.283022	0.282934	0.282723	4.85	0.63835	0.99	0.7934372
KM_SDF3_19	0.282201474	2.47109E-05	0.001866186	1213.8	0.282016	0.282371	0.282293	0.282159	5.07	0.86488	1.68	1.5084822
KM_SDF3_20	0.282443211	2.09071E-05	0.000901788	284.5	0.282606	0.283046	0.282957	0.282438	-5.94	0.73175	1.65	1.449547
KM_SDF3_21	0.282707425	2.02128E-05	0.000827895	293.6	0.282601	0.283039	0.282950	0.282703	3.62	0.70745	1.05	0.8529032
KM_SDF3_22	0.282791022	1.89757E-05	0.000532674	301.8	0.282595	0.283033	0.282945	0.282788	6.82	0.66415	0.86	0.656225
KM_SDF3_23	0.28275755	2.34499E-05	0.001130669	246.2	0.282630	0.283073	0.282984	0.282752	4.32	0.82075	0.97	0.7705504
KM_SDF3_24	0.282913599	1.66273E-05	0.000636089	130.7	0.282703	0.283156	0.283066	0.282912	7.39	0.58195	0.69	0.4803478
Sample SDF-5: GDA 94, 530316 mE, 6592874 mN												
KM_SDF5_01	0.282744536	1.65442E-05	0.000543697	297.7	0.282598	0.283036	0.282948	0.282742	5.08	0.57905	0.96	0.763517
KM_SDF5_02	0.282030003	1.93576E-05	0.000480361	1268.5	0.281981	0.282331	0.282253	0.282019	1.34	0.67752	1.95	1.7832258
KM_SDF5_03	0.28223913	2.818E-05	0.0013906	1052.2	0.282119	0.282489	0.282409	0.282212	3.28	0.9863	1.66	1.488353
KM_SDF5_04	0.281913887	1.72444E-05	0.000428462	1160.9	0.282050	0.282410	0.282331	0.281905	-5.14	0.60356	2.27	2.0953814
KM_SDF5_05	0.281555261	1.78859E-05	0.000444057	1710.8	0.281696	0.282005	0.281932	0.281541	-5.50	0.62601	2.71	2.5561506
KM_SDF5_06	0.282063293	2.99024E-05	0.000630497	996.5	0.282155	0.282530	0.282449	0.282051	-3.66	1.04658	2.05	1.8728569
KM_SDF5_07	0.282537624	1.97353E-05	0.000604405	441.7	0.282507	0.282932	0.282845	0.282533	0.90	0.69073	1.34	1.1440216
KM_SDF5_08	0.2829246	2.02399E-05	0.000322077	153	0.282689	0.283140	0.283050	0.282924	8.30	0.7084	0.64	0.4402988
KM_SDF5_09	0.282248634	4.19297E-05	0.000994672	963.6	0.282176	0.282554	0.282473	0.282231	1.95	1.46754	1.68	1.4993106
KM_SDF5_10	0.281858327	1.96587E-05	0.000368537	1167.1	0.282046	0.282405	0.282326	0.281850	-6.93	0.68805	2.38	2.2095864
KM_SDF5_11	0.282149994	2.33719E-05	0.000437428	550	0.282439	0.282854	0.282768	0.282145	-10.38	0.81802	2.12	1.9352749
KM_SDF5_12	0.282138118	2.17449E-05	0.000715369	1184	0.282035	0.282393	0.282314	0.282122	3.10	0.76107	1.78	1.6064815
KM_SDF5_13	0.282279104	3.01743E-05	0.001906756	931.1	0.282196	0.282577	0.282496	0.282246	1.75	1.0561	1.66	1.4854443

Analysis #	$^{176}Hf/^{177}Hf$	2 S.E.	$^{176}Lu/^{177}Hf$	U/Pb AGE	Hf Chur (t)	Hf DM (t)	Hf NC(t)	Hf_i	epsilon	1s	T(DM) (crustal)	T(NC) (crustal)
KM_SDF5_14	0.281950111	3.16909E-05	0.002341991	1620.4	0.281754	0.282072	0.281998	0.281878	4.41	1.10918	2.04	1.8814998
KM_SDF5_15	0.282089545	2.06138E-05	0.000755352	1169.1	0.282044	0.282404	0.282325	0.282073	1.01	0.72148	1.90	1.7232291
KM_SDF5_16	0.282153997	2.2942E-05	0.000971491	501.6	0.282469	0.282889	0.282803	0.282145	-11.48	0.80297	2.16	1.9659625
KM_SDF5_17	0.282480181	2.39448E-05	0.00044784	588.1	0.282414	0.282827	0.282741	0.282475	2.15	0.83807	1.37	1.1832062
KM_SDF5_18	0.281086969	2.4828E-05	0.001084368	2700.9	0.281049	0.281266	0.281205	0.281031	-0.65	0.86898	3.20	3.067671
KM_SDF5_19	0.282097448	1.80488E-05	0.00046684	1156.2	0.282053	0.282413	0.282334	0.282087	1.23	0.63171	1.87	1.6994107
KM_SDF5_20	0.282677526	1.91695E-05	0.000892389	285.4	0.282606	0.283045	0.282956	0.282673	2.37	0.67093	1.12	0.9255455
KM_SDF5_21	0.282331301	1.72314E-05	0.000509572	552.5	0.282437	0.282852	0.282766	0.282326	-3.93	0.6031	1.73	1.535857
KM_SDF5_22	0.282073951	2.32143E-05	0.000989278	725	0.282328	0.282727	0.282643	0.282060	-9.46	0.8125	2.20	2.0159142
KM_SDF5_23	0.282224069	1.25718E-05	0.000171761	588.1	0.282414	0.282827	0.282741	0.282222	-6.81	0.44001	1.93	1.7435563
KM_SDF5_24	0.28271915	2.54866E-05	0.000812479	276.2	0.282611	0.283052	0.282963	0.282715	3.66	0.89203	1.04	0.8363763
KM_SDF5_25	0.282135766	1.46356E-05	0.000161102	566.1	0.282428	0.282842	0.282757	0.282134	-10.42	0.51224	2.14	1.9506168
KM_SDF5_26	0.282116104	1.68842E-05	0.00054711	1152.2	0.282055	0.282416	0.282337	0.282104	1.74	0.59095	1.84	1.6646574
KM_SDF5_27	0.281869478	1.81778E-05	0.000573208	1232.9	0.282003	0.282357	0.282279	0.281856	-5.22	0.63622	2.33	2.1576915
KM_SDF5_28	0.282010641	2.49305E-05	0.001416157	1128.2	0.282071	0.282433	0.282354	0.281981	-3.19	0.87257	2.12	1.9493091
KM_SDF5_29	0.282474791	1.88545E-05	0.000435255	600.7	0.282406	0.282817	0.282732	0.282470	2.25	0.65991	1.38	1.1875094
KM_SDF5_30	0.282203378	1.45314E-05	0.000369231	818.8	0.282268	0.282659	0.282576	0.282198	-2.49	0.5086	1.84	1.6584555
KM_SDF5_31	0.281042354	2.28645E-05	0.000702958	2614.1	0.281106	0.281331	0.281269	0.281007	-3.52	0.80026	3.30	3.1666202

CHAPTER 7

Conclusions and Future Directions

"Their study involves many difficult problems,
but is of more than ordinary interest,
as they will, no doubt, throw light on the
early conditions of the Australian continent
and the development of its orographic features."

- Walter Howchin, 1906,
on the basement rocks in the Mount Lofty Ranges

The primary aim of this thesis is to build an understanding of the geological development of the Barossa Complex, with a view to incorporate it into continental reconstruction models for the Gawler Craton and Australia during the Late Palaeoproterozoic. The first part of this thesis systematically addresses this by first building the stratigraphic and structural framework in chapters 2 and 3, determining constraints on the depositional timing and likely provenance of sediment in chapter 4, before assessing the timing of metamorphic events in the Barossa Complex in chapter 5.

The secondary aim of the thesis is to assess the validity and usefulness of the detrital zircon method in the modern environment as well as in the geological record, with specific reference to studies conducted on the Gawler Craton and the Curnamona Province.

Part 1:
Chapter 2-3: Stratigraphy and Proterozoic Structures of the Barossa Complex

The Barossa Complex is exposed as 5 basement inliers in the southern Mt. Lofty ranges in South Australia (Figure 1), and are primarily composed of metasedimentary rocks. In all of the mapped areas of the Barossa Complex, younging indicators are not preserved and as such the depositional younging sequence has to be established through detrital zircon geochronology.

The Houghton Inlier preserves the best stratigraphic relationships. The detrital zircon geochronology in Chapter 4, and by Jagodzinski et al. (2017), indicate that the sedimentary pile is presently the correct way up. The oldest and structurally lowest units are a calcsilicate gneiss and a quartzofeldspathic gneiss, which in parts are separated by a discontinuous unit of now completely seritcised gneiss which was primarily composed of thick bands of micaceous and feldspathic material. These units are best exposed in the southern Houghton Inlier in a NNW-SSE trending anticline, with additional small exposures occurring in the north-western extent of the inlier. These lower units are overlain by a psammopelite which is mapped as biotite-sericite gneiss. This unit is partially migmitised and dominated by fine (~5mm) segregations of micaceous and quartzofeldspathic material. The psammopelitic unit then grades up into an aluminous metapelitic gneiss, which is defined by the appearance of sillimanite and mapped as Sillimanite Gneiss. Within the sillimanite gneiss, a discontinuous minor unit of garnetiferous gneiss occurs. It is unclear whether the discontinuous nature of this lithology is the result of prolithic variation or as a result of tectonic and metamorphic processes. The biotite-sericite gneiss and sillimanite gneiss make up the bulk of the exposure in the Houghton Inlier. In the south-eastern extent of the inlier the sillimanite gneiss appears to be structurally overlain by a second calcsilicate gneiss. The boundary of this calcsilicate is inferred from regional magnetic imagery which presents a magnetic low over areas corresponding to this unit, and is in contrast to the magnetic high of the rest of the inlier. This exposure of calcsilicate is inferred to be at least partially fault bound.

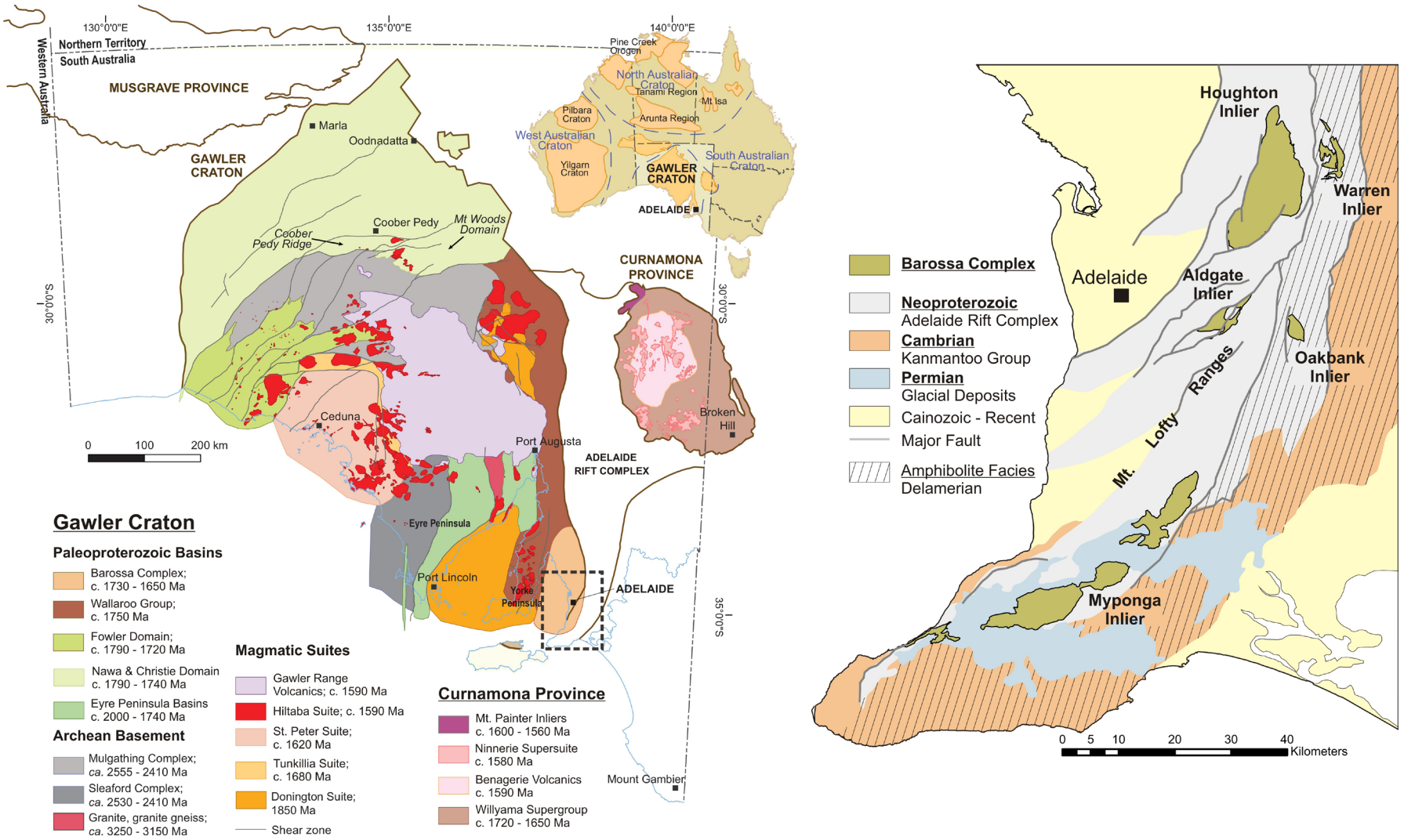

Figure 1: Geological map of the Gawler Craton and Curnamona Province in South Australia after Reid, et al. (2017), with inset geological domains of the Mount Lofty Ranges after Preiss (1993), with focus on the Barossa Complex basement inliers.

A layer parallel metamorphic fabric (S_1) is preserved in the Houghton Inlier, which is defined by the segregation of quartzofeldspathic material in psammopelitic gneisses, and sillimanite foliation in pelitic gneisses. This fabric is subsequently deformed by two Proterozoic folding phases. The first generation of folds produced west verging open to tight folds (F_2), and these were subsequently deformed by an apparently NE-SW oriented compressional regime generating regional scale open folds (F_3). Greenschist facies retrogression during the Delamerian Orogeny produced extensive phylonnisation and the development of a strong cleavage (S_4) which obliterates many of the Palaeo-Mesoproterozoic structures in many places in the Houghton Inlier.

In the Warren Inlier, mesoscopic structures are dominantly associated with foliation and fold development during the Delamerian Orogeny. A low angle muscovite-biotite foliation (S_4) dominates most outcrops. This is subsequently deformed by E-W to NE-SW oriented compression which generated folding from the mesoscopic to regional scale. In numerous outcrops, small wavelength (~5cm) folds are preserved refolded around larger (0.5-1m) wavelength folds, indicating at least two deformation stages after the formation of the S_4 foliation (F_5/F_6). The D_4-D_6 structures in the Warren Inlier are consistent with the D_1-D_3 structures in the overlying Neoproterozoic sequences.

Similar stratigraphic successions to those in the Houghton Inlier have been identified in the other Barossa Complex inliers (Figure 2). In the Warren Inlier, the structurally lowest unit is a quartzofeldspathic gneiss which appears to grade into a psammopelitic biotite-migmatite gneiss, which in turn grades into a dominantly muscovite schist. The muscovite schist is interpreted to be part of a retrograde assemblage, with remnant sillimanite gneiss identified in several localities that is interpreted to represent the primary metamorphic lithology. This psammopelite-pelite association is proposed to correlate to the similar assemblages in the Houghton Inlier (Figure 2). Similarly in the Aldgate Inlier, a psammopelitic gneiss is structurally overlain by a pelitic sillimanite bearing gneiss. The boundary between these two lithologies is still poorly defined. A calcsilicate also occurs in a small exposure in the southern part of the Aldgate Inlier. However, its relationship to the other lithologies is obscured by Neoproterozoic sequences. These three inliers all contain a succession of psammopelitic gneiss which appear to grade into a pelitic gneiss. In the case of the Warren and Houghton inliers, these are underlain by a quartzofeldspathic gneiss. A psammopelitic gneiss, locally schist, occurs in the Oakbank Inlier and records a comparable maximum depositional age (MDA) to that of the biotite-sericite gneiss in the Houghton Inlier, and this is also considered to represent a likely stratigraphic correlation (Figure 2).

In the southern Myponga Inlier, a different stratigraphic sequence occurs. A quartzofeldspathic gneiss is structurally overlain by a garnet-sillimanite bearing metapelite. This metapelite encloses quartzite and calcsilicate. A prominent domain of interlayered quartzite and calcsilicate gneiss occurs between the pelitic sillimanite-garnet gneiss and a psammopelitic biotite-quartzofeldspathic gneiss. These metasedimentary lithologies occur in association with mafic amphibolites which either erupted or intruded prior to granulite facies metamorphism. Post deformational pegmatites subsequently intruded at 1580 ±4 Ma (Jagodzinski et al. 2017).

Many of the lithological contacts are obscured in the Myponga Inlier by retrograde shear zones dominated by biotite-chlorite schists, which developed in at least two generations between the Mesoproterozoic and the Ordovician. One shear zone displaying east side down extensional kinematics preserves a monazite ages at c. 1560 Ma (Morrissey et al. 2013). These are comparatively rare

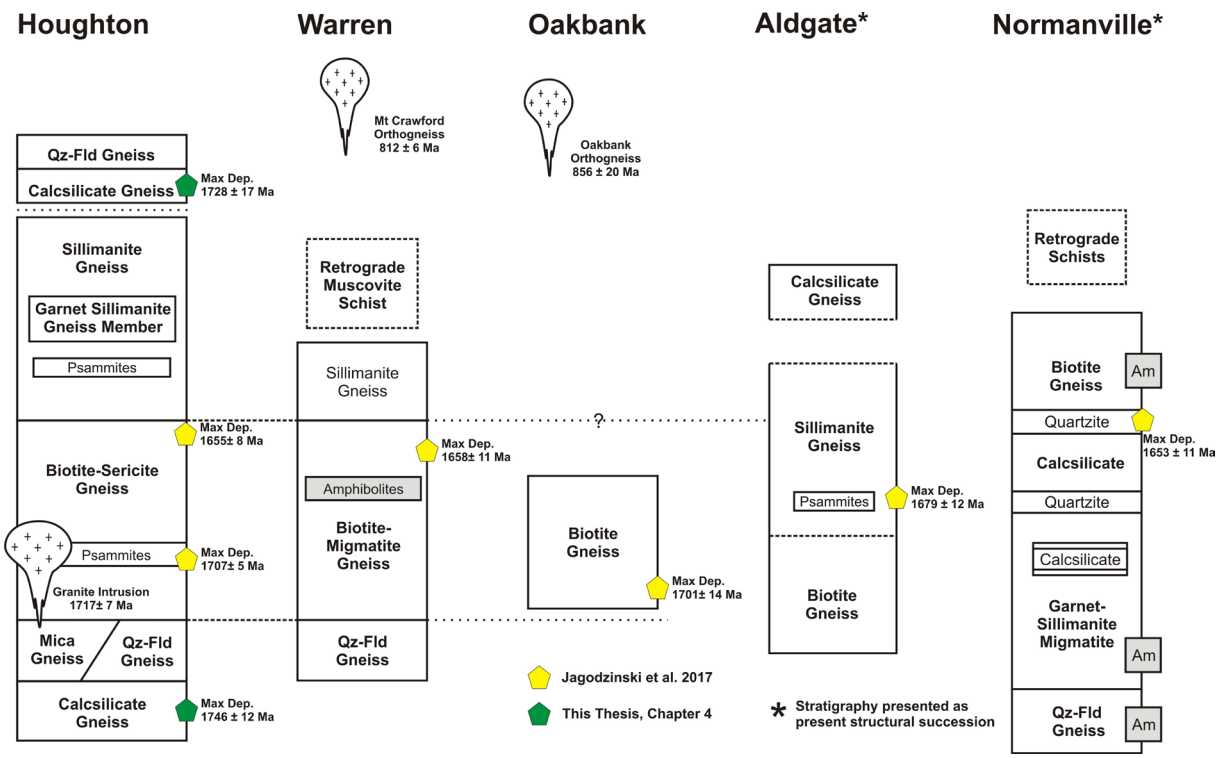

Figure 2: Proposed stratigraphic correlations between the 5 Barossa Complex inliers based on the lithological similarity and established maximum depositional ages, as established in Chapters 2-4 and Jagodzinski et al. (2017).

and the overall dominant shear sense is top to the west thrusting. These compressional shears also deform Neoproterozoic sequences and are attributed to the Cambro-Ordovician Delamerian Orogeny.

A quartzite layer from the Normanville exposure of the Myponga Inlier yields a maximum depositional age of 1653 ±11 Ma, which is comparable to that obtained in psammopelitic metasediments from the Houghton and Warren Inliers. Whether this represents the same depositional timing or merely the same sediment provenance is unclear, and as such the relationship between the southern Myponga Inlier and northern inliers is unknown.

Chapter 4: Depositional Timing

Detrital zircon U-Pb geochronology has revealed the depositional timing of the protoliths to the Barossa Complex occurred between c. 1740 Ma and 1655 Ma. In the Houghton Inlier, two calcsilicate samples yielded detrital zircon MDA of 1728 ±17 Ma and 1746 ±12 Ma. These samples were collected from the top and the bottom of the proposed stratigraphic column. However, the detrital zircon MDA from the upper extent of the biotite-sericite gneiss yielded 1655 ±8 Ma (Jagodzinski et al. 2017). This indicates that the upper calcsilicate unit in the Houghton Inlier, which is defined through geophysical imaging, is a structural repetition.

The South Para Orthogneiss (SPOG) has previously been reported as having a magmatic crystallisation age of 1717 ±7 Ma (Jagodzinski et al. 2017). However, this study yielded a magmatic crystallisation age of 1698 ±10 Ma. This discrepancy in ages is most likely the result of metamorphic disturbance. A further sample of quartzofeldspathic gneiss, which yielded a unimodal detrital zircon population of 1693 ±7 Ma. Again, this likely reflects a metamorphically disturbed population of zircon based on zircon morphologies and

the sample's position within the stratigraphy. The upper limits of the timing of deposition of protoliths to the Barossa Complex is given by the onset of metamorphism, recorded in metamorphic rims in zircon at between 1630-1620 Ma in the Houghton and Myponga inliers.

The oldest MDA's and the intrusion of the protolith to the SPOG confine the initiation of deposition to between 1740 Ma and 1717 Ma, which corresponds to the onset of the c. 1730-1690 Ma Kimban Orogeny in the eastern Gawler Craton. Given the proximity of this event to the Barossa Complex, the eastern Gawler Craton is a likely sediment source for the Barossa Complex metasedimentary rocks. This is supported by the detrital zircon provenance. The combined detrital zircon datasets from this work and Jagodzinski et al. (2017) reveal a detrital zircon age spectrum with major peaks at 1655 Ma, 1690 Ma, 1730 Ma, 1760 Ma, 1790 Ma, 1830 Ma, and 1850 Ma. The 1730-1790 Ma and 1850 Ma zircon populations are consistent with bimodal magmatic events in the eastern Gawler Craton of this age (e.g. Jagodzinski 2005, Fanning et al. 2007, Szpunar and Fraser 2010, Szpunar et al. 2011). Detrital zircon from the Barossa Complex records comparable Hf isotopic values to that found in other Paleoproterozoic basins in the central and northern Gawler Craton which were metamorphosed during the Kimban Orogeny (Payne et al. 2008, Howard et al. 2011a, Howard et al. 2011b). Uplift and erosion of these and equivalent sequences during the Kimban Orogeny is a likely source of sediment in the older Barossa Complex sequences. The 1690 Ma zircon populations in the Barossa Complex are consistent in age with volcanics in the Curnamona Province (Raetz et al. 2002, Page et al. 2005). Populations at 1655 Ma and 1830 Ma do not correspond to the Gawler Craton, and the sources of these zircons is unknown. 1655 Ma detrital zircon populations occur in sedimentary rocks in the Gawler Craton, Willyama Supergroup, and Mount Isa Inlier, which are associated with a whole rock shift in ε_{Nd} isotopic values from evolved to more juvenile signatures, and may be sourced from a juvenile magmatic source at 1655 Ma which has yet to be identified (Barovich and Hand 2008, Lambeck et al. 2012).

The depositional timing of parts of the Barossa Complex overlap with the depositional timing of the Willyama Supergroup in the Curnamona Province, which was deposited in a rift basin between 1720-1630 Ma (e.g. Page et al. 2005, Stevens et al. 2008). The Willyama Superbasin has previously been correlated to the Calvert – Isa Superbasin sequences in the Mount Isa Inlier based on similar depositional timing and setting, magmatism, and base metal mineralisation. Recent reconstruction models of Australia predict that this basin would continue south of the Curnamona Province into the eastern Gawler Craton (Aitken et al. 2016). The location, depositional timing, and timing of magmatic intrusives of the Barossa Complex is consistent with this being a part of this larger transcontinental basin system which dominated eastern Australia during the Late Paleoproterozoic.

Chapter 5: Metamorphic History

The Barossa Complex records an 80 million year metamorphic history during the Late Paleo- to Early Mesoproterozoic (Figure 3). The Houghton Inlier records extensive metamorphic zircon growth at c. 1630 Ma. This metamorphic period is poorly preserved in the other inliers. Previous high resolution zircon dating has revealed a second pulse of metamorphic zircon growth at c. 1610 Ma (Jagodzinski et al. 2017). The most pervasive and best recorded metamorphic age corresponds to the period of 1590-1580 Ma. The southern Myponga Inlier and Aldgate Inlier only preserve the 1590-1580 Ma event, and it is the most common metamorphic age preserved in the Warren Inlier.

Previous work has determined peak metamorphic conditions for the Houghton and Myponga inliers of 800-870^{o}C and 8-9 Kbar

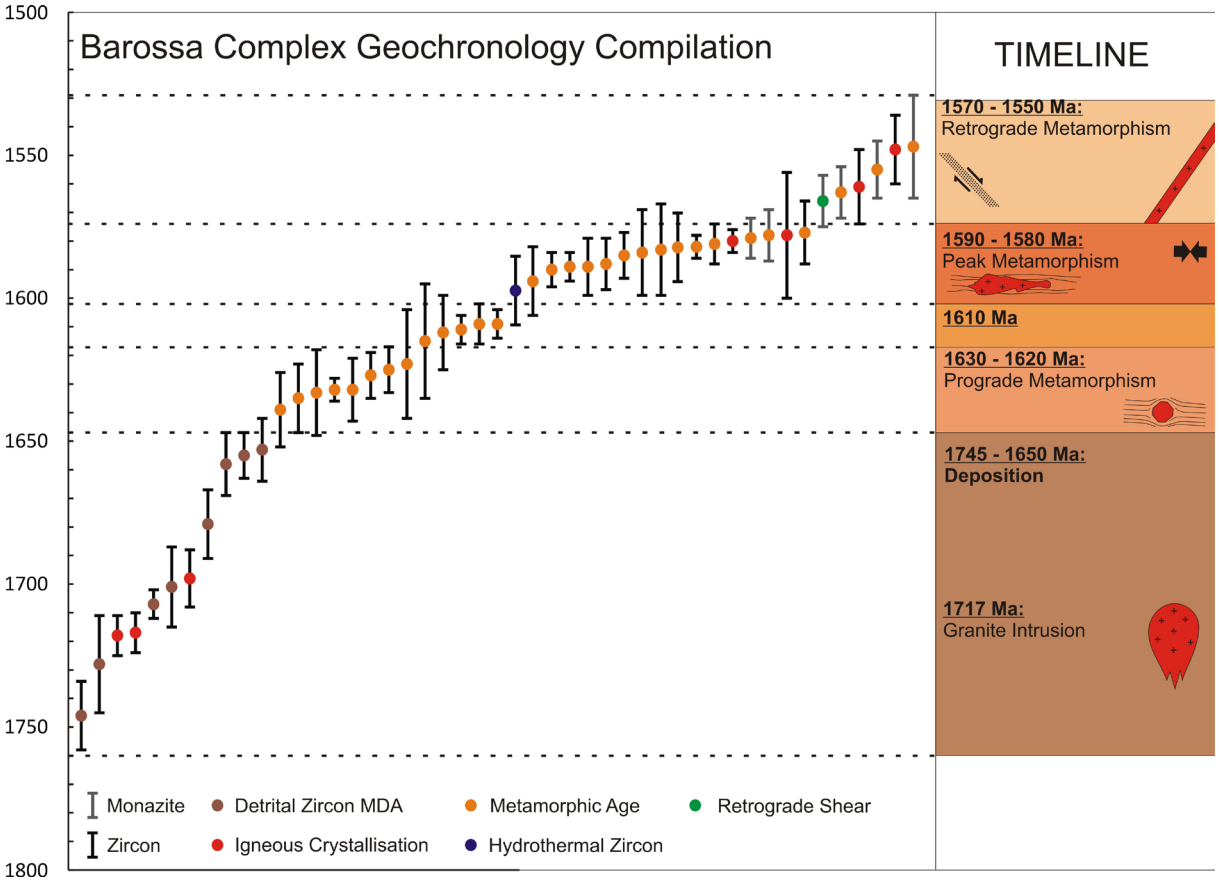

Figure 3: Compilation of published geochronology in addition to that from this thesis, illustrating the different stages of development of the Barossa Complex.

(Morrissey et al. 2013). However the timing of these peak conditions was unclear. Rare Earth Element (REE) partitioning coefficients between garnet and zircon reveal trends in granulite grade metapelite in the Myponga Inlier consistent with peak metamorphic garnet growth coinciding with the growth of zircon at 1581 ±12 Ma. In the Houghton Inlier, REE trends of a 1599 ±10 Ma zircon population are highly enriched in light REE as well as heavy REE; a highly unusual trend for metamorphic zircon. This trend is consistent with zircon grown or modified in hydrothermal conditions. The REE partitioning coefficients between garnet and zircon indicate disequilibrium growth, and makes 1630-1610 Ma the likely timing of development for preserved metamorphic features in the Houghton Inlier, namely the low angle metamorphic fabric (S_1). A small number of LREE enriched zircons also occur in the Myponga Inlier indicating that hydrothermal fluids were present throughout the exposed extent of the Barossa Complex between 1600-1580 Ma. The nature of these fluids is unknown. Several areas exist in the Houghton Inlier which contain quartz veining with fluid alteration halos, and these features may correspond to the 1600-1580 Ma hydrothermal event. Historically, some of these quartz veins have been found to be gold bearing (Brown 1885). If the 1600-1580 Ma hydrothermal fluids are responsible for these mineralised domains, they may be related to the wider Hiltaba event, which affected the Gawler Craton between 1590-1570 Ma. This event created numerous mineral deposits in the Gawler Craton through the interaction of hydrothermal fluids and magmatic intrusions, including the world class Olympic Dam deposit. As such further characterisation of the hydrothermal fluids in the Barossa Complex may provide further insight into this

economically significant event.

The implications of hydrothermal zircon in the Houghton Inlier and granulite-grade zircon in the Myponga inlier are that the peak mineral assemblages preserved in these two areas are not of the same age, and therefore that the metamorphic conditions described by Morrissey et al. (2013) are not the same age.

The intrusion of an undeformed pegmatite body at 1580 ±4 Ma in the southern Myponga Inlier marks the end deformation associated with high grade metamorphism (Jagodzinski et al. 2017). Monazite growth between 1570-1550 Ma corresponds to post-peak evolution of the Houghton Inlier and likely the development of retrograde shear zones in the Myponga Inlier (Morrissey et al. 2013). During this retrograde interval, a series of pegmatites intruded the northern Houghton and Warren inliers at 1561 ±13 Ma and 1548 ±12 Ma, which indicates a late thermal pulse or decompression generated conditions deeper in the crust capable of producing melt.

The metamorphic history recorded in the Barossa Complex is essentially identical to that recorded in other Paleoproterozoic basins in eastern Australia. In the Willyama Supergroup in the Curnamona Province, metamorphism initiated at c. 1620 Ma, producing a low angle to layer parallel fabric. This was subsequently deformed during peak metamorphism at c. 1600 Ma under relatively low pressure-high temperature conditions (i.e. Forbes et al. 2007a). Retrograde monazite in the Willyama Supergroup yields ages of c. 1570 Ma (Rutherford et al. 2007). An almost identical metamorphic history is recorded in the Mt. Isa Inlier, where a low angle metamorphic fabric developed at approximately 1620 Ma (Rubenach et al. 2008) before peak metamorphism occurred at 1600 Ma (Page and Sun 1998, Giles and Nutman 2002) with subsequent retrograde metamorphism at 1550-1540 Ma (Giles et al. 2006). The essentially identical metamorphic style and duration of the Barossa Complex to these other eastern Australian Paleoproterozoic terranes strongly suggests a continuation of this larger metamorphic event which incorporated the entire eastern margin of Proterozoic Australia.

Part 2:

Chapter 6: On the Use of Detrital Zircons

Chapter 6 addresses zircon U-Pb ages derived from modern stream sediment with comparison to the bedrock of the catchment areas of those streams. Modern stream sediments sampled from around the Broken Hill area in the eastern Curnamona Province, South Australia (Figure 1), contain catchment areas with bedrock physiology composed entirely of the 1710-1640 Ma Willyama Supergroup. The last period of known zircon growth in this area occurred during the c. 1600 Ma Olarian Orogeny. Therefore erosion of this basement should not generate sediment with zircon younger than the earliest Mesoproterozoic. However, the stream sediments sampled yield zircon populations as young as 100 Ma, with approximately 30% of all zircon analysed yielding ages between 1400-100 Ma. Despite the fact that the physical character of the sediment indicated that it is source proximal and immature, it is clear that an additional zircon sources are contributing to the sediment.

Zircon sampled from aeolian dunes 120km north of the Broken Hill area contain U-Pb and Lu-Hf isotopic values consistent with the incongruous populations in the Broken Hill stream sediments, and as such aeolian transport is the most plausible source for the exotic zircon populations in the stream sediments. However, the dune sands also contain zircon which preserve ages consistent with that found in the Willyama Supergroup, and as such the interpretation of any zircon isotopic values obtained from modern sediment in the Broken Hill area can have little certainty attributed to them regarding their source.

The sources of the dune sands are the dry inland lakes of the Lake Eyre Basin in southern Central Australia, which sample approximately one seventh of the Australian

continent. Catastrophic dust storm events in recent times have demonstrated how sediment from the now arid Lake Eyre Basin can be transported in excess of 2000km in a single event. Events such as this lead to widespread homogenisation of zircon populations in the modern environment and make identifying zircon sources difficult without in situ sampling for comparison.

In studies relying on the use of modern detrital zircon, the character of the regolith in addition to the bedrock of the catchment areas must be considered. One such example comes from the Gawler Craton, in which modern sediment sampling across the extent of the craton found significant populations of c. 1000-1400 Ma zircon, with some populations as young as 300 Ma (Belousova et al. 2009). The interpretation of this data was that during the Mesoproterozoic the Gawler Craton was tectonically active and received significant juvenile inputs during an as yet unidentified event. This is in spite of low temperature geochronometers not recording any significant activity in the Gawler craton after c. 1450 Ma (Webb et al. 1986, Fraser and Lyons 2006), and significant zircon deposits on the southwest margins of the craton having been derived from the Mesoproterozoic Albany-Fraser Orogen to the west (Reid et al. 2013). Despite the ambiguity surrounding it, this extensive modern detrital zircon data set has been widely used when considering the geodynamic evolution of the Gawler Craton throughout the Proterozoic (e.g. Smits et al. 2014, Mulder et al. 2015, Armit et al. 2017). This illustrates the risks involved in addressing provenance through detrital zircon in not only the modern environment, but also the ancient. While in the modern environment it is relatively straightforward to identify zircon sources, including natural sources of contamination, in the ancient environment the surface conditions such as aridity are much more difficult to establish.

Implications for reconstruction models: Australia through the Proterozoic

The depositional and metamorphic history of the Barossa Complex closely mimics that of other Paleoproterozoic terranes in eastern Australia. Deposition initiated between 1740-1720 Ma with initially shallow water or high energy depositional environments, before the intrusion of granitic melts at 1717 Ma. A subsequent progression to deep water or lower energy depositional environments occurred until at least 1655 Ma. At some point before the initiation of metamorphism, mafic magmatism also occurred in the Barossa Complex, which strongly suggests an active extensional basin.

During this interval, a rift basin was developing on the eastern margin of proto-Australia which accommodated the deposition of the Willyama supergroup in the Curnamona Province, and the Calvert-Isa Superbasin sequences in the Mt. Isa Inlier (i.e. Forbes et al. 2008, Foster and Austin 2008). In reconstruction models for the Paleo-Mesoproterozoic, the Gawler Craton is frequently rotated 52^{o} northwest of its current position such that the Curnamona Province and Mt. Isa Inliers are juxtaposed against one another (Giles et al. 2004, Betts and Giles 2006). In this configuration the position of the Barossa Complex becomes aligned with this rift basin system, and lies within the proposed extent of this superbasin (Aitken et al. 2016). The driving force of the geodynamic development of this system is proposed to be back arc spreading behind an east dipping subduction zone operating on the eastern margin of Australia (Cawood and Korsch 2008, Aitken et al. 2016).

This rift basin system was inverted and metamorphosed by the Isan-Olarian Orogeny (Page and Sun 1998, Betts et al. 2006, Conor and Preiss 2008). This event was accompanied by a low angle metamorphic fabric in the Willyama Supergroup and Mt. Isa Inlier (Giles et al. 2002, Forbes et al. 2007b), and was subsequently overprinted by folding and high grade metamorphism between 1600-1580 Ma

(Forbes et al. 2008, Giles et al. 2006). This metamorphic history closely mimics that recorded in the Barossa Complex, supporting the interpretation that the Barossa Complex is a continuation of the Willyama-Isa system.

The driving mechanism behind the c. 1600 Ma Olarian-Isan Orogeny is still poorly understood. The link to the Barossa Complex demonstrates that this basin and orogenic system spanned the length of the preserved eastern Australian continent during the Paleo-Mesoproterozoic. The development of a series of rift basins along the eastern Palaeoproterozoic margin is most likely driven by back arc extension behind a subduction zone (Figure 4). Whether the driver of compression was a continental collision (i.e. Betts and Giles 2006, Betts et al. 2015) or another factor remains ambiguous.

Future research directions

While the work presented in this thesis elucidates much of the development of the Barossa Complex and its significance in the Proterozoic development of Australia, there remain a number of avenues of research that deserve further examination. As a stratigraphic framework for much of the Barossa Complex has now been defined, targeted geochemistry could further establish links between this terrain and others in eastern Proterozoic Australia or formerly contiguous crust. One of the features of Late Paleoproterozoic basins in eastern Australia is a shift in Nd isotopic values from an evolved to distinctly more juvenile signature at c. 1655 Ma (Lambeck et al. 2012). These 1655 Ma sequences include those in the Willyama supergroup and in the Gawler Craton. If the Barossa Complex is linked to these basin systems, it will likely contain this Nd isotopic pattern. This shift to juvenile Nd signatures implies sediment input from a juvenile source region, and further characterisation of this isotopic signature could further characterise the basin connectivity and architecture of eastern Australia in the Late Palaeoproterozoic.

Another geochemical feature which has been used to link the basins of the Mt. Isa Inlier and the Willyama Supergroup is the geochemistry of mafic magmas which developed during the development of the rift basin (Baker et al. 2010). If the timing of mafic magmatism can be better established in the Barossa Complex, this avenue of research may provide stronger links between these terrains, as well as allowing for a better characterisation of the Paleoproterozoic rift basin into which these sequences were deposited.

Some ambiguity still remains regarding the metamorphic evolution of the Barossa Complex. The metamorphic conditions calculated by Morrissey et al. (2013) appear to largely reflect the 1590-1580 Ma period, while the prograde evolution between 1630-1610 Ma are essentially unknown. Further P-T analysis of rocks preserving the 1630 Ma signature would allow for a better understanding of the overall metamorphic evolution of the Barossa Complex, and therefore the tectonic regime controlling the metamorphic evolution of the eastern Gawler Craton in the Late Palaeo-Early Mesoproterozoic.

The identification of 1600-1580 Ma hydrothermal zircon in the Barossa Complex means that all subsequent work on metamorphic zircon in the Barossa complex must be accompanied by trace element analysis to accurately characterise its origin. In addition to this, the hydrothermal activity in the Barossa Complex requires further investigation in order to determine the source and effects of this fluid. The more regional c. 1600-1560 Ma hydrothermal activity in the Gawler Craton is linked to the genesis of major ore bodies and as such a better understanding of the source and distribution of hydrothermal fluids at this time may have significant economic implications.

The nature of the Kimban Orogen also deserves further study. This significant metamorphic event in the Gawler craton occurred synchronous with the opening of the Willyama-Barossa rift basin. While the

Kimban Orogen is generally thought of as a compressional event, little structural work exists for this time period outside of transpressional shear zones, and it is unclear what the tectonic regime of the Gawler Craton was during the 1730-1690 Ma interval. Understanding how the Kimban metamorphic event developed and how it relates to the basins of the Barossa and Willyama sediments will have a significant impact on the understanding of the development of the Gawler Craton.

Another major limitation of paleogeographic models is the poor understanding between the link between the Gawler Craton and the North Australian Craton. Recent models have proposed that the Gawler Craton is oroclinally bent (Betts et al. 2015). If this is the case then it is likely that the northern and western elements of the craton were formerly contiguous to the southeastern North Australian Craton. However it is these regions of the Gawler Craton which exhibit poor exposure and much of the work conducted there is limited to samples obtained from sparse drill core and geophysical interpretation. Further exploration of these less exposed regions will allow for better understanding of the development of these regions and allow better and more reliable correlations and reconstructions.

References

Aitken, A. R. A., Betts, P. G., Young, D. A., Blankenship, D. D., Roberts, J. L. & Siegert, M. J., 2016. The Australo-Antarctic Columbia to Gondwana transition. Gondwana Research, 29(1), 136-152.

Armit, R., Betts, P. G., Schaefer, B. F., Yi, K., Kim, Y., Dutch, R. A., Reid, A., Jagodzinski, L., Giles, D. & Ailleres, L., 2017. Late Palaeoproterozoic evolution of the buried northern Gawler Craton. Precambrian Research, 291, 178-201.

Baker, M. J., Crawford, A. J. & Withnall, I. W., 2010. Geochemical, Sm–Nd isotopic characteristics and petrogenesis of Paleoproterozoic mafic rocks from the Georgetown Inlier, north Queensland: Implications for relationship with the Broken Hill and Mount Isa Eastern Succession. Precambrian Research, 177(1–2), 39-54.

Barovich, K. & Hand, M., 2008. Tectonic setting and provenance of the Paleoproterozoic Willyama Supergroup, Curnamona Province, Australia: Geochemical and Nd isotopic constraints on contrasting source terrain components. Precambrian Research, 166(1–4), 318-337.

Belousova, E. A., Reid, A. J., Griffin, W. L. & O'Reilly, S. Y., 2009. Rejuvenation vs. recycling of Archean crust in the Gawler Craton, South Australia: Evidence from U–Pb and Hf isotopes in detrital zircon. Lithos, 113(3–4), 570-582.

Betts, P. G., Armit, R. J., Stewart, J., Aitken, A. R. A., Ailleres, L., Donchak, P., Hutton, L., Withnall, I. & Giles, D., 2015. Australia and Nuna. Geological Society, London, Special Publications, 424.

Betts, P. G. & Giles, D., 2006. The 1800–1100 Ma tectonic evolution of Australia. Precambrian Research, 144(1–2), 92-125.

Betts, P. G., Giles, D., Mark, G., Lister, G. S., Goleby, B. R. & Aillères, L., 2006. Synthesis of the proterozoic evolution of the Mt Isa Inlier. Australian Journal of Earth Sciences, 53(1), 187-211.

Brown, H. Y., 1885. Geological Map of Barossa and Para Wirra (ed Paper, P.).

Cawood, P. A. & Korsch, R. J., 2008. Assembling Australia: Proterozoic building of a continent. Precambrian Research, 166(1–4), 1-35.

Conor, C. H. H. & Preiss, W. V., 2008. Understanding the 1720–1640 Ma Palaeoproterozoic Willyama Supergroup, Curnamona Province, Southeastern Australia: Implications for tectonics, basin evolution and ore genesis. Precambrian Research, 166(1–4), 297-317.

Fanning, C. M., Reid, A. J. & Teale, G., 2007. A geochronological framework for the Gawler Craton, South Australia. Geological Survey of South Australia.

Forbes, C. J., Betts, P. G., Giles, D. & Weinberg, R., 2008. Reinterpretation of the tectonic context of high-temperature metamorphism in the Broken Hill Block, NSW, and implications on the Palaeo- to Meso-Proterozoic evolution. Precambrian Research, 166(1–4), 338-349.

Forbes, C. J., Betts, P. G., Weinberg, R. & Buick, I. S., 2007a. A structural metamorphic study of the Broken Hill Block, NSW, Australia: reply. Journal of Metamorphic Geology, 25(6), 719-723.

Forbes, C. J., Giles, D., Betts, P. G., Weinberg, R. & Kinny, P. D., 2007b. Dating Prograde Amphibolite and Granulite Facies Metamorphism Using In Situ Monazite U-Pb SHRIMP Analysis. The Journal of Geology, 115(6), 691-705.

Foster, D. R. W. & Austin, J. R., 2008. The 1800–1610 Ma stratigraphic and magmatic history of the Eastern Succession, Mount Isa Inlier, and correlations with adjacent Paleoproterozoic terranes. Precambrian Research, 163(1–2), 7-30.

Fraser, G. L. & Lyons, P., 2006. Timing of Mesoproterozoic tectonic activity in the northwestern Gawler Craton constrained by 40Ar/39Ar geochronology. Precambrian Research, 151(3–4), 160-184.

Giles, D., Betts, P. & Lister, G., 2002. Far-field continental backarc setting for the 1.80–1.67 Ga basins of northeastern Australia. Geology, 30(9), 823-826.

Giles, D., Betts, P. G., Aillères, L., Hulscher, B., Hough, M. & Lister, G. S., 2006. Evolution of the Isan Orogeny at the southeastern margin of the Mt Isa Inlier. Australian Journal of Earth Sciences, 53(1), 91-108.

Giles, D., Betts, P. G. & Lister, G. S., 2004. 1.8-1.5-Ga links between the North and South Australian Cratons and the Early-Middle Proterozoic configuration of Australia. Tectonophysics, 380(1-2), 27-41.

Giles, D. & Nutman, A. P., 2002. SHRIMP U–Pb monazite dating of 1600–1580 Ma amphibolite facies metamorphism in the southeastern Mt Isa Block, Australia. Australian Journal of Earth Sciences, 49(3), 455-465.

Howard, K. E., Hand, M., Barovich, K. M. & Belousova, E., 2011a. Provenance of late Paleoproterozoic cover sequences in the central Gawler Craton: exploring stratigraphic correlations in eastern Proterozoic Australia using detrital zircon ages, Hf and Nd isotopic data. Australian Journal of Earth Sciences, 58(5), 475-500.

Howard, K. E., Hand, M., Barovich, K. M., Payne, J. L., Cutts, K. A. & Belousova, E. A., 2011b. U–Pb zircon, zircon Hf and whole-rock Sm–Nd isotopic constraints on the evolution of Paleoproterozoic rocks in the northern Gawler Craton. Australian Journal of Earth Sciences, 58(6), 615-638.

Jagodzinski, E. A., 2005. Compilation of SHRIMP U-Pb geochronological data: Olympic Domain, Gawler Craton, South Australia, 2001-2003, pp. 197 pp, Geoscience Australia.

Jagodzinski, E. A., Meaney, K. J., Szpunar, M. A. & Fraser, G. L., 2017. SHRIPM U-Pb dating of the Barossa Complex, South Australia: exploring tectonic links between the Gawler Craton and Curnamona Province., Department of the Premier and Cabinet, South Australia, Adelaide.

Lambeck, A., Barovich, K., Gibson, G., Huston, D. & Pisarevsky, S., 2012. An abrupt change in Nd isotopic composition in Australian basins at 1655Ma: Implications for the tectonic evolution of Australia and its place in NUNA. Precambrian Research, 208, 213-221.

Morrissey, L. J., Hand, M., Wade, B. P. & Szpunar, M., 2013. Early Mesoproterozoic metamorphism in the Barossa Complex, South Australia: links with the eastern margin of Proterozoic Australia. Australian Journal of Earth Sciences, 60(8), 769-795.

Mulder, J. A., Halpin, J. A. & Daczko, N. R., 2015. Mesoproterozoic Tasmania: Witness to the East Antarctica–Laurentia connec-

tion within Nuna. Geology, 43(9), 759-762.

Page, R. W., Conor, C. H. H., Stevens, B. P. J., Gibson, G. M., Preiss, W. V. & Southgate, P. N., 2005. Correlation of Olary and Broken Hill Domains, Curnamona Province: Possible relationship to Mount Isa and other North Australian Pb-Zn-Ag-bearing successions. Economic Geology, 100(4), 663-676.

Page, R. W. & Sun, S. S., 1998. Aspects of geochronology and crustal evolution in the Eastern Fold Belt, Mt Isa Inlier. Australian Journal of Earth Sciences, 45(3), 343-361.

Payne, J. L., Hand, M., Barovich, K. M. & Wade, B. P., 2008. Temporal constraints on the timing of high-grade metamorphism in the northern Gawler Craton: implications for assembly of the Australian Proterozoic. Australian Journal of Earth Sciences, 55(5), 623-640.

Preiss, W. V., 1993. Basement Inliers of the Mount Lofty Ranges. In: The Geology of South Australia, Volume 1, The Precambrian (eds Drexel, J. F., Preiss, W. V. & Parker, A. J.), pp. 102-105, Geological Survey of South Australia, Adelaide.

Raetz, M., Krabbendam, M. & Donaghy, A. G., 2002. Compilation of Pb zircon data from the Willyama Supergroup, Broken Hill region, Australia: Evidence for three tectonostratigraphic successions and four magmatic events? Australian Journal of Earth Sciences, 49(6), 965-983.

Reid, A., Keeling, J., Boyd, D., Belousova, E. & Hou, B., 2013. Source of zircon in world-class heavy mineral placer deposits of the Cenozoic Eucla Basin, southern Australia from LA-ICPMS U–Pb geochronology. Sedimentary Geology, 286–287, 1-19.

Reid, A. J., Jourdan, F. & Jagodzinski, E. A., 2017. Mesoproterozoic fluid events affecting Archean crust in the northern Olympic Cu–Au Province, Gawler Craton: insights from 40Ar/39Ar thermochronology. Australian Journal of Earth Sciences, 64(1), 103-119.

Rubenach, M. J., Foster, D. R. W., Evins, P. M., Blake, K. L. & Fanning, C. M., 2008. Age constraints on the tectonothermal evolution of the Selwyn Zone, Eastern Fold Belt, Mount Isa Inlier. Precambrian Research, 163(1–2), 81-107.

Rutherford, L., Hand, M. & Barovich, K., 2007. Timing of Proterozoic metamorphism in the southern Curnamona Province: implications for tectonic models and continental reconstructions. Australian Journal of Earth Sciences, 54(1), 65-81.

Smits, R. G., Collins, W. J., Hand, M., Dutch, R. & Payne, J., 2014. A Proterozoic Wilson cycle identified by Hf isotopes in central Australia: Implications for the assembly of Proterozoic Australia and Rodinia. Geology, 42(3), 231-234.

Stevens, B. P. J., Page, R. W. & Crooks, A., 2008. Geochronology of Willyama Supergroup metavolcanics, metasediments and contemporaneous intrusions, Broken Hill, Australia. Australian Journal of Earth Sciences, 55(3), 301-330.

Szpunar, M., Hand, M., Barovich, K., Jagodzinski, E. & Belousova, E., 2011. Isotopic and geochemical constraints on the Paleoproterozoic Hutchison Group, southern Australia: Implications for Paleoproterozoic continental reconstructions. Precambrian Research, 187(1–2), 99-126.

Szpunar, M. A. & Fraser, G. L., 2010. Age of deposition and provenance of Palaeoproterozoic basins on north-eastern Eyre Peninsula, PIRSA Geological Survey Branch.

Webb, A. W., Thomson, B. P., Blissett, A. H., Daly, S. J., Flint, R. B. & Parker, A. J., 1986. Geochronology of the Gawler Craton, South Australia. Australian Journal of Earth Sciences, 33(2), 119-143.

Appendix 1

Jagodzinski, E.A., Meaney, K., Szpunar, M., and Fraser, G., 2017. *SHRIMP U-Pb dating of the Barossa Complex, South Australia: exploring tectonic links between the Gawler Craton and Curnamona Province.* Report Book 2017/00017. Department of the Premier and Cabinet, South Australia, Adelaide.

SHRIMP U-Pb dating of the Barossa Complex, South Australia: exploring tectonic links between the Gawler Craton and Curnamona Province

E.A.Jagodzinski[1], M.Szpunar[1], K.Meaney[1] and G.Fraser[1]

1 Geological Survey of South Australia, GPO Box 320 Adelaide, South Australia 5001
2 Geoscience Australia, GPO Box 378 Canberra ACT 2601

Report Book 2017/00017

Australian Government
Geoscience Australia

Resources and Energy
Department of the Premier and Cabinet
Level 7, 101 Grenfell Street, Adelaide
GPO Box 320, Adelaide SA 5001
Phone +61 8 8463 3037
Email dpc.minerals@sa.gov.au
www.minerals.dpc.sa.gov.au

South Australian Resources Information Gateway (SARIG)
SARIG provides up-to-date views of mineral, petroleum and geothermal tenements and other geoscientific data. You can search, view and download information relating to minerals and mining in South Australia including tenement details, mines and mineral deposits, geological and geophysical data, publications and reports (including company reports).
map.sarig.sa.gov.au

Preferred way to cite this publication
Jagodzinski, E.A., Szpunar, M., Meaney, K. and Fraser, G. 2017. SHRIMP U-Pb dating of the Barossa Complex, South Australia: exploring tectonic links between the Gawler Craton and Curnamona Province. Report Book 2017/00017. Department of the Premier and Cabinet, South Australia, Adelaide.

Contents

Tables

Figures

SHRIMP U-PB DATING OF THE BAROSSA COMPLEX: EXPLORING TECTONIC LINKS BETWEEN THE CURNAMONA PROVINCE AND GAWLER CRATON.

E.A. Jagodzinski, K. Meaney, M. Szpunar and G. Fraser

INTRODUCTION

The Barossa Complex is a Paleoproterozoic-Mesoproterozoic terrain which lies between the Gawler Craton and Curnamona Province forming the basement to the Neoproterozoic Adelaide Rift Complex. It outcrops as five basement inliers exposed throughout the N-S-trending Mount Lofty Ranges, which extend from Williamstown c. 50 km north of Adelaide to Normanville, c. 70 km south on the Fleurieu Peninsula (Fig. 1). The inliers are overlain by Neoproterozoic-Cambrian sequences of the Adelaide Rift Complex, and are exposed within partially fault bound anticlinal cores generated during the Cambrian-Ordovician Delamerian Orogeny (Offler and Fleming 1968, Mancktelow 1990).

The dominant lithologies of the Barossa Complex include sillimanite- and garnet-bearing gneisses, quartzites and psammites, calcsilicate gneisses, retrograde micaceous rocks and meta-igneous rocks including amphibolites and granitic orthogneisses (Preiss 1993 and references therein). Previous publications on the - evolution suggest up to four deformational events have affected the basement complex (Webb 1953, Davies 1972, Heaslip 1972, Mills 1973). In a more recent study of the northern Houghton and Warren inliers, six deformational events were recorded: three associated with the Proterozoic Olarian Orogeny and three with the Delamerian Orogeny (Meaney et al. in prep).

The Barossa Complex has been metamorphosed to upper amphibolite-granulite facies with peak metamorphism at c. 800 - 870ºC and 8 - 9 Kbar recorded in garnet–sillimanite-bearing gneisses, then retrogressed to greenschist-amphibolite facies during the Delamerian Orogeny and prior (Talbot 1963, Morrissey et al. 2013). Previous U-Pb dating of zircon suggests granulite facies metamorphism occurred at c. 1590 -1580 Ma (Preiss 1993, Szpunar et al. 2007a), with monazites recording ages between c. 1570-1550 Ma representing a pre-Delamerian retrograde phase (Morrissey et al. 2013). Stream sediment sampling by Belousova et al. (2006) identified metamorphic zircon approximately 1625 Ma in age in the northern Barossa Complex, hinting at a multi-stage Proterozoic metamorphic history.

Neoproterozoic granites emplaced during the onset of rifting of the Adelaide Rift Complex intrude the Barossa Complex in the Warren Inlier (812 ± 6 Ma) and Oakbank Inlier (856 ± 20 Ma, Preiss 2008). During the Cambrian-Ordovician Delamerian Orogeny (509.5 - 490 Ma), the Barossa Complex was variably deformed in a major crustal shortening event, and both the basement and cover were folded, and basement blocks thrust westward across the Neoproterozoic Adelaidean cover (Spry 1951, Campana et al. 1954, Heaslip 1972, Steinhardt 1991, Preiss 2000, Foden et al. 2006). A significant thrust fault (Williamstown -Meadows Fault) lies between the Houghton and Warren Inliers, juxtaposing two metamorphic grade zones of the Delamerian Orogeny (Mills 1973, Mancktelow 1990). The Houghton Inlier lies to the west in the lower greenschist facies grade zone and is dominated by Delamerian D_1 structures, while the Warren and Oakbank Inliers lie to the west in amphibolite facies grades, where fibrolitic sillimanite is present and D_2-D_3 structures dominate (Offler and Fleming 1968).

AIMS

SHRIMP dating was undertaken as part of the National Geoscience Agreement (NGA), as a collaborative research project between the Geological Survey of South Australia (GSSA) and Geoscience Australia (GA). Eight samples were collected from the five basement inliers of the Barossa Complex, selected to constrain timing of deposition and provenance of metasediments, early and late magmatism and timing of deformation and metamorphism.

The SHRIMP zircon dating study was initiated as part of a broader program investigating tectonic links between the Curnamona Province and Gawler Craton, both regions of economic significance, hosting some of the largest base metal ore bodies ever found. In Proterozoic palaeogeographic reconstructions, these two domains are often grouped together as the South Australian Craton, although whether they have a common tectonic history has not been comprehensively explored. Positioned on the eastern margin of the Gawler Craton through to the western edge of Curnamona Province, the Barossa Complex is a valuable region in understanding the relationship between the two domains, and this study seeks to provide dates that can be used to better understand the tectonothermal history this domain.

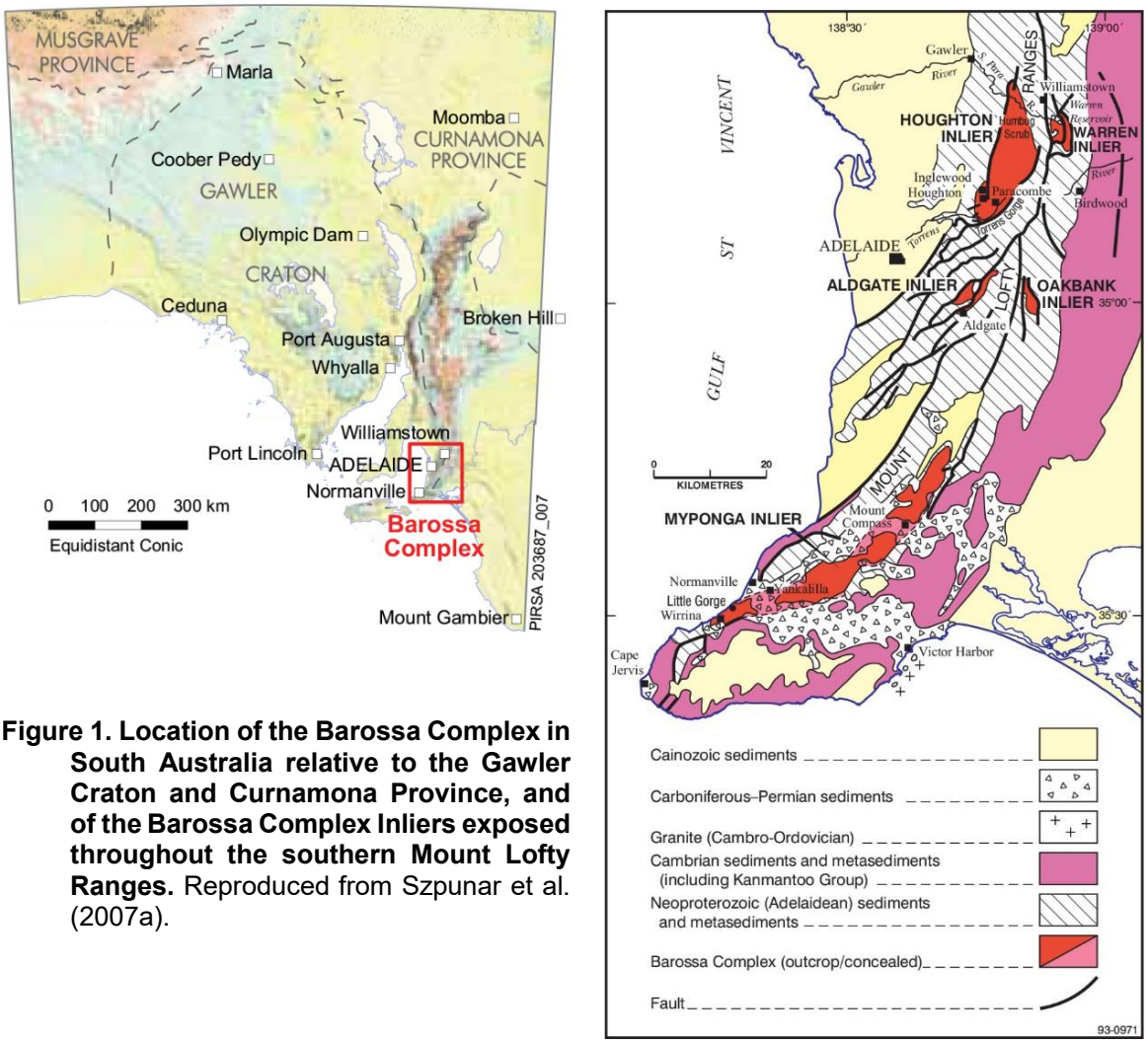

Figure 1. Location of the Barossa Complex in South Australia relative to the Gawler Craton and Curnamona Province, and of the Barossa Complex Inliers exposed throughout the southern Mount Lofty Ranges. Reproduced from Szpunar et al. (2007a).

Table 1. Summary of sample information and U-Pb zircon ages in this report.

Sampno	East	North	Zone	Lithology	Protolith Age			mmc range	Metamorphic peaks							
					Age	error	Age Type		Age1	err	Age 2	err	Age 3	err	Age 4	err
Houghton Inlier																
R695752	302617	6160174	54	granite gneiss	1717	7	Magmatic age	1647 - 1582	1632	4	1609	5	1589	10		
R695753	301614	6161240	54	metaquartzite	1707	5	Dmax (n=2)	1627 - 1582	1627		1605		1589			
R1009272	299633	6142480	54	paragneiss	1655	8	Dmax (n=4)	1616 - 1568			1609	7	1585	8		
Warren Inlier																
R1588241	309134	6157063	54	psammopelite	1658	11	Dmax (n=2)	1619 - 1579			1611	5	1589	5	518	40
Oakbank Inlier																
R1588240	305966	6126053	54	paragneiss	1701	14	Dmax (n=9)	1653 - 1576	1635	12	1612	13	1594	12		
Aldgate Inlier																
R1588243	297129	6127826	54	psammite	1679	12	Dmax (n=3)	1640 - 1576	1633	15			1582	4		
Myponga Inlier																
R1588242	254686	6071105	54	quartzite	1653	11	Dmax (n=2)	1599 - 1575					1590	6		
R695754	255330	6069800	54	coarse monzogranite	1580	4	Magmatic age									

R695752: ORTHOGNEISS, HOUGHTON INLIER

Field sample number:	HI 02		
Location GDA94:	302617 E	6160174 N	Zone 54
Location Lat-Long:	-34°40'53"	138°50'44"	
250K map sheet	Adelaide (SI 54-9)		
100K map sheet	Adelaide (6628)		
Location:	South Para River, Houghton Inlier		
Mount:	Z4597		
Date analysed:	03/08/2005		
Machine:	SHRIMP IIB		
Standard age QGNG:	Batch 1: 1848.3 ± 3.3 Ma Batch 2: 1843.0 ± 3.3 Ma		
Corrected for overcounts to:	Batch 1: 1851.9 ± 3.1 Ma Batch 2: 1851.5 ± 3.4 Ma		
Standard data	Appendix 2		
Interpreted age:	1632 ± 4 Ma and 1589 ± 9 Ma		
Age type:	Metamorphic crystallisation		
Interpreted age:	1716 ± 5 Ma		
Age type:	Magmatic crystallisation of protolith		

FIELD DESCRIPTION

Sample R695752 is a strongly foliated granitic gneiss forming a massive body 3-4 km thick and of unknown lateral extent, with a planar, locally undeformed gneissosity. The composition of this rock is dominated by quartz and plagioclase in roughly equal portions. Segregations of biotite define the gneissosity which is observed wrapping rounded K-feldspar augens up to 3 cm in size (Fig. 2). No minerals indicative of the magma source are observed (i.e. Hornblende, garnet, muscovite, etc). Plagioclase and biotite are often retrogressed to a fine grained sericite.

This sample is located in the northern Houghton Inlier approximately 4 km east of Williamstown in the South Para River gorge (Fig. 3), 100 m downstream from where the river crosses Bassnet Road, very close to the Terranechron sample site of Belousova et al. (2006).

This western margin of the granite gneiss has an intrusive contact with the surrounding psammopelitic and pelitic metamorphic rocks in the northern Houghton Inlier, and it has a sheared margin fabric (in contact with basement metasediments) which parallels the gneissic along its eastern edge. The orthogneiss contains a well-defined linear fabric throughout.

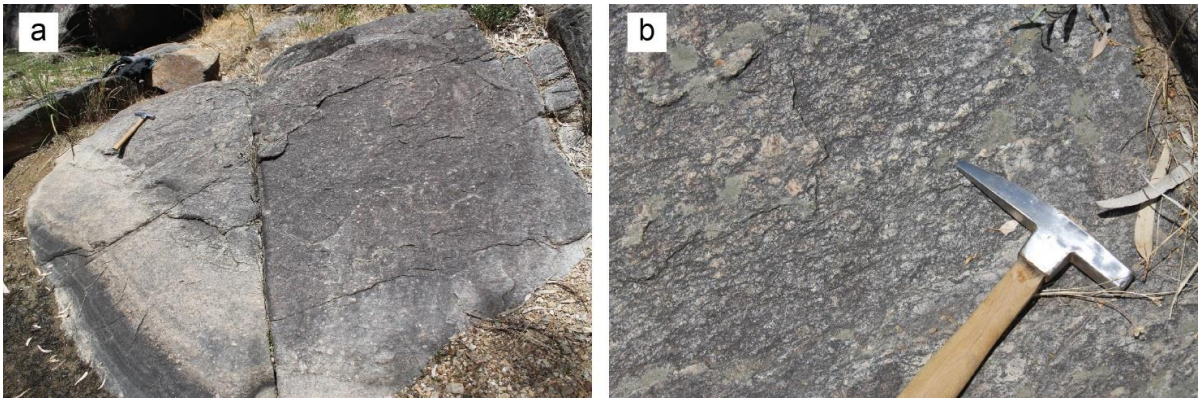

Figure 2. (a) Outcrop photo of granite gneiss in the South Para River gorge. **(b)** Close up of granite gneiss showing pink K-feldspar augens and biotite foliation.

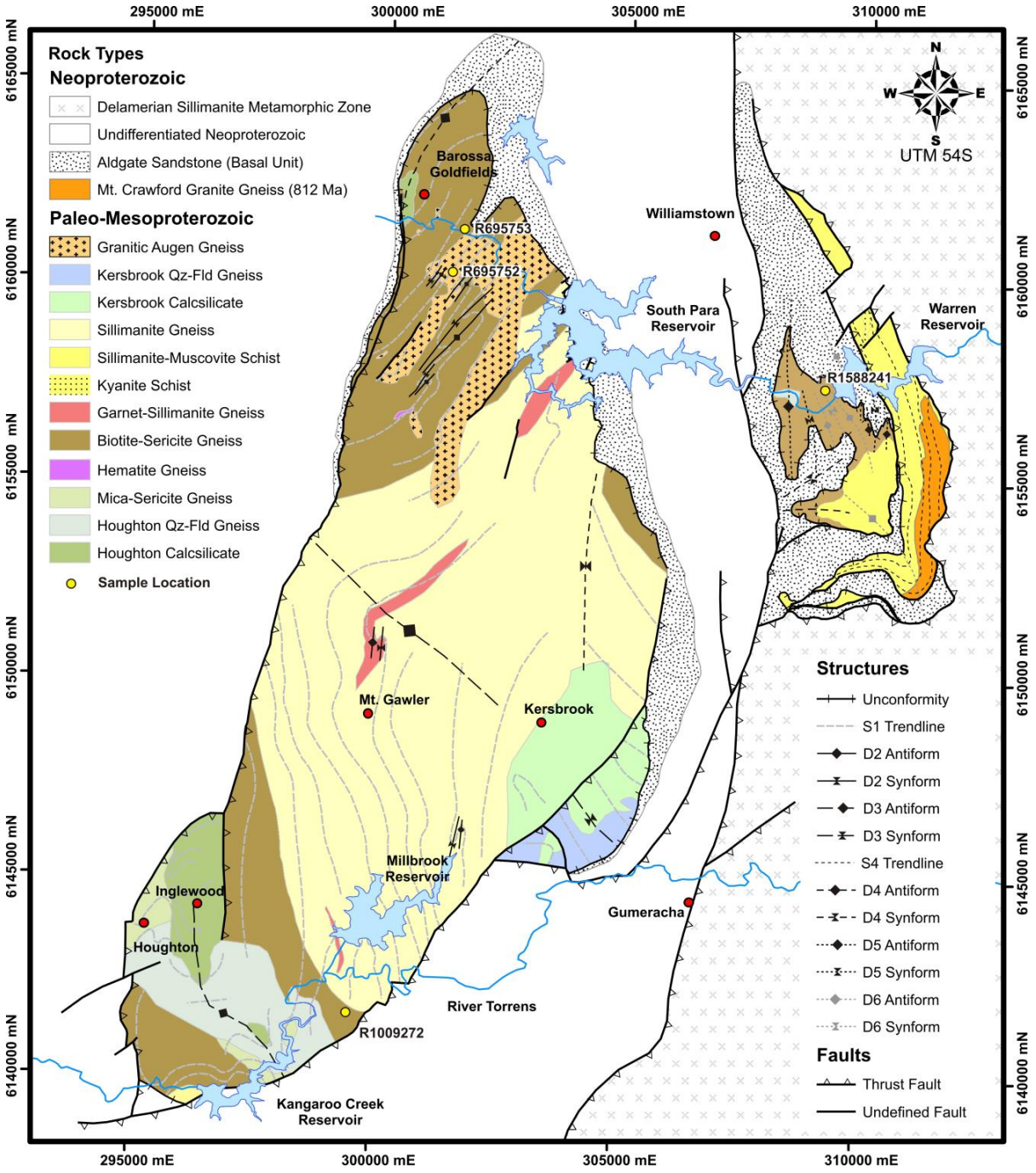

Figure 3. Location of the four samples in this study from the northernmost Houghton and Warren Inliers of the Barossa Complex. Map is reproduced from Meaney et al. in prep.

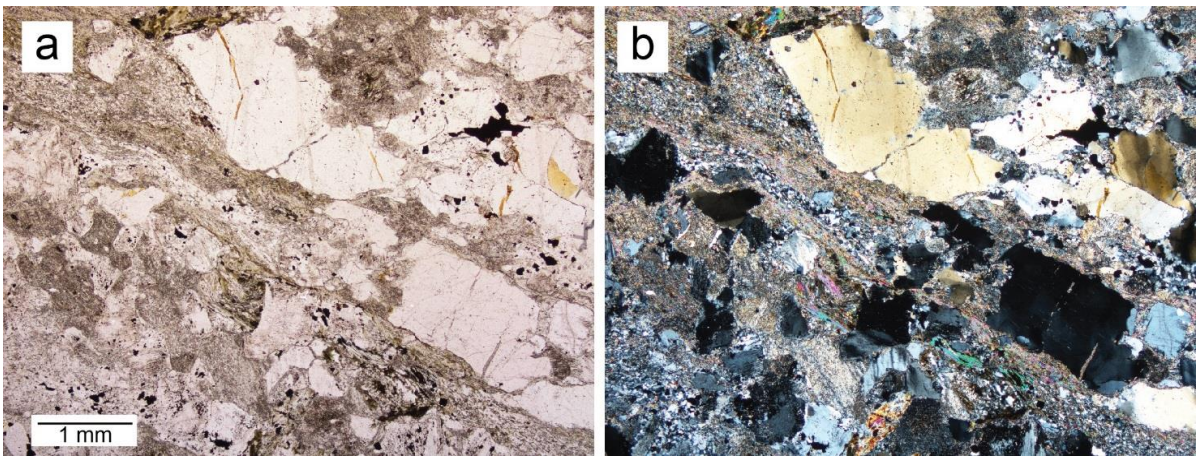

Figure 4. Sample R695752 under (a) plane polarised light; and (b) cross polars.

PETROLOGY

Lithology: Strongly deformed, phyllonitised granitoid (?monzogranite).

The following petrographic description is taken from Mason (2006).

Mineral	Vol %	Origin
Quartz	24	Relict igneous 1
K-feldspar (microcline)	24	Relict igneous 1 / metamorphic ?2
Albite	5	Metamorphic ?2
Biotite	Tr	Relict igneous 1 (inclusions in quartz 1)
Zircon	Tr	Igneous 1
Allanite	Tr	Igneous 1
Sericite	30	Metamorphic 2
Biotite	2	Metamorphic 2
Felsic mosaic (mainly quartz)	10	Metamorphic 2
Opaques (?magnetite)	3	Metamorphic 2
Titanite	Tr	Metamorphic 2
Tourmaline	Tr	Metamorphic 2

Description: In thin section, this sample displays a coarse-grained granitoid texture, severely modified by phyllonitic deformation and alteration (Fig. 4). Texturally the rock can be divided into two types of regions: elongated kernels (lithons) of relict coarse-grained granitoid, and subparallel to anastomosing bands and wispy trails dominated by foliated phyllosilicates (mainly sericite, lesser biotite).

Quartz is moderately abundant in the granitoid lithons, where it forms small to large anhedral grains with a moderate degree of shadowy strain extinction. The quartz clearly represents relict primary igneous quartz. K-feldspar is moderately abundant, occurring entirely in the granitoid lithons. The grains range in size, up to very large blocky prisms (phenocrysts) ~4 mm in size. Most of the K-feldspar grains display fine ‘tartan’ twinning typical of microcline, but the large K-feldspar phenocryst lacks such twinning and appears to represent relict primary orthoclase. Albite occurs in minor amount in some of the granitoid lithons, where it forms optically continuous replacements of precursor primary anhedral plagioclase grains.

Biotite occurs in minor amount in different forms: (i) Rare small but well-shaped plates of biotite occur as inclusions in some of the large quartz grains. This biotite is considered to represent

primary igneous biotite. It is pleochroic from dark chocolate brown to straw yellow. (ii) A small amount of biotite occurs as small flakes which are concentrated in aggregates in the granitoid lithons. This represents metamorphic biotite that has developed by recrystallisation of precursor ferromagnesian flakes (most likely biotite as per i) above). (iii) Most biotite occurs as small flakes, pleochroic from drab tan brown to pale yellow, that are concentrated in aggregates and trails elongated within subparallel sericite-rich bands that traverse the rock. This biotite appears to represent a new phase that has formed by recrystallisation and chemical modification of the precursor metamorphic biotite of ii) above.

Sericite is abundant. Most occurs as tiny flakes concentrated densely in subparallel bands that traverse the rock, enclosing the relict granitoid lithons. A strong foliation is defined by preferred orientation of individual flakes in the bands, and the subparallel orientation of the bands themselves. Some sericite also occurs in the granitoid lithons, where it forms small randomly oriented flecks that have partly replaced the albite-altered plagioclase grain sites. Fine-grained felsic mosaic (mostly quartz, possibly some albite) is intimately intergrown with the foliated sericite. Locally, the felsic mosaic appears to have formed by recrystallisation and alteration of the margins of the granitoid lithons.

Opaques occur in minor but significant amount as equant cubic crystals and aggregates of crystals, irregularly sprinkled through the altered granitoid lithons, and also in biotite-rich parts of recrystallised lithon margins. Sphene is present in trace amount as relatively large subhedral grains in the sericite-rich bands. They display the typical high relief, weak turbid pleochroism, and very high birefringence of this mineral. Zircon occurs in trace amount as relatively large euhedral stumpy prisms, located in some of the relict granitoid lithons and rarely in some of the sericite-rich bands. Allanite forms stumpy pleochroic dark brown prisms in some granitoid lithons, and also in some sericite-rich bands. Tourmaline occurs as rare small stumpy subhedral crystals, pleochroic in drab dark greens, in close association with fine-grained dense sericite and biotite in the phyllonitic bands.

Interpretation: This sample is considered to represent a strongly deformed granitoid. Paragenetic evolution of the rock progressed through the following stages:

1. Crystallisation of pluton. A granitoid pluton was emplaced and crystallised to form the coarse-grained assemblage of K-feldspar, quartz, plagioclase, minor ferromagnesian minerals (mainly biotite), and accessory zircon and allanite. Some large blocky K-feldspar phenocrysts were present. Primary mineral abundances are difficult to determine, but a monzogranitic composition is considered likely. It is notable that this granitoid shares textural and mineralogical similarities with the meta-monzogranite of R695752 (see previous description), including coarse grain size, proportions of primary minerals, and types and grain size of accessory minerals (allanite, zircon).

2a. Metamorphism. The granitoid may have experienced a low-grade regional metamorphic event, causing partial recrystallisation of primary biotite to form finer-grained biotite ± sericite. The possible effects of this event have been obscured by the subsequent event.

2b. Phyllonitic deformation. The rock body underwent strong ductile deformation in response to a dynamic regional metamorphic event, generating subparallel to anastomosing bands (high-strain zones) of fine-grained sericite + biotite ± tourmaline, enclosing elongated lithons of precursor granitoid. These bands also contain crystal fragments (K-feldspar, allanite, zircon) derived from the relict granitoid lithons. Parts of the lithons suffered partial recrystallisation and replacement by fine-grained sericite + biotite + quartz + opaques (?magnetite). The stability of biotite in this assemblage suggests that the deformation occurred at middle-greenschist metamorphic P-T conditions.

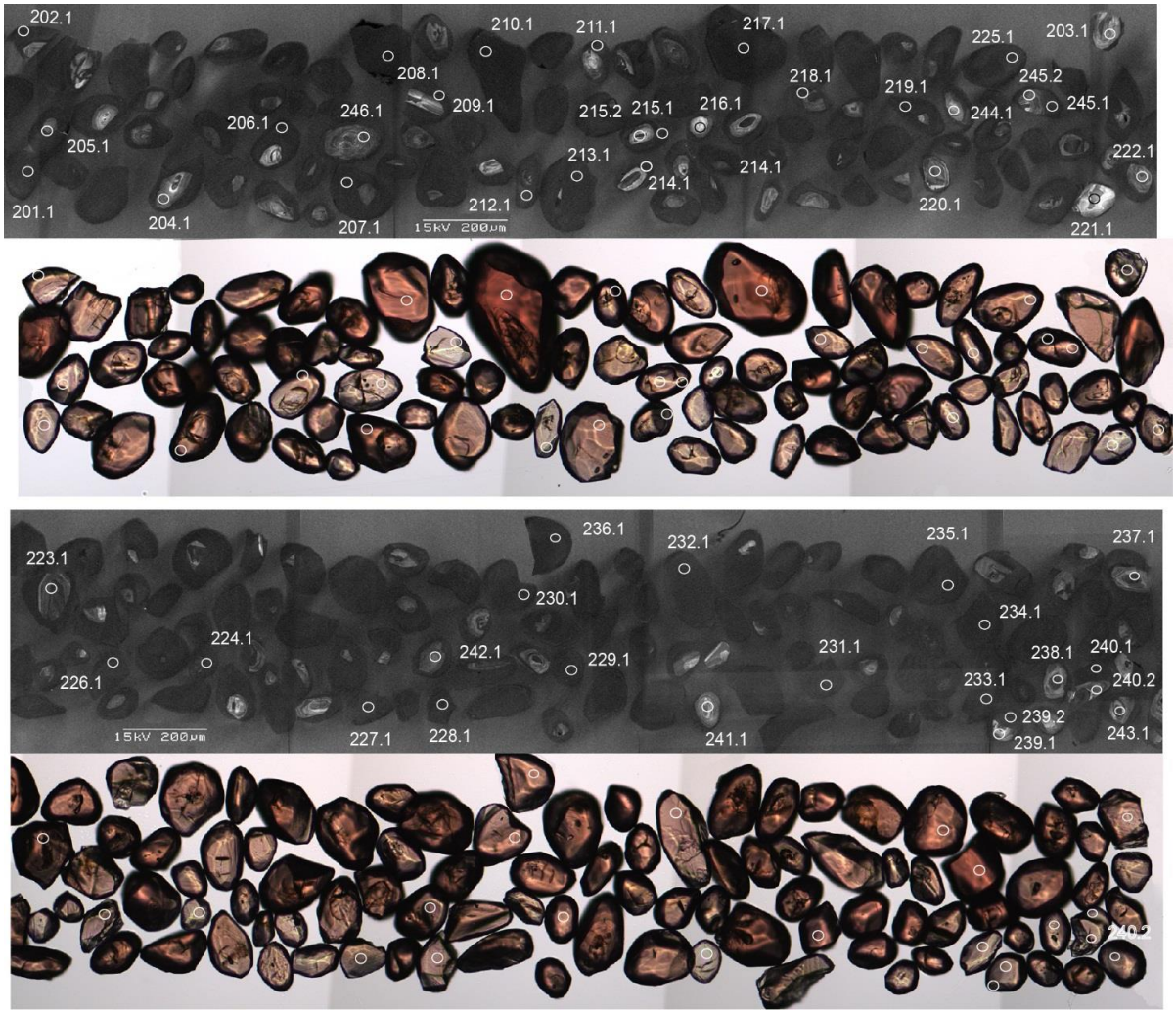

Figure 5. Transmitted light and CL images of zircon, R695752: foliated granite, Houghton Inlier.

ZIRCON CHARACTERISTICS

The sample contains abundant subhedral, spherical to oval-shaped zircons, some with multifaceted exteriors, ranging from 70 to 200 µm in size, with aspect ratios up to 3:1 (Fig. 5). The grains are hyacinth to brown in colour and clear, with few cracks or inclusions. Many of the dark CL homogenous grains contain 30-80 µm, light CL, subhedral to euhedral, concentrically zoned cores. The dark CL overgrowths truncate the oscillatory zoning. Some cores are fractured and contain small inclusions. The overgrowths have high uranium (500-800 ppm) and low Th/U ratios (0.02-0.03) typical of metamorphic zircon.

RESULTS

Fifty analyses were made on 46 grains, with both cores and rims targeted. All analyses are concordant and contain < 0.5 common Pb (Table, Fig. 6). Three analyses (214.1, 218.1 and 245.1) lie on or near a core boundary and are interpreted as core-rim mixing ages of no geological significance. Two other analyses (224.1 and 205.1) also located on a zircon rim but slightly overlapping a core. These analyses have high U and low Th/U characteristic of metamorphic zircon, but the same age as the cores, and are also considered to represent a core-rim isotopic mix.

CORES

Eighteen cores were analysed. One core is notably older (215.2, c. 1916 Ma), indicating a minor component of inheritance in the magmatic protolith. The remaining 17 analyses yield a weighted mean $^{207}Pb/^{206}Pb$ age of 1717 ± 7 Ma (MSWD = 1.6; probability of fit = 0.07). This is interpreted to be the crystallisation age of the granite protolith.

METAMORPHIC ZIRCON

Twenty seven analyses of dark CL metamorphic zircon yield concordant ages between 1582 and 1647 Ma; a range of $^{207}Pb/^{206}Pb$ much greater than expected for a single population (MSWD = 11, Fig. 7). The dispersed metamorphic ages suggest an extended period of metamorphism, producing a continuum of zircon ages. Apparent age peaks in the continuum may indicate two (or more) distinct pulses of metamorphic zircon growth within the long-lived metamorphic event.

Using MSWD as a guide to separating population, the four youngest analyses yield a weighted mean $^{207}Pb/^{206}Pb$ age of 1589 ± 10 Ma (MSWD = 1.5, probability of fit = 0.20), constraining the minimum age of metamorphism. This age coincides with the timing of granulite facies metamorphism in the southern Barossa Complex (c. 1590 Ma, Szpunar et al. 2007a), and is recorded in all metamorphosed samples in this study. The oldest 13 analysis have a weighted mean age of 1632 ± 4 Ma (MSWD = 1.7, probability = 0.05), recording a metamorphic event previously recognised in the Houghton Inlier by Belousova et al. (2006), in a geochronological study of zircon in stream sediments (1625 ± 9 Ma). This metamorphic age is also recorded in samples from the Oakbank Inlier and Aldgate Inlier (this study, Table 1). Ten intermediate analyses yield an age of 1609 ± 5 Ma (MSWD = 1.7, probability of fit = 0.09). This age is recorded in 5 samples in this study, from the Houghton, Warren and Oakbank Inliers.

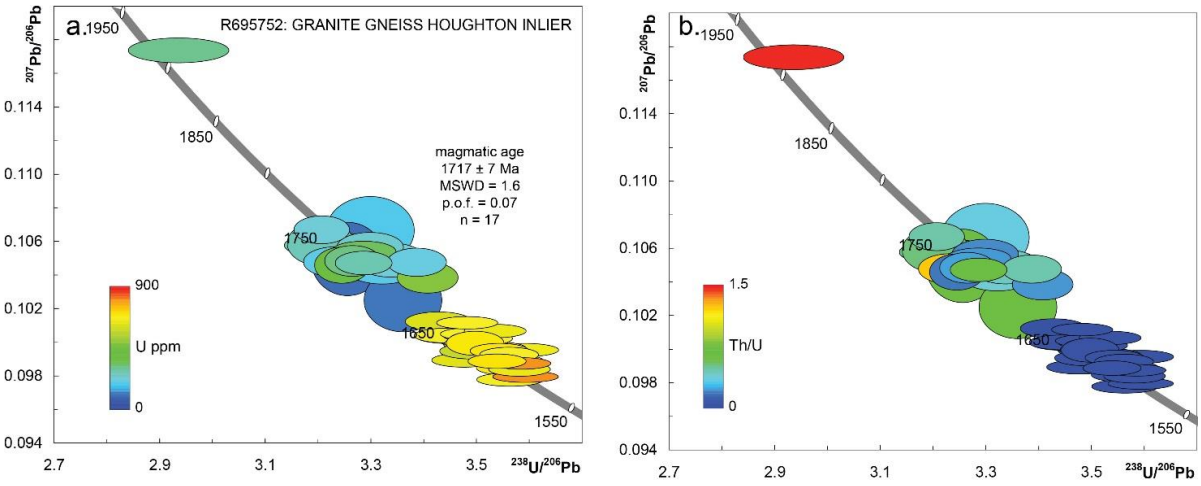

Figure 6. Tera-Wasserburg concordia diagrams for zircon in R695752, with error ellipses coloured according to (a) U content and (b) Th/U ratio, showing the difference in composition between igneous cores and metamorphic rims. Five analyses representing core-rim isotopic mixing ages are not plotted.

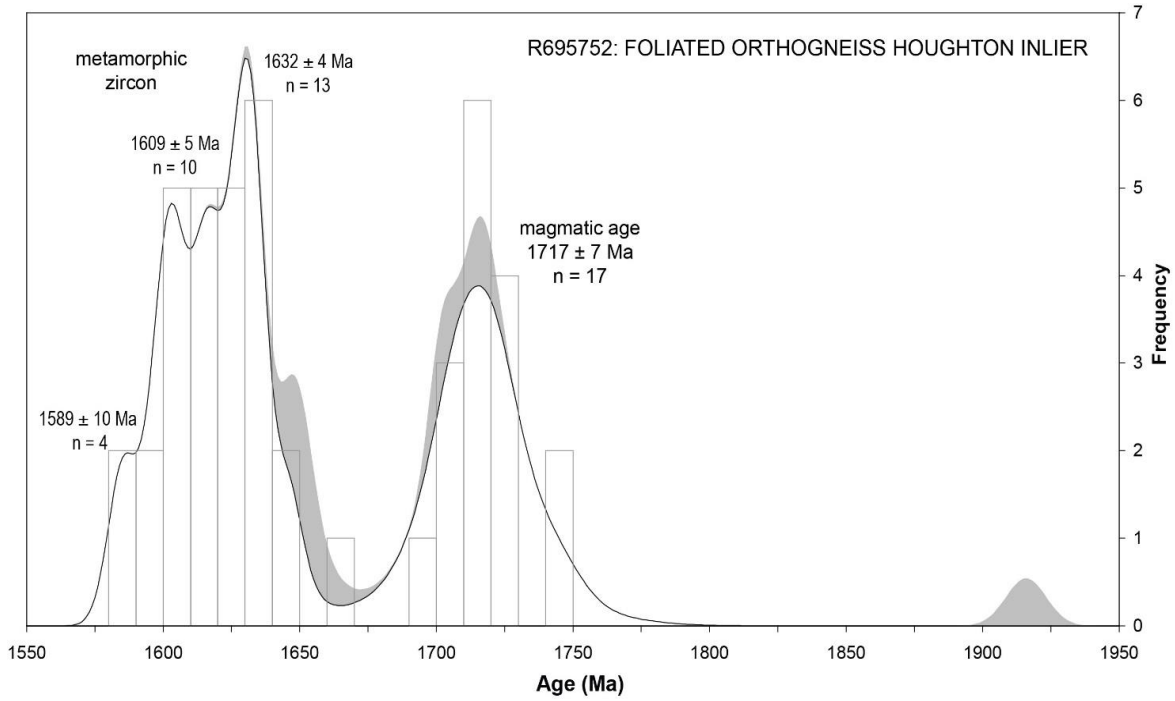

Figure 7. PDD of $^{207}Pb/^{206}Pb$ ages for R695752. All analyses are < 5% concordant. The grey curve represents core-rim isotopic mixing ages excluded from the age calculations, and one inherited core.

Table 2. SHRIMP analytical results for zircon from R695752, foliated granite, Houghton Inlier.

Spot	% $206Pb_c$	ppm U	ppm Th	232Th /238U	206Pb* /238U	±%	207Pb* /235U	±%	207Pb* /206Pb*	±%	207Pb /206Pb Age		% Disc
inherited core													
215.2	--	301	427	1.47	0.340	2.13	5.507	2.17	0.1173	0.41	1916	7	2
magmatic cores													
222.1	0.01	222	99	0.46	0.312	1.09	4.586	1.21	0.1067	0.52	1743	9	0
242.1	--	181	59	0.34	0.303	1.67	4.458	2.08	0.1066	1.25	1743	23	2
220.1	0.02	257	130	0.52	0.312	1.30	4.555	1.53	0.1059	0.82	1730	15	-1
246.1	--	279	133	0.49	0.310	1.84	4.518	1.90	0.1058	0.48	1727	9	-1
203.1	--	233	44	0.20	0.303	1.25	4.416	1.36	0.1057	0.54	1726	10	1
237.1	0.00	333	69	0.21	0.304	1.23	4.422	1.29	0.1054	0.38	1721	7	1
245.2	--	200	59	0.30	0.307	1.71	4.451	1.82	0.1053	0.61	1719	11	0
216.1	--	89	52	0.60	0.307	1.40	4.444	1.96	0.1049	1.36	1713	25	-1
240.2	--	221	91	0.43	0.300	1.31	4.333	1.46	0.1049	0.64	1712	12	2
204.1	0.01	309	68	0.23	0.306	1.07	4.426	1.21	0.1048	0.57	1711	11	-1
221.1	0.02	191	228	1.23	0.309	1.22	4.469	1.34	0.1048	0.56	1710	10	-2
239.1	--	204	90	0.45	0.295	1.09	4.265	1.21	0.1048	0.53	1710	10	3
241.1	--	187	68	0.38	0.301	1.57	4.346	1.76	0.1047	0.79	1709	14	1
238.1	0.00	268	162	0.62	0.304	1.07	4.393	1.16	0.1047	0.44	1709	8	0
243.1	0.02	368	61	0.17	0.308	1.05	4.443	1.25	0.1046	0.67	1707	12	-2
223.1	0.03	482	98	0.21	0.294	1.11	4.202	1.25	0.1038	0.58	1693	11	2
244.1	--	102	59	0.59	0.298	1.45	4.206	1.88	0.1025	1.20	1670	22	-1

Spot	% $206Pb_c$	ppm U	ppm Th	232Th /238U	206Pb* /238U	±%	207Pb* /235U	±%	207Pb* /206Pb*	±%	207Pb /206Pb Age		% Disc
metamorphic zircon													
225.1	--	614	11	0.02	0.292	1.21	4.072	1.26	0.1012	0.37	1647	7	0
227.1	--	673	13	0.02	0.287	1.09	4.007	1.12	0.1012	0.25	1645	5	1
229.1	0.01	643	13	0.02	0.283	1.10	3.927	1.13	0.1007	0.26	1636	5	2
228.1	--	677	14	0.02	0.286	1.14	3.968	1.17	0.1005	0.25	1633	5	1
236.1	0.01	584	14	0.03	0.286	1.20	3.963	1.22	0.1004	0.27	1632	5	1
231.1	--	525	13	0.03	0.286	1.14	3.959	1.17	0.1004	0.28	1632	5	1
207.1	--	668	13	0.02	0.290	1.16	4.021	1.20	0.1004	0.29	1631	5	-1
201.1	--	639	13	0.02	0.290	1.17	4.017	1.20	0.1004	0.28	1631	5	-1
206.1	--	675	14	0.02	0.285	1.11	3.939	1.15	0.1002	0.28	1628	5	1
233.1	0.00	585	16	0.03	0.287	1.16	3.959	1.19	0.1001	0.27	1627	5	0
226.1	--	606	15	0.03	0.286	1.14	3.942	1.20	0.1000	0.38	1623	7	0
210.1	--	676	12	0.02	0.286	1.12	3.938	1.16	0.0999	0.29	1623	5	0
208.1	0.00	695	15	0.02	0.286	1.03	3.941	1.14	0.0999	0.47	1623	9	0
235.1	--	688	16	0.02	0.283	1.19	3.893	1.21	0.0997	0.25	1618	5	1
232.1	--	650	13	0.02	0.278	1.17	3.822	1.19	0.0995	0.26	1615	5	2
213.1	0.01	697	16	0.02	0.282	1.03	3.873	1.08	0.0995	0.29	1615	5	1
219.1	0.03	575	11	0.02	0.287	1.14	3.930	1.18	0.0995	0.30	1614	6	-1
212.1	--	667	16	0.02	0.281	1.04	3.844	1.08	0.0993	0.30	1610	6	1
217.1	0.00	624	14	0.02	0.288	1.14	3.925	1.18	0.0989	0.27	1604	5	-2
209.1	--	625	13	0.02	0.282	1.21	3.850	1.25	0.0989	0.31	1604	6	0
230.1	0.02	635	13	0.02	0.280	1.07	3.821	1.10	0.0989	0.26	1604	5	1
211.1	--	699	16	0.02	0.283	1.03	3.853	1.07	0.0989	0.29	1603	5	0
240.1	0.01	803	18	0.02	0.279	1.03	3.799	1.05	0.0987	0.23	1600	4	1
215.1	--	690	16	0.02	0.280	1.22	3.809	1.26	0.0985	0.30	1596	6	0
239.2	--	644	14	0.02	0.279	1.07	3.789	1.11	0.0984	0.28	1594	5	0
234.1	0.01	805	18	0.02	0.278	1.13	3.761	1.16	0.0980	0.23	1586	4	0
202.1	0.01	663	15	0.02	0.281	1.16	3.785	1.19	0.0978	0.27	1582	5	-1
core-rim mixing ages													
205.1	--	590	21	0.04	0.306	1.18	4.437	1.21	0.1051	0.27	1717	5	0
224.1	0.00	726	11	0.02	0.301	1.08	4.326	1.11	0.1043	0.24	1702	4	0
214.1	--	697	11	0.02	0.291	1.03	4.071	1.13	0.1015	0.46	1652	9	0
218.1	0.00	615	17	0.03	0.296	1.10	4.139	1.13	0.1015	0.26	1651	5	-1
245.1	--	517	12	0.02	0.286	2.07	3.994	2.24	0.1014	0.85	1650	16	2

Data are 1σ precision. Pbc and Pb* indicate the common and radiogenic portions, respectively. All Pb data are initially common Pb corrected based on measured ^{204}Pb (after Stacey and Kramer 1975), then corrected for excess 204 counts inferred from average 207-corrected standard spots Grey coloured spot names are from Batch 2..

R695753: META-QUARTZITE, HOUGHTON INLIER

Sample Number:	Field sample number HI 03		
Location GDA94:	301614 E	6161240 N	Zone 54
Location Lat-Long:	-34°40'18"	138°50'05"	
250K map sheet	SI 54-09 Adelaide		
100K map sheet	6628 Adelaide		
Location:	South Para River, Houghton Inlier		
Mount:	Z4597		
Date analysed:	03/08/2005		
Machine:	SHRIMP IIB		
Standard age QGNG:	Batch 1: 1849.3 ± 2.9 Ma Batch 2: 1843.0 ± 3.3 Ma		
Corrected for overcounts to:	Batch 1: 1851.9 ± 3.1 Ma Batch 2: 1851.5 ± 3.4 Ma		
Standard Data:	Appendix 2		
Interpreted age:	1707 ± 5 Ma		
Age type:	Maximum age of deposition		
Interpreted age:	c. 1579 Ma, 1605 Ma, 1627 Ma		
Age type:	Metamorphic age		

FIELD DESCRIPTION

Sample R695753 was collected from the South Para River gorge in the Norther Houghton Inlier, approximately 5km east of Williamstown and 1km downstream from sample R695754 (Fig. 3, 8a).

Sample R695753 is a quartz dominated, K-feldspar bearing psammite (Fig. 8b, 8c). Minor biotite is also present defining a weak foliation. This sample comes from a 1 meter thick, laterally extensive psammite layer from the steeply dipping psammopelite unit which dominates the northern Houghton Inlier. The average grain size is 1-2 mm, however some coarser grained patches are enriched in K-feldspar which occurs as crystals up to 1 cm in size, suggestive that this rock has undergone partial melting. Some surfaces within this layer show slickenlines indicating some minor faulting present, however the psammite layer is not visibly offset.

The surrounding psammopelites are composed of very fine-grained biotite and retrograde sericite, as well as quartzofeldspathic material which is concentrated into fine (~5mm) bands. This segregation defines the gneissosity in these rocks which occurs at a low angle to the sedimentary structures in most areas. The gneissosity is obliterated by an overprinting cleavage in many areas. The psammopelite unit grades into a sillimanite bearing metapelite in the central and eastern Houghton Inlier.

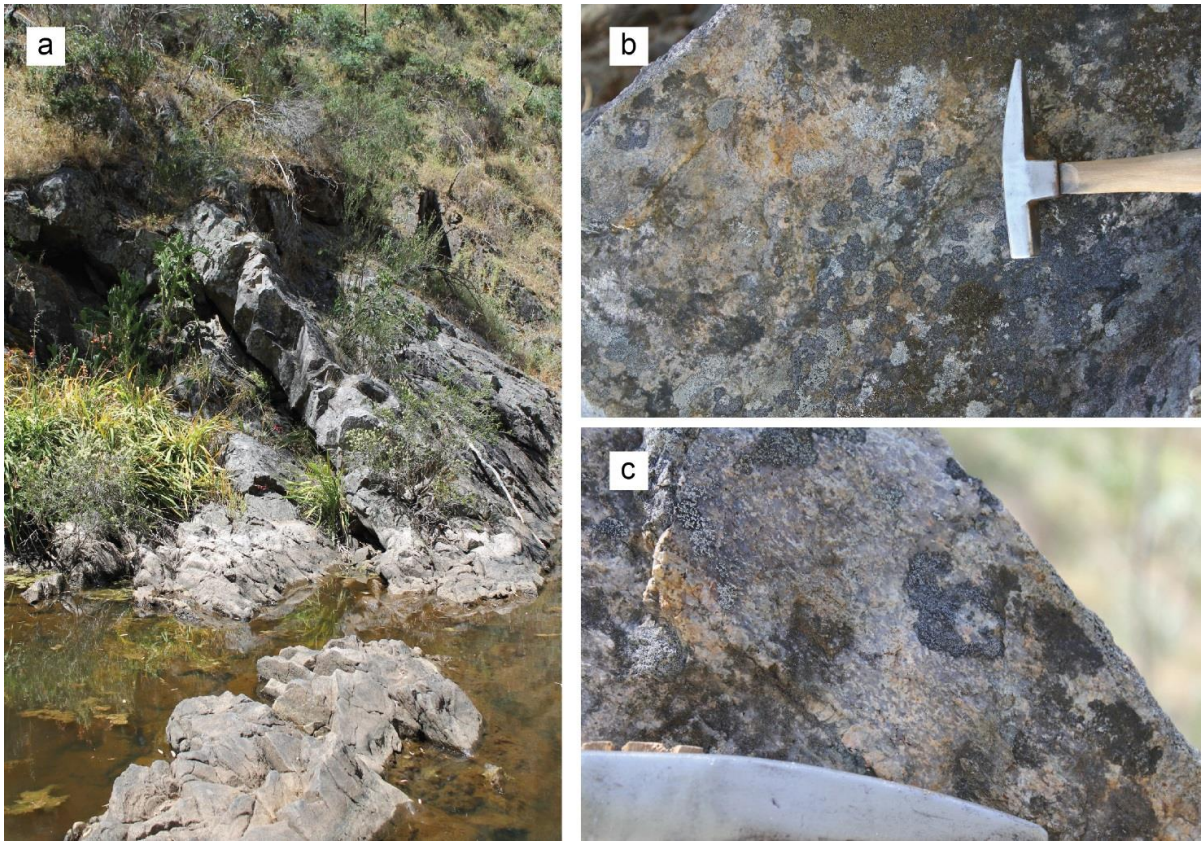

Figure 8. (a) Outcrop photo of psammite layer in the South Para gorge. **(b)** The sampled psammite. **(c)** Coarse grained area at the top of the psammite layer.

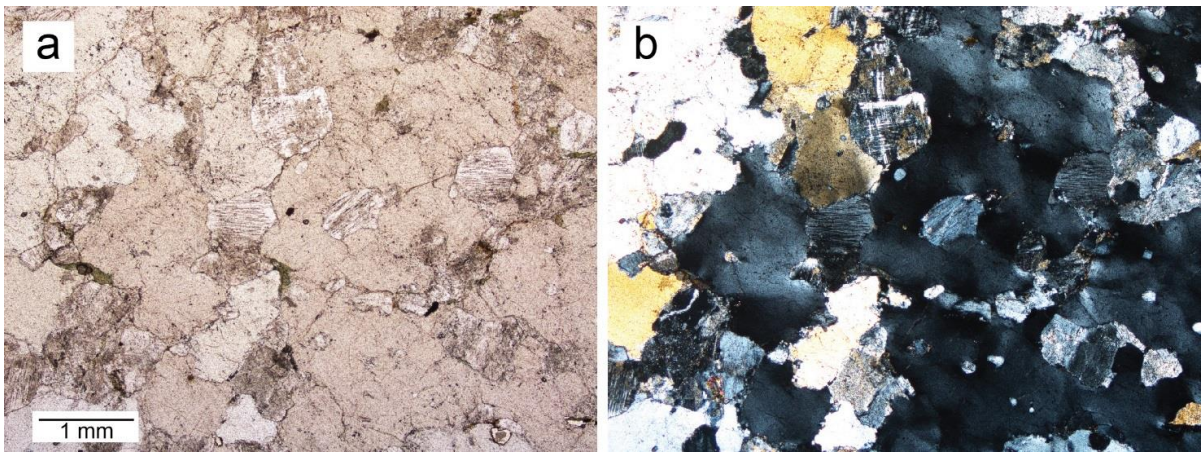

Figure 9. Sample R695753 under (a) plane polarised light; and (b) cross polars.

PETROLOGY

Lithology: Foliated biotite-sericite quartzite (meta-feldspathic sandstone)

The following petrographic description is taken from Mason (2006).

Mineral	Vol %	Origin
Quartz	90	Relict clastic 1 / metamorphic 2
Zircon	Tr	Clastic 1
K-feldspar	5	Metamorphic 2
Biotite	2	Metamorphic 2
Sericite	2	Metamorphic 2
Opaques	Tr	Metamorphic 2

Description: In thin section, this sample displays a poorly-preserved framework supported clastic sedimentary texture that has been severely modified by recrystallisation and deformation (Fig. 9). Quartz dominates the rock. It forms large anhedral grains ~1-2 mm long. Ductile deformation has caused grain elongation with aspect ratios mostly ~2:1 – ~3:1, although some grains retain a more-or-less equant grain shape (ie unstrained). Shadowy strain extinction is common, and grain boundaries display suturing which in places has progressed into granular recrystallisation mosaics. K-feldspar occurs in minor amount as small blocky anhedral grains and small aggregates, commonly smaller than the quartz grains. They display the 'tartan' twinning typical of microcline. Like the quartz grains, the K-feldspar grains and aggregates are partly entrained in the trace of the structure (foliation) through the rock.

Biotite occurs in minor amount as small pleochroic chocolate brown to straw yellow flakes. The preferred orientation of discrete flakes and aggregates of flakes contributes to definition of the foliation. Sericite occur as small flakes that tend to be concentrated in foliated trails that contribute to the foliation. Sericite locally is intergrown with biotite, confirming they formed synchronously as part of the same assemblage. Opaques occur in trace amount as small blocky grains sparsely scattered through the rock. Their positive identification is not possible in the absence of reflected light observations.

Interpretation: This sample is considered to have formed as a relatively well-sorted and compositionally mature quartz sandstone. It contained a minor proportion of clastic K-feldspar and a small amount of detrital argillaceous materials.

Following burial and diagenesis, regional metamorphism with accompanying ductile deformation modified the rock. Quartz and K-feldspar grains suffered elongation and partial recrystallisation, and argillaceous components recrystallised to form fine-grained small aggregates of foliated biotite and sericite. The presence of biotite in the assemblage suggests that P-T conditions reached the middle greenschist facies.

ZIRCON CHARACTERISTICS

Zircons from the quartzite range from rounded grains, to more euhedral crystals with rounded terminations, preserved crystal faces and aspect ratios of 2:1 (Fig. 10). They are predominantly small- to medium-sized grains (40 to 130 µm long). They are either brown or hyacinth in colour and clear, with few cracks and inclusions.

Cathodoluminescence imaging of the zircon shows that most grains have narrow dark overgrowths, suggesting a detrital population modified by metamorphism. The cores range from dark to moderately bright, and commonly display oscillatory zoning, typical of igneous crystallisation. The cores are subrounded or fragmented and in some cases, embayed.

Figure 10. Transmitted light and CL images of zircon, R695753, quartzite, Houghton Inlier. Large spots are Hf analyses.

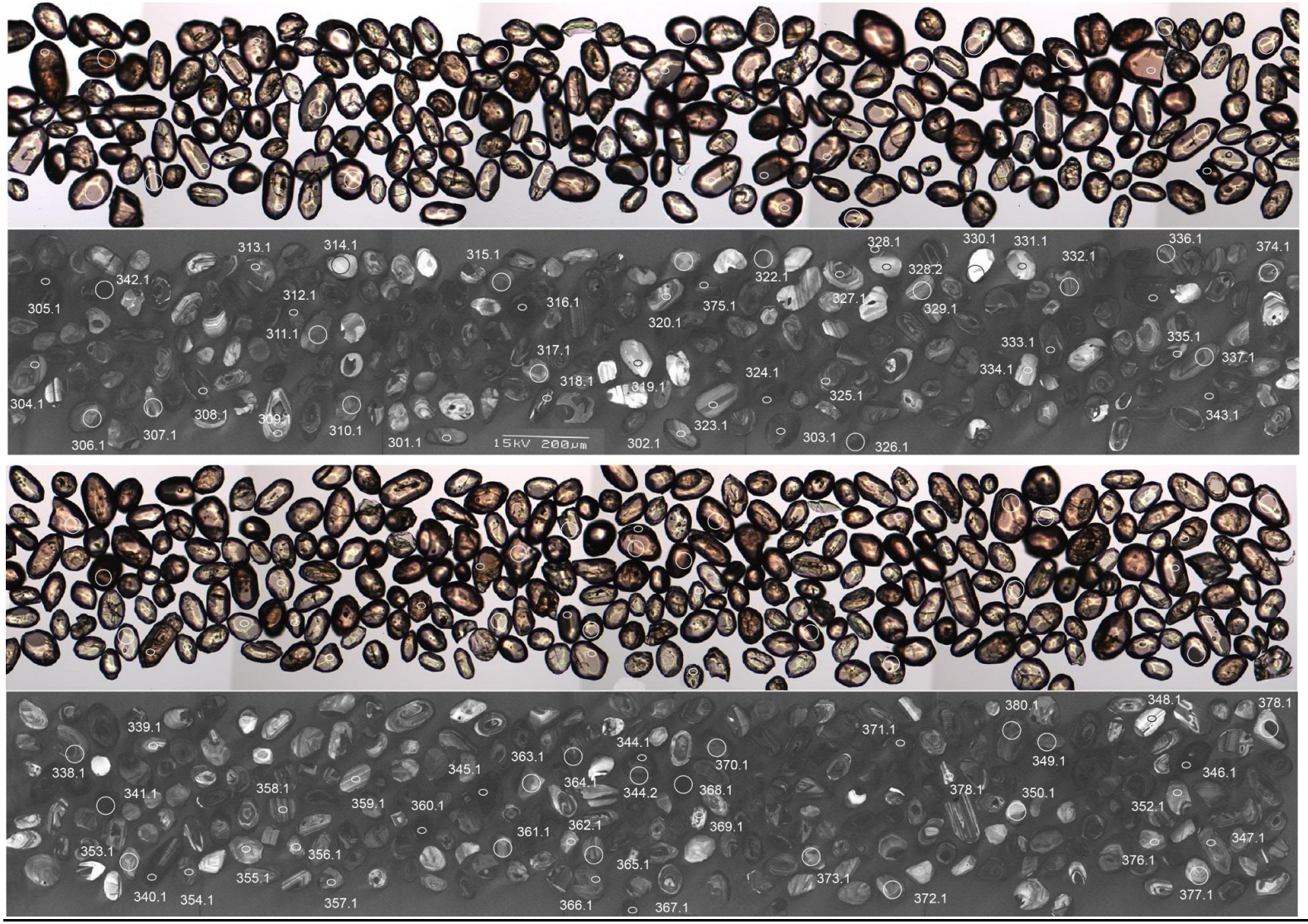

RESULTS

Eighty two analyses were made on 80 grains. All analyses are concordant or near concordant within analytical uncertainty (Fig. 11), and contain < 0.5% common Pb.

METAMORPHIC RIMS

Most of the metamorphic rims are too thin to analyse, but five grains with thicker overgrowths provided space for five analyses. Although based on only few analyses, the pattern of ages, mimics that of sample R695752, an orthogneiss collected in close proximity to the quartzite, with peaks at c. 1589 Ma, 1605 Ma and 1627 Ma (Fig. 12).

CORES

Seventy seven cores have a range of ages between c. 1705 – 3220 Ma (Fig.12). The two youngest analyses yield a weighted mean $^{207}Pb/^{206}Pb$ age of 1707 ± 5 Ma, constraining the maximum age of deposition of the sedimentary protolith. Two grains yield slightly older ages of c. 1722 Ma. About 60% of the analyses lie between c. 1740 – 1920 Ma, with merging peaks at c. 1765 Ma, 1799 Ma, 1834 Ma, 1890 Ma and 1922 Ma. Two analyses have older ages of c. 1984 Ma and 2032 Ma. A cluster of late Archaean - early Palaeoproterozoic cores range in age between c. 2326 – 2673 Ma, with older Archaean grains at c. 2811 Ma, 2842 Ma, 2936 Ma, 3096 Ma and 3221 Ma.

DISCUSSION

The maximum age of deposition of this sample is in conflict with the magmatic age of 1717 ± 7 Ma obtained for sample R695752, which appears to intrude the metasedimentary succession in South Para gorge. The youngest detrital cores in the meta-quartzite range between 1706 – 1722 Ma, indicating is particular sedimentary unit cannot have been intruded by the granite represented by sample R695752. This suggests some complexity in the steeply dipping psammopelite succession of the northern Houghton Inlier, it comprising perhaps juxtaposed tectonic slices of different crustal age, which have not been identified. That is, the metasedimentary succession hosting the psammite layer represented by sample R695753 could be younger than that intruded by the R695752 granite gneiss. Younger metasediments with maximum depositional ages of c. 1655 Ma have been identified elsewhere in the Houghton Inlier (sample R1009272, this study). Alternately, the granite gneiss could have been tectonically emplaced into the younger metasedimentary succession. Resolving this conflict warrants further geochronological study of the metasedimentary units of the Houghton Inlier, preferably coupled with more detailed structural and stratigraphic mapping.

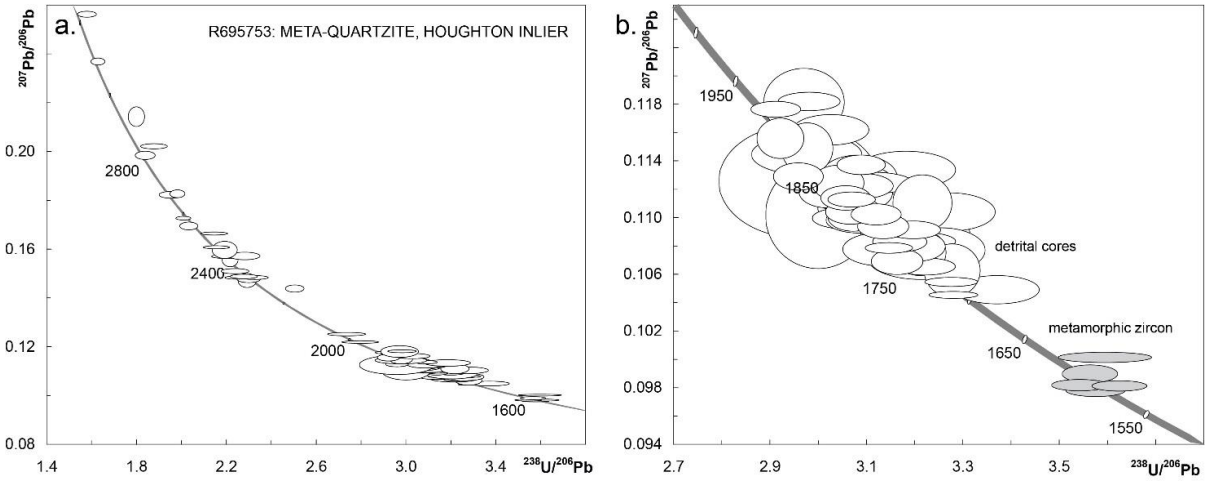

Figure 11. Tera-Wasserburg concordia diagrams for zircon in R695753. (a) All analyses; and **(b)** the dominant cluster of core analyses and metamorphic rims younger than 1930 Ma.

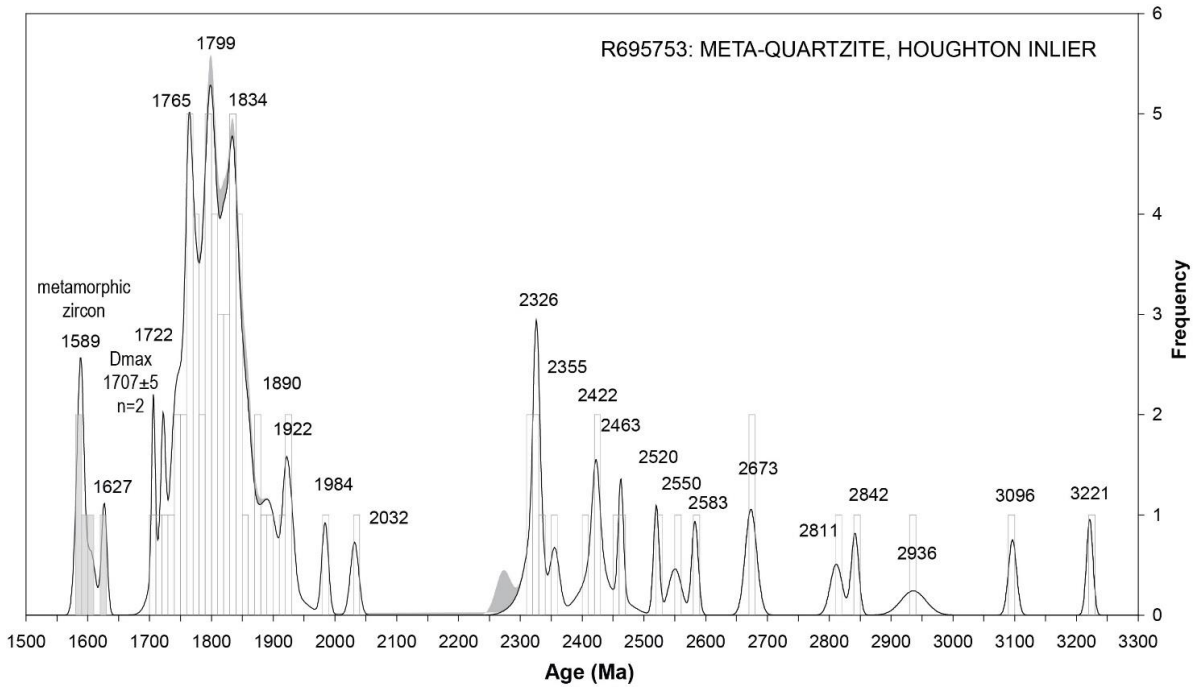

Figure 12. PDD of $^{207}Pb/^{206}Pb$ ages for R695753. The grey shaded curve represents analyses > 5% discordant, which are not included in the calculation of peak maxima (Sircombe 2004). The histogram and white area represent analyses < 5% discordant. Grey columns of the histogram represent metamorphic zircon and white represent detrital cores.

Table 3. SHRIMP analytical results for zircon from R695753, quartzite, Houghton Inlier.

Spot	% $206Pb_c$	ppm U	ppm Th	232Th /238U	206Pb* /238U	±%	207Pb* /235U	±%	207Pb* /206Pb*	±%	207Pb /206Pb Age ± Ma		% Disc
detrital cores													
359.1	--	124	168	1.39	0.631	1.74	22.25	1.76	0.2559	0.32	3221	5	3
319.1	--	93	63	0.70	0.612	1.25	19.96	1.32	0.2365	0.41	3096	6	1
328.2	--	79	28	0.36	0.554	1.31	16.34	1.80	0.2140	1.24	2936	20	4
369.1	--	136	108	0.82	0.531	2.05	14.79	2.08	0.2019	0.37	2842	6	4
318.1	--	440	34	0.08	0.542	1.60	14.82	1.71	0.1982	0.59	2811	10	1
325.1	0.00	266	109	0.42	0.503	1.09	12.66	1.24	0.1825	0.58	2675	10	2
348.1	--	95	60	0.66	0.511	1.78	12.82	1.85	0.1820	0.51	2672	8	1
307.1	--	219	205	0.97	0.496	1.11	11.81	1.16	0.1726	0.31	2583	5	-1
314.1	0.04	79	108	1.41	0.491	1.30	11.45	1.44	0.1693	0.63	2550	10	-1
364.1	0.00	333	485	1.51	0.465	1.84	10.66	1.86	0.1662	0.27	2520	4	3
368.1	--	1060	333	0.33	0.463	1.75	10.26	1.76	0.1607	0.24	2463	4	0
330.1	--	31	200	6.69	0.455	1.67	10.02	2.23	0.1596	1.48	2451	25	2
378.1	--	559	34	0.06	0.438	1.96	9.48	2.07	0.1570	0.65	2424	11	4
373.1	--	247	100	0.42	0.454	1.90	9.83	1.93	0.1569	0.34	2422	6	0
342.1	--	1098	82	0.08	0.450	1.03	9.65	1.57	0.1555	1.18	2407	20	1
339.1	--	153	215	1.45	0.446	1.81	9.28	1.87	0.1509	0.45	2356	8	-1

Spot	% $206Pb_c$	ppm U	ppm Th	232Th /238U	206Pb* /238U	±%	207Pb* /235U	±%	207Pb* /206Pb*	±%	207Pb /206Pb Age ± Ma		% Disc
357.1	0.01	371	151	0.42	0.438	1.74	8.98	1.79	0.1486	0.40	2330	7	-1
358.1	--	244	142	0.60	0.429	1.70	8.77	1.73	0.1482	0.35	2326	6	1
303.1	0.01	385	216	0.58	0.445	1.49	9.09	1.52	0.1482	0.27	2325	5	-2
309.1	--	201	109	0.56	0.434	1.50	8.83	1.63	0.1475	0.63	2317	11	0
302.1	0.03	136	62	0.47	0.435	1.19	8.83	1.74	0.1471	1.27	2312	22	-1
308.1	--	364	427	1.21	0.399	1.07	7.90	1.28	0.1437	0.70	2272	12	6
374.1	--	332	171	0.53	0.365	2.02	6.31	2.06	0.1252	0.38	2032	7	1
367.1	--	1010	320	0.33	0.357	1.93	6.01	1.96	0.1219	0.30	1984	5	1
340.1	0.02	906	256	0.29	0.335	1.41	5.46	1.45	0.1181	0.36	1928	6	4
360.1	--	1065	83	0.08	0.336	1.86	5.48	2.28	0.1181	1.33	1928	24	3
335.1	--	477	276	0.60	0.343	1.16	5.56	1.20	0.1176	0.31	1920	5	1
352.1	--	157	64	0.42	0.330	1.72	5.29	1.82	0.1161	0.62	1898	11	4
322.1	0.00	275	113	0.42	0.342	1.09	5.45	1.36	0.1155	0.81	1888	15	-1
321.1	--	147	57	0.40	0.336	1.17	5.32	1.56	0.1148	1.03	1877	19	1
377.1	--	111	66	0.61	0.336	2.52	5.30	2.65	0.1144	0.81	1870	15	0
344.2	--	381	93	0.25	0.324	1.08	5.07	1.15	0.1137	0.40	1859	7	3
380.1	--	368	210	0.59	0.314	2.13	4.91	2.26	0.1133	0.76	1854	14	6
332.1	--	192	100	0.54	0.338	1.13	5.26	1.26	0.1128	0.56	1846	10	-2
353.1	--	186	107	0.60	0.324	1.71	5.04	1.94	0.1128	0.90	1845	16	2
351.1	--	330	200	0.63	0.338	3.68	5.24	4.36	0.1125	2.34	1841	42	-2
362.1	--	125	52	0.43	0.325	1.77	5.05	1.91	0.1125	0.74	1840	13	2
372.1	--	321	184	0.59	0.321	1.77	4.98	1.82	0.1124	0.43	1839	8	3
301.1	--	149	59	0.41	0.329	1.17	5.10	1.38	0.1124	0.72	1839	13	0
361.1	0.05	144	80	0.58	0.325	2.16	5.03	2.28	0.1122	0.72	1836	13	1
338.1	0.02	231	72	0.32	0.324	1.45	5.01	1.54	0.1122	0.52	1835	9	2
371.1	--	521	214	0.42	0.326	1.74	5.04	1.77	0.1120	0.32	1833	6	1
343.1	0.00	453	88	0.20	0.331	1.28	5.10	1.44	0.1118	0.66	1828	12	-1
347.1	--	216	61	0.29	0.326	1.82	5.02	2.00	0.1117	0.82	1827	15	1
315.1	--	245	51	0.22	0.327	1.11	5.02	1.22	0.1114	0.50	1822	9	0
333.1	--	514	300	0.60	0.326	1.06	5.00	1.10	0.1112	0.32	1820	6	0
334.1	--	94	60	0.66	0.311	1.26	4.76	1.73	0.1110	1.18	1816	21	4
366.1	0.01	290	98	0.35	0.323	2.12	4.92	2.24	0.1107	0.71	1810	13	0
317.1	--	216	119	0.57	0.326	1.12	4.96	1.23	0.1104	0.52	1806	10	-1
379.1	0.03	201	62	0.32	0.306	1.93	4.65	2.09	0.1104	0.81	1806	15	5
329.1	0.05	186	74	0.41	0.325	1.14	4.94	1.32	0.1104	0.67	1805	12	-1
311.1	--	299	146	0.50	0.320	1.09	4.87	1.17	0.1102	0.44	1803	8	1
350.1	--	83	27	0.34	0.333	2.40	5.06	3.28	0.1102	2.25	1802	41	-3
337.1	0.00	212	56	0.27	0.325	1.13	4.94	1.28	0.1100	0.60	1800	11	-1
370.1	0.04	245	44	0.19	0.319	2.24	4.85	2.30	0.1100	0.52	1800	9	1
365.1	0.00	271	118	0.45	0.326	1.68	4.94	1.74	0.1099	0.48	1798	9	-1
310.1	--	226	62	0.28	0.324	1.44	4.91	1.54	0.1098	0.54	1796	10	-1
363.1	--	317	51	0.17	0.318	1.87	4.81	1.90	0.1098	0.37	1796	7	1
336.1	0.04	249	123	0.51	0.319	1.11	4.81	1.23	0.1094	0.53	1789	10	0
326.1	0.05	435	146	0.35	0.313	1.16	4.70	1.22	0.1091	0.38	1785	7	2
349.1	--	204	82	0.42	0.312	2.33	4.68	2.58	0.1088	1.12	1779	20	2
306.1	--	153	47	0.32	0.315	1.16	4.71	1.35	0.1084	0.68	1773	12	0
354.1	0.02	315	102	0.34	0.312	1.67	4.66	1.72	0.1083	0.39	1771	7	1

Spot	% $206Pb_c$	ppm U	ppm Th	232Th /238U	206Pb* /238U	±%	207Pb* /235U	±%	207Pb* /206Pb*	±%	207Pb /206Pb Age ± Ma		% Disc
341.1	0.01	918	304	0.34	0.316	1.18	4.71	1.26	0.1083	0.44	1771	8	0
313.1	0.03	204	188	0.95	0.312	1.13	4.64	1.29	0.1079	0.62	1765	11	1
375.1	--	374	309	0.86	0.310	2.07	4.61	2.11	0.1079	0.40	1764	7	2
312.1	--	882	438	0.51	0.318	1.03	4.72	1.06	0.1078	0.23	1763	4	-1
355.1	--	151	62	0.43	0.319	1.71	4.74	1.86	0.1077	0.72	1762	13	-2
331.1	0.00	106	70	0.69	0.307	1.82	4.56	2.06	0.1077	0.96	1760	18	2
323.1	0.00	259	112	0.45	0.311	1.12	4.62	1.50	0.1075	1.00	1758	18	1
376.1	--	110	52	0.49	0.311	2.25	4.59	2.42	0.1071	0.91	1750	17	0
304.1	0.05	268	104	0.40	0.316	1.11	4.66	1.24	0.1069	0.56	1747	10	-2
327.1	0.00	412	231	0.58	0.310	1.27	4.56	1.32	0.1065	0.37	1741	7	0
320.1	--	156	87	0.57	0.305	1.17	4.47	1.65	0.1062	1.16	1736	21	1
316.1	0.00	1263	457	0.37	0.305	1.09	4.44	1.11	0.1054	0.20	1722	4	0
356.1	--	209	121	0.60	0.297	1.71	4.29	1.82	0.1049	0.63	1713	12	3
345.1	0.01	1811	14	0.01	0.305	1.02	4.39	1.03	0.1045	0.15	1706	3	-1
metamorphic zircon													
346.1	--	819	131	0.17	0.278	1.77	3.84	1.79	0.1001	0.24	1627	4	3
328.1	0.02	447	114	0.26	0.281	1.06	3.83	1.14	0.0990	0.42	1605	8	1
305.1	0.04	884	123	0.14	0.282	1.09	3.82	1.12	0.0982	0.27	1590	5	-1
344.1	--	1034	139	0.14	0.276	1.03	3.73	1.06	0.0981	0.25	1589	5	1
324.1	--	737	96	0.13	0.280	1.13	3.77	1.17	0.0978	0.29	1583	5	-1

Data are 1σ precision. Pbc and Pb* indicate the common and radiogenic portions, respectively. All Pb data are initially common Pb corrected based on measured ^{204}Pb (after Stacey and Kramer 1975), then corrected for excess 204 counts inferred from average 207-corrected standard spots Batch 1: 301.1-345.1. Batch 2: 346.1-380.1.

R1009272: PARAGNEISS, HOUGHTON INLIER

GA Sample Number:	2008371001		
Field Number:	HI1		
Stratigraphic Unit:	Barossa Complex		
Location:	Houghton Inlier		
Location GDA94:	299633 E	6142480 N	Zone 54
Location Lat-Long:	-34°50'25"	138°48'31"	
250K map sheet	SI 54-09 ADELAIDE		
100K map sheet	6628 Adelaide		
Mount:	GA6054		
Date analysed: 1.1-68.1 73.1-111.1	LIMS session 80083: 16-18 May 2008 LIMS session 80126: 30Sep-2Oct 2008		
Machine:	SHRIMP IIe (GA)		
Standard age (α*)	LIMS session 80083: 3465.9 ± 3.5 Ma (1.00027) LIMS session 80126: 3465.6 ± 2.9 Ma (1.00013)		
Standard data	LIMS session 80083: Appendix 3.2 LIMS session 80126: Appendix 3.3		
Interpreted age:	1655 ± 8 Ma		
Age type:	Maximum age of deposition		
Interpreted age:	1585 ± 8 Ma, 1609 ± 7 Ma		
Age type:	Metamorphic age		

* α is a correction for Instrumental Mass Fractionation (Stern et al. 2009). For more information, see Appendix 3.

FIELD DESCRIPTION

Sample R1009272 was collected from a large road cutting on Gorge Road in the River Torrens gorge, approximately half a kilometre west of Cudlee Creek, in the southern Houghton Inlier (Fig. 3, 13a).

This lithology is dominated by quartz, biotite, and a fine grained retrograde mineral that is most likely sericite (Fig. 13b). Coarse quartz and K-feldspar occurs in leucosomes throughout the rock, indicating partial melting has occurred. A subtle layering of quartz rich and quartz poor domains is present and may reflect a primary sedimentary feature. Retrogression of the primary mineral assemblage obscures many of the structures within this rock.

Similar quartz-biotite-sericite gneisses occur throughout the southern Houghton Inlier, and structurally overly (younging uncertain) calcsilicate and quartofeldspathic gneisses. Retrogression is much more extensive in the southern Houghton Inlier than the north, and minor faults and hydrous alteration around quartz veins is common, which often obscures lithological boundaries and sedimentary or metamorphic structures.

Figure 13. (a) Outcrop photo of the location of R1009272. **(b)** The sampled lithology showing banding (near hammer point) and K-feldspar rich leucosome (below hammer).

ZIRCON CHARACTERISTICS

Zircons are predominantly elongate and subrounded exhibiting some crystal facets, and vary between 30-150 µm in length (Fig. 14). They are hyacinth in colour and clear, with few cracks or inclusions. Under CL they consist of dull CL homogenous to faintly zoned rims enclosing smaller (10-80µm), brighter CL, oscillatory zoned cores.

Figure 14. Transmitted light and CL images of zircon, R1588272: paragneiss, Houghton Inlier.

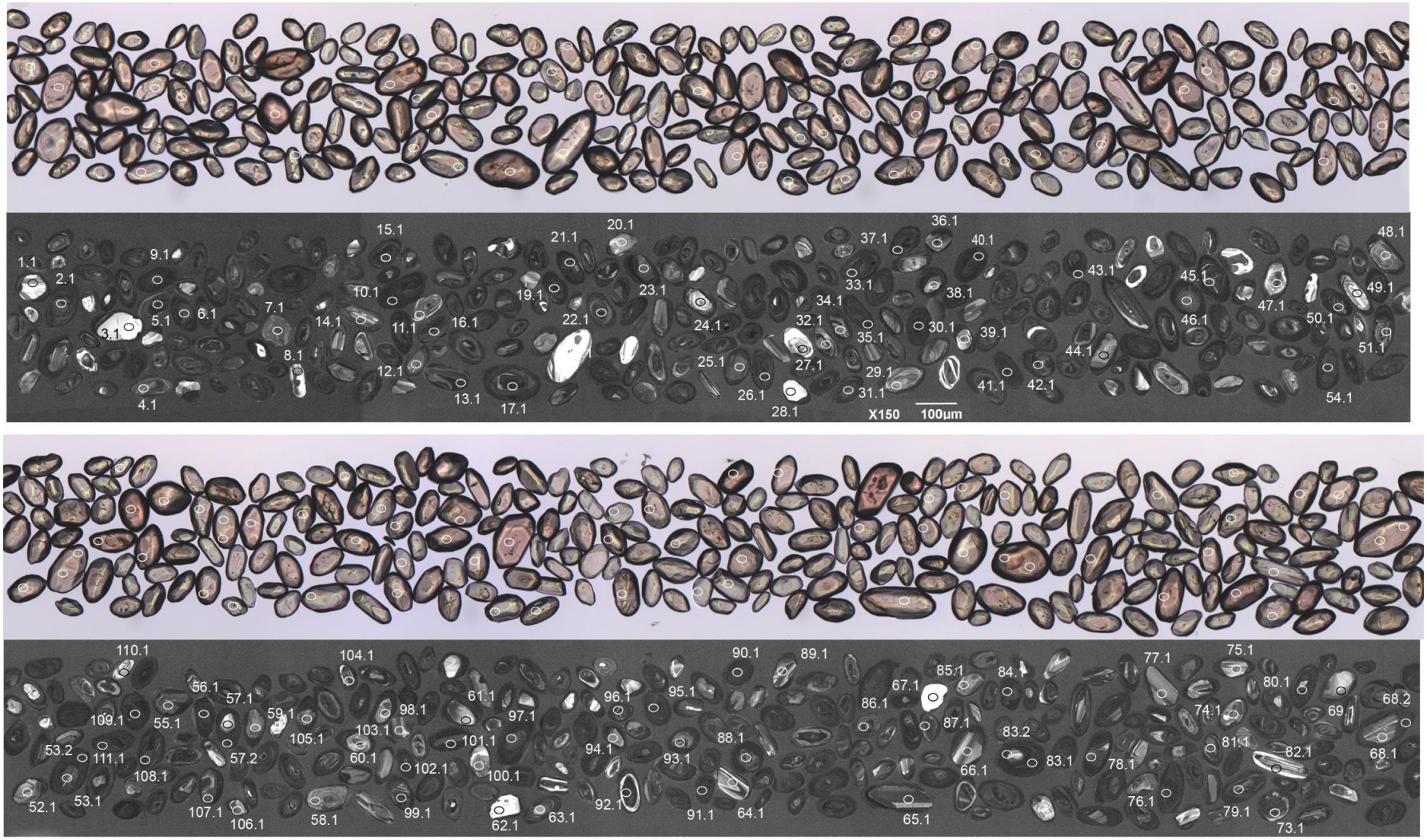

RESULTS

One hundred and twelve analyses were made on 105 grains over two analytical sessions. Only 11 analyse are > 5% discordant (Fig. 15), and all contain < 0.5% common lead. Three analyses (108.1, 83.2 and 15.1) overlap the boundary between core and rim, producing isotopic mixing ages of no geological significance.

CORES

Eighty three cores have a range of ages between c. 1653 – 3133 Ma (Fig. 16). The four youngest analyses yield a weighted mean $^{207}Pb/^{206}Pb$ age of 1655 ± 8 Ma, constraining the maximum age of deposition of the sedimentary protolith. Over two thirds of the analyses lie between c. 1690 – 1900 Ma, with merging peaks at c. 1691 Ma, 1713 Ma, 1733 Ma, 1772 Ma, 1787 Ma, 1813 Ma, |1827 Ma and 1862 Ma. Five analyses form an older group at 1962 ± 15 Ma (MSWD = 0.67, probability of fit = 0.61), and one analysis is c. 2064 Ma. A cluster of late Archaean - early Palaeoproterozoic cores range in age between c. 2285 – 2595 Ma, with older Archaean grains at c. 2717 Ma, 2802 Ma, and 3133 Ma.

METAMORPHIC RIMS

Twenty five analyses represent dark CL metamorphic zircon. With a high MSWD of 3.6, the analyses do not conform to a simple population at the 95% confidence level, and have a bimodal distribution (Fig. 16). Using mixture modelling as a guide to separating the two populations (Sambridge and Compston 1994), the 15 youngest analyses have a weighted mean $^{207}Pb/^{206}Pb$ age of 1585 ± 8 Ma (MSWD = 0.87, probability of fit = 0.59), and ten older analyses an age of 1609 ± 7 Ma (MSWD = 0.56, probability of fit = 0.83), and one analysis is older, at 1631 ± 6 Ma (1σ).

The 1585 ± 8 Ma age coincides with the timing of granulite facies metamorphism in the southern Barossa Complex (c. 1590 Ma, Szpunar et al. 2007a). The 1609 ± 7 Ma lies within a range of 1605-1612 Ma ages recorded in five of the samples analysed in this study and might represent an earlier peak in metamorphic conditions, during a prolonged period of metamorphism that affected the Barossa Complex between c. 1635-1590 Ma.

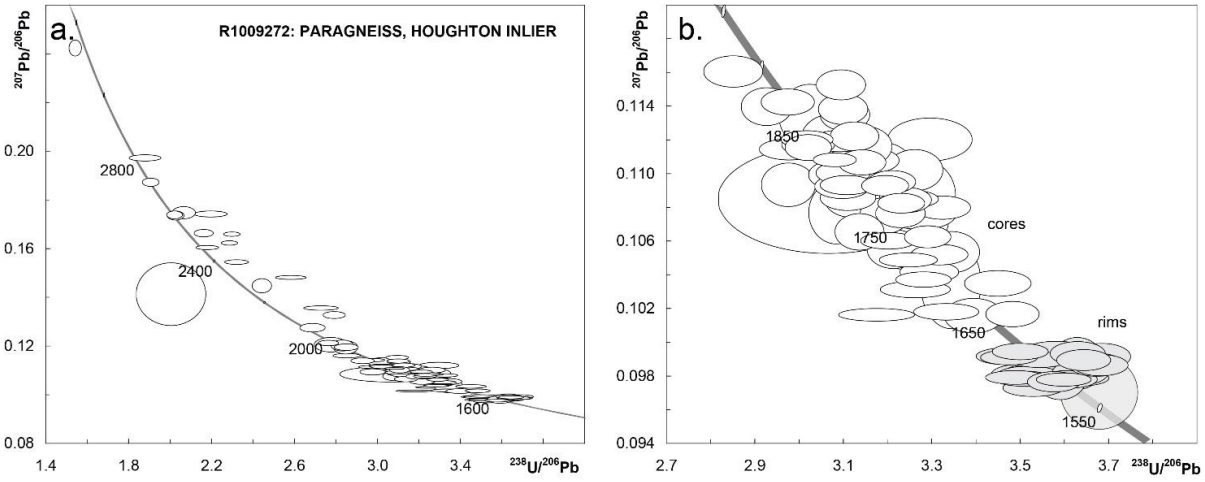

Figure 15. Tera-Wasserburg concordia diagrams for zircon in R1588272. (a) All analyses; and **(b)** the dominant cluster of core analyses and metamorphic rims younger than 1900 Ma.

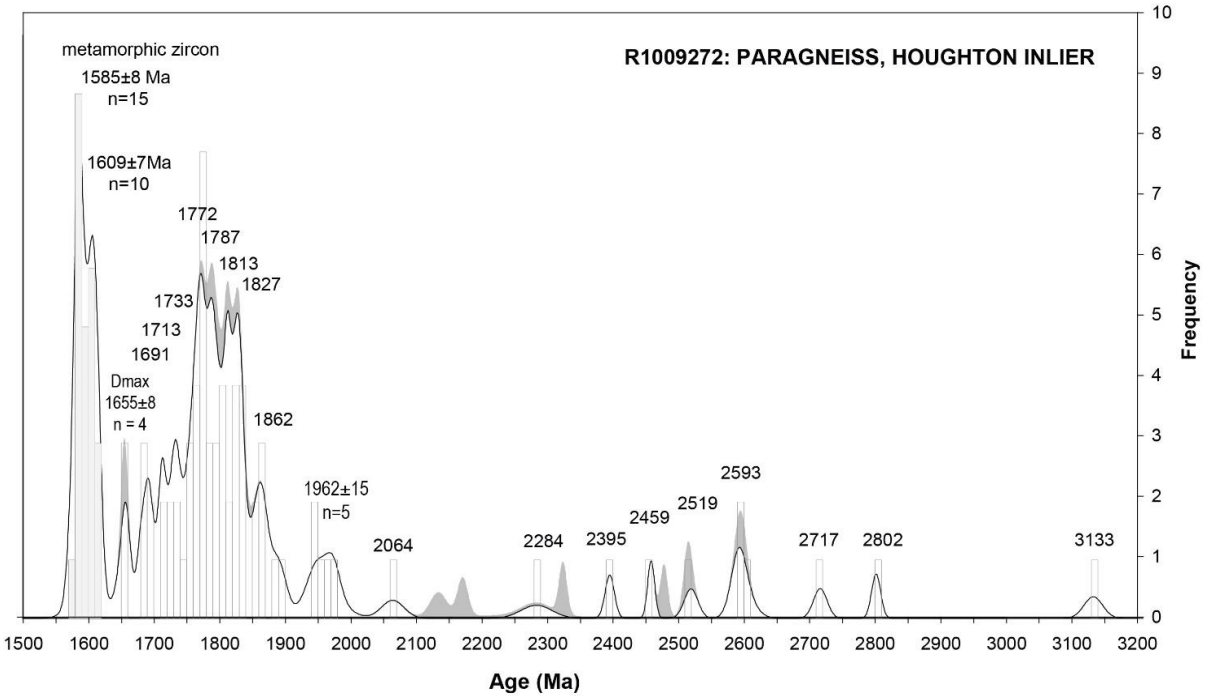

Figure 16. PDD of $^{207}Pb/^{206}Pb$ ages for R1009242. The grey shaded curve represents analyses > 5% discordant, which are not included in the calculation of peak maxima (Sircombe 2004). The histogram and white curve represent analyses < 5% discordant. Shaded histogram bars represent metamorphic zircon.

Table 4. SHRIMP analytical results for zircon from R1588272: paragneiss, Houghton Inlier. Analyses from LIMS session 80126 have grey spot names.

Spot	% $206Pb_c$	ppm U	ppm Th	232Th /238U	206Pb* /238U	±%	207Pb* /235U	IMF-corr 207Pb* /235U	±%	207Pb* /206Pb*	IMF-corr 207Pb* /206Pb*	±%	207Pb /206Pb Age	IMF-corr 207Pb /206Pb Age	± Ma	% Disc
detrital cores																
1001.18.1.1	0.03	84	28	0.35	0.645	1.29	21.535	21.529	1.57	0.24204	0.24197	0.90	3133	3133	14	-3
1001.48.1.1	0.08	223	178	0.82	0.531	2.71	14.428	14.424	2.74	0.19708	0.19703	0.42	2802	2802	7	2
1001.110.1.1	0.04	150	251	1.73	0.523	1.36	13.486	13.484	1.50	0.18709	0.18706	0.63	2717	2717	10	0
1001.62.1.1	0.40	67	97	1.51	0.483	1.75	11.626	11.623	2.01	0.17463	0.17458	0.98	2603	2602	16	3
1001.39.1.1	0.16	231	90	0.41	0.454	2.37	10.905	10.902	2.42	0.17401	0.17397	0.49	2597	2596	8	8
1001.92.1.1	0.01	658	348	0.55	0.493	1.25	11.817	11.816	1.40	0.17370	0.17368	0.63	2594	2593	11	0
1001.98.1.1	0.05	258	85	0.34	0.492	1.31	11.762	11.761	1.48	0.17339	0.17337	0.71	2591	2590	12	1
1001.49.1.1	0.15	145	69	0.49	0.461	1.39	10.569	10.566	1.52	0.16620	0.16616	0.62	2520	2519	10	4
1001.45.1.1	0.07	388	172	0.46	0.434	1.16	9.929	9.926	1.22	0.16574	0.16569	0.37	2515	2515	6	9
1001.54.1.1	0.01	500	98	0.20	0.437	1.14	9.763	9.760	1.19	0.16219	0.16214	0.34	2479	2478	6	7
1001.105.1.1	0.03	259	74	0.29	0.458	1.64	10.121	10.119	1.67	0.16029	0.16027	0.32	2459	2459	5	1
1001.53.1.1	0.06	335	122	0.38	0.430	1.63	9.165	9.163	1.68	0.15445	0.15441	0.42	2396	2395	7	4
1001.106.1.1	0.07	262	78	0.31	0.387	1.90	7.898	7.897	1.93	0.14811	0.14809	0.35	2324	2324	6	11
1001.101.1.1	--	389	166	0.44	0.409	1.28	8.154	8.153	1.87	0.14466	0.14464	1.37	2284	2284	24	4
1001.23.1.1	0.01	275	176	0.66	0.497	5.45	9.690	9.687	8.12	0.14129	0.14125	6.01	2243	2243	104	-20
1001.51.1.1	0.09	392	251	0.66	0.366	2.00	6.848	6.846	2.06	0.13558	0.13554	0.46	2171	2171	8	9
1001.93.1.1	0.03	337	88	0.27	0.358	1.29	6.552	6.552	1.48	0.13272	0.13271	0.72	2134	2134	13	9
1001.57.1.1	0.22	111	75	0.70	0.372	1.51	6.543	6.541	1.79	0.12756	0.12753	0.97	2065	2064	17	1
1001.47.1.1	0.07	485	314	0.67	0.362	1.19	6.043	6.041	1.33	0.12120	0.12117	0.58	1974	1974	10	-1
1001.67.1.1	0.53	54	61	1.17	0.360	1.88	5.988	5.986	2.46	0.12062	0.12059	1.60	1965	1965	28	-1
1001.6.1.1	0.05	408	120	0.30	0.353	1.26	5.851	5.849	1.74	0.12023	0.12020	1.20	1960	1959	21	1
1001.3.1.1	0.26	68	100	1.52	0.351	1.35	5.783	5.782	2.01	0.11948	0.11944	1.49	1948	1948	27	1
1001.38.1.1	0.14	197	156	0.82	0.351	1.33	5.777	5.775	1.52	0.11947	0.11944	0.74	1948	1948	13	1
1001.27.1.1	0.13	161	132	0.85	0.350	1.53	5.608	5.606	1.62	0.11604	0.11601	0.53	1896	1896	9	-2
1001.65.1.1	0.03	374	840	2.32	0.323	1.18	5.132	5.131	1.29	0.11524	0.11521	0.51	1884	1883	9	5

1001.99.1.1	0.01	505	291	0.59	0.336	1.35	5.292	5.291	1.42	0.11421	0.11419	0.45	1867	1867	8	0
1001.78.1.1	0.03	329	119	0.37	0.341	1.28	5.365	5.364	1.44	0.11395	0.11393	0.65	1863	1863	12	-2
1001.55.1.1	0.10	359	232	0.67	0.323	1.18	5.062	5.061	1.29	0.11382	0.11379	0.53	1861	1861	10	4
1001.34.1.1	0.07	348	123	0.36	0.322	1.20	5.039	5.038	1.32	0.11349	0.11346	0.56	1856	1856	10	3
1001.11.1.1	0.09	314	97	0.32	0.331	1.51	5.169	5.168	1.87	0.11341	0.11338	1.10	1855	1854	20	1
1001.32.1.1	0.10	420	193	0.47	0.320	1.16	4.949	4.947	1.27	0.11220	0.11217	0.51	1835	1835	9	3
1001.4.1.1	0.05	278	77	0.28	0.325	1.64	5.014	5.012	1.86	0.11205	0.11202	0.88	1833	1832	16	1
1001.104.1.1	0.03	421	213	0.52	0.331	1.27	5.114	5.114	1.31	0.11201	0.11200	0.31	1832	1832	6	-1
1001.63.1.1	0.12	227	59	0.27	0.303	1.91	4.686	4.685	2.05	0.11202	0.11199	0.75	1832	1832	14	8
1001.7.1.1	0.03	313	121	0.40	0.323	1.36	4.987	4.986	1.42	0.11193	0.11190	0.38	1831	1830	7	2
1001.82.1.1	0.01	250	70	0.29	0.331	1.30	5.096	5.095	1.36	0.11170	0.11169	0.38	1827	1827	7	-1
1001.52.1.1	0.05	199	146	0.76	0.318	1.30	4.887	4.885	1.48	0.11162	0.11159	0.70	1826	1825	13	3
1001.36.1.1	0.04	459	119	0.27	0.331	1.15	5.089	5.088	1.24	0.11154	0.11151	0.45	1825	1824	8	-1
1001.74.1.1	0.14	379	267	0.73	0.336	1.49	5.156	5.155	1.54	0.11141	0.11140	0.38	1823	1822	7	-3
1001.13.1.1	0.03	736	123	0.17	0.324	1.04	4.957	4.956	1.07	0.11082	0.11079	0.24	1813	1812	4	0
1001.42.1.1	0.08	480	211	0.45	0.317	1.50	4.840	4.839	1.57	0.11077	0.11074	0.46	1812	1812	8	2
1001.57.2.1	0.08	701	112	0.17	0.318	1.12	4.853	4.852	1.21	0.11066	0.11063	0.45	1810	1810	8	2
1001.60.1.1	0.14	291	145	0.52	0.319	1.70	4.869	4.868	1.80	0.11064	0.11061	0.61	1810	1809	11	2
1001.44.1.1	0.15	173	77	0.46	0.313	1.34	4.774	4.773	1.57	0.11048	0.11045	0.82	1807	1807	15	3
1001.5.1.1	0.03	622	80	0.13	0.322	1.05	4.891	4.890	1.30	0.11024	0.11021	0.77	1803	1803	14	0
1001.58.1.1	0.11	216	64	0.31	0.306	1.28	4.657	4.656	1.47	0.11020	0.11017	0.73	1803	1802	13	5
1001.103.1.1	0.06	282	130	0.48	0.322	1.30	4.892	4.891	1.37	0.11002	0.11001	0.41	1800	1800	7	0
1001.75.1.1	0.07	162	185	1.18	0.324	1.36	4.911	4.910	1.46	0.10991	0.10990	0.53	1798	1798	10	-1
1001.25.1.1	0.03	284	60	0.22	0.311	1.10	4.704	4.703	1.17	0.10953	0.10950	0.40	1792	1791	7	3
1001.85.1.1	0.14	198	70	0.36	0.336	1.35	5.062	5.061	1.56	0.10932	0.10931	0.77	1788	1788	14	-5
1001.81.1.1	0.03	351	138	0.41	0.322	1.28	4.847	4.846	1.33	0.10930	0.10928	0.35	1788	1788	6	-1
1001.14.1.1	0.02	280	295	1.09	0.313	1.09	4.715	4.714	1.15	0.10928	0.10925	0.37	1787	1787	7	2
1001.100.1.1	0.07	235	152	0.67	0.323	1.32	4.860	4.860	1.39	0.10923	0.10922	0.44	1787	1786	8	-1
1001.66.1.1	0.02	284	283	1.03	0.309	2.15	4.633	4.631	2.60	0.10882	0.10879	1.45	1780	1779	26	3
1001.28.1.1	0.34	45	176	4.00	0.305	1.51	4.573	4.572	1.98	0.10873	0.10871	1.28	1778	1778	23	4

1001.77.1.1	0.08	220	355	1.67	0.321	1.32	4.811	4.810	1.40	0.10856	0.10854	0.46	1775	1775	8	-1
1001.46.1.1	0.00	199	89	0.46	0.326	5.37	4.875	4.874	5.71	0.10849	0.10846	1.96	1774	1774	36	-3
1001.80.1.1	0.00	414	56	0.14	0.307	1.27	4.597	4.597	1.31	0.10847	0.10845	0.32	1774	1774	6	3
1001.107.1.1	0.03	251	164	0.68	0.320	1.31	4.789	4.789	1.46	0.10845	0.10844	0.65	1774	1773	12	-1
1001.50.1.1	0.04	496	156	0.32	0.308	1.14	4.609	4.608	1.23	0.10844	0.10841	0.46	1773	1773	8	3
1001.69.1.1	0.25	134	58	0.45	0.312	1.41	4.656	4.654	1.72	0.10833	0.10830	0.99	1772	1771	18	1
1001.2.1.1	0.04	408	113	0.29	0.309	1.08	4.619	4.617	1.13	0.10825	0.10822	0.36	1770	1770	7	2
1001.64.1.1	0.06	268	17	0.06	0.309	2.11	4.601	4.600	3.11	0.10808	0.10805	2.28	1767	1767	42	2
1001.109.1.1	0.01	680	70	0.11	0.301	1.26	4.479	4.478	1.33	0.10798	0.10797	0.42	1766	1765	8	5
1001.89.1.1	0.09	223	38	0.18	0.324	1.32	4.812	4.811	1.74	0.10768	0.10767	1.14	1761	1760	21	-3
1001.8.1.1	0.10	187	189	1.04	0.310	1.14	4.595	4.593	1.25	0.10764	0.10761	0.51	1760	1759	9	1
1001.29.1.1	0.10	191	52	0.28	0.305	1.61	4.529	4.527	1.69	0.10754	0.10751	0.51	1758	1758	9	3
1001.20.1.1	0.16	157	52	0.34	0.313	1.17	4.641	4.639	1.34	0.10750	0.10747	0.65	1758	1757	12	0
1001.24.1.1	0.21	151	132	0.90	0.319	1.17	4.682	4.680	1.35	0.10655	0.10652	0.67	1741	1741	12	-3
1001.19.1.1	0.06	818	62	0.08	0.304	1.04	4.452	4.451	1.12	0.10626	0.10623	0.40	1736	1736	7	2
1001.79.1.1	0.02	471	75	0.16	0.312	1.27	4.565	4.564	1.31	0.10602	0.10600	0.31	1732	1732	6	-1
1001.1.1.1	0.16	138	135	1.01	0.311	1.23	4.528	4.526	1.42	0.10555	0.10552	0.72	1724	1723	13	-1
1001.68.1.1	0.16	229	150	0.67	0.299	1.27	4.345	4.343	1.48	0.10536	0.10533	0.76	1721	1720	14	2
1001.95.1.1	--	362	42	0.12	0.301	1.29	4.372	4.372	1.34	0.10520	0.10518	0.38	1718	1718	7	1
1001.94.1.1	0.02	666	63	0.10	0.308	1.33	4.452	4.452	1.36	0.10488	0.10487	0.26	1712	1712	5	-1
1001.22.1.1	0.09	611	143	0.24	0.303	1.33	4.359	4.358	1.39	0.10418	0.10416	0.40	1700	1699	7	-1
1001.96.1.1	0.03	596	274	0.47	0.305	1.26	4.357	4.356	1.29	0.10371	0.10370	0.29	1692	1691	5	-2
1001.12.1.1	0.08	244	145	0.61	0.290	1.43	4.137	4.136	1.51	0.10351	0.10348	0.48	1688	1688	9	3
1001.59.1.1	0.16	186	79	0.44	0.299	1.34	4.268	4.267	2.16	0.10350	0.10347	1.70	1688	1687	31	0
1001.73.1.1	0.05	469	189	0.42	0.306	1.60	4.357	4.357	1.63	0.10313	0.10312	0.32	1681	1681	6	-3
1001.86.1.1	0.05	443	19	0.04	0.300	1.45	4.211	4.210	1.48	0.10181	0.10179	0.31	1657	1657	6	-2
1001.31.1.1	0.10	489	48	0.10	0.287	1.13	4.027	4.026	1.24	0.10170	0.10167	0.49	1655	1655	9	2
1001.102.1.1	0.02	728	47	0.07	0.315	1.78	4.412	4.412	1.80	0.10164	0.10163	0.25	1654	1654	5	-8
1001.88.1.1	0.04	340	28	0.09	0.295	1.29	4.125	4.125	1.45	0.10158	0.10156	0.66	1653	1653	12	-1

metamorphic zircon																
1001.9.1.1	0.04	626	36	0.06	0.279	1.24	3.836	3.835	1.28	0.09962	0.09959	0.31	1617	1616	6	2
1001.17.1.1	0.05	720	24	0.03	0.286	1.19	3.919	3.917	1.23	0.09947	0.09945	0.31	1614	1614	6	0
1001.56.1.1	0.02	552	19	0.04	0.275	1.13	3.774	3.773	1.22	0.09936	0.09934	0.47	1612	1612	9	3
1001.87.1.1	0.02	416	25	0.06	0.288	1.27	3.944	3.944	1.32	0.09919	0.09918	0.33	1609	1609	6	-2
1001.33.1.1	0.03	482	28	0.06	0.271	1.15	3.710	3.709	1.26	0.09916	0.09914	0.52	1608	1608	10	4
1001.16.1.1	0.02	743	44	0.06	0.288	1.23	3.932	3.931	1.26	0.09911	0.09909	0.30	1607	1607	6	-2
1001.26.1.1	0.03	575	16	0.03	0.282	1.25	3.852	3.851	1.29	0.09899	0.09896	0.31	1605	1605	6	0
1001.41.1.1	0.06	730	18	0.03	0.275	1.10	3.746	3.745	1.18	0.09897	0.09894	0.42	1605	1604	8	3
1001.35.1.1	0.02	676	19	0.03	0.276	1.11	3.754	3.753	1.51	0.09878	0.09875	1.03	1601	1601	19	2
1001.37.1.1	0.07	561	18	0.03	0.272	1.12	3.705	3.704	1.21	0.09869	0.09867	0.46	1600	1599	9	3
1001.43.1.1	0.03	681	24	0.04	0.272	1.11	3.695	3.694	1.19	0.09866	0.09863	0.43	1599	1598	8	4
1001.30.1.1	0.06	583	15	0.03	0.281	1.49	3.814	3.813	1.53	0.09850	0.09847	0.31	1596	1595	6	0
1001.68.2.1	0.03	483	17	0.04	0.275	1.14	3.726	3.725	1.25	0.09824	0.09822	0.50	1591	1591	9	2
1001.76.1.1	0.04	467	17	0.04	0.283	1.27	3.834	3.834	1.31	0.09821	0.09820	0.34	1590	1590	6	-1
1001.84.1.1	0.03	502	30	0.06	0.284	1.26	3.844	3.844	1.30	0.09812	0.09811	0.32	1589	1588	6	-2
1001.53.2.1	0.05	528	17	0.03	0.279	1.14	3.767	3.766	1.52	0.09810	0.09808	1.00	1588	1588	19	0
1001.97.1.1	0.08	336	14	0.04	0.285	1.29	3.861	3.860	1.35	0.09808	0.09807	0.42	1588	1588	8	-2
1001.91.1.1	0.02	611	18	0.03	0.287	1.26	3.871	3.870	1.28	0.09792	0.09791	0.27	1585	1585	5	-3
1001.111.1.1	0.06	557	19	0.04	0.275	1.26	3.718	3.718	1.30	0.09790	0.09788	0.32	1584	1584	6	1
1001.83.1.1	0.03	571	15	0.03	0.285	1.26	3.847	3.847	1.29	0.09786	0.09784	0.29	1584	1583	5	-2
1001.21.1.1	0.07	535	18	0.04	0.277	1.21	3.739	3.738	1.26	0.09783	0.09780	0.35	1583	1583	6	0
1001.10.1.1	0.03	801	19	0.02	0.278	1.13	3.748	3.747	1.16	0.09782	0.09779	0.26	1583	1582	5	0
1001.40.1.1	0.02	735	19	0.03	0.280	1.11	3.767	3.766	1.18	0.09769	0.09767	0.40	1581	1580	8	-1
1001.90.1.1	0.06	466	15	0.03	0.283	1.27	3.803	3.802	1.31	0.09731	0.09729	0.34	1573	1573	6	-3
1001.61.1.1	0.46	96	25	0.27	0.272	1.55	3.639	3.638	2.15	0.09707	0.09705	1.49	1569	1568	28	1
rejected analyses: mixing ages																
1001.15.1.1	0.04	724	80	0.11	0.285	1.04	3.972	3.971	1.08	0.10094	0.10092	0.27	1642	1641	5	2
1001.83.2.1	0.05	530	47	0.09	0.288	1.26	3.996	3.996	1.45	0.10047	0.10046	0.71	1633	1633	13	0
1001.108.1.1	0.00	502	30	0.06	0.289	1.27	4.002	4.002	1.30	0.10037	0.10035	0.31	1631	1631	6	0

R1588241: PSAMMOPELITE, WARREN INLIER

GA sample number:	2008371004		
Field Number:	WI2		
Stratigraphic Unit:	Barossa Complex		
Location:	Warren Inlier		
Location GDA94:	309134 E	6157063 N	Zone 54
Location Lat-Long:	-34° 42' 38"	138° 54' 57"	
250K map sheet	SI5409 ADELAIDE		
100K map sheet	6628 ADELAIDE		
Mount:	GA6054		
Date analysed:	LIMS session 100027: 15-17 Feb 2010		
Machine:	SHRIMP IIe (GA)		
Standard age (α*)	3462.4 ± 2.5 Ma (0.99803)		
Standard data	Appendix		
Interpreted age:	1658 ± 11 Ma		
Age type:	Maximum age of deposition		
Interpreted age:	1589 ± 5 Ma, 1611 ± 5 Ma		
Age type:	Peak metamorphism		
Interpreted age:	518 ± 40 Ma		
Age type:	Delamerian metamorphism		

* α is a correction for Instrumental Mass Fractionation (Stern et al. 2009). For more information, see Appendix 3.

FIELD DESCRIPTION

Sample R1588241 was collected from the South Para River in the Warren Inlier, approximately 3.5 km southeast of Williamstown and 400 m downstream from the Warren Reservoir dam, from a muscovite and biotite rich psammopelite (Fig. 3). A strong gneissic fabric is present, which segregates quartzofeldspathic minerals from the micaceous minerals forming 0.5-1.0 cm gneissic bands (Figs 17, 18). Larger quartz rich layers up to 5 cm thick, possibly a relict sedimentary feature, closely follow the gneissic layering. Thin leucosomes, several centimetres thick, parallel the gneissic foliation, and in some places are boudinaged. Larger pegmatites which cross the foliation are common in the surrounding area.

The gneissosity of this rock has been multiply deformed. Larger wavelength folds are commonly observed disturbing older crenulations, indicating at least 2 folding events. The sampled psammopelite grades into a structurally overlying muscovite sillimanite schist to the south. The Warren Inlier lies within the sillimanite isograd of the Delamerian Orogen, and is positioned in an area of intense deformation as mapped by Mills (1973).

Figure 17. (a) Outcrop photo of psammopelite R1588241. **(b)** Folded gneissosity in psammopelite from the sample location. **(c)** Leucosomes (thin light bands, above the hammer) and pegmatites from the sample location, both displaying boudinage**.**

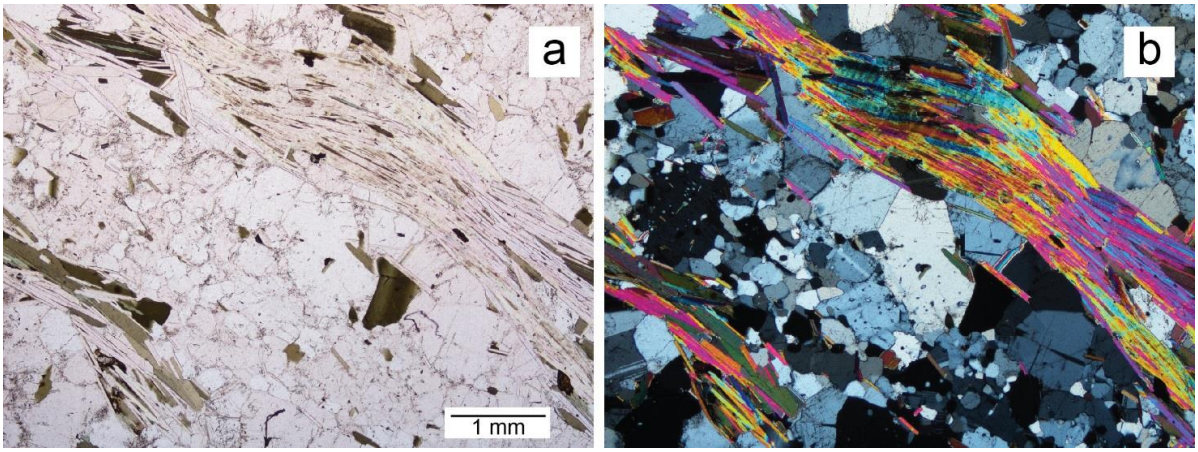

Figure 18. Sample R695752 under (a) plane polarised light; and (b) cross polars.

ZIRCON CHARACTERISTICS

The 50 -150 µm zircons are subhedral to slightly elongate and subrounded, with a blocky to tabular aspect. Many of the larger grains are subhedral while the smaller grains are more euhedral and prismatic. In transmitted light, zircons are light brown in colour, and somewhat metamict, with many fractures. Under CL the zircon exhibits three distinct growth structures (Fig. 19). The dominant zircon phase has a dull luminescence with faint growth zoning, high U, low Th (median 1521 ppm

and 81 ppm, respectively), and low Th/U ratios (median 0.06). This is interpreted to be metamorphic zircon, some grains of which enclose small cores, generally of brighter luminescence and with moderate U and Th contents and Th/U ratios, more typical of igneous zircon (median 572 ppm, 276 ppm and 0.50, respectively). The cores display a range of textures including oscillatory and complex growth zoning. All grains have a luminescent outer rim mantling the dark CL metamorphic zircon, which display faint convolute and oscillatory zoning. The luminescent rims contain moderate U, low Th (median 292 ppm and 44 ppm, respectively) and a wide range of Th/U ratios (0 – 2.37).

Figure 19. Transmitted light and CL images of zircon, R1588241: psammopelite, Warren Inlier.

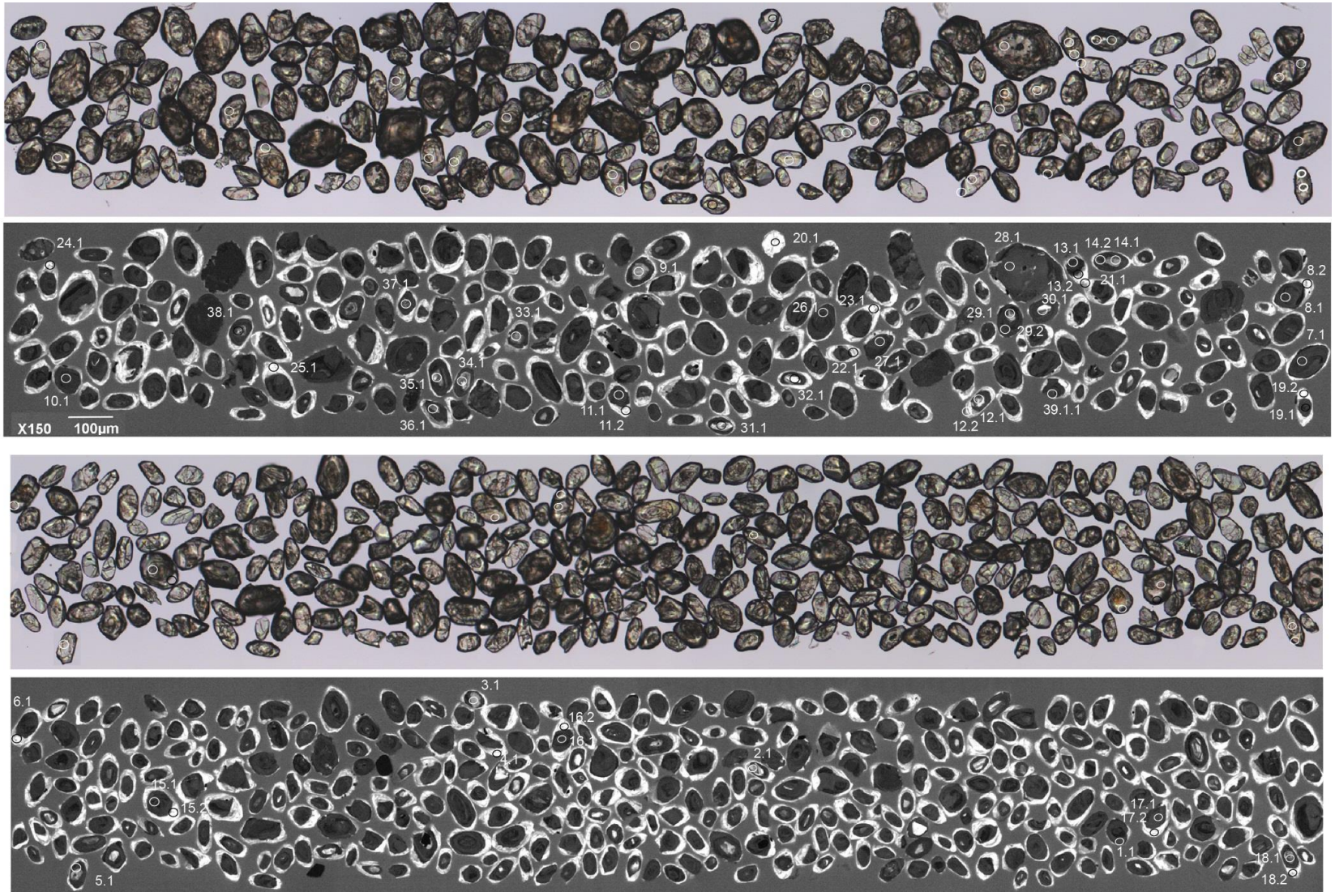

RESULTS

Fifty one analyses were made on 39 grains. Analyses targeted dark CL, homogeneous zircon and their thin, outermost, highly luminescent rims and light CL cores.

LIGHT CORES

Sixteen Palaeoproterozoic-Mesoproterozoic cores range between c. 1650 – 1805 Ma in age, with one older c. 2600 Ma Archaean core (Figs 20, 21). The two youngest analyses constrain the maximum age of deposition of the protolith at 1658 ± 11 Ma. The cluster of analyses between c. 1700 - 1800 Ma has dominant peaks at c. 1733 Ma, 1750 Ma and 1788 Ma (Fig. 21).

DARK METAMORPHIC ZIRCON

Eighteen analyses represent dark CL metamorphic zircon, of which 4 analyses are > 10% discordant and not included in the age calculations. With a high MSWD of 5, the remaining 14 analyses do not conform to a simple population at the 95% confidence level, and have a bimodal distribution (Fig. 21). The eight youngest analyses yield a weighted mean $^{207}Pb/^{206}Pb$ age of 1589 ± 5 Ma (MSWD = 0.65, probability of fit = 0.72). The $^{207}Pb/^{206}Pb$ age of the six oldest is 1611 ± 5 Ma (MSWD = 1.10, probability of fit = 0.36).

The 1589 ± 5 Ma age is the same as the timing of granulite facies metamorphism in the southern Barossa Complex (c. 1590 Ma, Szpunar et al. 2007a). The c. 1611 Ma age lies within a range of 1600-1615 Ma ages recorded in five of the samples analysed in this study and might represent an earlier peak in metamorphic conditions, during a prolonged period of metamorphism that affected the Barossa Complex between c. 1635-1590 Ma.

LUMINESCENT RIMS

Seventeen analyses of the brighter luminescent rims produced variably discordant $^{207}Pb/^{206}Pb$ ages ranging between c. 420 and 1330 Ma (Fig. 22) suggesting this is partially recrystallised zircon, with some grains containing an ‘isotopic memory’ of the protolith to produce a range of mixing ages of no geological significance (Hoskin and Black 2000). The 17 analyses lie on a scattered discordia (MSWD = 19), with intercepts of 1564 ± 230 Ma and 459 ± 40 Ma. The youngest 10 analyses conform to a single population with a weighted mean $^{207}Pb/^{206}Pb$ age of 518 ± 40 Ma (MSWD = 1.8, probability of fit = 0.08). The ages suggest recrystallisation of Proterozoic grains occurred in the early Phanerozoic. Given that three generations of Delamerian-aged deformation and folding are recognised in the Warren Inlier and surrounding Neoproterozoic cover (Mills (1973), it is likely that the isotopic system was disturbed during the 514-490 Ma Delamerian Orogeny (Foden et al. 2006), which locally reached amphibolite facies in the Warren Inlier (Offler and Fleming 1968; Mancktelow 1990).

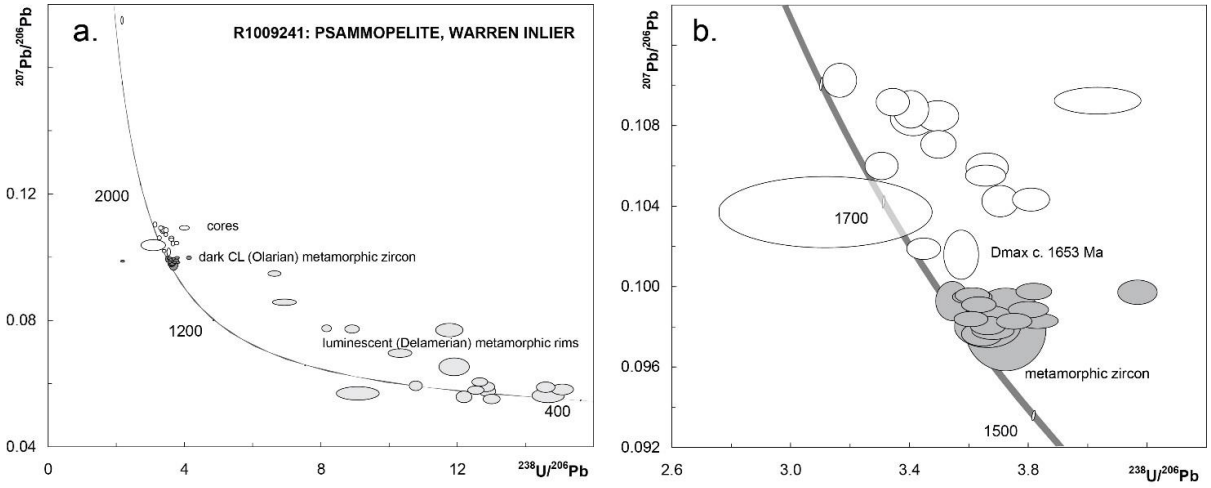

Figure 20. Tera-Wasser Concordia diagrams for zircon in R1009241. (a) all analyses; and **(b)** dark CL metamorphic zircons and light CL cores. Archaean core (grain 38) and the two most discordant analyses of metamorphic zircon are excluded from Figure b.

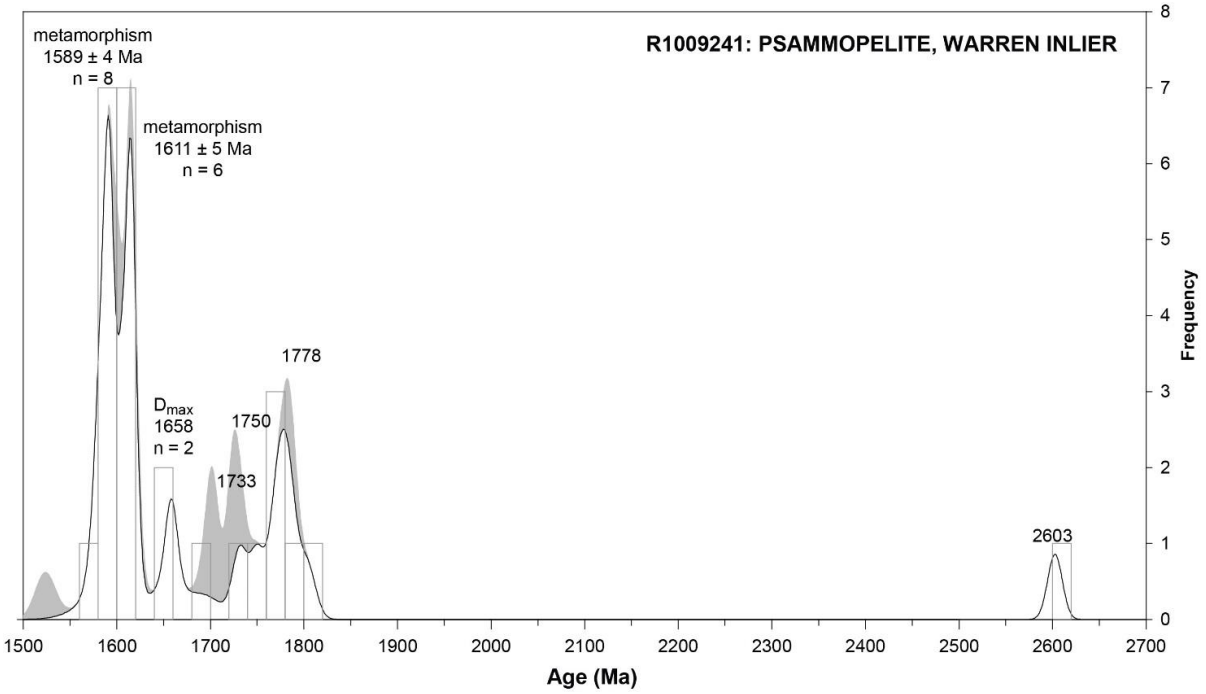

Figure 21. PDD of $^{207}Pb/^{206}Pb$ ages for dark CL metamorphic zircon and light CL cores in sample R1009241. The grey shaded area represents analyses > 10% discordant, which are not included in the calculation of peak maxima (Sircombe 2004). The histogram and white area represent analyses < 10% discordant.

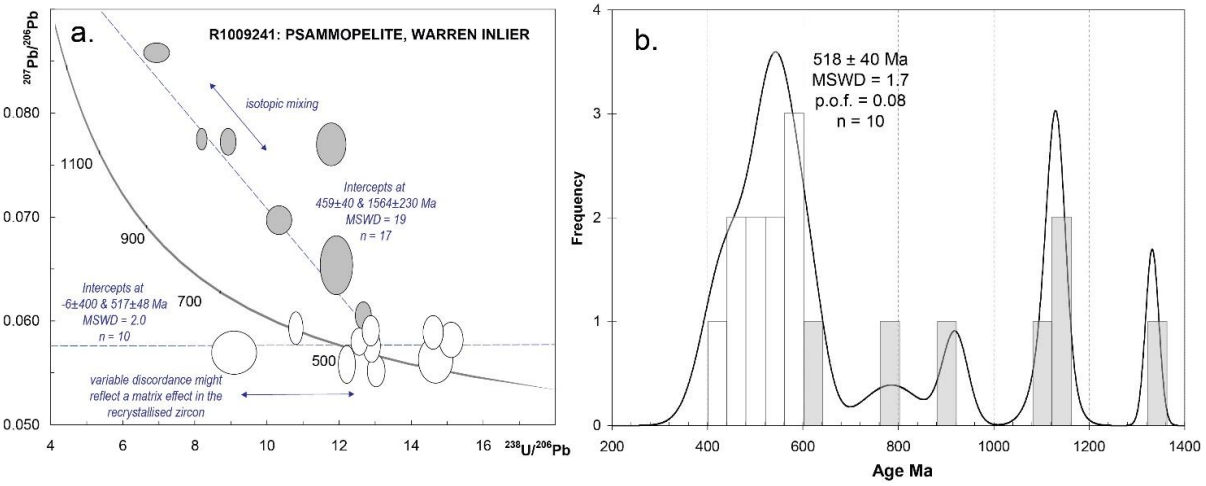

Figure 22. (a) Tera-Wasser concordia diagram; and (b) PDD for the luminescent metamorphic rims in sample R1009241. White analyses are included in the mean $^{207}Pb/^{206}Pb$ age calculation.

Table 5. SHRIMP analytical results for zircon from R1588241, psammopelite, Warren Inlier.

Spot	% $206Pb_c$	ppm U	ppm Th	232Th /238U	206Pb* /238U	±%	207Pb* /235U	IMF-corr 207Pb* /235U	±%	207Pb* /206Pb*	IMF-corr 207Pb* /206Pb*	±%	207Pb /206Pb Age	IMF-corr 207Pb /206Pb Age	± Ma	% Disc
light CL cores																
1004.38.1.1	--	830	411	0.51	0.452	1.09	10.851	10.873	1.19	0.17429	0.17463	0.47	2599	2603	8	9
1004.9.1.1	0.03	296	110	0.38	0.316	1.18	4.789	4.798	1.28	0.11000	0.11022	0.51	1799	1803	9	2
1004.18.1.1	0.23	860	743	0.89	0.248	2.37	3.727	3.734	2.40	0.10899	0.10920	0.40	1783	1786	7	22
1004.2.1.1	0.05	479	269	0.58	0.299	1.11	4.489	4.498	1.19	0.10892	0.10913	0.41	1781	1785	8	6
1004.30.1.1	0.09	340	102	0.31	0.294	1.16	4.394	4.403	1.29	0.10856	0.10877	0.57	1775	1779	10	7
1004.14.1.1	0.18	547	79	0.15	0.286	1.33	4.268	4.276	1.41	0.10824	0.10845	0.46	1770	1774	8	9
1004.35.1.1	0.11	332	284	0.88	0.293	1.50	4.368	4.376	1.60	0.10815	0.10836	0.54	1768	1772	10	7
1004.36.1.1	--	499	136	0.28	0.286	1.12	4.211	4.219	1.20	0.10683	0.10705	0.43	1746	1750	8	8
1004.33.1	0.00	436	204	0.48	0.302	1.13	4.410	4.419	1.20	0.10577	0.10598	0.42	1728	1731	8	2
1004.3.1.1	0.07	522	206	0.41	0.273	1.30	3.979	3.987	1.37	0.10567	0.10588	0.45	1726	1730	8	11
1004.37.1.1	0.08	941	527	0.58	0.274	1.22	3.971	3.979	1.26	0.10529	0.10549	0.33	1719	1723	6	10
1004.12.1.1	0.11	848	779	0.95	0.263	1.07	3.768	3.776	1.13	0.10410	0.10431	0.36	1698	1702	7	13
1004.29.1.1	0.26	596	359	0.62	0.270	1.10	3.871	3.878	1.21	0.10402	0.10423	0.50	1697	1701	9	10
1004.34.1.1	0.02	762	842	1.14	0.321	7.58	4.575	4.584	7.66	0.10348	0.10368	1.12	1687	1691	21	-7
1004.32.1.1	0.03	755	314	0.43	0.290	1.08	4.065	4.073	1.13	0.10167	0.10187	0.34	1655	1659	6	1
1004.31.1.1	0.13	817	138	0.17	0.280	1.08	3.910	3.918	1.34	0.10136	0.10156	0.79	1649	1653	15	4
dark CL metamorphic overgrowths																
1004.17.1.1	0.12	1700	337	0.20	0.262	1.04	3.595	3.602	1.08	0.09955	0.09975	0.27	1616	1619	5	8
1004.19.1.1	0.50	1488	655	0.45	0.240	1.04	3.293	3.300	1.12	0.09951	0.09970	0.40	1615	1619	7	16
1004.10.1.1	0.01	1433	29	0.02	0.277	1.05	3.793	3.801	1.07	0.09935	0.09955	0.25	1612	1616	5	3
1004.7.1.1	0.01	1507	29	0.02	0.277	1.12	3.796	3.803	1.15	0.09928	0.09948	0.24	1611	1614	5	2
1004.16.1.1	0.02	1640	96	0.06	0.276	1.13	3.784	3.791	1.15	0.09927	0.09946	0.25	1610	1614	5	3
1004.29.2.1	0.01	1568	22	0.01	0.282	1.05	3.854	3.861	1.23	0.09908	0.09927	0.64	1607	1611	12	0
1004.11.1.1	0.01	1541	91	0.06	0.275	1.05	3.753	3.760	1.08	0.09888	0.09908	0.26	1603	1607	5	3
1004.5.1.1	0.02	1222	71	0.06	0.263	1.17	3.579	3.586	1.21	0.09865	0.09885	0.28	1599	1602	5	7

1004.34.2.1	0.03	1075	3079	2.96	0.449	1.57	6.099	6.111	1.59	0.09852	0.09872	0.22	1596	1600	4	-60
1004.13.1.1	0.01	1654	55	0.03	0.277	1.04	3.752	3.760	1.08	0.09818	0.09837	0.25	1590	1593	5	1
1004.8.1.1	0.02	1535	143	0.10	0.261	1.21	3.530	3.537	1.24	0.09809	0.09828	0.25	1588	1592	5	7
1004.1.1.1	0.01	1279	128	0.10	0.266	1.05	3.603	3.611	1.08	0.09807	0.09826	0.26	1588	1591	5	5
1004.27.1.1	--	1096	41	0.04	0.273	1.06	3.682	3.690	1.10	0.09786	0.09805	0.30	1584	1587	6	2
1004.14.2.1	0.03	1218	72	0.06	0.273	2.01	3.682	3.689	2.13	0.09782	0.09801	0.71	1583	1587	13	2
1004.39.1.1	0.33	1986	677	0.35	0.269	2.39	3.616	3.624	2.77	0.09766	0.09785	1.38	1580	1584	26	3
1004.28.1.1	0.01	1070	39	0.04	0.272	1.28	3.657	3.665	1.31	0.09761	0.09780	0.30	1579	1583	6	2
1004.26.1.1	0.01	1654	59	0.04	0.274	1.26	3.686	3.694	1.32	0.09744	0.09764	0.40	1576	1579	8	1
1004.15.1.1	1.02	1558	4702	3.12	0.150	1.92	1.953	1.957	2.01	0.09458	0.09477	0.58	1520	1524	11	44
luminescent outer rims																
1004.15.2.1	0.00	411	26	0.07	0.144	3.36	1.695	1.698	3.43	0.08556	0.08573	0.72	1328	1332	14	37
1004.17.2.1	--	334	3	0.01	0.122	1.16	1.300	1.302	1.46	0.07728	0.07743	0.88	1128	1132	18	36
1004.16.2.1	0.08	282	91	0.33	0.112	1.63	1.189	1.192	1.96	0.07705	0.07720	1.09	1123	1126	22	41
1004.8.2.1	0.17	419	221	0.55	0.085	2.29	0.899	0.901	2.89	0.07680	0.07695	1.77	1116	1120	35	55
1004.22.1.1	0.12	304	6	0.02	0.097	2.24	0.928	0.930	2.59	0.06954	0.06968	1.30	915	919	27	37
1004.13.2.1	0.69	311	260	0.86	0.084	2.47	0.754	0.756	3.78	0.06522	0.06535	2.86	781	786	60	35
1004.6.1.1	--	281	99	0.36	0.079	1.19	0.658	0.659	1.86	0.06040	0.06052	1.43	618	622	31	22
1004.4.1.1	0.11	303	30	0.10	0.093	1.21	0.756	0.757	2.12	0.05918	0.05929	1.73	574	578	38	0
1004.20.1.1	--	226	1	0.00	0.078	1.23	0.632	0.633	2.06	0.05894	0.05906	1.65	565	569	36	15
1004.11.2.1	--	190	188	1.03	0.069	1.25	0.555	0.556	2.20	0.05880	0.05891	1.81	560	564	40	24
1004.18.2.1	0.26	321	98	0.32	0.066	1.44	0.531	0.532	2.40	0.05807	0.05818	1.92	532	537	42	23
1004.24.1.1	--	233	2	0.01	0.080	1.22	0.636	0.637	1.94	0.05788	0.05800	1.51	525	530	33	6
1004.25.1.1	--	193	1	0.00	0.078	1.26	0.615	0.616	2.23	0.05749	0.05760	1.84	510	515	40	6
1004.12.2.1	0.34	599	422	0.73	0.110	4.54	0.861	0.863	5.13	0.05684	0.05695	2.40	485	490	53	-41
1004.19.2.1	0.55	292	670	2.37	0.068	2.15	0.528	0.529	3.37	0.05613	0.05624	2.60	458	462	58	7
1004.21.1.1	0.21	242	2	0.01	0.082	1.26	0.629	0.631	2.49	0.05571	0.05582	2.15	441	445	48	-16
1004.23.1.1	0.11	235	44	0.19	0.077	1.22	0.584	0.585	2.19	0.05511	0.05522	1.81	417	421	41	-15

Data are 1σ precision. Pbc and Pb* indicate the common and radiogenic portions, respectively. All Pb data are initially common Pb corrected based on measured ^{204}Pb (after Stacey and Kramer 1975), then corrected for instrumental mass fractionation (IMF). Both uncorrected data, and IMF-corrected data (grey columns) are presented. All data are from LIMS Session 100027, analysis date 15/02/10; SHRIMP IIe, Geoscience Australia.

R1588240: PARAGNEISS, OAKBANK INLIER

Sample Number:	GA sample number 2008371003		
Field Number:	OI2		
Stratigraphic Unit:	Barossa Complex		
Location:	Oakbank Inlier		
Location GDA94:	305966 E	6126053 N	Zone 54
Location Lat-Long:	-34.9895323	138.8740785	
250K map sheet	SI 54-09 Adelaide		
100K map sheet	6628 Adelaide		
Mount:	GA6054		
Date analysed: 1.1-3.1 4.1-20.1 21.1-48.1 49.1-75.1	LIMS session 80081: 12-16 May 2008 LIMS session 80126: 30 Sep-2 Oct 2008 LIMS session 90032: 7-8 April 2009 LIMS session 100027: 15-17 Feb 2010		
Machine:	SHRIMP IIe (GA)		
Standard age (α*)	LIMS session 80081: 3467.6 ± 2.0 Ma (1.00137) LIMS session 80126: 3465.6 ± 2.9 Ma (1.00013) LIMS session 90032: 3466.3 ± 8.3 Ma (0.99957) LIMS session 100027: 3462.4 ± 2.5 Ma (0.99803)		
Standard data	LIMS session 80081: Appendix 3.1 LIMS session 80126: Appendix 3.3 LIMS session 90032: Appendix 3.4 LIMS session 100027: Appendix3.5		
Interpreted age:	1701 ± 14 Ma		
Age type:	Maximum age of deposition		
Interpreted age:	1594 ± 12 Ma, 1612 ± 13 Ma, 1635 ± 12 Ma.		
Age type:	Metamorphic age		

* α is a correction for Instrumental Mass Fractionation (Stern et al. 2009). For more information, see Appendix 3.

FIELD DESCRIPTION

Sample R1588240 was collected from a small outcrop in a drainage depression near Downers Road, approximately 2km east of the Oakbank township, on the eastern limit of the Oakbank inlier Fig. 23, 24a).

Sample R1588240 is a biotite- and muscovite-rich gneiss, with a fine-grained quartz and K-feldspar groundmass (Fig. 24b). Biotite is the dominant mica, defining a well-developed foliation which is deformed into open folds at the outcrop scale. The groundmass of quartz and feldspars is fine grained, averaging 0.5 mm grain sizes, with some coarse K-feldspar crystals up to 5 mm which are wrapped by the biotite foliation (Fig. 25). This sample site is weathered and friable which casts some uncertainty on the identification of the fine grained groundmass minerals.

The metasediments of the Oakbank inlier are poorly exposed and have not been mapped or described in any detail previously. This inlier is intruded by the 856 ± 20 Ma granite of Preiss et al. (2008), as well as a large pegmatite dykes of an unknown age. The Oakbank Inlier lies within the andalusite-staurolite isograd of the Delamerian Orogen which makes a potential Cambrian overprint or retrogression likely.

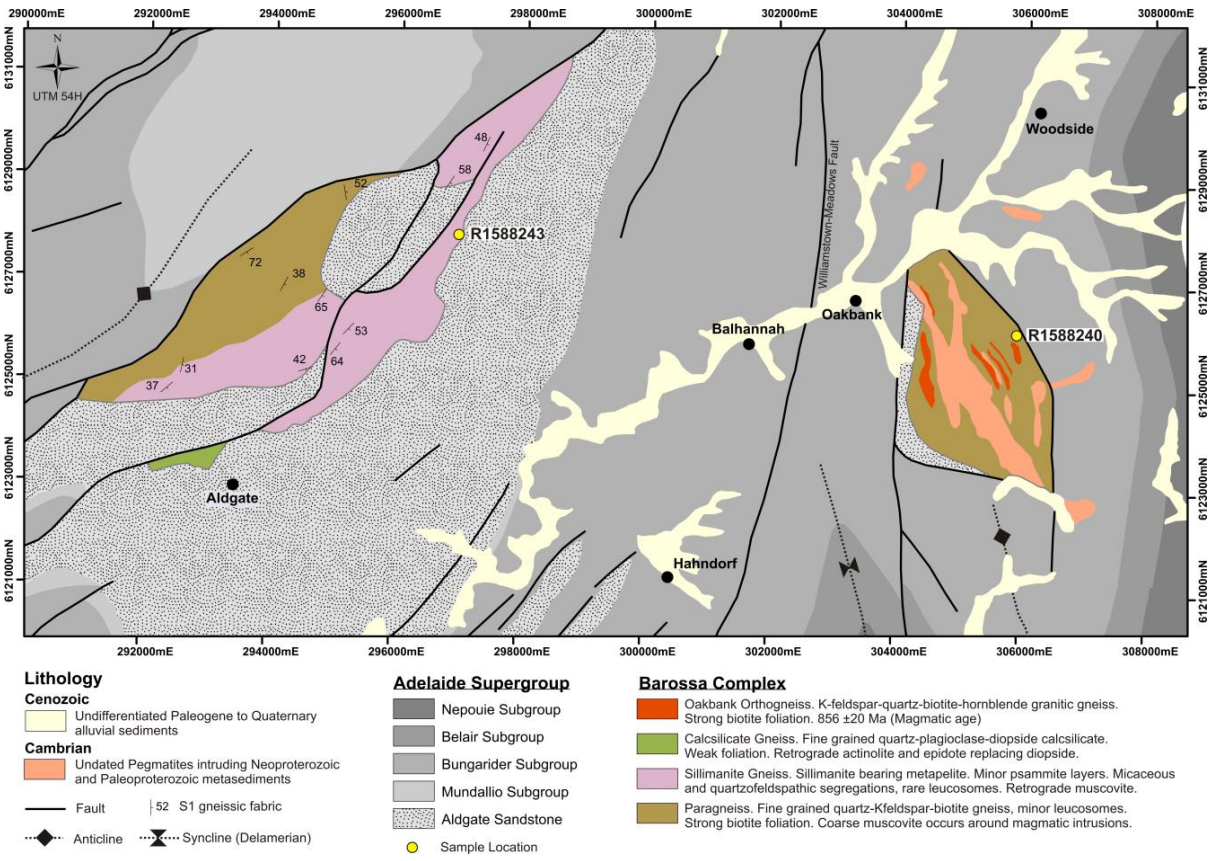

Figure 23. Location of the two samples in this study from the Aldgate and Oakbank Inliers of the Barossa Complex. Map is reproduced from Meaney et al. in prep.

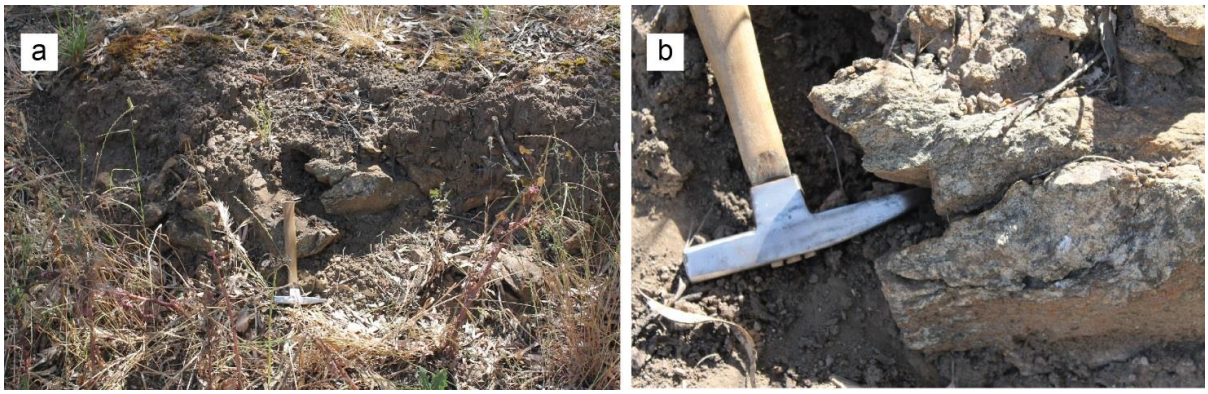

Figure 24. (a) Outcrop photo of R1588240 in a small exposure in drainage depression. **(b)** Close up of sampled lithology

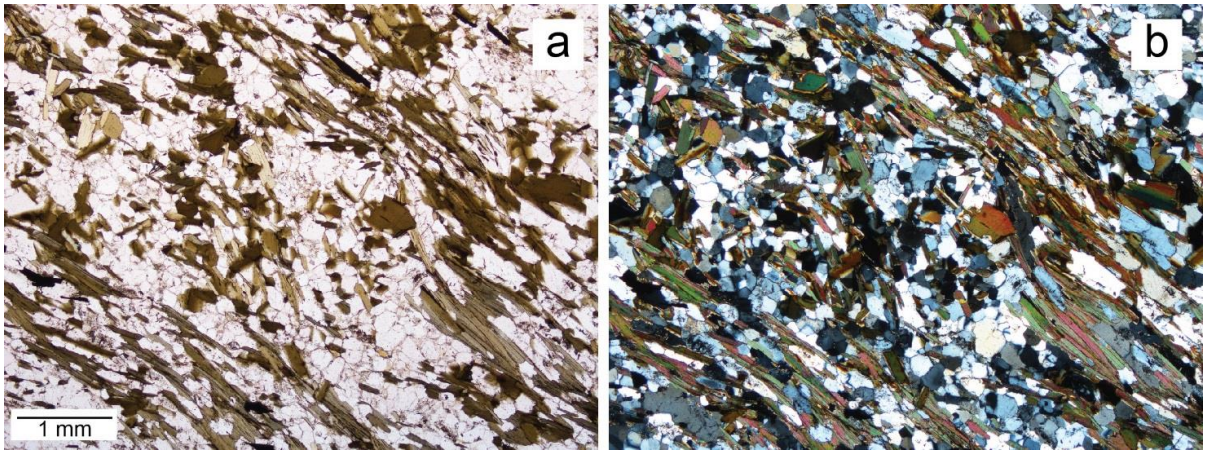

Figure 25. Sample R695752 under (a) plane polarised light; and (b) cross polars.

ZIRCON CHARACTERISTICS

Zircons are subhedral to sub rounded, elongate grains about 50 to 120µm long, and typically have a stubby, rounded to sub-rounded oval like morphology (Fig. 26). They are clear to pale brown wit few cracks and inclusions. Thick, light grey CL, homogenous to sector or oscillatory zoned rims enclose smaller, oval shaped cores that emit a range of CL responses from luminescent with well-defined oscillatory zoning, to homogeneous black-dull grey. Many crystals have thin, black CL grain edges.

Figure 26. CL and transmitted light images, R1588240: paragneiss, Oakbank Inlier.

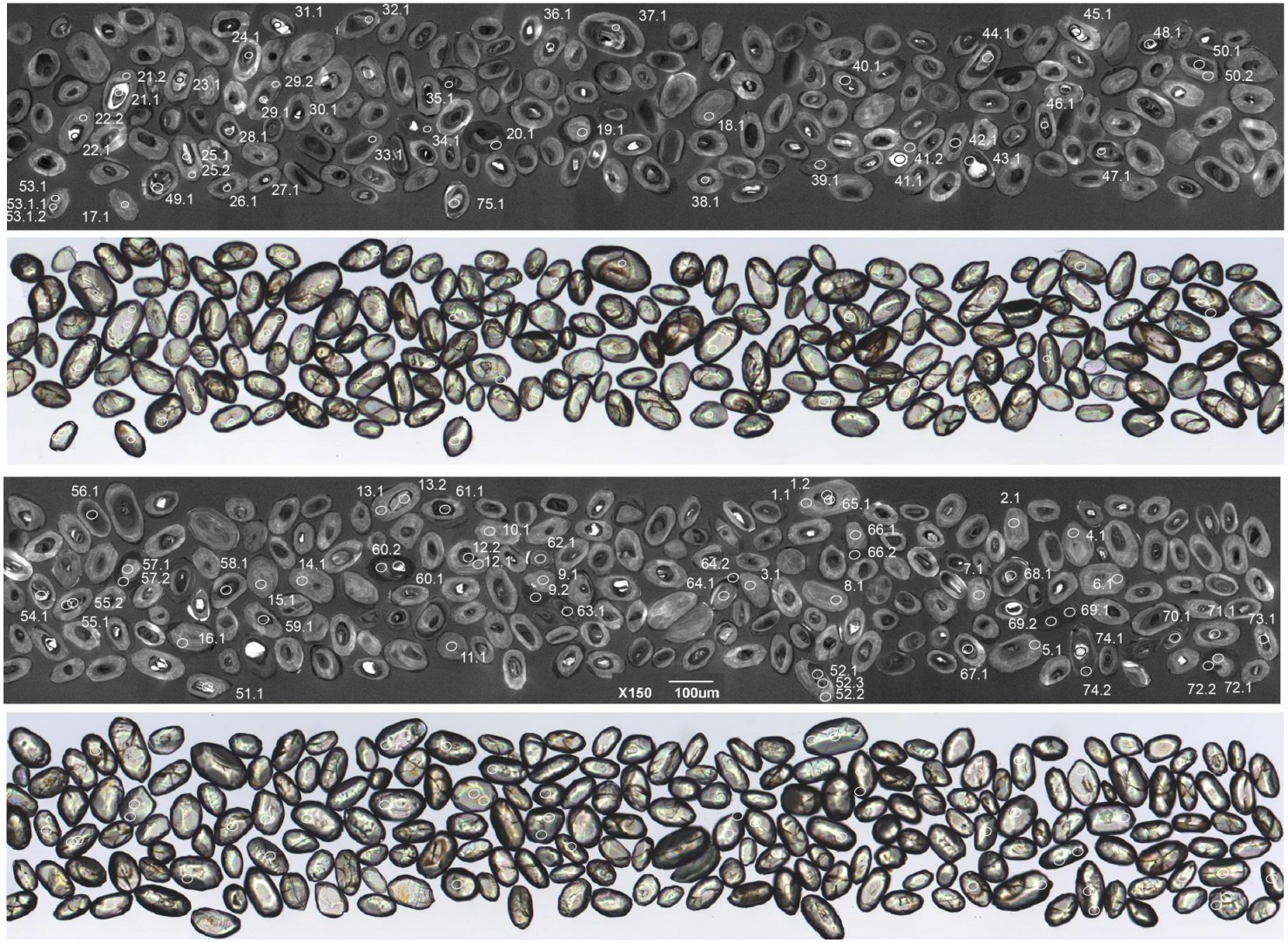

RESULTS

Ninety seven analyses made on 75 grains over four analytical sessions. The youngest analysis (64.2.1) overlapped the grain edge and is 17% discordant and not considered further. Analysis 1003.53.1.2, a downhole duplicate of 1003.53.1.1, is also eliminated due to the likelihood of element fractionation during sputtering.

CORES

Forty seven near-concordant analyses of cores range in age between c. 1675 - 2642 Ma (Figs 27, 28). Using MSWD as a guide to separating populations, the nine youngest analyses constrain the maximum age of deposition of the protolith at 1701 ± 9 Ma (MSWD = 1.8, probability of fit = 0.07). When the errors for the sessions are added to the uncertainties, the age becomes 1701 ± 14 Ma. Nearly half the cores are c. 1690 - 1770 Ma in age, with dominant peaks at c. 1701 Ma, 1727 Ma and 1759 Ma. Ten older analyses between 1808 - 1858 Ma have a bimodal distribution with peaks at c. 1820 Ma and 1855 Ma. Older peaks in the age spectrum occur at c. 1914 Ma, 1965 Ma, 2001 Ma and 2072 Ma, and there is a group of predominantly discordant analyses with late Archaean-early Palaeoproterozoic ages (c. 2320 – 2640 Ma).

METAMORPHIC RIMS

Forty eight analyses of metamorphic zircon range in age between c. 1575 – 1655 Ma. A high MSWD of 4.9, indicates that this cluster of analyses is not a single population, although there are no obvious peaks within the spectrum of merging metamorphic ages (Fig. 28). Mixture modelling was used to interpret possible age groups. The maximum number of age groups that can be modelled is three, which gives the youngest age at 1594 ± 6 Ma, with other ages of 1612 ± 5 Ma and 1635 ± 5 Ma. When the errors for the four sessions are added to the uncertainties, the ages become 1594 ± 12 Ma, with other ages of 1612 ± 13 Ma and 1635 ± 12 Ma. These three ages are in good agreement with metamorphic ages for other samples reported in this study, and so may be geologically meaningful.

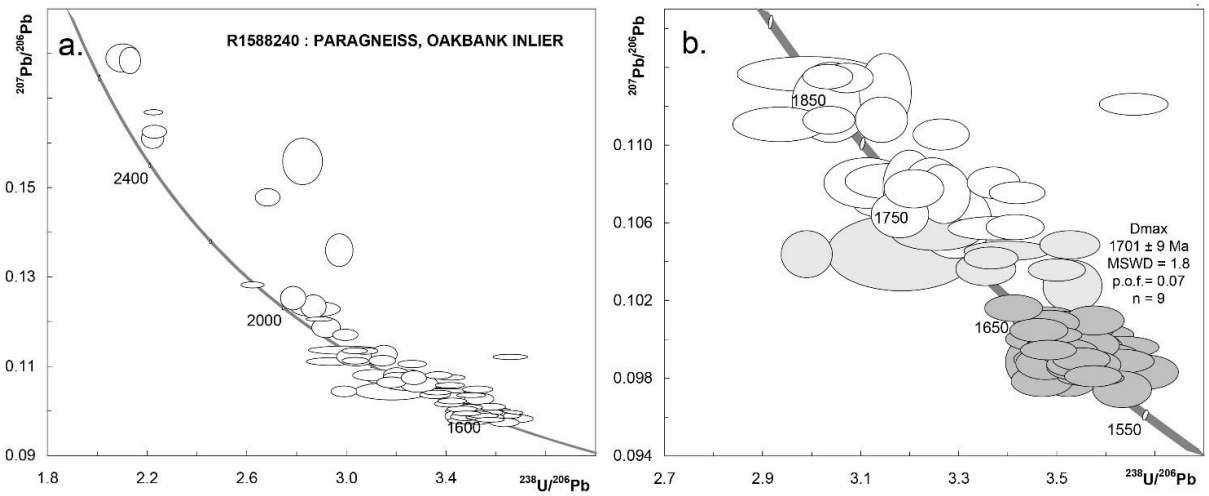

Figure 27. Tera-Wasser Concordia diagrams for zircon in R1009240. (a) all analyses; and **(b)** analyses younger than 1860 Ma**.** Dark grey ellipses represent metamorphic zircon and light grey represent the youngest detrital population.

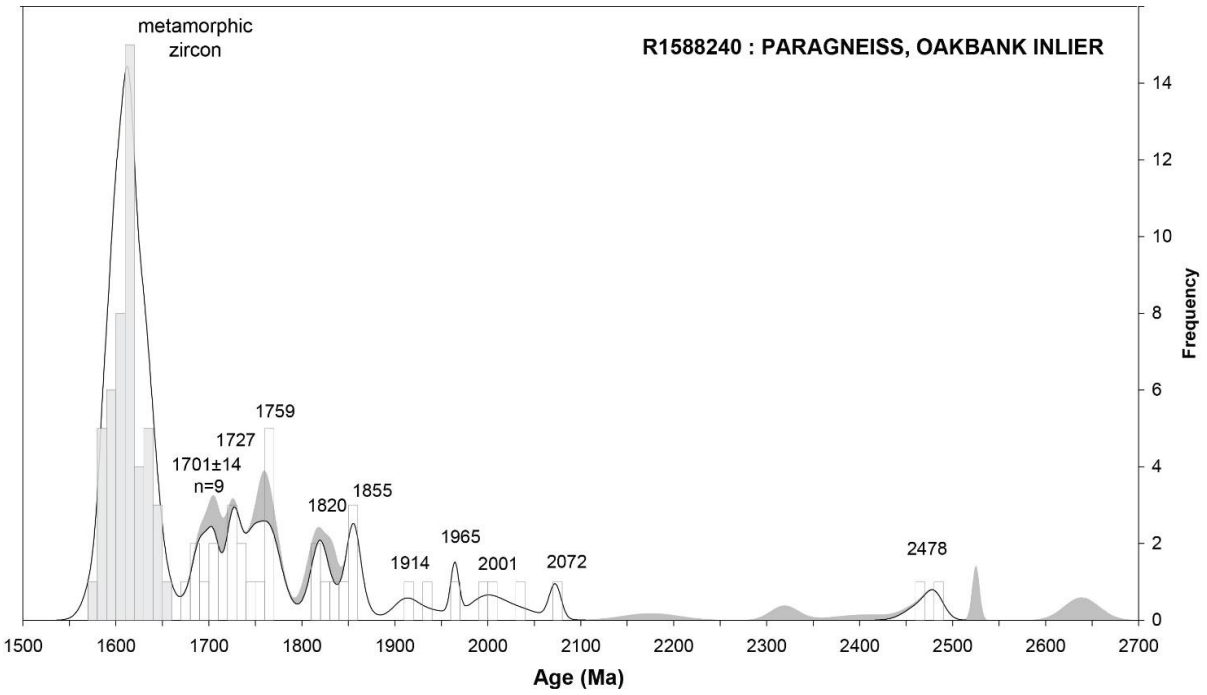

Figure 28. PDD of $^{207}Pb/^{206}Pb$ ages for R1009240. The grey shaded curve represents analyses > 5% discordant, which are not included in the calculation of peak maxima (Sircombe 2004). The histogram and white area represent analyses < 5% discordant. Grey columns of the histogram represent metamorphic zircon and white represent detrital cores.

Table 6. SHRIMP analytical results for zircon from R1588240, paragneiss, Oakbank Inlier.

Spot	% $206Pb_c$	ppm U	ppm Th	232Th /238U	206Pb* /238U	±%	207Pb* /235U	IMF-corr 207Pb* /235U	±%	207Pb* /206Pb*	IMF-corr 207Pb* /206Pb*	±%	207Pb /206Pb Age	IMF-corr 207Pb /206Pb Age	± Ma	% Disc
detrital cores																
1003.45.1.1	--	357	286	0.83	0.474	2.14	11.686	11.691	2.44	0.17872	0.17880	1.16	2641	2642	19	6
1003.27.1.1	0.03	244	40	0.17	0.468	1.33	11.491	11.496	1.71	0.17810	0.17818	1.09	2635	2636	18	7
1003.54.1.1	0.02	634	530	0.86	0.448	1.08	10.286	10.306	1.11	0.16639	0.16672	0.23	2522	2525	4	6
1003.31.1.1	0.00	126	79	0.65	0.448	1.47	10.019	10.023	1.58	0.16229	0.16236	0.59	2480	2480	10	5
1003.60.1.1	0.03	170	57	0.35	0.449	1.34	9.937	9.956	1.62	0.16048	0.16080	0.91	2461	2464	15	3
1003.26.1.1	0.00	589	94	0.17	0.354	1.83	7.595	7.598	2.86	0.15566	0.15573	2.20	2409	2410	37	22
1003.39.1.1	0.02	438	187	0.44	0.372	1.20	7.574	7.577	1.49	0.14759	0.14766	0.87	2318	2319	15	14
1003.25.1.1	0.00	322	137	0.44	0.336	1.24	6.299	6.302	2.16	0.13584	0.13590	1.77	2175	2176	31	16
1003.36.1.1	0.10	537	143	0.28	0.381	1.14	6.723	6.726	1.20	0.12807	0.12813	0.36	2072	2072	6	0
1003.67.1.1	0.00	861	164	0.20	0.359	1.21	6.181	6.193	1.85	0.12500	0.12525	1.40	2029	2032	25	3
1003.46.1.1	0.23	551	210	0.39	0.348	1.16	5.922	5.925	1.83	0.12325	0.12331	1.42	2004	2005	25	4
1003.28.1.1	--	356	108	0.31	0.347	2.24	5.872	5.875	2.42	0.12269	0.12274	0.90	1996	1996	16	4
1003.59.1.1	0.01	996	874	0.91	0.346	1.22	5.739	5.750	1.24	0.12032	0.12056	0.24	1961	1965	4	3
1003.23.1.1	--	212	26	0.13	0.342	1.30	5.599	5.601	1.79	0.11859	0.11864	1.24	1935	1936	22	2
1003.73.1.1	0.02	606	86	0.15	0.334	1.09	5.372	5.383	1.31	0.11678	0.11701	0.71	1908	1911	13	3
1003.21.1.1	0.02	272	60	0.23	0.334	3.18	5.229	5.232	3.22	0.11356	0.11361	0.52	1857	1858	9	0
1003.49.1.1	0.02	503	313	0.64	0.330	1.10	5.146	5.156	1.16	0.11324	0.11347	0.36	1852	1856	7	1
1003.47.1.1	0.04	509	164	0.33	0.325	1.16	5.086	5.088	1.25	0.11335	0.11340	0.44	1854	1855	8	2
1003.48.1.1	0.00	777	145	0.19	0.317	1.11	4.929	4.931	1.61	0.11263	0.11268	1.17	1842	1843	21	4
1003.41.1.1	0.21	72	27	0.39	0.329	1.73	5.083	5.085	2.11	0.11211	0.11216	1.21	1834	1835	22	0
1003.63.1.1	0.05	746	130	0.18	0.274	1.26	4.219	4.227	1.31	0.11184	0.11207	0.33	1830	1833	6	17
1003.68.1.1	0.02	462	108	0.24	0.318	1.12	4.871	4.881	1.31	0.11106	0.11128	0.69	1817	1820	13	2
1003.75.1.1	0.00	385	91	0.25	0.329	1.14	5.041	5.051	1.22	0.11103	0.11125	0.42	1816	1820	8	-1
1003.13.2.1	0.03	301	99	0.34	0.341	2.14	5.203	5.214	2.20	0.11081	0.11103	0.52	1813	1816	9	-5

Spot	% $206Pb_c$	ppm U	ppm Th	232Th /238U	206Pb* /238U	±%	207Pb* /235U	IMF-corr 207Pb* /235U	±%	207Pb* /206Pb*	IMF-corr 207Pb* /206Pb*	±%	207Pb /206Pb Age	IMF-corr 207Pb /206Pb Age	± Ma	% Disc
1003.51.1.1	0.01	335	146	0.45	0.306	1.16	4.660	4.669	1.25	0.11030	0.11052	0.48	1804	1808	9	5
1003.44.1.1	--	286	94	0.34	0.317	1.87	4.718	4.720	1.95	0.10808	0.10812	0.55	1767	1768	10	0
1003.55.2.1	0.05	980	607	0.64	0.297	1.06	4.410	4.419	1.17	0.10782	0.10803	0.49	1763	1767	9	6
1003.24.1.1	0.00	1381	432	0.32	0.321	1.84	4.782	4.784	2.00	0.10798	0.10803	0.79	1766	1766	14	-2
1003.71.1.1	0.01	284	90	0.33	0.308	1.18	4.574	4.583	1.46	0.10771	0.10793	0.85	1761	1765	16	2
1003.35.1.1	0.01	1012	251	0.26	0.312	1.10	4.644	4.646	1.59	0.10779	0.10784	1.15	1762	1763	21	1
1003.74.1.1	0.08	238	76	0.33	0.312	1.24	4.619	4.628	1.37	0.10751	0.10772	0.60	1758	1761	11	1
1003.58.1.1	0.01	681	99	0.15	0.292	1.10	4.328	4.336	1.15	0.10731	0.10752	0.35	1754	1758	6	6
1003.61.1.1	0.01	795	100	0.13	0.306	1.07	4.521	4.530	1.42	0.10725	0.10746	0.93	1753	1757	17	2
1003.42.1.1	0.18	711	105	0.15	0.314	2.08	4.617	4.619	2.13	0.10678	0.10683	0.43	1745	1746	8	-1
1003.37.1.1	--	681	209	0.32	0.314	1.22	4.610	4.612	1.42	0.10635	0.10639	0.74	1738	1739	14	-2
1003.22.1.1	--	194	278	1.48	0.304	1.51	4.441	4.443	1.92	0.10602	0.10606	1.19	1732	1733	22	1
1003.65.1.1	0.00	481	126	0.27	0.293	1.14	4.262	4.271	1.21	0.10555	0.10576	0.40	1724	1728	7	4
1003.52.3.1	0.02	730	86	0.12	0.297	1.78	4.316	4.325	1.81	0.10549	0.10569	0.38	1723	1726	7	3
1003.32.1.1	0.04	323	75	0.24	0.307	1.86	4.463	4.465	1.94	0.10537	0.10542	0.54	1721	1722	10	0
1003.38.1.1	0.03	572	38	0.07	0.284	1.14	4.099	4.101	1.23	0.10481	0.10485	0.45	1711	1712	8	7
1003.1.2.1	0.04	527	89	0.17	0.294	1.71	4.247	4.241	1.74	0.10468	0.10454	0.31	1709	1706	6	3
1003.43.1.1	0.09	847	34	0.04	0.314	3.15	4.521	4.523	3.39	0.10440	0.10444	1.23	1704	1704	23	-4
1003.29.1.1	0.14	611	96	0.16	0.334	1.14	4.808	4.810	1.38	0.10432	0.10437	0.77	1702	1703	14	-11
1003.53.1.1	0.00	633	61	0.10	0.297	1.08	4.260	4.268	1.14	0.10396	0.10417	0.36	1696	1700	7	1
1003.55.1.1	0.01	1111	127	0.12	0.298	1.21	4.250	4.258	1.33	0.10342	0.10362	0.55	1686	1690	10	0
1003.52.1.1	0.02	626	84	0.14	0.286	1.09	4.072	4.081	1.15	0.10335	0.10356	0.37	1685	1689	7	4
1003.53.2.1	0.03	468	59	0.13	0.283	1.13	4.003	4.011	1.41	0.10252	0.10272	0.85	1670	1674	16	4
metamorphic zircon																
1003.33.1.1	0.10	595	54	0.09	0.293	1.13	4.104	4.106	1.22	0.10155	0.10159	0.44	1653	1653	8	0
1003.16.1.1	0.06	319	65	0.21	0.288	1.30	4.008	4.007	1.36	0.10105	0.10104	0.42	1643	1643	8	1
1003.50.2.1	--	380	77	0.21	0.280	1.14	3.886	3.894	1.23	0.10077	0.10097	0.48	1638	1642	9	3

Spot	% $206Pb_c$	ppm U	ppm Th	232Th /238U	206Pb* /238U	±%	207Pb* /235U	IMF-corr 207Pb* /235U	±%	207Pb* /206Pb*	IMF-corr 207Pb* /206Pb*	±%	207Pb /206Pb Age	IMF-corr 207Pb /206Pb Age	± Ma	% Disc
1003.19.1.1	0.01	375	61	0.17	0.284	1.29	3.948	3.948	1.34	0.10090	0.10089	0.37	1641	1640	7	2
1003.34.1.1	0.00	544	74	0.14	0.287	1.15	3.988	3.990	1.22	0.10080	0.10084	0.43	1639	1640	8	1
1003.10.1.1	0.05	309	63	0.21	0.286	1.30	3.962	3.962	1.37	0.10051	0.10049	0.43	1633	1633	8	1
1003.40.1.1	0.02	667	23	0.04	0.289	1.12	3.998	4.000	1.19	0.10041	0.10046	0.40	1632	1633	7	0
1003.50.1.1	0.06	839	25	0.03	0.282	1.35	3.902	3.910	1.39	0.10025	0.10045	0.33	1629	1632	6	2
1003.8.1.1	--	354	71	0.21	0.285	1.29	3.943	3.943	1.35	0.10044	0.10042	0.38	1632	1632	7	1
1003.2.1.1	0.06	361	73	0.21	0.281	1.73	3.884	3.878	1.77	0.10036	0.10022	0.41	1631	1628	8	3
1003.12.2.1	0.02	1016	25	0.03	0.287	1.15	3.952	3.960	1.19	0.10002	0.10022	0.29	1624	1628	5	0
1003.18.1.1	0.02	323	67	0.21	0.289	1.32	3.981	3.981	1.38	0.10002	0.10001	0.41	1625	1624	8	-1
1003.3.1.1	0.01	358	71	0.21	0.284	1.74	3.915	3.910	1.78	0.09994	0.09980	0.39	1623	1620	7	1
1003.7.1.1	0.03	318	69	0.22	0.285	1.30	3.920	3.920	1.36	0.09973	0.09972	0.42	1619	1619	8	0
1003.72.1.1	0.04	376	65	0.18	0.281	1.14	3.848	3.856	1.25	0.09950	0.09970	0.51	1615	1619	9	1
1003.70.1.1	0.04	690	50	0.07	0.275	1.39	3.775	3.783	1.44	0.09940	0.09960	0.38	1613	1617	7	3
1003.56.1.1	0.05	693	41	0.06	0.284	1.32	3.891	3.899	1.37	0.09937	0.09956	0.35	1612	1616	7	0
1003.62.1.1	0.00	644	43	0.07	0.286	1.34	3.917	3.925	1.39	0.09934	0.09954	0.36	1612	1615	7	-1
1003.5.1.1	0.07	343	66	0.20	0.286	1.29	3.921	3.920	1.36	0.09953	0.09952	0.41	1615	1615	8	0
1003.57.1.1	0.01	384	67	0.18	0.280	1.49	3.838	3.845	1.56	0.09931	0.09950	0.48	1611	1615	9	1
1003.29.2.1	0.03	294	61	0.21	0.280	1.23	3.843	3.845	1.37	0.09944	0.09948	0.60	1614	1614	11	1
1003.72.2.1	0.02	838	23	0.03	0.287	1.08	3.930	3.938	1.13	0.09926	0.09945	0.34	1610	1614	6	-1
1003.4.1.1	0.08	294	68	0.24	0.284	1.30	3.891	3.890	1.38	0.09945	0.09944	0.45	1614	1614	8	0
1003.15.1.1	0.06	342	63	0.19	0.286	1.29	3.916	3.915	1.36	0.09944	0.09943	0.42	1614	1613	8	0
1003.14.1.1	0.04	304	63	0.22	0.283	1.30	3.884	3.883	1.37	0.09943	0.09942	0.44	1613	1613	8	0
1003.12.1.1	0.06	330	76	0.24	0.284	1.31	3.892	3.892	1.50	0.09942	0.09940	0.74	1613	1613	14	0
1003.30.1.1	0.01	575	54	0.10	0.284	1.14	3.887	3.888	1.21	0.09930	0.09934	0.43	1611	1612	8	0
1003.11.1.1	0.00	377	73	0.20	0.282	1.29	3.861	3.860	1.34	0.09927	0.09925	0.38	1610	1610	7	1
1003.17.1.1	0.03	313	69	0.23	0.278	1.30	3.800	3.799	1.37	0.09914	0.09913	0.43	1608	1608	8	2

Spot	% $206Pb_c$	ppm U	ppm Th	232Th /238U	206Pb* /238U	±%	207Pb* /235U	IMF-corr 207Pb* /235U	±%	207Pb* /206Pb*	IMF-corr 207Pb* /206Pb*	±%	207Pb /206Pb Age	IMF-corr 207Pb /206Pb Age	± Ma	% Disc
1003.13.1.1	0.04	337	65	0.20	0.280	1.41	3.826	3.826	1.47	0.09899	0.09898	0.41	1605	1605	8	1
1003.69.2.1	--	638	39	0.06	0.282	1.09	3.837	3.844	1.16	0.09878	0.09898	0.38	1601	1605	7	0
1003.6.1.1	0.05	334	64	0.20	0.287	1.29	3.922	3.921	1.36	0.09899	0.09897	0.41	1605	1605	8	-2
1003.74.2.1	--	597	59	0.10	0.276	1.28	3.752	3.759	1.34	0.09868	0.09887	0.41	1599	1603	8	2
1003.41.2.1	--	382	69	0.19	0.289	1.19	3.940	3.942	1.53	0.09880	0.09884	0.97	1602	1602	18	-3
1003.66.1.1	0.03	361	71	0.20	0.288	1.14	3.909	3.917	1.27	0.09857	0.09877	0.56	1597	1601	10	-2
1003.9.1.1	0.06	342	67	0.20	0.287	1.29	3.908	3.907	1.36	0.09874	0.09873	0.42	1601	1600	8	-2
1003.60.2.1	0.03	506	41	0.08	0.283	1.11	3.838	3.846	1.19	0.09851	0.09870	0.44	1596	1600	8	-1
1003.52.2.1	0.02	378	70	0.19	0.280	1.14	3.806	3.814	1.24	0.09850	0.09869	0.49	1596	1600	9	0
1003.20.1.1	0.00	667	49	0.08	0.281	1.26	3.827	3.827	1.29	0.09863	0.09862	0.27	1598	1598	5	0
1003.64.1.1	--	424	68	0.16	0.283	1.13	3.833	3.841	1.22	0.09841	0.09860	0.47	1594	1598	9	-1
1003.69.1.1	0.01	849	42	0.05	0.275	1.52	3.728	3.735	1.55	0.09826	0.09846	0.33	1591	1595	6	2
1003.25.2.1	--	323	66	0.21	0.272	1.21	3.683	3.685	1.35	0.09827	0.09831	0.59	1592	1592	11	3
1003.1.1.1	0.06	344	64	0.19	0.283	1.81	3.830	3.825	1.87	0.09831	0.09818	0.45	1592	1590	8	-1
1003.66.2.1	0.01	751	34	0.05	0.280	1.08	3.777	3.785	1.14	0.09791	0.09811	0.36	1585	1588	7	0
1003.22.2.1	0.05	582	114	0.20	0.284	1.19	3.837	3.838	1.38	0.09805	0.09809	0.70	1587	1588	13	-2
1003.9.2.1	0.01	773	39	0.05	0.280	1.25	3.787	3.786	1.28	0.09802	0.09800	0.27	1587	1586	5	0
1003.21.2.1	0.03	354	69	0.20	0.288	1.19	3.888	3.889	1.31	0.09781	0.09785	0.54	1583	1584	10	-4
1003.57.2.1	0.01	852	52	0.06	0.275	1.08	3.691	3.699	1.26	0.09724	0.09743	0.63	1572	1576	12	0
rejected analysis (see text)																
1003.53.1.2	0.03	574	51	0.09	0.292	1.11	4.111	4.119	1.19	0.10207	0.10227	0.41	1662	1666	8	1
1003.64.2.1	0.17	889	56	0.06	0.219	1.06	2.835	2.841	1.15	0.09383	0.09402	0.44	1505	1508	8	17

Data are 1σ precision. Pbc and Pb* indicate the common and radiogenic portions, respectively. All Pb data are initially common Pb corrected based on measured ^{204}Pb (after Stacey and Kramer 1975), then corrected for instrumental mass fractionation (IMF). Both uncorrected data, and IMF-corrected data (grey columns) are presented. LIMS session 80081: 1003.1.1-1002.3.1, LIMS session 80126: 1003.4.1-1003.20.1, LIMS session 90032: 1003.21.1-1003.48.1, LIMS session 100027: 1003.49.1-1003.75.1.

R1588243: ALDGATE INLIER PSAMMITE

Sample Number:	GA sample number 2008371006		
Field Number:	AI1		
Stratigraphic Unit:	Barossa Complex		
Location:	Aldgate Inlier		
Location GDA94:	297129 E	6127826 N	Zone 54
Location Lat-Long:	-34.9718229	138.7777517	
250K map sheet	SI 54-09 Adelaide		
100K map sheet	6628 Adelaide		
Mount:	GA6054		
Date analysed: 1.1-66.1 68.1-83.1 84.1-95.1	LIMS session 80081: 12-16 May 2008 LIMS session 80083: 16-18 May 2008 LIMS session 80126: 30/9-2/10/10/2008		
Machine:	SHRIMP IIe (GA)		
Standard age (α*)	LIMS session 80081: 3467.6 ± 2.0 Ma (1.00137) LIMS session 80083: 3465.9 ± 3.5 Ma (1.00027) LIMS session 80126: 3465.6 ± 2.9 Ma (1.00013)		
Standard data	LIMS session 80081: Appendix 3.1 LIMS session 80083: Appendix 3.2 LIMS session 80126: Appendix 3.3		
Machine:	SHRIMP IIe (GA)		
Interpreted age:	1679 ± 12 Ma		
Age type:	Maximum age of deposition		
Interpreted age:	1582 ± 4 Ma, 1633 ± 15 Ma		
Age type:	Metamorphic age		

* α is a correction for Instrumental Mass Fractionation (Stern et al. 2009). For more information, see Appendix 3.

FIELD DESCRIPTION

Sample R1588243 was collected from the north eastern Aldgate Inlier, adjacent Greenhill Road approximately 5km north of Bridgewater (Fig. 23).

Sample R1588243 is a psammite layer from within a weathered sillimanite-bearing gneiss (Fig. 29). The psammite is coarse grained (up to 2mm) and dominated by quartz with minor weathered feldspar (variety uncertain). The surrounding pelites clearly preserve a sillimanite- and mica-dominated assemblage. The mica species are difficult to identify due to weathering, however biotite is a likely constituent due to iron oxide staining, with finer-grained muscovite which may be related to retrogression. Leucosomes are uncommon but are observed on a 2-5 cm scale, which parallel a weak gneissosity defined by segregation of quartzofeldspathic minerals and the pelitic minerals

The basement rock at the sample location is directly overlain 50 meters away by the basal units of the Neoproterozoic Aldgate Sandstone, which in this location include interlayered phyllites containing fine grained muscovite and a strong cleavage, which is also observed in the basement lithology.

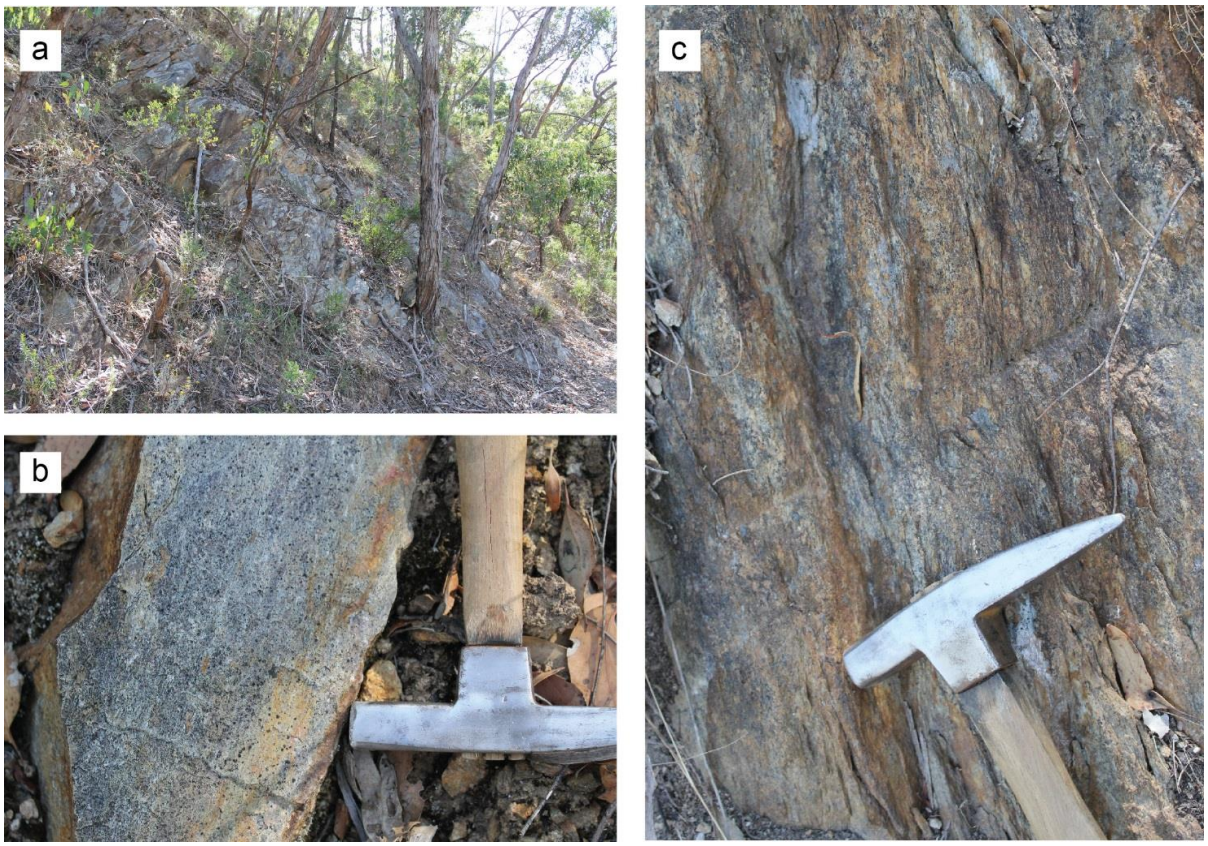

Figure 29. (a) Outcrop photo of the sample location for R1588243. **(b)** Psammite layer selected for dating. **(c)** Weathered sillimanite-bearing pelitic gneiss from the sample location.

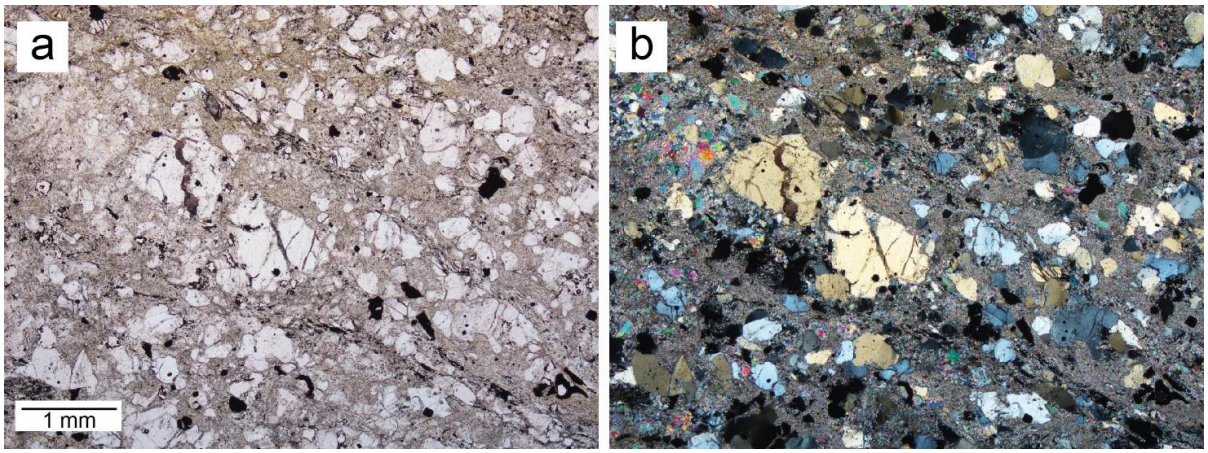

Figure 30. Sample R695752 under (a) plane polarised light; and (b) cross polars.

Figure 31. Transmitted light and CL images of zircon, R1588243: psammite layer in sillimanite-bearing gneiss, Aldgate Inlier.

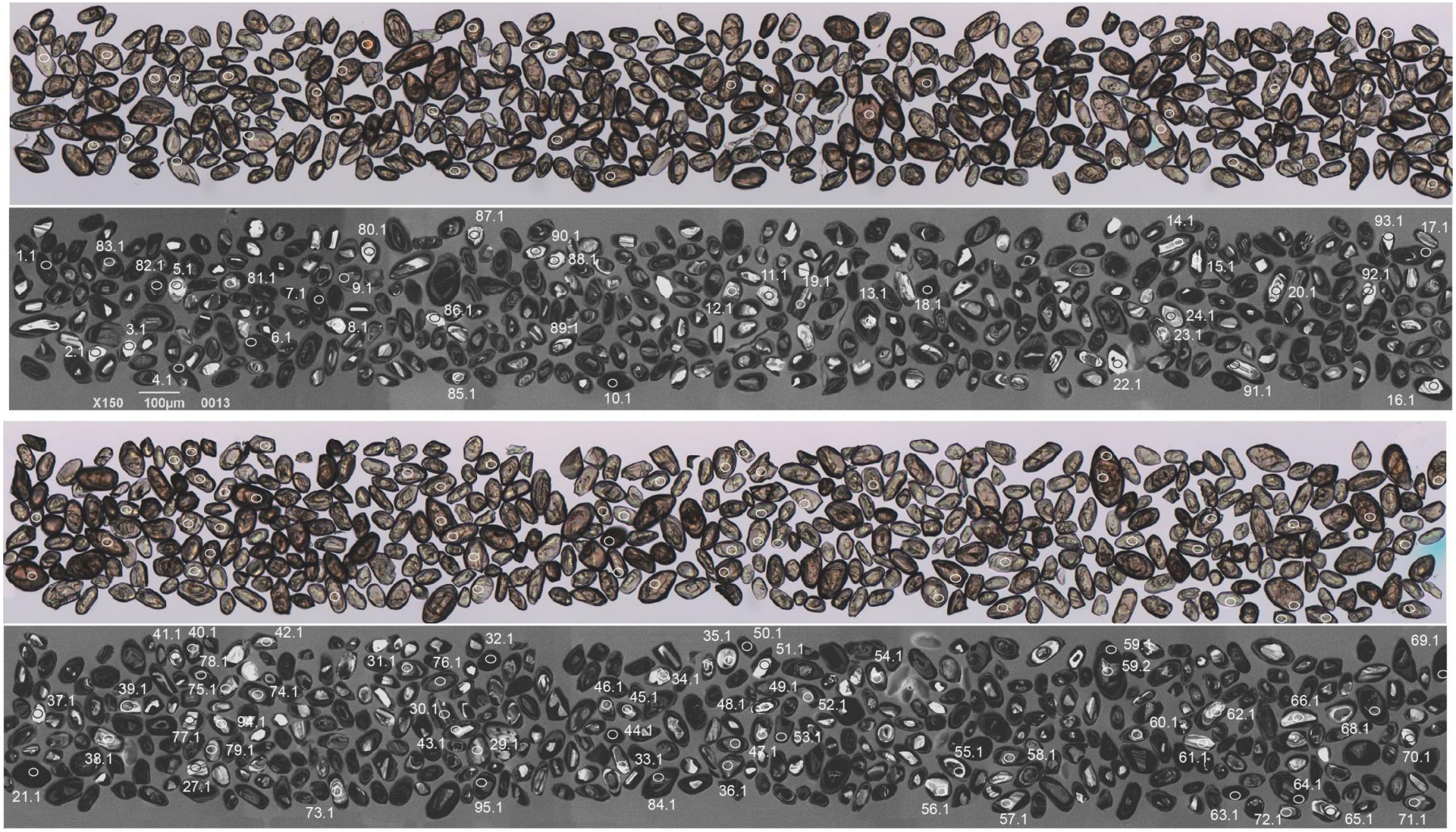

ZIRCON CHARACTERISTICS

Zircon range in length from ~30 to 100µm and are typically sub-rounded to ovoid in shape, with aspect ratios between 2:1 and 3:1 (Fig. 31). Habits vary between rounded, elongate grains and subhedral - tabular forms with sub rounded prisms. Under transmitted light, zircon is typically clear to smoky brown colour, cracks are prevalent, and core regions have a range of appearances from clouded-metamict, to clear-translucent. When viewed under CL, zircon exhibit two distinct growth zones. These include xenocrystic cores which have a CL response varying from luminescent to dull grey-black, and a growth zone immediately mantling the core which is dull grey to black in appearance. Growth textures within xenocrystic cores include oscillatory zoning and more complex sector and convolute zoning. Growth zone textures within regions of overgrowths are poorly defined and are typically homogenous grey-black in appearance although some regions exhibit broad, oscillatory zoning. In some zircon, growth zones mantling xenocrystic cores are enclosed within a thin, non luminescent, black rim. Xenocrystic cores often comprise the bulk of the volume of zircon and the thickness of overgrowths mantling the cores varies from <10µm to 30µm.

RESULTS

Seventy eight analyses were made on 68 zircon grains over 3 analytical sessions. There is some discordance in the data set, with only 41 analyses < 5% discordant (68 analyses < 10% discordant), although most analyses contain < 0.5% common Pb (Table 7, Fig. 32). One imprecise analysis with 13% common Pb (1006.59.2) is not considered further.

CORES

Sixty eight cores have a range of ages between c. 1675 – 2825 Ma (Fig. 33). The three youngest analyses yield a weighted mean $^{207}Pb/^{206}Pb$ age of 1679 ± 12 Ma (MSWD = 0.14, probability of fit = 0.87), constraining the maximum age of deposition of the sedimentary protolith. Over two thirds of the analyses lie between c. 1720 – 1885 Ma, with merging peaks at c. 1737 Ma, 1765 Ma, 1798 Ma, 1839 Ma and 1855 Ma. A few older analyses form peaks at c. 1910 Ma (n = 2), 1959 Ma (n = 3) and 2100 Ma (n = 1). A cluster of late Archaean - early Palaeoproterozoic cores range in age between c. 2330 – 2690 Ma, with one older Archaean grain at c. 2824 Ma.

METAMORPHIC RIMS

Nine analyses represent homogeneous dark CL rims and crystals. Five analyses are concordant, and yield a weighted mean $^{207}Pb/^{206}Pb$ age of 1582 ± 4 Ma (MSWD = 0.86, probability of fit = 0.49). The remaining four analyses are significantly discordant, with older apparent ages between 1624 Ma and 1640 Ma indicating an earlier period of metamorphism. The weighted mean $^{207}Pb/^{206}Pb$ age of this group, 1633 ± 15 Ma (MSWD = 1.8, probability of fit = 0.15), could be geologically significant, if Pb loss in the grains is recent, as suggested by a discordia through the analyses (Fig. 32b). An older metamorphic event of similar age (c. 1630 Ma) has been recognised in the Houghton Inlier (Belousova et al. 2006, and see sample R695752, this study).

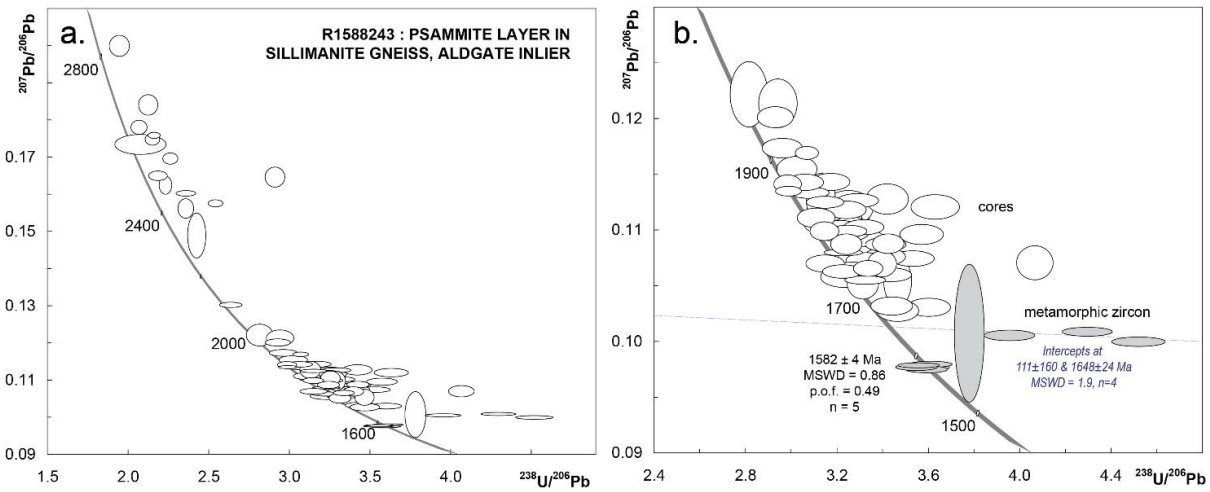

Figure 32. Tera-Wasser Concordia diagrams for zircon in R1009243. (a) all analyses; and **(b)** analyses < 2000 Ma.

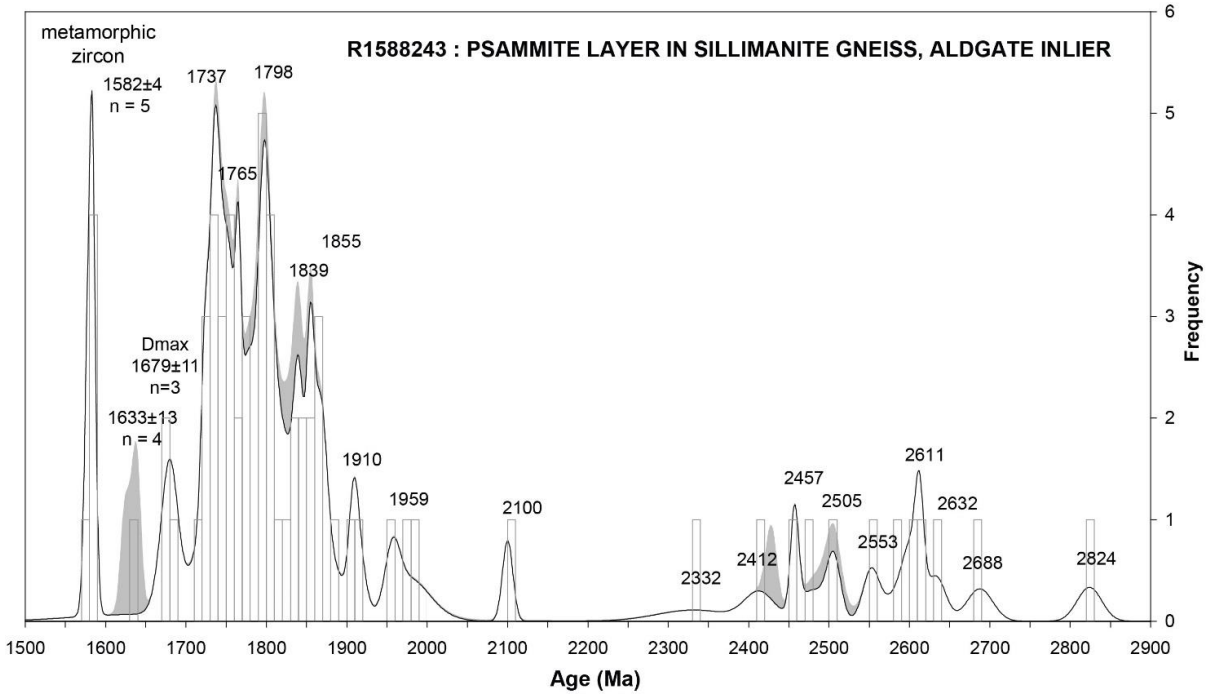

Figure 33. PDD of $^{207}Pb/^{206}Pb$ ages for R1009243. The grey shaded area represents analyses > 10% discordant, which are not included in the calculation of peak maxima (Sircombe 2004). The histogram and white area represent analyses < 10% discordant.

Table 7. SHRIMP analytical results for zircon from R1588243, psammite layer in sillimanite-bearing gneiss, Aldgate Inlier.

Spot	% $206Pb_c$	ppm U	ppm Th	232Th /238U	206Pb* /238U	±%	207Pb* /235U	IMF-corr 207Pb* /235U	±%	207Pb* /206Pb*	IMF-corr 207Pb* /206Pb*	±%	207Pb /206Pb Age	IMF-corr 207Pb /206Pb Age	± Ma	% Disc
detrital cores																
1006.3.1.1	0.07	82	36	0.46	0.512	2.09	14.105	14.086	2.29	0.19999	0.19972	0.94	2826	2824	15	7
1006.73.1.1	0.08	375	10	0.03	0.469	1.85	11.884	11.881	2.09	0.18386	0.18381	0.97	2688	2688	16	9
1006.73.1.1	0.09	332	120	0.38	0.482	1.54	11.823	11.821	1.70	0.17791	0.17789	0.71	2633	2633	12	4
1006.83.1.1	0.06	531	237	0.46	0.461	1.13	11.165	11.162	1.17	0.17571	0.17566	0.32	2613	2612	5	8
1006.70.1.1	0.16	167	52	0.32	0.464	1.36	11.164	11.161	1.48	0.17463	0.17458	0.60	2603	2602	10	7
1006.49.1.1	0.01	807	243	0.31	0.480	5.01	11.472	11.456	5.11	0.17346	0.17323	1.01	2591	2589	17	3
1006.76.1.1	0.19	214	49	0.24	0.440	1.34	10.294	10.293	1.48	0.16949	0.16947	0.62	2553	2552	10	9
1006.52.1.1	0.02	280	131	0.48	0.456	1.74	10.388	10.374	1.81	0.16505	0.16483	0.51	2508	2506	9	4
1006.81.1.1	1.02	146	83	0.59	0.343	1.40	7.778	7.777	1.78	0.16448	0.16446	1.10	2502	2502	18	28
1006.68.1.1	0.09	460	156	0.35	0.447	1.15	10.003	10.001	1.52	0.16233	0.16229	1.00	2480	2480	17	5
1006.32.1.1	0.02	1024	316	0.32	0.423	1.70	9.351	9.338	1.72	0.16036	0.16014	0.30	2459	2457	5	9
1006.71.1.1	0.11	399	306	0.79	0.393	1.17	8.525	8.522	1.24	0.15748	0.15744	0.42	2429	2428	7	14
1006.74.1.1	0.07	155	99	0.66	0.423	1.37	9.105	9.104	1.76	0.15608	0.15606	1.10	2414	2413	19	7
1006.77.1.1	0.20	312	103	0.34	0.411	1.50	8.433	8.432	3.09	0.14878	0.14876	2.70	2332	2332	46	6
1006.48.1.1	0.06	272	142	0.54	0.379	1.74	6.804	6.795	1.78	0.13034	0.13016	0.37	2103	2100	6	2
1006.39.1.1	0.05	285	163	0.59	0.355	1.91	5.977	5.969	2.48	0.12228	0.12211	1.58	1990	1987	28	2
1006.54.1.1	1.36	230	142	0.64	0.339	1.88	5.685	5.677	2.23	0.12148	0.12132	1.18	1978	1976	21	5
1006.65.1.1	0.17	212	198	0.97	0.341	1.76	5.649	5.641	1.83	0.12021	0.12005	0.52	1959	1957	9	4
1006.35.1.1	0.09	220	251	1.18	0.337	1.93	5.460	5.452	1.99	0.11744	0.11728	0.49	1918	1915	9	3
1006.82.1.1	0.03	828	833	1.04	0.325	1.09	5.243	5.242	1.14	0.11689	0.11686	0.33	1909	1909	6	6
1006.33.1.1	0.08	265	98	0.38	0.330	1.90	5.262	5.255	2.02	0.11556	0.11541	0.67	1889	1886	12	3
1006.41.1.1	0.14	251	14	0.06	0.315	1.74	4.966	4.960	1.80	0.11442	0.11427	0.45	1871	1868	8	7
1006.61.1.1	0.05	237	168	0.73	0.326	1.74	5.146	5.139	1.79	0.11438	0.11423	0.42	1870	1868	8	3
1006.80.1.1	0.13	222	252	1.17	0.335	1.34	5.265	5.264	1.42	0.11410	0.11408	0.48	1866	1865	9	0

1006.84.1.1	0.01	667	307	0.48	0.334	1.26	5.227	5.226	1.28	0.11347	0.11346	0.25	1856	1855	5	0
1006.30.1.1	0.03	559	439	0.81	0.324	1.82	5.073	5.066	1.84	0.11347	0.11332	0.29	1856	1853	5	3
1006.57.1.1	0.33	209	65	0.32	0.292	1.75	4.547	4.541	1.92	0.11287	0.11272	0.80	1846	1844	14	12
1006.78.1.1	0.03	179	98	0.57	0.319	1.37	4.958	4.958	1.93	0.11272	0.11271	1.36	1844	1844	25	4
1006.45.1.1	0.07	425	99	0.24	0.304	1.79	4.718	4.712	1.83	0.11274	0.11258	0.36	1844	1842	7	8
1006.58.1.1	0.00	465	234	0.52	0.317	1.71	4.925	4.918	1.74	0.11261	0.11245	0.30	1842	1839	5	4
1006.74.1.1	0.14	326	65	0.21	0.275	1.93	4.254	4.253	2.03	0.11205	0.11202	0.65	1833	1833	12	16
1006.50.1.1	0.39	88	44	0.52	0.307	2.17	4.748	4.741	2.36	0.11206	0.11191	0.92	1833	1831	17	7
1006.38.1.1	0.13	225	91	0.42	0.308	1.76	4.756	4.749	1.82	0.11194	0.11179	0.47	1831	1829	9	6
1006.8.1.1	0.12	147	65	0.46	0.321	1.76	4.927	4.921	1.84	0.11121	0.11106	0.52	1819	1817	9	1
1006.37.1.1	0.01	158	79	0.52	0.316	2.10	4.825	4.818	2.16	0.11060	0.11044	0.52	1809	1807	9	2
1006.79.1.1	0.04	379	137	0.37	0.307	1.18	4.676	4.675	1.66	0.11047	0.11044	1.17	1807	1807	21	5
1006.46.1.1	0.06	342	158	0.48	0.301	1.72	4.582	4.576	1.77	0.11037	0.11021	0.41	1805	1803	8	7
1006.81.1.1	0.24	347	52	0.15	0.306	1.77	4.652	4.651	1.89	0.11010	0.11007	0.65	1801	1801	12	5
1006.66.1.1	0.08	202	127	0.65	0.311	1.76	4.716	4.710	1.83	0.11015	0.11000	0.49	1802	1799	9	4
1006.78.1.1	0.03	1015	603	0.61	0.307	1.68	4.659	4.658	1.71	0.10989	0.10986	0.32	1798	1797	6	4
1006.79.1.1	0.13	252	178	0.73	0.317	1.32	4.808	4.808	1.41	0.10987	0.10985	0.50	1797	1797	9	1
1006.76.1.1	0.70	394	101	0.27	0.304	1.18	4.594	4.593	1.95	0.10973	0.10970	1.55	1795	1794	28	5
1006.36.1.1	0.06	362	138	0.39	0.315	1.74	4.767	4.760	1.77	0.10978	0.10963	0.36	1796	1793	7	2
1006.2.1.1	0.13	145	90	0.64	0.280	1.76	4.233	4.227	1.84	0.10972	0.10957	0.54	1795	1792	10	13
1006.82.1.1	0.15	225	69	0.32	0.292	1.33	4.376	4.375	1.44	0.10875	0.10874	0.54	1779	1778	10	8
1006.75.1.1	0.01	163	80	0.50	0.308	1.38	4.620	4.620	1.48	0.10872	0.10870	0.55	1778	1778	10	3
1006.40.1.1	0.18	427	149	0.36	0.293	1.72	4.392	4.386	1.76	0.10882	0.10867	0.39	1780	1777	7	8
1006.42.1.1	0.17	494	329	0.69	0.299	1.82	4.461	4.455	2.10	0.10834	0.10819	1.04	1772	1769	19	6
1006.63.1.1	0.01	1383	202	0.15	0.309	1.72	4.612	4.606	1.73	0.10810	0.10795	0.18	1768	1765	3	2
1006.56.1.1	0.10	221	151	0.71	0.293	1.75	4.354	4.348	1.82	0.10772	0.10757	0.49	1761	1759	9	7
1006.51.1.1	0.10	1329	168	0.13	0.283	1.75	4.198	4.192	1.80	0.10755	0.10740	0.44	1758	1756	8	10
1006.34.1.1	0.09	247	191	0.80	0.302	2.00	4.478	4.472	2.14	0.10740	0.10725	0.77	1756	1753	14	3
1006.47.1.1	0.08	425	304	0.74	0.300	1.72	4.443	4.437	1.78	0.10735	0.10721	0.45	1755	1752	8	4
1006.77.1.1	0.33	237	204	0.89	0.246	1.28	3.630	3.629	1.59	0.10704	0.10701	0.94	1750	1749	17	21

1006.5.1.1	0.13	167	60	0.37	0.317	1.75	4.685	4.678	1.81	0.10711	0.10696	0.48	1751	1748	9	-2
1006.75.1.1	0.23	265	154	0.60	0.294	1.23	4.339	4.337	1.43	0.10696	0.10693	0.72	1748	1748	13	6
1006.83.1.1	0.06	732	73	0.10	0.299	1.26	4.398	4.398	1.33	0.10654	0.10653	0.44	1741	1741	8	3
1006.62.1.1	0.07	231	222	0.99	0.306	1.75	4.489	4.483	1.81	0.10649	0.10635	0.48	1740	1738	9	1
1006.60.1.1	0.11	431	285	0.68	0.310	1.73	4.545	4.539	1.76	0.10641	0.10627	0.37	1739	1736	7	0
1006.55.1.1	0.05	593	274	0.48	0.304	1.81	4.460	4.454	1.83	0.10640	0.10625	0.27	1739	1736	5	2
1006.7.1.1	0.05	1124	252	0.23	0.291	1.71	4.254	4.248	1.75	0.10610	0.10595	0.39	1733	1731	7	6
1006.11.1.1	0.01	187	142	0.78	0.309	2.14	4.509	4.503	2.21	0.10590	0.10576	0.58	1730	1728	11	0
1006.9.1.1	0.04	640	164	0.27	0.301	1.76	4.377	4.371	1.78	0.10564	0.10550	0.24	1725	1723	4	2
1006.72.1.1	0.32	458	277	0.62	0.288	1.14	4.190	4.189	1.78	0.10540	0.10537	1.37	1721	1721	25	6
1006.80.1.1	0.10	157	107	0.71	0.301	1.38	4.373	4.372	1.63	0.10520	0.10517	0.88	1718	1717	16	1
1006.29.1.1	0.08	226	98	0.45	0.290	1.77	4.137	4.132	1.84	0.10331	0.10317	0.52	1684	1682	10	3
1006.43.1.1	0.41	336	76	0.23	0.277	1.73	3.948	3.943	1.80	0.10320	0.10306	0.51	1682	1680	9	7
1006.31.1.1	0.11	447	32	0.07	0.288	1.73	4.089	4.084	1.83	0.10288	0.10274	0.61	1677	1674	11	3
metamorphic zircon																
1006.44.1.1	0.19	1187	125	0.11	0.233	1.69	3.243	3.239	1.71	0.10101	0.10087	0.26	1643	1640	5	20
1006.69.1.1	4.19	912	41	0.05	0.264	1.12	3.674	3.673	4.19	0.10077	0.10074	4.04	1638	1638	75	9
1006.59.1.1	0.15	801	116	0.15	0.253	1.84	3.510	3.505	1.87	0.10067	0.10053	0.29	1636	1634	5	13
1006.64.1.1	0.33	1144	572	0.52	0.221	1.69	3.056	3.052	1.72	0.10011	0.09997	0.28	1626	1624	5	23
1006.1.1.1	0.02	1220	23	0.02	0.277	1.72	3.744	3.739	1.73	0.09810	0.09796	0.19	1588	1586	4	1
1006.10.1.1	0.01	1884	26	0.01	0.281	1.69	3.796	3.791	1.69	0.09798	0.09785	0.15	1586	1583	3	-1
1006.6.1.1	0.01	1025	19	0.02	0.282	1.69	3.800	3.795	1.71	0.09783	0.09770	0.20	1583	1581	4	-1
1006.53.1.1	0.04	605	18	0.03	0.278	1.81	3.752	3.747	1.84	0.09782	0.09768	0.32	1583	1580	6	0
1006.4.1.1	0.03	997	20	0.02	0.278	1.69	3.744	3.739	1.70	0.09763	0.09750	0.20	1579	1577	4	0
high common Pb																
1006.59.2.1	13.07	322	390	1.25	0.570	5.94	9.203	9.190	17.23	0.11714	0.11698	16.17	1913	1911	290	-65

Data are 1σ precision. Pbc and Pb* indicate the common and radiogenic portions, respectively. All Pb data are initially common Pb corrected based on measured ^{204}Pb (after Stacey and Kramer 1975), then corrected for instrumental mass fractionation (IMF). Both uncorrected data, and IMF-corrected data (grey columns) are presented. Data were collected during three analytical sessions: LIMS session 80081: 1006.1.1-1006.66.1, LIMS session 80083: 1006.68.1-1006.83.1, LIMS session 80126: 1006.84.1-1006.95.1

R1588242: QUARTZITE, MYPONGA INLIER

GA sample number:	2008371005		
Field number:	MI3		
Stratigraphic Unit:	Barossa Complex		
Location:	Myponga Inlier		
Location GDA94:	254686 E	6071105 N	Zone 54
Location Lat-Long:	-35° 28' 24"	138° 17' 47"	
250K map sheet	SI 5413 BARKER		
100K map sheet	6527 YANKALILLA		
Mount:	GA6054		
Date analysed:	LIMS session 80081: 12-16 May 2008		
Machine:	SHRIMP IIe (GA)		
Standard age (α)*	3467.6 ± 2.0 Ma (1.00137)		
Standard data	Appendix 3.1		
Interpreted age:	1653 ± 11 Ma (n=2)		
Age type:	Maximum age of deposition		
Interpreted age:	1590 ± 6 Ma		
Age type:	Metamorphic age		

* α is a correction for Instrumental Mass Fractionation (Stern et al. 2009). For more information, see Appendix 3.

FIELD DESCRIPTION

Sample R1588242 was collected from a large ridge of quartzite 4km south of Normanville, in the southernmost exposure of the Myponga inlier, and approximately 1.5km northwest of sample R695754 (Fig. 34).

The rock collected for analysis is a medium-grained (up to 1mm), impure quartzite to psammite which varies from 95% to 60% quartz. K-feldspar and biotite make up the remainder of the rock in varying amounts, with biotite < 5% of the rock (Fig. 35). A weak foliation is observed where biotite is present (Fig. 36).

The quartzite is one of two quartzite beds which bound a northeast-southwest trending unit of calcsilicate. The south eastern extent of this package is bound by a shear zone displaying extensional kinematics (Morrissey et al. 2013), against which a migmatised garnet-sillimanite gneiss is juxtaposed. This area is intruded by coarse K-feldspar dominated granite and pegmatite intrusions similar to that of sample R695754.

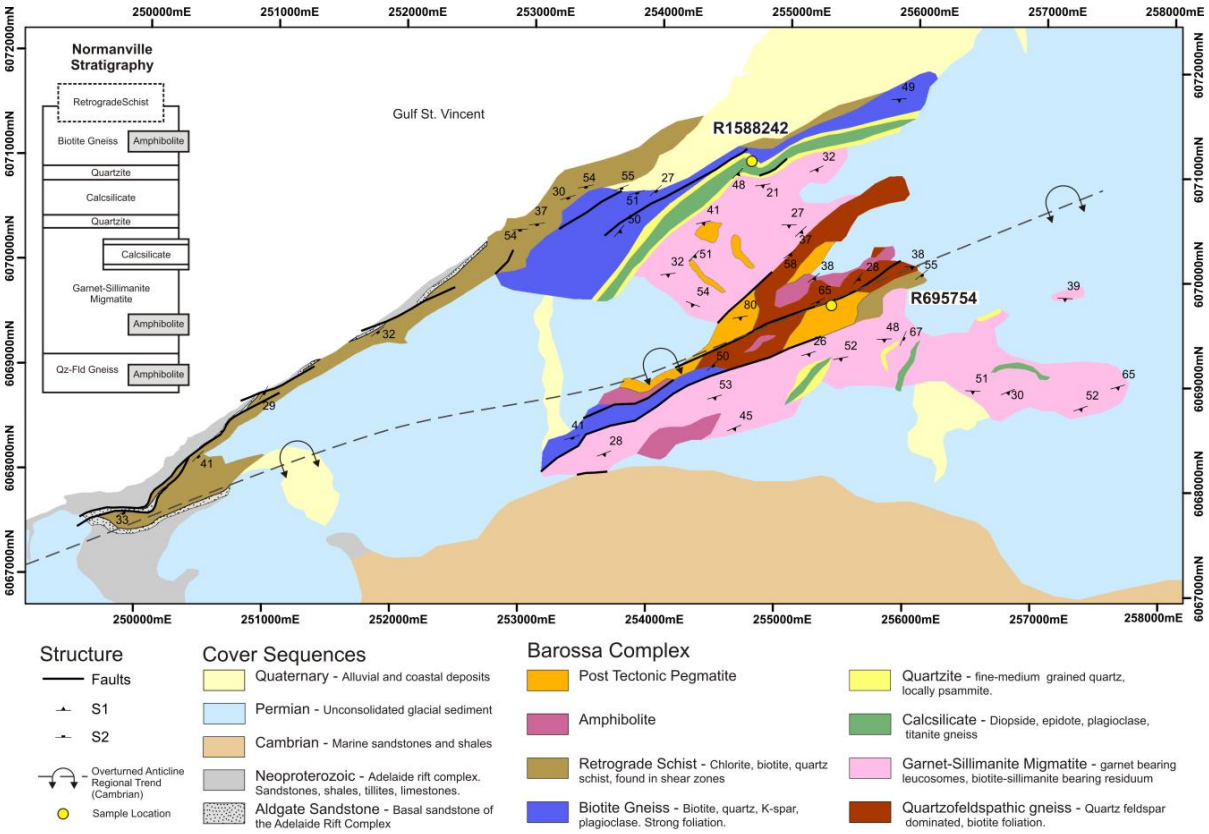

Figure 34. Location of the two samples in this study from the Aldgate and Oakbank Inliers of the Barossa Complex. Map is reproduced from Meaney et al. in prep.

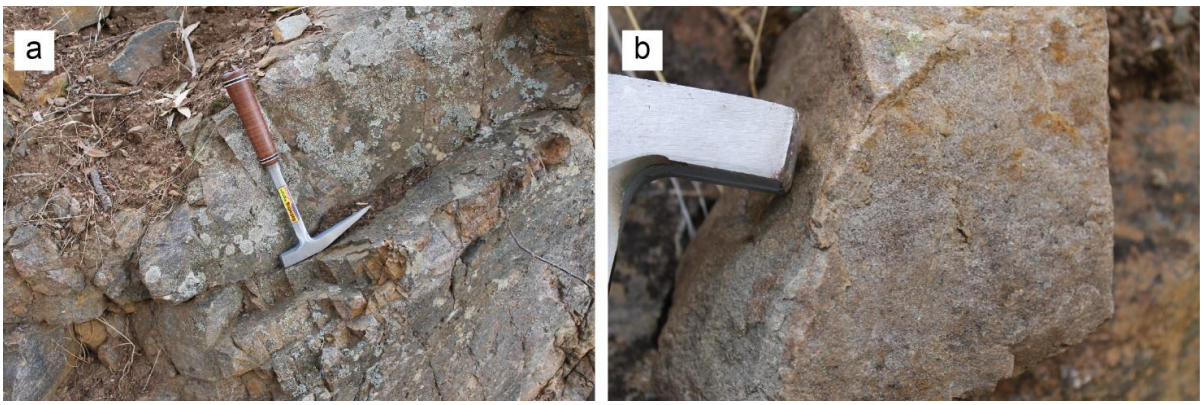

Figure 35. (a) Outcrop of R1588242. **(b)** Hand specimen.

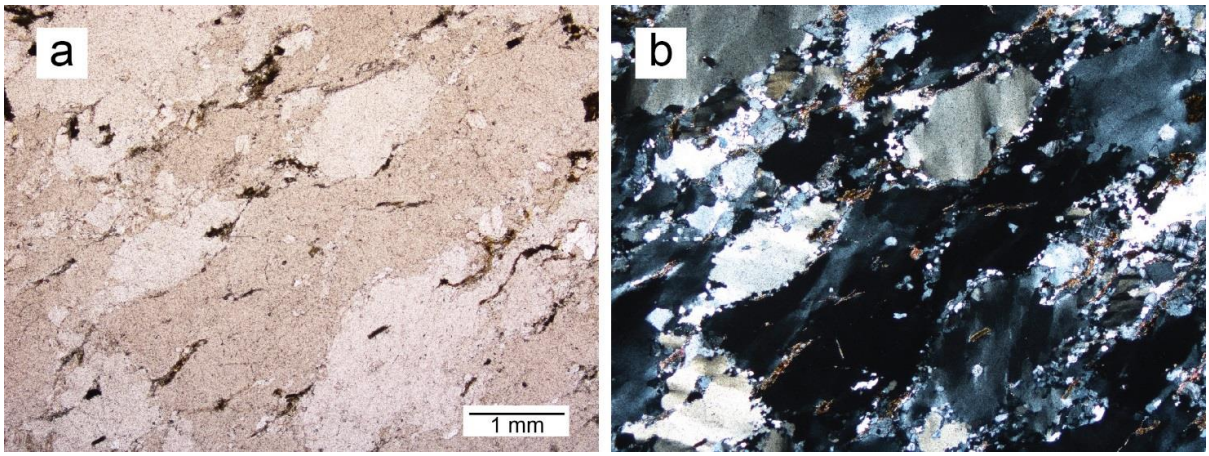

Figure 36. Sample R695752 under (a) plane polarised light; and (b) cross polars.

ZIRCON CHARACTERISTICS

Zircons are subequant to elongate, subrounded to rounded and small, between 80µm and 120µm in length (Fig. 37). The grains are hyacinth to colourless and clear, with few cracks or inclusions. They comprise homogenous to broadly zoned, dark grey CL overgrowths enclosing cores with a varied CL response from highly luminescent to dull (black). Well defined growth zoning is pronounced in most cores. Zonation textures within core regions include oscillatory, sector, irregular, concentric and convoluted zoning.

RESULTS

Seventy two analyses were made on 69 grains, of which 61 are < 5% discordant (Fig. 38). Nine analyses targeted metamorphic zircon, occurring as homogeneous grey zircons and zircon rims, and have a weighted mean $^{207}Pb/^{206}Pb$ age of 1590 ± 6 Ma (MSWD = 0.97, probability of fit = 0.45). This dates the timing of high grade metamorphism in the Myponga Inlier, during a regional granulite facies event.

The cores range between c. 1650 - 3120 Ma. The two youngest analyses constrain the maximum age of deposition of the protolith at 1653 ± 11 Ma. Two grains yield slightly older, discordant ages of c. 1680 Ma. About a third of the core analyses cluster between c. 1730 - 1850 Ma with dominant peaks at c. 1733 Ma, 1748 Ma, 1799 Ma and 1850 Ma. Other clusters occur at c. 2320-2620 Ma and c. 2930 – 3120 Ma (Fig, 39).

A weighted mean age of 1590 ± 6 Ma is interpreted to be the timing of a high grade metamorphic event which effected this sample. The age of c. 1590 Ma is consistent with a $^{207}Pb^{206}Pb$ age of 1588 ± 9 Ma, which is the timing from zircon of granulite facies metamorphism in the southern Myponga Inlier (Szpunar et al. 2007). The timing of deposition of MI3 is interpreted to be between c. 1650 Ma and 1590 Ma and the sample is interpreted to have undergone high grade metamorphic event at ca 1590 Ma, as part of a regional, granulite facies event.

Figure 37. CL and transmitted light images of zircon, R1588242: quartzite, Myponga Inlier

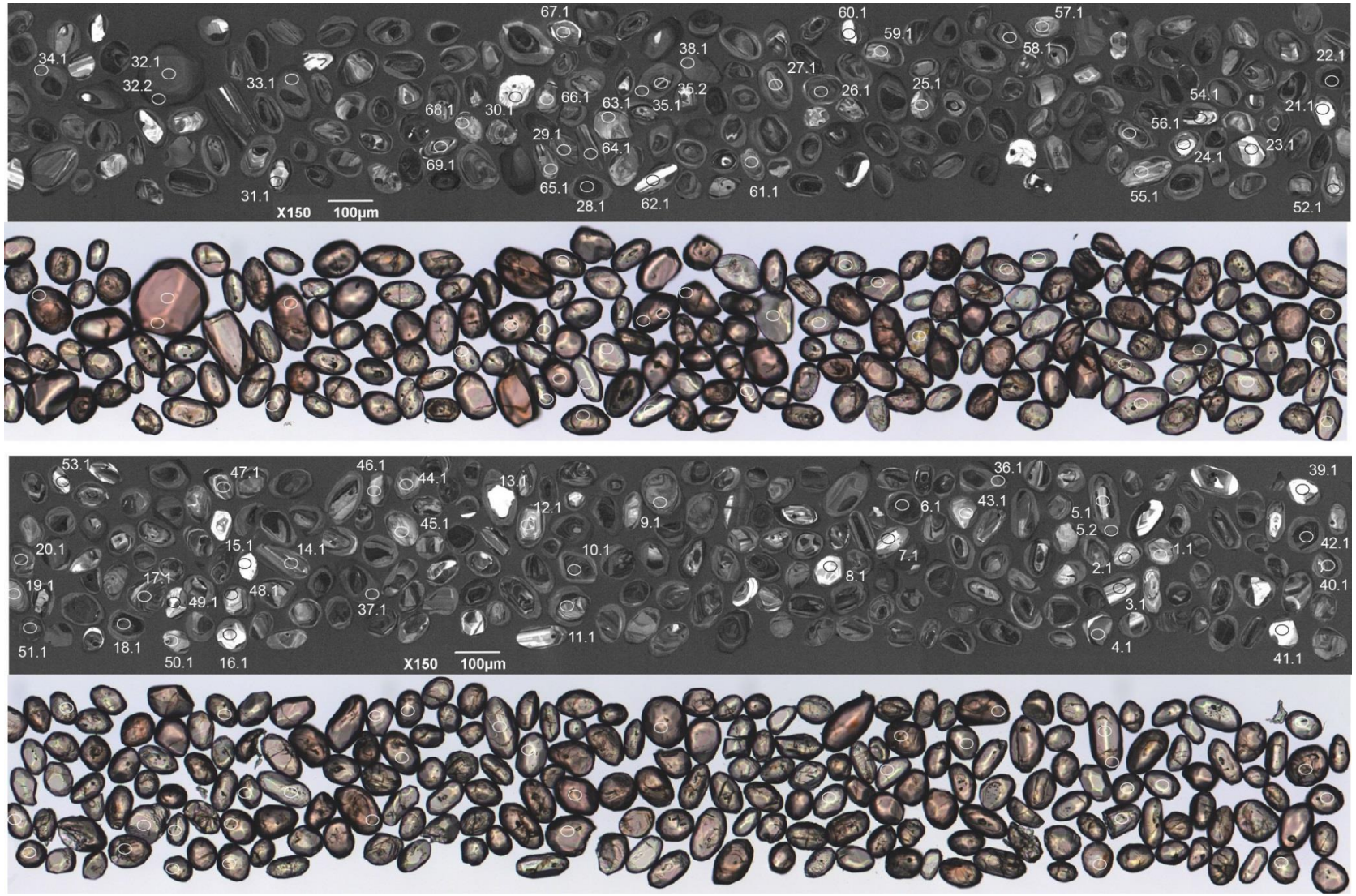

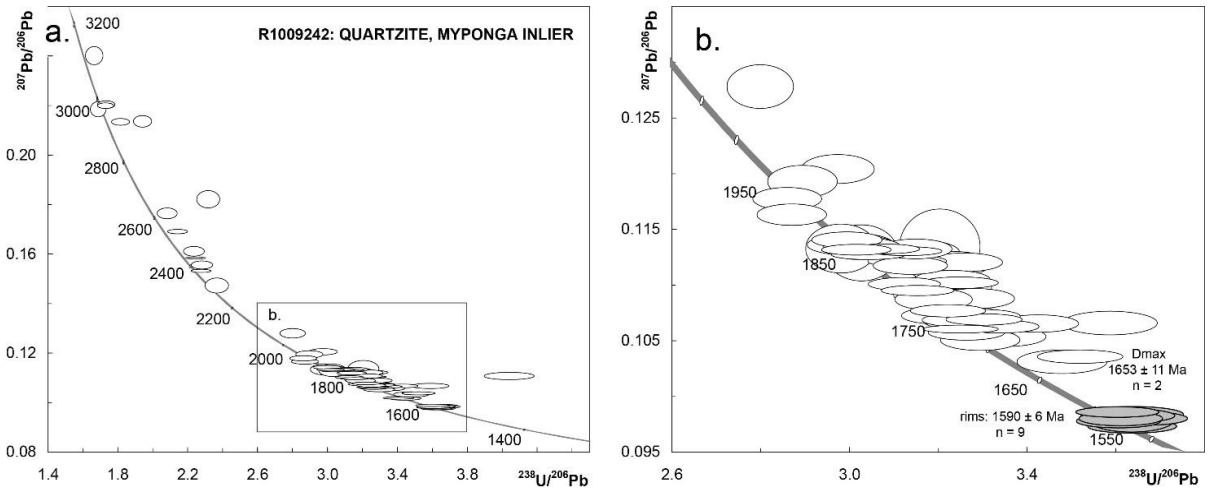

Figure 38. Tera-Wasserburg concordia diagrams for zircon in R1009242. (a) All analyses; and **(b)** analyses younger than 2100 Ma and ≤10% discordant.

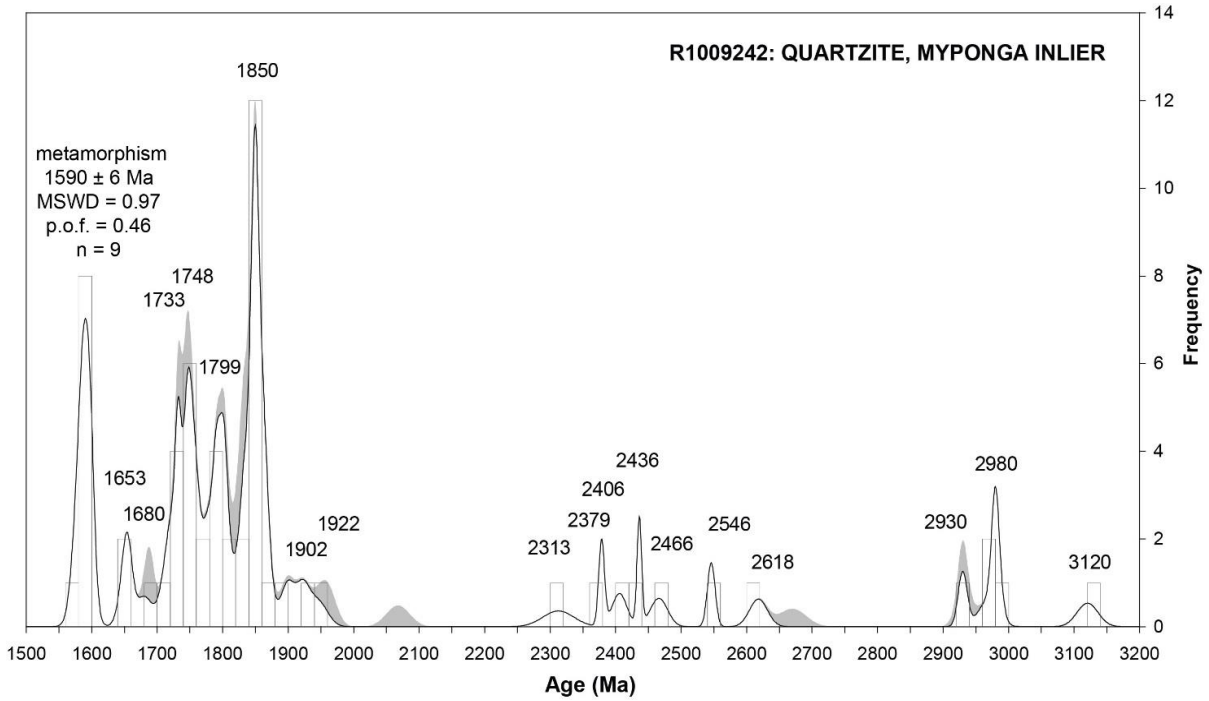

Figure 39. PDD of $^{207}Pb/^{206}Pb$ ages for R1009242. The grey shaded area represents analyses > 5% discordant, which are not included in the calculation of peak maxima (Sircombe 2004). The histogram and white area represent analyses < 10% discordant.

Table 8. SHRIMP analytical results for zircon from R1588242, quartzite, Myponga Inlier.

Spot	% $206Pb_c$	ppm U	ppm Th	232Th /238U	206Pb* /238U	±%	207Pb* /235U	IMF-corr 207Pb* /235U	±%	207Pb* /206Pb*	IMF-corr 207Pb* /206Pb*	±%	207Pb /206Pb Age	IMF-corr 207Pb /206Pb Age	± Ma	% Disc
detrital cores																
005.39.1.1	0.14	43	26	0.62	0.598	1.94	19.837	19.810	2.19	0.24040	0.24007	1.01	3123	3120	16	4
005.41.1.1	0.11	63	27	0.44	0.576	1.87	17.495	17.471	1.93	0.22047	0.22017	0.46	2984	2982	7	2
005.8.1.1	0.05	105	67	0.66	0.576	1.78	17.492	17.468	1.81	0.22012	0.21982	0.33	2982	2979	5	2
005.16.1.1	0.05	94	60	0.65	0.591	1.79	17.812	17.788	2.01	0.21867	0.21837	0.91	2971	2969	15	-1
005.52.1.1	0.04	142	55	0.40	0.514	1.77	15.138	15.117	1.92	0.21373	0.21344	0.75	2934	2932	12	11
005.21.1.1	0.11	65	25	0.40	0.549	1.87	16.173	16.150	1.92	0.21348	0.21318	0.43	2932	2930	7	5
005.13.1.1	0.21	64	23	0.36	0.431	1.85	10.813	10.798	2.24	0.18210	0.18185	1.27	2672	2670	21	16
005.54.1.1	0.67	107	93	0.89	0.479	1.79	11.660	11.644	1.97	0.17650	0.17626	0.82	2620	2618	14	4
005.2.1.1	0.05	124	91	0.76	0.466	1.77	10.864	10.850	1.80	0.16905	0.16882	0.35	2548	2546	6	4
005.51.1.1	0.01	420	55	0.13	0.447	1.77	9.924	9.911	1.94	0.16120	0.16098	0.78	2468	2466	13	4
005.35.2.1	0.03	438	254	0.60	0.445	1.71	9.717	9.703	1.72	0.15839	0.15817	0.21	2439	2436	4	3
005.65.1.1	0.04	176	84	0.49	0.438	1.76	9.386	9.373	1.88	0.15558	0.15536	0.67	2408	2406	11	3
005.69.1.1	0.03	383	171	0.46	0.439	1.71	9.261	9.249	1.73	0.15310	0.15289	0.26	2381	2379	4	2
005.4.1.1	0.04	203	95	0.48	0.422	1.89	8.573	8.561	2.34	0.14731	0.14711	1.39	2315	2313	24	2
005.31.1.1	0.44	146	45	0.32	0.357	1.76	6.295	6.286	2.02	0.12796	0.12779	1.01	2070	2068	18	6
005.53.1.1	0.32	99	110	1.15	0.336	1.80	5.583	5.576	1.94	0.12053	0.12037	0.71	1964	1962	13	6
005.24.1.1	0.07	118	154	1.35	0.345	1.77	5.683	5.676	1.95	0.11941	0.11924	0.82	1947	1945	15	2
005.30.1.1	0.10	90	57	0.65	0.349	1.80	5.676	5.668	1.89	0.11786	0.11770	0.58	1924	1922	10	0
005.66.1.1	0.11	118	82	0.72	0.348	1.79	5.587	5.579	1.87	0.11642	0.11626	0.55	1902	1900	10	-1
005.25.1.1	0.06	175	81	0.48	0.334	1.74	5.252	5.245	1.79	0.11418	0.11402	0.41	1867	1864	7	1
005.45.1.1	0.11	149	79	0.55	0.331	1.76	5.185	5.178	1.83	0.11371	0.11355	0.50	1860	1857	9	1
005.55.1.1	0.11	127	75	0.62	0.333	2.08	5.223	5.216	2.15	0.11372	0.11356	0.54	1860	1857	10	0
005.60.1.1	0.61	83	51	0.64	0.312	1.85	4.885	4.879	2.70	0.11357	0.11342	1.96	1857	1855	35	7
005.67.1.1	0.08	169	98	0.60	0.329	1.76	5.155	5.148	1.82	0.11354	0.11338	0.48	1857	1854	9	1
005.19.1.1	0.10	156	81	0.53	0.331	1.75	5.175	5.168	1.88	0.11355	0.11339	0.68	1857	1854	12	1

005.63.1.1	0.13	154	87	0.58	0.335	1.76	5.240	5.233	2.18	0.11338	0.11322	1.28	1854	1852	23	-1
005.6.1.1	0.05	464	305	0.68	0.317	1.70	4.960	4.953	1.78	0.11334	0.11318	0.51	1854	1851	9	5
005.28.1.1	0.04	514	104	0.21	0.325	1.70	5.074	5.067	1.72	0.11335	0.11319	0.25	1854	1851	5	3
005.58.1.1	0.03	416	130	0.32	0.331	1.71	5.176	5.169	1.73	0.11328	0.11312	0.28	1853	1850	5	0
005.42.1.1	0.03	707	301	0.44	0.320	1.70	4.985	4.979	1.71	0.11315	0.11300	0.23	1851	1848	4	4
005.57.1.1	0.13	181	109	0.62	0.330	1.75	5.143	5.136	2.29	0.11301	0.11285	1.47	1848	1846	27	1
005.48.1.1	0.20	111	59	0.55	0.316	1.79	4.926	4.920	1.91	0.11302	0.11286	0.64	1848	1846	12	5
005.64.1.1	0.03	535	216	0.42	0.328	1.79	5.110	5.103	1.81	0.11282	0.11266	0.26	1845	1843	5	1
005.40.1.1	0.04	342	177	0.54	0.319	1.86	4.943	4.936	1.89	0.11224	0.11209	0.31	1836	1834	6	3
005.50.1.1	0.11	203	95	0.48	0.307	1.75	4.744	4.737	1.81	0.11215	0.11200	0.49	1835	1832	9	7
005.3.1.1	0.06	269	165	0.63	0.309	1.72	4.775	4.768	1.84	0.11201	0.11185	0.65	1832	1830	12	6
005.12.1.1	0.05	138	77	0.57	0.319	1.76	4.913	4.906	1.81	0.11184	0.11169	0.46	1830	1827	8	3
005.15.1.1	1.05	218	223	1.06	0.248	2.33	3.777	3.771	2.50	0.11061	0.11046	0.91	1809	1807	16	24
005.9.1.1	0.21	170	72	0.44	0.309	1.74	4.717	4.711	1.82	0.11058	0.11043	0.51	1809	1806	9	4
005.18.1.1	0.08	408	143	0.36	0.308	1.77	4.680	4.674	1.79	0.11030	0.11015	0.31	1804	1802	6	5
005.29.1.1	0.05	307	58	0.20	0.320	1.72	4.860	4.854	1.75	0.11017	0.11002	0.36	1802	1800	7	1
005.7.1.1	0.26	59	206	3.64	0.310	1.86	4.691	4.684	2.07	0.10988	0.10973	0.91	1797	1795	17	4
005.17.1.1	--	393	269	0.71	0.317	1.71	4.791	4.785	1.73	0.10961	0.10946	0.27	1793	1790	5	1
005.23.1.1	0.08	71	85	1.24	0.314	1.83	4.725	4.719	1.96	0.10927	0.10912	0.69	1787	1785	13	2
005.1.1.1	0.14	153	60	0.40	0.304	1.75	4.570	4.563	1.84	0.10889	0.10874	0.55	1781	1778	10	4
005.62.1.1	0.14	114	142	1.29	0.313	1.79	4.703	4.696	1.89	0.10881	0.10866	0.60	1780	1777	11	1
005.20.1.1	0.08	315	197	0.65	0.310	1.71	4.611	4.604	1.75	0.10778	0.10763	0.35	1762	1760	6	1
005.68.1.1	0.07	172	133	0.80	0.312	1.75	4.619	4.613	1.81	0.10734	0.10720	0.47	1755	1752	9	0
005.27.1.1	0.04	257	46	0.19	0.303	1.72	4.485	4.479	1.76	0.10728	0.10714	0.37	1754	1751	7	3
005.47.1.1	0.08	262	201	0.79	0.308	1.83	4.547	4.541	1.96	0.10720	0.10706	0.73	1752	1750	13	2
005.26.1.1	0.04	350	141	0.42	0.303	1.71	4.468	4.462	1.74	0.10702	0.10688	0.31	1749	1747	6	3
005.10.1.1	0.06	325	218	0.69	0.308	1.71	4.537	4.531	1.75	0.10695	0.10680	0.37	1748	1745	7	1
005.49.1.1	0.10	272	90	0.34	0.279	1.96	4.102	4.097	2.07	0.10668	0.10653	0.66	1743	1741	12	10
005.46.1.1	0.05	218	68	0.32	0.292	1.74	4.292	4.286	1.81	0.10663	0.10649	0.48	1743	1740	9	6
005.14.1.1	0.08	257	134	0.54	0.299	1.72	4.391	4.385	1.76	0.10637	0.10623	0.36	1738	1736	7	3
005.22.1.1	0.04	918	313	0.35	0.308	1.72	4.502	4.496	1.73	0.10616	0.10601	0.22	1734	1732	4	0

005.44.1.1	0.07	208	106	0.53	0.306	1.74	4.470	4.463	1.79	0.10582	0.10568	0.44	1729	1726	8	0
005.59.1.1	0.09	136	67	0.51	0.298	1.77	4.337	4.332	1.86	0.10547	0.10533	0.55	1723	1720	10	3
005.43.1.1	0.12	128	71	0.57	0.303	1.77	4.401	4.395	1.87	0.10517	0.10503	0.58	1717	1715	11	1
005.5.1.1	0.07	307	57	0.19	0.284	1.81	4.061	4.056	1.85	0.10367	0.10352	0.38	1691	1688	7	5
005.61.1.1	0.09	225	111	0.51	0.287	1.91	4.091	4.086	2.03	0.10321	0.10307	0.68	1683	1680	13	4
005.56.1.1	0.10	336	132	0.40	0.294	1.72	4.121	4.115	1.76	0.10180	0.10166	0.38	1657	1655	7	0
005.11.1.1	0.13	195	115	0.61	0.290	1.74	4.064	4.059	1.81	0.10157	0.10143	0.50	1653	1650	9	1
metamorphic rims																
005.32.2.1	--	472	39	0.08	0.278	1.71	3.786	3.780	1.73	0.09880	0.09867	0.31	1602	1599	6	1
005.32.1.1	0.05	246	32	0.13	0.275	2.09	3.743	3.738	2.15	0.09860	0.09846	0.47	1598	1595	9	2
005.34.1.1	0.04	255	48	0.20	0.275	1.73	3.737	3.732	1.78	0.09847	0.09833	0.41	1595	1593	8	2
005.35.1.1	0.09	257	29	0.12	0.275	1.73	3.730	3.725	1.78	0.09835	0.09822	0.43	1593	1591	8	2
005.5.2.1	0.07	271	36	0.14	0.273	1.72	3.699	3.694	1.77	0.09821	0.09808	0.41	1591	1588	8	2
005.37.1.1	0.10	305	48	0.16	0.277	1.72	3.755	3.750	1.77	0.09822	0.09809	0.43	1591	1588	8	1
005.38.1.1	0.14	251	35	0.15	0.275	1.73	3.725	3.720	1.88	0.09809	0.09796	0.74	1588	1586	14	1
005.33.1.1	0.09	275	36	0.13	0.278	1.72	3.751	3.746	1.77	0.09798	0.09784	0.41	1586	1583	8	0
005.36.1.1	0.10	248	44	0.19	0.275	1.81	3.702	3.697	1.86	0.09752	0.09738	0.42	1577	1575	8	1

Data are 1σ precision. Pbc and Pb* indicate the common and radiogenic portions, respectively. All Pb data are initially common Pb corrected based on measured ^{204}Pb (after Stacey and Kramer 1975), then corrected for instrumental mass fractionation (IMF). Both uncorrected data, and IMF-corrected data (grey columns) are presented. All data are from LIMS Session 80081, analysis date 12/05/08; SHRIMP IIe, Geoscience Australia.

R695754: COARSE-GRAINED POST-TECTONIC GRANITE/PEGMATITE, MYPONGA INLIER

Field sample number:	MI 01		
Stratigraphic Unit:	Barossa Complex		
Location:	Yankalilla River, Myponga Inlier		
Location GDA94:	255330 E	6069800 N	Zone 54
Location Lat-Long:	-35°29'07"	138°18'11"	
250K map sheet	Barker (SI 54-13)		
100K map sheet	Yankalilla (6527)		
Mount:	Z4697		
Date analysed:	03/08/2005		
Machine:	SHRIMP IIB, Curtin University		
Standard age QGNG:	Batch 1: 1849.3 ± 2.9 Ma		
Correction?	corrected for overcounts to 1851.9 ± 3.1 Ma		
Standard data	Appendix 2		
Interpreted age:	1580 ± 4 Ma		
Age type:	Magmatic crystallisation, intrusive		

FIELD DESCRIPTION

Sample R695754 was taken from the 5km south of Normanville in the Yankalilla River, approximately 2 km upstream from where the river crosses Main South Road (Figs 34, 40a). This area is the southernmost extent of the Myponga Inlier and was mapped in detail by Davies (1972), and is near the sample sites of Szpunar et al. (2007) and Morrissey et al. (2013).

Figure 40. (a) Outcrop photo of sample location for R695754 in the Yankalilla River gorge. An example of typical outcrop of this rock type. The dominant K-feldspar gives the rock an overall pink-orange colour. **(b)** Typical example of this rock type. Quartz (white) can be seen interlocking with K-feldspar (pink) with little other mineralogical variety.

Sample R695754 is a coarse-grained, K-Feldspar-dominated granitic intrusion (Fig. 40b). K-Feldspar makes up approximately 70% of the rock with crystal sizes averaging 2-4 cm. Quartz makes up approximately 25%, usually interlocking between K-feldspar crystals, but also forming coarser pegmatitic concentrations where books of muscovite also occur. No foliation or structural features are observed, suggesting this intrusion is post-deformation.

This granitic intrusion is one of a series of K-Feldspar-rich coarse-grained granites that occur in the southern Myponga Inlier. It intrudes and truncates fabrics present in metasedimentary and meta-igneous units, which include coarse grained garnet-sillimanite migmatite, psammite gneisses, calcsilicates, and cpx-opx metabasites.

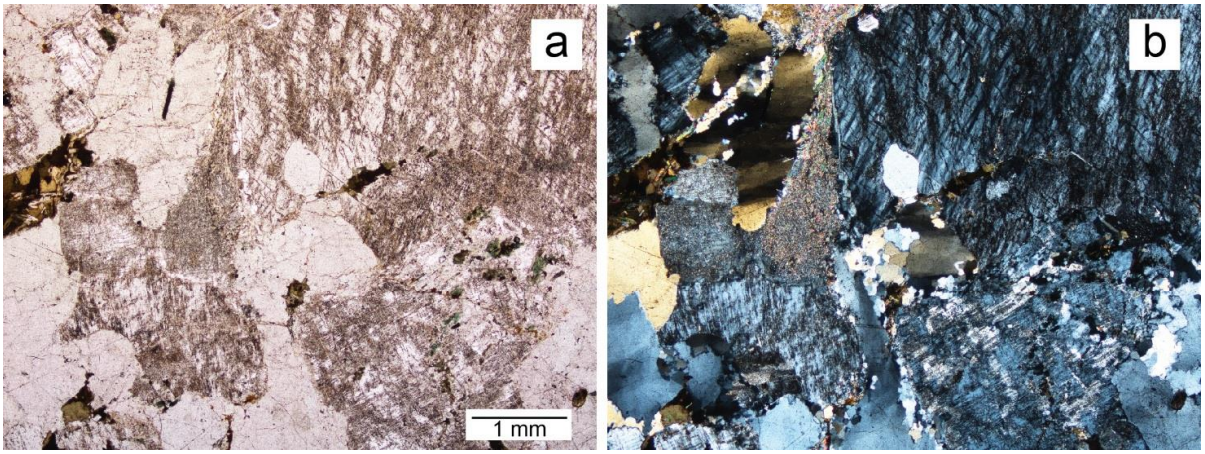

Figure 41. Sample R695752 under (a) plane polarised light; and (b) cross polars.

PETROLOGY

The following petrographic description is taken from Mason (2006).

LITHOLOGY: Weakly deformed albite-biotite-sericite meta-monzogranite

Mineral	Vol %	Origin
Quartz	25	Igneous 1
Zircon	Tr	Igneous 1
Allanite (includes trace epidote)	Tr	Igneous 1 (includes alteration 2)
K-feldspar (microcline microperthite)	34	Metamorphic 2
Albite	34	Metamorphic alteration 2
Biotite	3	Relict igneous 1 / metamorphic alteration 2
Sericite	3	Metamorphic alteration 2
Chlorite	Tr	Metamorphic alteration 2
Opaques (?sulphide)	Tr	Metamorphic alteration 2

DESCRIPTION: In thin section, this sample displays a well-preserved coarse-grained massive granitoid texture, modified by mild deformation, recrystallisation and alteration (Fig. 41). K-feldspar is abundant, forming large anhedral grains commonly ~3-4 mm in size. All display fine 'tartan' twinning confirming identification as microcline, and all grains contain a moderate proportion of ragged patches of twinned albite exsolution patches. Clearly, the K-feldspar has inverted from a precursor primary K-feldspar phase (orthoclase). Plagioclase formed large anhedral twinned grains comparable in size with the K-feldspar grains. All have suffered complete replacement by optically continuous albite and sericite (see sericite below). Quartz is moderately abundant, forming large anhedral grains mostly ~2-3 mm in size. Although they retain their primary shapes, all display mild

deformation effects including shadowy strain extinction and local partial recrystallisation to finer-grained sutured mosaics.

Biotite is the sole ferromagnesian phase. It forms small pleochroic chocolate brown to straw yellow flakes ~0.1-0.4 mm long that occur in different sites: i) As flaky aggregates that represent recrystallised primary biotite plates ~1-2 mm long. Locally, the recrystallised aggregates are entrained along discontinuous trails (sealed fractures or deformation planes). ii) As small ragged replacement flakes along cleavage traces in K-feldspar and plagioclase grain sites. Clearly, this biotite has formed by a subsolidus alteration process. In places, this biotite displays pleochroism that ranges to greener colours (ie variable biotite composition; not chlorite, see chlorite below).

Sericite is present in significant amount, and occurs in different sites: i) Most occurs as clouds of tiny flecks that pervade albite-altered plagioclase grains. In places the sericite flakes are randomly oriented, but elsewhere they display a preferred orientation suggesting they formed synchronous with mild deformation. ii) Some sericite forms small flakes intergrown with the small biotite flakes in recrystallised primary biotite plate sites. iii) Some sericite is concentrated along thin discontinuous fracture surfaces, in places with intergrown biotite.

Chlorite is uncommon, forming local small ragged pleochroic green flakes. This is readily distinguished by its anomalous interference colours, compared with the moderately high birefringence of the local greenish biotite. Allanite is uncommon, forming large prismatic crystals ~2-3 mm long that display the typical dark brown pleochroism and high birefringence of this mineral. A small amount of pale yellow epidote is developed along cleavage traces and crystal margins. Opaques occur rarely as equant blocky crystals. It may be ?pyrite.

INTERPRETATION: This sample formed as a coarse-grained massive granitoid of monzogranitic composition. It was originally composed of subequal abundances of K-feldspar, plagioclase and quartz, with minor biotite and accessory allanite and zircon.

The rock body suffered mild deformation and alteration. This generated the new alteration assemblage of microcline + albite + sericite + biotite + trace chlorite + opaques (?pyrite). In more detail, primary orthoclase inverted to microcline microperthite ± replacement sericite ± biotite, primary plagioclase was replaced by albite + sericite ± biotite, primary biotite suffered recrystallisation and alteration to biotite ± sericite, primary accessory allanite suffered incipient replacement by epidote, and small amounts of chlorite and opaques (?pyrite) formed sparsely through the rock. Mild deformation during this event produced shadowy strain extinction and local recrystallisation patches in primary quartz, and thin discontinuous deformation planes (commonly along primary grain boundaries) were sealed by intergrown biotite + sericite. Note that the concentration of biotite along these planes defines a weak structure through the rock that is evident in the thin section viewed by the unaided eye.

The timing of the alteration event with respect to emplacement is difficult to determine petrographically. It is possible that it represents subsolidus adjustments in the intrusion during slow cooling. However, the presence of mild deformational effects including microstructure development suggests that the alteration might have accompanied a regional stress event, and may therefore be attributed to a low-grade regional metamorphic event in the middle-greenschist facies.

ZIRCON CHARACTERISTICS

Zircons from the pegmatite have a uniform morphology, consisting of light- to red-brown, inclusion-free grains with very high clarity, and largely devoid of fractures (Fig. 42). Most are broken fragments of formerly much larger grains, probably broken during crushing and milling procedures in the lab, ranging in size from 100-250 μm with a few smaller grains (50 μm). Aspect ratios are about 2:1. Where original grain morphology is preserved, the grains are oval in shape with rounded terminations, and crystal facets preserved, but with no pyramidal terminations. The grains contain no cores and emit a dark to dull uniform cathodoluminescence, or weak oscillatory zoning that is not visible in transmitted light.

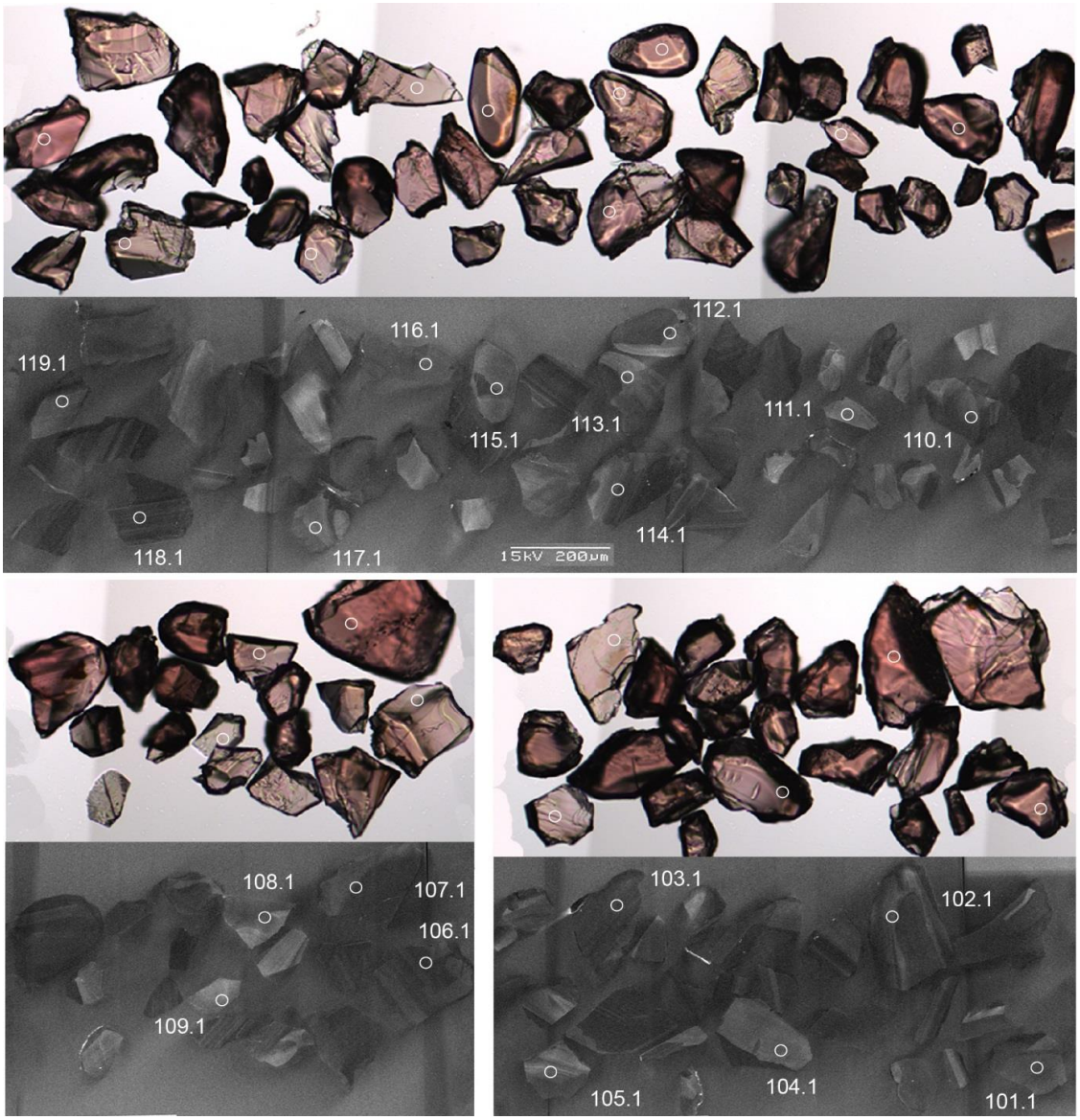

Figure 42. Transmitted light and CL images of zircon, R695752, coarse-grained granite, Myponga Inlier.

RESULTS

Nineteen grains were analysed. The grains have uniform, moderate U contents (270-570 ppm), low Th and Th/U in the range 0.03-0.33 (median 0.24). All analyses contain negligible common Pb (< 0.1% $^{206}Pb_c$) and plot on concordia at c. 1580 Ma (Fig. 43a). They have indistinguishable $^{207}Pb/^{206}Pb$ ages (MSWD = 0.51; probability of fit = 0.96), which yield a weighted mean $^{207}Pb/^{206}Pb$ age of 1580 ± 4 Ma (Fig. 43b). This is interpreted to be the crystallisation age of the coarse-grained granite. As the non-foliated granite body cross cuts the foliated metasediments, this date also provides a minimum age of deformation for the Myponga Inlier.

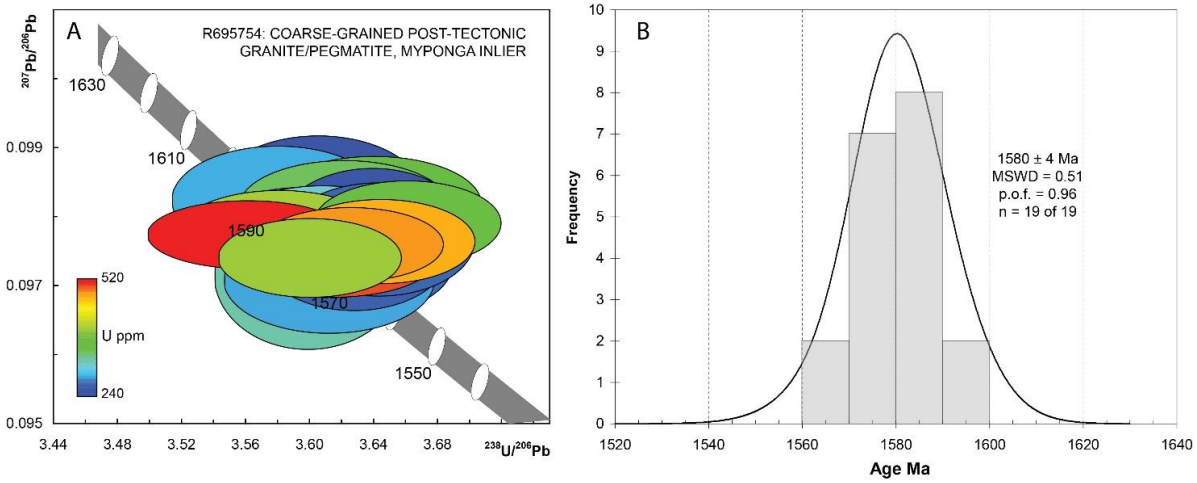

Figure 43. (a) Tera-Wasser Concordia diagram; and (b) probability density diagram (PDD) for R695754. Error ellipses are coloured according to U content.

Table 9. SHRIMP analytical results for R695754, post-tectonic granite, Myponga Inlier.

Spot	% 206Pbc	ppm U	ppm Th	232Th /238U	206Pb* /238U	±%	207Pb* /235U	±%	207Pb* /206Pb*	±%	207Pb /206Pb Age	± Ma	% Disc
101.1	0.01	360	36	0.10	0.273	1.05	3.687	1.13	0.0979	0.41	1584	8	2
102.1	0.00	342	40	0.12	0.278	1.20	3.746	1.28	0.0978	0.45	1582	8	0
103.1	0.02	505	235	0.48	0.277	1.14	3.714	1.19	0.0973	0.34	1574	6	0
104.1	0.00	267	62	0.24	0.276	1.24	3.706	1.36	0.0973	0.55	1574	10	0
105.1	-0.05	249	72	0.30	0.277	1.21	3.758	1.36	0.0983	0.61	1591	11	1
106.1	0.02	489	152	0.32	0.276	1.05	3.711	1.11	0.0976	0.36	1579	7	1
107.1	-0.03	365	37	0.10	0.275	1.20	3.719	1.29	0.0982	0.46	1590	9	2
108.1	-0.03	344	50	0.15	0.276	1.20	3.736	1.28	0.0981	0.46	1589	9	1
109.1	0.00	251	59	0.24	0.275	1.09	3.704	1.25	0.0978	0.62	1582	12	1
110.1	0.01	312	98	0.32	0.277	1.16	3.735	1.25	0.0977	0.47	1581	9	0
111.1	0.05	260	60	0.24	0.276	1.08	3.706	1.23	0.0975	0.58	1577	11	1
112.1	0.06	326	69	0.22	0.278	1.07	3.722	1.29	0.0971	0.72	1570	14	-1
113.1	-0.02	264	51	0.20	0.275	1.08	3.697	1.22	0.0977	0.55	1580	10	1
114.1	-0.02	480	148	0.32	0.274	1.05	3.694	1.13	0.0976	0.41	1579	8	1
115.1	0.00	399	129	0.33	0.278	1.04	3.730	1.11	0.0974	0.39	1575	7	0
116.1	0.00	401	23	0.06	0.279	1.14	3.765	1.21	0.0978	0.40	1582	7	0
117.1	0.03	283	9	0.03	0.277	1.19	3.706	1.30	0.0971	0.52	1569	10	0
118.1	0.00	518	161	0.32	0.281	1.16	3.784	1.20	0.0977	0.33	1581	6	-1
119.1	-0.02	285	81	0.29	0.279	1.21	3.783	1.32	0.0982	0.53	1591	10	0

Data are 1σ precision. Pbc and Pb* indicate the common and radiogenic portions, respectively. All Pb data are initially common Pb corrected based on measured ^{204}Pb (after Stacey and Kramer 1975), then corrected for excess 204 counts inferred from average 207-corrected standard spots.

DISCUSSION

DEPOSITIONAL TIMING CONSTRAINTS

The age spectra for six metasedimentary rocks collected from the five inliers of the Barossa Complex are remarkably similar, with all samples sharing a common thermal (metamorphic) history, confirming that the now isolated inliers were once part of a single cratonic block. All samples record Palaeoproterozic to Mesoarchaean ages in the detrital cores, comprising a substantial fraction of c. 1735 – 1850 Ma zircons (60%), with smaller populations of c. 1920 – 2100 Ma and 2325 – 2720 Ma, and rare Mesoarchaean ages (Fig. 44). About 10% of the cores are younger than c. 1735 Ma, forming peaks at c. 1658 Ma, 1690 Ma and 1707 Ma. Maximum depositional ages range between c. 1655 – 1707 Ma, and at c. 1655 Ma; the youngest detrital cores are only c. 20 million years older than the onset of metamorphism in the northern inliers.

The earliest magmatic activity recognised is intrusion of the orthogneiss in South Para Gorge at 1717 ± 7 Ma. Given the comparative age of the metasedimentary successions, it is clear that this intrusion does not post-date their deposition. The crystallisation age is within the range of the youngest detrital populations in the Barossa Complex metasediments (c. 1660 – 1735 Ma). Although an intrusive contact has been reported between the orthogneiss and some metasedimentary units within the South Para Gorge (a biotite-sericite gneiss and sillimanite gneiss, Meaney et al. in prep), the orthogneiss is older than other units in the metasedimentary succession (sample R695753 representing a quartzite bed within the psammopelitic biotite-sericite gneisses contains a few c. 1705 - 1720 Ma detrital cores), indicating some complexity in the depositional and/or tectonic history of the Houghton Inlier. The deformation preserved in the orthogneiss is consistent with that in the surrounding metasediments (Meany et al. in prep), and it has been metamorphosed with the metasedimentary succession, supporting the interpretation that it is an early syn-depositional intrusion.

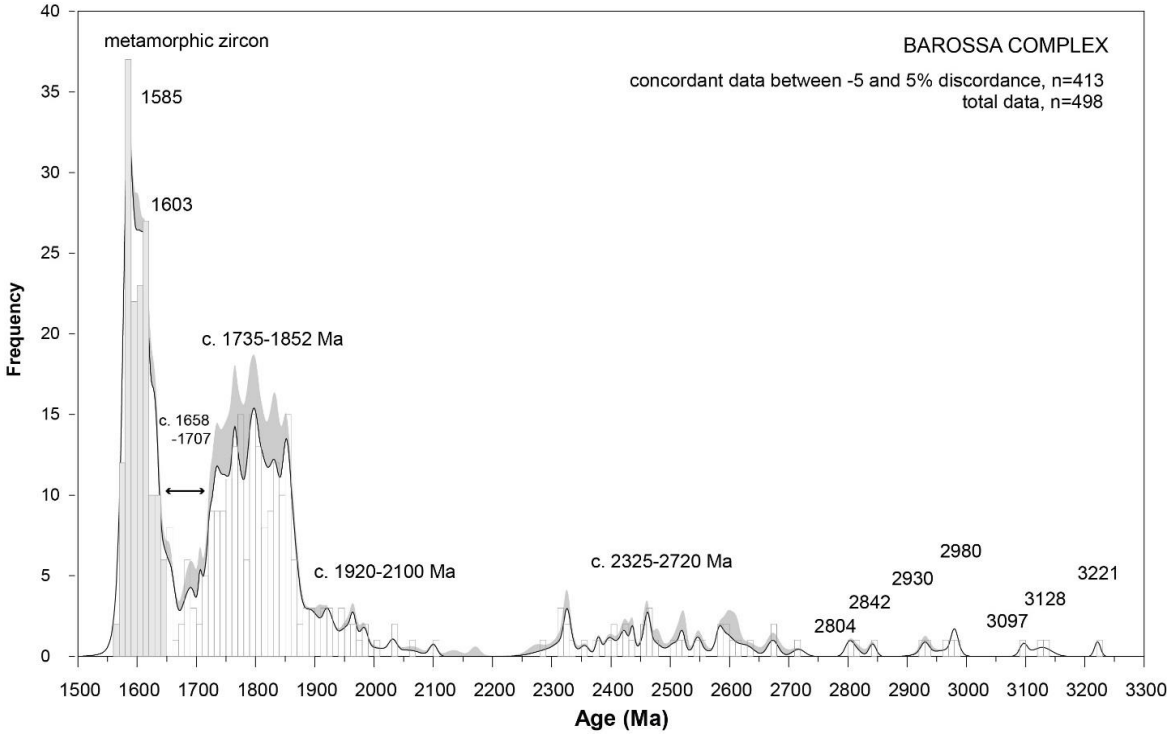

Figure 44. PDD of all $^{207}Pb/^{206}Pb$ ages for six metasedimentary rocks representing all inliers of the Barossa Complex. The grey-shaded curve represents analyses > 5% discordant, which are not used to calculate peak maxima. The histogram and white curve represent analyses < 5% discordant. Grey columns represent metamorphic zircon, white columns detrital zircon.

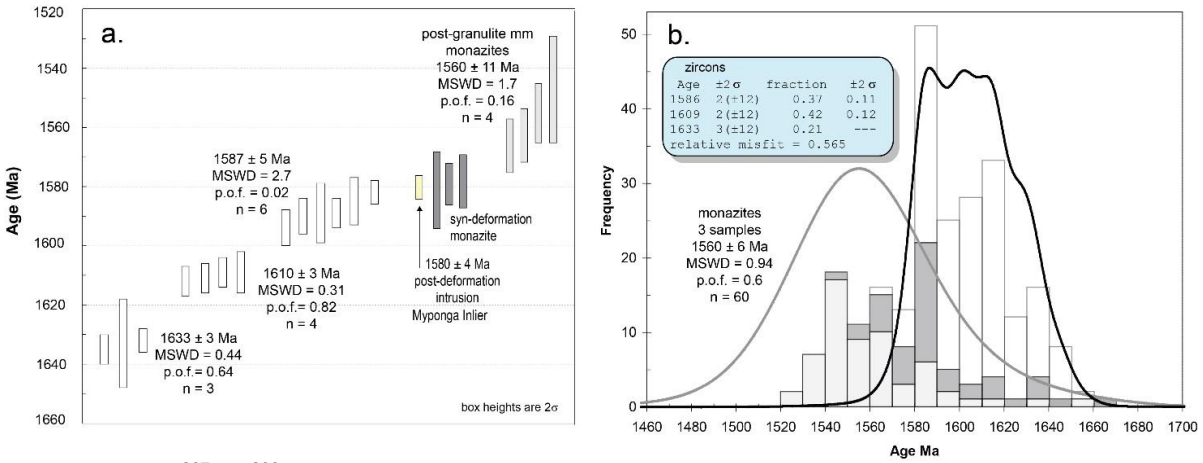

Figure 45. (a) $^{207}Pb/^{206}Pb$ ages for metamorphic zircon (this study) and monazite (Szpunar et al. 2007a, Morrissey et al. 2013). **(b)** PDDs of individual analyses. White symbols (error bars and histogram columns) represent metamorphic zircon. Yellow represents magmatic zircon. Light grey represents c. 1560 Ma monazite. Dark grey represents c. 1635-1580 Ma monazite in samples from the Myponga Inlier. These analyses are not used in the c. 1560 Ma age calculation. Monazite analyses for 2 samples (MI5 and R1473458) were not plotted in (b) as analyses were not provided in publications.

TIMING OF METAMORPHISM

Metamorphic zircon returned a range of ages, between c. 1645 – 1575 Ma, indicating a long-lived thermal event, with the pattern of ages suggesting three peak periods of zircon growth (Table 1, Fig. 45). The youngest age is recorded in all samples, and has been linked to high grade granulite facies metamorphism in the southern-most Myponga Inlier (Szpunar et al. 2007a). Pooling the ages of six samples produces weighted mean of 1587 ± 5 Ma (MSWD = 2.7, probability of fit = 0.02). Four samples from the Houghton, Warren and Oakbank inliers also record an older age at 1610 ± 3 Ma (MSWD = 0.31, probability of fit = 0.82), and three from the Houghton, Oakbank and Aldgate inliers record an age of 1633 ± 3 Ma (MSWD = 0.44, probability of fit = 0.64). Zircons from the Myponga Inlier do not record these earlier ages in zircon. However, c. 1630 Ma and 1613 Ma ages have been recorded in monazite cores from samples collected in the northern Myponga Inlier (Morrissey et al. 2013). A second method of calculating the age peaks by mixture modelling of individual analysis from all samples (Fig. 45b) produces near-identical results of 1586 ± 2 Ma (37% of analyses), 1609 ± 2 Ma (42%) and 1633 ± 3 Ma (21%). When the uncertainties are augmented with session errors, the final ages become 1586 ± 12 Ma, 1609 ± 12 Ma and 1633 ± 12 Ma.

In the Myponga Inlier, garnet-bearing leucosome formed by partial melting of a prograde biotite-sillimanite-bearing assemblage in a metapelitic granulite produced a LA-ICP-MS zircon age of 1588 ± 9 Ma (Szpunar et al. 2007a). This age was reproduced using SHRIMP in sample R1588242, which contains metamorphic zircon of 1590 ± 6 Ma. Magmatic zircon from a post-deformation, coarse-grained pegmatitic granite (R695754), provides some constraint on the timing of deformation, indicating the high grade fabric developed before 1580 ± 4 Ma. LA-ICP-MS monazite ages of 1579 ± 7 Ma (MI5, Szpunar et al. 2007a), 1581 ± 13 Ma and 1578 ± 9 Ma (WD2a and WD5c, Morrissey et al. 2013) recorded in garnet-bearing leucosomes appear to be younger than the syn-deformation zircon ages and the same as post-deformation zircon in the pegmatite. However, the apparent age difference between the monazites and zircons could be an analytical artefact. A Student's T test carried out between zircon (R1588242) and monazite (WD5c) indicates the age difference is not significant at the 95% confidence level of error (*t*-value 1.72, *p*-value .095). The other two monazite ages could not be tested as analyses were not published, but given the larger uncertainties on the ages, a null hypothesis is also likely.

Some monazites from the Myponga Inlier, however, are significantly younger than the c. 1590 Ma age recorded for prograde granulite facies metamorphism. Morrissey et al. (2013) report younger LA-ICP-MS $^{207}Pb/^{206}Pb$ monazite ages in both the Myponga and Houghton Inliers, ranging between c. 1570 – 1550 Ma (Fig. 45b). Sixty analyses from three samples (MY05, HOW4, HOW5) yield a

weighted mean age of 1560 ± 6 Ma (MSWD = 0.94, probability of fit = 0.6, Fig. 45b). Morrissey et al. (2013) attribute this younger episode to a retrograde phase post dating peak metamorphism, with monazite growth occurring on the retrograde path as pressure and temperature decreases and partial melts crystallise. This is consistent with the pre-Delamerian retrograde phase suggested by Talbot (1963).

In the Warren Inlier, where metamorphic grades reached lower amphibolite facies during the Delamerian Orogeny, the dark CL c. 1610 - 1590 Ma zircon overgrowths are enclosed by lighter CL rims, interpreted to have been variably recrystallised at 518 ± 40 Ma.

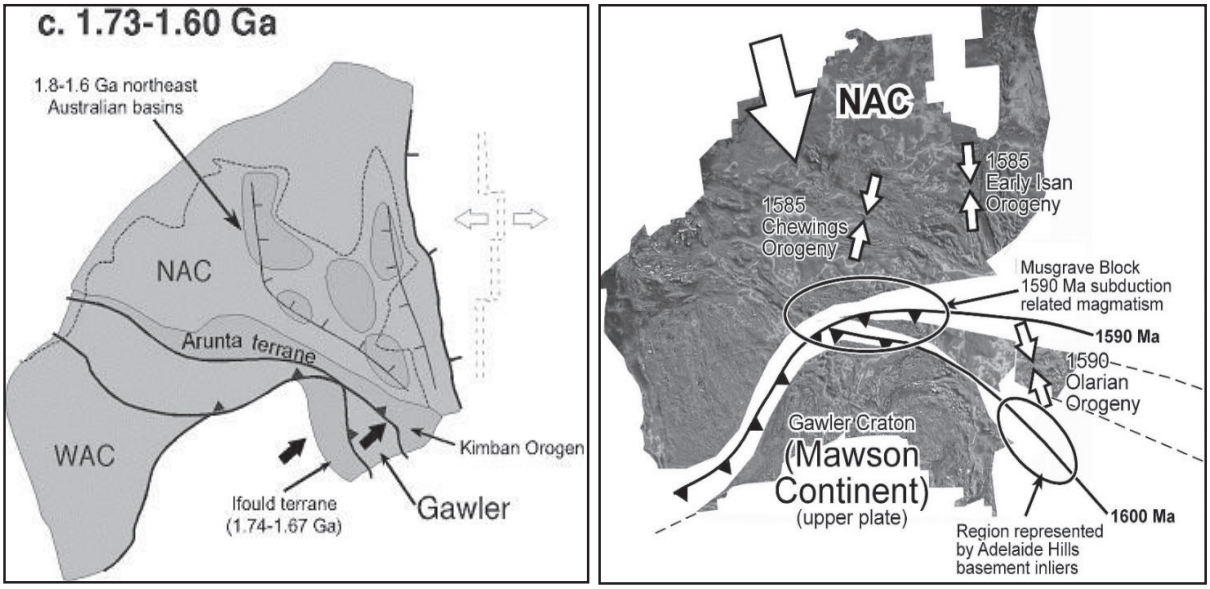

Figure 46. Models for the proposed collision of the Gawler Craton with the Northern Australian Craton during north-directed subduction. (a) Collision at c. 1730 Ma, continuing for about 100 Ma (eg Ferris et al. 2002, adapted from Betts et al. 2002). **(b**) Collision at c. 1630-1580 Ma encompassing the development of the Olarian Orogeny in the Curnamona Province and eastern Gawler Craton, emplacement of the Hiltaba and Bimbowrie Suites, and intrusion of c. 1590 Ma granitic rocks in the Musgrave Province (eg Wade et al. 2006, 2008, Morrissey et al. 2013).

COMPARISONS WITH THE GAWLER CRATON AND CURNAMONA PROVINCE

In terrains where craton boundaries are obscured by thick cover sequences, a multi analytical approach targeting craton margins and basement inliers can help provide a coherent tectonic synthesis between geographically separate domains. In models of Proterozoic continental evolution, the Gawler Craton and Curnamona Province are often grouped together as the South Australian Craton. It is clear that the key to developing a coherent model for their interconnected evolution is to understand the tectonic relationship between the two cratonic blocks. This is inhibited by the extensive Adelaide Rift Complex, which obscures the transition between the two domains. Key areas that can potentially bridge the gap are (1) the SE Gawler Craton in the Yorke Peninsula region and extending northward through the Olympic Domain (Proterozoic basement to the Stuart Shelf); and (2) the basement inliers of the Barossa Complex in the Adelaide Hills.

The c. 1750 Ma Wallaroo Group forms part of the leading edge of the eastern Gawler Craton, a region which in some models is interpreted to be involved in collision with elements of a proto-Curnamona Craton and north-directed subduction of Gawler lithosphere beneath the Northern Australian Craton during the c. 1700 Ma Kimban Orogeny (e.g. Betts et al. 2002, Giles et al. 2004, Betts et al. 2006; Fig. 46a). In the context of this model, the subsequent evolution of the Gawler Craton is envisaged to have occurred via a series of accretionary events that added material to the southwestern margin of the craton over the interval 1700-1600 Ma (e.g. Ferris et al. 2002). As the

Wallaroo Group was deposited before the Kimban Orogeny, an important implication of this model is that the c. 1720-1640 Ma Willyama Supergroup in the Curnamona Province should show some provenance input of this age from the eastern Gawler Craton, since it would have developed in a continental interior setting flanked by the Gawler Craton. In addition, the Wallaroo Group should record some evidence of this collisional event. These models also indicate that the Kalinjala shear zone, a 400km long transpressional crustal shear developed during the Kimban orogeny (Vasallo & Wilson 2002), is the suture between the Gawler Craton and Curnamona Province. This assertation has been refuted by several works which show detrital zircons in the Cleve Group were partly sourced from the Donnington suite, despite these two rock packages being separated by the proposed suture (Howard et al. 2006, Szpunar et al. 2011).

Other models have amalgamation of the Gawler Craton and Northern Australian Craton at c. 1600 Ma, with the Olary Orogeny representing a collisional system involving the Curnamona Province, eastern margin of the Gawler Craton, basement inliers of the Adelaide Hills and the Musgrave Province (e.g. Wade et al. 2006, 2008, Fig. 46b). Some authors suggest the orogenic system extends across eastern Proterozoic Australia from the Georgetown-Coen and Mt Isa Inliers of the north Australian Craton into Antarctica (Morrissey et al. 2013), and perhaps into the Wernecke Mountain region of Laurentia (Thorkelson et al. 2001). Viewed in this context, the Hiltaba Suite in the Gawler Craton is a syn-collisional magmatic system developed in the overriding Mawson continent above south-directed subduction of the northern Australian Craton. Importantly, in this model, the ~1720-1640 Ma Willyama Supergroup in the Curnamona Province will not share a common pre-Kimban provenance with the Gawler Craton, since it accumulated on a separate continental domain.

Recent models have suggested that the Gawler Craton and North Australian Craton were amalgamated prior to the Paleoproterozoic (Cawood & Korsch 2008, Payne et al. 2009, Betts et al. 2015, Aitken et al. 2016). In these models, the Willyama Supergroup is deposited in part of a large rift basin that also encompasses the Paleoproterozoic basins of the Mt. Isa Inlier and Georgetown and Coen Inliers. This rift is widely considered to have developed in response to subduction on the eastern Australian margin between c. 1800-1640 Ma (e.g. Cawood & Korsch 2008, Payne et al. 2009, Aitken et al 2016). The proposed extent of this basin includes the location of the Barossa Complex, and in this context the sediments of the Barossa Complex may be an extension of the Willyama Supergroup, or at least represent another sub-basin I this larger rift basin. This basin is proposed to have been inverted during the Isan-Olarian Orogeny at c. 1600 Ma during collision with an as yet unidentified collider, which has been proposed by some to be Laurentia (Betts et al. 2015, Thorkelson and Laughton 2016).

Provenance

It is not known whether the inliers of the Barossa Complex represent the eastern-most Gawler Craton or are an extension of the Curnamona Province, or if they represent separate basin(s) that evolved independently of both terrains. The results of this U-Pb zircon study can provide an insight into sedimentary provenance and thermal (metamorphic and magmatic) history, providing direct comparisons with adjacent terrains, and constraining the timing of amalgamation of the larger cratonic blocks.

The meta-sedimentary units of the Barossa Complex have maximum depositional ages between c. 1710- 1655 Ma for the sedimentary protolith, which are about 40 million years younger than the c. 1750 Ma Wallaroo Group of the south-eastern Gawler Craton, but very similar to depositional and eruption ages recorded in metasediments and metavolcanics of the Willyama Supergroup in the Curnamona Province (Fig. 47). Detrital zircon age spectra for the Barossa Complex and Willyama Supergroup are remarkably similar, suggesting a close spatial relationship between the two domains. They share the same broad clustering of ages, with about 70% of detrital zircon ages between c. 1690 – 1900 Ma, and peaks at c. 1660 Ma, 1795 Ma and 1850 Ma common to both provinces. Both contain zircon ages in the time range of the Kimban Orogeny, with c. 1690 Ma, 1710 Ma and 1735 Ma peaks recorded in the Barossa Complex and c. 1715 Ma in the Willyama Supergroup. The youngest maximum depositional ages of c. 1655 Ma for the Barossa Complex suggest that at least part of the meta-sedimentary succession is a temporal correlative of the Upper Willyama Supergroup; that is, the c. 1670-1640 Ma Paragon and Strathearn Groups (Fig.

47). The 1717 ± 7 Ma magmatic age for the granite gneiss intrusion in South Para gorge indicates other parts of the metasedimentary sequence must be older, perhaps equivalent to the Lower Willyama Supergroup. The Curnamona Group records maximum depositional ages of c. 1715 – 1790 Ma in the metasediments, and volcanism between c. 1716 - 1710 Ma. Syn-depositional granite intrusion of the Basso Suite at c. 1719 – 1711 Ma Suite (Conor and Preiss 2008) is contemporary with the South Para gorge orthogneiss.

Deposition of the Barossa Complex and Willyama Supergroup metasediments postdates the period of widespread basin deposition and associated bimodal magmatism across the Gawler Craton at c. 1770 – 1740 Ma (Hand et al. 2007), which included the Wallaroo Group on Yorke Peninsula and extending northward below the Stuart Shelf. Their depositional ages are similar to the c. 1715 Ma Labyrinth Formation and c. 1655 Ma Tarcoola Formation, deposited in younger, fault-bounded basins confined to the central and northern Gawler Craton during the Kimban Orogeny (Cowley and Martin 1991, Daly et al. 1998; Budd 2006, Fanning et al. 2007). LA-ICP-MS detrital zircon data from the Labyrinth Formation yield dominant age peaks at c. 1720 Ma, 1840 Ma, 2520 Ma, and 3100 Ma, and is considered to be derived from locally sourced Gawler Craton sources, while the Tarcoola Formation yields a broad dominant age peak between 1660-1770 Ma, with additional peaks at 1850 Ma and 2520 Ma (Howard et al. 2011a). The Tarcoola Formation detrital signature is similar to the Barossa Complex and has been interpreted to be related to the upper Willyama Supergroup based on isotopic composition. The Tarcoola Formation contains a comparatively juvenile ε_{Nd} values (ε_{Nd} -4.1 to +0.5) when compared to the isotopically evolved Archean Gawler Craton. An influx of juvenile material is recorded in many Paleoproterozoic basins in eastern Australia after c. 1655 Ma (e.g. Barovich and Hand 2008, Lambeck et al. 2012) which further supports some level of continuity in the Paleoproterozoic basins of eastern Australia. The source of this juvenile material is unknown and is suggested to be a now eroded or unexposed magmatic province in Australia, or be from a now rifted continental fragment.

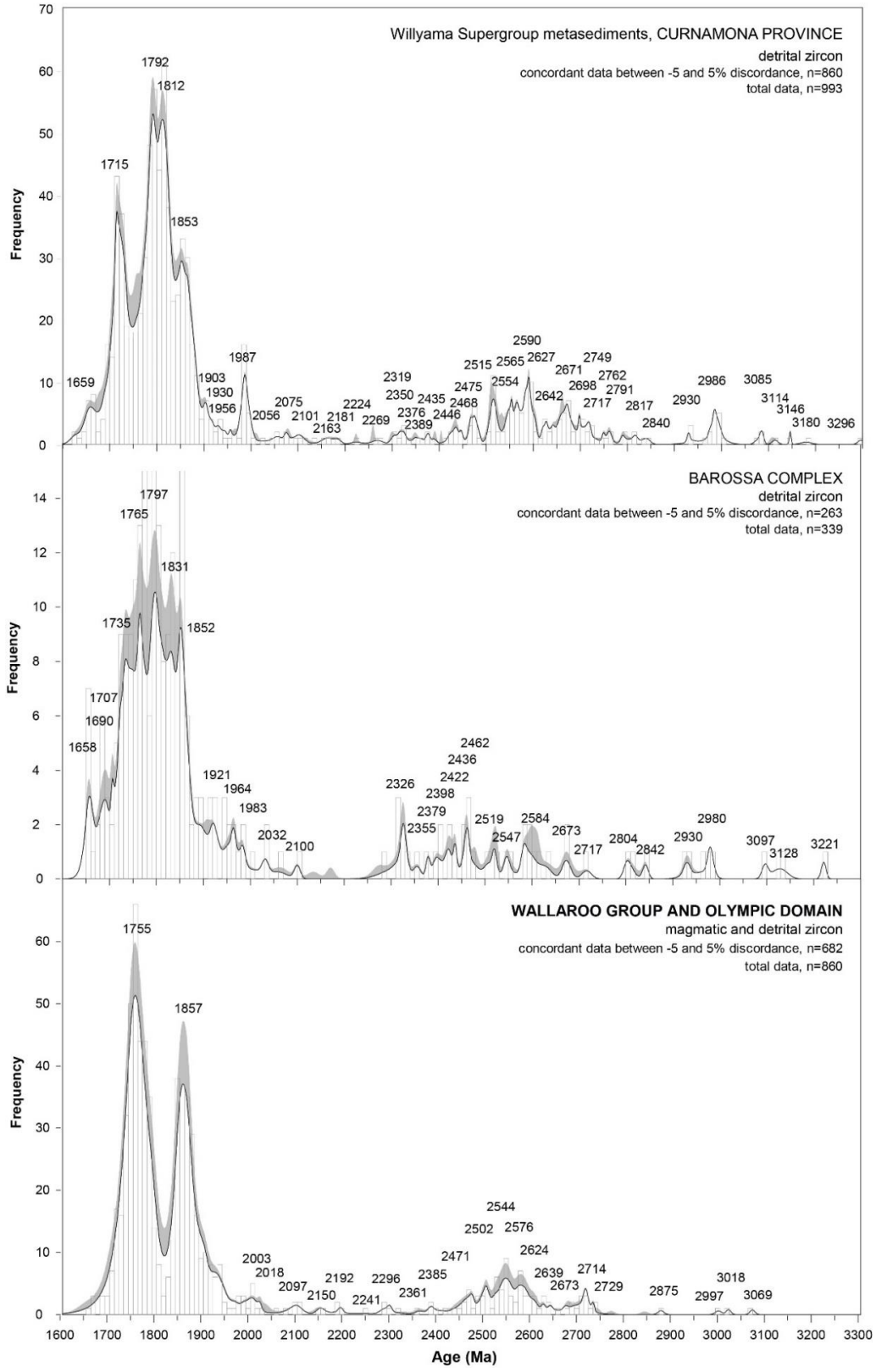

Figure 47. A comparison of detrital age spectra for the Willyama Supergroup (unpublished data from the BHEI, collected by Rod Page between 1998 – 2002), Barossa Complex metasediments (this study) and detrital and magmatic zircon of the Wallaroo Group (Jagodzinski and Szpunar 2017). The grey curve represents analyses > 5% discordant, which are not used to calculate peak maxima. The histogram and white curve represent analyses < 5% discordant.

In the Wallaroo Group, magmatism occurred between c. 1735 – 1770 Ma, and the metasedimentary rocks record maximum ages of deposition between c. 1750 – 1780 Ma (Jagodzinski 2005, Fanning et al. 2007, Jagodzinski and Szpunar 2017). Plotted together, the magmatic and detrital zircon ages form a dominant peak at c. 1755 Ma, which is not seen in the Barossa-Willyama detritus (Fig. 47). A point of difference between the Barossa Complex and Curnamona Province is that the former does contain detritus of Wallaroo Group age, with peak ages of c. 1735 and 1765 Ma corresponding with the age of Wallaroo Group magmatism. The Willyama Supergroup contains no c. 1750 Ma detritus, negating models for continental evolution involving amalgamation during the Kimban Orogeny, in which the Wallaroo basin uplifts and collides with the Northern Australian Craton during the Kimban Orogeny and sheds detritus into the Willyama basin in the continental interior (Fig. 46a). Also contradicting this model is the fact that across the eastern Gawler Craton, the Wallaroo Group was essentially unmetamorphosed prior to the Olary Orogeny, and records no evidence of Kimban-aged deformation or metamorphism (eg Reid and Fabris 2015). Although the Wallaroo Group and equivalents do not appear to be a viable source region for the Willyama Supergroup, it seems plausible that in the central -western-southern Gawler Craton the Kimban Orogen was uplifted at the time the Willyama rift basins formed, and that detritus was transported across what is now Yorke Peninsula with its as yet undeformed Wallaroo Group to the Barossa-Willyama basins. The data do not rule out possible eastward extension of the Wallaroo Group beneath the Willyama Supergroup, where seismic data suggest there may be many kilometres of thick, layered stratigraphy below the oldest outcropping rocks (Goleby et al. 2006).

Many authors have suggested a northern Australian (Arunta) provenance, as the source of the lower Willyama Supergroup rather than the nearby Gawler Craton (Barovich and Hand 2008, Payne et al. 2006, Page et al. 2000). However, the more comprehensive dataset for the Willyama Supergroup presented in this study (Fig. 47) indicates that the eastern Gawler Craton, Barossa Complex and Curnamona Province all contain detrital zircon clusters that allow for the central and western Gawler Craton as a potential source: c. 1790 Ma (corresponding with the Myola Volcanics, Broadview Schist, Hutchison Group), 1850 Ma (Donington Suite), 2000 Ma (Miltalie Gneiss) and 2420 – 2580 Ma (Sleaford and Mulgathing Complexes). Other significant clusters at c. 2200 – 2400 Ma and c. 2600 – 2840 Ma do not favour a Gawler Graton provenance and could derive from the Northern Australian Craton. The apparent mixing of detrital zircons from both the Gawler and North Australian Cratons supports models such as Aitken et al. (2016), which propose a continuity between the Late Paleoproterozoic basins of the Mt. Isa Inlier, Curnamona Province, and Northern Gawler Craton.

Lu-Hf isotopic data support a common provenance for the Palaeoproterozoic basins of the southern Gawler Craton, Barossa Complex and lower Willyama Supergroup, of evolved crust (ε_{Nd} (1.7Ga) = -3 to -7) and REE-enriched upper crust, compared with Post-Archean Average Australian Shale (Szpunar et al. 2007b). Detrital zircon of c. 1790 Ma age have similar initial εHf values (-4 to +5). The c. 1850 Ma Donington Suite (initial εHf -4 to +5) is a likely source for detrital zircon in the southern Gawler Craton and Barossa Complex (εHf values of -4 to +4). In the lower Willyama Supergroup, c. 1850 Ma detrital zircon is more juvenile (initial εHf 0 to +6), which may indicate it also contains detritus from a source that was not available to the Southern Gawler Craton and Barossa Complex.

Thermal history

By the late Paleoproterozoic to early Mesoproterozoic, the Curnamona Province and Gawler Craton share a common history. The best evidence of this is the recognition of a silicic large igneous province (SLIP), which encompasses the c. 1595 – 1587 Ma Gawler Range Volcanics and the c. 1587 Ma Benagerie Volcanic Suite in the northern Curnamona Province (Wade et al. 2012, Jagodzinski et al. in prep).

In the Curnamona Province, this period encompasses the extrusion of bimodal A-type volcanics of the Benagerie Volcanic Suite of the Mudguard Domain, intrusion of the c. 1600–1570 Ma Ninnerie Supersuite (Wade 2011) and regional high-temperature metamorphism of the Olarian Orogeny (Conor and Preiss 2008). The metamorphic grade and deformational intensity of the Olarian Orogeny varies across the Curnamona province, with the highest grades preserved in the southeast in the Broken Hill and adjacent Redan Domains, reaching granulite facies conditions of

c. 750°C and 4 – 6 kB (Page and Laing 1992, Forbes et al. 2005, McFarlane and Frost 2009, Clark and Hand 2010). The Olary Domain is less intensely metamorphosed, generally decreasing from upper amphibolite facies in the south to greenschist facies, with less extensive deformation, to the north and west (Phillips and Wall 1981, Clarke et al. 1987, Webb and Crooks 2005, Conor and Preiss 2008).

In the southern Curnamona Province, peak metamorphic conditions are closely associated with intense deformation during the Olarian Orogeny at c. 1600 –1590 Ma (Page and Laing 1992, Page et al. 2000, Forbes and Betts 2004, Gibson and Nutman 2004). However, as with the Barossa Complex, there is evidence of an extended tectonothermal history. McFarlane and Frost (2009) report earlier monazite growth at 1630 ± 6 Ma, near-identical to the 1633 ± 3 Ma zircon age population for the Barossa Complex reported in this study. Teale and Fanning (2000) also published c. 1630 Ma monazite ages and Forbes et al. (2007a) ages of c. 1620 Ma. A later episode of high grade metamorphism in the Broken Hill region, and heterogeneously-distributed retrograde metamorphism in the Olary Domain and western Broken Hill Domain, occurred between ca 1570 and 1550 Ma (Rutherford et al. 2007).

In the early Mesoproterozoic, the Gawler Craton experienced the voluminous magmatism of the c. 1595 – 1575 Ma Hiltaba Suite and Gawler Range Volcanics which, with the Benagerie Volcanic Suite and Ninnerie Supersuite of the northern Curnamona Province, form a SLIP of estimated 110 000 km^3 volume. Contemporary with this large magmatic system and the Olarian Orogeny in the Curnamona Province, UHT to high-temperature granulite facies metamorphism is recorded in the north – north-western Gawler Craton; in the Coober Pedy Ridge (c. 925 °C and 6.5 kbar at 1585 – 1565 Ma), Mabel Creek Ridge (c. 850 °C and 9 kbar at 1595 – 1575 Ma) and Mt Woods 2007, Cutts et al. 2011, Forbes et al. 2011). In the Mount Woods Inlier, monazite ages of c. 1615 Ma have large uncertainties (c. 20 Ma) that overlap the peak metamorphic event and zircon growth at c. 1595 Ma, but may represent early monazite growth during prograde metamorphism (c. 2–3 kbar and 550–610 ◦C, Forbes et al. 2011). Younger U–Pb monazite ages between 1570–1540 Ma, contemporary with the c. 1560 Ma retrograde phase recorded in the Barossa Complex, are recorded elsewhere in high-grade metamorphic rocks in the Gawler Craton, associated with the Kararan Orogeny (Daly et al. 1998, Hand et al. 2007, Payne et al. 2008, Howard et al. 2011b).

CONCLUSIONS

It has been proposed that the Barossa Complex is part of a series of eastward-younging basins within the South Australian Craton, from the c. 1790 Ma Cleve group (Hutchison Group, Szpunar et al. 2011) on the Eyre Peninsula and c. 1750 Ma Wallaroo Group on the Yorke Peninsula to the west, to the c. 1720 – 1640 Ma Willyama Supergroup to the east (Szpunar et al. (2006) Kositcin (2010). The detrital spectra indicate a close spatial relationship between the Barossa Complex and Curnamona Province, suggesting these now separated domains were once contiguous parts of the same crustal fragment. The only point of difference is additional age peaks at 1735 - 1765 Ma in the Barossa Complex, recording some input from the Wallaroo Group or a contemporary source. This could be explained if, during deposition, the Wallaroo Group formed a slightly elevated hinterland more proximal to the Barossa Complex.

The apparent eastward younging of the Wallaroo Group – Barossa Complex – Willyama Supergroup may be driven by an eastward migrating back arc or continental rift, with a continuation of the Wallaroo group forming the basement of the Willyama Supergroup and Barossa Complex. The metasedimentary successions have a common pre-1850 Ma provenance, with the range of ages suggesting a combined central–western Gawler Craton - northern Australian Craton (Arunta Province) source. The common provenance supports models which propose the Gawler and North Australian Cratons were contiguous throughout the Late Paleoproterozoic.

In the early Mesoproterozic the Gawler Craton, Barossa Complex, and Curnamona Province have a shared post-depositional geological history. In the past two decades, suggestions of pre-Olarian (c. 1600 – 1590 Ma) prograde metamorphism in the Curnamona Province have not met universal acceptance (Stevens 2007, Forbes et al. 2007b), mainly because c. 1660 – 1640 Ma zircon ages generated by Nutman and Ehlers (1998) could be dismissed as mixing ages or aberrant ages generated by a particular approach to statistical modelling of complex datasets (Page et al. 2000,

Stevens 2000, Page et al. 2005). However, whereas conditions may not have favoured zircon growth, in situ monazites record
c. 1630 – 1620 Ma prograde amphibolite facies metamorphism (Teale and Fanning 2000, Forbes et al. 2007a, McFarlane and Frost 2009), which Forbes et al. (2008) attribute to a short-lived M1/D1 mid-crustal extensional event, and Conor and Preiss (2008) to burial of the sedimentary succession at mid crustal depths.

In the Barossa Complex, the evidence for pre-Olarian metamorphism is more compelling, with two episodes of zircon growth recorded at 1633 ± 3 Ma and 1610 ± 3 Ma, prior to peak metamorphic conditions at 1587 ± 5 Ma. Without more targeted in situ monazite studies, it is unknown whether the older ages are relics from an earlier event that has been overprinted or, as with the Curnamona Province, represent growth during the prograde evolution of a long-lived event.

In both provinces monazites, but not zircon, record metamorphism between c. 1570 and 1550 Ma (Rutherford et al. 2007, Morrissey et al. 2011), which appears to be diachronously prograde in the Paragon Group near Broken Hill, but retrograde elsewhere in the Olary and Broken Hill Domains. In the Barossa Complex, monazite grew during post peak retrogresstion between 1570-1550 Ma, with one 1566 ± 9 Ma age representing a retrograde shear zone in the Myponga Inlier..The similar metamorphic timing indicates that during the Mesoproterozoic, both provinces have a shared tectonic history, recording what appears to be a single, long-lived high-grade metamorphic event at c. 1630–1550 Ma. The northern Gawler Craton experienced similar granulite facies metamorphic conditions between c. 1595 – 1575 Ma, and 1570–1540 Ma, and in the Mount Woods Inlier, monazite ages of c. 1615 may represent early monazite growth during prograde metamorphism.

REFERENCES

Aitken A. R. A., et al. 2016 *The Australo-Antarctic Columbia to Gondwana transition*, Gondwana Research, vol. 29, no. 1, pp. 136-152.

Barovich, K. and Hand, M. 2008. Tectonic setting and provenance of the Palaeoproterozoic Willyama Supergroup, Curnamona Province, Australia: Geochemical and Nd isotope constraints on contrasting source terrain components. *Precambrian Research*, 318–337.

Belousova, E., Preiss, W. V., Schwarz, M. P. and Griffin, W. L. 2006. Tectonic affinities of the Houghton Inlier, South Australia: U–Pb and Hf isotope data from zircons in modern stream sediments. *Australian Journal of Earth Sciences* 53, 971–989.

Betts, P.G., Giles, D., Lister, G.S. and Frick, L.R. 2002. Evolution of the Australian lithosphere. *Australian Journal of Earth Sciences* 49, 661–695.

Betts, P. G. and Giles, D. 2006 *The 1800–1100 Ma tectonic evolution of Australia*, Precambrian Research, vol. 144, no. 1–2, pp. 92-125.

Betts, P. G., Armit, R. J., Stewart, J., Aitken, A. R. A., Ailleres, L., Donchank, P., Hutton, L., Withnall, I., and Giles, D. 2015 *Australia and Nuna*, Geological Society, London, Special Publications, vol. 424.

Black, L.P., Kamo, S.L., Williams, I.S., Mundil, R., Davis, D.W., Korsch, R.J. and Foudoulis, C. 2003. The application of SHRIMP to Phanerozoic geochronology; a critical appraisal of four zircon standards. *Chemical Geology* 200, 171–188.

Black, L.P., Kamo, SL, Allen, CM, Davis, DW, Aleinikoff, JN, Valley, JW, Mundil, R, Campbell, IH, Korsch, RJ, Williams, IS and Foudoulis, C. 2004. Improved 206Pb/238U microprobe geochronology by the monitoring of a trace-element-related matrix effect; SHRIMP, ID-TIMS, ELA-ICP-MS and oxygen isotope documentation for a series of zircon standards. *Chemical Geology* 205, 115–140.

Budd, A. 2006. The Tarcoola Goldfield of the central Gawler gold province, and the Hiltaba Association Granites, Gawler craton, South Australia: PhD. thesis, Australian National University,365 p.

Campana, B., Wilson, R. B. and Whittle, A. W. G. 1954. Geological Atlas of South Australia, Yankallila Sheet 1:63 360. Geological Survey of South Australia, Adelaide.

Cawood P. A. and Korsch R. J. 2008 Assembling Australia: Proterozoic building of a continent, Precambrian Research, vol. 166, no. 1–4, pp. 1-35.

Chalmers, N. 2007. *Mount Woods Domain: Proterozoic metasediments and intrusives.* Report Book 2007/20. Department of Primary Industries and Resources South Australia, Adelaide.Claoué–Long, J.C., Compston, W., Roberts, J. and Fanning, C.M. 1995. Two Carboniferous ages: a comparison of SHRIMP zircon dating with conventional zircon ages and 40Ar/39Ar analysis. In WA Berggren, DV Kent, MP Aubry and J Hardenbol eds, *Geochronology, Time Scales and Global Stratigraphic Correlation. SEPM Special Publication*. Society for Sedimentary Geology, Tulsa, USA 3–21.

Clark, C. and Hand, M. 2010. Decoding Mesoproterozoic and Cambrian metamorphic events in Willyama Complex metapelites through the application of Sm–Nd garnet geochronology and P–T pseudosection analysis. *Gondwana Research* 17, 59–74.

Clarke, G.L., Guiraud, M., Powell, R. and Burg, J.P. 1987. Metamorphism in the Olary Block, South Australia: compression with cooling in a Proterozoic fold belt. *Journal of Metamorphic Geology* 5, 291–306.

Conor, C. H. H. and Preiss, W. V. 2008. Understanding the 1720–1640 Ma Palaeoproterozoic Willyama Supergroup, Curnamona Province, Southeastern Australia: Implications for tectonics, basin evolution and ore genesis. *Precambrian Research* 166, 297–317.

Copeland, P., Parrish, R. R. and Harrison, T. M. 1988. Identification of inherited radiogenic Pb in monazite and its implications for U–Pb systematics. *Nature* 333, 760–763.

Cowley, W.M. and Martin, A.R. 1991, *Kingoonya, South Australia*. Primary Industries and Resources South Australia, Adelaide 64 p.

Cutts, K., Hand, M. and Kelsey, D. E. 2011. Evidence for early Mesoproterozoic (ca 1590 Ma) ultrahigh–temperature metamorphism in southern Australia. *Lithos* 124, 1–16.

Daly, S.J., Fanning, C. M. and Fairclough, M. C. 1998. Tectonic evolution and exploration potential of the Gawler Craton, South Australia. *AGSO Journal of Australian Geology and Geophysics* 17, 145–168.

Davies M. B. 1972. A. The geology and petrology of an Archean Inlier south of Normanville. B. The geochemistry of the 'Houghton' granulite. BSc Hons Thesis, University of Adelaide.

Fanning, C. M, Reid, A.J. and Teale, G.S. 2007. *A geochronological framework for the Gawler Craton, South Australia.* Bulletin 55. Geological Survey of South Australia, Adelaide.

Ferris, G.M., Schwarz, M.P. and Heithersay, P. 2002. The geological framework, distribution and controls of Fe–Oxide Cu–Au mineralisation in the Gawler Craton, South Australia, Part I – Geological and tectonic framework. In TM Porter ed. *Hydrothermal iron oxide copper-gold and related deposits: a global perspective,* vol. 2. PGC Publishing, Adelaide, 9–31.

Foden, J., Elburg, M. A., Dougherty-Page, J. and Burtt, A. 2006. The timing and duration of the Delamerian Orogeny: correlation with the Ross Orogen and implications for Gondwana assembly. *Journal of Geology* 114, 189–210.

Forbes, C. J. and Betts, P. G. 2004. Development of type 2 fold interference patterns in the Broken Hill Block: implications for strain partitioning across a detachment during the Olarian Orogeny. *Australian Journal of Earth Sciences* 51, 173–188.

Forbes, C. J., Betts, P. G., Giles, D. and Weinberg, R. 2008. Reinterpretation of the tectonic context of high-temperature metamorphism in the Broken Hill Block, NSW, and implications on the Palaeo- to Meso-Proterozoic evolution. *Precambrian Research* 166, 338–349.

Forbes, C. J., Betts, P. G., Weinberg, R. and Buick, I. S. 2005. A structural metamorphic study of the Broken Hill Block, NSW, Australia. *Journal of Metamorphic Geology* 23, 745–770.

Forbes, C. J., Betts, P. G., Weinberg, R. and Buick, I. S. 2007b. A structural metamorphic study of the Broken Hill Block, NSW, Australia: reply. *Journal of Metamorphic Geology* 25, 719–723.

Forbes, C. J., Giles, D., Betts, P. G., Weinberg R. and Kinny, P. D. 2007a. Dating prograde amphibolite and granulite facies metamorphism using in situ monazite U–Pb SHRIMP analysis. *Journal of Geology* 115, 691–705.

Forbes, C. J., Giles, D., Hand, M., Betts, P. G., Suzuki, K., Chalmers, N. and Dutch, R. 2011. Using P–T paths to interpret the tectonothermal setting of prograde metamorphism: An example from the northeastern Gawler Craton, South Australia. *Precambrian Research* 185, 65–85.

Gibson, G.M. and Nutman, A.P. 2004. Detachment faulting and bimodal magmatism in the Palaeoproterozoic Willyama Supergroup, south-central Australia: keys to recognition of a multiply deformed Precambrian metamorphic core complex. *Journal of the Geological Society of London* 161, 55–66.

Giles D., Betts P. G. and Lister G. S. 2004 1.8-1.5-Ga links between the North and South Australian Cratons and the Early-Middle Proterozoic configuration of Australia, Tectonophysics, vol. 380, no. 1-2, pp. 27-41.

Goleby, B.R., Korsch, R.J., Fomin, T., Conor, C.H.H., Preiss, W.V., Robertson, R.S. and Burtt, A. 2006. *The 2003–2004 Curnamona Province seismic survey: workshop notes.* Record 2006/12. Geoscience Australia, Canberra.

Hand, M., Reid, A. J. and Jagodzinski E. 2007. Tectonic Framework and Evolution of the Gawler Craton, Southern Australia. *Economic Geology* 102, 1377–1395.

Heaslip, J. E. 1972. Review of the geology of the Mt. Magnificent area. BSc Hons. Thesis, University of Adelaide.

Howard K., Ried, A. J., Hand, M., Barovich,K. M., and Belousova, E. 2006 Does the Kalinjala Shear Zone represent a paleosuture zone? Implications for distribution of styles of Mesoproterozoic mineralisation in the Gawler Craton, MESA Journal, vol. 43, pp. 16-20.

Howard K. E., Hand, M., Barovich, K. M., and Belousova, E. 2011a Provenance of late Paleoproterozoic cover sequences in the central Gawler Craton: exploring stratigraphic correlations in eastern Proterozoic Australia using detrital zircon ages, Hf and Nd isotopic data, Australian Journal of Earth Sciences, vol. 58, no. 5, pp. 475-500.

Howard, K. E., Hand, M., Barovich, K. M., Payne, J. L., Cutts, K. A. and Belousova E. A. 2011. U–Pb zircon, zircon Hf and whole-rock Sm–Nd isotopic constraints on the evolution of Paleoproterozoic rocks in the northern Gawler Craton. *Australian Journal of Earth Sciences* 58, 615–638.

Jaffey, A.H., Flynn, K.F., Glendenin, L.F., Bentley, W. C. and Essling, A.M. 1971. Precision measurements of half-lives and specific activities of 235U and 238U. *Physical Review C4*: 1889–1906.

Jagodzinski, E.A. 2005. *Compilation of SHRIMP U–Pb geochronological data, Olympic Domain, Gawler Craton South Australia, 2001–2003.* Record 2005/20. Geoscience Australia, Canberra.

Jagodzinski, E.A. and Szpunar, M. 2017. *SHRIMP U-Pb dating of the Wallaroo Group, Yorke Peninsula, South Australia.* Report Book 2017/00018. Department of the Premier and Cabinet, South Australia, Adelaide.

Jagodzinski, E.A., Reid, A.J., Chalmers, N., Swain, G., Frew, R.A. and Foudoulis, C. 2007. *Compilation of SHRIMP U–Pb geochronological data for the Gawler Craton, South Australia, 2007.* Report Book 2007/21. Department of Primary Industries and Resources South Australia, Adelaide.

Jagodzinski, E.A., Reid, A.J., Crowley, J.L., McAvaney, S. and Wade, C.E. in prep. Precise zircon U-Pb dating of a Mesoproterozoic silicic large igneous province: the Gawler Range Volcanics and Benagerie Volcanic Suite, South Australia

Kositcin, N. 2010. *Geodynamic Synthesis of the Gawler Craton and Curnamona Province.* Record 2010/27, Geoscience Australia, Canberra.

Lambeck A., Barovich, K. M., Gibson, G., Huston, D., and Pisarevsky, S. 2012 An abrupt change in Nd isotopic composition in Australian basins at 1655Ma: Implications for the tectonic evolution of Australia and its place in NUNA, Precambrian Research, vol. 208, pp. 213-221

Ludwig, K.R. 2009. SQUID 2.50: A user's manual. Berkeley Geochronology Center Special Publication No. 5. Berkeley California, USA.

Ludwig, K.R. 2003. *Isoplot 3.00 - a geochronological toolkit for Microsoft Excel.* Berkeley Geochronology Center Special Publication No. 4.

Mancktelow, N. S. 1990 The structure of the southern Adelaide Fold Belt, South Australia. In JB Jago and PJ Moore eds. *The evolution of a Late Precambrian-Early Paleozoic Rift Complex: The Adelaide Geosyncline.* Geological Society of Australia Special Publication, pp. 483–495.

Mason, D. 2006a. Petrographic Descriptions for Four rock thin sections. Report no. 3172; Mason Geoscience Pty Ltd. *Unpublished report.*

McFarlane, C. R. M. and Frost, B. R. 2009. Constraints on the early metamorphic evolution of Broken Hill, Australia, from in situ U–Pb dating and REE geochemistry of monazite. *Journal of Metamorphic Geology* 27, 3–17.

Meaney, K., Hand, M. and Collins, A. in prep The Paleo-Mesoproterozoic Stratigraphy and Structure of the Northern Barossa Complex, Mount Lofty Ranges, South Australia.

Mills, K. J. 1973. The structural geology of the Warren National Park and the western portion of the Mount Crawford State Forest, South Australia., *Transactions of the Royal Society of South Australia* 97, Part 4, 281–315.

Morrissey, L. J., Hand, M., Wade, B.P and Szpunar, M. 2013. Early Mesoproterozoic metamorphism in the Barossa Complex, South Australia: links with the eastern margin of Proterozoic Australia, *Australian Journal of Earth Sciences* 60, 769–795.

Offler, R. and Fleming, P. D. 1968 A synthesis of folding and metamorphism in the Mt Lofty Ranges, South Australia, *Journal of the Geological Society of Australia* 15, 245–266.

Page, R. W. and Laing, W. P. 1992. Felsic metavolcanic rocks related to the Broken Hill Pb–Zn–Ag orebody, Australia: geology, depositional age and timing of high-grade metamorphism. *Economic Geology*, 87, 2138–2168.

Page, R. W., Stevens, B. P. J. and Gibson, G. M. 2005. Geochronology of the sequence hosting the Broken Hill Pb-Zn-Ag orebody, Australia. *Economic Geology*, 100, 633–661.

Page, R.W., Stevens, B.P.J., Gibson, G.M. and Conor, C. H.H. 2000. Geochronology of the Willyama Supergroup rocks between Olary and Broken Hill and comparison to northern Australia. In M Peljo ed. *Broken Hill Exploration Initiative: abstracts of papers presented at the May 2000 conference in Broken Hill.* Record 2000/10. Australian Geological Survey Organisation, Canberra. 72–75.

Payne, J. L., Barovich, K. and Hand, M. 2006. Provenance of metasedimentary rocks in the northern Gawler Craton, Australia: implications for Palaeoproterozoic reconstructions. *Precambrian Research* 148, 275–291.

Payne, J. L., Hand, M., Barovich, K. M. and Wade, B. P. 2008. Temporal constraints on the timing of high-grade metamorphism in the northern Gawler Craton: implications for assembly of the Australian Proterozoic. *Australian Journal of Earth Sciences* 55, 623–640.

Payne J. L., Hand, M., Barovich, K. M., Reid, A., and Evans, D. A. D., 2009 Correlations and Reconstruction Models for the 2500-1500 Ma evolution of the Mawson Continent. In Reddy S. M., et al. eds. Paleoproterozoic Supercontinents and Global Evolution. pp. 319-357. London: Geological Society.

Phillips, G.N. and Wall, V.J. 1981. Evaluation of prograde regional metamorphic conditions: their implications for the heat source and water activity during metamorphism in the Willyama Complex, Broken Hill, Australia. *Bulletin de Mineralogie* 104, 801–810.

Preiss, W. V. 1993. Basement inliers of the Mount Lofty Ranges. In JF Drexel, WV Preiss and AJ Parker eds, *The geology of South Australia, Volume 1, The Precambrian,* Bulletin 54. Geological Survey of South Australia, Adelaide, pp. 102–105.

Preiss, W. V. 2000. The Adelaide Geosyncline of South Australia and its significance in Neoproterozoic continental reconstruction. *Precambrian Research* 100, 21–63.

Preiss, W. V., Fanning, C.M., Szpunar, M.A. and Burtt, A.C. 2008. Age and tectonic significance of the Mount Crawford Granite Gneiss and a related intrusive in the Oakbank Inlier, Mount Lofty Ranges, South Australia. *MESA Journal* 49, 21–27. Department of Primary Industries and Resources South Australia, Adelaide.

Reid, A.J. and Fabris, A. 2015. Influence of pre-existing low metamorphic grade sedimentary successions on the distribution of iron oxide copper-gold mineralization in the Olympic Cu-Au Province, Gawler Craton. *Economic Geology* 110, 2147–2157.

Rutherford, L., Hand, M. and Barovich, K., 2007b. Timing of Proterozoic metamorphism in the southern Curnamona Province: implications for tectonic models and continental reconstructions. *Australian Journal of Earth Sciences* 54, 1–17.

Sambridge, M. and Compston, W. 1994. Mixture modeling of multi-component data sets with application to ion-probe zircon ages: *Earth and Planetary Science Letters* 128, 373–390.

Sircombe, K.N. 2004. AgeDisplay: an EXCEL workbook to evaluate and display univariate geochronological data using binned frequency histograms and probability density distributions. *Computers and Geosciences* 30, 21–31.

Spry, A. H. 1951 The Archaean Complex at Houghton, South Australia, *Transactions of the Royal Society of South Australia,* 74, 115–134.

Stacey, J.S. and Kramers, J.D. 1975. Approximation of terrestrial lead isotope evolution by a two-stage model. *Earth and Planetary Science Letters 26*, 207–221

Steiger, R.H. and Jäger, E. 1977. Subcommission of geochronology: Convention on the use of decay constants in geo- and cosmochronology. *Earth and Planetary Science Letters* 36, 359–362.

Stern, R.A., Bodorkos, S., Kamo, S.L., Hickman, A.H., Corfu, F., 2009. Measurement of SIMS instrumental mass fractionation of Pb isotopes during zircon dating. *Geostandards and Geoanalytical Research*, 33, 145–168.

Stevens, B. P. J. 2000. Evaluating models for tectonic development of the Willyama Supergroup. In M Peljo ed. *Broken Hill Exploration Initiative: abstracts of papers presented at the May 2000 conference in Broken Hill.* Record 2000/10. Australian Geological Survey Organisation, Canberra. 89–90.

Stevens, B.P.J. 2007. A structural metamorphic study of the Broken Hill Block, NSW, Australia: discussion. *Journal of Metamorphic Geology* 25, 715–717.

Szpunar, M., Hand, M., Barovich, K. and Jagodzinski, E. 2006. Tectonics links between the Gawler Craton and Curnamona Province. *Broken Hill Exploration Initiative*, Abstracts. Geoscience Australia, Canberra, p. 176.

Szpunar, M., Wade, B., Hand, M. and Barovich, K. 2007a. Timing of Proterozoic high-grade metamorphism in the Barossa Complex, southern South Australia: exploring the extent of the 1590 Ma event. *MESA Journal* 47, 21–27. Department of Primary Industries and Resources South Australia, Adelaide.

Szpunar, M.A., Hand, M., Barovich, K.M., Jagodzinski, E.A. and Belousova, E. 2007b. Detrital zircon in the southern Gawler, Curnamona and Barossa Complex: Where does it come from? In Reid A and McAvaney S eds. *Primary Industries and Resources SA, University of Adelaide and Monash University, ARC Linkage Program: 2007 Reporting day abstract volume*. Report Book 2008/1. Department of Primary Industries and Resources South Australia, Adelaide.

Talbot, J. L. 1963. Retrograde metamorpism of the Houghton Complex, South Australia. *Transactions of the Royal Society of South Australia* 87, 185–196.

Teale, G. S., and Fanning, C. M. 2000. The timing of Cu-Au mineralisation in the Curnamona Province. In M Peljo ed. *Broken Hill Exploration Initiative: abstracts of papers presented at the May 2000 conference in Broken Hill.* Record 2000/10. Australian Geological Survey Organisation, Canberra. 98–100.

Thorkelson, D.J., Mortensen, J.K., Davidson, G.J., Creaser, R.A., Perez, W.A. and Abbott, J.G. 2001. Early Mesoproterozoic intrusive breccias in Yukon, Canada: the role of hydrothermal systems in reconstructions of North America and Australia. *Precambrian Research,* 111, 31–35.

Vassalo J. J. and Wilson C. J. L. 2002 Palaeoproterozoic regional-scale non-coaxial deformation: an example from eastern Eyre Peninsula, South Australia, Journal of Structural Geology, vol. 24, no. 1, pp. 1-24.

Wade C. E., Reid A. J., Wingate M. T. D., Jagodzinski E. A. and Barovich K. 2012. Geochemistry and geochronology of the c. 1585 Ma Benagerie Volcanic Suite, southern Australia: relationship to the Gawler Range Volcanics and implications for the petrogenesis of a Mesoproterozoic silicic large igneous province. *Precambrian Research* 206–207, 17–35.

Wade, B. P., Barovich, K. M., Hand, M., Scrimgeour, I. and Close, D. F. 2006. Evidence for early Mesoproterozoic arc magmatism in the Musgrave Block, Central Australia: implications for Proterozoic crustal growth and tectonic reconstructions of Australia. *Journal of Geology* 114, 43–63.

Wade, B., Kelsey, D. E., Hand, M. and Barovich, K. M. 2008. The Musgrave Province: Stitching north, west and south Australia. *Precambrian Research* 166, 370–386.

Wade, C. E. 2011. Definition of the Mesoproterozoic Ninnerie Supersuite, Curnamona Province, South Australia. *MESA Journal* 62, 35–42. Department of Primary Industries and Resources South Australia, Adelaide.

Webb, B.P. 1953. Structure of the Archaean complex of the Mount Lofty Ranges. MSc thesis, University of Adelaide.

Webb, G. and Crooks, A. 2005. Metamorphic investigation of the Palaeoproterozoic metasediments of the Willyama Inliers, southern Curnamona Province—a new isograd map. *MESA Journal* 37, 53–57. Department of Primary Industries and Resources South Australia, Adelaide.

Williams, I.S. 1998. U–Th–Pb geochronology by ion microprobe, *in* Applications of Microanalytical Techniques to Understanding Mineralizing Processes *edited by* MA McKibben, WC Shanks III, WI Ridley: *Reviews in Economic Geology*, 7, 1–35.

APPENDIXES

Contents

Tables

Figures

APPENDIX 1: ANALYTICAL PROCEDURES

SAMPLE PROCESSING

The locations of field samples (± 50 m) were determined using a hand-held GPS. Unless otherwise stated, grid references in this record refer to the Geocentric Datum of Australia 1994 (GDA94). Locations mentioned in the text are referenced using Map Grid Australia (MGA) coordinates.

All samples were processed at the Geoscience Australia Geochronology Laboratories. Zircons were separated and concentrated by crushing, Wilfley table, Franz magnetic separation, density separation in methylene iodide (3.3 g/ml) and handpicking. For all samples, zircon selection was biased towards the least magnetic, clearest grains, without discrimination between grain morphologies. Where available, several hundred zircon grains per sample were selected for mounting by handpicking using a binocular microscope. The zircon grains were encapsulated in 25mm diameter epoxy discs, together with the multi-grain zircon standards QGNG (Mount Z4697) or for mount GA6054, Temora 2 (U-Pb standard) and OG1 ($^{207}Pb/^{206}Pb$ standards). A small quantity of U concentration standard SL13 was also mounted. The epoxy discs were polished to expose the interiors of the crystals in section. All grains were photographed in transmitted and reflected light, and with a cathodoluminescence (CL) detector, to ensure that analyses were made on discrete growth phases. These images were obtained with a JEOL JSM-6490LV scanning electron microscope located at Geoscience Australia and operating at 15 keV with a working distance of 16 mm. All SHRIMP mounts were ultrasonically cleaned in petroleum spirit, rinsed in quartz-distilled water and gold-coated with high purity gold.

DATA ACQUISITION AND PROCESSING

Data were collected during six analytical sessions on SHRIMP IIA at Curtin University in Perth (Z4697) and SHRIMP IIe at Geoscience Australia in Canberra (GA6054) using a primary oxygen ion beam of variable intensity (1.1 – 3.7 nA) and c. 20 microns diameter. Secondary ions were collected on a single electron multiplier via cycling of the magnet through 6 scans across the mass range of interest.

Differential fractionation between U and Pb was monitored by reference to a $^{206}Pb/^{238}U$ ratio of 0.11261 for interspersed analyses of the QGNG zircon standard (1851.6 ± 0.6 Ma; Black et al. 2003) for mount Z4697, and a ratio of 0.0668 for interspersed analyses of the Temora 2 zircon standard (416.8 ± 0.3 Ma; Black et al. 2004) for mount GA6054, based on the power law relationship $^{206}Pb^+/U^+ = a(UO^+/U^+)^b$, where a and b are session-dependent constants determined from measurements of Temora 2. The calibration exponent b has a canonical value of 2 (Williams et al. 1998, Claouè-Long et al. 1995), but its value is calculated independently for each session by calculating the slope of the robust regression of $\ln(^{206}Pb^+/^{238}U^+)$ vs $\ln(^{254}UO^+/^{238}U^+)$.

Elemental U concentrations in the unknown zircons were calibrated using SL13 reference zircon (238 ppm U), and the power law relationship $[^{196}Zr_2O^+/^{238}U^+] = A[^{254}UO^+/^{238}U^+]^{0.66}$, where A is a session-dependent constant determined from measurements of the reference zircon (Claouè-Long et al. 1995). Th/U ratios were derived from the linear relationship $^{232}ThO/^{238}U = (0.03446.UO^+/U^+ + 0.868).ThO^+/UO^+$ (Williams et al. 1998).

The U-Pb standards QGNG and Temora 2 were also used to monitor isobaric interference at the ^{204}Pb mass peak. On mount GA6054, the OG1 zircon standard (3465.4 ± 0.6 Ma; Stern et al. 2009) was used to monitor $^{207}Pb/^{206}Pb$ reproducibility and accuracy.

DATA PRESENTATION

Data were processed using the SQUID 2.5 software of (Ludwig 2001), using the U and Th decay constants of Jaffey et al. (1971), as recommended by Steiger and Jäger (1977). Correction for common Pb was made using measured $^{204}Pb/^{206}Pb$ and contemporaneous common-Pb isotopic compositions determined according to the model of Stacey and Kramers (1975). Uncertainties are quoted at the 95% ($t\sigma$) confidence level. Ages and the corresponding uncertainties are rounded to the nearest integer. All data from individual analyses are tabulated with 1σ uncertainty, and the tabulated data are all common-Pb corrected. Data are plotted using ISOPLOT/EX 3.71 (Ludwig 2003) and AgeDisplay (Sircombe 2004), and are displayed with 1σ precision.

APPENDIX 2: MOUNT Z4697: SHRIMP IIB, CURTIN UNI, 3-8 AUG 2015

Samples R695754 (MI1), R695753 (HI3) and R695752 (HI2).

Primary beam ~2.8-3.2 nA. 7 scan data through 9 mass stations (R695752 and R695754), 5 scan data through 9 mass stations (R695753).

Analyst and data processing: E.A.Jagodzinski

Only one standard, QGNG, was analysed during this session (n = 52). A significant shift in the Pb/U calibration occurred on day 3 of the analytical session, corresponding to the Duo Plasmatron switching off several times (i.e. the arc dropping out). The calibration shift is clearly defined, following the 26th analysis of the QGNG standard (Fig. A.1). Data for this session are consequently processed as two separate batches. The analyses for both batches are corrected for overcounts at mass ^{204}Pb (calculated assuming ^{206}Pb/^{238}U-^{207}Pb/^{235}U age concordance). This forces the weighted mean ^{207}Pb/^{206}Pb age for QGNG to the TIMS reference value (1851.6 ± 0.6 Ma) and improves the scatter in the data set.

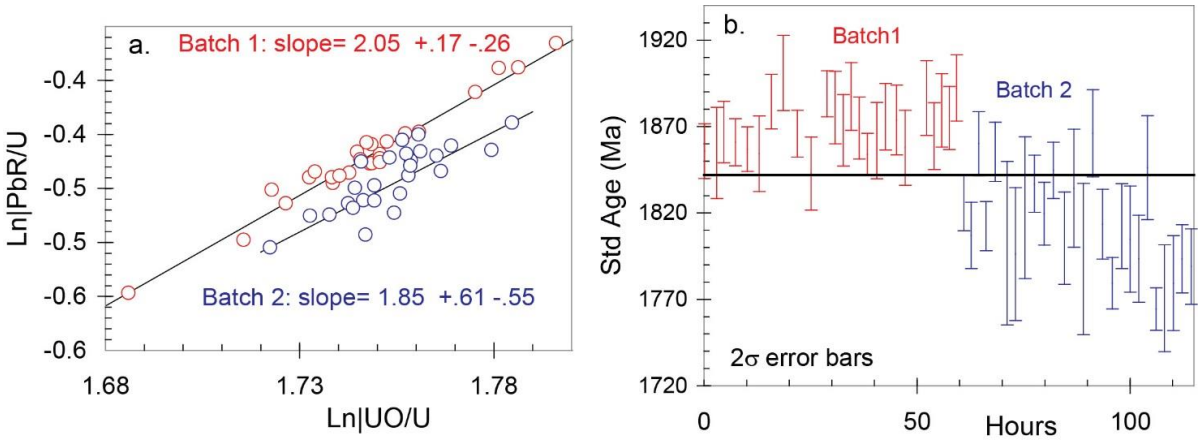

Figure A1 (a) Pb/U calibrations for mount Z4697 (analysis date 3-8 Aug 2005; SHRIMP IIB, Curtin University); and **(b)** variation in ^{206}Pb/^{238}U ages for QGNG with time, showing an obvious calibration shift in the middle of the session.

BATCH 1

The QGNG analyses for batch 1 (901.1-926.1) yield a calibration exponent of 2.05, with an upper limit of 2.22 and lower limit of 1.79 (at 95% confidence level). Thus the nominal value of 2.0 has been used in data reduction. The ^{206}Pb/^{238}U calibration error is 0.17% (1σ), with an external spot-to-spot error of 0.63% (1σ; MSWD = 2.41, probability of fit = 0). A more realistic value of 1% has been applied to the data processing. There is evidence overcounts on the Pb peaks (Table A.1), and an overcount correction has been applied to the data from this batch.

The analyses yield a weighted mean ^{207}Pb/^{206}Pb age of 1848.3 ± 3.3 Ma (MSWD = 1.5; probability of fit = 0.06; n = 26 of 26). After the overcount correction is applied, the age becomes 1851.9 ± 3.1 Ma (MSWD = 0.91, probability of fit = 0.59).

BATCH 2

The standard analyses for batch 2 (927.1-952.1) have a calibration exponent of 1.85, with an upper limit of 2.46 and a lower limit of 1.30 (at 95% confidence level). Thus the nominal value of 2.0 has been used in data reduction. The ^{206}Pb/^{238}U calibration error is 0.35% (1σ), with a high external spot-to-spot error of 1.62% (1σ; n = 26 of 26). There is evidence overcounts on the Pb peaks (Table A.1), and an overcount correction has been applied to the data from this batch.

The analyses yield a weighted mean $^{207}Pb/^{206}Pb$ age of 1842.3 ± 2.9 (MSWD = 0.87, probability of fit = 0.64, n = 26 of 26). After the overcount correction is applied, the age becomes 1851.5 ± 3.4 Ma (MSWD = 0.59, probability of fit = 0.95).

Element abundance calibration was based on two analyses of SL13 (U = 238 ppm).

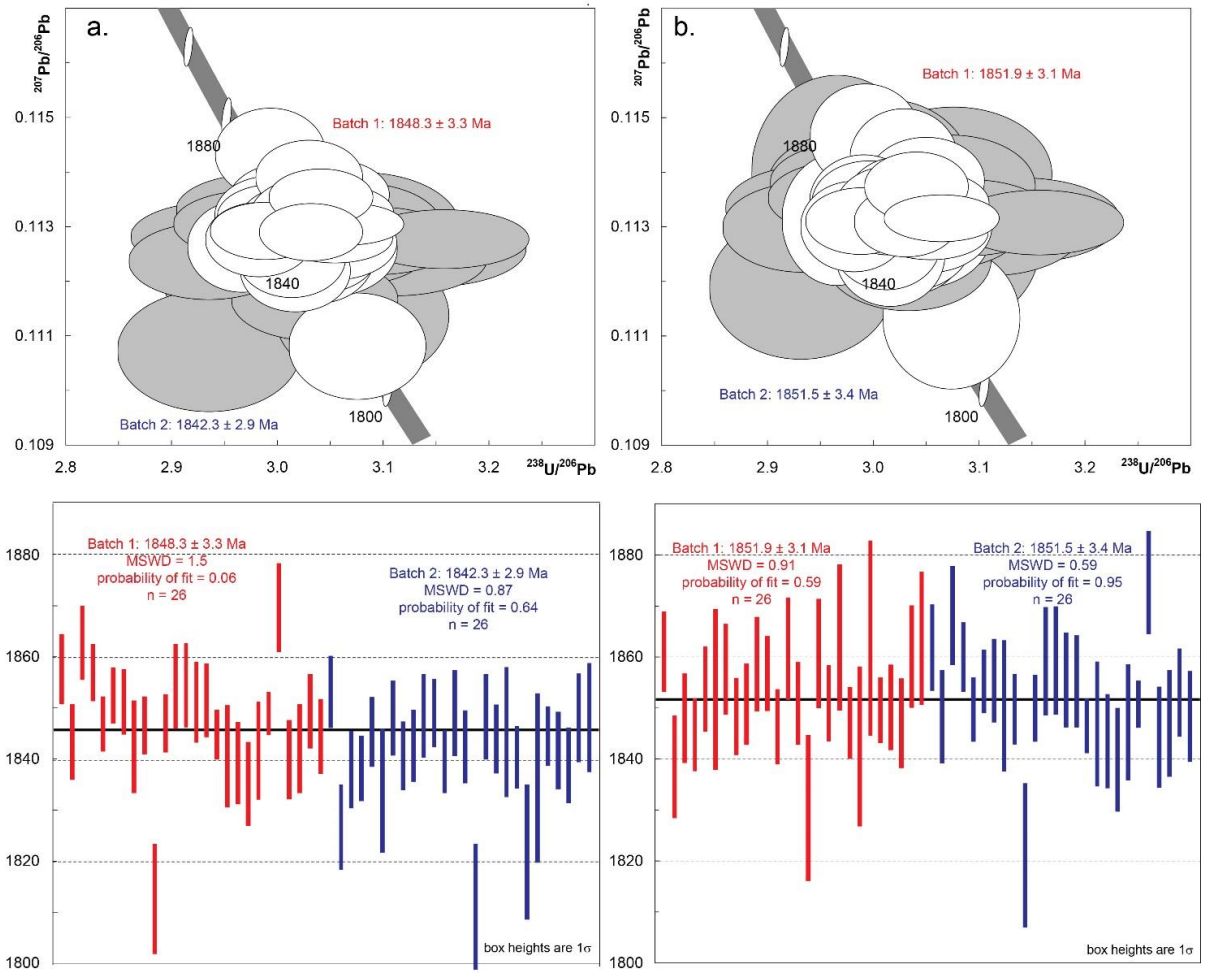

Figure A2 A comparison of **(a)** uncorrected; and **(b)** overcount-corrected data for QGNG. Tera-Wasserburg concordia plots (above). White ellipses represent analyses collected in Batch 1 and grey Batch 2. $^{207}Pb/^{206}Pb$ ages plotted in order of acquisition below). Red analyses represent Batch 1 and blue Batch 2.

Table A.1 SHRIMP analyses of the zircon standard QGNG, 3-8 AUG 2015, SHRIMP IIB, Curtin University

Batch 1 Spot Name	4-corr %com 206	ppm U	ppm Th	232Th /238U	4-corr 206Pb /238U calibr. const	% err	Age (Ma)	±1σ	Ln UO/U	Ln PbR/U	204 overcts /sec (fr. 207)	204 overcts /sec (fr. 208)	4-corr 207Pb /206Pb age	±1σ	4-corr 207Pb /206Pb	% err
901.1	0.05	213	113	0.55	0.01964	0.63	1827	10	1.75	-0.43	-0.11	0.13	1858	7	0.11358	0.37
902.1	0.06	226	153	0.70	0.01963	0.82	1826	13	1.74	-0.44	0.13	0.18	1843	7	0.11270	0.40
903.1	0.01	201	205	1.05	0.01977	0.46	1838	7	1.74	-0.44	-0.16	0.35	1863	7	0.11391	0.39
904.1	-0.01	352	336	0.98	0.01970	0.35	1832	6	1.75	-0.42	-0.13	0.34	1857	5	0.11354	0.30
905.1	0.02	416	374	0.93	0.01965	0.58	1828	9	1.74	-0.44	0.14	0.27	1847	5	0.11291	0.29
906.1	0.03	416	369	0.92	0.01962	0.68	1826	11	1.75	-0.43	-0.02	0.02	1852	5	0.11326	0.29
907.1	-0.01	220	232	1.09	0.01999	0.64	1856	10	1.73	-0.44	0.01	-0.08	1851	6	0.11318	0.34
908.1	0.03	132	117	0.91	0.02019	0.55	1872	9	1.72	-0.45	0.09	0.21	1842	9	0.11264	0.49
909.1	0.02	296	291	1.02	0.01976	0.35	1837	6	1.73	-0.46	0.13	0.49	1847	6	0.11290	0.31
910.1	0.14	110	57	0.53	0.01948	0.95	1815	15	1.72	-0.50	0.37	0.12	1813	11	0.11081	0.58
911.1	0.05	337	342	1.05	0.02005	0.55	1860	9	1.73	-0.43	0.13	0.56	1847	6	0.11292	0.31
912.1	-0.01	194	173	0.92	0.01995	0.54	1852	9	1.75	-0.41	-0.04	0.13	1854	8	0.11337	0.45
913.1	-0.01	191	160	0.86	0.01979	0.53	1839	9	1.75	-0.41	-0.04	0.08	1854	8	0.11338	0.45
914.1	-0.02	217	157	0.75	0.02003	0.50	1859	8	1.74	-0.42	0.01	-0.19	1851	8	0.11318	0.43
915.1	-0.01	259	254	1.01	0.01980	0.46	1841	7	1.75	-0.42	0.00	0.50	1851	7	0.11320	0.39
916.1	0.02	585	343	0.60	0.01962	0.60	1825	10	1.75	-0.42	0.33	0.10	1845	5	0.11278	0.26
917.1	0.06	176	123	0.72	0.01971	0.57	1833	9	1.69	-0.55	0.14	-0.06	1841	10	0.11252	0.54
918.1	0.04	233	232	1.03	0.01988	0.49	1847	8	1.75	-0.41	0.23	0.16	1839	8	0.11244	0.44
919.1	0.02	211	216	1.06	0.01986	0.52	1845	8	1.76	-0.40	0.28	0.19	1835	8	0.11219	0.44
920.1	0.07	183	172	0.97	0.01966	1.02	1829	16	1.74	-0.44	0.14	-0.23	1842	9	0.11259	0.52
920.0	0.01	562	257	0.47	0.01955	0.60	1820	9	1.75	-0.43	0.12	-0.13	1849	4	0.11304	0.22
922.1	-0.05	172	127	0.77	0.02001	0.55	1858	9	1.80	-0.32	-0.29	0.07	1870	9	0.11434	0.48
923.1	0.01	216	225	1.08	0.01975	0.81	1836	13	1.76	-0.40	0.21	0.08	1840	8	0.11248	0.42
924.1	0.05	186	118	0.66	0.01993	0.54	1851	9	1.79	-0.34	0.15	0.39	1842	9	0.11261	0.47
925.1	0.02	246	254	1.07	0.01987	0.47	1846	8	1.77	-0.36	0.05	0.62	1849	7	0.11307	0.39
926.1	-0.01	225	236	1.08	0.02009	0.49	1863	8	1.78	-0.34	0.15	0.45	1844	7	0.11276	0.40
										ave	0.08	0.18	1847			
										err	0.06	0.09	±4			

Spot Name	4-corr %com 206	% err	ppm U	ppm Th	232Th /238U	4-corr 206Pb /238U calibr. const	% err	Age (Ma)	±1σ	Ln UO/U	Ln PbR/U	204 overcts /sec (fr. 207)	204 overcts /sec (fr. 208)	4-corr 207Pb /206Pb age	±1σ	4-corr 207Pb /206Pb	% err
927.1	0.05	0.55	325	203	0.65	0.01939	0.48	1864	8	1.73	-0.48	-0.04	0.10	1853	7	0.11330	0.38
928.1	0.03	0.57	214	176	0.85	0.01905	0.51	1835	8	1.75	-0.46	0.42	0.14	1827	8	0.11167	0.45
929.1	0.02	0.49	236	225	0.99	0.01969	0.48	1889	8	1.76	-0.41	0.27	0.36	1838	7	0.11236	0.41
930.1	0.05	0.41	422	393	0.96	0.01911	0.38	1841	6	1.72	-0.50	0.41	0.42	1838	6	0.11237	0.34
931.1	0.01	0.44	275	276	1.04	0.01964	0.86	1884	14	1.76	-0.40	0.15	1.09	1845	7	0.11282	0.37
932.1	0.13	0.99	103	61	0.61	0.01899	1.50	1831	24	1.74	-0.46	0.18	0.12	1834	12	0.11210	0.66
933.1	-0.01	0.48	254	241	0.98	0.01892	1.23	1824	19	1.74	-0.47	0.07	-0.58	1848	7	0.11299	0.40
934.1	0.02	0.48	323	233	0.74	0.01924	1.29	1852	21	1.76	-0.42	0.28	0.04	1841	7	0.11253	0.36
935.1	0.04	0.45	298	280	0.97	0.01941	0.74	1866	12	1.76	-0.42	0.22	0.03	1843	7	0.11265	0.38
936.1	0.07	0.53	251	221	0.91	0.01920	0.48	1848	8	1.75	-0.45	0.06	0.22	1848	8	0.11301	0.44
937.1	-0.02	0.42	328	342	1.08	0.01950	0.42	1873	7	1.76	-0.42	0.07	0.79	1849	7	0.11305	0.36
938.1	0.00	0.39	264	265	1.03	0.01903	0.85	1834	14	1.74	-0.47	0.35	0.80	1840	6	0.11246	0.33
939.1	0.01	0.55	159	147	0.95	0.01938	1.07	1863	17	1.74	-0.45	0.04	0.06	1849	8	0.11305	0.46
940.1	0.04	0.96	217	194	0.92	0.01888	1.40	1821	22	1.75	-0.46	0.22	0.26	1842	7	0.11264	0.39
941.1	0.15	0.99	107	63	0.61	0.01977	0.65	1895	11	1.75	-0.43	0.42	0.10	1811	12	0.11072	0.67
942.1	0.01	0.52	172	179	1.08	0.01913	0.53	1842	9	1.77	-0.41	0.05	0.27	1848	8	0.11300	0.45
943.1	0.06	0.84	324	236	0.75	0.01871	0.40	1807	6	1.77	-0.43	0.22	0.26	1844	7	0.11273	0.36
944.1	0.22	0.79	124	111	0.93	0.01911	0.65	1841	10	1.77	-0.42	0.07	0.14	1845	13	0.11281	0.69
945.1	0.01	0.42	371	302	0.84	0.01902	0.98	1833	16	1.76	-0.44	0.33	-0.50	1840	6	0.11251	0.33
946.1	0.19	1.11	123	70	0.58	0.01889	0.67	1822	11	1.76	-0.43	0.29	0.24	1822	13	0.11137	0.72
947.1	0.30	1.31	92	57	0.65	0.01952	0.78	1875	13	1.75	-0.42	0.11	0.24	1836	16	0.11226	0.90
948.1	0.09	0.36	427	407	0.99	0.01854	0.33	1792	5	1.75	-0.47	0.28	0.46	1844	6	0.11277	0.32
949.1	0.09	0.47	277	275	1.02	0.01861	1.00	1798	16	1.75	-0.49	0.23	0.31	1842	7	0.11259	0.41
950.1	0.08	0.53	244	174	0.74	0.01872	0.88	1807	14	1.78	-0.41	0.31	0.32	1839	7	0.11241	0.40
951.1	0.05	0.70	173	101	0.60	0.01888	0.53	1822	8	1.78	-0.39	0.06	0.18	1848	9	0.11299	0.47
952.1	0.12	1.00	149	70	0.48	0.01883	1.09	1817	17	1.76	-0.45	0.04	0.05	1848	11	0.11299	0.58
											ave	0.20	0.23	1841			
											err	±0.06	±0.13	±3			

APPENDIX 3: MOUNT GA6054

Mount GA6054 was analysed over five sessions, between May 2008 and February 2010. For three of the 6 samples on the mount, data from multiple sessions have been merged to produce the final data set (Table A.). For two of the five sessions, the measured age of the $^{207}Pb/^{206}Pb$ standard, OG1, was not within error of its TIMS reference value of 3465.4 ± 0.6 Ma, and over the five sessions, the SHRIMP ages varied by 5 m.y. (Table A.). For these reasons a $^{207}Pb/^{206}Pb$ correction for instrumental mass fractionation (IMF) has been applied to all unknown $^{207}Pb/^{206}Pb$ ages and ratios collected from this mount, following the recommendations outlined in Stern et al. (2009). This normalises all unknown ages, so that ages generated in different sessions can be directly compared. The IMF correction factor (α) is calculated as follows:

$$\alpha = [^{207}Pb^*/^{206}Pb^*]_{STD}/[^{207}Pb^*/^{206}Pb^*]_{RM}$$

That is, tthe measured ratio of OG1 in the analytical session, divided by the reference value determined by multiple TIMS analyses. For all sessions, the calculated IMF correction is applied by dividing the $^{207}Pb^*/^{206}Pb^*$ ratio of each analysis of an unknown sample by α. The IMF-corrected ratios (and their uncorrected errors) are then pooled as appropriate, and the pooled ratios are used to calculate weighted mean $^{207}Pb^*/^{206}Pb^*$ ages using the Isoplot worksheet toolbar.

Uncertainties in pooled $^{207}Pb^*/^{206}Pb^*$ ages are augmented by adding in quadrature the relative uncertainty of the pooled $^{207}Pb^*/^{206}Pb^*$ ratio of the sample age and the relative uncertainty of the $^{207}Pb^*/^{206}Pb^*$ ratio of the standard in that session. That is,

$$\sigma = \sqrt{(\sigma_{unk}^2 + \sigma_{OG1}^2)}$$

where each of the σ refers to a “relative” uncertainty (ie expressed as a percentage), unk refers to the pooled $^{207}Pb^*/^{206}Pb^*$ ratio measured on the unknown sample, and OG1 refers to the pooled $^{207}Pb^*/^{206}Pb^*$ ratio measured on OG1 for the session. This formula gives you a “relative” uncertainty on the corrected $^{207}Pb^*/^{206}Pb^*$ age, which then must be converted to an absolute uncertainty (Ma). For multiple sessions, the relative uncertainty of the $^{207}Pb^*/^{206}Pb^*$ ratio of OG1 for each session is added to the formula.

$$\sigma = \sqrt{(\sigma_{unk}^2 + \sigma_{OG1}(session1)^{2+} + \sigma_{OG1}(session2)^{2+} + \sigma_{OG1}(session3)^{2+} \ldots\ldots etc)}.$$

Table A2. Key to analyses collected in the different sessions for mount GA6054

LIMS	date	1001	1002	1003	1004	1005	1006
80081	12-16th May 2008		1.1 - 16.1	1.1 - 3.1		1.1 - 69.1	1.1 - 66.1
80083	16-18th May 2008	1.1-68.1					68.1 - 83.1
80126	30 Sep-2 Oct 2008	73.1-111.1		4.1-20.1			84.1-95.1
90032	7-8th Apr 2009			21.1 - 48.1			
100027	15-17th Feb 2010			49.1-75.1	1.1-39.1		

Table A3. Results for OG1 reference zircon analysed during all SHRIMP sessions for mount GA6054.

GA LIMS session	n	weighted mean $^{207}Pb^*/^{206}Pb^*$ age (Ma)	± Ma (MSWD)	weighted mean $^{207}Pb^*/^{206}Pb^*$	±	IMF factor α
80081	18	3467.6	2.0 (1.20)	0.29948	0.00038 [0.13%]	1.00137
80083	11	3465.9	3.5 (1.30)	0.29915	0.00068 [0.23%]	1.00027
80126	9	3465.6	2.9 (1.30)	0.29911	0.00057 [0.19%]	1.00013
90032	5	3466.3	8.3 (1.6)	0.29920	0.0016 [0.53%]	0.99957
100027	12	3462.4	2.5 (0.47)	0.29849	0.00048 [0.16%]	0.99803

Appendix 3.1: SHRIMP IIE Ga; 12-16 MAY 2008, Mount Ga6054

Samples R1588240 (analyses 1003.1.1.1 – 1003.3.1.1, n=4), R1588243 (analyses 1006.1.1.1 – 1006.66.1.1), R1009273 (all 17 analyses) and R1009242 ((all 72 analyses).

LIMS session 80081. Analyst G.Fraser and M.Szpunar. Data processing E.Jagodzinski. Processing software: SQUID 2.50.11.02.03, rev. 03 Feb 2011

6 scan data through 10 mass stations. Primary beam ~3.7 nA, dropping to ~ 2.5 nA after 8.00 a.m. on 15th May, after resuming session following a primary beam drop out and auto run failure overnight (2.00 a.m. – 7.30 a.m.).

In the middle of this session, the arc dropped out during an overnight autorun. Data continued to be collected for the next 5 hours with a low beam current. High ^{204}Pb counts (Table A3.), causing high % common Pb, and imprecise analyses (Fig. A3), indicate there was a problem with peak centring, so all analyses collected during this interval are discarded. That is, T.26-T.28, OG14.1.1 and OG.14.2.1, and 1006.12.1.1-24.1.1.

ASSESSMENT OF CALIBRATION

When the three imprecise analyses collected during the failed autorun are eliminated, the remaining analyses have a calibration exponent of 1.72 (lower limit 1.26 upper limit 2.08, Figure), which is still within error of the nominal value of 2, and a calibration error 0.31% (1σ). The external spot to spot error is high, at 1.67 % (1σ).

ASSESSMENT OF ^{207}PB/^{206}PB AGES

When the two analyses of OG1 collected during the failed autorun are eliminated, the remaining 19 analyses do not conform to a simple population (MSWD = 2.3). SQUID identifies the youngest analysis (OG1.4.2.1) as an outlier (Fig.). The remaining eighteen analyses yield a ^{207}Pb/^{206}Pb age of 3467.6 ± 2.0 Ma (MSWD = 1.2, probability = 0.23, Fig. A). A correction for instrumental mass fractionation (IMF) of 1.00137 has been applied to the session.

The ^{207}Pb /^{206}Pb age of Temora is 394 ± 32 Ma (Tukey's biweight), or 430 ± 24 Ma (weighted mean), and there is no evidence of overcounts on the Pb peaks (Table A.1).

Element abundance calibration was based on standard SL13 (n = 1, U = 238 ppm).

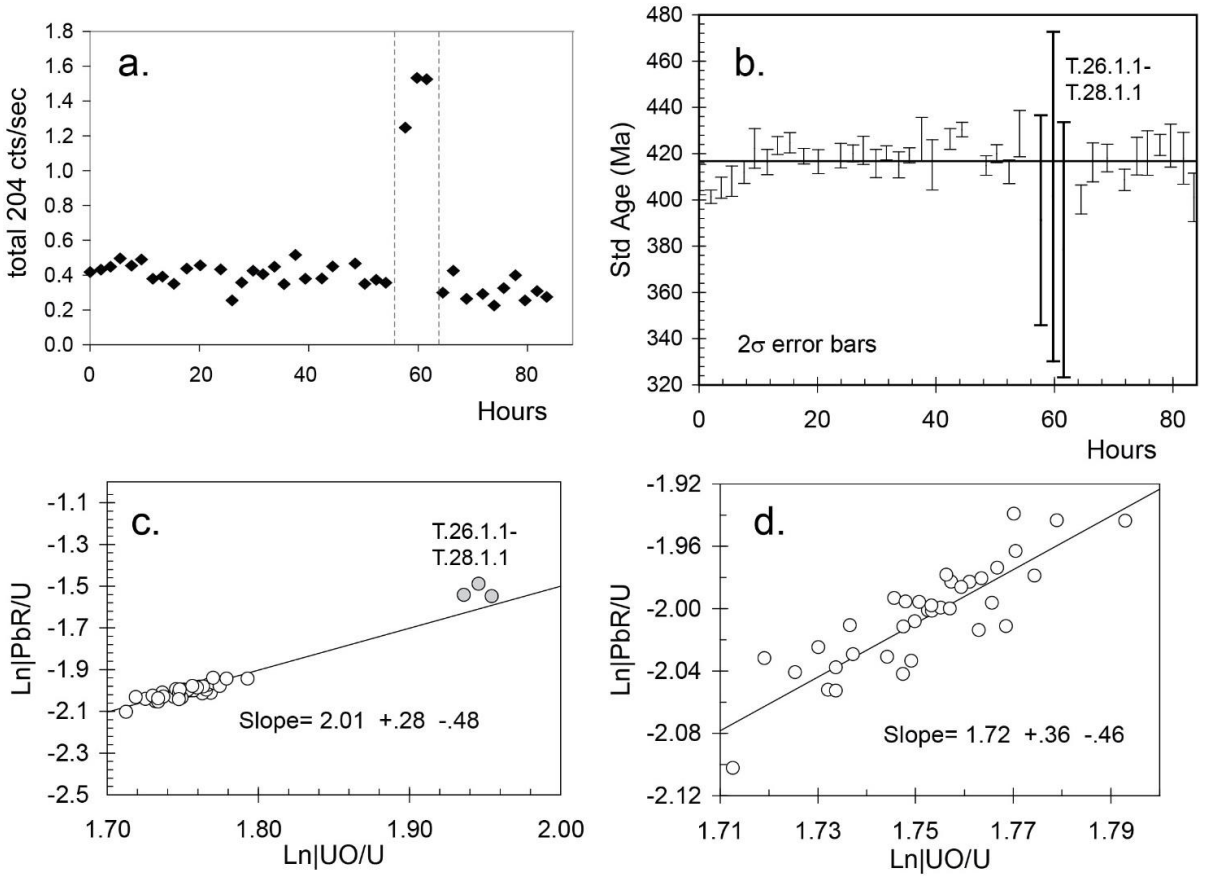

Figure A3. (a) Change in the ^{204}Pb counts vs time, showing the five hour period when the primary beam failed, between the dashed lines. All data collected during this period have been removed from the final data sets **(b)** ^{206}Pb/^{238}U ages for Temora 2. Thick lines represent iscarded analyses **(c)** Pb/U calibration for mount GA6054, analysis date 12-16 May 2008; SHRIMP IIe, GA: all analyses **(d)** Pb/U calibration reconstructed with the aberrant analyses eliminated. The slope changes, but is still within error of the nominal value of 2.

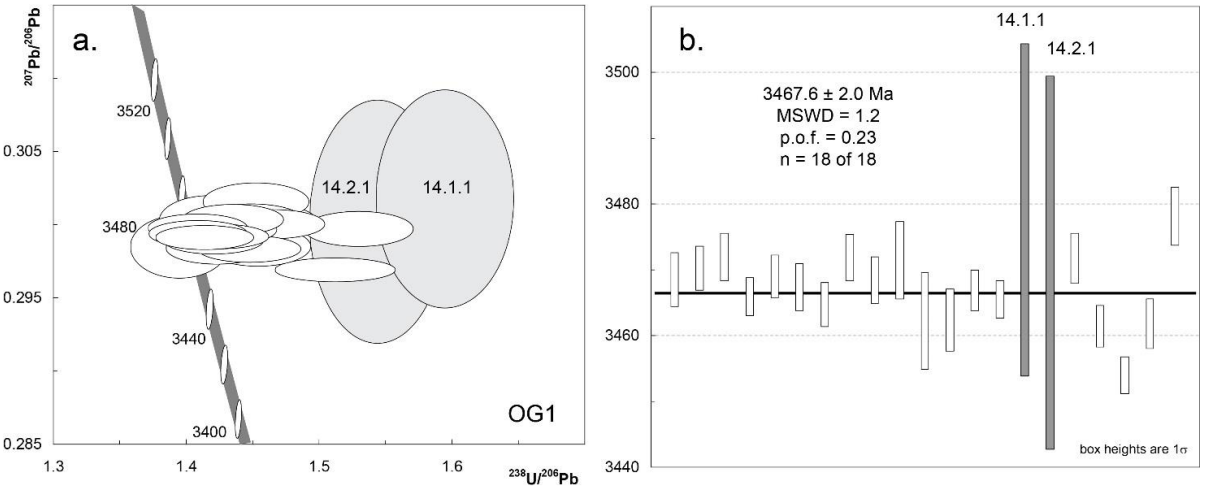

Figure A4. (a) ^{207}Pb/^{206}Pb ages for OG1 standard analyses. **(b)** Concordia diagram for all analyses of OG1. Discarded analyses are grey.

Table A4. SHRIMP analyses of the zircon standard Temora, for 12-16 May 2008, SHRIMP IIe, Geoscience Australia.

Spot Name	4-corr %com 206	ppm U	ppm Th	232Th /238U	Ln UO/U	Ln PbR/U	4-corr 206Pb /238U calibr. const	% err	Age (Ma)	±1σ	204 overcts /sec (fr. 207)	204 overcts /sec (fr. 208)	4-corr 207Pb /206Pb age	±1σ	4-corr 207Pb /206Pb	% err
T.1.1.1	0.26	227	84	0.384	1.79	-1.94	0.0039	0.83	409	3	0.00	0.01	417	31	0.0551	1.40
T.2.1.1	0.22	296	143	0.499	1.77	-2.01	0.0039	0.38	401	1	-0.08	-0.26	456	27	0.0561	1.22
T.3.1.1	0.56	120	38	0.324	1.76	-2.01	0.0039	0.58	405	2	-0.05	0.06	474	53	0.0565	2.39
T.4.1.1	0.59	187	89	0.491	1.77	-2.00	0.0039	0.82	408	3	0.11	0.20	366	61	0.0539	2.73
T.4.2.1	0.97	115	34	0.303	1.73	-2.05	0.0040	0.61	412	2	0.05	0.13	344	73	0.0534	3.24
T.5.1.1	1.08	111	30	0.278	1.74	-2.01	0.0041	1.05	422	4	0.12	0.16	251	81	0.0512	3.53
T.6.1.1	0.83	88	26	0.311	1.75	-2.00	0.0040	0.67	416	3	-0.04	-0.06	479	70	0.0567	3.16
T.7.1.1	0.18	181	80	0.457	1.75	-2.00	0.0041	0.47	423	2	-0.15	-0.11	532	31	0.0581	1.42
T.8.1.1	0.30	143	41	0.297	1.73	-2.04	0.0041	0.53	425	2	-0.05	-0.02	473	41	0.0565	1.87
T.10.1.1	0.40	269	138	0.532	1.77	-1.97	0.0040	0.41	419	2	0.09	0.20	362	35	0.0538	1.55
T.11.1.1	0.91	116	38	0.334	1.75	-2.00	0.0040	0.64	416	3	0.11	0.09	251	94	0.0512	4.09
T.12.1.1	0.92	109	33	0.317	1.77	-1.96	0.0040	0.65	419	3	-0.03	-0.05	460	70	0.0562	3.15
T.12.2.1	0.04	228	58	0.263	1.75	-2.01	0.0040	0.45	420	2	-0.15	-0.17	526	25	0.0579	1.16
T.13.1.1	0.61	85	30	0.369	1.76	-1.98	0.0041	0.75	421	3	-0.01	0.04	445	71	0.0558	3.20
T.14.1.1	0.84	83	26	0.331	1.77	-1.98	0.0040	0.75	416	3	0.01	-0.01	403	100	0.0548	4.48
T.15.1.1	0.25	335	172	0.530	1.76	-1.98	0.0040	0.38	420	2	-0.05	0.00	444	27	0.0558	1.23
T.16.1.1	1.26	108	54	0.518	1.74	-2.03	0.0040	0.70	415	3	0.14	0.15	159	116	0.0492	4.98
T.15.2.1	0.11	304	151	0.515	1.76	-2.00	0.0040	0.40	419	2	-0.09	-0.04	466	25	0.0563	1.14
T.17.1.1	0.67	170	79	0.478	1.75	-1.99	0.0041	1.15	426	5	0.14	0.26	326	126	0.0529	5.57
T.18.1.1	0.76	73	23	0.329	1.76	-1.98	0.0040	1.35	415	5	-0.05	0.02	538	80	0.0582	3.65
T.19.1.1	0.63	147	56	0.397	1.73	-2.02	0.0041	0.55	426	2	0.09	0.03	310	57	0.0526	2.49
T.20.1.1	0.34	317	81	0.264	1.77	-1.94	0.0041	0.38	430	2	0.11	0.20	366	30	0.0539	1.33
T.21.1.1	0.70	153	50	0.334	1.76	-2.00	0.0040	0.53	415	2	0.05	0.12	366	54	0.0539	2.41
T.22.1.1	0.40	197	95	0.499	1.75	-2.00	0.0040	0.47	420	2	0.04	0.09	384	40	0.0543	1.80
T.23.1.1	0.55	111	30	0.281	1.73	-2.05	0.0040	0.65	412	3	-0.03	-0.01	465	60	0.0563	2.70

Spot Name	4-corr %com 206	ppm U	ppm Th	232Th /238U	Ln UO/U	Ln PbR/U	4-corr 206Pb /238U calibr. const	% err	Age (Ma)	±1σ	204 overcts /sec (fr. 207)	204 overcts /sec (fr. 208)	4-corr 207Pb /206Pb age	±1σ	4-corr 207Pb /206Pb	% err
T.24.1.1	0.57	156	74	0.488	1.72	-2.03	0.0041	1.21	428	5	0.04	0.10	376	53	0.0541	2.36
T.29.1.1	0.84	116	56	0.495	1.75	-2.03	0.0038	0.81	400	3	0.06	0.09	302	85	0.0524	3.73
T.30.1.1	1.16	152	46	0.313	1.74	-2.03	0.0040	1.05	416	4	0.16	0.18	160	92	0.0493	3.94
T.31.1.1	0.76	112	32	0.290	1.76	-1.99	0.0040	0.73	418	3	0.00	0.07	418	76	0.0551	3.39
T.32.1.1	0.31	183	83	0.469	1.71	-2.10	0.0039	0.58	408	2	0.02	-0.05	392	49	0.0545	2.16
T.33.1.1	0.17	303	92	0.314	1.75	-2.01	0.0040	1.01	419	4	-0.07	0.07	464	30	0.0563	1.35
T.34.1.1	0.40	209	98	0.485	1.78	-1.94	0.0040	1.18	420	5	-0.05	-0.05	469	43	0.0564	1.94
T.35.1.1	0.58	195	59	0.311	1.75	-2.00	0.0041	0.55	424	2	0.06	0.13	354	54	0.0536	2.40
T.35.2.1	0.48	197	59	0.308	1.76	-1.98	0.0041	1.13	423	5	0.03	-0.06	382	49	0.0543	2.20
T.36.1.1	0.61	221	72	0.337	1.73	-2.04	0.0040	1.38	418	6	0.12	0.10	294	54	0.0522	2.39
T.37.1.1	1.28	78	22	0.296	1.75	-2.04	0.0039	1.35	401	5	-0.01	0.03	456	111	0.0561	5.00
										ave	0.02	0.05	394			
										err	0.03	0.04	±32			

Table A5. SHRIMP analyses of the zircon standard OG1 for 12-16 May 2008, SHRIMP IIe, Geoscience Australia.

Spot	4-corr %com 206	ppm U	ppm Th	232Th /238U	206Pb* /238U	±%	207Pb* /235U	±%	207Pb* /206Pb*	±%	207Pb /206Pb Age ± Ma		% Disc
OG1.1.1.1	0.05	133	77	0.60	0.653	1.76	27.00	1.78	0.2997	0.26	3469	4	8
OG1.2.1.1	0.03	160	98	0.63	0.682	1.75	28.21	1.76	0.3000	0.22	3470	3	4
OG1.3.1.1	0.03	146	131	0.92	0.690	1.76	28.57	1.77	0.3003	0.23	3472	4	3
OG1.4.1.1	0.02	214	207	1.00	0.701	1.73	28.93	1.74	0.2992	0.19	3466	3	1
OG1.5.1.1	0.02	166	78	0.48	0.709	1.74	29.32	1.76	0.2998	0.21	3469	3	0
OG1.6.1.1	0.05	147	136	0.95	0.708	1.76	29.23	1.77	0.2995	0.23	3467	4	1
OG1.6.2.1	0.04	196	93	0.49	0.703	1.74	28.99	1.76	0.2989	0.21	3465	3	1
OG1.7.1.1	0.04	200	169	0.88	0.696	1.74	28.83	1.76	0.3003	0.23	3472	4	2
OG1.8.1.1	0.03	161	140	0.90	0.699	1.76	28.88	1.77	0.2997	0.23	3468	4	2
OG1.9.1.1	0.02	157	135	0.89	0.705	1.76	29.18	1.80	0.3002	0.38	3471	6	1
OG1.10.1.1	0.04	304	208	0.71	0.716	1.73	29.48	1.79	0.2985	0.47	3462	7	-1
OG1.11.1.1	0.03	109	56	0.53	0.687	1.79	28.28	1.81	0.2985	0.30	3462	5	3
OG1.12.1.1	0.04	258	306	1.22	0.709	1.72	29.27	1.74	0.2994	0.20	3467	3	0
OG1.13.1.1	0.01	255	201	0.82	0.707	1.72	29.15	1.73	0.2991	0.18	3466	3	1
OG1.9.2.1	0.01	203	153	0.78	0.687	1.95	28.45	1.96	0.3003	0.25	3472	4	4
OG1.1.2.1	0.03	267	244	0.94	0.690	1.75	28.40	1.76	0.2983	0.20	3461	3	3
OG1.4.2.1	0.12	351	450	1.33	0.661	1.97	27.06	1.98	0.2969	0.18	3454	3	7
OG1.16.1.1	0.05	186	186	1.04	0.702	1.76	28.89	1.78	0.2984	0.24	3462	4	1
OG1.2.3.1	0.09	153	109	0.74	0.688	1.80	28.60	1.82	0.3015	0.28	3478	4	4
OG1.1.1.1	0.05	133	77	0.60	0.653	1.76	27.00	1.78	0.2997	0.26	3469	4	8
OG1.2.1.1	0.03	160	98	0.63	0.682	1.75	28.21	1.76	0.3000	0.22	3470	3	4

Appendix 3.2: SHRIMP II RSES; 16-18 MAY 2008, Mount Ga 6054

Samples R1009272 (analyses 1001.1.1.1 - 1001.68.1.1) and R1588243 (analyses 1006.68.1.1 – 1006.83.1.1)

LIMS session 80083. Analyst G.Fraser and M.Szpunar. Data processing E.Jagodzinski. Processing software: SQUID 2.50.11.02.03, rev. 03 Feb 2011

6 scan data through 10 mass stations (1001.1.1.1-1001.30.1.1). 3 scan data through 10 mass stations (1001.31.1.1-1001.68.1.1, and all 1006 analyses). The decision was made to include all analyses in the data processing. Primary beam ~ 2.5 nA.

ASSESSMENT OF CALIBRATION

Two standards, OG1 and Temora 2, were analysed during this session. Twenty three analyses of Temora have a calibration exponent of 1.81 (upper limit 1.99, lower limit 1.63). The nominal slope of 2 was applied to the session. The calibration error is 0.3% (1σ, MSWD = 1.96), with an external spot to spot error of 0.93%. A value of 1.0% was assigned.

ASSESSMENT OF ^{207}PB/^{206}PB AGES

11 analyses of OG1 yield a weighted mean ^{207}Pb/^{206}Pb age of 3465.9 ± 3.5 Ma (MSWD = 1.3, probability = 0.24, Figure), which is near identical to the TIMS reference age of 3465.4 ± 0.6 Ma. The IMF correction for the session is 1.00027.

The ^{207}Pb /^{206}Pb age of Temora is 335 ± 94 Ma (Tukey's biweight), or 430 ± 54 Ma (weighted mean), and there is no evidence of overcounts on the Pb peaks (Table A.1).

Element abundance calibration was based on standard SL13 (n = 1, U = 238 ppm).

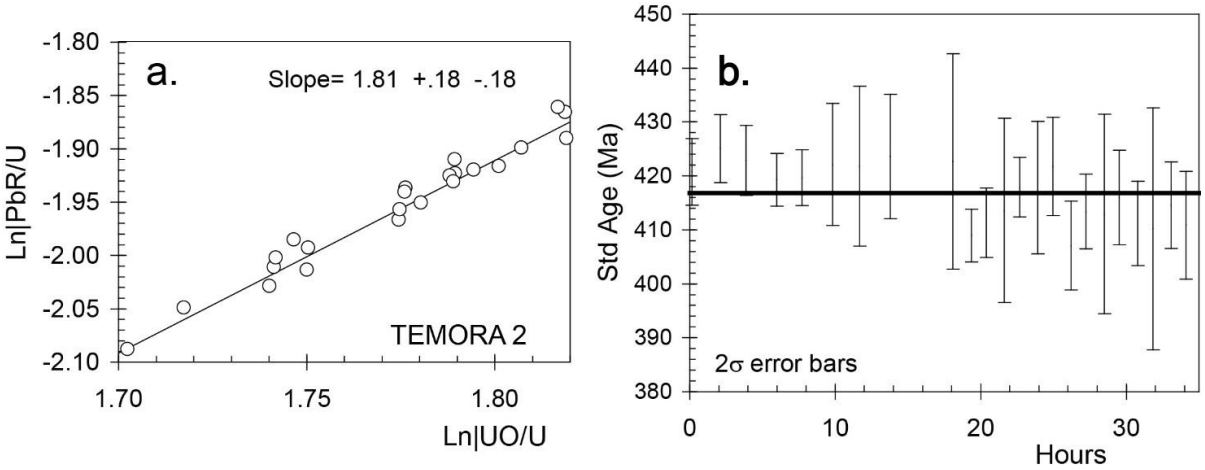

Figure A5. (a) Pb/U calibration for mount GA6054, analysis date 12-16 May 2008; SHRIMP IIe, GA. **(b)** ^{206}Pb/^{238}U ages for Temora 2.

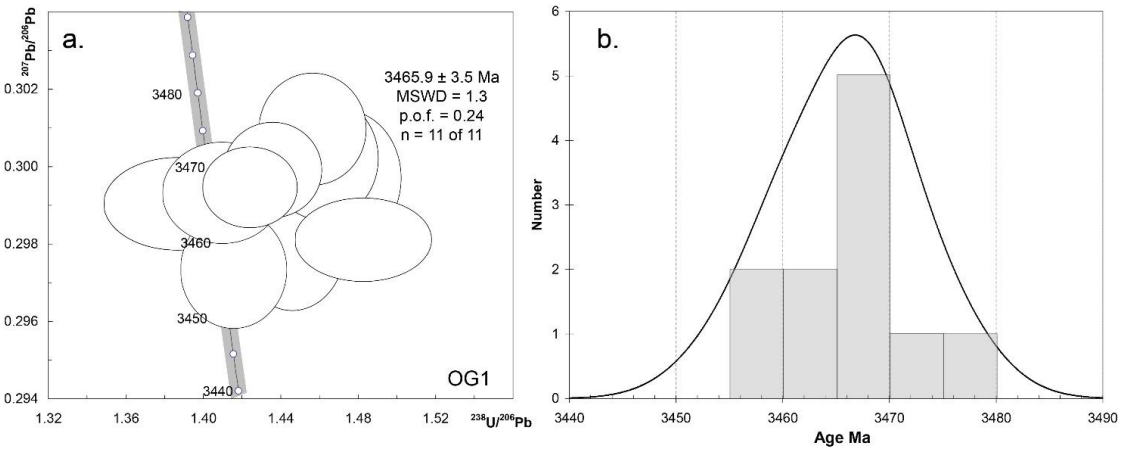

Figure A6. (a) Concordia diagram for all analyses of OG1. **(b)** PDD showing the $^{207}Pb/^{206}Pb$ ages for OG1 standard analyses.

Table A6. SHRIMP analyses of the zircon standard OG1 (16-18 May 2008, SHRIMP IIe, GA

Spot	206Pbc %	U ppm	Th ppm	232Th /238U	206Pb* /238U	±%	207Pb* /235U	±%	207Pb* /206Pb*	±%	207Pb /206Pb Age ± Ma		% Disc
OG1.17.1.1	0.02	214	234	1.13	0.695	1.13	28.60	1.21	0.2987	0.42	3463	7	2
OG1.17.2.1	0.05	175	81	0.48	0.696	1.16	28.80	1.19	0.2999	0.27	3470	4	2
OG1.18.1.1	0.03	208	104	0.52	0.702	1.13	28.99	1.15	0.2995	0.23	3467	4	1
OG1.18.2.1	0.08	143	118	0.85	0.709	1.44	29.27	1.47	0.2993	0.29	3467	4	0
OG1.19.1.1	0.20	263	219	0.86	0.692	1.24	28.41	1.29	0.2979	0.37	3460	6	3
OG1.20.1.1	0.01	252	264	1.09	0.687	1.25	28.49	1.29	0.3010	0.32	3475	5	4
OG1.21.1.1	0.04	457	773	1.75	0.675	1.56	27.73	1.58	0.2981	0.24	3460	4	5
OG1.21.2.1	0.10	356	451	1.31	0.721	1.80	29.73	1.82	0.2990	0.26	3465	4	-1
OG1.22.1.1	0.07	179	163	0.94	0.679	1.34	28.07	1.39	0.2997	0.39	3469	6	5
OG1.22.2.1	0.06	233	196	0.87	0.706	1.27	28.95	1.32	0.2973	0.34	3456	5	0
OG1.23.1.1	0.03	209	192	0.95	0.684	1.28	28.32	1.33	0.3002	0.35	3471	5	4

Spot Name	% comm 206	ppm U	ppm Th	232Th /238U	204-corr Pb/U: UO/U^2	% err	4-corr 206Pb /238U age (Ma)	±1σ	Ln Pb/U	Ln Pb*/U	204 overcts /sec (fr. 207)	204 overcts /sec (fr. 208)	4-corr 207 /206 age (Ma)	± Ma	4-corr 207Pb /206Pb	% err
T.38.1.1	0.63	110	58	0.54	0.004	0.8	421	3	1.74	-2.01	-0.03	0.07	483	72	0.0568	3.26
T.38.2.1	0.86	118	58	0.51	0.004	0.8	425	3	1.72	-2.05	0.02	0.05	376	111	0.0541	4.93
T.38.3.1	0.98	107	55	0.53	0.004	0.8	423	3	1.74	-2.00	0.07	0.03	256	128	0.0513	5.57
T.39.1.1	0.69	204	87	0.44	0.004	0.6	419	2	1.79	-1.91	0.06	0.15	357	54	0.0537	2.40
T.39.2.1	0.42	188	100	0.55	0.004	0.6	420	3	1.74	-2.03	0.01	-0.03	400	51	0.0547	2.26
T.35.3.1	0.31	189	60	0.33	0.004	1.4	422	6	1.70	-2.09	-0.02	0.05	443	46	0.0558	2.07
T.40.1.1	0.17	99	29	0.30	0.004	1.8	422	7	1.75	-1.99	-0.10	-0.12	623	50	0.0606	2.30
T.40.2.1	0.29	104	32	0.31	0.004	1.4	424	6	1.75	-1.99	-0.09	-0.03	612	56	0.0602	2.58
T.41.1.1	0.51	442	152	0.36	0.004	2.4	423	10	1.78	-1.94	0.01	0.30	414	51	0.0550	2.29
T.42.1.1	0.48	413	150	0.37	0.004	0.6	409	2	1.82	-1.89	0.07	0.35	380	51	0.0542	2.26
T.42.2.1	0.37	231	66	0.29	0.004	0.8	411	3	1.77	-1.97	-0.07	0.11	492	61	0.0570	2.78
T.43.1.1	0.41	259	71	0.28	0.004	2.1	414	9	1.78	-1.95	-0.07	0.08	481	60	0.0567	2.72
T.43.2.1	0.45	338	155	0.47	0.004	0.7	418	3	1.79	-1.92	0.06	-0.09	374	56	0.0541	2.51
T.43.3.1	0.53	284	75	0.27	0.004	1.5	418	6	1.79	-1.93	0.07	0.13	357	67	0.0537	2.96
T.43.4.1	1.04	129	38	0.31	0.004	1.1	422	5	1.78	-1.94	0.04	0.15	343	127	0.0533	5.59
T.44.1.1	1.93	158	65	0.43	0.004	1.0	407	4	1.75	-2.01	0.34	0.21	-241	217	0.0418	8.59
T.44.2.1	0.67	197	77	0.40	0.004	0.9	413	3	1.79	-1.92	0.05	0.24	355	83	0.0536	3.66
T.45.1.1	1.27	220	67	0.31	0.004	2.3	413	9	1.79	-1.93	0.29	0.42	84	120	0.0477	5.07
T.46.1.1	0.82	125	57	0.47	0.004	1.1	416	4	1.77	-1.96	0.00	0.13	422	111	0.0552	4.96
T.46.2.1	0.29	146	86	0.61	0.004	1.0	411	4	1.80	-1.92	-0.08	-0.10	526	68	0.0579	3.11
T.47.1.1	1.18	181	59	0.34	0.004	2.8	410	11	1.81	-1.90	0.19	0.19	161	120	0.0493	5.15
T.48.1.1	1.40	144	67	0.48	0.004	1.0	415	4	1.82	-1.87	0.22	0.12	67	208	0.0473	8.72
T.49.1.1	2.37	101	34	0.34	0.004	1.3	411	5	1.82	-1.86	0.26	0.21	-239	270	0.0418	10.69
										ave	+0.05	+0.11	335			
										error	±0.05	±0.06	±94			

Appendix 3.3: SHRIMP II RSES; 30 SEP–2 Oct 2008, Mount GA 6054

R1009272 (analyses 1001.73.1.1 – 1001.111.1.1), R1588240 (analyses 1003.4.1.1 – 1003.20.1.1) and R1588243 (analyses 1006.84.1.1 – 1006.95.1.1).

LIMS session 80126. Analyst G.Fraser and M.Szpunar.. Data processing E.Jagodzinski. Processing software: SQUID 2.50.11.02.03, rev. 03 Feb 2011

6 scan data through 10 mass stations. Primary beam ~ 2.0-2.4 nA.

ASSESSMENT OF CALIBRATION

Two standards, OG1 and Temora 2, were analysed during this session. Nineteen analyses of Temora have a calibration exponent of 1.41 (upper limit 1.77, lower limit 1.17), which is significantly lower than the nominal value of 2. However the nominal slope 2 is applied. The calibration error for the session is 0.32% (MSWD 4.72) and the external spot to spot error 1.21%.

ASSESSMENT OF ^{207}PB/^{206}PB AGES

OG1 yields a ^{207}Pb/^{206}Pb age of 3465.6 ± 2.9 Ma (MSWD = 1.3, probability = 0.26, n = 9, Figure A.), which is near identical to the TIMS reference age of 3465.4 ± 0.6 Ma. However, for consistency in merging data sets from the many sessions, a correction for instrumental mass fractionation (IMF) has still been applied to the individual ^{207}Pb/^{206}Pb ages of the unknowns for detrital spectra collected during this session, and their errors appropriately augmented. The IMF correction factor = 0.99987.

The ^{207}Pb /^{206}Pb age of Temora is 386 ± 70 Ma (Tukey's biweight), or 438 ± 43 Ma (weighted mean), and there is no evidence of overcounts on the Pb peaks (Table A.1).

Element abundance calibration was based on standard SL13 (n = 1, U = 238 ppm).

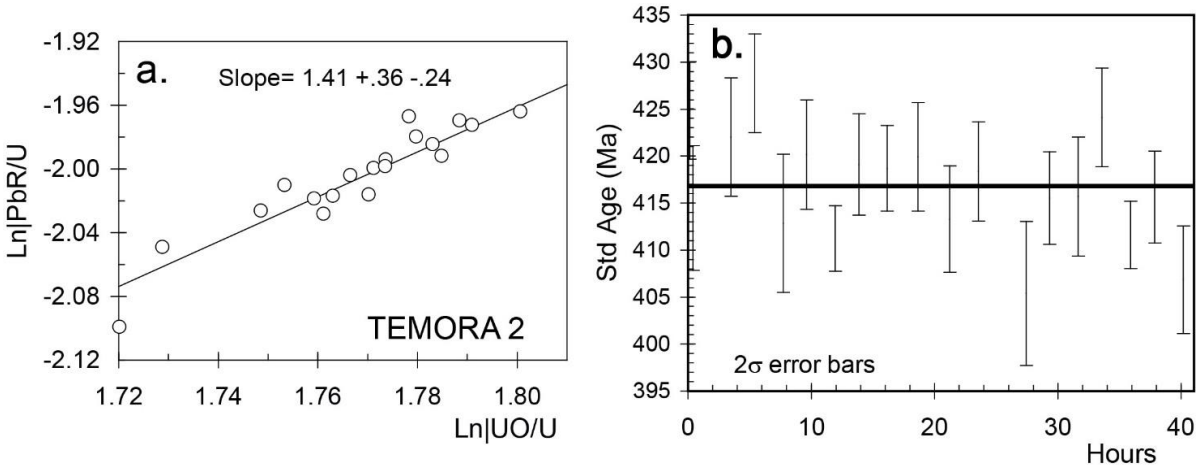

Figure A7. (a) Pb/U calibration for mount GA6054, analysis date 30 Sep – 2 Oct 2008; SHRIMP IIe, GA. **(b)** ^{206}Pb/^{238}U ages for Temora 2.

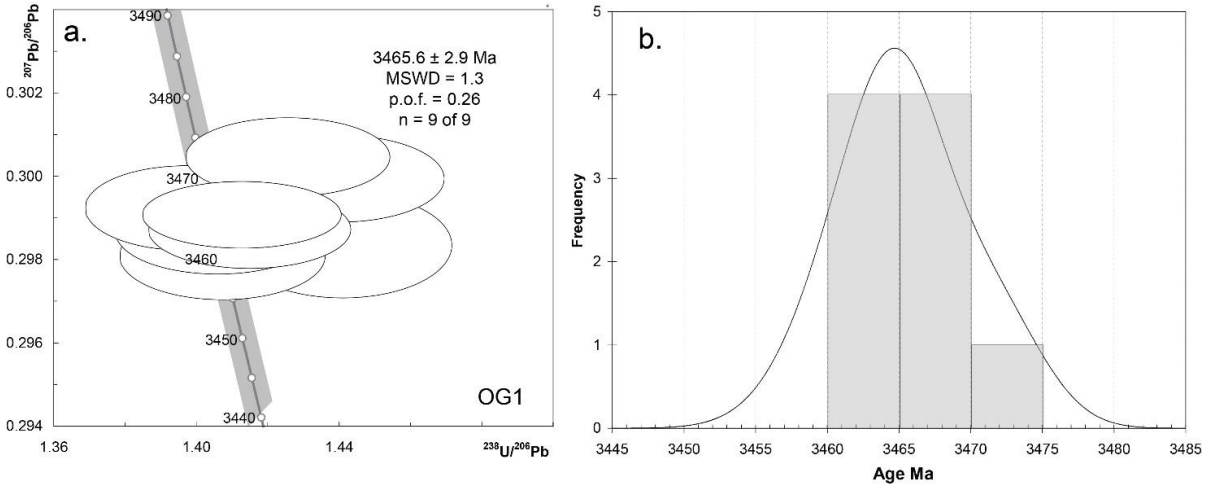

Figure A8. (a) Concordia diagram for all analyses of OG1. **(b)** PDD showing the $^{207}Pb/^{206}Pb$ ages for OG1 standard analyses.

Table A8. SHRIMP analyses of the zircon standard OG1, 30 Sep – 2 Oct 2008, SHRIMP IIe, GA

Spot	U ppm	Th ppm	232Th /238U	206Pbc %	206Pb* /238U	±%	207Pb* /235U	±%	207Pb* /206Pb*	±%	207Pb /206Pb Age		% Disc
OG.17.3.1	157	55	0.36	0.05	0.710	1.4	29.27	1.4	0.2992	0.24	3466	4	+0
OG.21.3.1	342	468	1.41	0.01	0.708	1.3	29.20	1.3	0.2991	0.18	3465	3	+1
OG.22.3.1	178	161	0.93	0.03	0.716	1.4	29.54	1.4	0.2992	0.22	3466	3	-1
OG.22.4.1	213	192	0.93	0.02	0.702	1.4	29.07	1.4	0.3004	0.21	3473	3	+2
OG.23.2.1	175	163	0.96	0.04	0.711	1.4	29.22	1.4	0.2981	0.23	3460	4	-0
OG.24.1.1	238	276	1.20	0.04	0.707	1.4	29.12	1.4	0.2987	0.21	3464	3	+1
OG.25.1.1	204	120	0.61	0.02	0.712	1.4	29.30	1.4	0.2986	0.22	3463	3	-0
OG.26.1.1	196	131	0.69	0.01	0.695	1.4	28.73	1.4	0.2999	0.23	3470	4	+3
OG.27.1.1	146	87	0.62	0.04	0.694	1.5	28.56	1.5	0.2983	0.28	3462	4	+2

Table A9. SHRIMP analyses of the zircon standard Temora, for 30 Sep – 2 Oct 2008, SHRIMP IIe, Geoscience Australia

Spot Name	204 /206	4-corr 206Pb /238U calibr. const	% err	4-corr 206Pb /238U age (Ma)	±1σ	4-corr ppm 206*	ppm U	ppm Th	232Th /238U	Ln UO/U	Ln Pb/U	204 overcts /sec (fr. 207)	204 overcts /sec (fr. 208)	4-corr 207Pb /206Pb age (Ma)	% err
T.55.1.1	2.7E-4	0.00396	0.75	425	3	0.49	152	69	0.47	1.729	-2.049	0.06	-0.06	327	60
T.56.1.1	6.6E-4	0.00386	0.97	415	4	1.19	97	32	0.34	1.720	-2.099	0.10	0.16	131	123
T.57.1.1	6.3E-4	0.00393	0.91	422	4	1.13	108	35	0.33	1.749	-2.026	0.12	0.14	160	106
T.58.1.1	3.4E-5	0.00398	0.76	428	3	0.06	135	64	0.49	1.753	-2.010	0.02	0.03	383	38
T.59.1.1	7.0E-4	0.00384	1.08	413	4	1.27	73	26	0.36	1.763	-2.017	0.08	0.11	167	134
T.60.1.1	-1.9E-4	0.00391	0.86	420	3	-0.34	113	36	0.32	1.771	-1.999	-0.11	-0.11	607	50
T.61.1.1	1.1E-4	0.00382	0.52	411	2	0.19	322	169	0.54	1.762	-2.016	-0.01	0.03	423	30
T.62.1.1	----	0.00390	0.80	419	3	0.00	132	37	0.29	1.767	-2.004	-0.05	-0.03	500	35
T.63.1.1	-1.7E-5	0.00390	0.67	419	3	-0.03	184	52	0.29	1.774	-1.994	-0.03	-0.03	456	31
T.64.1.1	1.1E-4	0.00391	0.85	420	3	0.19	121	37	0.32	1.759	-2.019	-0.01	0.04	429	50
T.65.1.1	5.2E-5	0.00384	0.71	413	3	0.09	504	196	0.40	1.761	-2.028	-0.01	0.16	420	22
T.66.1.1	8.7E-5	0.00389	0.78	419	3	0.16	157	71	0.46	1.780	-1.980	-0.02	0.04	447	43
T.67.1.1	4.2E-4	0.00377	0.75	406	3	0.76	171	103	0.62	1.801	-1.964	0.17	0.18	171	73
T.68.1.1	-7.7E-5	0.00387	0.73	416	3	-0.14	181	54	0.31	1.783	-1.985	-0.13	-0.15	581	36
T.69.1.1	1.9E-4	0.00387	0.94	416	4	0.35	108	34	0.32	1.774	-1.998	-0.04	-0.03	504	61
T.70.1.1	2.0E-4	0.00395	0.76	424	3	0.37	166	69	0.43	1.778	-1.967	0.01	0.10	398	52
T.71.1.1	1.5E-4	0.00383	0.54	412	2	0.26	349	100	0.30	1.791	-1.972	0.06	0.19	373	33
T.72.1.1	-1.0E-4	0.00387	0.73	416	3	-0.18	189	60	0.33	1.788	-1.969	-0.09	-0.06	535	39
T.73.1.1	4.3E-4	0.00378	0.86	407	3	0.77	134	37	0.29	1.785	-1.992	0.06	0.10	290	81
											ave	0.01	0.04		
											error	0.04	0.05		

Appendix 3.4: SHRIMP IIE GA; 7-8 April 2009, Mount GA 6054

R1588240 (1003.21.1.1 – 1003.48.1.1). LIMS session 90032.
This session was cut short after 22 hours, as the primary beam was unstable, and the duo required servicing. Primary beam 1.1-1.5 nA and 70 μm aperture, 5 scan data through 10 mass stations Analyst E.A.Jagodzinski. Data processing E.A.Jagodzinski. Processing software: SQUID 2.50.11.02.03, rev. 03 Feb 2011.

ASSESSMENT OF CALIBRATION

Two standards, OG1 and Temora 2, were analysed during this session. Eleven analyses of Temora have a calibration exponent of 2.16 (lower limit 1.95 upper limit 2.39), which agrees well with the nominal value of 2. A very high calibration error of 1.40% (MSWD 4.15) and external spot to spot error of 4.15 % (1σ) is removed by eliminating one low analysis (T.10.1.1), to become 0.49% and 0%, respectively. A more realistic Pb/U external error of 1.0% has been assigned for data reduction. There is little change to the slope after eliminating analysis TEM.10.1.1 (2.12 +.22 -.25).

ASSESSMENT OF ^{207}PB/^{206}PB AGES

Five analyses of OG1 yield a ^{207}Pb/^{206}Pb age of 3466.3 ± 8.3 Ma (MSWD = 1.6, probability of fit = 0.18, Figure A.10. The IMF correction factor = 0.99957. The ^{207}Pb /^{206}Pb age of Temora is 385 ± 140 Ma (Tukey's biweight), or 376 ± 100 Ma (weighted mean), and there is no evidence of overcounts on the Pb peaks (Table A.11).

Element abundance calibration was based on standard SL13 (n = 1, U = 238 ppm).

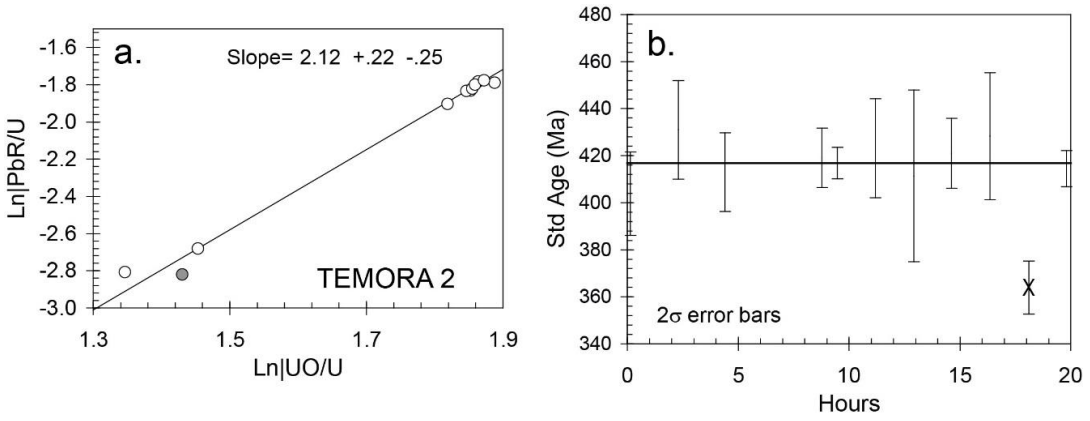

Figure A9. (a) Pb/U calibration for mount GA6054, analysis date 7-8 April 2009; SHRIMP IIe, GA. Rejected analysis TEM.10.1 is marked **(b)** ^{206}Pb/^{238}U ages for Temora 2 vs time.

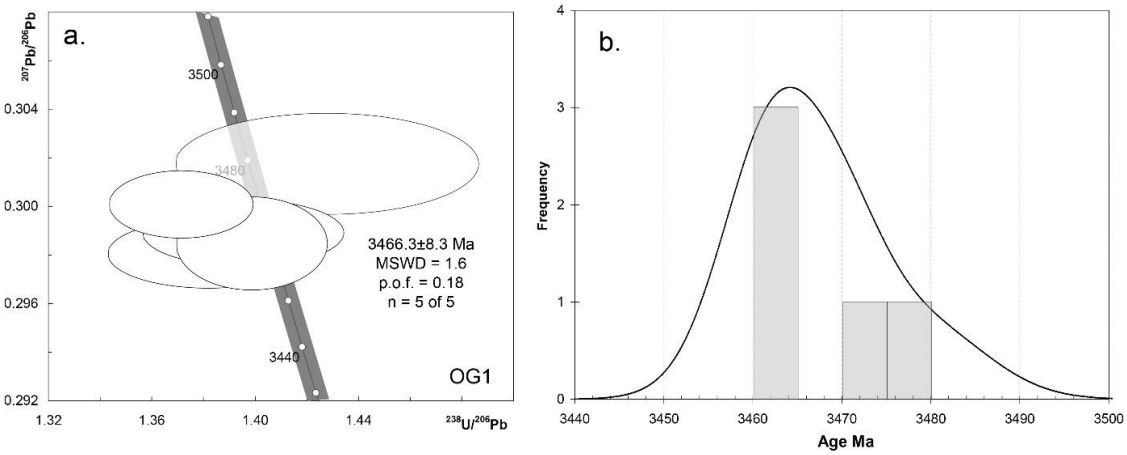

Figure A10. (a) Concordia diagram for all analyses of OG1. **(b)** PDD showing the ^{207}Pb/^{206}Pb ages for OG1 standard analyses

Table A10. SHRIMP analyses of the zircon standard Temora, for 7-8 April 2009, SHRIMP IIe, Geoscience Australia.

Spot Name	4-corr %com 206	ppm U	ppm Th	232Th /238U	4-corr 206Pb /238U calibr. const	% err	4-corr 206Pb /238U age (Ma)	±1σ	Ln UO/U	Ln Pb/U	204 overcts /sec (fr. 207)	204 overcts /sec (fr. 208)	4-corr 207Pb /206Pb age (Ma)	% err	4-corr 207Pb /206Pb	% err
TEM.1.1.1	0.10	113	33	0.30	0.0038	2.26	404	9	1.89	-1.79	-0.020	0.017	483	62	0.0568	2.82
TEM.2.1.1	-0.80	291	76	0.27	0.0040	2.52	431	11	1.35	-2.81	-0.054	-0.010	737	124	0.0639	5.85
TEM.3.1.1	0.54	79	28	0.37	0.0039	2.10	413	8	1.85	-1.83	0.038	0.040	236	122	0.0509	5.29
TEM.4.1.1	-0.35	163	74	0.47	0.0039	1.55	419	6	1.85	-1.83	-0.076	-0.013	584	62	0.0595	2.85
TEM.5.1.1	-0.05	213	107	0.52	0.0039	0.83	417	3	1.86	-1.82	-0.033	0.020	475	69	0.0566	3.12
TEM.6.1.1	0.57	85	26	0.32	0.0040	2.58	423	11	1.86	-1.78	0.033	0.055	256	127	0.0513	5.53
TEM.7.1.1	1.14	118	42	0.36	0.0038	4.58	411	18	1.45	-2.68	0.025	0.028	59	307	0.0472	13
TEM.8.1.1	0.40	181	56	0.32	0.0039	1.83	421	7	1.86	-1.80	0.026	0.012	358	73	0.0537	3.23
TEM.9.1.1	0.27	140	38	0.28	0.0040	3.26	428	14	1.87	-1.78	0.055	0.033	246	79	0.0511	3.42
TEM.11.1.1	-0.08	158	71	0.47	0.0039	0.96	415	4	1.82	-1.90	-0.001	-0.001	418	54	0.0551	2.41
										ave	0.00	0.01	385			
										error	0.03	0.02	±140			

Table A11. SHRIMP analyses of the zircon standard OG1 for 7-8 April 2009, SHRIMP IIe, GA

Spot	$206Pb_c$ %	U ppm	Th ppm	232Th /238U	$206Pb^*$ /238U	±%	$207Pb^*$ /235U	±%	$207Pb^*$ /$206Pb^*$	±%	207Pb /206Pb Age ± Ma		% Disc
OG.1.1.1	--	197	178	0.93	0.724	1.84	29.73	1.87	0.2980	0.31	3460	5	-2
OG.2.1.1	0.38	108	80	0.76	0.700	2.70	29.14	2.73	0.3017	0.46	3479	7	2
OG.3.1.1	0.01	188	150	0.82	0.729	1.33	30.16	1.37	0.3001	0.30	3471	5	-2
OG.4.1.1	0.04	260	125	0.50	0.715	1.37	29.42	1.44	0.2985	0.42	3462	7	-1
OG.5.1.1	--	226	119	0.54	0.717	1.83	29.54	1.86	0.2989	0.30	3465	5	-1

Appendix 3.5: SHRIMP IIE Ga; 15-17 Feb 2010, Mount Ga 6054

Samples R1588241 (all 49 analyses), R1588240 (analyses 1003.49.1.1 – 1003.75.1.1).

LIMS session 100027. Analyst E.A.Jagodzinski.
Processing software: SQUID 2.50.11.02.03, rev. 03 Feb 2011.
5 scan data through 10 mass stations. Primary beam 1.8-2.3 nA,

ASSESSMENT OF CALIBRATION

Two standards, OG1 and Temora 2, were analysed during this session. Nineteen analyses of Temora have a calibration exponent of 1.96 (lower limit 1.47 upper limit 2.41), which is within error of nominal value of 2. The calibration error is 0.16% (MSWD = 0.90, probability of fit = 0.57). An external spot to spot error of 0 % (1σ) is recorded, so a more realistic value of 1.0% has been assigned for data reduction.

ASSESSMENT OF ^{207}PB/^{206}PB AGES

OG1 yields a ^{207}Pb/^{206}Pb age of 3462.4 ± 2.5 Ma (MSWD = 0.47, probability = 0.92, Figure A.), which is younger than the TIMS reference age of 3465.4 ± 0.6 Ma. A correction for instrumental mass fractionation (IMF) has been applied to the individual ^{207}Pb/^{206}Pb ages of the unknowns for this session, and their errors appropriately augmented. The IMF correction is 0.99803.

The ^{207}Pb /^{206}Pb age of Temora is 373 ± 53 Ma (Tukey's biweight), or 412 ± 26 Ma (weighted mean), and there is no evidence of overcounts on the Pb peaks (Table A.1).

Element abundance calibration was based on standard SL13 (n = 1, U = 238 ppm).

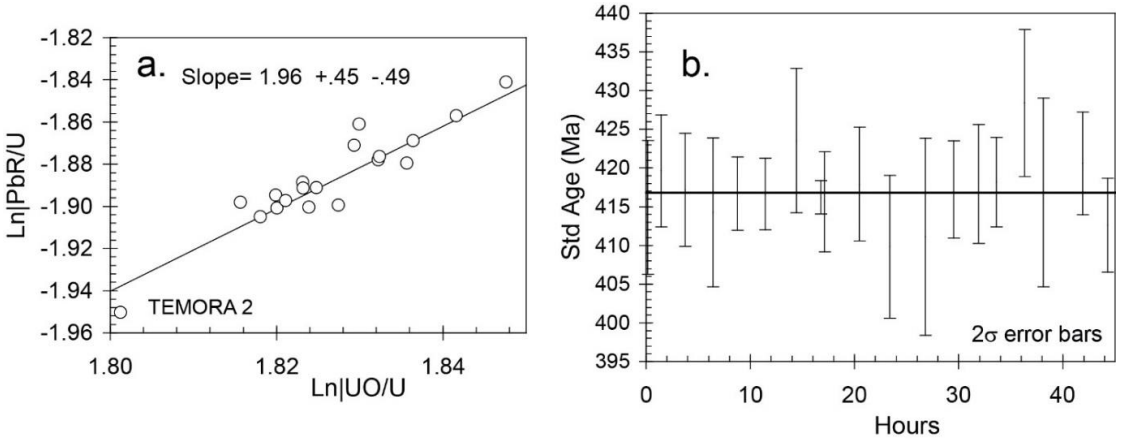

Figure A11. (a) Pb/U calibration for mount GA6054, analysis date 15-17 February 2010; SHRIMP IIe, GA **(b)** ^{206}Pb/^{238}U ages for Temora 2 in order of acquisition.

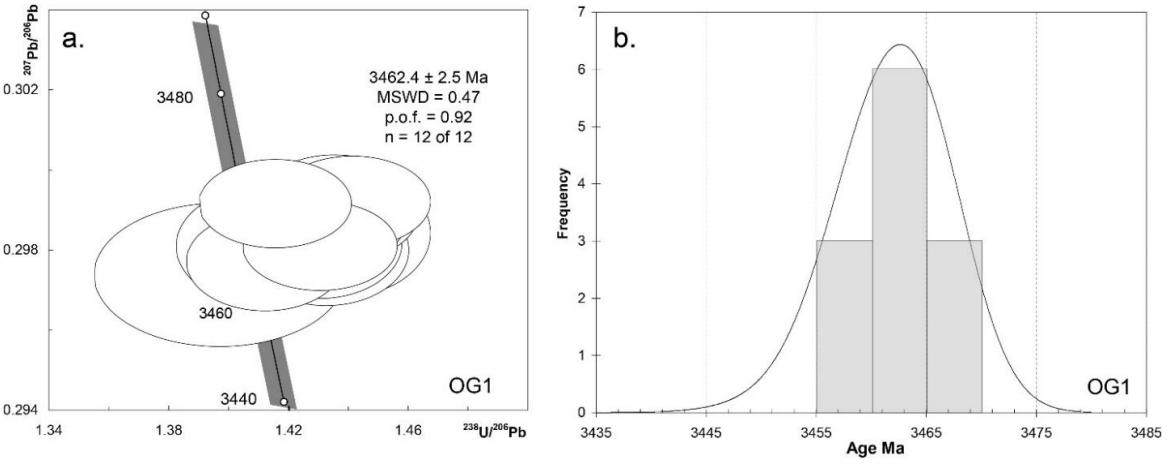

Figure A12. (a) Tera-Wasserburg concordia diagram for OG1. **(b)** PDD showing the $^{207}Pb/^{206}Pb$ ages for OG1.

Table A12. SHRIMP analyses of the zircon standard OG1, 15-17 February 2010, SHRIMP IIe, GA.

Spot	$^{206}Pb_c$ %	U ppm	Th ppm	232Th /238U	$^{206}Pb^*$ /238U	±%	$^{207}Pb^*$ /235U	±%	$^{207}Pb^*$ /$^{206}Pb^*$	±%	207Pb /206Pb Age	±	% Disc
OG.1.1.1	--	156	133	0.88	0.709	1.30	29.14	1.34	0.2981	0.32	3460	5	0
OG.2.1.1	--	169	156	0.95	0.699	1.27	28.74	1.31	0.2982	0.30	3461	5	2
OG.3.1.1	--	264	303	1.19	0.699	1.19	28.73	1.21	0.2981	0.25	3460	4	2
OG.4.1.1	--	236	221	0.97	0.696	1.21	28.68	1.24	0.2989	0.26	3464	4	2
OG.5.1.1	0.01	288	319	1.14	0.706	1.18	29.14	1.21	0.2991	0.24	3466	4	1
OG.6.1.1	0.01	226	202	0.93	0.716	1.97	29.35	2.01	0.2974	0.40	3457	6	-1
OG.7.1.1	0.04	145	80	0.57	0.695	1.32	28.61	1.37	0.2984	0.35	3462	5	2
OG.8.1.1	--	199	205	1.06	0.697	1.25	28.73	1.28	0.2990	0.29	3465	5	2
OG.9.1.1	0.00	223	111	0.51	0.708	1.23	29.06	1.26	0.2977	0.27	3458	4	0
OG.10.1.1	--	283	333	1.22	0.694	1.19	28.62	1.21	0.2992	0.25	3466	4	3
OG.11.1.1	0.01	254	155	0.63	0.698	1.20	28.74	1.23	0.2987	0.25	3464	4	2
OG.12.1.1	--	201	104	0.54	0.698	1.27	28.68	1.30	0.2980	0.31	3460	5	2

Table A13. SHRIMP analyses of the zircon standard Temora, 15-17 February 2010, SHRIMP IIe, Geoscience Australia

Spot Name	4-corr ppm 206*	ppm U	ppm Th	232Th /238U	4-corr 206Pb /238U calibr. const	% err	4-corr 206Pb /238U age (Ma)	±1σ	Ln UO/U	Ln Pb/U	204 overcts /sec (fr. 207)	204 overcts /sec (fr. 208)	4-corr 207Pb /206Pb age (Ma)	±	4-corr 207Pb /206Pb	±%
T.1.1.1	0.59	94	28	0.31	0.0039	1.08	415	4	1.82	-1.90	0.05	0.05	254	107	0.0513	4.67
T.2.1.1	0.00	128	41	0.33	0.0039	0.89	420	4	1.82	-1.89	0.02	0.02	381	48	0.0542	2.14
T.3.1.1	0.14	134	48	0.37	0.0039	0.91	417	4	1.82	-1.90	0.01	-0.06	382	59	0.0543	2.62
T.4.1.1	0.65	85	29	0.35	0.0039	1.20	414	5	1.83	-1.90	0.05	0.06	222	120	0.0506	5.17
T.5.1.1	0.20	319	111	0.36	0.0039	0.59	417	2	1.84	-1.86	0.10	0.15	318	41	0.0527	1.80
T.6.1.1	0.00	339	171	0.52	0.0039	0.57	417	2	1.83	-1.88	-0.04	-0.13	456	28	0.0561	1.28
T.7.1.1	-0.55	87	24	0.28	0.0039	1.13	424	5	1.82	-1.90	-0.04	-0.05	559	90	0.0588	4.14
T.8.1.1	-0.02	1991	823	0.43	0.0039	0.27	416	1	1.84	-1.87	-0.02	-0.21	420	13	0.0552	0.57
T.9.1.1	0.39	171	75	0.45	0.0039	0.80	416	3	1.82	-1.89	0.07	-0.02	289	69	0.0521	3.02
T.10.1.1	0.14	134	42	0.33	0.0039	0.91	418	4	1.82	-1.89	0.00	-0.01	416	58	0.0551	2.59
T.11.1.1	0.79	87	35	0.42	0.0038	1.16	410	5	1.82	-1.90	0.09	0.14	32	147	0.0467	6.12
T.12.1.1	0.12	166	63	0.39	0.0038	1.60	411	6	1.84	-1.88	0.00	-0.01	408	51	0.0549	2.27
T.13.1.1	-0.15	190	60	0.33	0.0039	0.78	417	3	1.83	-1.86	-0.03	-0.04	467	47	0.0564	2.11
T.14.1.1	0.08	125	65	0.54	0.0039	0.95	418	4	1.82	-1.89	0.03	0.10	336	59	0.0532	2.60
T.15.1.1	-0.17	232	104	0.47	0.0039	0.71	418	3	1.83	-1.88	0.00	-0.06	420	45	0.0552	2.02
T.16.1.1	0.09	114	32	0.29	0.0040	1.15	428	5	1.83	-1.87	0.03	0.04	317	62	0.0527	2.75
T.17.1.1	0.23	183	55	0.31	0.0039	1.51	417	6	1.82	-1.90	0.01	0.04	396	57	0.0546	2.55
T.18.1.1	-0.06	177	91	0.53	0.0039	0.81	421	3	1.85	-1.84	-0.02	0.01	462	44	0.0562	2.00
T.19.1.1	-0.20	216	59	0.28	0.0038	0.76	413	3	1.80	-1.95	-0.04	-0.11	477	50	0.0566	2.26
										ave	0.01	0.00	373			
										error	0.02	0.04	±53			